Recent Progress on Two-Dimensional Materials

Cheng Chang [1], Wei Chen [2], Ye Chen [3], Yonghua Chen [4], Yu Chen [5], Feng Ding [6], Chunhai Fan [7], Hong Jin Fan [8], Zhanxi Fan [9], Cheng Gong [10], Yongji Gong [11], Qiyuan He [12], Xun Hong [13], Sheng Hu [14], Weida Hu [15], Wei Huang [4], Yuan Huang [16], Wei Ji [17], Dehui Li [18], Lain-Jong Li [19], Qiang Li [20], Li Lin [21], Chongyi Ling [20], Minghua Liu [22], Nan Liu [23], Zhuang Liu [24], Kian Ping Loh [2], Jianmin Ma [25], Feng Miao [26], Hailin Peng [27], Mingfei Shao [28], Li Song [29], Shao Su [30], Shuo Sun [31], Chaoliang Tan [32], Zhiyong Tang [33], Dingsheng Wang [34], Huan Wang [35], Jinlan Wang [20], Xin Wang [36], Xinran Wang [37], Andrew T. S. Wee [31], Zhongming Wei [38], Yuen Wu [36], Zhong-Shuai Wu [39], Jie Xiong [40], Qihua Xiong [41], Weigao Xu [42], Peng Yin [43], Haibo Zeng [44], Zhiyuan Zeng [12], Tianyou Zhai [45], Han Zhang [43], Hui Zhang [4], Qichun Zhang [12], Tierui Zhang [46], Xiang Zhang [47], Li-Dong Zhao [11], Meiting Zhao [48], Weijie Zhao [20], Yunxuan Zhao [46], Kai-Ge Zhou [49], Xing Zhou [45], Yu Zhou [50], Hongwei Zhu [51], Hua Zhang [9,*], Zhongfan Liu [27,*]

[1] Institute of Science and Technology Austria, Am Campus 1, 3400 Klosterneuburg, Austria.

[2] Department of Chemistry, National University of Singapore, 3 Science Drive 3, 117543, Singapore.

[3] Department of Chemistry, The Chinese University of Hong Kong, Shatin, New Territories, Hong Kong, China.

[4] Key Laboratory of Flexible Electronics and Institute of Advanced Materials, Nanjing Tech University, Nanjing 211816, China.

[5] School of Life Sciences, Shanghai University, Shanghai 200444, China.

[6] Centre for Multidimensional Carbon Materials, Institute for Basic Science, Ulsan 44919, Korea.

[7] School of Chemistry and Chemical Engineering, Shanghai Jiao Tong University, Shanghai 200240, China.

[8] School of Physical and Mathematical Sciences, Nanyang Technological University, Singapore 637371, Singapore.

[9] Department of Chemistry, City University of Hong Kong, Kowloon, Hong Kong, China.

[10] Department of Electrical and Computer Engineering and Quantum Technology Center, University of Maryland, College Park, Maryland 20742, USA.

[11] School of Materials Science and Engineering, Beihang University, Beijing 100191, China.

[12] Department of Materials Science and Engineering, City University of Hong Kong, Kowloon, Hong Kong, China.

[13] Center of Advanced Nanocatalysis (CAN), Hefei National Laboratory for Physical Sciences at the Microscale, Department of Applied Chemistry, University of Science and Technology of China, Hefei 230026, China.

[14] College of Chemistry and Chemical Engineering, State Key Laboratory of Physical Chemistry of Solid Surfaces, Collaborative Innovation Center of Chemistry for Energy Materials (iChEM), Xiamen University, Xiamen, 361005, Fujian Province, China.

[15] State Key Laboratory of Infrared Physics, Shanghai Institute of Technical Physics, Chinese Academy of Sciences, Shanghai 200083, China.

[16] Advanced Research Institute of Multidisciplinary Science, Beijing Institute of Technology, Beijing, 100081, China.

[17] Beijing Key Laboratory of Optoelectronic Functional Materials & Micro-Nano Devices, Department of Physics, Renmin University of China, Beijing 100872, China.

[18] School of Optical and Electronic Information, Wuhan National Laboratory for Optoelectronics, Huazhong University of Science and Technology, Wuhan 430074, China.

[19] Department of Mechanical Engineering, The University of Hong Kong, Pokfulam Road, Hong Kong, China.

[20] School of Physics, Southeast University, Nanjing 211189, China.

[21] Department of Materials Science and Engineering, National University of Singapore, Singapore 117575, Singapore.

[22] CAS Key Laboratory of Colloid, Interface and Chemical Thermodynamics, Institute of Chemistry, Chinese Academy of Sciences, Beijing 100190, China.

[23] College of Chemistry, Beijing Normal University, Beijing 100875, China.

[24] Institute of Functional Nano & Soft Materials (FUNSOM), Jiangsu Key Laboratory for Carbon-based Functional Materials and Devices, Soochow University, Suzhou 215123, Jiangsu Province, China.

[25] School of Materials and Energy, University of Electronic Science and Technology of China, Chengdu 611731, China.

*Corresponding authors. Emails: Hua.Zhang@cityu.edu.hk (H.Z.); zfliu@pku.edu.cn (Z.L.).

[26] School of Physics, Nanjing University, Nanjing 210093, China.

[27] Center for Nanochemistry (CNC), Beijing National Laboratory for Molecular Sciences, College of Chemistry and Molecular Engineering, Beijing Graphene Institute (BGI), Peking University, Beijing 100871, China.

[28] State Key Laboratory of Chemical Resource Engineering, Beijing University of Chemical Technology, Beijing 100029, China.

[29] National Synchrotron Radiation Laboratory, CAS Center for Excellence in Nanoscience, University of Science and Technology of China, Hefei 230029, China.

[30] State Key Laboratory of Organic Electronics and Information Displays & Jiangsu Key Laboratory for Biosensors, Institute of Advanced Materials (IAM), Nanjing University of Posts and Telecommunications, Nanjing 210023, China.

[31] Department of Physics, National University of Singapore, 2 Science Drive 3, 117551, Singapore.

[32] Department of Electrical Engineering, City University of Hong Kong, Kowloon, Hong Kong, China.

[33] CAS Key Laboratory of Nanosystem and Hierarchical Fabrication, CAS Center for Excellence in Nanoscience, National Center for Nanoscience and Technology, Beijing 100190, China.

[34] Department of Chemistry, Tsinghua University, Beijing 100084, China.

[35] Key Laboratory of Advanced Energy Materials Chemistry (Ministry of Education), Renewable Energy Conversion and Storage Center (RECAST), College of Chemistry, Nankai University, Tianjin 300071, China.

[36] School of Chemistry and Materials Science, iChEM (Collaborative Innovation Center of Chemistry for Energy Materials), Hefei National Laboratory for Physical Sciences at the Microscale, University of Science and Technology of China, Hefei 230026, China.

[37] National Laboratory of Solid State Microstructures, School of Electronic Science and Engineering, Collaborative Innovation Center of Advanced Microstructures, Nanjing University, Nanjing 210023, China.

[38] Institute of Semiconductors, Chinese Academy of Sciences, Beijing 100083, China.

[39] State Key Laboratory of Catalysis, Dalian Institute of Chemical Physics, Chinese Academy of Sciences, Dalian 116023, Liaoning Province, China.

[40] State Key Laboratory of Electronic Thin Film and Integrated Devices, University of Electronic Science and Technology of China, Chengdu 610054, China.

[41] State Key Laboratory of Low Dimensional Quantum Physics, Department of Physics, Tsinghua University, Beijing 100084, China.

[42] Key Laboratory of Mesoscopic Chemistry, School of Chemistry and Chemical Engineering, Nanjing University, Nanjing 210023, China.

[43] Institute of Microscale Optoelectronics, Shenzhen University, Shenzhen 518060, Guangdong Province, China.

[44] MIIT Key Laboratory of Advanced Display Materials and Devices, College of Material Science and Engineering, Nanjing University of Science and Technology, Nanjing 210094, China.

[45] School of Materials Science and Engineering, Huazhong University of Science and Technology, Wuhan 430074, China.

[46] Technical Institute of Physics and Chemistry, Chinese Academy of Sciences, Beijing 100190, China.

[47] Faculties of Sciences and Engineering, The University of Hong Kong, Hong Kong, China.

[48] Tianjin Key Laboratory of Molecular Optoelectronic Sciences, Department of Chemistry, Institute of Molecular Aggregation Science, Tianjin University, Tianjin 300072, China.

[49] Institute of Molecular Plus, Tianjin University, Tianjin 300072, China.

[50] School of Physics and Electronics, Hunan Key Laboratory of Nanophotonics and Devices, Central South University, Changsha 410083, China.

[51] State Key Lab of New Ceramics and Fine Processing, School of Materials Science and Engineering, Tsinghua University, Beijing 100084, China.

Abstract: Research on two-dimensional (2D) materials has been explosively increasing in last seventeen years in varying subjects including condensed matter physics, electronic engineering, materials science, and chemistry since the mechanical exfoliation of graphene in 2004. Starting from graphene, 2D materials now have become a big family with numerous members and diverse categories. The unique structural features and physicochemical properties of 2D materials make them one class of the most appealing candidates for a wide range of potential applications. In particular, we have seen some major breakthroughs made in the field of 2D materials in last five years not only in developing novel synthetic methods and exploring new structures/properties but also in identifying innovative applications and pushing forward commercialisation. In this review, we provide a critical summary on the recent progress made in the field of 2D materials with a particular focus on last five years. After a brief background
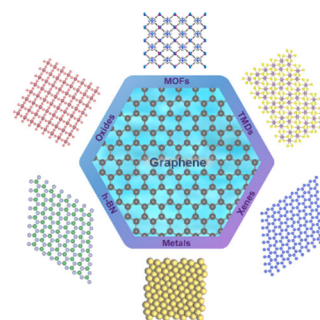
introduction, we first discuss the major synthetic methods for 2D materials, including the mechanical exfoliation, liquid exfoliation, vapor phase deposition, and wet-chemical synthesis as well as phase engineering of 2D materials belonging to the field of phase engineering of nanomaterials (PEN). We then introduce the superconducting/optical/magnetic properties and chirality of 2D materials along with newly emerging magic angle 2D superlattices. Following that, the promising applications of 2D materials in electronics, optoelectronics, catalysis, energy storage, solar cells, biomedicine, sensors, environments, *etc.* are described sequentially. Thereafter, we present the theoretic calculations and simulations of 2D materials. Finally, after concluding the current progress, we provide some personal discussions on the existing challenges and future outlooks in this rapidly developing field.

Key Words: Two-dimensional materials;　Transition metal dichalcogenides;　Phase engineering of nanomaterials;　Electronics;　Optoelectronics;　Catalysis;　Energy storage and conversion

CONTENTS

1 Introduction

The first report on the mechanical cleavage of atomically thin single-crystalline carbon film, namely graphene, and its extraordinary transport properties by Geim, Novoselov and co-workers [1] in 2004 had ignited the resurgence of a class of fascinating functional nanomaterials, *i.e.*, two-dimensional (2D) materials [2–10]. 2D materials now have been recognized as a type of nanomaterials which have a sheet-like morphology featuring with a large lateral size from hundreds of nanometers to tens of micrometers or even larger but a thickness in single or few atomic layer [2,3]. Such a unique structural feature of 2D materials

endows them with various unconventional physical, chemical, optical, electronic and magnetic properties as compared to their bulk, zero-dimensional (0D) and one-dimensional (1D) counterparts [2]. Owing to their unusual properties, 2D materials have been proven to be one of the most promising candidates for numerous potential applications like electronics [11–14], optoelectronics [15–20], catalysis [21–26], energy storage [27–34], solar cells [35–38], biomedicine [39–45], sensors [46–49], environments [50–54], *etc*. Driven by their unusual properties and promising applications, a large number of novel 2D materials beyond graphene, such as transition metal dichalcogenides (TMDs including MoS_2, $MoSe_2$, $MoTe_2$, WS_2, WSe_2, ReS_2, TaS_2, *etc*.) [55,56], hexanol boron nitride (h-BN) [57,58], graphyne [59,60], noble metal dichalcogenides (NMDs: $PdSe_2$, $PtSe_2$, PtS_2, *etc*.) [61,62], elemental 2D materials (e.g., black phosphorus (BP), tellurium, silicene, germanene, borophene, *etc*.) [63–65], layered metal oxides [66,67], layered double hydroxides (LDHs) [68,69], graphitic carbon nitride (g-C_3N_4) [70,71], MXenes [72], metals [73], organics/polymers [74,75], metal-organic frameworks (MOFs) [76,77], covalent-organic frameworks (COFs) [78,79], organic-inorganic hybrid perovskites [80–82], and transition metal halides [83,84], have been synthesized by various synthetic methods in the last decade. It is worth pointing out that the number of materials in the family of 2D materials is still continuously growing every year.

On the basis of the previous research works, the last five years have witnessed some major breakthroughs made in the field of 2D materials in all aspects. Firstly, a large number of novel 2D materials have been reported, including NMDs [85–87], tellurium [88,89], selenium [90], and so on. Secondly, some novel methods have been developed for synthesis of 2D materials with higher quality, larger size, or better control, such as oxygen plasma- or Au-enhanced mechanical exfoliation [91,92], organic intercalation-assisted liquid exfoliation of layered materials (e.g., BP, TMDs, InSe, *etc*.) [93–95], salt-assisted chemical vapor deposition (CVD) growth of a library of 2D thin layers [96,97], CVD growth of wafer-scale high-quality 2D thin films [98,99], pulsed laser deposition (PLD) of BP thin films [100], vapor phase synthesis of high-purity 1T'-phase 2D TMD crystals [101], and liquid metal-assisted synthesis of metal oxide nanosheets [102]. Thirdly, some new promising applications of 2D materials have been demonstrated, such as integrated circuits based on wafer-scale 2D thin films [103] and infrared imaging sensor systems based on graphene [104]. More importantly, some newly emerging research directions have been extensively explored on 2D materials in recent years. For example, the phase engineering of nanomaterials (PEN) including 2D materials has been recognized as a promising way to fine tune their physicochemical properties and enhance their performances in addition to other conventional structural characteristics, such as size, thickness, defects, vacancies, and interlayer spacing [105,106]. As another typical example, by simply stacking two 2D graphene in a specific magic angle, namely magic angle 2D superlattices, the properties of graphene can be tuned from a conductor to a superconductor or insulator [107,108].

Inspired by the unexpected properties of magic angle graphene superlattices, magic angle 2D superlattices have become one of the most interesting materials to explore new properties in condensed matter physics.

Although many review articles related to 2D materials have been published previously, most of them were published in several years ago or even earlier, and most of them focused on a selected type 2D materials (e.g., graphene, graphyne, TMDs, MOFs, elemental ones, metals, MXenes, *etc*.) [4,55,73], or specific application (e.g., electronics, optoelectronics, energy storage, electrocatalysis, sensors, biomedicine, *etc*.) [27,31,39]. Bearing this mind, offering a comprehensive review article to cover all of the 2D materials from all aspects with highlights on recent progress in this growing field is of great significance for its further development. To this end, this review aims to critically summarize the recent progress on 2D materials with particular focus on the last five years. Following a brief background introduction, the major synthetic methods for 2D materials, including the mechanical exfoliation, liquid exfoliation, vapour phase deposition, and wet-chemical synthesis as well as phase engineering of 2D materials are first discussed. The superconducting, optical, magnetic properties and chirality of 2D materials along with newly emerging magic angle 2D superlattices are then introduced. Thereafter, we summarize the great potential of 2D materials in various applications like electronics, optoelectronics, catalysis, energy storage, solar cells, biomedicine, sensors, environments, *etc*. Following that, recent progress on the theoretic calculations and simulations of 2D materials is also discussed. Finally, we conclude this Review by summarizing the current process and offering some personal insights on the existing challenges and future opportunities in this promising field.

2 Synthetic methods

2.1 Mechanical exfoliation

Mechanical exfoliation has been recognized as an efficient method to obtain fresh atomically flat surface of layered materials [109,110]. In 2004, a new tape-based exfoliation method developed in Geim's group was used to prepare monolayer and few-layer graphene from graphite [1,111]. As one of the most popular "top-down" strategy to date, this mechanical exfoliation technique has been widely used to get a large number of 2D crystals, such as MoS_2 [112,113], WS_2 [114], SnS_2 [115] and BP [115,116]. The exfoliated 2D materials are ideal samples to study their intrinsic electronic [117,118], optical [119] and mechanical properties. However, there are a few shortcomings for the conventional mechanical exfoliation. Firstly, the sample size of exfoliated 2D materials is usually in the range of few to tens of micrometers. Secondly, the yield is quite low. With the discovery of new layered materials, novel mechanical methods are desired to prepare high-quality, large-area 2D materials with relatively high efficiency.

Although the exfoliation processes are generally simple, some scientific questions were not well understood at the beginning.

In the early stage, many researchers believed that a bulk crystal should be exfoliated many times to get thin layers on tape and then transferred onto SiO₂/Si substrate, which has been demonstrated to be wrong later [120]. The interaction between tape and monolayer or few layers is stronger than the interaction between the solid substrate surfaces (e.g., SiO₂) and 2D materials. Therefore, it is difficult to transfer a monolayer flake from tape to solid substrates. Besides, when the bulk crystal is exfoliated by tape for many times, it will be broken into small pieces. It is worth pointing out that the monolayer or few-layer flakes are exfoliated from multilayer crystal adhered on the tape instead of the ones adhered on the tape itself. More importantly, the interaction between layered crystals and solid substrates depends on the dipole interaction of different atoms. For example, the interaction between C atoms and O atoms is stronger than the one between C and other atoms [121]. As a result, the oxide substrates could work well for graphene but not so well for BP, FeSe or some other layered materials.

In the year 2015, Huang *et al*. proposed a new oxygen plasma enhanced exfoliation method, which is very effective for getting large-area monolayer graphene and $Bi_2Sr_2CaCu_2O_x$ [120]. They pointed out that the surface of oxide substrates has a thin layer of absorbed molecules, which serves as a buffer layer between layered crystal and oxide substrate surface. The oxygen plasma treatment could remove the absorbed molecules and enhance the interaction between 2D materials and substrate. As shown in Fig. 1, there are four steps for this optimized exfoliation. (1) Oxygen plasma is used to remove the small molecules on SiO₂/Si substrate surface. (2) A new cleaved graphite surface is put together with tape onto substrate. (3) The tape/graphite/substrate are baked at about 100 °C for 1–2 min. (4) The sample is taken out from hot plate and cooled down to room temperature, then

the tape with graphite is removed. After these steps, large-area monolayer and few-layer graphene with a size ranging from few hundred micrometers to millimeters can be easily observed by optical microscope or even naked eyes [120,122]. Some graphene bubbles formed in the baking process are often observed on these samples [120,123]. The unique structure of the bubble provides an ideal model for exploring some interesting phenomena of graphene and other 2D materials under strain, such as standing wave oscillation and band structure changes [123,124].

However, the oxygen plasma enhanced exfoliation is not very effective on exfoliating MoS₂, WS₂ and many other 2D materials, because these materials do not have strong interaction with oxide substrates. Magda *et al*. deposited a thick layer of Au (100 nm) on mica and peeled off the metal layer, then the Au layer was put into contact with fresh cleaved MoS₂ and heated at 90 °C [125]. This method can get MoS₂ in the size of several hundreds of micrometers, but it still consumes the precious gold and induces many cracks on 2D materials. Desai *et al*. optimized this gold-layer enhanced exfoliation using thermal-release tape and transferring the sample onto other substrates [92]. KI/I₂ solvent was used to etch Au layer and obtain large-area monolayer MoS₂, WS₂, *etc*.

Commonly, based on the lattice structure of common layered materials, the out-most atoms in the unit layer are non-metallic elements such as P, As, S, Se, Te, Cl, Br, I, *etc*., while the inner elements are usually transition metals (Mo, W, Ti, Fe, Cr, Ni, Ta, *etc*.) or some main group metals (Ga, Sn, In). Thus, the roadmap for optimizing mechanical exfoliation can be considered as selecting suitable substrates which have strong interaction with these non-metallic elements. In 2020, Huang *et al*. reported a more universal mechanical exfoliation method based on their systematic experimental and calculation results (Fig. 2) [126]. They
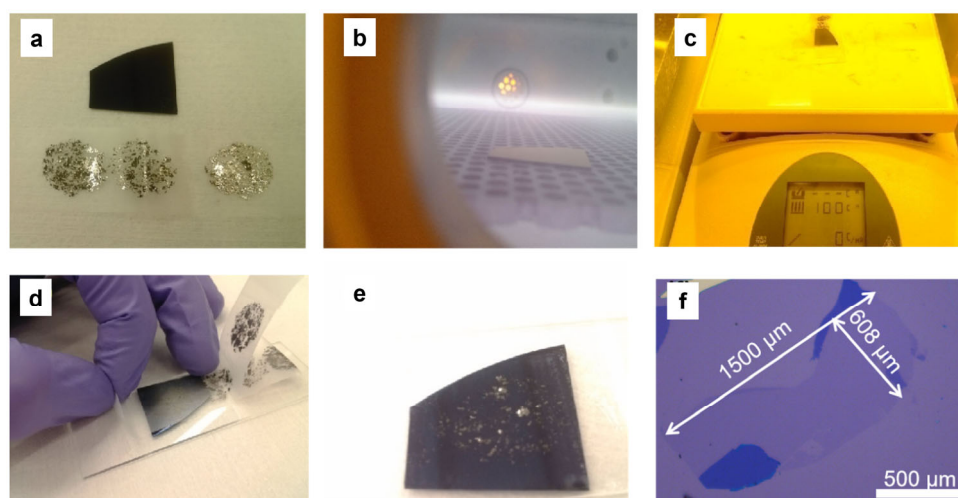
Fig. 1　Illustration of the oxygen-plasma-enhanced exfoliation process for graphene. (a) Optical image of the SiO₂/Si substrate and adhesive tape with graphite flakes. (b) Oxygen plasma cleaning of the substrate. (c) Contact between the graphite decorated tape and the substrate surface, followed by heating of the substrate (with tape) on a hot plate in air at ~100 °C for 2 min. (d) Removal of the substrate from the hot plate and peeling off the tape. (e) Optical image of the substrate after graphene exfoliation. (f) Optical micrograph of one large scale graphene flake on the substrate. (a–e) Reproduced with permission from Ref. [120], Copyright 2015 American Chemical Society. (f) Reproduced with permission from Ref. [122], Copyright 2018 *Acta Physica Sinica*.

pointed out that the adhesion energy at the interface of 2D materials and substrate is the key parameter for exfoliation. Their calculation results suggested that the 2D crystal-Au interaction could be sufficient to overcome the interlayer interaction to realize the successful exfoliation of monolayers from a wide range of layered materials. Based on the theoretical guidance, Huang *et al*. developed a new gold-assisted mechanical exfoliation, which was successful to get 40 different 2D materials, including MoS_2, BP, $PtTe_2$, FeSe, $CrCl_3$, *etc*. The size of exfoliated monolayer ranges from millimeter to sub-centimeter, which is visible to the naked eyes (Fig. 2). The new gold-assisted mechanical exfoliation method has two main steps. Firstly, two metal layers of Au/Ti (or Au/Cr) in sub-nanometer range are deposited onto SiO_2/Si or other substrates by electron-beam or thermal evaporator instruments. The second step is to put a bulk crystal with fresh surface onto the Au/Ti, and peel off the tape with crystal after gentle press.

In summary, mechanical exfoliation technique has greatly promoted the rapid development of the field of 2D materials in the past 17 years. While this technology has received extensive attention and undergone in-depth research in the past five years, it is believed to continue to play important roles in the research of 2D materials in the future. There are two aspects which may be crucial for the development of mechanical exfoliation. The first one depends on the progress of developing high-quality bulk crystals. Growing wafer-scale and high-quality layered materials is the prerequisite for exfoliating a single layer of wafer size. Secondly, promoting the development of this technology towards cheap and controllable industrial applications is also an important question. With breakthroughs in these two aspects, mechanical exfoliation will be widely used not only in basic scientific research but also in industrial applications, especially for 2D semiconducting materials.

2.2 Liquid exfoliation

Liquid exfoliation methods, mainly including direct exfoliation in solvents and intercalation-based exfoliation, offer
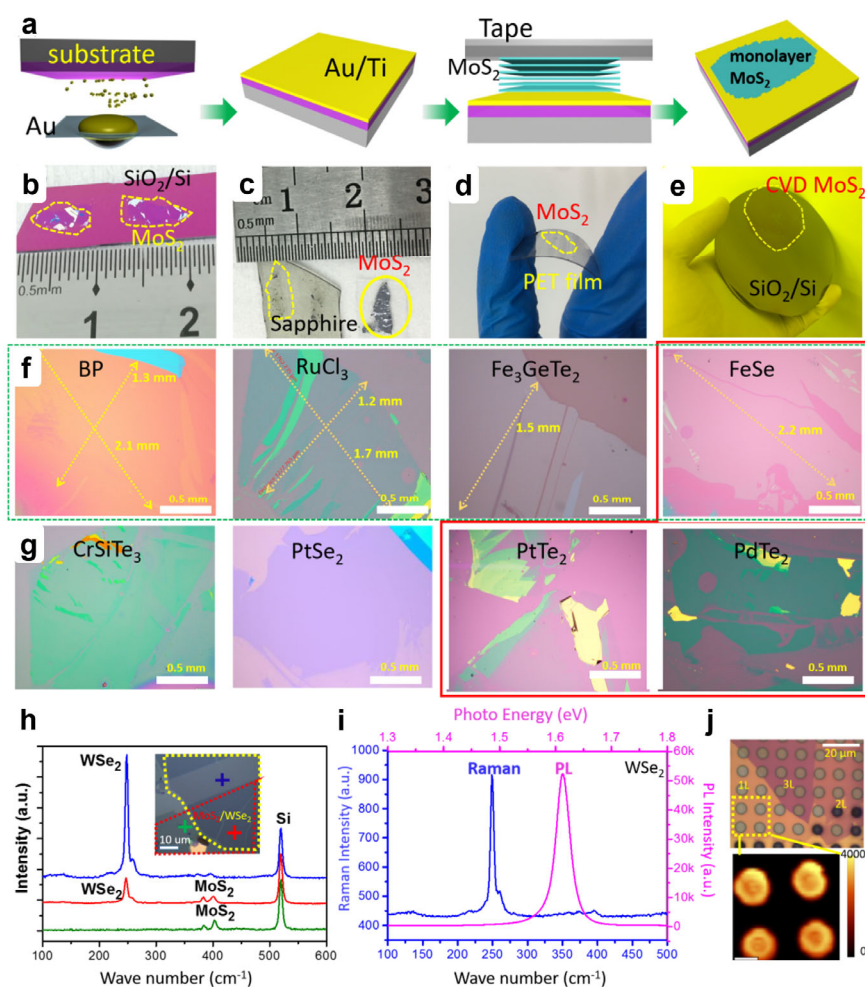
Fig. 2 (a) Schematic of the Gold-assisted mechanical exfoliation process of different monolayer materials. (b–d) Optical images of exfoliated MoS_2 on SiO_2/Si, sapphire, and plastic film. (e) 2-inch CVD-grown monolayer MoS_2 film transferred onto a 4 inch SiO_2/Si substrate. (f–g) Optical images of large exfoliated 2D crystals: BP, $RuCl_3$, Fe_3GeTe_2, FeSe, $CrSiTe_3$, $PtSe_2$, $PtTe_2$, and $PdTe_2$. Those exfoliated monolayers highlighted in the red box are, so far, not accessible using other mechanical exfoliate method. (h) Optical image and Raman spectra of a MoS_2/WSe_2 heterostructure. (i) Raman and photoluminescence (PL) spectra of suspended monolayer WSe_2. (j) Optical image of suspended WSe_2 with different thicknesses (1L to 3L) and a PL intensity map of the suspended monolayer. Reproduced from Ref. [126].

versatile and scalable routes for preparation of solution-dispersed 2D materials [127–130]. Previous studies have demonstrated the successful production of monolayer or few-layer 2D nanosheets (e.g., MoS_2, $MoSe_2$, $MoTe_2$, WS_2, $TaSe_2$, $NbSe_2$, $NiTe_2$, Bi_2Te_3, BN, graphene, and BP) by direct sonication of layered crystals in a number of solvents, such as *N*-methyl-pyrrolidone (NMP), *N,N*-dimethylformamide (DMF), *N*-vinyl-pyrrolidinone (NVP), cyclohexyl-pyrrolidinone (CHP), isopropanol (IPA), dimethylsulphoxide (DMSO), and acetone [128–130]. Recently, other kinds of 2D materials have also been exfoliated by this method, such as tin sulfide (SnS) [131], lead iodide (PbI_2) [132], topological insulators Bi_2TeI [133], calcium metal-organic framework (Ca-MOF) [134], hematene [135], metal hydride (e.g., $TiH_{1.924}$, ZrH_2, CaH_2, and $HfH_{1.983}$) [136], and various organic nanosheets [137,138]. Meanwhile, the available solvents are still limited by the matching degree of surface tension between the layered materials and the solvent. For example, surface tension of solvent need to close to 40 mJ·m^{-2} for the exfoliation of graphite [129]. Although adding mixed-solvent [139], surfactant [140–142], or polymer [143,144] has been proven to be an effective solution for this limitation, direct liquid exfoliation is also plagued by the low yield of the monolayers and low efficiency.

Intercalation-based exfoliation of layered materials has been recognized as a mature and controllable method for production of 2D materials with a remarkable advantage of high-yield monolayers [127,145–147]. It involves chemical or electrochemical intercalation of foreign species into the interlayer gap of layered bulk materials and a subsequent mild sonication process in solvent (e.g., water). Studies about intercalation and exfoliation of layered materials date back to several decades ago [127,148–150]. Very recently, the development of this method has been greatly boosted since 2011 by the chemical [151] and electrochemical [152,153] lithium-ion intercalation-based exfoliation of 2D TMDs. Since then, lithium-ion intercalation-based exfoliation method has been wildly reported for preparation of 2D monolayers [25,154–161]. However, the rising prices of lithium, and the sensitivity of lithium intercalation compounds to ambient conditions along with its flammability make finding alternative intercalation species necessary. Up to now, a host of intercalation species beyond lithium ion have been proven to be effective for the intercalation-based exfoliation, including cations (e.g., Na^+ and K^+ [162,163], O_2^+ [164], quaternary ammonium cation [165–168]), anions (e.g., SO_4^{2-} [169–172], BF_4^- [173,174]), and molecules (e.g., H_2O [175], Lewis bases [176], Brønsted acids [177], dimethyl sulfoxide [178], 4,4′-dipyridyl disulfide [179], *n*-propylamine [180]). For example, Ding *et al.* used 4,4′-dipyridyl disulfide as intercalation species to exfoliate MOFs and obtained ultrathin (~1 nm) 2D MOF nanosheets in ~57% overall yield [179]. In addition, Liu *et al.* demonstrated the production of BP nanobelts by electrochemical BF_4^- intercalation-based exfoliation method [173]. As a notable example, Wang *et al.* have demonstrated that monolayer BP molecular superlattices can be produced from bulk BP by electrochemical intercalation-based exfoliation method using

cetyl-trimethylammonium bromide (CTAB) as intercalant [93]. Very recently, CTAB intercalation-based exfoliation method have also used for production of mica (eMica) nanosheets [181], and the exfoliation of the sodalite precursor RUB-15 into the crystalline 0.8-nm-thick nanosheets [182]. Besides, Lin *et al.* have also reported the exfoliation of a large number of 2D nanosheets, including MoS_2, WSe_2, Bi_2Se_3, $NbSe_2$, In_2Se_3, Sb_2Te_3 and BP, by electrochemical intercalation-based exfoliation strategy with tetraheptylammonium bromide (THAB) as intercalant [94]. Importantly, this method prevented the undesired phase transition from 2H to 1T during the intercalation-based exfoliation process, achieving the preparation of high-purity 2H phase MoS_2 nanosheets.

Alternatively, multiple intercalation species as tandem intercalants [176] or as co-intercalants [183] have also been recently reported for the production of 2D materials. For example, very recently, Li *et al.* demonstrated an electrochemical co-intercalation-based exfoliation process [183]. Using quaternary ammonium cations solvated with propylene carbonate molecule as co-intercalants, they successfully prepared a series of TMD nanosheets, including $NbSe_2$, $NbTe_2$, $TaSe_2$, TaS_2, $TiSe_2$, TiS_2, and $MoTe_2$. As a general and scalable synthesis method, it realized a high-yield (> 75%) preparation of TMD monolayers with large lateral dimensions (up to 300 μm) and high-crystallinity, which is better than the monolayers grown by molecular beam epitaxy [184] or chemical vapor deposition [185] methods.

As mentioned above, a number of intercalation-based exfoliation methods have been established based on different intercalation species. However, there is still room for improvement for effective and high-yield production of monolayers. Therefore, reasonable selection of intercalants and rational design of the exfoliation process remain crucial for the synthesis of atomically thin nanosheets to achieve specific application purposes.

2.3 Gas vapor growth

In comparison with the top-down approaches, the bottom-up approaches based on the gas-phase vapor growth has been regarded as an efficient and controllable synthesis strategy for growth of high-quality large-area 2D materials, which are promising for meeting the requirements of industrial applications, especially in electronics and optoelectronics [186–188]. Gas-vapor growth generally occurs in the system composed of a tube furnace. Under high temperature, gaseous precursors containing the elements of 2D materials are transported into the reaction zone, followed by nucleation, growth and final formation of 2D flakes or continuous films on the target substrates. Common gas vapor growth includes chemical vapor deposition (CVD), thermally assisted conversion (TAC) and physical laser deposition (PLD)

2.3.1 Chemical vapor deposition

Since the first successful demonstration of CVD growth of monolayer graphene on Cu foils [189], CVD approaches have

gradually become the dominant method for preparing various kinds of 2D materials including graphene, h-BN [190], metal disulfides (MX$_2$, M=Mo, W, Ta, Cr, Nb, Re, *etc.*, X = Se, S, Te) [191–195], ternary compounds as well as 2D material-based heterostructures [196,197]. The properties and applications of 2D materials are highly dependent on the thickness, domain size, geometric morphology and crystalline orientation, defect densities and dopant types, all of which can be controlled by optimizing the parameters in CVD growth. Accordingly, the strategies can be categorized to precursor design, space-confined growth, additive-assisted growth and substrate engineering.

As for graphene growth, methane (CH$_4$) is commonly used gaseous precursors, enabling the precise control on the elementary steps of CVD growth for graphene by accurately tuning the gas flow rate [187,189]. In contrast, the growth of MX$_2$ usually requires two kinds of solid precursors, metal-containing precursors (e.g., metal foil, metal oxides, metal chloride) and non-metal precursors (e.g., S, Se, Te), which are located at different heated regions [191]. In this case, the metal and non-metal precursors are separately volatilized by heating and transported to the substrate in the high-temperature reaction zone assisted by carrier gas. Subsequently the chemical reaction occurs to form MX$_2$ on the substrates. Since the heating temperature of the solid precursors is the key parameter which would determine the vapor pressure of the solid precursors. Hence, it is still challenging to accurately control the amount of volatilized solid precursors by solely setting the temperature, making it rather

difficult to effectively adjust the growth process of MX$_2$. To this end, metal-organic precursors hold great promise for controlled synthesis of the 2D materials, which can ensure introducing a precise and stable amount of precursors into the CVD system [198]. In this respect, Kang *et al.* grew continuous 4-inch wafer-scale MoS$_2$ and WS$_2$ films by employing Mo(CO)$_6$, W(CO)$_6$ as metal precursor and (C$_2$H$_5$)$_2$S as non-metal precursors, respectively.

Since precursors are the reactants for growing 2D materials, tuning the elemental compositions of the precursors can enable the direct growth of doped, alloyed as well as ternary 2D materials [199–203]. For example, Wu *et al.* employed Bi$_2$O$_3$ and Bi$_2$Se$_3$ as two isolated precursors to successfully prepared ultrathin Bi$_2$O$_2$Se flakes (Fig. 3a), which exhibited excellent air stability and high-mobility semiconducting behaviors [201,202]. In another recent work, Hong *et al.* grew 2D layered MoSi$_2$N$_4$ by CVD on a Cu/Mo bilayer substrate, in which NH$_3$ gas and pure Si plate were employed as the N and Si sources, respectively [203]. The as-grown MoSi$_2$N$_4$ demonstrated semiconducting behaviors, high mechanical strength and excellent ambient stability. This synthetic strategy can be also extended to other ternary MXene such as WSi$_2$N$_4$.

In a regular CVD system, the thickness and domain size of as-received 2D materials can only be controlled by adjusting the related growth parameters including the growth temperature, the gas flow of carrier gas and precursors, and the chamber pressure. However, the complex intermediate reactions inevitably result in the non-uniformity of thickness, adsorption of impurities and
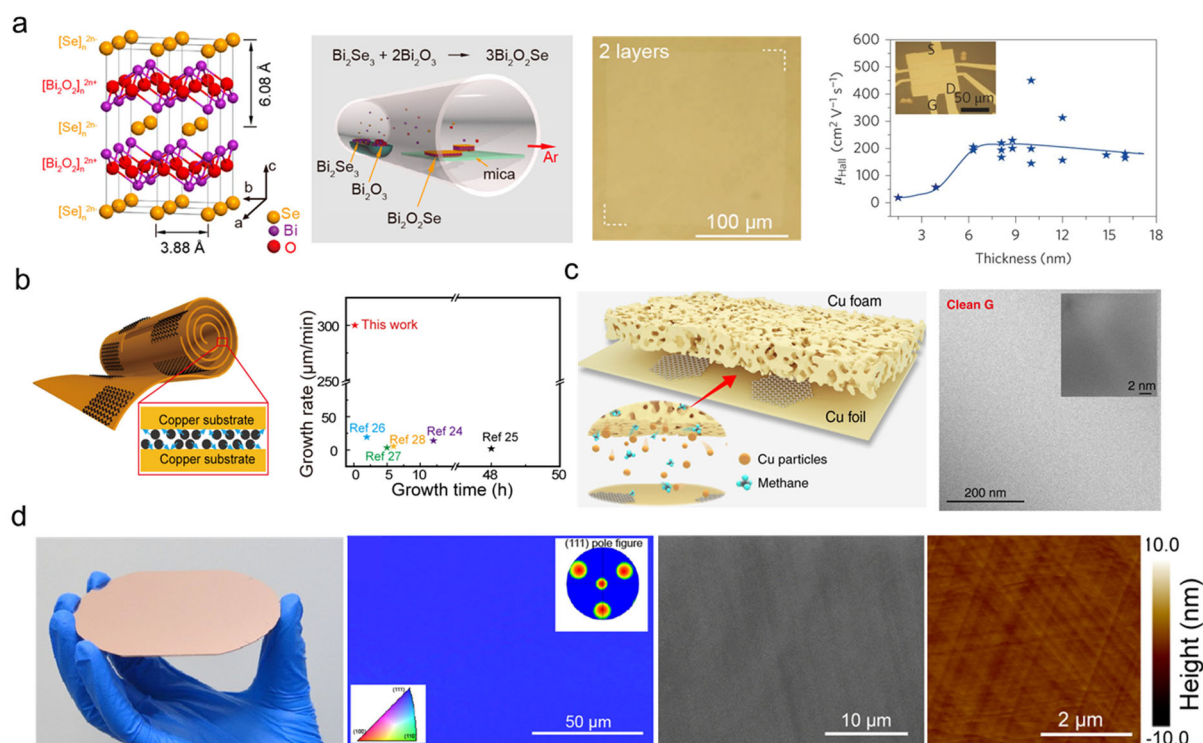
Fig. 3 **(a) Layered crystal structure and CVD growth of Bi$_2$O$_2$Se with Bi$_2$Se$_3$ and Bi$_2$O$_3$ as precursors [201,202]. (b) Fast growth of millimeter-sized graphene within confined space; reproduced with permission from Ref. [204], Copyright 2016 John Wiley and Sons. (c) Experimental design of Cu foil-foam stacked structure for the growth of super-clean graphene [206]. (d) Epitaxial growth of single-crystal graphene wafer with free wrinkles on as-deposited Cu (111) thin film; reproduced with permission from Ref. [209], Copyright 2017 American Chemical Society.**

slow growth rate. To improve the uniformity and growth rate, space-confined growth has emerged as a promising growth strategy. With this novel configuration, growth of large graphene single crystals can be achieved with a high growth rate by facilitating the decomposition of CH_4 precursors and decreasing the nucleation density (Fig. 3b) [204,205]. In another work, Lin *et al.* relies on a new configuration of catalyst to achieve the scalable production of super-clean graphene (> 99% clean regions) *via* the stacking of Cu foil and Cu foam [206], where the Cu foam can provide sufficient supply of Cu vapor during the entire growth to continuously catalyze the decomposition of carbon species (Fig. 3c). For other 2D materials, Wang *et al.* achieved the preparation of 2D all-inorganic halide perovskites (2D AIHP) with adjustable morphologies *via* a vertical mass transport with the space-confined channel [207]. Confined spaces can improve the vapor pressure of sulfur, so that PtS_2 thin films can be readily achieved in a scalable and controlled manner in a modified quartz tube [208].

Despite recent progress on the growth of 2D materials, many 2D crystals remains difficult to be directly grown on substrates *via* direct CVD growth owing to high melting points of their metal/metal oxide precursors as well as thermodynamics instabilities of metastable phases. To this end, molten salts as additives are introduced into CVD process for achieving the growth of high-quality 2D materials [97,210,211]. With the assistance of NaCl and KI, Zhou *et al.* synthesized the growth of 47 compounds including 32 binary compounds, 13 alloys and two heterostructures [97]. Investigation of the related growth mechanism confirmed that the salt can decrease the melting point of the reactants and facilitates the formation of oxychloride compound as intermediate products that are energetically favorable to be sulfurized or selenized. Meanwhile, the alkali metal ions can also reduce the growth barrier, synergistically increasing the overall reaction rate and promoting large-scale production of high-quality 2D materials with fine uniformity. With the aid of trace amount of Na catalysts released from the glass substrates, Yang *et al.* successfully prepared a 6-inch uniform MoS_2 monolayer film with the domain size larger than 400 μm on solid soda-lime glass with an improved growth speed, relying on a face-to-face metal-precursor supply method [212]. However, the residue of molten salts and possible dopants might influence the stability and pristine property of as-grown 2D materials, which still needs further study.

High-quality 2D materials single crystal with no grain boundaries are highly desired for the applications in electronics and optoelectronics, in which a high carrier mobility of 2D materials is highly needed. Therefore, main focus becomes the synthesis of wafer-scale single crystals of 2D materials. CVD technique shows a unique merit in producing wafer-scale 2D thin films. By deliberately designing the single-crystal substrates which have fine lattice matching with the target 2D materials, the epitaxy growth of well-aligned 2D crystal domains can be realized. After the well-aligned nucleation, the subsequent

seamless stitching would enable the growth of wafer-scale 2D single crystal. Hence, the epitaxy growth of graphene with identical orientations on a Cu (111) substrate toward single-crystal graphene film has received great attention [209,213]. In this regard, Deng *et al.* synthesized a 4-inch wrinkle-free single-crystal graphene wafer on a twin-boundary-free single-crystal Cu (111) thin film prepared on sapphire substrate through strain engineering (Fig. 3d) [209]. Furthermore, the growth of 100-square-centimetre single-crystal BN monolayer on Cu (110) and wafer-scale growth of WS_2 film on *c*-plane (0001) sapphire have been successfully demonstrated [214,215].

2.3.2 Thermally assisted conversion in CVD system

One effective strategy to prepare wafer-scale continuous films involves the sulfurization (or selenization) of pre-deposited metal films or metal oxide on the substrates in a conventional CVD system. The pre-deposition process can be realized *via* thermal deposition, atomic layer deposition, electron beam deposition, magnetron sputtering and spin coating. For instance, the preparation of wafer-scale and homogenous 2D $PdSe_2$ film with thickness of 1.2–20 nm can be readily achieved by thermally assisted conversion of the as-deposited Pd layer with gaseous Se [216]. Likewise, other 2D noble disulfides (such as $PtSe_2$) as well as MoS_2 and $MoSe_2$ with adjustable layers are achieved relying on the TAC approaches [217–219]. It is worth mentioning that this strategy cannot only offer good control on film uniformity and thickness, but also can contribute to an improved air stability of as-received 2D crystals. Gao discovered that the direct selenization of magnetron-sputtered Nb film for 2D $NbSe_2$ films can effectively avoid the reaction of the $NbSe_2$ with H_2O and O_2, which can exhibit a superior and stable superconductivity [220].

2.3.3 Pulsed laser deposition

PLD is an effective and controllable approach to deposit 2D materials on target substrates, which has demonstrated the following advantages: (i) the active species from the precursors can reduce the surface activation for the deposition; (ii) the thickness of the deposited film can be manipulated by the repetition rate, laser energy and deposition pressure; (iii) further sulfurization or selenization is not required; (iv) the use of expensive and potentially dangerous precursors can be avoided [221]. Wu *et al.* recently reported the controlled PLD strategy for the growth of high-quality, few-layer BP on the centimeter-sized scale [100]. The unique plasma-activated region induced by laser ablation is energetically favorable for the formation of BP cluster and the following coalescence of monolayer BP flakes into continuous films. Moreover, manipulating the number of laser pulses during the deposition can enable the precise control over the thickness of as-received film. Moreover, few-layer WSe_2 thin film on a centimeter-scale can be achieved *via* a PLD method, in which the thickness can be readily controlled by varying the number of introduced laser pulses [222]. In addition, the PLD technology also enables the preparation of uniform tellurium films with a thickness of sub-7 nm over a centimeter square,

which exhibited hexagonal, $P3_121$ structure [223].

2.4 Chemical synthesis

Besides vapor phase growth and exfoliation methods, chemical synthesis methods are also explored extensively owing to their simple, low-cost and high-output characteristics. This section discusses recent advances developed in the wet-chemical synthesis of representative 2D materials.

2.4.1 2D metal nanomaterials

Despite the intrinsic non-layered characteristics and strong isotropic metallic bond, various strategies have been developed for synthesizing metallic nanosheets [73]. The template method is one of the strategies by means of confined-space effect and metal-support interaction. The template used could be divided as hard templates and soft templates. 2D materials like graphene and TMDs are commonly used hard templates. For example, Huang *et al.* adopted single-layer MoS_2 nanosheets as templates to produce small Pd, Pt and Ag nanosheets through epitaxial growth [161]. Jiang *et al.* synthesized single-crystalline Pd square nanosheets enclosed by (100) facets on reduced graphene oxide [224]. Confined growth of metal in the interlayer of layered materials is another effective hard template method. Wang *et al.* controlled the crystal growth of ultrathin Au nanosheets by introducing $AuCl_4^-$ into the interlayer space of LDHs through anion exchange and followed by chemical reduction (Fig. 4a) [225]. The acquired nanosheets are [001] oriented and have the thickness of only a few atomic layers. Furthermore, inorganic salts have been found as a useful temple to synthesize 2D materials. Wu *et al.* reported a general synthesis method for ultrathin amorphous noble metal nanosheets through adjusting the heating temperature between metal acetylacetone precursors and inorganic salts [226]. Besides hard templates, some soft materials with lamellar structures are also used. For instance, Niu *et al.* reported a polymer-free lamellar hydrogel as soft template to synthesize large area single-crystalline Au membranes [227]. The acquired membranes are flexible, ultrathin and with atomically flat surface because of the slow diffusion of precursor ions in the confined 2D space.

Another popular method for preparing metallic nanosheets is using molecule adsorbents [229,230]. For example, ultrathin PdMo nanosheets were synthesized by Luo *et al.* through one-pot wet-chemical approach with mixing of $Pd(acac)_2$ and $Mo(CO)_6$,

which is curved and has the sub-nanometer thickness [231]. Yang *et al.* synthesized 2D PdCu alloy nanosheets by co-reduction of $Pd(acac)_2$ and $Cu(acac)_2$ with $Mo(CO)_6$ [232]. Besides CO and analogues, halide ions also show potential as shape guider by adsorption in specific crystal face and changing the reduction potential of metal. For instance, triangular Au nanoplates are obtained by selective binding and oxidative etching role of iodide ions [233].

In addition to the two common methods mentioned above, a variety of effective means are developed in regulating the morphology of metallic nanosheets, such as photocatalytic synthesis, self-assembly method, mechanochemical method, and oxidation etching [234–239]. Besides noble metal 2D materials, nanosheets of non-noble metals are also acquired [240,241]. 2D Cu nanosheets were prepared by Luc *et al.* by chemical reduction of Cu precursor with the presence of surfactants [240]. Luo *et al.* synthesized sub-2-nm Al nanosheets by wet-chemical synthesis using $AlCl_3$ and $LiAlH_4$ (Fig. 4b) [228]. The ultrathin Al nanosheets were steadied by oxygen adsorption on (111) facets.

2.4.2 Layered double hydroxides

Among various 2D materials, LDHs have attracted much attention in the field of energy storage and conversion owing to their large surface area, low cost, adjustable structure and composition [242–244]. As a typical class of layered anionic compounds, LDHs compose of divalent cations (M^{2+}, such as Mg^{2+}, Ni^{2+}, Co^{2+}, Zn^{2+} or Fe^{2+}), trivalent cations (M^{3+}, such as Al^{3+}, Fe^{3+}, Mn^{3+}, Ga^{3+} or Cr^{3+}) and hydroxyl groups in laminate, and charge-compensating anions (A^{n-}, such as CO_3^{2-}, SO_4^{2-}, NO_3^- or Cl^-) in interlayer, which can be represented by the general formula $[M_{1-x}^{2+}M_x^{3+}(OH)_2]^{z+}[A^{n-}]_{z/n}\cdot mH_2O$ (Fig. 5). LDHs can not only be used as catalysts, but also act as carriers to support other active materials to achieve synergistically enhanced performance. In this section, we summary the recent progress of LDHs and LDH-based materials in the field of energy storage and conversion from the perspective of synthesis.

In recent years, a variety of methods have been explored to prepare LDHs and LDH-based materials. Among them, coprecipitation and electrochemical deposition can directly synthesize LDHs with controlled structure [245]. Exfoliation (-reassembling) strategies provide effective ways for preparing LDHs with few layers and single layer, as well as other LDH-
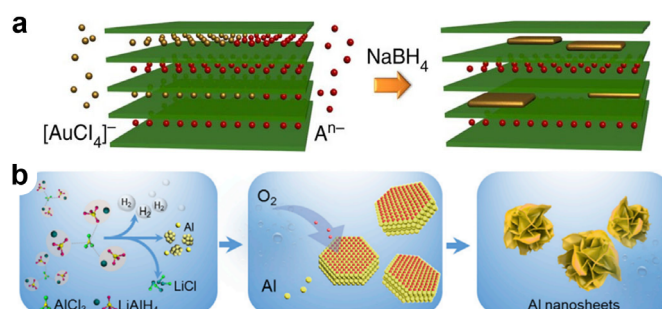
Fig. 4 (a) Schematic illustration of the synthetic route of 2D Au nanosheets using LDH as template [225].

(b) The synthesis process of ultrathin Al nanosheets [228].

based multi-functional nanomaterials [246,247]. Furthermore, LDHs can be used as precursors to synthesize various 2D transition metal compounds through topological transformation [248]. In order to achieve excellent electrochemical performance, it is necessary to construct active sites with high intrinsic activity or expose more active sites, which puts forward higher demands for the design and synthesis of novel LDHs [249]. With the development of synthetic techniques, more effective methods have been developed in addition to conventional methods, providing wider options in promoting the synthesis and application of LDHs.

The coprecipitation method is one of the most used methods for preparing LDH-based materials, however, the thickness and microstructure of the obtained material cannot be precisely controlled, which prevents the full exposure of the active sites. Thus, it is necessary to update the synthetic conditions of coprecipitation to obtain more exposed active sites. Li *et al.* synthesized ultrathin Ga doped CuZn-LDH nanosheets *via* the aqueous miscible organic solvent treatment method and applied the products as catalyst precursors for the further synthesis of other active materials [250]. This ultra-thin structure is conducive to the full exposure of active sites. Intercalating large-size molecules between the LDH layers can increase the layer spacing, promote the mass transfer, and even bring other useful functions. Up to date, various guest species, including inorganic and organic molecules, have been successfully intercalated into LDHs, which usually requires a separate interlayer anion exchange process. Calhau *et al.* incorporated a kind of photoactivatable CO-releasing molecule into the ZnAl-LDH host by a one-pot coprecipitation method, which simplified the synthesis process [251]. Doping is another effective way to improve the intrinsic activity of LDH-based materials. A variety of metal elements have been introduced into the LDH laminate *via* hydrothermal coprecipitation method, such as highly charged metal ions (V^{4+} and Mn^{4+}) and precious metal ions. The doped

sites can modify the electronic structure of LDHs, thereby enhance the electrochemical properties [252,253]. Other modified coprecipitation methods have also been reported, such as separate nucleation and aging method [254].

In the past few years, electrodeposition method was developed to fabricate LDHs facilely on conductive matrices, using nitrate or sulfate solutions which contained appropriate metal ions at negative potential. Li *et al.* has successfully fabricated various ultrathin LDH nanosheet arrays (200–300 nm in lateral length and 8–12 nm in thickness) on various macro/micro conductive substrates *via* electrodeposition method [255]. To further expand the types of elements suitable for the synthesis of LDHs, the lanthanides (La^{3+}) was introduced and NiLa-LDH with adjustable Ni/La ratio were prepared [256]. Owing to the advantages of simplicity, electrodeposition can combine with other methods to controllably prepare composite materials with complex structures [257,258].

Exfoliation(-reassembling) strategy allows us to obtain LDHs with few layers or even single layer with maximal exposure of active sites. It also allows to further assemble LDHs with other guest species to produce LDH-based multi-functional nanomaterials. During this process, exfoliating bulk LDHs into uniform monolithic layers is a critical step. However, conventional exfoliation methods that require toxic organic solvents are time-consuming and less controllable, and the resulting monolithic layer is easily reunited during applications. To overcome this, Wang *et al.* developed a "dry exfoliation" method that uses Ar plasma to etch bulk CoFe LDHs into ultrathin LDH nanosheets with multiple vacancies [259]. Zhao *et al.* successfully explored an electrostatic layer-by-layer technique to assemble the exfoliated LDH nanosheets with commercial conductive polymer into a superlattice heterostructure without accumulation [260]. In this heterostructure, LDH can provide a restricted microenvironment for the accommodation of the conductive polymer, allowing the high

Fig. 5   Illustration, synthesis and applications of LDHs.

charge carrier mobility.

In addition, LDHs can be used as precursors for synthesizing various 2D transition metal compounds *via* topological transformation [261]. Until now, various transition metal oxides, sulfides, nitrides, phosphides and selenides have been prepared by Shao's and Wei's groups and have demonstrated excellent electr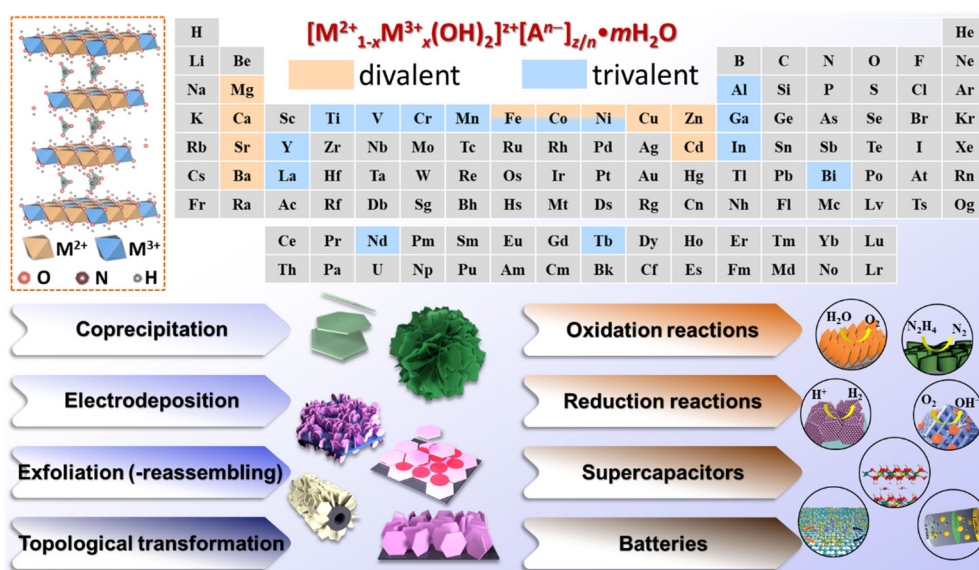ocatalytic activity [262–266]. In addition, they recently reported a new strategy for constructing Co single atom-based integrated electrodes through topological transformation of organic molecules intercalated LDHs, which further expanded the choices of materials that can be prepared using LDH [267]. Apart from topological transformation from LDHs to transition metal compounds, the resulted compounds can be reversibly transformed back to LDHs owing to the unique memory effect [268]. Taking advantage of the memory effect of LDH, Yuan *et al.* synthesized NiFe-LDH with multiple vacancy defects that significantly improved the electrical conductivity and electrochemical surface area, which exhibits enhanced performance toward water splitting [269].

2.4.3　2D metal-organic framework

During the last decade, a series of methods have been developed to prepare 2D metal-organic framework (MOF) nanosheets, which can be categorized into bottom-up synthesis (e.g., modulated synthesis [270,271], sonication-assisted synthesis [272,273], surfactant-assisted synthesis [274–276], three-layer synthesis [277,278], and interfacial synthesis [279,280]) and top-down exfoliation (e.g., sonication exfoliation [281–283], chemical exfoliation [179], and Li-intercalation exfoliation [284]). These methods have been summarized in some review articles [77,285–287]. Here, we only introduce some recent progress in the preparation of 2D MOF nanosheets.

Recent reports demonstrated that 2D metal oxide/hydroxide nanosheets could be used as hard sacrificial templates for the bottom-up synthesis of 2D MOF nanosheets [288,289]. In this method, metal ions are leached in a controllable manner under hydrothermal/solvothermal conditions. Therefore, metal ions are enriched near the surface of metal oxide nanosheets, which induces the confined growth of 2D MOF nanosheets. In a typical work, aqueous dispersions of monometallic (Ni, Fe, Co and Cu) and bimetallic (FeCo, NiFe, CoCu) oxide nanosheets, prepared by the reduction of corresponding metal nitrates with sodium borohydride, were added into an DMF-water-ethanol solution of H_4DOBDC (DOBDC = 2,5-dihydroxyterephthalate) ligand, respectively, and corresponding 2D MOF-74 (M_2DOBDC, M = Fe, Co, Ni, Cu or their combination) nanosheets were formed after keeping the mixtures at 100 °C for 24 h (Fig. 6a) [289].

In another report, carbon dioxide has been used as a capping agent to control the growth of MOF nanosheets. For example, CuBDC (BDC = terephthalate) nanosheets were prepared *via* solvothermal treatment of the methanol solution of $Cu(NO_3)_2$, H_2BDC and triethylamine under CO_2 atmosphere. As nano-sized CuBDC building blocks initially formed, CO_2 molecules were preferably adsorbed on ($20\overline{1}$) plane, thereby selectively

eliminating ($20\overline{1}$) crystal facets stacking along [$20\overline{1}$] axis (Fig. 6b). As a result, the growth of (110) plane was much faster than that of ($20\overline{1}$) plane, thus enabling the formation of 2D CuBDC nanosheets. Meanwhile, the dissolution of CO_2 caused liquid volume expansion and viscosity reduction, which accelerated the growth of MOF crystal; hence, a higher pressure of CO_2 led to a smaller size and a higher yield of the resultant CuBDC nanosheets [290].

For the top-down synthesis of MOF nanosheets, alkali etching route has been proposed for exfoliating 3D MOFs into 2D nanosheets. Generally, as for certain metal cations (e.g., Mn, Co, Ni, Cu, and Zn), the coordinative bonding with nitrogen-based ligands is more stable than that with carboxylate ligands in alkali media. Based on this, when multivariant MOFs containing both nitrogen-based linkers and carboxylate linkers are treated with alkali, the carboxylate linkers can be selectively removed (Fig. 6c). In a typical study, Zn-TRZ-TDA (TDA = 2,5-thiophene-dicarboxylic acid, TRZ = 1,2,4-triazole), a 3D bulk MOF consisting of Zn-TRZ layers connected with each other by TDA, was etched with sodium hydroxide in methanol-water system, and Zn-TRZ nanosheets were obtained as expected [291]. In
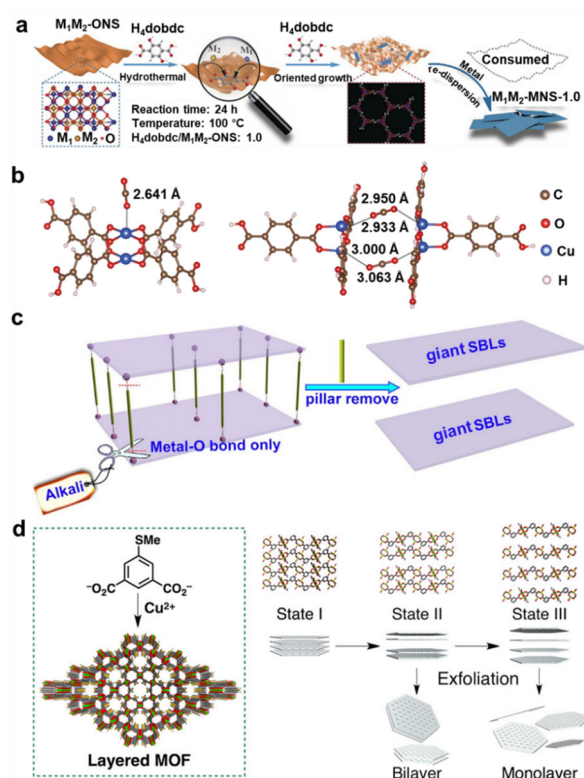
Fig. 6　(a) 2D oxide sacrifice preparation of MOF-74 nanosheets; reproduced with permission from Ref. [289], Copyright 2019 John Wiley and Sons. (b) Structural units of CuBDC and CO_2 along [$20\overline{1}$] axis (left) and ($20\overline{1}$) plane (right) [290]. (c) Alkali etching exfoliation for the preparation of MOF nanosheets; reproduced with permission from Ref. [291], Copyright 2019 American Chemical Society. (d) Stepwise expansion and exfoliation of layered kgm^SMe MOF; reproduced with permission from Ref. [292], Copyright 2018 American Chemical Society.

addition, stepwise expansion has been observed in some layered MOFs, which enables the exfoliation of MOFs in a layer-number-controlled fashion. For example, kgm^{SMe}, a layered MOF fabricated with 5-methylthioisophthalate and Cu^{2+} in a kagomé lattice, underwent a stepwise expansion that formed bilayer or monolayer expanded structures when being immersed in certain solvents, and a gentle agitation led to the exfoliation into bilayer or monolayer nanosheets accordingly. The layer number of nanosheets depends on the type of solvents (Fig. 6d). For example, methyltetrahydrofuran and cyclopentanone tend to the formation of bilayer nanosheets, while tetrahydrofuran, dioxane and DMF favor monolayer nanosheets [292].

2.4.4 Xenes

Elemental 2D materials, often referred to as Xenes, are elemental materials with layered or sheet-like structures (Fig. 7a) [293]. The name Xenes derives from graphene, the first and most studied 2D material. Beyond graphene and its derivatives, over a dozen emerging Xenes, including antimonene, arsenene, bismuthine, borophene, BP, gallenene, germanene, silicene, and tellurene, have been experimentally realized, while others like aluminene and indiene are still in theoretically prediction, as summarized in Table 1 [90,199,294–308]. Xenes have attracted a considerable amount of recent attention due to distinct properties and performances across various research fields. Xenes possess rich atomic structures, such as puckered structure for BP [302] and black arsenene [309] and buckled structure for β-antimonene [310] and grey arsenene [311], which have also lead to structural anisotropicity. In addition, Xenes possess various electronic structures from metallic to semiconductors. For example, different from other 2D semiconductors like TMDs, Xenes such as BP and arsenene often exhibits direct bandgap and high mobility [311–313]. Their distinct properties render extensive applications in diverse research fields, including (opto-) electronics and many energy storage and conversion applications [64,314–316].

Despite significant synthetic challenges, many Xenes were successfully prepared and characterized with controlled crystal structure and morphologies in recent years. The synthetic strategies can be generally categorized into top-down and bottom-up methods. Top-down methods mainly include various exfoliation techniques such as mechanical exfoliation, liquid-phase exfoliation and electrochemical exfoliation, which break the van der Waals (vdW) interaction between the atomic layers in source crystals. Top-down approaches are straightforward and relatively cost-effective, however also limited by the dependence on the source materials, low yield and inhomogeneity. Xenes including BP, antimonene, arsenene and bismuthene have been obtained *via* facile liquid exfoliation method. On the other hand, electrochemical exfoliation strategy is highly efficient, controllable and productive, showing excellent results in BP, antimonene and bismuthene. Unfortunately, electrochemical intercalation is not suitable for most Xenes due to either the difference in intercalation kinetics or the lack of layered source crystals.

Bottom-up methods refer to the direct synthesis of monolayer to few-layer Xenes through chemical reactions in either liquid (wet chemistry) or gas (CVD and molecular beam epitaxy). "Bottom-up" methods generally show good yield and does not require source crystals. However, the most used methods like MBE and CVD rely on the chemical interaction/bonding between precursors and substrates and largely limited by their lattice parameters. Currently, MBE is conveniently used in the synthesis of Xenes in IIIA and IVA groups, such as borophene [294], silicene [320] and germanene [321] with fine-tuned combination of chemical composition, substrate lattice and deposition conditions. Meanwhile, wet-chemical methods generally produce Xenes with limited control in chemical composition and morphologies. And they are incapable of producing self-support monolayer Xenes. And the surfactants resulted from the synthesis process are undesirable in the consequence applications. Currently, only a few Xene members have been obtained in wet-chemical processes, such as silicene [317],

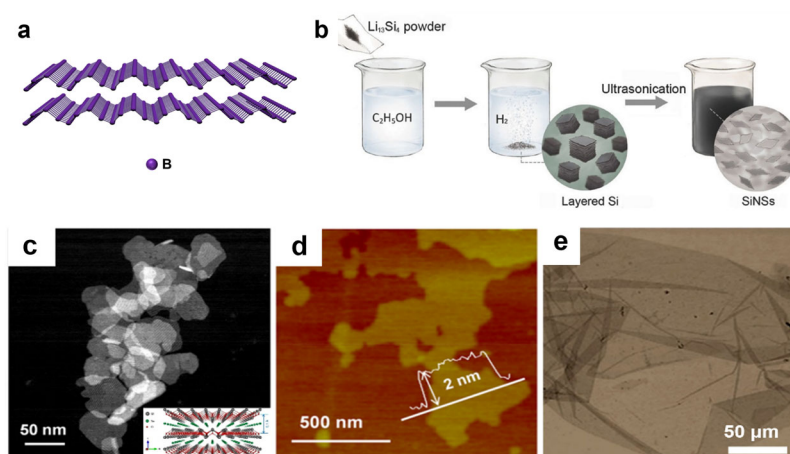**Fig. 7　(a) Schematic model of one example of Xenes (borophene). (b) The synthesis process of Si nanosheets through chemical etching. Reproduced with permission from Ref. [317], Copyright 2017 John Wiley and Sons. (c) HAADF-STEM image and (d) AFM image of Bi$_2$O$_2$Se nanosheets. Reproduced with permission from Ref. [318], Copyright 2019 American Chemical Society. (e) TEM images of PtSe$_2$ nanosheets [319].**

Table 1   Overview of elemental 2D materials explored by experimental and theoretical methods.

IIIA	IVA	VA	VIA	VIIA
5	6	7	8	9
B	C	N	O	F
13	14	15	16	17
Al*	Si	P	S	Cl
31	32	33	34	35
Ga	Ge	As	Se	Br
49	50	51	52	53
In*	Sn	Sb	Te	I
81	82	83	83	85
Ti	Pb	Bi	Po	At

The shaded elements are yet to be explored by any method. * represents theoretical exploration. The experimental realization and theoretical prediction can be found in references [90,199,294–308].

tellurene [89], antimonene [322] and bismuthene [323]. The 2D Si nanomaterials show novel properties and have plenty of applications towards optical, electronic devices and energy storage and conversion. As shown in Fig. 7b, Lang *et al.* prepared ultrathin Si nanosheets by chemical leaching of $Li_{13}Si_4$ using ethyl alcohol [317]. Group VI tellurium displays distinct in-plane anisotropic properties due to the unique chiral-chain vdW crystal structure. Te nanostructures tend to adopt the 1D form because of the chain structure. Inspiringly, Wang *et al.* synthesized 2D Te nanosheets using sodium tellurite as precursor and hydrazine hydrate as reducing agent with the presence of polyvinylpyrrolidone [89]. Layered materials black arsenic, which is the analogue of black phosphorus with the orthorhombic structure, shows the tunable bandgap and great potential in optical properties. Besides mechanical and liquid exfoliation method, Antonatos *et al.* prepared the black arsenic through crystallization of amorphous arsenic using mercury vapors [324]. Up until now, it is still very challenging to realize general, effective, high-yield and low-cost synthesis of Xenes.

2.4.5   2D covalent organic framework

Besides MOFs, 2D covalent organic frameworks (COFs) are another important class of organic crystalline porous materials due to their charming advantages including the pre-designable

structure, manageable function, small mass density and good chemical stability (Fig. 8a). Since the first COF appeared in year 2005 [325], a large number of 2D/3D COFs materials have been designed and synthesized for broad applications in gas storage and separation [326,327], drug delivery [328,329], catalysis [330–332], photoelectronic devices [333,334], supercapacitors [335,336], and batteries [337–339]. Normally, 2D COFs can be prepared through the polycondensation reactions or coupling reactions, and their structures are confirmed through the structural simulation together with the powder X-ray diffraction (PXRD) pattern matching. More recently, their single crystal structures can be determined by electron diffraction or single-crystal XRD [337,339]. In principle, AA and AB stacking modes can be adopted. In order to further evaluate the structures and compositions of 2D COFs, other general methods for characterization could also be applied, such as solid-state nuclear magnetic resonance (ssNMR), Fourier transform infrared spectroscopy (FT-IR), and so on. Herein, the recent progress, design strategies, and future perspectives of 2D COFs regarding their luminescence, stimulus-responsive ability, and electrochemical properties will be briefly discussed.

Until now, numerous luminescent 2D COFs have been designed and prepared through introducing various luminophores into the skeleton [338], and their luminescent mechanisms involve excimers, aggregation-induced emission (AIE), excited state intramolecular proton transfer (ESIPT), intramolecular charge transfer (ICT), two-photon induced (TPI) emission, and phosphorescence. In one pioneering work, Wan *et al.* developed the first luminescent boronated-linked 2D COF through the condensation reaction, which exhibits strong blue fluorescence peaks at 474 nm originating from the excimer emission of pyrene [340]. Later on, these excimers emission properties in 2D COFs can be tuned by changing building blocks, linkage types, or stacking distances. Besides, the introduction of AIE luminogens (such as tetraphenylethene) into skeleton can also construct the luminescent 2D COFs because the π–π stacking in COFs can restrict the rotation of the four phenyl groups and obtain high luminescence quantum yield [341]. Moreover, choosing different linkages can effectively change their stacked rhombic topology together with π–π stacking, thus leading to different fluorescent behaviors. By introducing
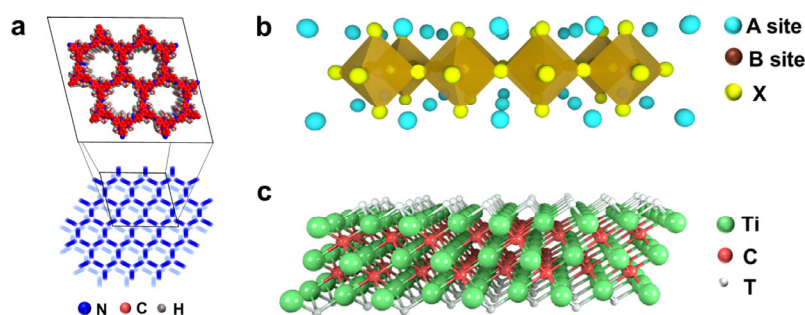
Fig. 8   Schematic models of examples of (a) 2D covalent organic frameworks (COFs), (b) 2D perovskite and (c) 2D Mxenes ($Ti_3C_2T_x$).

resorcinol units with ESIPT property into COFs system [342], a kind of luminescent COFs with dual emission properties are developed, in which the dual emission of COFs originates from the enol state and ESIPT emission, respectively. When these COFs are dissolved in different polar solvents, their emission colors can be tunned because the equilibrium of keto and enol forms is broken. However, these polar solvents also could influence their chemical stabilities. Furthermore, combining the large π-conjugation area with strong charge transfer character, COFs with TPI emission can be realized [343]. Note that the larger conjugation extension and strong charge transfer between electron acceptors and donors are vital for TPI emission. Recently, several phosphorescent 2D COFs have been reported by introducing organic phosphors as building units [344], but so far, none of them shows persistent RTP behavior under ambient conditions.

The physicochemical properties of COFs could be dynamically varied under external stimuli, which are defined as stimulus-responsive 2D COFs [345]. Generally, stimulus-responsive 2D COFs consist of physical and chemical-responsive COFs, depending on the different stimuli manners. Since the first nitro explosives responsive 2D COF was reported in 2013 [346], more stimulus-responsive 2D COFs materials have been widely developed [347–349]. Such stimulus can be metal ions, pH values, gas molecules, solvents, temperature, light, electricity, and so on. In general, stimulus-responsive 2D COFs are prepared by rational incorporation of functional groups into the conjugated skeletons or the active sites that can capture different guest molecules. The responsive performances of functional monomers and linkers endow these resulting 2D COFs with dynamically controlled optical or electrical properties. Moreover, the ordered and porous structures of COFs make real-time responses possible. Nevertheless, the responsive behaviors of most smart 2D COFs always occur in the presence of structure changes or solvents [181,350], leading to possible structure collapses and shortened lifetime of COFs. Therefore, suitable stimulus types with no solvent contact or structure variations are necessary. In order to achieve smart 2D COFs with good durability, two key countermeasures should be adopted in the future: one is to develop more and new electrochromic COFs, in which the red-shifted absorption is triggered by new formation of the stable cation radical without structure changes, and the other is to introduce photoinduced radical molecules into COFs, where radical can bring improved optical properties upon light excitation.

Besides, 2D COFs materials attract increasing attention in extensive electrochemical applications (e.g., fuel cells [351], supercapacitors [352], batteries [353] and so on) due to the following reasons: (1) the well-defined active sites and controllable porosities in COFs favor electrocatalytic processes and efficient mass transport; (2) various redox-active sites can be rationally introduced into COFs, which endows them with the enhanced pseudocapacitive performance; (3) the mass transport, electrical conductivity and mechanical stability of COFs materials can be improved by compositing other materials, such as poly(3,4-ethylenedioxythiophene) and 3D graphene. Although many efforts have been paid to the development of COF-based materials for electrocatalytic applications, they still suffer from several challenges, such as low chemical stabilities, limited durability, and the poor processability. Therefore, it is desirable to construct novel COFs materials with good stability and processability through synthetic approaches and processing methodologies. Particularly, new cyanovinylene- or olefin-linked COFs should be developed due to its good recyclability (robustness) and superior charge transport properties under strong aqueous acidic/alkaline electrolytes.

2.4.6 Other emerging 2D materials

In addition to the abovementioned 2D materials, new promising 2D materials are rapidly expanding the family of 2D materials. This section briefly discusses a few representative examples.

Layered bismuth oxychalcogenide (Bi_2O_2Se) has appeared as a compelling 2D material with high carrier mobility and thickness-dependent bandgap [354]. As shown in Fig. 7c, d, Ghosh *et al.* relied on the electrostatic interactions between oppositely charged alternating layers to assemble the single crystalline Bi_2O_2Se nanosheets by a wet chemical method [318]. Because the nearly full occupation of *d* orbitals brings unique interlayer vibration, 2D noble-transition-metal dichalcogenides have emerged as a more attractive materials compared with other transition metal dichalcogenides. Therein, straightforward aqueous-phase reaction method with thermal annealing were developed by Umar *et al.* to acquire mesoporous $PtSe_2$ nanosheets (Fig. 7e) [319].

2D halide perovskites (Fig. 8b) have arisen as the next-generation halide perovskites with intriguing physical properties and improved performances in optoelectronics [355]. Particularly, 2D perovskites and their hybrids demonstrated great potentials in outperforming conventional 3D perovskites in terms of stability and conversion efficiency [356,357]. As a result, engineering the phase and heterostructures of 2D halide perovskite and integrating them with other 2D materials have become an effective strategy to expand the possibility of future perovskite-based applications [358]. The preparation of 2D perovskites can be realized by solution-based synthesis, mechanical exfoliation, epitaxial growth, as well as space-confined growth [359]. Recently, the direct growth of atomically thin, square-shape $(C_4H_9NH_3)_2PbBr_4$ perovskite has been achieved in a solution based method [80]. The growth solution containing precursors of the perovskite was drop-casted directly on the substrate and majority of the products were molecularly thin with $n = 1$. In another work, solution-based crystallization method was applied to synthesize a series of 2D organic-inorganic hybrid perovskites [360]. The authors made use of different types of bulky ligands to sterically prevent the intermolecular aggregation and thickening during the crystal

growth, resulting in the formation of nanometer-thick 2D perovskites.

MXenes are another group of 2D nanocrystals composed of transition metal carbides, nitrides, or carbonitrides. MXenes adopts a general formula of $M_{n+1}X_nT_x$ ($n = 1$–3), where M is the transition metal, X represents carbon and/or nitrogen, and T_x is the surface terminations (a typical example of MXenes, $Ti_3C_2T_x$, is shown in Fig. 8c). Thanks to the conductive layered structure and tuneable surface properties [361], MXenes have demonstrated excellent performances in applications such as energy storage [362,363], sensing [364], and catalysis [365,366]. The synthesis of MXenes can be realized *via* the high-temperature molten-salt approach, as well as wet etching [362]. Particularly, the most used method is selective wet etching from a layered precursor followed by delamination. To date, different strategies have been employed in the etching and/or delamination processes to modulate the structure and composition of the resultant MXenes towards desired properties and functions. Examples include edge functionalization [367], single metal atom substitution [366,368], controlled self-assembly of MXenes [369], and so on.

2.5 Phase engineering of 2D materials

2.5.1 Overview of phase engineering in 2D materials

Phase engineering of nanomaterials (PEN) focuses on the significant impact of the distinct atomic arrangement on the physiochemical properties of nanomaterials, and its incorporation towards unique properties and applications [105]. PEN has gradually become a powerful strategy to engineer the property and performance of nanomaterials in applications across a multitude of research fields such as photonics, electronics, condensed matter and energy applications [106,370]. The concept of PEN has deep root in 2D materials, showing intriguing development in TMDs, noble metals, metal oxides, MOFs, COFs and perovskites. In addition, amorphous 2D materials which lack long-range atomic ordering is a new development in PEN, showing enhanced performance in many energy applications. In this section, we will elaborate on the PEN-related studies in 2D materials with a particular focus on TMDs.

2.5.2 Phase engineering of transition metal dichalcogenides

TMDs are among the most studied nanomaterials in the field of PEN. The early attempt of phase engineering in TMDs could date back to the 1980s when the phase transition was observed during the Li intercalation of MoS_2 [371]. Phase engineering of TMDs gains significant tracking in the last decade and finds importance in both fundamental science [101] and practical applications [370,372,373]. Polymorphism is one of the key characteristics that defines TMDs and their applications in various research fields [145,374,375]. In general, layered TMDs can be categorized into different phases based on their atomic arrangement of chalcogen atom and transition metal atom, including 2H, 3R, 1T, 1T' and 1T$_d$. The importance and effectiveness of phase engineering in TMDs is largely attributed

to the unique band-structure modulation upon phase transformation. Specifically, group VIB TMDs, such as MoS_2 and WSe_2, in their conventional phase (hexagonal, 2H) are semiconductors, with large bandgaps range from ~1 to ~2 eV, which are intensively studied in next-generation electronics [113]. However, their unconventional phases (octahedral, 1T and 1T') are semi-metals with metallic charge transport, demonstrating extensive application in energy storage and conversion applications [154,370]. Such dramatic change in electronic properties is a result of the change in the filling state of the *d* orbitals of the transition metal upon change of the crystal phases [375]. Although various PEN strategies have been developed in the past decade, the continuous progress of this field is largely limited by the difficulty to obtain metastable TMDs with high phase-purity and high yield, due to the unstable nature of these unconventional-phase materials. There are currently two main PEN strategies in obtained metastable-phase TMDs, phase transition and direct chemical synthesis. The former refers to the various methods to tune the TMDs materials from their thermodynamically stable phases to metastable phases, while the later refers to the more recent development in the CVD and solid-gas phase reactions. In this section, we will elaborate on the synthetic success of metastable TMD materials. More comprehensive review of the phase engineering of TMDs and their application in specific fields can be found in these recent reviews [105,370,375].

2.5.2.1 Phase transition of TMDs

Phase transformation from thermodynamically stable phase to metastable phase is the most studied strategy to obtain metastable phases of TMDs. The various phase transformation methods not only provide convenient and effective approaches readily applicable in many applications, but also play critical roles in understanding the fundamentals of how crystal phases impact the properties. Early discovery of phase transition of TMDs is a byproduct of Li intercalation process as a general route to exfoliate TMDs into colloid suspensions [371]. However, the extensive studies of phase transition process in the recent decade show its true potential in many applications including electronics and catalysis. Based on the difference in transition mechanism, phase transition in TMDs can be roughly divided into two categories, those based on the direct injection of electrons into the lattice and the ones based on thermal activation of the lattice.

2.5.2.1.1 Phase transition *via* direct electron injection

The direct injection of electrons into TMDs can be achieved by lithium intercalation process which simultaneously induces phase transition. Most chemical intercalation methods roughly follow the similar procedures where 2H TMDs can be chemically intercalation with Li ions by immersed TMD flake or powders into the *n*-butyllithium solution under various reaction conditions. As shown in Fig. 9a, the intercalation of alkyli ions (in most case Li^+) results in electron injection into the TMDs which induces phase transition from hexagonal (2H) to

octahedral (1T) or distorted octahedral (1T'). Although very convenient and widely adopted, chemical intercalation methods generally lack control over the intercalation and phase transition processes and show excess damage over of integrity of 2D structures. Such defect-rich morphology is often favored in catalytic applications such as electrocatalytic hydrogen evolution (HER) [154], due to its richness in active sites combined with the enhanced charge transport from the semi-metallic metastable phases [155].

Inspired by the electrochemical cells used in Li-ion battery, the electrochemical intercalation was development in 2011 to overcome these disadvantages [152]. It not only assures a fine control over the whole intercalation processes, but also enable diverse intercalant ions for different applications such as various alkali metal-ion (Li, Na, and K) and organic intercalants [93,376]. Till now, various metal ions and organic cations have been used to intercalate TMD crystals to produce high-quality suspension of nanosheets in large quantity. Electrochemical intercalation has found extensive utilization in thin-film applications in both electronics and catalysis. More importantly, it is a highly versatile method that can be easily integrated with various *in situ* characterization techniques to monitor the intercalation process, as well as study the evolution of the structure and properties.

Aside from the intercalation methods, there are other means to directly inject electron into TMD lattice such as electron beam irradiation [377] and hot electrons injection from plasmonic metal nanostructrure [378]. However, such processes generally produce localized phase transition at the contact area, therefore are unfavored in practical applications. Notably, it is also possible to reverse the phase transition process by extract electron from 1T/1T' TMDs *via* electrochemical reduction [379]. In a more recently and rather unique study, field-induce phase transition was observed in MoTe2 nanosheet when a high magnitude of gate modulation was applied *via* ionic gating in ionic liquid [380]. The phase transition is induced by the ultrahigh carrier (electron) injection under high electrostatic doping, and only occurs at the first layer of MoTe2 that directly contacts the electrolyte.

2.5.2.1.2 Phase transition *via* thermal activation

In addition to the electron injection approaches, thermal activation is another viable and widely used strategy to induce phase transition in TMDs. Both thermodynamically stable and metastable phases of TMDs could undergo phase transition upon absorption of various forms of thermal energy in crystal lattice. The simplest form in this category is the phase transition of TMDs upon thermal annealing at elevated temperature. For example, metastable TMDs spontaneously transfer back to their thermodynamically stable phase upon thermal annealing with a clear transition temperature, as experimentally observed in the TGA experiments in high-purity metastable TMD crystals [101,372]. On the other hand, due to the extremely small energy difference (tens of meV) between 2H- and 1T'-MoTe2, reversible phase transition between these two phases was observed upon thermal treatment (Fig. 9b) [381]. Alternatively, the thermal energy from
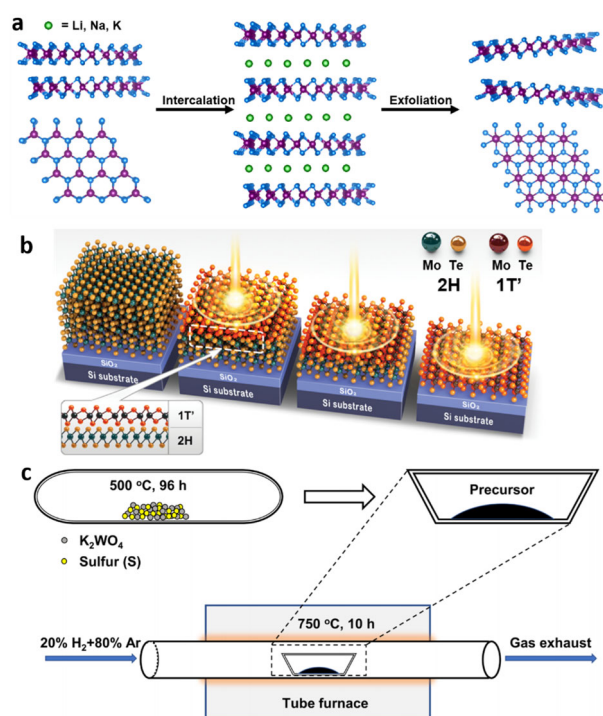
Fig. 9 **(a) Schematic illustration of the intercalation of TMD crystals with alkali metal to exfoliate 2D nanosheets while induce phase transition. Reproduced with permission from Ref. [105], Copyright 2020 Springer Nature. (b) Schematic illustration of laser-induced phase transition of MoTe2 at the top layer. Reproduced with permission from Ref. [381], Copyright 2015 Association for the Advancement of Science. (c) Schematic illustration of the gas-solid reaction for the synthesis of 1T'-WS2 crystals. Reproduced with permission from Ref. [101], Copyright 2021 Springer Nature.**

laser irradiation could induce localized phase transition on TMD nanosheets, which is much favored in electronic devices [381]. It is however worth mentioning that laser irradiation often induces structural defects and thinning effect [372,381], suggesting undesirable burning of the materials to a certain degree.

Other examples of phase transition in TMDs that cannot be generally categorized include mechanical strain applied *via* AFM tips [382] or in a diamond avil cell [383], plasma treatment [384], and surface functionalization [385].

2.5.2.2 Direct synthesis of metastable-phase TMDs

Compared with phase transition methods, the direct synthesis of metastable TMDs is more favored to achieve phase purity for exploration in important fundamental properties. Although several wet-chemical syntheses of metastable TMDs have been reported [386,387], the products generally lack well-defined morphologies and is highly dependent on the underlying substrates which is not ideal for practical applications. On the other hand, the direct synthesis of metastable TMDs crystals has gaining increasing attention due to the high quality of products, representing an important breakthrough in 2D material synthesis. The earliest success in of direct synthesis of metastable TMD crystals dated back to 1992, when Wypych *et*

al. obtained 1T-MoS₂ (the detail crystal phase is unclear due to the limitation in TEM techniques at the time) by synthesizing KMoS₂ and consequently removing the K⁺ from the compound [388]. Upon further improvement on the strategy of solid-state reaction, the synthesis1T-MoS₂ and 1T'-MoSe₂ with high phase purity were recently reported [372]. The high phase-purity enables the resolution of the critical role of crystal phases in electrocatalysis. More recently, Lai *et al*. further reported a general method for the large-scale synthesis of metastable 1T'-phase group-VIB TMDs, using a modified solid-gas phase reaction, as shown in Fig. 9c [101]. More importantly, the high quality of the 1T'-TMD crystals makes it possible to clearly solve the crystal structures of 1T'-MoS₂, 1T'-WS₂, 1T'-MoSe₂ and 1T'-WSe₂ with single-crystal X-ray diffraction.

2.5.3 Phase engineering of other 2D nanosheets

Although the vast majority of PEN-related studies in 2D materials focus on TMDs, the concept is expending to other 2D materials such as 2D noble metal nanosheets, metal oxides [389], Mexene [390] and perovskites [391]. Take noble metal nanosheets for example. The vast majority of noble metals nanomaterials crystalize into face-centered cubit (fcc) phase, same as their bulk counterparts. However, it was found that some thermo-dynamically unstable phases, such as hexagonal close-packed (hcp) phase (2 h or 4 h type) of gold can be stabilized in 2D gold nanosheets and ribbons obtained by phase-controlled wet-chemical synthesis [392–396]. Phase transformation from fcc to hcp can be realized *via* ligand exchange process [393] and electron-beam irradiation [394]. Fig. 10a elaborates the phase transition from unconventional hcp Au square sheet (2 h) to conventional fcc phase *via* ligand exchange process [393]. In addition, the 4H Au nanosheets or ribbons can be used as template to epitaxially grow the other metals in 4H phase such as Pt, Pd, Ag, Ir, and

Cu [395,397]. More recently, a general one-pot wet-chemical method was reported to prepare ultrathin Pd alloy nanosheets with a novel face-centered tetragonal (fct) phase [398].

2.5.4 Amorphous 2D materials

Distinctive from crystalline materials with long-range periodicity, amorphous 2D materials refer to a specific type of nanomaterials with 2D morphology, showing no long-range atomic order. Currently studies in this aspect mainly focused on metal, metal oxides/hydroxides [399] and TMDs. Various top-down and bottom-up methods have been utilized in the controlled synthesis of amorphous 2D materials such as supercritical CO₂-assisted exfoliation in TMDs and wet-chemical synthesis in noble-metal nanosheets. However, the research in this area is still in its infancy and most of the synthetic successes are case specific. Recently, a relatively general synthetic approach was reported for the synthesis of noble metal nanosheets (Ir, Rh and Ru) [226]. In this work, the amorphization is achieved *via* direct annealing of metal acetylacetonates with alkali salt at elevated temperature in air, as shown in Fig. 10b. The amorphous nanosheets show much enhanced performance in electrocatalytic OER compared to their crystalline counterpart. In a more recent study, amorphous domains were introduced into Pd nanosheets in a one-pot wet-chemical method to create amorphous/crystalline phase heterostructures as heterogeneous catalyst in hydrogenation of 4-nitrostyrene [400]. It was found that the amorphous-phase rich Pd nanosheets exhibit high chemo-selectivity while the crystalline-rich ones exhibit high catalytic activity.

2.5.5 X-ray based characterizations on phase engineering in 2D materials

In principle, controlling the phase of a material is accompanied by initial atomic structure, chemical or electronic make-up. Notably, various X-ray-based techniques have been employed to provide edges in understanding phase engineering of 2D materials. Among the plethora, synchrotron-based X-ray absorption spectroscopy (XAS) and angle-resolved photo-emission spectroscopy (ARPES) are often employed to probe the local atomic environment, electronic states and band structure of 2D materials. Thus, we will mainly focus on XAS and ARPES characterizations herein.

2.5.5.1 XAS study on phase engineering in 2D materials

XAS is the X-ray absorption coefficient of an incident X-ray with an energy range of the absorption edge of a target element in a material, thus becomes a valuable tool in studying the local structure near a particular atom of interest [401]. In principle, XAS can be distinguished into the X-ray absorption near edge structure (XANES) and the extended X-ray absorption fine structure (EXAFS), from which structural information such as the chemical bonding, coordination number, site symmetry, and interatomic distances can be extracted [402]. As shown in Fig. 11a, the XANES and EXAFS spectra are demonstrated to provide detailed information on the oxidation state and coordination environment of Mn atom [403], implying that XAS analysis can
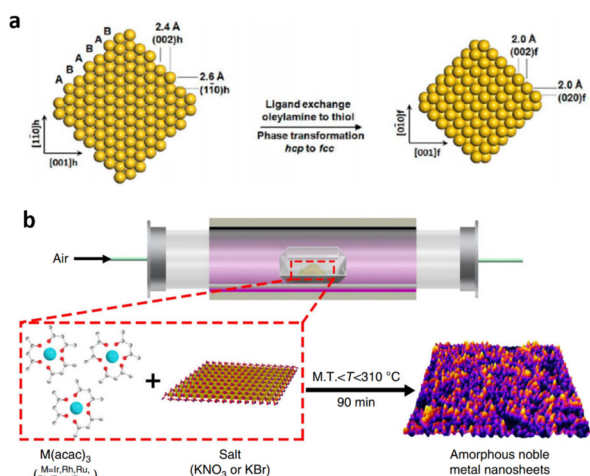
Fig. 10　(a) Schematic illustration of ligand exchange induced phase transformation of Au square sheets from hcp to fcc. Reproduced with permission from Ref. [393], Copyright 2015 Springer Nature. (b) Schematic illustration of the general synthetic process for amorphous noble metal nanosheets. M.T.: the melting point of metal acetylacetonate [226].
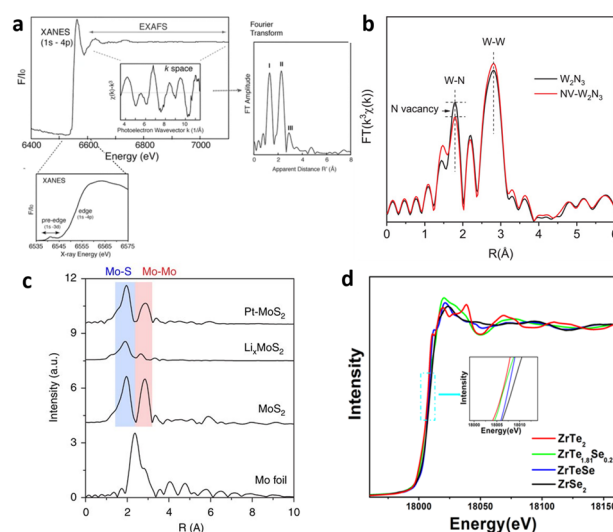
Fig. 11 **(a) The Mn K-edge XANES and EXAFS spectra. Inset (top left) the X-ray absorption spectrum from a sample showing the XANES and EXAFS regions of the spectrum. The enlargements show the Mn K-edge XANES and the *k*-space EXAFS data with the corresponding Fourier transform (shown on the right) [403]. (b) The FT-EXFAS plots of NV-W_2N_3 and W_2N_3. Reproduced with permission from the Ref. [405], Copyright 2019 John Wiley and Sons. (c) k^2-weighted Mo K-edge EXAFS spectra of Pt-MoS_2 in comparison to Mo foil, bulk MoS_2 and Li_xMoS_2 [406]. (d) Zr K-edge XANES spectra of $ZrTe_{2(1-x)}Se_{2x}$ single crystals [407].**

reveal the nature of interaction sites and the structural changes cause by the intercalation or doping process in 2D materials. In fact, XAS can focus on various atomic sites of different atoms in the same compounds with independent absorption signals [404]. For examples, Jin *et al*. utilized XAS to investigate the local coordination of nitrogen vacancies in 2D W_2N_3, as shown in Fig. 11b [405]. Both the pristine and nitrogen vacant samples show the prominent coordination peak at 2.8 Å (1 Å = 0.1 nm), which corresponds to a W—W bonding [405]. Moreover, there is a weakening in the intensity at the W—N bond, with the peak at 1.8 Å of the vacancy-induced sample compared to the pristine sample. This weakening in the W—N bonding intensity shows decreased coordination between W and N and an increase in N vacancies. Chen *et al*. investigated the local bonding environment in Li and Pt intercalated MoS_2 using EXAFS, as shown in Fig. 11c [406]. The EXAFS spectrum of the pristine MoS_2 is consistent with the trigonal prismatic phase; in the spectrum of the Li_xMoS_2 sample, the Mo—S and Mo—Mo bonds peaks appear much weaker in comparison to the pristine. This suggests a change in the site symmetry caused by a phase transition from 2H to 1T' phase. In the Pt_xMoS_2, the K-edge EXAFS spectrum indicates the structure is consistent with the 2H phase [406]. To probe the influence of the Se dopant in the $ZrTe_2$, Zahir *et al*. studied the XANES spectra of $ZrTe_{2(1-x)}Se_{2x}$ single crystals, as shown in Fig. 11d [407]. The Zr K-edges were found to shift to higher energies with an increase in the amount of dopant, showing an increase in the oxidation number of the dopant.

2.5.5.2 ARPES study on phase engineering in 2D materials

ARPES is one of the most essential experimental techniques used to study the electronic bands of solids [408]. Demonstrating the change of phase from a metal to insulator, Han *et al*. report

the surface doped 2H-$MoTe_2$ [409]. As shown in Fig. 12a, they used ARPES to show the emergence of gapped phase indicating a phase transition from metal to an insulator. Zahir *et al*. intercalated Cu atoms into $ZrSe_2$. The introduction of copper into the material facilitated electron doping into the system and induced a phase transition from semiconducting to a metallic phase [410]. As shown in Fig. 12b, the ARPES results in the intercalated samples reveal a conduction band crossing the Fermi level around L high symmetry point in Fig. 12b(iv). Zia *et al*. also demonstrated the use of ARPES to study the phase transition of 2D material from semiconducting to a metallic characteristics [411].

3 Physical properties
3.1 Optical properties

In this part, we will review recent progresses on how various 2D materials interact with light and the related spectroscopic features and optoelectronic functionalities, encompassing a broad range of research topics: absorption, reflection, scattering, emission, light-matter strong coupling and nonlinear optical properties.

3.1.1 Optical absorption

Absorption and reflection spectroscopy have been well-established to probe inter-electronic band transition, exitonic fine structures and lattice anisotropy down to the monolayer limit. For instance, the evolution of electronic band structure (Fig. 13a, b) [412,413] and $1s$ and $2s$ exciton states of E_{11} transition (Fig. 13c) [414] from bulk BP to its monolayer counterpart have been investigated using reflection and IR extinction spectra. Other intriguing properties of excitons like valley effect [415], optical Stark effect [416,417], exciton-phonon coupling [418], linewidth and lifetime coherence [419], transport behavior [420] and
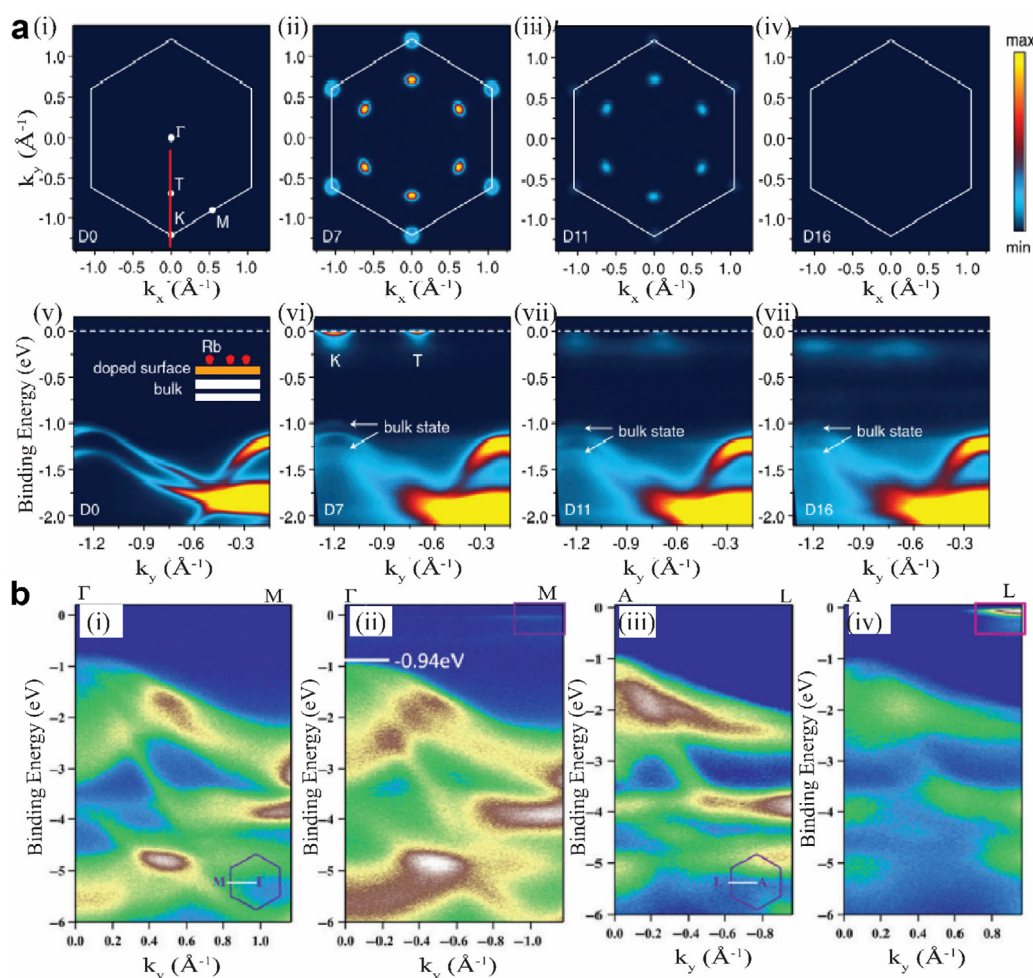
Fig. 12 **(a) Doping evolutions of Fermi surface and band structure in the surface-doped 2H-MoTe₂. (i–iv) Fermi surface mapping taken in the as-grown sample. (v–vi) the energy-momentum cut taken along the G-K direction in the as-grown sample. (ii) and (vi), (iii) and (vii), (iv) and (vii) are the same as (i) and (v). Reproduced with permission from Ref. [409], Copyright 2021 American Physical Society. (b) (i) and (ii) shows the photoemission intensity plots along the G-M direction in the pristine ZrSe₂ and Cu intercalated ZrSe₂ single crystals, respectively. (b) (iii) and (iv) shows the photoemission intensity plots along the A-L direction in the pristine ZrSe₂ and Cu intercalated ZrSe₂ single crystals, respectively [410].**

interlayer exciton absorptions [421–423], are extensively studied. The lattice anisotropy induced polarization dependent optical responses are observed in BP [412,414] and other anisotropic 2D materials [416,424–429]. Furthermore, absorption spectroscopy is a powerful tool to reveal unique excitonic properties modulated by external fields, including dielectric environment [430], electrical filed [421,431,432], and optomechanical fields [433]. There are also continuous efforts and progresses on 2D materials with tailored optical functionalities, such as optical absorbers with tunable polarization [434], wavelength [435–438], and efficiency [439].

3.1.2 Raman scattering

Raman spectroscopy reveals abundant information on spin-phonon couplings, phonon-fingerprints, electron-photon interactions, interlayer couplings, *etc*. For instance, Huang *et al*. reported extraordinarily large magneto-optical Raman effects of A_{1g} phonon 2D magnet CrI₃ due to spin-phonon coupling (Fig. 13d, e) [440,441]. Deep insights are needed on the observation of forbidden Raman modes, including new edge modes related to electromagnetic field distortion of incident and scattered light [442],

acoustic phonons under double-resonance excitation [443] and cross-dimensional electron-phonon coupling between 3D phonons and 2D excitons [444].

Exotic electron-phonon coupling effects attract significant research interest for 2D matters in a strain/electric/plasmonic field. Huang *et al*. investigated size-dependent G-band oscillations originated from optical standing waves of a graphene bubble [123]. Gate-dependent electronic Raman scattering [449] and phonon polarization [450] have been studied. To improve the sensitivity and spatial resolution, tip-enhanced Raman spectroscopy (TERS) are often exploited to study local lattice vibrations [451,452].

3.1.3 Optical emission

Group VIB TMDs are the most attractive 2D semiconductors owing to their extraordinary properties and great potential in novel optoelectronic and photonic applications. With a direct bandgap and strong excitonic effects at the ultimate 2D limit, monolayer TMDs are expected to show high photoluminescence quantum yield (PLQY). However, the PLQY was greatly
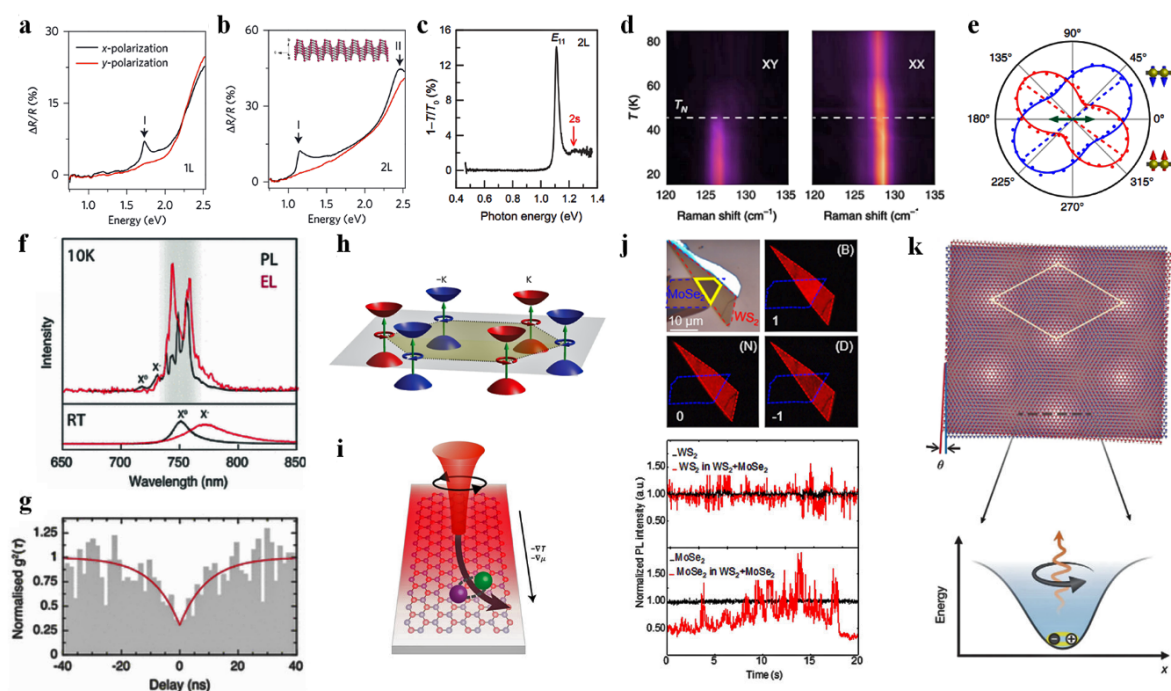
Fig. 13　Reflection contrast spectra of monolayer (a) and bilayer (b) BP [413]. (c) 1*s* and 2*s* exciton states of E_{11} Exciton absorption spectra for bilayer BP [414]. (d, e) Extraordinarily large magneto-optical Raman effects of A_{1g} phonon due to spin-phonon coupling [441]. Single photon emission (f) and photon correlation measurements (g) [445]. Schematics of valley polarization of excitons (h) and the exciton Hall effect in monolayer MoS₂ (i) [446]. (j) Fluorescence blinking effect in a WS₂/MoSe₂ heterobilyer [447]. (k) Schematics of the moiré superlattice and moiré excitons formed in a heterobilayer [448]. (h, i) reproduced with permission from Ref. [446], Copyright 2018 John Wiley and Sons.

constrained below 1% at room temperature by the non-radiative recombination owing to trap states from defects or impurities and inherently enhanced Auger-type exciton-exciton interaction [453,454]. Tremendous research efforts have been devoted to improving the PLQY of TMDs [453–456].

Meanwhile, 2D semiconductors are becoming a unique platform to study many-body physics of excitons. Coulomb interactions among excitons or between excitons and free carriers could facilitate the formation of excitonic complexes, such as charged exciton (trion), biexciton and charged biexciton (or exciton-trion). Several research groups [457–460] have demonstrated independently that individual emission peaks of excitonic complexes can be observed in monolayer WSe₂, and their resonance energy and PLQY can be substantially modulated by applying gate voltages or magnetic fields.

Moreover, when excitons are strongly localized in a point defect or strain field in TMDs, they can serve as quantum light sources to emit single photons [445,461–463]. Fig. 13f, g show that extremely sharp emission peaks of excitons are observed at 10 K in both PL and electroluminescence spectra of monolayer WSe₂. Photon correlation measurements are employed to justify the single-photon nature of these sharp emission. Klein *et al.* [461] show that point defects as single-photon emitters can be controllably introduced into monolayer MoS₂ by irradiating He²⁺ beams. He *et al.* [462] reported that strongly localized biexcitons leads to an emission cascade of single photons. Most interestingly, Chen *et al.* [464] proposed that the entanglement

between chiral phonons and single photons. These intriguing results render TMDs as potential candidates for developing next-generation quantum-optic devices.

Because of the valley degree of freedom in monolayer TMDs, excitons at the *K* and *K′* points in the Brillouin zone are energetically degenerate, but inequivalent, as shown in Fig. 13h, which can directly couple with σ^+ and σ^- circularly polarized light [446,465,466]. Valley-polarized excitons have finite Berry curvatures in Fig. 13i, and therefore are expected to show quantum transport phenomenon analogue to those of spin degree of freedom. Indeed, Onga *et al.* [465] investigated exciton Hall effect in monolayer MoS₂. Excitons at *K* and *K′* valleys after diffusing over a distance of several microns accumulate at opposite directions as evident from polarization-resolved PL mapping. Such transverse splitting indicates the occurrence of the exciton Hall effect in monolayer MoS₂ and are promising for novel valleytronic application in 2D semiconductors.

However, exciton valley coherence time is only on a time scale of ~100 fs which is a tradeoff for strong excitonic effect in monolayer TMDs. The prominent Coulomb force between electrons and holes inevitably lead to a strong intervalley electron-hole exchange effect and ultrashort exciton lifetimes [466–468]. A promising strategy for overcoming this constraint is to construct heterostructures with two TMD monolayers. As a result of a type-II band alignment, electrons and holes can accumulate in different monolayers. Consequently, they can bound together through Coulomb force

to form interlayer excitons (IEs) carrying valley information [469]. IEs show long PL lifetime and valley coherence time on a timescale of ns. In addition, optical properties of IE can be effectively modulated by applying gate voltages or magnetic fields since they have an out-of-plane electric dipole moment [469,470]. With such a long lifetime, IE condensation is experimentally observed with distinct electroluminescence signatures in MoSe2/WSe2 heterobilayers [471].

Over the past few years, tremendous progress and significant breakthroughs has been made in understanding and controlling the interlayer coupling in TMD heterobilayers [447,472–475]. Fluorescence blinking effect was observed in a weakly coupled WS2/MoSe2 heterobilayer with limited overlap of electronic wavefunctions (Fig. 13j) [447]. Periodic superlattices, known as moiré patterns, will form as two monolayers with incommensurate lattice constant or a twist are stacked vertically, as shown in Fig. 13k [448]. For both intralayer and interlayer excitons, their optical properties are substantially influenced by the periodic potential of moiré patterns [472–477]. These so-called moiré excitons show distinct PL emission with valley polarization functionalities and can be fine-tuned by changing the twist angles. For example, Lui *et al.* [478] demonstrated moiré trion in a WSe2/MoSe2 heterobilayer recently.

3.1.4　Light-matter strong coupling and exciton polaritons

Excitons can strongly couple with photons to form new quasiparticles, known as exciton-polaritons, in a hybrid structure of semiconductors and optical cavities. Exciton-polaritons are half-matter and half-light bosonic quasiparticles. They can condense to a single quantum state at high temperature and low density, which can bring quantum effects to a macroscopic scale and provide great opportunities for developing all-optical devices. Thanks to the 2D confinement and large exciton bonding energies with giant oscillator strength, exciton-polaritons based on monolayer TMDs are stable at room temperature promising for practical optoelectronic and valleytronic devices [479]. Zhao *et al.* [480] reported the observation of polariton condensation and lasing with ultralow thresholds in monolayer WS2 microcavity at room temperature (Fig. 14a–d).

3.1.5　Nonlinear optical properties

Nonlinear optics examines the behavior of light in nonlinear media. The photoelectric field generated by irradiation of light will produce optical linear and nonlinear polarization properties [449,450]. Generally, since the intensity of natural light is relatively weak, the resulting nonlinear properties are much smaller than linear optical properties, and the nonlinear optical properties can be ignored at this time. When the light source is changed to a higher intensity laser, the nonlinear optical properties will be observed obviously. Nonlinear absorption and refraction are distinct properties of nonlinear materials [479,481,482], which are widely used in lasers [483], saturable absorbers [484], optical switch, photovoltaic cell [485,486], and many other applications [487–491].

Borophene is a promising nonlinear optical material with both nonmetallic and metallic properties which can facilitate polymorphism in low-dimensional structures. Ma *et al.* [492] studied intriguing nonlinear properties of borophene prepared with the liquid-phase exfoliation method and their potential applications. The broadband nonlinear photonic characteristics of borophene are shown in the Fig. 14. The fundamental mode-locked spectrum in Fig. 14e reveals that the 3 dB bandwidth and central wavelength are 4.2 and 1560.76 nm, respectively and the output power is 1.1 mW. Fig. 14f shows a pulse train within the span of 500 ns with a pulse interval of ~101 ns. The radio frequency spectrum with a resolution of 100 Hz is shown in the Fig. 14g and a strong peak with a signal-to-noise ratio of 63 dB can be observed at 10.09 MHz. Furthermore, Fig. 14h presents the single pulse duration measured by the intensity autocorrelation and fitted by the hyperbolicsecant function, and
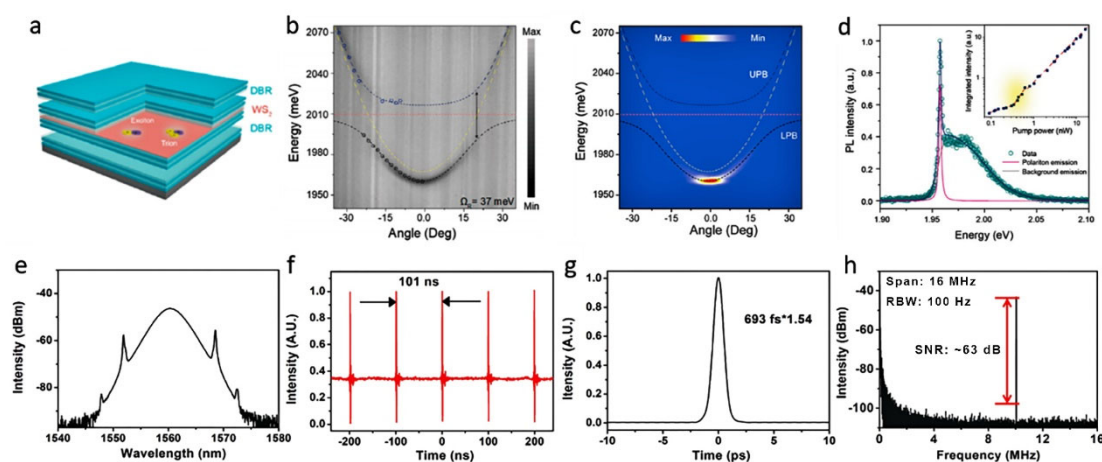
Fig. 14　(a–d) Exciton-polariton condensation and lasing of monolayer WS2 [480]: (a) Sample structure of monolayer WS2 embedded in an optical cavity formed by two DBRs; (b) Angle-resolved reflectivity map of the polariton in a monolayer WS2; (c) Above-threshold angle-resolved PL map; (d) Real space PL spectrum. (e–h) Pulse Q-switching characteristics when the pump power is 263.1 mW [492]: (e) The mode-locked spectrum of borophene; (f) Typical oscilloscope pulse trains of mode-locking; (g) Autocorrelation race fitted by a *sech*² profile; (h) RF spectrum of the mode-locked pulses.

the full width at half-maxima of the pulse is 693 fs.

In the meantime, a variety of emerging materials has been demonstrated with remarkable nonolinear optical properties and applications recently. Shi *et al*. [493] applied black arsenic-phosphorus saturable absorber to passively Q-switched erbium-doped fiber laser for the first time. Tian *et al*. [494] studied the mid-infrared ultra-wideband saturable absorber made of Bi_2O_2Se. Wu *et al*. [495] synthesized a new infrared material, Na_2BaMQ_4, and studied its nonlinear optical properties. Guo *et al*. [496] grew Se on Te nanotubes to construct a Te@Se heterostructure by making use of the instability of light absorption. Saouma *et al*. [497] and several research teams [498,499] studied the nonlinear optical properties of 2D perovskite materials. In addition, MOFs, COFs and graphyne also exhibit excellent nonlinear optical properties [500–504]. 2D layered NMDs have been attracting extensive attention because of their unique nonlinear optical properties [505–508]. Tsang *et al*. [509] studied the nonlinear absorption properties of PtS_2 and demonstrated that it can be used in optical limiters and biosensors. The nonlinear optical properties of MXenes include saturable absorption, nonlinear refractive index, and so on are also comprehensively investigated [510,511].

3.2 Magnetic properties

The discovery of magnetic vdW 2D materials (*i.e.* $Cr_2Ge_2Te_6$ [512,513] and CrI_3 [514]) in 2017 successfully added the fundamental physics — magnetism — into 2D materials. The emergent 2D magnets [513,515,516] not only provide ideal platforms for the experimental study of 2D spin and magnon physics [192,517], but also can couple with disparate electronic, photonic, superconducting and topological materials to create a large influx of new designer heterostructures [518–522]. These new materials and heterostructures have been enabling superior device performances such as the very large tunneling magnetoresistance in graphite-CrI_3-graphite tunneling junctions [523–526].

Due to the strong thermal fluctuations in 2D magnetic systems according to Mermin-Wagner theorem [527], many researchers had long believed that it was unlikely to experimentally realize 2D magnets. Efforts on seeking 2D magnetism have started since the advent of graphene in 2004 and they can be primarily classified into three categories. Firstly, defects including structural imperfections (*i.e.*, vacancies, edges and grain boundaries) and foreign atoms (e.g., adatoms and substitutional doping) [528–532] have been widely applied to create local magnetic moments. Yet, it poses severe challenges to align these local moments to make long-range magnetic order. Secondly, magnetic proximity effect [533,534] has been leveraged by integrating non-magnetic 2D materials with conventional magnetic substrates (e.g., yttrium iron garnet and europium sulfide). This approach can effectively spin polarize the wavefunction of 2D materials [535]. Yet, such extrinsically induced magnetic responses in 2D materials primarily rely on the properties of the non-vdW magnetic substrates, and any potential device developments have to include the proximitized heterogeneous materials as a whole.

Thirdly, flat bands [536,537] have been actively sought in new materials by theoreticians, since the extraordinarily large density of states (DOS) at van Hove singularity potentially causes Stoner instability and itinerant ferromagnetism. However, it leaves great challenges for experimentalists to prepare the required materials at atomic precision or under extreme conditions (e.g., high p-doping in deep valence bands [537]). It is worthwhile to highlight that such flat band related ferromagnetism was recently observed in twisted bilayer graphene and graphene/hBN Moire heterostructures [538,539].

It is always instructive to reflect on the challenges confronted during the course of finding and observing intrinsic 2D magnets. A few important causes couple together. Firstly, there have been no mature theoretical calculation methods to predict Curie temperatures of 2D ferromagnets accurately [512,536]. Even if a first-principles calculation predicted the ground state of a 2D material is ferromagnetic, the absence of precise knowledge on the Curie temperature sets hurdles for experimental exploration. Secondly, many 2D materials in atomic-thinness region are unstable in the air [512,514,540], leading to the substantially degraded properties if samples are not carefully protected. Thirdly, it is difficult to characterize the small amount of magnetization from the atomic-thin micrometer-size magnets. The commonly adopted electrical characterizations of magnetism based on anomalous Hall effect cannot be applied on many 2D magnets that are electrically insulating [541]. Meanwhile, the commonly used bulk characterization techniques such as vibrating sample magnetometry (VSM) is not reliable for 2D flake characterization, since small amount of magnetic impurities or defects in the bulk could bury the true magnetic signal from the 2D flake if any. In contrast, magneto-optical effects [512,514] (e.g., magneto-optical Kerr effect and magnetic circular dichroism) could enable the convenient magnetic characterization of as-exfoliated micrometer-size 2D flakes, no matter samples are electrically conductive or insulating.

The original discovery of 2D magnets were carried out by magneto-optical Kerr microscopy on two magnetic insulators, $Cr_2Ge_2Te_6$ [512] and CrI_3 [514]. Afterwards, metallic 2D magnets such as Fe_xGeTe_2 ($x = 3$, 4, 5, or some non-integer numbers) have been reported [542–547]. Generally, metallic 2D magnets have higher Curie temperatures than insulating 2D magnets. Intrinsic magnetic topological insulators such as $MnBi_2Te_4$ and $MnBi_2Se_4$ [548,549] are another intriguing class of layered magnets that closely link 2D magnetism with topological physics. Though many new 2D magnets were claimed to be synthesized by molecular beam epitaxy or CVD, the adopted VSM-based characterizations are unable to reliably distinguish 2D flakes from bulk substrates.

Magnetism lays the foundation for spintronics and so it is important to develop the electrical control, which means either voltage or current control. In voltage control scheme [542,550–556], one can use voltage to cause electric field or electrostatic doping in 2D magnets. In current control scheme [518,557,558], one usually aims to utilize electrical current to switch magnetization *via* spin

orbit torque. Besides electrical control, many other stimuli have been attempted to control 2D magnetism, including pressure [559–563], chemical synthesis [545], light incidence [564], to name a few. For example, pressure can artificially change the lattice constants of vdW magnets, chemical synthesis [545] can easily modify the elemental concentration and stoichiometry, and optical incidence can cause photo-induced doping in 2D magnets [565], all of which could lead to the effective control of magnetic properties.

There has also been a surge of interest in 2D antiferromagnets. Due to the absence of net magnetization, it is hard to utilize magneto-optical Kerr effect, magnetic circular dichroism and anomalous Hall effect to directly probe antiferromagnetism. Indirect evidence based on the spin-phonon coupling or spin-photon interaction can be acquired. For example, temperature-dependent Raman spectroscopy [566] shows observable changes in peak frequency, intensity or linewidth across the Néel temperatures. Exciton emission [567–569] or second harmonic generation [570,571] may have linear polarization with a certain direction relative to the spin ordering orientation in layered antiferromagnets.

2D magnetic heterostructure is a vital direction that still leaves vast room unexplored. Magnetic proximity effects have been reported when 2D magnets interface with 2D semiconductors [519] or topological insulators [521]. More attentions were paid to the induced effect on the non-magnetic side but not the opposite way (*i.e.*, how the magnetic properties are affected by adjacent materials). When 2D magnets interface with other low-symmetry materials, the proximitized materials [518,519] with further reduced symmetry hold the possibility to generate exotic particles. These prospects appear looming on the horizon and we have many reasons to believe a superlative range of exotic physics and phenomena will be discovered in numerous 2D magnetic heterostructures [572,573].

3.3 Thermoelectric properties

Due to the increasing demand for clean energy and net-zero CO_2 emissions goal, the development of renewable energy technology has never been more critical. Thermoelectric (TE) technology, which enables the direct conversion between heat and electricity, provides a promising approach to achieving sustainable energy production, as shown in Fig. 15a [574]. The TE conversion efficiency is determined by the figure of merit $ZT = \sigma S^2 T/\kappa$, where σ, S, κ, T are the electrical conductivity, Seebeck coefficient, thermal conductivity and absolute temperature respectively. These parameters are all governed by the electronic structure and phonon scattering properties which counteract each other. Great progress has been achieved in 2D materials since Hicks and Dresselhaus predicted that superlattices may show high TE performance based on quantum mechanics [575].

The initial TE superlattice enhancement contains two main strategies [576,577]: (1) the quantum-confinement forms a unique step-like shape DOS which contributes to S enhancement and decoupling between S and σ; (2) a new kind of Umklapp process, which is confined in a small Brillouin zone due to the finite thickness and large superlattice constant, is introduced by quantum-confinement, creating preferential interface scattering for phonons than electrons. The development of these concepts has successfully promoted ZT of superlattice above 2. However, the complex fabrication technology limits the superlattice's application. To address this problem, researchers start to pay attention to bulk materials with superlattice-like 2D structures, as shown in Fig. 15b.

Like superlattice, TE materials with 2D structures possess superior charge and phonon transport compared with conventional bulk materials with 3D structures (such as cubic structure), *i.e.*, high S and low κ. However, the underlying mechanisms are very different from superlattices. Since bulk materials with 2D structures are macroscopically 3D and microscopically 2D, quantum confinement is no longer applicable. Instead, complex band structure (none-single parabolic band edges) and strong anharmonicity play critical roles in charge and phonon transport, as shown in Fig. 15c. The complex band structure derives from the anisotropic bonding conditions, leading to anisotropic effective mass (m^*) along different crystallographic directions. Generally, the in-plane direction has smaller m^* than the out-of-plane direction, indicating higher carrier mobility (μ) along the in-plane direction. More importantly, complex band structures projected by 2D crystal structures enable an effective approach to enhancing S, because the multiple band edges with a small energy offset of several $k_B T$ could simultaneously participate in
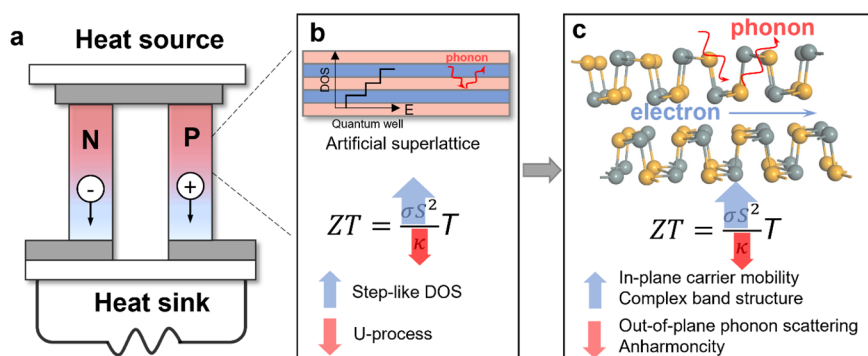

Fig. 15 **Schematic of (a) thermoelectric module, (b) electrical and thermal transports in a given superlattice structure;**
(c) advanced thermoelectric parameters are also elucidated in the bulk materials with a layered structure.

the charge transport [578,579]. As for the phonon transport, due to the different anisotropic chemical bondings between the in-plane and out-of-plane, 2D structures can be regarded as adjacent layers with different electromagnetic properties. Accordingly, low κ could be obtained in the in-plane direction due to the strong anharmonicity, which has been extensively observed in 2D materials, originating from lone pair electrons [580], resonant bonding [581], rattling model [582], *etc*. Moreover, phonons with high frequency are also severely scattered along the out-of-plane direction than the in-plane direction, leading to lower κ.

Here we choose SnSe as an example to give a brief review of advanced TE performance in 2D materials. SnSe crystal has a distorted rock-salt structure, as shown in Fig. 16a. Each Sn atom is bonded with seven Se atoms to form a highly distorted SnSe7 coordination polyhedral with strong Sn—Se bonding within *a* and *b* axis and weak Sn—Se bonding along the *c* axis. Additionally, a lone electron pair of Sn^{2+} is sterically accommodated between the weak Sn—Se bonds. The unique chemical bonding conditions lead to a 2D structure with two-atom-thick SnSe slabs, which is the foundation of the outstanding TE performance in SnSe with low κ and high σS^2. The low κ in SnSe originates from the strong anharmonicity due to the ferroelectric-like lattice instability [583]. The DFT calculated Grüneisen parameters (γ), an indicator of anharmonicity, are all very high, reaching 4.1, 2.1, 2.3 along the *a*, *b*, *c* axis, respectively. Inelastic neutron scattering measurements also reveal significant phonon dispersion softening in both transverse acoustic and transverse optical phonons propagation (Fig. 16b), in accordance with high γ. TA modes are considerably softer along the Γ–*X* direction than that along Γ–*Y*, in line with the weaker bonding along the out-of-plane direction and the corresponding highest Grüneisen parameter. As a result, low κ is expected according to the relation $\kappa \propto \gamma^{-2}$ [584]. On the other side, the anisotropic crystal structure leads to the complex

electronic band structure in SnSe, as shown in Fig. 16c. The first valence band maximum (VBM1) lies in the Γ–*Z* direction, alongside which lies another VBM2. Moreover, VBM3 lies in the *U*–*X* direction within a narrow energy offset of ~0.13 eV [578]. As for the conduction band minimum (CBM), there are also two CBM with an energy offset of ~0.1 eV [585]. The complex band structure in valence/conduction bands facilitate multiple-bands transport when Fermi level is pushed toward CBM or VBM, leading to enhanced m^* and thus high S. Moreover, the energy offset even exhibits complex temperature-dependent behaviors [579], as shown in Fig. 16d. The dynamic band structure enables the wide-range optimization of $\mu m^{*3/2}$, therefore high σS^2. The complex band structure has been confirmed by angle-resolved photoemission spectroscopy (ARPES) [586], Fig. 16e reveals two distinct VBMs along Γ–*Z* and Γ–*Y* direction, corresponding to VBM1 and VBM2 in DFT calculations. By fitting the dispersion slope, the effective mass can be extracted. It can be seen that dispersions along Γ–*Z* are flatter than Γ–*Y*, indicating larger *m* along the out-of-plane direction than the in-plane direction.

Besides SnSe, many other TE materials, such as Bi_2Te_3 [587], BiCuSeO [588] and $NaCoO_2$ [582], also exhibit excellent TE performance, benefiting from theoretical and experimental achievements in 2D structures. Even though different crystal structures need to be taken into consideration when it comes to a specific 2D material, the common features of 2D materials, complex band structure and strong anharmonicity, are the most fundamental aspects contributing to the high TE performance. It is very likely that continued investigations on 2D materials will further improve their TE performance, including intercalation, bilayer mismatch, vacancy and so forth.

3.4 Ferroelectric properties

The research topics of 2D ferroelectricity have been explored on the theoretical predictions and experimental developments in
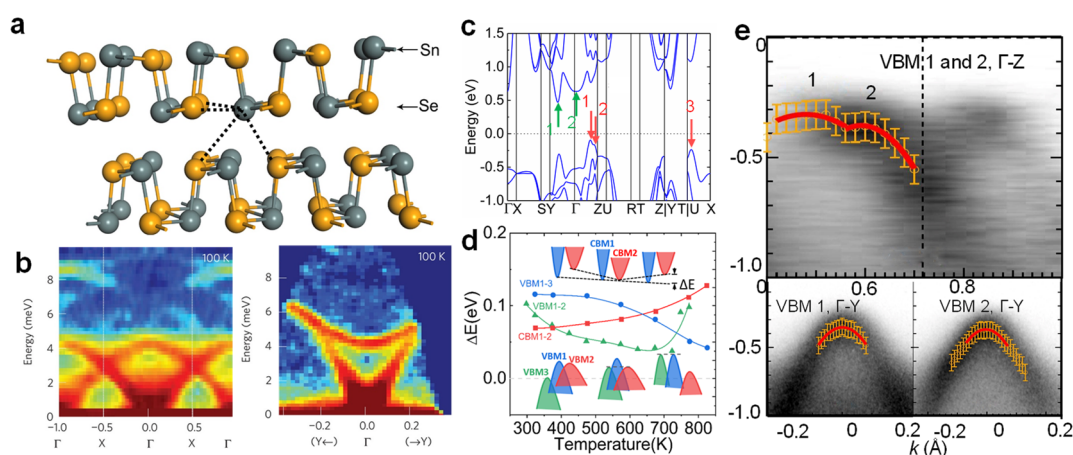
Fig. 16 **(a) Crystal structure of SnSe. (b) Phonon dispersions measured by inelastic neutron scattering; reproduced with permission from Ref. [583], Copyright 2015 Springer Nature. (c) Band structure of SnSe, green arrows (1, 2) indicate the conduction bands, red arrows (1, 2, 3) indicate the valence bands. (d) Temperature-dependent energy offset in the valence band and conduction band, which enable the high electrical performance through reasonable manipulating band structures. (e) Valence band structure measured by angle-resolved photoemission spectroscopy. Reproduced with permission from Ref. [586], Copyright 2016 American Physical Society.**

many systems since last century, including the ultrathin inorganic perovskite oxide and organic fluoride-based polymer systems [589,590]. The key scientific question of 2D ferroelectricity is to reduce the influence of the suppression for spontaneous polarization from depolarization fields, thus raising a fundamental question whether there is a critical thickness for all of ferroelectric behaviors [591]. As the rapid development of various growth technologies, the critical thickness has been pushing towards the thickness of sing-unit cell limit in the PVDF, $BiFeO_3$ and $YMnO_3$ films, which indicate the upcoming bloom future of 2D ferroelectricity [589,590,592,593]. Very recently, the discovery of emerging 2D ferroelectrics have experimentally and theoretically demonstrated that the stable and switchable electrical polarization could be observed in a lot of atomically-thin layered and non-layered films, thus giving the possibility of fabricating polarization-dependent electronic and optoelectronic devices even at monolayer limit [593]. The low-density dangling bonds and defects density at the surfaces of vdW materials render a rise of 2D ferroelectricity, which could provide relatively inert and stable surfaces to stabilize the electric polarizations. Essentially the chemical bonds of 2D ferroelectrics are normally shown with local covalent bonds

other than the long-range interactions for the traditional perovskite oxides, therefore the surface charge accumulated depolarization fields have been confirmed with rather weaker strength that are not enough to suppress the electric polarization.

Layered group IV-VI materials, especially for the group IV monochalcogenides MX (M = Sn, Ge; X = S/Se) and tellurides (MTe), have been predicted to possess intrinsic in-plane ferroelectricity in the monolayer limit, due to their low-level crystal symmetry [594–596]. In 2016, Chang *et al.* discovered unconventional ferroelectricity in the molecular beam epitaxial grown atomic-thick SnTe, in which the Currie temperature of one-unit cell SnTe film are 270 K and much higher than that of the bulk states (98 K) (Fig. 17a–c) [597]. Nagashio *et al.* reported the purely in-plane 2D ferroelectricity for monolayer SnS obtained from physical vapor deposition, in which the odd-even effects are distinguished and the critical thickness are explored with 15 layers [598]. The clear ferroelectric switching phenomena is founded in the in-plane few-layered SnS nanoflakes devices [598]. More interestingly, Bao *et al.* observed the gate tunable ferroelectricity in the MBE grown few-layered SnS nanoflakes (Fig. 17d–f) [599]. Some more intriguing theoretical calculations give out the interesting physical properties such as
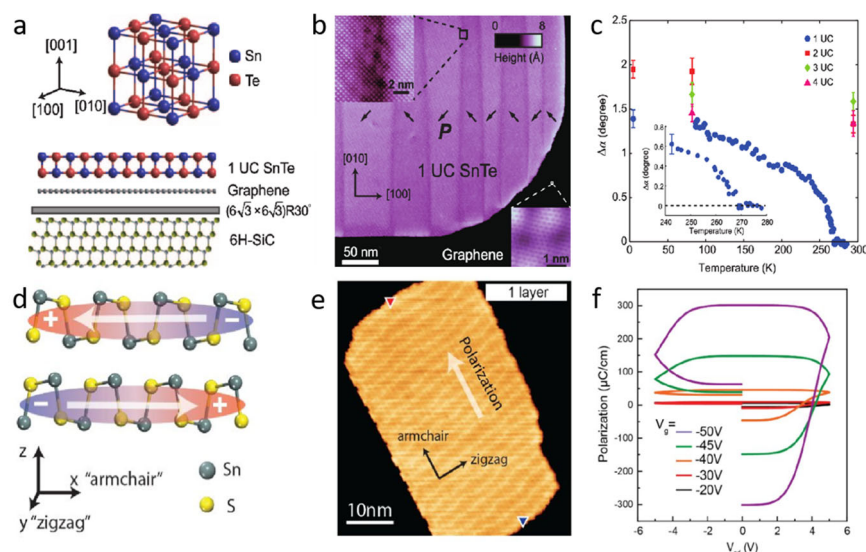
Fig. 17 **(a) Schematics of the SnTe crystal structure (upper) and the SnTe film (lower). (b) The stripe domain of a1-UC SnTe film (imaging conditions: −0.2 V, 30 pA, 4.7 K). The arrows in each domain indicate the direction of lattice distortion. (Upper inset) Topography image across a domain boundary (−0.2 V, 100 pA). (Lower inset) The graphene substrate (−0.1 V, 200 pA). (c) Temperature dependence of the distortion angle for the 1- to 4-UC SnTe films. (Inset) The distortion angle near T_c = 270 K for the 1-UC film exhibiting the behavior of a second-order phase transition. (d) Schematic side view of a bilayer SnS structure. Each SnS layer is ferroelectrically polarized with a net dipole moment aligned with the *x*-axis. Adjacent SnS layers are anti-ferroelectrically coupled due to the inversion symmetry in the AB-stacked structure (top panel); Schematic view of the wedding-cake morphology of MBE-grown SnS crystals, which are inversion-symmetry broken with non-zero net polarizations at the terraces (bottom panel). (e) (left) STM image of one ML SnS island with the nanoripple pattern. The in-plane armchair and zigzag directions are determined from the lattice constants and marked by the black arrows. The net ferroelectric polarization of this island, determined by the LCPD measurements, is marked by the white arrow. (right) Frequency shift measured as a function of the voltage, collected above the two edges marked by red and blue triangles respectively. Measurements are performed in constant-height mode after compensating the surface tilting and thermal drifting effects. Parabolic fits and corresponding parabola peaks are indicated. (f) The corresponding *P-V* hysteresis curves of the memory device at different gate voltages. (a–c) Reproduced with permission from Ref. [597], Copyright 2016 American Association for the Advancement of Science. (d–f) Reproduced with permission from Ref. [599], Copyright 2019 American Chemical Society.**

photostriction induced by an inverse piezoelectric effect, selective valley excitation and persistent spin currents [594,596,600]. Chang *et al.* also observed the robust ferroelectricity with microscopic domain structure and a critical temperature of 400 K in SnSe monolayer by the scanning tunneling microscopy [601]. The large-scale synthesis of high-quality monolayer group IV monochalcogenides MX is still very difficult for multiple applications due to the strong interlayer interaction that could benefit the growth in the vertical direction [602]. Meantime multiferroic states of monolayer group IV monochalcogenides also have been predicted by the theoretical calculations.

Bulk layered metal thio- and seleno-phosphates (MTPs) originally crystallize in the crystal structures with inversion symmetry, in which metal cations and the framework of $[P_2S(Se)_6]^{4-}$ bonds in the in-plane layers and form VDH structures [603]. These family materials are discovered in the late 1800s by Friedel and Ferrand, which have later been extensively explored with ferroic ordering including ferromagnetic, antiferromagnetic and ferroelectric properties. Very recently, size-effect in one of layered MTP material, $CuInP_2S_6$, has been discussed for the possible ferroelectricity under the monolayer limit. Both Maksymovych and Kalinin groups reported the switchable polarization could be suppressed below the thickness of 50 nm, in which the ferroelectricity disappears at the thickness of 10 nm [604,605]. On the contrary, Liu *et al.* reported the nanoflakes show clear hysteresis loops down to the thickness of 4 nm, in which the polarization dependent diodes are shown the superior performance with the current on/off ratio ~100 [606]. Furthermore, Deng *et al.* found the critical thickness for in-plane ferroelectricity of $CuInP_2S_6$ should be between 90 and 100 nm [607]. The out-of-plane ferroelectricity of ultrathin $CuInP_2S_6$ nanoflakes seems like still under debate, in which the key questions are from polarization screening and interfacial chemistry. However, from the views of the device's application, it is clear that the ferroelectric fields of ultrathin MTPs plays an important role in affecting the carriers' transport.

Wu *et al.* reported the tunable barrier height by the ferroelectric polarization in the asymmetric chromium-$CuInP_2S_6$-graphene devices could be high as 1 eV, thus achieving the tunneling electro-resistance of above 10^7 [608]. Wang *et al.* reported a negative capacitance transistor based on the multilayer MoS_2 and ferroelectric $CuInP_2S_6$ (20 nm) heterostructures, which shows with a minimum subthreshold swing of 28 mV·dec^{-1} and negligible hysteresis thanks to the NC effect of CIPS that strongly correlated to interface ferroelectric domain switching [609]. Niu *et al.* also presents the pyroelectricity of CIPS could be clearly seen at bilayer samples, where the pyroelectric nanogenerators also has been fabricated to convert the thermal induced charges into electric currents [610].

Ding *et al.* firstly predicted the intrinsic in-plane and out-of-plane ferroelectricity for the zincblende and wurtzite structured In_2Se_3 (α-phase) and other III$_2$-VI$_3$ VDH materials (Al_2S_3, Al_2Se_3, Al_2Te_3, Ga_2S_3, Ga_2Se_3, Ga_2Te_3, In_2S_3 and In_2Te_3) by the first-principles DFT calculations [611]. The origin of ferroelectricity has been interpreted as the Se atom's displacement in the vertical direction, which also could arouse the intercorrelated lock-in in-plane switchable polarization [612]. Based on the exfoliated and vapor-phase grown α-In_2Se_3 nanoflakes, Zhou *et al.* have clarified the vertical displacement of Se atoms by the atomically-resolution TEM imaging and revealed its space group as R3m for the first time, and confirmed the noncentral-symmetry by second Harmonic generation and switchable electrical polarizations by piezoelectric force microscopy [612]. Subsequently, several groups independently reported the layer-dependent ferroelectricity on In_2Se_3 nanoflakes even at the monolayer limit, in which the Curie temperature T_c, the coercive filed E_c and the piezoelectric coefficient were determined with 700 K and 200 kV·cm^{-1}, 0.34 pm·V^{-1}, respectively [613]. Then the ferroelectricity of α-In_2Se_3 nanoflakes has applied in the ferroelectric semiconductor field-effect transistor (FET), tunneling electro-resistance junction devices, neuromorphic computing devices and strain sensing devices [614–616]. Other groups also reported either in-plane ferroelectricity or antiferroelectricity on the other polymorphs of In_2Se_3 nanoflakes [617–620].

The first prediction for 2D ferroelectricity was proposed in the T_d phase MoS_2 monolayer [621]. Traditionally only insulators could be considered as the ferroelectrics and the ferroelectric metal are very rare, because the high concertation of electrons in metals or semimetals should screen the external electric fields and the polarization between ions. However, it is quite interesting that the direct evidence of switchable electrical polarization has been confirmed in the semi-metallic and metallic 2D materials [622,623]. Fei *et al.* has differentiated the polarization switching of two or three-layer WTe_2 by the
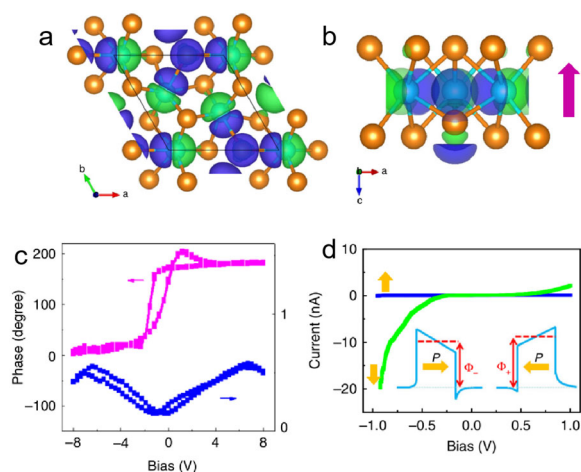
Fig. 18　(a, b) Top-view and side-view of charge density difference between ferroelectric MoTe₂ *d*1T and paraelectric 1T phases (green, purple, cyan, orange, and pink colors denote negative charge, positive charge, Mo atom, Te atom, and polarization, respectively); (c) PFM phase hysteretic and butterfly loops of monolayer *d*1T-MoTe₂; (d) *I–V* characteristic of monolayer *d*1T-MoTe₂ on Pt and inset shows the energy diagram of ferroelectric tunneling junction devices [616].

conductivity measurements using graphene as an electric gate electrode, while the monolayer WTe2 nanoflakes does not observed the electric hysteresis loops due to the nonpolar crystal structure [622]. All of the above results confirm that the electric field could penetrate through the ultrathin 2D polar metal to switch the electrical polarization and indicate the possibility for the integration of ferroelectricity into other physical properties and multiple functional devices [622]. As shown in Fig. 18, in the meantime, Yuan *et al.* discovered the out-of-plane ferroelectricity in single-layer 1T' MoTe2 at the room temperature (Fig. 18c), in which the origin of symmetry breaking is from the relative atom's displacement of Mo and Te atoms [624]. Recently, unconventional 2D bilayer Bernal-stacked graphene and boron nitride moiré heterostructures were explored with switchable ferroelectricity, which is attributed by the introducing superlattice potential from the moiré patterns and shows the hysteretic resistance behaviors [625]. The new ferroelectricity mechanism of unconventional, odd-parity electronic ordering in the bilayer graphene/boron nitride moiré system has been clearly understood [625]. The emerging of 2D ferroelectric materials not only show us much more rich physical pictures, but also give us the potential opportunities for the high-density polarization controlled functional devices, therefore which apparently raise the important requirements for the large-scale ferroelectric phase-controlled synthesis [626–628].

3.5 Superconductivity

The emergence of superconductivity in 2D materials has attracted tremendous research interests because of the presence of unprecedented physical properties. With the first discovery of superconductivity in Hg at 4.15 K, the intriguing phenomenon has been observed in many other systems. At extremely low temperature (less than 40 K), the superconductivity can be well explained by the Bardeen-Cooper-Schrieffer (BCS) theory [629], in which the famous "Cooper pair" plays an essential role. However, this theory fails to explain the high-temperature superconductivity (higher than 40 K). Owing to the emerging 2D superconductors, researchers can study the intriguing superconductivity at the 2D limit with possible tunability, both experimentally and theoretically, which could provide new clues in high-temperature superconductor research. In this section, we review recent advances in the field of 2D superconductors with unique characteristics. We first discuss the 2D superconductors that can be explained by BCS theory, in which some distinguishing properties such as Berezinskii-Kosterlitz-Thouless (BKT) transition [630], charge density wave (CDW) phase [631], and Ising superconductivity [632] will be introduced. Next, we review the field of 2D high-temperature superconductors, including Fe-based and Cu-based 2D superconductors. Finally, we review the unconventional superconductivity in moiré superlattices.

3.5.1　BCS 2D superconductors

BCS theory [629] describes the "Cooper pair", paired electrons through the electron–phonon interactions, which can be used to explain superconductivity below the McMillan limit. With advances in fabrication techniques, such as MBE and mechanical exfoliation, researchers can now access the superconductivity in 2D materials. Fortunately, the BCS theory is still applicable in many 2D superconductors, such as metallic thin films and TMDs materials. Nevertheless, there are still many unique properties emerging in these 2D BCS superconductors. In particular, the BKT transition, a topological phase transition derived from symmetry broken in terms of the vortex, can be treated as the signature of a 2D superconducting transition [630]. It is worth noting, apart from the superconducting phase, that there are many other phases observed with the variation of physical parameters in 2D superconductors. Among them, the CDW phase, a periodic modulation of electronic densities induced by the lattice distortion, is one of the most investigated in 2D superconducting systems. Prototypical systems include NbSe2 and TaS2 materials [631,633]. Understanding the relationship between the superconducting phase and CDW phase is important for understanding the underlying mechanism of superconductivity. However, there are still debates about their relationship [634], *i.e.*, whether it is cooperative, co-existing, or competitive. Thus, further experiments and theoretical calculations are still needed.

Considering that the time reversal and spatial inversion symmetries are preserved in BCS theory, new superconducting properties can emerge by breaking inversion symmetry. Particularly, in a non-centrosymmetric superconductor with strong spin–orbit coupling (SOC), a unique Ising superconductivity has been proposed and experimentally verified in the NbSe2 system [632]. Furthermore, type-II Ising superconductivity was recently proposed without the participation of inversion symmetry breaking, where spin-orbit locking is suggested to play a critical role [635]. This type-II Ising superconductivity has been verified [636] in few-layer stanene in 2020. It is important to mention that the quantum transition phases [637–639], *i.e.*, quantum metallic ground state, quantum Griffith singularity phase and enhancement of the Pauli limit, have also been intensively investigated at extreme conditions, such as at extremely low temperature and large magnetic field.

3.5.2　2D high-temperature superconductors

Extremely low temperatures are required in BCS superconductors, which poses the main obstacle for device applications. Thus, the search for high-temperature superconductors is definitely important. Since the discovery of Cu-based high-temperature superconductors in 1986 and Fe-based superconductors in 2008, this field has received much research attention. However, conventional BCS theory fails to explain the high-temperature superconductivity. In this case, high-temperature superconductors at the 2D limit could function as a new platform with fine tunability to investigate the underlying mechanism of superconductivity.

As for Fe-based 2D high-temperature superconductors, FeSe on SrTiO3 heterostructure is one of the most investigated

systems [640]. Notably, only MBE-grown FeSe monolayer on SrTiO₃ substrates displays high-temperature superconductivity with a transition temperature (T_c) of 60–100 K, in which the interfacial electron-phonon interaction between the monolayer FeSe and the underlying SrTiO₃ substrate plays an import role in this unique high-temperature superconductivity. However, with the increasing number of layers, the T_c drops rapidly and no longer behaves as a high-temperature superconductor. Thus, it is believed that the monolayer FeSe/SrTiO₃ heterostructure system is significantly different from previously investigated bulk Fe-based high superconductors.

To date, most bulk Cu-based high-temperature superconductors are limited to the $Bi_2Sr_2CaCu_2O_{8+x}$, $La_{2-x}Sr_xCuO_4$ and $YBa_2Cu_3O_{7-x}$ systems. Previous studies demonstrated that the high-temperature superconductivity is lifted when the bulk materials were exfoliated down to few monolayers. In fact, it is caused by the degradation of the exfoliated samples under ambient conditions. Recently, monolayer Bi-2212 with good conditions [641] (here, the monolayer refers to a half unit cell that contains two CuO₂ planes) has been successfully prepared on a cold stage, which was kept at −40 °C, inside an Ar-filled glove box with water and oxygen content below 0.1 ppm. Most importantly, monolayer Bi-2212 features all the fundamental physical attributes of a high-temperature superconductor, e.g., pseudogap, charge order and the Mott insulating state. Therefore, the monolayer Bi-2212 can serve as an ideal platform to study its high-temperature superconductivity and other strongly correlated phenomena.

In this section, we have given a short and simple understanding of the recent developments in 2D superconductors, which may stimulate further studies in the area and other strongly correlated systems.

3.6　Magic-angle 2D superlattices

As the thickness of graphene increases, the electronic band structure of graphene would be modified under the influence of interlayer coupling. When two graphene layers are stacked together, rotation between layers would enable the production of moiré superlattices, and the moiré pattern period would be determined by the rotation angle. Therefore, by altering periodicity of moiré superlattices accordingly, the rotation angle can produce a significant impact on the electronic band structures and properties of twisted bilayer graphene [642]. In this aspect, in the presence of a small twist angle, the strong interlayer coupling will induce the dramatic changes in the low-energy spectrum. As predicted theoretically in 2011 [642], when the twist angle is close to a discrete set of magic angles (1.05°, 0.5°, 0.35°, 0.24°, and 0.2°), the Fermi velocity vanishes at the Dirac cones, and the lowest moiré band flattens with an enhanced counterflow conductivity (Fig. 19a). With slow movement, electrons would be localized in the superlattices, which would cause the strong correlation in magic-angle superlattice. However, after its initial prediction, it was not until the sensational discovery by Cao *et al.* in 2018 [107,108] that the

experimental observation of strongly correlated physics in magic-angle twisted bilayer graphene (MATBG) was achieved. The fabrication of MATBG devices with uniform twist angle is an important issue that needed to be addressed before the real experimental progress in MATBG. The accurate control over twist angle is the prerequisite to fabricate MATBG devices, which was achieved by the "tear and stack" approach, reported by Kim *et al.* and later Cao *et al.* [643,644]. In detail, after tearing a monolayer graphene single crystal into two pieces using h-BN stamping method, the stamp with one piece of graphene would be subsequently used to pick up the other piece on the substrate after rotating the substrate by 1.1° (Fig. 19b). Another issue is how to avoid the further interlayer rotation of MATBG to form the most energetically stable configuration, AB-stacked bilayer graphene (zero-twist angle stacking of bilayer structure). To achieve this, the fabrication of MATBG devices should avoid high temperature, the formation of bubble between two graphene layers, and the additional strains. Note that, CVD approach, which is suitable for the production of graphene films on a large scale, is also capable of growing twist bilayer graphene [645]. However, it remains difficult to produce twist bilayer graphene with fine control over twist angle, especially the magic angle near zero, owing to the overwhelming stability of AB-stack bilayer graphene. Recent progress in the synthesis of wafer-sized graphene single crystals by CVD approaches also provides an alternative route to fabricate MATBG on large scale, the vertical stacking of wafer-sized single crystals with a controllable rotation angle (magic angle) [209].

By successfully fabricating the MATBG devices, Cao *et al.* experimentally confirmed that when the twisted angle is close to the magic angle, the band structure near the Fermi level would become flat, as theoretically predicted [107,108]. At around 4 K, metal-insulator transition was also observed at half filling of the flat moiré band, indicating the Mott-like insulator behavior and the presence of strong interlayer electrons coupling in MATBG (Fig. 19c). Surprisingly, in the temperature-carrier density phase diagram, there exists superconducting domes flanking the Mott insulator states at low temperature (< 2 K), when tuning the Fermi level away from the charge neutrality to be near half-filling of the moiré band (Fig. 19d). The superconducting states were observed both in the MATBG devices with twist angle of 1.05° and 1.16°, in which the critical temperature of 1.05° MATBG device (1.7 K) is higher than that of 1.16° MATBG device (0.5 K). The phase diagram is similar with the superconducting states that flanks Mott states in the unconventional superconductors. The other evidence confirming the similarities between MATBG and unconventional superconductor is the observed linear-in-temperature resistance at higher temperature [648]. The superconducting behavior occurs in low carrier densities, which is significantly lower than those of other 2D superconductors. This makes the MATBG promising for the investigation of strongly correlated physics. It should be also noted that, the nature of the superconducting states remains
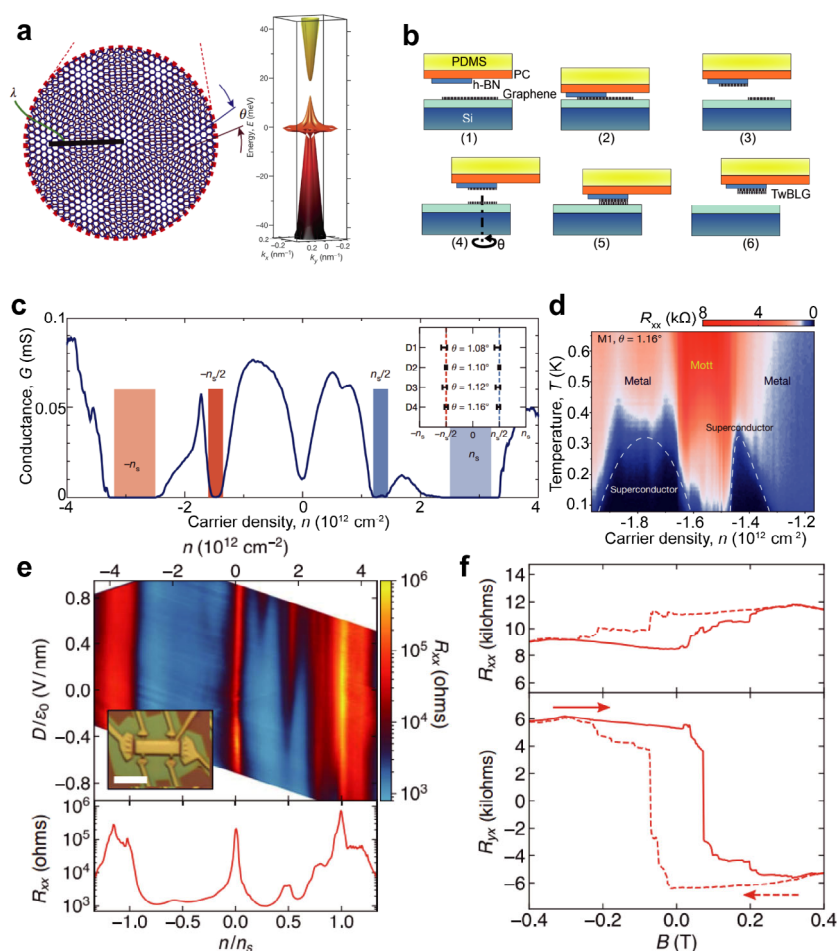
Fig. 19 **(a) The moiré patterns formed in the twisted bilayer graphene (left). The calculated band energy of the twisted bilayer graphene with twist angle of 1.05° using an *ab initio* tight-binding method (right) [646]. (b) Schematic illustration of the "tear and stack" approach for fabricating the MATBG; (c) measured conductance of MATBG device with a twist angle of 1.08° at the temperature of 0.3 K, the lighter-shaded regions denote the locations of superlattice gaps, while the darker-shaded regions highlight the half-filling states; (d) measured Resistance as function of temperature and carrier densities of the MATBG device with twist angle of 1.08°; (e) measured R_{xx} as function of carrier density and perpendicular displacement field (D) (Top), inset: the OM image of as-fabricated MATBG device, line cut of R_{xx} as function of carrier density at $D/D_0 = -0.22$ V·nm^{-1} (bottom); (f) magnetic field dependence of R_{xx} and R_{xy} with $n/n_s = 0.746$ (three-quarter filling) and $D/D_0 = -0.62$ V·nm^{-1} at 30 mK, the solid and dash line correspond to the results measured while sweeping the magnetic field up and down, respectively [647].**

unresolved and needs further investigations.

Afterwards, through the investigation of MATBG by STM and STS [649], the changes in DOS caused by the formation of superlattices and charge distribution at different filling of moiré band were clearly visualized. In detail, a pseudo-gap phase was observed at partial-filling of the flat band, which is consistent with high-temperature superconductors. In addition, without the formation of a perfect twist angle, it is still possible to achieve the superconducting states by applying hydrostatic pressure, which can reduce the interlayer spacing [650].

Beyond the twisted bilayer graphene, superconducting states and correlated insulator were also observed in ABC-trilayer-hBN moiré superlattices, in which a vertical displacement field enabled the formation of flat band by breaking the inversion symmetry and isolating the moiré band [651,652]. In twisted AB-stacked bilayer structure with magic angle, the similar correlated insulating states were achieved by several research groups [653,654],

and in contrast with MATBG, there was residual resistance after the superconducting-like transition. Recently, displacement field-tunable superconductivity with a maximum critical temperature of 2.1 K was realized in the heterostructure composed of three graphene layers that were stacked with alternating twist angles of 1.56° [655].

After the observation of the superconducting states in MATBG, Sharpe and coworkers [538] reported the observation of stable ferromagnetism in MATBG when the moiré unite cell is three-quarters filled. The longitudinal and Hall resistance as functions of carrier densities or vertical displacement field exhibited several additional resistance peaks at the filling of 1/4, 1/2 and 3/4 (Fig. 19e). Only at the three-quarters filling region, in the magneto-transport results, the resistance exhibited a hysteretic behavior under the external magnetic field (Fig. 19f). Although the hysteresis can be observed over a wide range of displacement field, it should be noted that, it only appears near

the three-quarters filling of the conduction moiré band. In addition, this ferromagnetism is sensitive to the current direction, enabling the formation of hysteresis loop between ±50 nA dc bias. Later, well-developed quantum anomalous Hall effects was observed in the MATBG system, in which the quantum anomalous Hall effects should be the result of ferromagnetic topological insulator (Chern insulator) [656].

The advent of MATBG-based research has already brought many exciting breakthroughs and discoveries in the scientific community. The future research might focus on the construction of theories to understand the nature of superconducting behaviors of MATBG. It would also be promising that we can produce new superlattice using other emerging 2D materials, including 2D superconductors and 2D magnetic materials.

3.7 Chirality

3.7.1 General concepts of 2D chirality

Chirality is a basic property of nature and exists at various scales from subatom to molecule, supramolecule, nanoscale, macroscale and even to the galaxy [657]. The chirality at a molecular level is strongly related to the biological structures and functions which controls the DNA duplication and protein folding as well as enzymatic catalysis. Thus, the synthesis of chiral molecules, drug discovery and the understanding of their interaction with the biological systems has long been the main topic of chirality research. On the other hand, chiral molecules can rotate the polarization plane of light when the light passes through the substance, thus leading in a series of unique new properties in materials. Therefore, a deep understanding of chirality at the molecular to nanoscale level will add new values of chirality to the materials. For example, the chirality of the carbon nanotube determines their metallic or semi-metallic properties. Accordingly, when chirality meets 2D materials, many new chirality-related issues would emerge. The integration of chirality will endow 2D materials with advanced chiroptical properties including electronic/vibration circular dichroism (ECD/VCD), Raman optical activity (ROA), circularly polarized luminescence (CPL) and so on. These properties not only provide new insights into the material chirality but also afford potential functional applications. This has been well exemplified by the recent achievements in the syntheses of chiral 2D materials and application developments in the fields of chiral recognition/sensing, asymmetric catalysis, enantioselective separation, pharmaceutical chemistry, biological application, optics, and electric and spintronic devices and so on. As an emergent class of 2D materials, many topics have been documented. For example, Dong *et al.* [658] reviewed the construction, optical properties, and electronic properties of novel chiral perovskites and Long *et al.* [659] provided a comprehensive summary of the optoelectronic activities and applications. Dang *et al.* and Ma *et al.* supplemented informative discussions on recent advances of chiral perovskites with an emphasis on crystal structures and underlying chirality transfer mechanism, respectively [660,661]. Zhao *et al.* reviewed the

structures, properties and applications of chiral graphene hybrid materials [662]. Fig. 20 summarizes the main topics related to the chiral 2D materials. Here, we just address some basic issues covering the origin of chirality and some typical functional applications of chiral 2D materials with the application focus on chiral 2D perovskites.

So far, many types of 2D materials have been fabricated into chiral ones, including the 2D perovskites [302,663–670], graphene [671–673], TMDs [674–677], 2D organic nanoassemblies [678] and many more. A key scientific issue is how the chirality is originated and how to endow the 2D materials with chirality. Essentially, the synthesis of chiral 2D materials can be produced with or without the introduction of chiral species. When chiral species are participated in generating chiral 2D materials, these chiral molecules can be covalently, non-covalently or coordinated to the surface or inserting into the layers of 2D nanomaterial. Depending on the types of 2D nanomaterials, different ways of synthesis can be used. For 2D perovskites, the introduction of chiral amines, either on the surface on inserting into the layers is efficient inducing the chirality. In this case, amines are used one of coordination components and play important role in inducing chirality as well as their chiroptical performances. Till now, various types of chiral amines have been used [666,679–681]. For chiral TMDs, the surface modification by chiral molecules is frequently used. L- or D-cysteine and related sulfur-containing chiral molecules are mostly used as the chiral modifiers [676,677]. For graphene and its analogues, GO and rGO, the modification by chiral species is frequently used and a large number of chiral molecules can be selected [682–684]. Besides typical inorganic nanomaterials, supramolecular chiral 2D materials have also attracting great interest. Using Bottom-up strategy and the elegant design of the starting building blocks, supramolecular 2D nanosheet, 2D COFs have been fabricated and unique properties are shown [685].
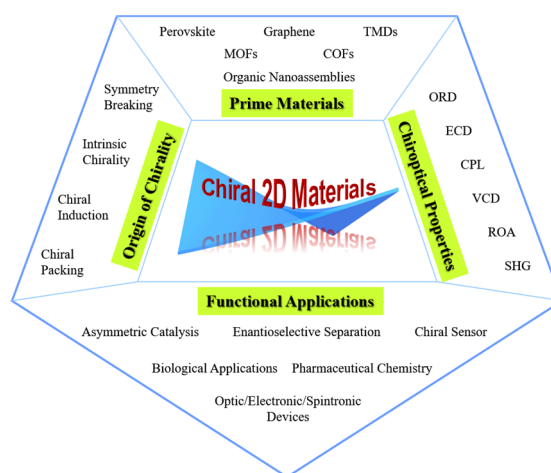
Fig. 20 Main topics related to the chiral 2D nanomaterials.
ORD: optical rotatory dispersion; ECD: electronic circular dichroism; CPL: circularly polarized luminescence; VCD: vibration circular dichroism; ROA: Raman optical activity; SHG: Second-harmonic generation.

However, upon interaction of the chiral molecules and the achiral 2D materials, the chirality is not always produced. Four different induction mechanisms of chirality generation in chiral 2D materials can be summarized as follows: (i) chiral molecules induce crystallization into individual chiral structure; (ii) electronic interactions induced by the large dipole moments between the chiral molecules and achiral structure; (iii) an achiral core and a chiral surface induced by chiral distortion or chiral ligand aggregation; and (iv) achiral nanomaterials-based chiral self-assembly [686–690]. These formation mechanisms of chirality are essential for the future designs and performance improvements of chiral 2D materials.

3.7.2　Some typical application of chiral 2D materials

3.7.2.1　Chiral graphene

Graphene is the most famous 2D materials. Although twisted stacking and buckling can cause intrinsic chirality into graphene [691–693], direct introduction or post modification of chiral small molecules or chiral macromolecules is the most powerful way of fabricating 2D graphene and its analogy (e.g., GO and rGO) [672]. The 2D graphene are more investigated in their chemical and biological applications rather than photonics. The structures, properties, and chirality of graphene-based chiral materials have recently been reviewed [662]. It appears that the chiral hybrid materials can demonstrate promising applications in nearly all specific areas related to chirality, including asymmetric catalysis, enantio-differentiating detection, and enantioselective crystallization, biological applications and luminescent materials. It should be addressed that many of properties of 2D graphene can be rather like a larger pi-conjugate and many functional materials can be developed.

3.7.2.2　Chiral TMDs

TMD semiconductors have shown a wide range of applications in spintronics and electronic devices. Among the family of TMDs, MoS_2 is particular interest as a chiral material. For example, Purcell-Milton *et al*. reported the fabrication of chiral MoS_2 nanosheets based on sonication-assisted exfoliation using the chiral ligands like cysteine and penicillamine [676]. Combined with the theoretical calculation, they showed that circular dichroism (CD) of 2D nanosheets arises from folding in preferential direction induced by chiral ligands. Additionally, Lin *et al*. demonstrated circularly polarized (CP) photoluminescence from the atomic layers of WSe_2, which was precisely controlled with chiral metamolecules (MMs) and results in 4-times enhancement in optical chirality [675]. Both the enhanced and reversed CD had been achieved. However, in comparison with the other system, there are still fewer reports on TMDs.

3.7.2.3　Chiral 2D perovskites

Chirality can be introduced from chiral molecules into halide perovskites, leading to a series of physical features, including CD, CPL, nonlinear optics, ferroelectricity, photovoltaic effects, spintronics and ferromagnetism (Fig. 21). Billing and Lemmerer first reported chiral 1D hybrid inorganic-organic perovskites in as early as 2003 and gave insight into the crystalline structure of

a series of chiral perovskites in 2006 and 2013 [694–696].

In 2017, the CD optical behavior of chiral 2D perovskite films were explored [686]. Subsequent studies further demonstrated that the chiroptical properties of chiral perovskites can be generated by the incorporation of organic cations and be manipulated by changing the chemical compositions, crystal orientations, film thicknesses, and electronic band structure [666,679,686]. Based on the chiroptical properties, chiral perovskites-based circularly polarized light detection was achieved without requiring extra optical elements, and thus is promising for integrated and flexible devices [697,701–705]. Besides the differential absorption of left-handed and right-handed circularly polarized lights (LCPL and RCPL), the differential emission of LCPL and RCPL in chiral HOIPs have been also widespread realized without an external magnetic field [688,697,701,706,707]. Since the mole fraction of the chiral ligands was positively associated with chirality in chiral 2D perovskites, pure chiral 2D perovskites exhibit the largest chiroptical activity and circularly polarized electroluminescence enable room-temperature spin-polarized light-emitting diode (LED) [698]. In addition, the incorporation of chiral cation can result in broadband white-light emission, which can be ascribed to the synergetic effects of the organic component and self-trapped excitons induced by the incorporation of organic molecules [708].

The non-centrosymmetric chemical structure of chiral perovskites implies their potential in nonlinear optics applications. Second-harmonic generation (SHG), a special type of the second-order nonlinear optics response, was first performed in chiral 2D perovskite nanowires (R- and S-MPEA)$_{1.5}$PbBr$_{3.5}$(DMSO)$_{0.5}$ and thereafter in various chiral perovskites [699,709–714]. Those studies shown that SHG signals always depend on polarization, particle size, temperature or
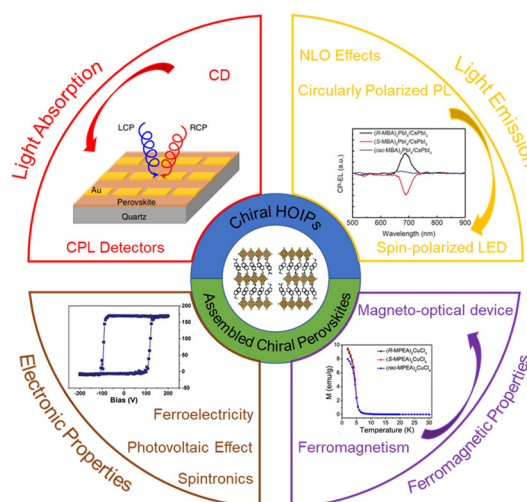
Fig. 21　Physical properties of chiral perovskites.
Top left panel reproduced from Ref. [697]. Top right panel reproduced with permission from Ref. [698], Copyright 2021 American Association for the Advancement of Science. Bottom left panel reproduced with permission from Ref. [699], Copyright 2019 John Wiley and Sons. Bottom right penal reproduced with permission from Ref. [700], Copyright 2020 American Chemical Society.

wavelength. Therefore, inherent non-centrosymmetric crystal structure renders chiral perovskites promising candidates for nonlinear optics-associated applications.

Chiral perovskites have also gained tremendous research attention in electronic properties such as ferroelectrics, photovoltaic effects and spintronics. Recent studies have shown that the ferroelectric behaviors in chiral perovskites are originated from the broken of spatial-inversion symmetry. Yang *et al*. synthesized the first homochiral chiral 2D perovskite ferroelectric (R- and S-CMBA)$_2$PbI$_4$ with a high Curie temperature of 333 K, which exhibited multiaxial ferroelectric characteristics [699]. The substitution strategy was applied to obtain chiral 1D perovskite ferroelectric with a higher Curie temperature [715,716]. The utilization of chiral molecules facilitates the materials crystallized in the special point groups, allowing ferroelectric performance. Moreover, chiral perovskites combine polarity and chirality together and thus drive bulk photovoltaic effects (BPVE), which can generate a steady-state photocurrent without a bias voltage. In 2019, BPVE in a pair of chiral-polar perovskites altered by chirality of the assembled organic cations has been demonstrated [717]. The chiral components defined the direction of electric polarization produced by the alignment of electric dipole moments in a crystal. Later, spin-dependent photovoltaic and photogalvanic responses of optoelectronic devices based on chiral 2D perovskites were further achieved, leading to the potential applications in optoelectronic devices that are sensitive to the helicity of the circularly polarized light [718]. In those devices, chiral molecules break the inversion symmetry and further give rise to the chiral-induced spin selectivity (CISS) effect and the circular photogalvanic effect (CPGE) response, which result in light-helicity-sensitive photovoltaic devices.

Symmetry breaking in chiral perovskites also contributes to spin polarization and subsequent spintronics. It had been verified that spin-related CPL emission could be modulated by magnetic field [706] and the CISS effect can directly control spin-polarized properties in chiral perovskites, which are essential for chiral spintronic applications [666,719]. Furthermore, the high spin polarizations enable chiral perovskites to manipulate the valley polarization (average valley polarization surpassing 10%) of monolayer TMDs in chiral 2D perovskite/monolayer TMD heterostructures *via* efficient spin injection (average spin-injection efficiency of 78%) without external magnetic fields [663,670]. In addition, regulating spin injection in chiral perovskites/ monolayer TMD heterostructures by applying an external electric and magnetic fields would be expected to greatly promote the development of chiral perovskite-based spintronic and valleytronic devices.

CISS effect also plays an important role in the opto-spintronic response of chiral perovskites. Recently, magneto-optical detection of photoinduced magnetism *via* CISS in chiral 2D perovskites/ferromagnetic NiFe heterostructures has been investigated, which laid a foundation for the primary exploration

of magneto-optical and spintronic applications [720]. Afterwards, the breakthrough of the first chiral 2D perovskite ferromagnets (R-/S-MPEA)$_2$CuCl$_4$ with clear ferromagnetic behaviors further revealed the potential of chiral perovskites for opto-spintronic applications [700]. Undoubtedly, the outstanding physical properties of chiral perovskites offer an advantage in various applications especially in next-generation optoelectronic and spintronic devices.

3.7.2.4 Other chiral 2D materials

g-C$_3$N$_4$ is also a well-developed 2D materials that demonstrates chirality. Chen *et al*. fabricated a mesoporous chiral nematic g-C$_3$N$_4$ for efficient hydrogen evolution, which could be modulated by polarized light [721]. It was found that the mesoporous nematic chiral g-C$_3$N$_4$ shows a high enhancement factor of 55 in hydrogen evolution in nematic chiral g-C$_3$N$_4$ than that in the bulk g-C$_3$N$_4$. Most interestingly, the chiral g-C$_3$N$_4$ material shows unique photocatalytic activity, which is modulated by CPL within the absorption region. Besides, the self-assembled organic 2D materials have also attracting great interest. Shen *et al*. have reviewed the recent progress in supramolecular 2D materials [678]. The easy design of the building blocks and the unique structural properties of the chiral 2D materials open new avenue in broad applications such as enantiomeric separation, asymmetric catalysis, and optoelectronic devices.

4 Potential applications
4.1 Electronics
4.1.1 Fabrication and architecture of 2d field-effect transistors

The metal-oxide-semiconductor field-effect transistor (MOSFET) is widely used in both analog and digital circuits. Depending on the channel polarity of MOSFETs, they can be divided into n-channel type with most electrons and p-channel type with most holes, which are usually called n-MOSFETs and p-MOSFETs, respectively. Moore's law has supported the global information technology industry to nearly double the performance and functionality of integrated circuit every two years within a fixed cost and area. However, with the development of Moore's law, the decreasing trend of node series and size becomes slower. Traditional silicon-based semiconductors are difficult to meet the requirements of International Technology Roadmap for Semiconductors (ITRS). Because of atomic-scale thickness, 2D materials benefit from dangling-bond-free surfaces and from good gate control ability in electronics application. Black phosphorus, like other 2D semiconductors, exhibits the steep subthreshold swings due to the suitable band gap. Moreover, black phosphorus holds a reasonably high mobility (exceed 1000 cm$^2 \cdot$V$^{-1} \cdot$s^{-1}). Taking advantage of these exotic features, 2D semiconductors have received significant attention in the post-Moore era. Particularly, owing to natural passivation and gate electrostatics, 2D field-effect transistors (FETs) have great potential for next-generation

integrated electronics applications.

4.1.1.1 Status of n-FET and p-FET

Different from traditional silicon-based FETs, the channel material of 2D FETs is usually 2D semiconductors at the atomic level. The metal-oxide-semiconductor capacitor locates in the center of the device is the core of the FETs. Metal electrodes are usually used for the source and drain, such as Au, Pt, Cu, *etc*. Utilizing the application of a gate voltage that passes through the 2D channel, the current is controlled between the source and drain electrodes. On the one hand, the gate voltage can generate a transverse electric field that depletes the carrier channel. Then, there is no current flow between the source and drain electrodes, namely off-state. On the other hand, the transverse electric field also can enhance the concentration of carriers to allow current to flow in the channel region, namely on-state. Usually, the off-state current is as small as possible, and the on-state current is larger than 10^4–10^5 compared with the off-state current.

For n-MOSFETs based on monolayer TMDs, the electrons in the conduction bands of TMD are the transport carriers in the channel region. Analogously, the holes in the valance bands of TMD are the transport carriers in the channel region of p-MOSFETs. Experimentally, the carrier types of 2D channel materials can be controlled by doping, passivation, and surface modification. When a positive voltage is applied to the gate, the negatively charged electrons are attracted to the surface, forming channels that allow most of the n-type semiconductor's carrier electrons to flow from the source to the drain. If this voltage is removed, the channel cannot form and carriers cannot flow between the source and drain, which is the gate voltage that can be used to switch the channel on and off. When a negative voltage is applied to the gate of p-MOSFET, the holes in the semiconductor are attracted to the surface to form channels, and most of the carrier holes in the semiconductor can flow from the source to the drain. If this negative voltage is removed, or if a positive voltage is applied, then no channel can be formed and carriers cannot flow between the source and drain.

Usually, the performance of a FET can be assessed in two forms: the output characteristics and transfer characteristics. Transfer characteristics, or transfer curves can be obtained by plotting drain current (I_d) as a function of the gate voltage (V_g), often refer to as the I_d–V_g curve. At a fixed drain voltage, the different gate voltage could change the energy levels, which are filled at the injection point of the source electrode. On-state and off-state current (I_{on} and I_{off}, respectively) are obtained from transfer characteristics. Additionally, the subthreshold slope (SS), often used to evaluate the switching speed of the FET, can be extracted from the transfer curve. In general, the SS of MOSFET can not be lower than 60 mV·dec^{-1} at room temperature (300 K). Output characteristics are obtained by drawing drain current (I_d) as a function of drain-source voltage (V_{ds}). A FET should present I_d saturation above certain V_{ds}. In an integrated circuit, the constant saturation current with V_{ds} is important because devices are interconnected. As a result, even

when the V_{ds} being supplied to individual device is different, the current from each device will remains the same [722].

4.1.1.2 CMOS demonstration

n-type MOSFETs and p-type MOSFETs are basic components that can be produced on a silicon wafer template. Because n-MOS and p-MOS are complementary in physical properties, it is called Complementary Metal-Oxide-Semiconductor (CMOS). CMOS has the advantage of consuming energy only when the transistor needs to be switched on and off. Therefore, it saves power and generates less heat, and it is also the most basic and commonly used semiconductor device in terms of technology. Low static power consumption and high noise immunity are two important characteristics of CMOS devices. Since one transistor of the MOSFET pair is always at off state, the series combination only draws significant power momentarily during switching phase between on and off states. As a result, CMOS does not generate as much waste heat as other forms of logic devices like transistor logic and NMOS logic, which usually involves some constant current even outside of the switching phase. These features allow CMOS to integrate with high-density on a chip. Consequently, CMOS is without doubt the most widely used technology in very large-scale integration (VLSI) chips.

4.1.2 Key challenges for 2D electronics

4.1.2.1 Contact issue

As the size of transistors continues to shrink, the influence of contact resistance (R_c) on the performance of transistors becomes increasingly critical, especially the current density improvement at the limiting channel size. The main cause of R_c is the energy barrier (Schottky barrier) formed between the contact metal and semiconductor, owing to the energy difference between the work function of the metal and the electron affinity of the semiconductor [723]. Low R_c is essential in device operation, and can be generally achieved *via* two approaches: (1) reduce the Schottky barrier width using highly doped contact; (2) minimize the energy barriers for charge carrier transport (Schottky-Mott rule) *via* choosing appropriate metals with work functions matching the semiconductor band edges [724,725]. In advanced microelectronics industry, silicon based devices realize low contact resistance (R_c < 0.1 kΩ·μm) and high current density (I_{on} > 1 mA·μm^{-1}) by doping the contact region with ion implementation. However, 2D materials do not have good compatibility with ion implementation because the high energy of ion beam will easily destroy the atomically thin lattice structure of 2D materials. Although some methods of chemically doping the contact region have been developed to reduce the R_c, these methods have the disadvantage of being unstable [726]. In order to achieve Ohmic contact, many metals matched with the electron affinity energy of 2D materials are used as the source/drain electrodes of the devices [727]. However, it is difficult to reduce the Schottky barrier and R_c to the ideal level because of the unavoidable chemical disorder and Fermi-level pinning effect at metal-semiconductor interfaces [728].

To address this challenge, many approaches have been developed to reduce the R_c of devices. For example, phase engineering to create lateral metal-semiconductor-metal hetero-junctions [373]; formation of clean interfaces *via* vdW contacts using graphene and low-melting-point metal [729–732]; mechanical transfer of metal films and using h-BN as the tunnel barrier [733–735]. These methods can effectively reduce the R_c, but which are still far from the level of silicon-based devices. Recently, researchers from MIT and TSMC reported the Ohmic contact between semimetal Bi and semiconducting monolayer TMDs where the Femi-level pining effect are sufficiently suppressed and the degenerate states in TMDs are spontaneously formed in contact with Bi (Fig. 22a, b). In this work, they achieved a zero Schottky barrier height (Fig. 22c), a R_c of 123 $\Omega \cdot \mu m$ (Fig. 22d) and an on-state current density of 1135 $\mu A \cdot \mu m^{-1}$ (Fig. 22e) on monolayer MoS_2, which is a hallmark breakthrough in the field of 2D electronics (Fig. 22f) [736]. Due to the low melting temperature, the issue of reliability and process compatibility of Bi still need to be

further considered. Nevertheless, achieving similar contact resistance with Si CMOS significantly boosts the potential of TMDs as channel materials for sub-2 nm technology node.

4.1.2.2 Doping of 2D semiconductors

In general, doping of semiconductors has two important functions for electronic devices. One is to heavy-doping the contact region to reduce the R_c of the device; the other is to realize n-type and p-type material features to construct complementary circuits. For example, in the 22 nm node Si CMOS, the well-designed doping concentration with a relatively high value (> 10^{20} cm^{-3}) under the contact regions and a moderate value (~10^{18} cm^{-3}) within the channel is carefully realized using the advanced implementation technique with ultra-steep doping profiles [737]. Nevertheless, conventional doping by ion implantation is not suitable for 2D materials due to their atomic thickness [722]. Hence, sophisticated doping techniques are required to preserve the structure and intrinsic properties of 2D materials as well as modulate them according
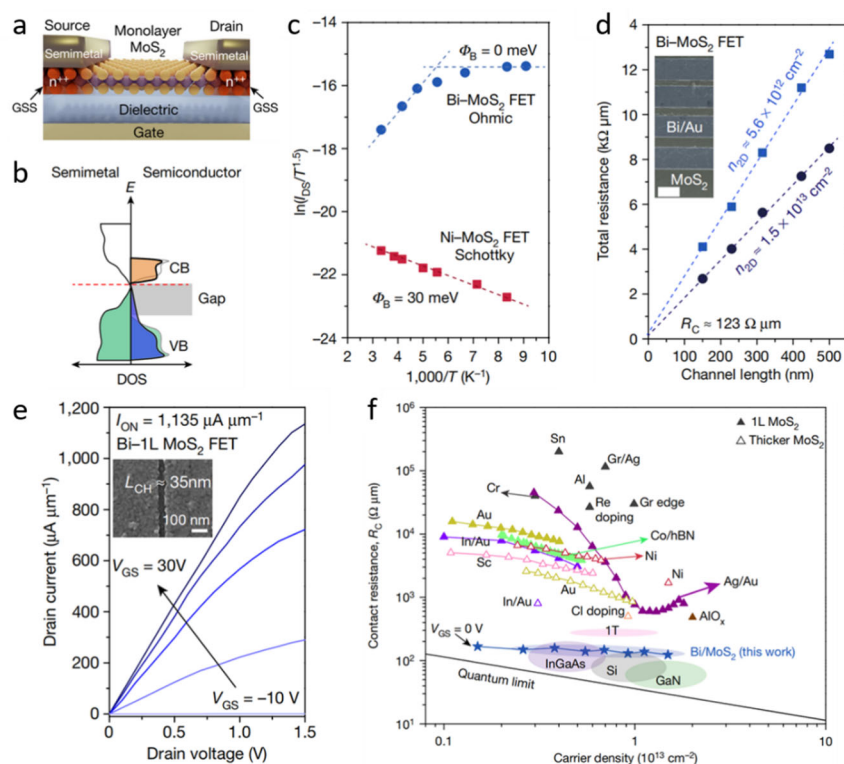
Fig. 22 **(a) Schematic of a 2D FET with a monolayer semiconductor (MoS₂) channel and semimetal (Bi) contacts. The degenerate part of Bi-contacted MoS₂ due to gap-state saturation (GSS) is marked in orange colour. (b) The DOS of semimetal and semiconductor contact. Because the Fermi level of the semimetal aligns with the conduction band of the semiconductor, and the DOS at the Fermi level of the semimetal is near-zero, conduction-band contributed metal-induced gap states (MIGS) are suppressed and the branching point is elevated into the conduction band. The MIGS, now mostly contributed by the valence band, are saturated, leading to gap-state saturation. (c) Arrhenius plots of the Ohmic Bi-MoS₂ (blue) and Schottky Ni-MoS₂ (red) FETs at a carrier density (n_{2D}) of 1.5 × 10¹² cm⁻² and V_{DS} of 1 V. A 30-meV and negligible barrier for Ni-MoS₂ and Bi-MoS₂ FETs, respectively, are extracted. (d) Contact resistance (R_c) extraction using the transfer-length method (TLM) for Bi-MoS₂ FETs on 100-nm-thick SiN$_x$ dielectrics. Blue squares and black circles are total resistance *vs.* channel length at carrier densities of 5.6 × 10¹² and 1.5 × 10¹³ cm⁻², respectively. Inset, False colour SEM image of the TLM structure. Scale bar, 1 μm. (e) I_{DS}–V_{DS} curves of a 35 nm L_{CH} Bi-MoS₂ FET. V_{GS} changes from −10 V to 30 V with steps of 10 V. Inset, SEM image of the 35 nm L_{CH} device. (f) State-of-the-art contact technology for MoS₂ transistors plotted as a function of carrier density, showing the respective R_c of various semiconductor technologies (Si, III–Vs, and MoS₂). The black line represents the quantum limit of R_c [736].**

to required applications. n-type or p-type doping can be realized by substitution depending on the number of valence electrons in the dopant atom [738]. However, due to the reduced screening in atomically thin materials, the ionization energy is much higher than in bulk semiconductors, leading to low doping efficiency [739]. Novel synthetic methods have been developed to confront this challenge. For example, the surface doping takes advantage of the charge transfer interaction between the host material and surface adatoms [726,740], gas molecules and supporting substrates [741]. Since the dopants lie out of the transport pathways of the charge carriers, such modulated doping successfully avoid lattice distortion, resulting in high carrier mobility. Among them, doping by surface adatoms and gas molecules may lead to ideal performance however is not practical due to the poor stability. To this end, a promising solution would be the incorporation of high-κ dielectrics through industrially friendly atomic layer deposition to transfer charge from the solid dopants [742].

4.1.2.3 Mobility engineering

Carrier mobility is the most important figure of merit for the performance of semiconductor devices. Taking monolayer MoS_2 and WS_2 as examples, the theoretical phonon limiting mobility at room temperature is about 410 $cm^2 \cdot V^{-1} \cdot s^{-1}$ [743] and 1100 $cm^2 \cdot V^{-1} \cdot s^{-1}$ [744], respectively, which are much higher than the value of silicon on insulator at the same thickness (Fig. 23c). This is a clear advantage of 2D materials for transistor dimension scaling and continuation of Moore's Law. But the experimentally measured results are often much lower than the theoretical

values, which is in practice limited by disorder and the presence of scattering sources [745]. The intrinsic charged point defects or other defects at the semiconductor/dielectric interface or the surrounding dielectric media can trap charges or scatter mobile charge carriers. At close to room temperature, the intrinsic and remote optical phonons in the 2D semiconductor environment can further limit the mobility [55].

In order to improve the mobility of 2D materials, the carrier transport process of 2D materials has been analyzed in detail by the theoretical model [746]. It has been found that the factors limiting carrier transmission mainly include intrinsic electron-phonon scattering [743,747], surface optical phonon [743], coulomb impurities [748,749], atomic defect scattering [750] and charge trap [751] (Fig. 23a). Many approaches have been attempted to improve the performance of 2D transistors (Fig. 23c). For example, reducing the atomic defects in 2D materials by optimized synthetic methods [98,752,753] and by defect repairing [745]; *in situ* annealing in vacuum to eliminate the impurities originating from the fabrication process or adsorbates from the atmosphere [754]; using interface engineering (such as high-κ dielectrics [113,755], h-BN encapsulation [749,756] and self-assembled monolayer [745]) to reduce the coulomb scattering by dielectric screening [755]. Especially the room temperature mobility of monolayer MoS_2 can reach ~150 $cm^2 \cdot V^{-1} \cdot s^{-1}$ combining with sulfur vacancy repairing and high-κ substrate (Fig. 23b), which is close to the theoretical value considering remote optical phonon scattering [757]. At present, high performance single transistors have been experimentally verified, but most of them are based on the preparation of
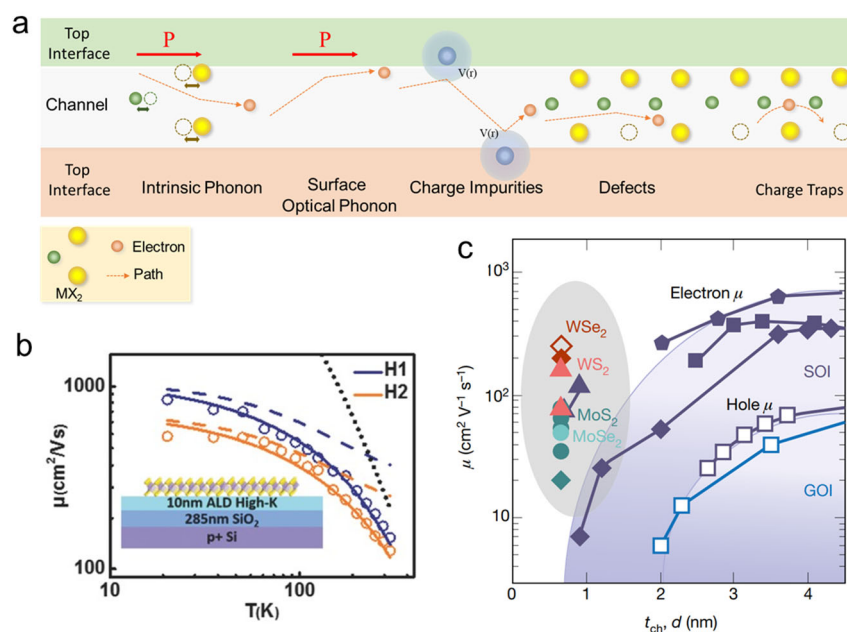
Fig. 23 **(a) Electron transport mechanism in MoS₂ channel devices, including electron-phonon scattering, remote phonon scattering, charge impurity scattering, defection scattering and electron trap. Reproduced with permission from Ref. [758], Copyright 2017 *Acta Physica Sinica*. (b) Field-effect mobility as a function of temperature for two monolayer MoS₂ FETs on HfO₂ substrate with thiol treatment under *n* = 10.5 × 10¹² cm⁻² (symbols), together with the best theoretical fittings (solid lines), the calculated CI-limited mobility (dashed lines), and the calculated phonon-limited mobility (black dotted line). Reproduced with permission from Ref. [757], Copyright 2018 John Wiley and Sons. (c) Mobility *vs.* semiconductor channel thickness, covering silicon on insulator, some promising 2D materials [5].**

mechanically exfoliated samples [736,757]. How to achieve the performance of large-area thin film transistor arrays is urgently need to be considered by optimizing CVD or MOCVD growth processes [742].

4.1.2.4 Gate dielectrics

The dielectric-semiconductor interface has been a central topic not only for conventional Si but also for the emerging 2D semiconductors. The utilization of high-κ dielectrics on thin 2D layers is critical to the application of 2D FETs in advanced technology nodes, where the criteria of the high-κ dielectrics are similar to the Si FETs, such as good dielectric integrity and wafer-scale uniformity, ultrathin electrical thickness for avoiding short-channel" effects, scalable deposition for top-gate devices, and low defects density in 2D-dielectric interfaces. To achieve high electrical performance in either planar FETs, FinFETs or stacked nanosheet FETs [759], it is critical to have the top-gate or gate-all-around process compatibility. Therefore, high-κ oxides based on atomic layer deposition (ALD) are still the most promising dielectrics for 2D FET applications.

The surface of 2D semiconductors such as TMDs is in principle free-of dangling bonds, which makes the seeding of ALD oxides challenging. Various approaches have been proposed to overcome the issue. Treatment on surfaces to generate reactive sites and improve precursor wetting on 2D layers: A variety of surface treatment methods have been reported, including UV-ozone [760] and exposure with different plasma gases (H_2, O_2, H_2 *etc.*) [761,762]. However, these methods typically introduce damages to the 2D lattices, leading to deterioration in electrical quality. Extended studies involve the modification of conventional ALD process to improve the high-κ deposition. Low-temperature physical adsorption of H_2O and ALD precursors was used for nucleation and a continuous Al_2O_3 gate oxide with a thickness of less 10 nm on WS_2 was achieved [763] as shown in Fig. 24a. Adding a buffer layer to promote seeding and avoid damages on 2D: There has been demonstration on the deposition of thin metal seed layer on 2D followed by mild oxidation to form a seeding oxide layer [764] and the potential damages of 2D were likely related to the initial metal deposition step. Other approaches using organic film or molecules have led to success to avoid damages on 2D layers owing to their low-temperature processes [765] although there might be concerns on the controllability of the molecular deposition. A recent work by Li *et al.* has demonstrated the use of the vapor-phase-deposited PTCDA molecules as the seeding layer followed by ALD HfO_2 to achieve a high-κ oxide with an EOT of ~1 nm film (Fig. 24b) [766]. The reliability of the ultrathin oxides by this approach has also been demonstrated promising [767] if it can be reproduced more broadly.

4.1.3 Emerging computing technology based on 2D materials

With many unique electronic and optoelectronic properties [768,769], 2D materials are promising for emerging computing technologies. In this section, we will provide a brief overview of recent progress in 2D material-based logic circuits, neuromorphic computing.

4.1.3.1 Logic circuits

The excellent electrostatic control of electrical field over the atomically-thin channel enables 2D materials to be useful not only for ultra-scaled FET [770] and logic circuits [94,771–776], but also in drastically simplifying the complex design of conventional silicon-based circuits [777–787]. Most of semiconducting TMDs are intrinsically n-type doped and can be used for the fabrication of
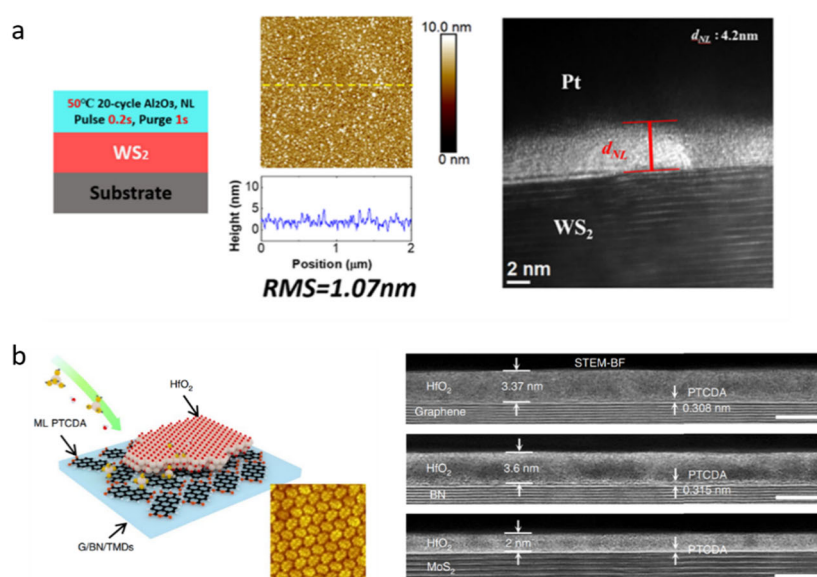
Fig. 24 (a) Schematic layer structure, AFM topography image and the TEM cross-sectional image of the Al₂O₃ nucleation layer grown on WS₂ layers with 20 ALD cycles at 50 °C with a short N₂ purge time of 1 s. Reproduced with permission from Ref. [763], Copyright 2020 American Chemical Society. (b) Schematic of using evaporated PTCDA molecular layer as the seeding layer for growing ultrathin HfO₂ ALD oxides as shown on the cross-sectional TEM images. Reproduced with permission from Ref. [766], Copyright 2019 Springer Nature.

n-type FET (Fig. 25a). Integrating a large number of n-type FETs allows for the realization of logic circuits with complex functions [94,771–774]. As shown in Fig. 25b, a 1-bit microprocessor consisting of 115 CVD-grown MoS_2 film transistors was successfully demonstrated [773]. With further advances in the CVD synthesis of wafer-scale 2D materials, higher density integration of MoS_2 transistors (*i.e.* 1518 devices per cm^2) has been demonstrated for flexible integrated logic circuits applications including five-stage ring oscillators [774]. In addition to the widely used CVD method, solution-processable 2D semiconductor nanosheets have been used for high-performance large-area logic circuits, opening up an alternative way for scalable fabrication of large-area arrays of 2D FETs [94]. Alternative to conventional size downscaling, improving area-efficiency may offer another promising solution to improve the performance of logic circuits. By using two surface channels of individual 2D semiconductors, dual-gate single devices can serve as distinct logic gates with higher area-efficiency than silicon-based circuits (Fig. 25c) [785,787]. Changing the dual-gate geometry into splitting gate architecture, 8 different switching states can be realized in the ambipolar WSe_2 material based electrically-tunable homojunction devices (Fig. 25d), which is desirable for constructing reconfigurable multifunctional logic circuits in a high area-efficiency manner [783]. Similarly, 2D semiconductor heterostructure based multifunctional logic circuit (*i.e.* three-value logic inverter) was reported by using gate-tunable band

alignment, showing great potential for future logic applications [778,788].

4.1.3.2 Neuromorphic computing

Nonvolatile memory devices are the building block for in-memory computing and neuromorphic computing [788–790], which hold promise in solving the challenges associated with the von Neumann bottleneck. As one typical nonvolatile memory, silicon-based flash memory devices have been commercialized, but suffering from the issues of slow writing/erasing speed. By employing the high-quality interface and suitable band offset of vdW heterostructures (vdWHs), around 20 ns writing/erasing speed has been recently achieved in the vdWH based floating gate transistors (FGT), which is orders of magnitude faster than that of the traditional silicon-based floating gate devices (Fig. 26a) [791–793]. When such atomically thin 2D materials based floating gate transistor is used as the memory element, it is suitable for designing a programmable inverter and implementing more complex programmable logic circuits for future low-power electronics [794]. Thermal stability is critical to the robust operation of the nonvolatile memory devices. Traditional silicon-device cannot be operated above 200 °C without any cooling, limiting their applications in high-temperature electronics. Wang *et al.* for the first time fabricated the graphene/$MoS_{2-x}O_x$/graphene vdWH robust memristor with operating temperature up to 340 °C (Fig. 26b) [795], by exploiting superior thermal and chemical stabilities of graphene
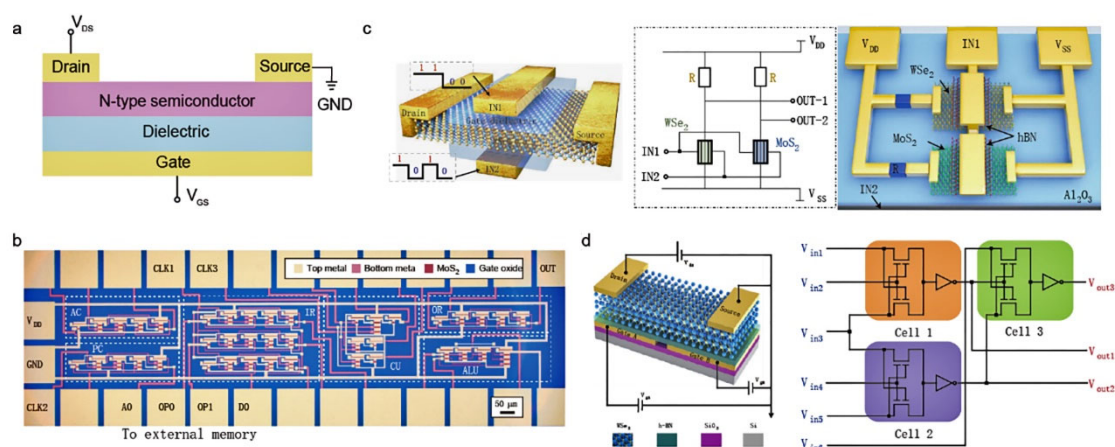
Fig. 25　Logic circuits based on 2D materials. (a) The schematic of a typical n-type FET. (b) A 1-bit microprocessor based on 115 CVD-grown MoS_2 transistors [773]. (c) High-efficiency logic gate circuit based on 2D materials [787]. (d) Reconfigurable logic circuit based on 2D ambipolar transistors [783].
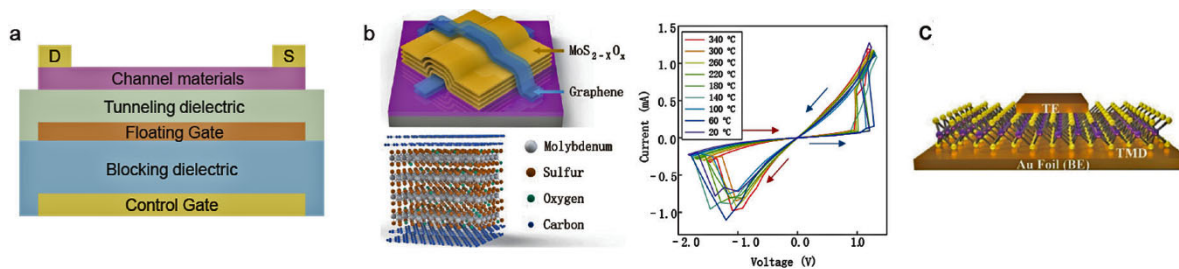
Fig. 26　Neuromorphic computing based on 2D materials. (a) The schematic of a typical floating gate transistor [791]. (b) Robust memristor based on graphene/$MoS_{2-x}O_x$/graphene vdWH [795]. (c) Atomristor based on monolayer MoS_2; reproduced with permission from Ref. [799], Copyright 2018 American Chemical Society.

and MoS_2. The memristive behavior was also observed in few-layer 2D insulator h-BN, which had been used to emulate synaptic behaviors [796,797]. By further reducing down to monolayer, the memristive behaviors have been recently demonstrated in many 2D semiconducting materials and vdWHs, which are attributed to different working mechanisms (Fig. 26c) [798,799]. Besides the reported field-driven ionic migration mechanism, field-driven lateral migration of grain boundary in the polycrystalline 2D semiconducting materials [800] and field-driven structural phase transition in 2D thin films [801] have also been utilized for the implementation of memristive devices for neuromorphic computing.

4.2 Optoelectronics

4.2.1 Categorization and figure of merit for optoelectronics

4.2.1.1 Categorization of optoelectronics

4.2.1.1.1 Photodetectors

The photodetector is a type of device which converts a light signal into an electrical signal and plays an important role in various applications, such as imaging, temperature measurement and fire alarm. According to the wavelength of the incident light, photodetectors include ultraviolet, visible, and infrared detectors. On the other hand, due to different photocurrent generation mechanisms, two kinds of photodetectors are introduced. One is a photon detector, in which the photon makes free carriers in semiconductors transit, including the photoconductive effect, photovoltaic effect, and photogating effect. The other is related to the thermal effect, including the photothermoelectric and bolometric effect [802].

For example, Lv *et al*. reported 2D homojunction diodes and multifunctional devices based on the spatially controlled ferroelectric domains [803]. A MoS_2 lateral homojunction device was obtained by a probe technique. MoS_2 homojunction photodetector exhibits an obvious photoresponse under 520 nm laser illumination. The open-circuit voltage is over 0.6 V. Atomically thin 2D heterojunctions with vdW heterointerfaces are fabricated. However, due to serious interlayer Shockley-Read-Hall (SRH) and Langevin recombination, thin 2D heterojunction devices don't meet the requirements of electronic and optoelectronic applications [804]. Tan *et al*. also demonstrated a WSe_2/PtS_2 vdW tunneling heterojunction because PtS_2 is narrow-bandgap 2D material with high mobility [805]. The reverse rectification ratio of WSe_2/PtS_2 is over 10^8. Compared to conventional semiconductors-based backward diodes, vdW tunneling diodes exhibit a higher rectification ratio and show great potential in high-speed and low-power devices [806,807]. On the other hand, Wu *et al*. designed a unilateral depletion structure based on AsP and MoS_2. A unilateral depletion can effectively reduce the severe interface recombination. Furthermore, a narrow bandgap AsP is an excellent contact layer. Finally, a high external quantum efficiency of 71% and a fast response time of 9 μs are obtained [808]. It is noteworthy that Chen *et al*. design a novel vdW nBn structure [809]. A thick h-BN is inserted and used

to block the major carriers. nBn WS_2/h-BN/$PdSe_2$ devices with perfect interfaces are achieved. Since a large conduction band barrier of h-BN exists, the major carrier-electrons in WSe_2 and $PdSe_2$ do not transport. Therefore, the dark-current of WS_2/h-BN/$PdSe_2$ photodetector is severely suppressed in contrast to that of vdW junction devices. Further, WS_2/h-BN/$PdSe_2$ exhibits an obvious superiority in light on/off ratio.

4.2.1.1.2 Photovoltaic devices

Photovoltaic processes mainly occur in the junction (p-n junction or Schottky junction) [810,811]. During irradiation, electron-hole pairs (photogenerated carriers) are generated from incident photons with energy equal to or higher than the semiconductor bandgap. Due to the internal electric field of the junction, electron-hole pairs are separated and can be collected by the electrodes to generate electricity, so the device's *I–V* curve will be shifted vertically when exposed to light. Under the working condition, the maximum output voltage generated by the device in the open circuit state is called the open circuit voltage, and the maximum output current of the device when the external circuit load is zero is called the short-circuit current. In order to make a quantitative performance evaluation of photovoltaic devices, one of the important characteristic quality factors is the filling factor (FF), which is defined as the ratio of the maximum available power and the product of the open-circuit voltage V_{OC} and short-circuit current I_{SC}. FF represents the ratio of the maximum power output by the device to the theoretical power. The formula is expressed as

$$FF = P_{max}/V_{OC}I_{SC}$$

where, P_{max} is the maximum power obtained. The shunt resistance $R_{SH} = dV/dI$ is mainly related to carrier compound loss, and the device characteristic resistance is $R_{CH} = V_{OC}/I_{SC}$. FF can be further improved by lowering the parameter of R_{CH}/R_{SH}. In addition, the power conversion efficiency (PCE), which is the percentage of the power of the incident photon converted to electrical power, can also be used as a device performance criterion. PCE can be calculated by the following formula:

$$PCE = P_{max}/P_{in}$$

where P_{in} is the input power. In fact, the atomic thickness of 2D crystals makes them extremely sensitive to the surroundings environments. In photovoltaic devices, the defects and unwanted interface states can not only significantly limit carrier mobility, but also act as recombination centers for the photogenerated electrons and holes, seriously affecting the device's internal quantum efficiency and overall performance [812,813].

4.2.1.1.3 Optical modulator and lasers

Optical modulator is a key functional device in optical fiber communication network and optical interconnection. At present, people have put forward higher requirements for such devices in terms of speed, volume, power consumption, integration and so on. When 2D materials are used to make modulator, the absorbance of the material is controlled by electric field: the absorption characteristics of 2D materials are changed by using different voltages to achieve the purpose of modulation [814]. The

refractive index of a material can usually be written in the form of a complex refractive index:

$$n = n_r + in_i$$

where n_r represents the real part of the refractive index and n_i represents the imaginary part of the refractive index. Both the real part and the imaginary part are changed by voltage regulation. If the voltage is used to change the real part of the refractive index, the phase of light transmission in the medium will change to some extent, and a phase-type modulator can be made. In addition, a better modulation effect can be obtained by enhancing the interaction between the light field and the 2D material. The integrated optical modulator with high modulation speed, small size and large bandwidth is expected to be a low power device for optical interconnection. By integration of modulator and photodetector into waveguide or fiber laser system, high performance ultrafast laser can be realized to produce ultrashort, low loss and wide-band laser. The modulation part can control the laser stability by active mode locking, while the detection part can provide feedback of the laser stability.

In fact, the fundamental cause of modulator operation depends on the nonlinear optical properties of the material which originates from the non-resonant motion of bound electrons under the applied electric field [815]. Thus, the formulas for simulating the linear and nonlinear responses under the applied electric field, E, can be expressed as:

$$P = \varepsilon_0 (\chi^{(1)} \cdot E + \chi^{(2)} : E + \chi^{(3)} \vdots E + \cdots)$$

where ε_0 is vacuum permittivity, the main factor that concerns the optical nonlinearity of materials is the third-order susceptibility $\chi^{(3)}$. The real part of $\chi^{(3)}$ is related to the nonlinear phase transition of incident light field caused by material, which is known as Kerr effect.

The laser mainly consists of a gain medium which can produce photons, an optical resonator which can make photons get feedback and can resonate and amplify in the gain medium, and a pump source device which can make the medium in the excited state. Due to the strong exciton-photon interaction, the thin layer 2D semiconductor material can be used as the gain medium, and different resonator structures can be designed to obtain ultra-low threshold and ultra-fast optical/electrically modulated lasers [816–820]. The laser also can be controlled by passive mode-locking without adding a modulator in the fiber. Its basic principle is to use of optical fiber nonlinear effect on the dependence of the intensity of the input pulse, and the effect can be equivalent to a saturated absorber effect. It is equivalent to a special material that has a smaller absorption coefficient for a larger light intensity and a larger absorption coefficient for a smaller light intensity. Thus, the optical pulse can be narrowed. Therefore, it is modeled as

$$\alpha = \alpha_{ns} + \frac{\alpha_s}{1 + I / I_{sat}}$$

where α_{ns} is non-saturable loss and α_s is modulation depth (saturable loss), I_{sat} is the saturation intensity.

4.2.1.2　Figure of merit of optoelectronics based on photocurrent generation mechanisms

4.2.1.2.1　Photoconductive effect

For the photoconductive effect, the photogenerated excess carriers make free carrier concentration in semiconductors increase, as illustrated in Fig. 27. The excess carriers are driven and collected under the applied bias thus forming the photocurrent. For instance, the device possesses a small dark current in dark conditions. When the device is illuminated, electron-hole pairs produced by the absorbed photons are separated by the applied bias and collected by the electrodes, respectively. The photocurrent of the device is larger than the dark current. It is worth noting that the photocurrent of
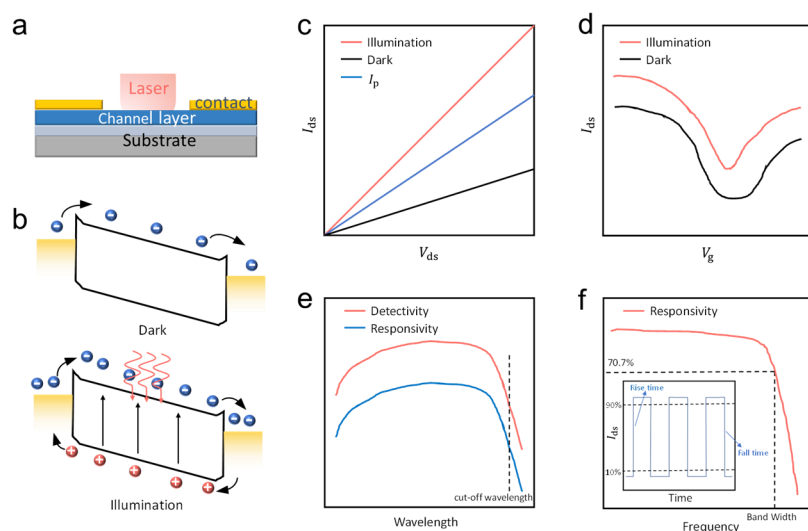
Fig. 27　(a) Schematic image of PC detector. (b) The energy band structure of PC devices with and (c) without illumination.

(c) Typical output characteristic (*I–V*) curves of PC device in dark and light states and photogenerated current *I*p as a function of bias voltage.

(d) Typical transfer characteristic (*I–V*g) curves of PC devices in dark and light states. (e) Two key parameters (Responsivity and

Detectivity) of a detector as a function of wavelength. (f) A key parameter (Response speed) of a detector with two typical presentations.

photoconductive effect has to be produced with an applied bias voltage.

4.2.1.2.2 Photovoltaic effect

The photogenerated electron-hole pairs are separated and accelerated by the built-in electric field of a Schottky or p-n junction. The direction of the junction determines the direction of the photocurrent. The junctional devices have a low dark current and fast response speed due to the built-in electric field. Thus, this kind of device often works under zero or reverse bias. Meanwhile, a higher quantum efficiency could be realized. By fabricating heavily doped p-n junctions, the avalanche photodiodes can be obtained, which are used to detect weak light, even down to single photon.

4.2.1.2.3 Photogating effect

It is actually a special case of the photoconductive effect. The corresponding devices are considered photoconductive photodetectors. Since low-dimensional materials have a higher defect concentration, this effect is introduced. Generally, the e-h pairs are produced under illumination. If the photogenerated electrons or holes are trapped in the defects or the adjacent semiconductor layer. These charged defects could act as an external and local gate, which would change the channel conductance. The devices usually possess higher responsivity and gain due to a long carrier lifetime.

4.2.1.2.4 Photothermoelectric effect

It is a thermal effect caused by the localized lighting that results in a temperature gradient across the device, when the spot of the illumination is smaller than the size of the channel. This temperature difference would result in a thermoelectric voltage. Alternatively, temperature gradient on the channel could also be induced under a globe lighting when the light absorption at different parts of the device varies. The produced thermoelectric voltage is often small and changes from μV to mV. It is closely related to the Seebeck coefficient of semiconductors and metals [821].

4.2.1.2.5 Bolometric effect

The bolometric effect refers to the phenomenon that the resistivity of a temperature-sensitive material increases or decreases when the materials are illuminated and heated by a uniform light. The photocurrent caused by the bolometric effect changes linearly with the applied bias voltage. The key difference between PTE and PBE is that the PTE photocurrent is self-driven, which is similar to that in photovoltaic devices, while PBE photocurrent could be only observed under applying external bias.

4.2.2 Key challenges for optoelectronics

4.2.2.1 Wide and narrow bandgap

Although 2D optoelectronics have been developed rapidly in recent years, there are still several key challenges for 2D optoelectronics. Among 2D materials, those 2D materials with wide bandgaps (3 eV) and narrow bandgaps (< 1 eV) usually exhibit more attractive optical properties. Taking photodetection as an example, 2D semiconductor materials (Fig. 28a) with wide bandgaps can be used for ultraviolet (UV) photodetection due to

the band-absorption cut-off wavelength. Yang *et al*. reported UV photodetection under 325 nm based on 2D GeS$_2$ with a bandgap of 3.71 eV (Fig. 28b) [822]. Furthermore, Wei *et al*. reported a new 2D material (GaPS$_4$) with an ultralarge bandgap of 4.5 eV at monolayer condition in Fig. 28c, showing high responsivity (4.89 A·W^{-1}), high detectivity (1.98 × 10^{12} Jones), and high quantum efficiency (2390%) in the solar-blind ultraviolet region [823]. There are more and more 2D materials with wide bandgaps are discovered recently [824–827], which is meaningful for the missile tracking and national security. On the other hand, 2D materials with narrow bandgaps are also important especially for infrared photodetection. Narrow-bandgap semiconductors have been studied intensively such as black phosphorous (0.3 eV for bulk to 2.0 eV for monolayer) [828] for near-wave infrared (NWIR) and mid-wave infrared (MWIR) photodetection [829,830], AsP (0.3–0.15 eV with varying stoichiometric ratio) for MWIR photodetection [831–833], and noble metal chalgenides for MWIR photodetection [834,835], and so on [836–839]. However, most reported 2D semiconductors with narrow bandgaps exhibit poor gate-modulated carrier-transportation characteristics, resulting in uncontrollable optoelectrical properties. Recently, the electrical and optical properties of Te have been simulated indicating that its effective charge carriers masses are three to four times smaller than that of MoS$_2$ [840], and the optical bandgap has been proved to be ~0.3 eV [841]. Thus, it is promising for gate-tunable MWIR photodetection. Recently Furukawa *et al*. synthesized ultrathin Te flakes (Fig. 28d) [842], which exhibit air-stable performance at room temperature for more than 2 months, on/off ratios on the order of 10^6, and field-effect mobilities of about 700 cm^2·V^{-1}·s^{-1} [89]. Then Hu *et al*. reported high performance MWIR photodetection based on 2D Te flakes under 3 μm [840]. Thus, 2D Te quickly became one of the most promising candidates for NWIR and MWIR photodetection. However, 2D semiconductors are much
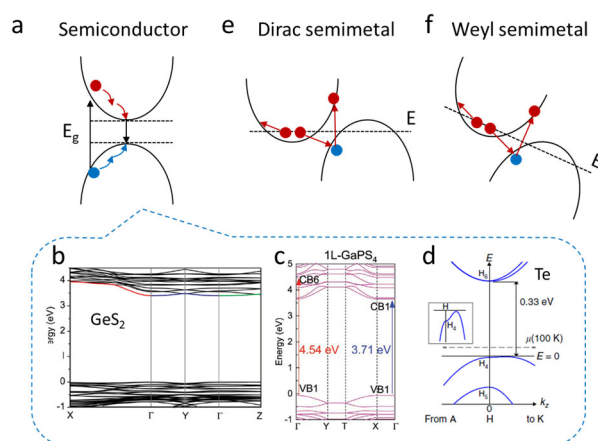

Fig. 28 (a, e, f) Schematics of band structure of semiconductor and semimetal. Calculated band structures of GeS$_2$ (b), monolayer GaPS$_4$ (c), Te (d); (b) reproduced with permission from Ref. [822], Copyright 2019 John Wiley and Sons; (c) reproduced with permission from Ref. [823], Copyright 2021 John Wiley and Sons. (d) Schematic band structure of trigonal tellurium [842].

difficult for further long-wave infrared (LWIR) detection due to the intrinsic bandedge-absorption. 2D semimetals are promising for LWIR even terahertz photodetection due to the nearly zero bandgaps (Fig. 28b).

On the other hand, graphene is a typical Dirac semimetal with zero-bandgap or small bandgap induced by chemical doping, shows great promise in LWIR and terahertz photodetectors [843]. However, the high dark current and low photoabsorption of grapheme photodetectors result in high noise, lower responsivity and low detectivity, which are not ideal in practical application [844–846]. Recently, 2D metallic TMDs, such as $PdTe_2$ and $PtTe_2$ have been discovered as topological semimetals showing exotic band structure such as type-II Dirac cone [847,848]. Without Lorentz invariance, type-II Weyl fermions can also be realized when inversion symmetry or time-reversal is broken, and possibly exhibit chiral-related transport, such as quantized photogalvanic effect, anomalous thermoelectric, and chiral anomaly. Chen *et al*. reported a $PdTe_2$-based photodetector with large photogalvanic effects and high anisotropy at terahertz frequency. A responsivity of 10 A·W^{-1} and a noise-equivalent power lower than 2 pW·Hz$^{-0.5}$ is achieved at room temperature [847]. 2D Weyl semimetals (Fig. 28c) are a new family of 2D family such as $TaIrTe_4$ [849], T_d-WTe_2 [850], T_d-$MoTe_2$ [851], and so on, which have exhibited much attractive exotic optoelectronic phenomena. For example, under 4-μm excitation at room temperature, $TaIrTe_4$ shows a large photoresponsivity of 130.2 mA·W^{-1}, arising from the third-order nonlinear optical response, which approaches the performance of commercial low-temperature detectors [852]. In another example, robust edge photocurrent response was demonstrated on layered type II Weyl semimetal WTe_2, mainly due to crystalline-symmetry breaking along certain crystal fracture directions [853].

4.2.2.2　2D heterostructures for optoelectronics

vdWHs fabricated by stacking 2D materials one by one artificially, but open unprecedented possibilities of combining them for technological use. Due to the lack of lattice matching at the interfaces, such stacking is very different from the traditional bulk semiconductor heterostructures. What's more, the charge transfers between the layers could be very large which induces large electric fields at the interface and offers possibilities in band-structure engineering, which will affect the optoelectrical properties significantly [854,855]. For example, infrared photodetectors based on single 2D material usually exhibit photoconductive or photogating effect, resulting in slow response rates from milliseconds to minutes, and high dark currents or low detectivity [856]. This can be solved by fabricating heterostructures with strong built-in electric fields easily. Hu *et al*. reported that $PdSe_2/MoS_2$ based photodetector shows a fast response rate of 51.3 μs and a high detectivity as 10^9 Jones even for 10.6 μm LWIR detection [856]. Also, the ballistic avalanche phenomenon was observed in vertical InSe/BP heterostructures with suitable thickness. In contrast to the conventional avalanche behavior, the ionization collision coefficient per primary carrier

is equal to one in the ballistic avalanche effect, resulting in a small avalanche breakdown voltage, a lower avalanche noise, and positive temperature coefficients with an almost constant multiplication factor. Thus, the device are impact-ionization transistors with a steep subthreshold swing (< 0.25 mV·dec^{-1}) and sensitive mid-infrared light detection (4 μm wavelength) [857]. In another example, an infrared photodetector was realized by the interlayer excitons (ILEs) generated between tungsten and hafnium disulfide. Peak responsivities of 8.2×10^2 and 9.5×10^2 A·W^{-1} were observed for 3L = WS_2/HfS_2 heterostrucrure on laser illuminations of λ = 4.7 and 4.3 μm, respectively [858].

2D semiconductors with strong exciton binding energies are promising for room-temperature excitonic. However, single 2D semiconductors usually show short exciton diffusion length. To this end, taking advantage of of the spatial separation of e-h pairs in adjacent layers of vdWHs, it is possible to overcome this limitation and enable the operation of mesoscale devices at room-temperature. For example, Lukman *et al*. realized the electrical control of exciton flux in a vdWH based on WSe_2/MoS_2 at room temperature, the long-lived nature of the interlayer excitons in these devices result in diffusing over a distance of five micrometres [858]. Except for electrical control of excitons diffusion, it is also important for control of valley-polarized excitons for next-generation encoding data and information processing. Kis *et al*. show the generation and transport over mesoscopic distances of valley-polarized excitons in a type-II heterostructure based on $WSe_2/hBN/MoS_2$. Engineering of the interlayer coupling can enhance the diffusion of valley-polarized excitons, which can be controlled electrically. The exciton concentration can be further increased by an order of magnitude using electrostatic traps, opening the way for achieving a coherent quantum state of valleypolarized excitons *via* Bose-Einstein condensation [859].

4.2.3　Unique applications of 2D functional optoelectronics

With the increasing unique applications of 2D functional optoelectronics, devices that can cover multi-band wide spectrum are demanded. In addition, the research of polarized-sensitive photodetector adapted to new applications is also important. 2D materials have been considered to be able to improve the performance of devices and have been widely studied [860,861]. The neural network, which is based on the development of 2D materials, can simultaneously complete the two major tasks of photosensitive behavior and processing images without delay.

4.2.3.1　Wide-spectrum photodetectors

The wide-spectrum 2D photodetectors show great potential in solving the problem of improving the device integration while controlling the cost. In the family of 2D materials, graphene is a promising broadband photodetector material [862]. However, the zero gap, large dark current and low absorption limited its application in photodetectors. Researchers are gradually studying other low-dimensional materials [863]. From the first-

principles calculations, the theoretical photoabsorption region of different 2D materials can be obtained. The 2D semiconductor materials with narrow band gap are the favorable candidates for wide spectral detection [864]. For example, photodetector based on Sb_2Se_3 exhibited the ultrafast response speed, while the wide absorption spectrum of Sb_2Se_3 from ultraviolet to near-infrared (300–1000 nm) [865]. However, the narrow band gap materials have disadvantages of low infrared band gain and low quantum efficiency. The polarized photodetection based on 2D materials can also achieved by defect engineering or building of heterojunctions. For instance, In_2Se_3 is a natural defect crystal material, therefore the photodetector based on In_2Se_3 has a wide-spectrum response [866]. A self-driven photodetector based on WS_2/ GaAs heterojunction broke the limitation of bandgap and achieves a rapid response from 200 to 1550 nm. It also has strong weak light detection ability [867]. The 2D/3D $MoTe_2$/Si photodiode also can achieve the ultrafast-wide-spectrum photodetection from 300–1800 nm [868]. The advantages of silicon compatibility of such devices have enable the development of the 2D broad-spectrum photodetector in the commercial application, which are expected to achieve large-scale integration [869].

4.2.3.2　2D polarization-sensitive photodetectors

Due to the ever-increasing requirements for the devices and device size, 2D materials with natural anisotropic structure have been well developed in the field of polarization photodetection. In addition to studying the circular polarization information of the incident light [870], the linear polarization of light can also be further studied. In 2015, the polarized-sensitive device based on BP/MoS_2 heterojunction was developed for the first time [871]. In 2019, a batch of 2D materials that may have polarization sensitivity can be obtained through first-principles calculations [872]. In 2021, photodetectors based on SiP and Ta_2NiSe_5 materials have polarization sensitivity, which are able to quickly response in visible light 532 nm and near-infrared 1064 nm with the anisotropic current ratio of 2.3 and 3.3 respectively [873,874]. Currently, the 2D materials with triangular, tetragonal, rhombic, monoclinic and triclinic crystal structures are reported, which can cover ultraviolet to infrared band [875]. Some of the 2D materials can be used for both broad-spectrum polarization detection, Fig. 29 shows some polarized-sensitive photodetectors with broad-spectrum. The photodetector based on $(BA)_2(GA)Pb_2I_7$ (Fig. 29a) has obvious anisotropic photocurrent in some different wavelengths of the visible band [876]. The $PdSe_2$-based device, shown in Fig. 29b, has obvious light absorption in visible and near infrared bands, and has obvious polarization sensitivity [877]. In addition to the single materials, heterostructures are also applied to polarization detection. As shown in Fig. 29c, the device based on the $Gr/PdSe_2/Ge$ heterojunction has a quick response in the deep ultraviolet to the infrared band, while the anisotropic photocurrent ratio of the device at 650 nm is about 112.2 [878]. Polarization images of targets can be obtained by the polarized-sensitive photodetectors [840,879]. Fig. 29d shows the polarization imaging of the GeSe-based

device in near-infrared band. The diagram is clear, and the patterns obtained by different polarization directions have significantly different [879].

4.2.3.3　2D neural network image sensors

In order to obtain higher quality image, it is necessary to fabricate an array and integrated a 2D single photodetector. An array device based on MoS_2/Graphene heterojunction were reported, which can be directly obtained under different lighting conditions [880]. Further integration of 2D materials and CMOS transistors can be used to complete the information collection at once with the read out integrated circuit, but it also be affected by the response time of the single device [104]. In practice, the imaging system that mimics the neural biology architecture can minimize the impact of device response. There is still a lot of work to be done to develop imaging system that imitates mimic the function of the human eyes [881–883]. The biomimetic human eyes, composed of multiple imaging sensors, are highly similar to the human eye. And the high image resolution can be achieved through electrical addressing [884]. The lens of the derived machine vision technology is its eyes, which can be passed to the processing unit and realized various visual capabilities after obtaining rich visual information. The construction of artificial neural network (ANN), and some clear images are presented [885,886]. Such systems can process optical images without delay, and have completed ultra-high-speed machine vision simulations [787,887].

4.2.3.4　Near/in-sensor computing

Near/In-sensor computing allows for placing computational tasks near or in the sensory devices and can mitigate the issues related to time delay and power consumption suffered by traditional visual information processing [888]. Many 2D materials and vdWHs with superior electronic and optoelectronic properties are suitable for near/in-sensor computing applications [883,885–887,889–896]. With the weight control layer able to trap or de-trap electrons in vdW interface, an optical neural network based on WSe_2/h-BN heterostructure synaptic devices (with distinct photoresponse to different visible wavelengths) has been proposed to recognize colored and color-mixed pattern (Fig. 30a) [883]. Similarly, an optical neural network was implemented by integrating 1Kb in-memory sensor arrays and in-memory computing arrays based on MoS_2 photodetectors that show persistent photoconductivity effect (Fig. 30b) [886]. Compared to near-sensor computing, in-sensor computing enables to perform low-level computations in the sensor and represents a paradigm shift to realize real-time information processing. By using continuously tunable photoresponse of 2D ambipolar WSe_2 semiconductors, Mennel *et al.* demonstrated a unique image sensor that can simultaneously sense and process optical images within 50 ns, which highlights the huge potential of 2D materials based in-sensor computing in future machine vision (Fig. 30c) [887]. Human retina with a stack of distinct cell layers naturally integrates the functionality of sensing and processing and offers an ideal template for implementing in-sensor computing. By highly mimicking the vertical structure
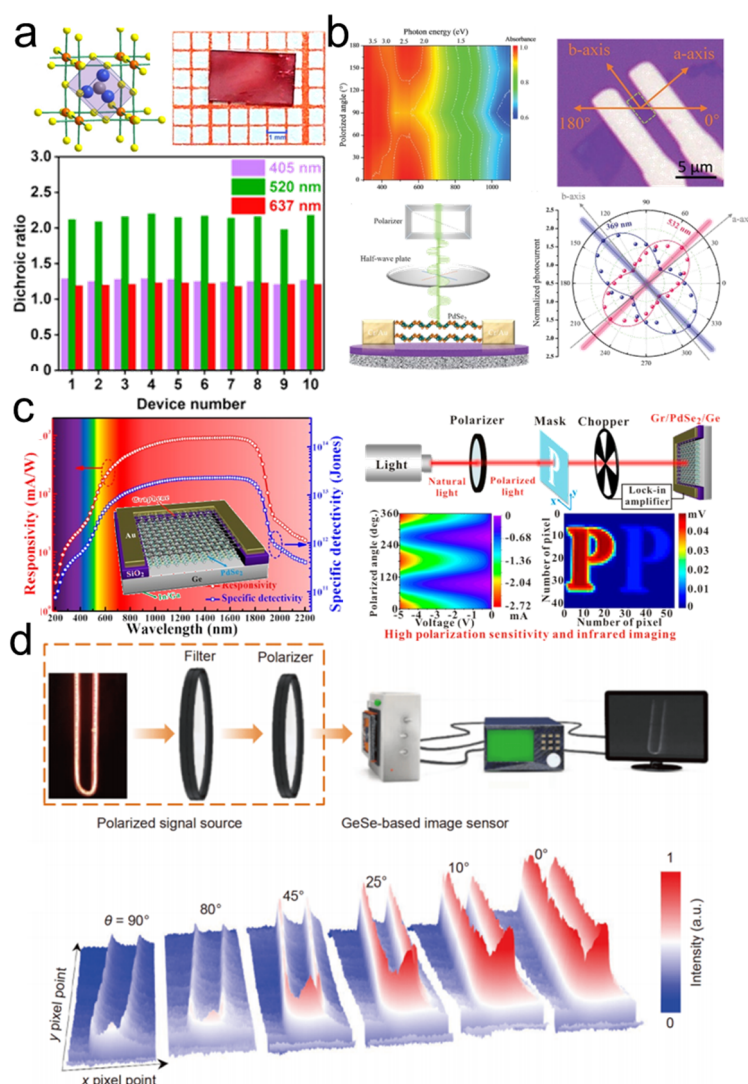
Fig. 29　Polarized-sensitive photodetectors with broad-spectrum. (a) Obvious anisotropic photocurrent of photodetector based on (BA)₂(GA)Pb₂I₇, inset are the crystal structure of material and the image of device; reproduced with permission from Ref. [876], Copyright 2021 John Wiley and Sons. (b) 2D absorption spectrum of PdSe₂ flake from 300 to 1100 nm, and the performance of polarization-sensitive photodetector; reproduced with permission from Ref. [877], Copyright 2021 John Wiley and Sons. (c) Wavelength-dependent responsivity, specific detectivity and the polarimetric imaging of the Gr/PdSe₂/Ge heterojunction device, inset is schematic diagram of the device; reproduced with permission from Ref. [878], Copyright 2019 American Chemical Society. (d) Schematic layout of the image scanning system and the NIR polarimetric imaging of GeSe-based image sensor; reproduced with permission from Ref. [879], Copyright 2021 Science China Press.

and biological functionality of human retina, Wang *et al.* designed a reconfigurable retinomorphic sensor based on gate-tunable photoresponse of vdWHs and showed its promising aplication in reconfigurable image processing (Fig. 30d) [885]. By taking a further step to emulating human vision system, they networked the retinomorphic sensor and memristive crossbar array to build a proof-of-concept neuromorphic vision system, (Fig. 30e), which may open up a new avenue for future exploration of neuromorphic vision systems [891].

4.3　Catalysis

4.3.1　Electrocatalysis

4.3.1.1　Oxygen reduction reaction

Proton exchange membrane fuel cell (PEMFC) is the zero-emission vehicle that best preserves the advantages of gasoline automobiles: long-distance driving, fast start-up speed and fast refueling [897]. However, the cathode reaction of oxygen reduction reaction (ORR) has become the bottleneck of PEMFC development due to sluggish reaction kinetics [898–900]. Consequently, the development of high-performance, stable and low-cost ORR catalysts is particularly urgent. Generally, the ORR occurs through either four proton-electron transfers ($O_2 + 4H^+ + 4e^- \rightarrow H_2O$) to reduce oxygen to water in acidic environment or a two-proton-electron pathway ($O_2 + 2H^+ + 2e^- \rightarrow H_2O_2$) to produce hydrogen peroxide (H_2O_2) [249]. For the fuel cell or metal-air batteries, the excellent efficiency, and durability in cathode strongly depend on $4e^-$ reduction reaction, while the intermediate product H_2O_2 will destroy the catalyst activity and accelerate the aging of batteries. On the other hand, as the
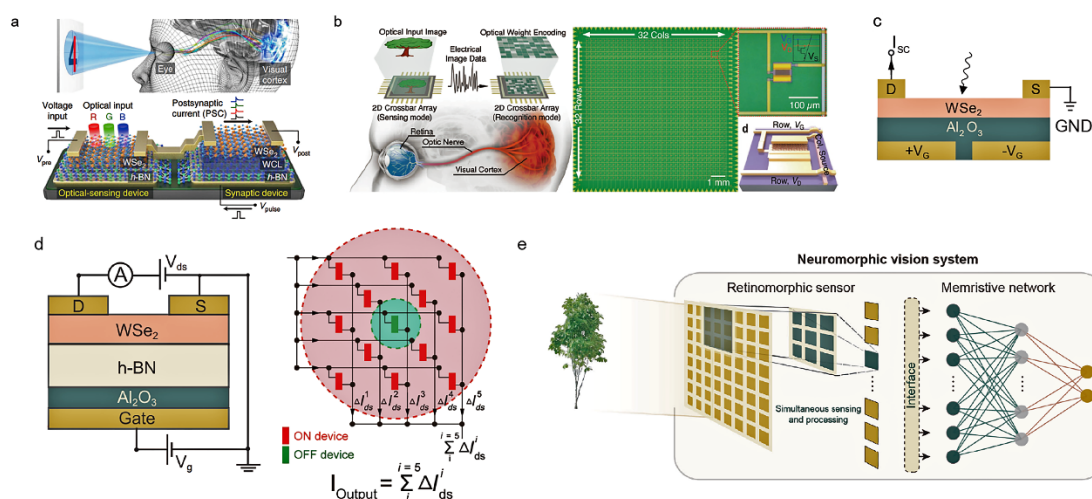
Fig. 30 Near-/In-sensor computing based on 2D materials. (a) Optic-neural synaptic device based on h-BN/WSe$_2$ heterostructure [883]. (b) 1 Kb vision processor based on MoS$_2$ photosensitive FET crossbar array; reproduced with permission from ref. [886], Copyright 2020 John Wiley and Sons. (c) Ultrafast machine vision sensor based on split-gate WSe$_2$ transistors. (d) Reconfigurable vision sensor based on vdWHs [885]. (e) A prototype neuromorphic vision system based on the retinomorphic sensor and the memristive crossbar array [891].

byproduct of 2e$^-$ pathway of ORR, H$_2$O$_2$ is a crucial chemical in the paper-bleaching and water treatment industries [901]. Such side production could be a promising alternative strategy towards H$_2$O$_2$ production, compared to the traditional synthetic methods [902–904]. In recent years, the application of various 2D materials including 2D carbon materials, metal-loaded graphene-based materials, noble metal nanoplatelets, 2D MOFs and MXenes as efficient ORR catalysts have been widely reported.

Carbon electrocatalysts have been widely studied for ORR because of their low cost, good conductivity and high stability [905]. As one of the most attractive 2D materials, graphene-derived materials have been applied as active ORR electrocatalysts through decorating and heteroatom doping [906,907]. Loading metal particles or single atoms (SAs) on graphene substrates with huge specific surface area and excellent conductivity is a good strategy to obtain high ORR performance. Graphene flakes coupled with isolated Fe atoms (FeN$_x$/graphene) exhibited high activity and durability towards ORR in alkaline solutions [908]. Besides, Qu *et al*. reported metal SAs on graphene oxide (GO), which were obtained by mixing GO slurry with bulk metals (such as Cu, Fe, Co, and Ni) (Fig. 31a) [909]. Moreover, the half-wave potential ($E_{1/2}$) for Fe SAs/n-G is 0.92 V *vs*. reversible hydrogen electrode (RHE), 90 mV higher than that of commercial Pt/C catalyst (Fig. 31b). After 10000 voltage cycles, the activity decay is negligible, illustrating their excellent long-term durability. Moreover, when employed as a cathode electrocatalyst for homemade Zn-air batteries, Fe SAs/N-G delivers a maximum power density up to 275 mW·cm^{-2}.

As state-of-the-art electrocatalysts, the Pt-based 2D materials play a very important role in the development of 2D catalysts for ORR. Hu *et al*. reported the 2D coplanar Pt-carbon nanomeshes (NMs) which were composed of interconnected Pt networks and carbon (Fig. 31c) [910]. The Pt/C NMs achieved current densities of 0.360 A·cm^{-2} at 0.80 V and peak power density of 1.21 W·cm^{-2} in the H$_2$/O$_2$ cell (Fig. 31d). Furthermore, the PEMFC showed superior stability against aggregation after high current density of 1000 mA·cm^{-2} for 120 h in H$_2$/O$_2$ system. The density functional theory (DFT) analysis supports that the suitable 2D morphology and open structure with rich active edges are the predominant factors for the PEMFC activity and durability.

As 2D MOF nanosheets exhibit controllable structures, more exposed metal sites and excellent electrical conductivity. They have been widely studied in the field of electrocatalysis for ORR [76,911,912]. As shown in Fig. 31e, f, Zhong *et al*. developed a new type of PcCu-O$_8$-Co 2D conjugated MOF mixing with carbon nanotubes, which shows excellent electrocatalytic ORR activity ($E_{1/2}$ = 0.83 V *vs*. RHE, j_L = 5.3 mA·cm^{-2}) [913]. The *in situ* Raman spectro-electrochemistry demonstrated that good activity is owing to the layer-stacked structures, highly ordered porous framework and well-defined Co-O centers of catalyst. Furthermore, the PcCu-O$_8$-Co material exhibited high performance for air cathode in the Zn-air battery. In addition to metal active sites, high-valence Ni^{4+} active sites in lattice-strained 2D NiFe MOF has also shown to be active catalyst for ORR [914].

In recent years, MXenes have been emerging as next-generation nanomaterials and received increasing attention [916]. Jiang *et al*. utilized the iron-cluster-directed cationic Fe-N-C nanosheets and anionic MXenes to assemble a superlattice-like heterostructure with a surface area of 30 m^2·g^{-1} and ultra-thin structures with repeating thickness of 0.4 and 2.1 nm (Fig. 31g, h) [915]. The synthesized Fe-N-C/MXene heterostructure has an excellent ORR performance, achieving the initial potential of 0.92 V and good stability of 20 h [915].

Besides, various LDH-based core-shell structures, such as CNT@CoMn-LDH (CNT, carbon nanotube) and Co$_3$O$_4$@NiFe-
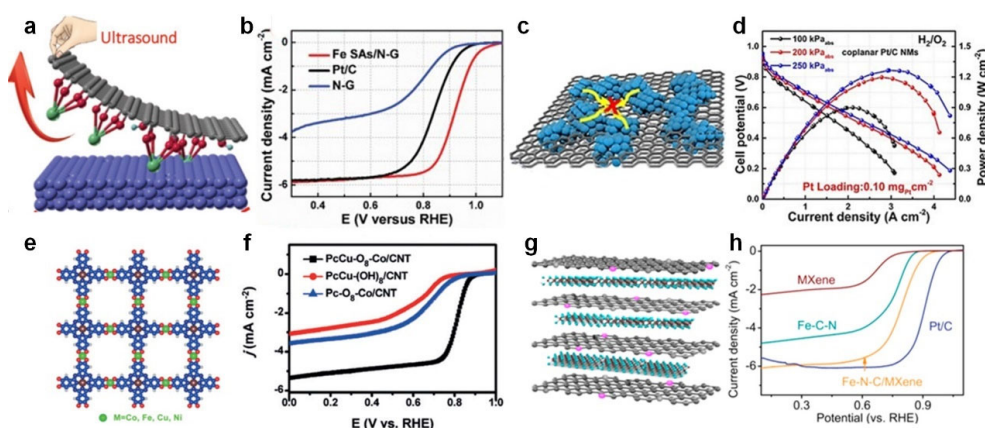
Fig. 31 **(a) Schematic illustration for the preparation and (b) the rotating ring-disk electrode polarization curves in 0.1 mol·L^{-1} KOH of Fe SAs/GO;**
reproduced with permission from Ref. [909], Copyright 2019 John Wiley and Sons. (c) Schematic illustration of 2D coplanar Pt-C nanomeshes.
(d) H$_2$-O$_2$ fuel cell *i–V* polarization and power density plots recorded under different O$_2$ pressure with the cathode Pt loading of 0.10 mg·cm^{-2} for
coplanar Pt/C NMs; reproduced with permission from Ref. [910], Copyright 2020 John Wiley and Sons. (e) Schematic structure of PcCu-O$_8$-M,
(f) ORR polarization curves of PcCu-O$_8$-Co/CNT in 0.1 mol·L^{-1} KOH; reproduced with permission from Ref. [913], Copyright 2019 John Wiley and
Sons. (g) Schematic illustration and (h) LSV plots at the scan rate of 5 mV·s^{-1} in O$_2$-saturated in 0.1 mol·L^{-1} KOH electrolyte for Fe-N-C/MXene
superlattice-like heterostructure; reproduced with permission from Ref. [915], Copyright 2020 American Chemical Society.

LDH, were reported, which exhibit superior activity for ORR. The cores can not only promote the uniform dispersion of LDHs, but also facilitate the transport of electron [917,918].

4.3.1.2　CO$_2$ reduction reaction

CO$_2$ reduction reaction (CO$_2$RR) could not only put a positive role in reducing greenhouse gas emissions but also serve as an efficient route to directly synthesize high value-added chemicals and energy storage molecules for energy conversion and utilization [919]. In recent years, CO$_2$RR has become a continuous research hot-spot in energy- and material-related fields. However, there are still many challenges in the large-scale application of CO$_2$RR, including improving conversion efficiency (reducing overpotential, increasing current density, *etc.*), regulating selectivity (especially for higher-order

hydrocarbons and oxygenates products, *etc.*) and optimization of related materials and catalytic mechanism study [920]. The properties of 2D catalysts can be readily adjusted by variations in their thickness, heteroatom modification, and/or external stimulation (electric field, strain, light, *etc.*), which provides a new route for engineering nanosheets for CO$_2$ electrocatalysis [921]. Accordingly, 2D electrocatalysts, including metals and metal oxides, 2D carbon-based materials, crystalline porous 2D materials and TMDs, have been intensively investigated.

Compared to their bulk materials, 2D metal nanosheets have shown positive results in electrocatalytic performances. Liu *et al*. successfully synthesized triangular Ag nanoplates (Tri-Ag-NPs), which have yielded one of the excellent performances for aqueous CO$_2$ reduction to CO (Fig. 32a) [922]. Compared with Ag
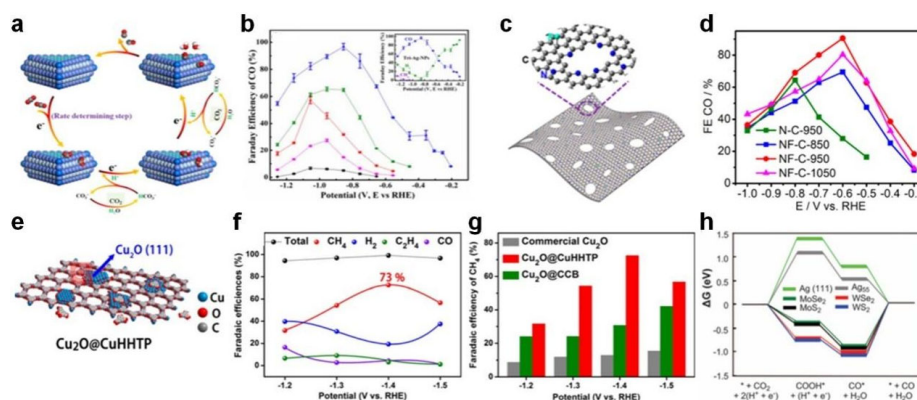
Fig. 32 **(a) Proposed mechanism for CO$_2$RR to CO on Tri-Ag-NPs. (b) Faradaic efficiencies of CO at various applied potentials (the inset shows the**
CO, CH$_4$ and H$_2$ overall FE for Tri-Ag-NPs); reproduced with permission from Ref. [922], Copyright 2017 American Chemical Society. (c) Schematic
illustration of holey NF-C layers. (d) CO FEs over N-C and NF-C; reproduced with permission from Ref. [925], Copyright 2019 American Chemical
Society. (e) Illustration of prepared Cu$_2$O@CuHHTP. (f) Faradaic efficiencies of different products for Cu$_2$O@CuHHTP. (g) Comparison of
CH$_4$ faradaic efficiencies between Cu$_2$O@CuHHTP, Cu$_2$O@CCB, and commercial Cu$_2$O; reproduced with permission from Ref. [926], Copyright 2020
John Wiley and Sons. (h) Calculated free energy diagrams for CO$_2$ electroreduction to CO on Ag(111), Ag$_{55}$ nanoplates, MoS$_2$, WS$_2$, MoSe$_2$, and
WSe$_2$ nanoflakes at 0 V *vs*. RHE; reproduced with permission from Ref. [931], Copyright 2016 Association for the Advancement of Science.

NPs, the Ag nanoplates exhibit a significantly enhanced current density and Faradaic efficiencies (FEs) for CO formation at a low overpotential of 0.746 V, suggesting that the CO₂RR catalytic efficiency in connection with the morphology of catalyst (Fig. 32b). A cheaper, leaf-shaped Bi nanosheet catalyst was reported to catalyze the electrochemical reduction of CO_2 to formic acid (HCOOH) in 1 mol·L⁻¹ KHCO₃ or KOH solution with a much higher FE (over 85% or 90%) by the flow cell configuration [923].

Nitrogen-doped graphene has proven to be a promising metal-free catalyst for electrocatalytic production of CO, $HCOO^-$ and CH₄ [921,924]. Pan *et al*. developed an N, F-co-doped 2D holey carbon nanostructure (NF-C) (Fig. 32c, d) [925]. After 40 h of testing, the CO₂RR performance of NF-C reached CO faradaic efficiencies of 90% and the overpotential as low as 490 mV. The performance is far superior to the comparative n-doped 2D holey carbon nanostructure (N-C) and most of the carbon-free catalysts that have been reported. A large number of pyridinic N provides rich ultrahigh active and selective sites and the high surface area makes these active sites fully accessible.

Crystalline porous 2D materials, such as MOFs and COFs, are promising candidates for electrocatalytic reduction of CO_2 due to their porous crystalline structures and periodically arranged isolated active sites. As shown in Fig. 32e–g, Yi *et al*. reported that Cu₂O(111) quantum dots synthesized *in situ* on a porous conductive 2D MOF and it can be served as a single type of active sites for electroreduction of CO_2 to produce CH₄ with high selectivity of 73%, outperforming most of the reported catalysts (especially MOF-based catalysts) [926]. In some other works, phthalocyanine molecules as active sites were implanted into 2D conductive MOFs for efficiently CO_2 electroreduction reaction to CO [927,928]. Donor-acceptor heterojunctions or tetrathiaful-valene units were integrated into 2D COFs to increase the electron transfer rate, resulting in good catalytic performance towards CO [929,930].

In addition, TMDs have been found to significantly improve CO_2 reduction for CO generation in ionic liquids, and the selenides appear to be the more effective [921]. On a series of TMD nanoflakes (WSe₂, MoSe₂, WS₂, and MoS₂), the formation of CO* from CO_2 is kinetically more favorable than on Ag (Fig. 32h), resulting in high current densities and high CO selectivity [931]. In addition, LDH-based materials are also reported for catalyzing CO₂RR. With NiZnAl-LDH/rGO (rGO, reduced graphene oxide) as precursor, Li *et al*. reported the synthesis of rGO/Al₂O₃ supported NiO/ZnO which could effectively electrocatalyze CO_2 reduction to CO with a high Faradaic efficiency of 92% [932].

4.3.1.3 Nitrogen reduction reaction

Ammonia (NH₃) is an important industrial raw material [933,934]. However, the conventional Haber-Bosch method is a low efficiency and high energy consumption process under the conditions of high temperatures (400–600 °C) and high pressures (150–350 atm, 1 atm =1.01325 × 10⁵ Pa) [935,936].

Therefore, a sustainable and low-energy consumption method to generate NH₃ is urgently needed. Electrochemical nitrogen reduction reaction (NRR) is an advanced method for sustainable NH₃ synthesis without carbon emission under ambient conditions [937,938]. But the NRR process needs suitable electrocatalysts due to the difficult to break strong N≡N triple bond [939,940].

4.3.1.3.1 2D metal-based NRR catalysts

Great efforts have been made to explore novel catalysts that can efficiently promote NRR while simultaneously limit the HER. To this end, different methods like constructing superhydrophobic surface layer, alloying, and Li⁺ incorporation have been developed [941–943]. To date, NRR electrocatalysts based on 2D materials are very rare, but already showing great promise in theoretical studies. DFT simulations suggested that individual Mo atoms supported on the defect-rich boron nitride (BN) monolayers could be used as a promising electrocatalyst for NRR, in which the well dispersed Mo SAs coordinated to the N atoms would contribute good performances in activating the inert N₂ molecules, stabilizing the N₂H intermediate and destabilizing the NH₂ species [944]. Han *et al*. prepared and optimized Mo SAs supported on the n-doped porous carbon (SA-Mo/NPC) as a low-cost catalyst (Fig. 33) for the electrochemically catalyzed NRR. Because of the hierarchically porous carbon frameworks and high density of catalytically active sites, SA-Mo/NPC delivers a large NH₃ yield rate of 34.0 ± 3.6 µg·h⁻¹·mg⁻¹ in 0.1 mol·L⁻¹ KOH aqueous solution at ambient conditions, which is much higher than that of the other non-precious-metal NRR electrocatalysts. Furthermore, SA-Mo/NPC also possesses excellent catalytic durability. No obvious current decrease was observed during the N₂ electrolysis for 50000 s. These results indicate that the rational design and synthesis of non-precious-metal SA catalysts could favor the electrocatalytic NRR [945].

MXenes have been widely investigated because of their important applications in lithium batteries, electrocatalysis, membrane separation, and photocatalysis [134,946–950]. Theoretical studies revealed that MXenes with M atoms exposing on the surface can effectively activate the adsorbed N₂ molecules, and thus favor the reduction of N₂ to NH₃ [951]. Actually, the basal planes of MXenes are typically terminated by OH*, O* and F*, which are bonded with surface M atoms [72,952]. Note that MXenes with surface terminated by O* would favor the hydrogen evolution rather than NRR due to their relatively weak binding ability toward N₂ molecules [953]. Bearing this in mind, great research efforts have been devoted to exposing the active sites of MXenes for N₂ adsorption and the subsequent activation and reduction. Peng *et al*. reported a single-atomic Ru modified Mo₂CTX MXene nanosheets (SA Ru-Mo₂CTX) for high-performance electrocatalytic NRR under ambient conditions (Fig. 34). The obtained SA Ru-Mo₂CTX shows a high FE of 25.77%, and large NH₃ yield rate of 40.57 µg·h⁻¹·mg⁻¹ at the potential of −0.3 V (*vs*. RHE). DFT calculations and operando
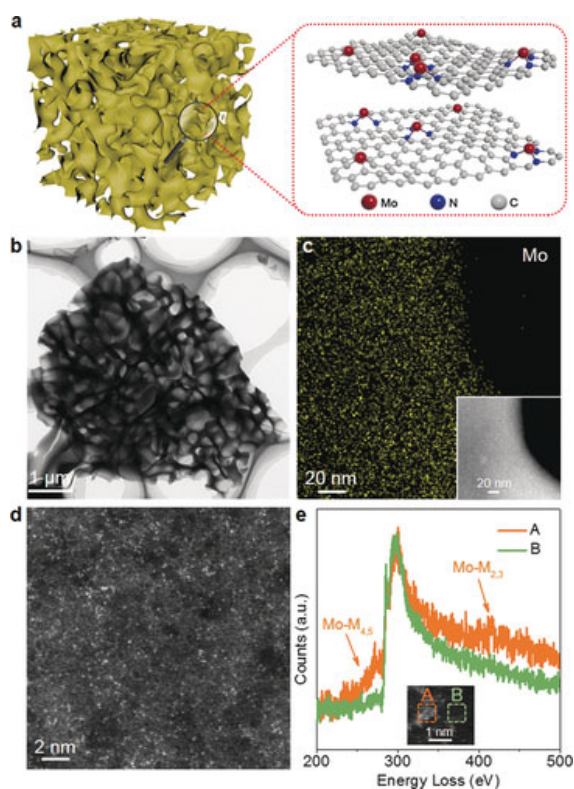
Fig. 33　(a) An illustration of SA-Mo/NPC and its corresponding atomic structure model. (b) A TEM image of SA-Mo/NPC. (c) Mo EDS mapping reveals the homogeneous distribution of Mo on the carbon support; the figure inset is the corresponding HAADF-STEM image. (d) Atomic-resolution HAADF-STEM image. (e) EELS spectra from areas A and B in the atomic-resolution HAADF-STEM image of the inset; area A does contain single Mo atoms whereas area B does not. The two orange arrows point to the signals of the Mo $M_{4,5}$ and $M_{2,3}$ edges, respectively. Reproduced with permission from Ref. [945], Copyright 2019 John Wiley and Sons.

X-ray absorption spectroscopy investigations suggested that Ru SAs supported on the Mo_2CT_X MXene nanosheets serve as essential electron back-donation centers for the activation of N_2 molecules, which could favor the N_2 adsorption and activation behaviors of SA Ru-Mo_2CT_X, as well as decrease the energy barriers of the first hydrogenation reaction. This study provides an important atomic-level engineering strategy of modulating the NRR performance of catalysts [954].

To better understand the reaction mechanism of NRR, it is essential to design transition metal nitrides (TMNs) with simple structure and durable surface vacancy for the correlation of real-world catalysts and theoretical models. 2D materials possess onefold and entirely exposed crystal surfaces, which have been extensively utilized as a platform for both practical application and theoretical calculation in electrocatalysis [955–958]. Simultaneously, various studies reveal that 2D materials possess surface distortions, which could greatly increase the structural stability of both 2D materials as well as their surface vacancies [959–961]. As a result, vacancy engineering of 2D TMNs is an effective strategy to prepare advanced NRR catalysts. Liu

et al. synthesized atomically ultrathin Rh nanosheet nanoassemblies (Rh NNs), which were used as an electrocatalyst for NRR. The obtained Rh NNs exhibit an outstanding catalytic performance toward NRR, with a large NH_3 yield rate of 23.88 $\mu g \cdot h^{-1} \cdot mg^{-1}$ and excellent catalytic selectivity (no N_2H_4 was observed) at a very low potential of −0.2 V (*vs*. RHE), which is much better than most of present NRR electrocatalysts [962]. The superior NRR performance of Rh NNs is attributed to their extremely large specific surface area as well as the modulated electronic structure. He *et al*. fabricated 2D mosaic bismuth nanosheets (Bi NSs) by using an *in situ* electrochemical method. Notably, the obtained Bi NSs showed a large NH_3 yield rate of about 13.23 $\mu g \cdot h^{-1} \cdot mg^{-1}$ and FE of 10.46% ± 1.45% at the potential of −0.8 V (*vs*. RHE), which is much better than the Bi NPs. It was proposed that the exposure of abundant edge sites and the decreased Bi–Bi interlayer distance in Bi NSs could contribute to their enhanced NRR performance in comparison with the Bi NPs [963].

4.3.1.3.2　Graphene-based NRR catalysts

Graphene is a classic 2D material with superior electronic transport and excellent catalytic performance of many electrocatalytic reactions and its functionalization can improve its pristine properties [964–966]. Through the functionalization of graphene, it is expected graphene could be an excellent NRR electrocatalysts for effective N_2 to NH_3 conversion [967]. Here, we will discuss the recent works of nanohybrids and heteroatom doped graphene for electrochemical NRR.

The noble metal catalysts are excellent for NRR, but the low abundance and high costs greatly restrict the large-scale applications. Meanwhile, nanomaterials have faced the problem of serious aggregation. To address this problem, the hybrid catalysts consisting of metal NPs and graphene are proposed. As shown in Fig. 35a, the metal precursors mixed with reductants, and then formed a highly dispersed PdCu NPs/rGO composites, where the rGO sheets are highly desirable for loading the metal NPs and promote the mass transfer of reactants on the surface of catalyst [941]. Au is a well-known excellent material for NRR. Li *et al*. reported an amorphous Au NPs anchored on rGO material [968]. The N_2 molecule shows stronger binding with amorphous Au NPs, which possess high catalytic activity. Due to the high price of noble metals, replacing it with non-noble metals is the rational strategy. A series of materials, *i.e.*, TiO_2 NPs/rGO [969], CuO/rGo [970], Mn_3O_4 NPs/rGO [971], MoP NPs/rGO [972], and MoS_2 nanosheet/rGO [973] composites, *etc.*, are reported to exhibit high NH_3 yields. From the viewpoint of size, the NPs and nanosheets are too large to weak the properties of high surface area and conductivity of 2D graphene. To enlarge the advantage of non-noble metal oxide/graphene composites, the QDs/graphene composites have been widely studied for NRR. The metal oxide QDs show exceptional NRR performance equal to and even higher than those of noble metal-based catalysts. The NRR activity of CoO QDs/rGO [974], NiO QDs/rGO [975], and SnO_2 QDs/rGO [967] could efficiently and stably
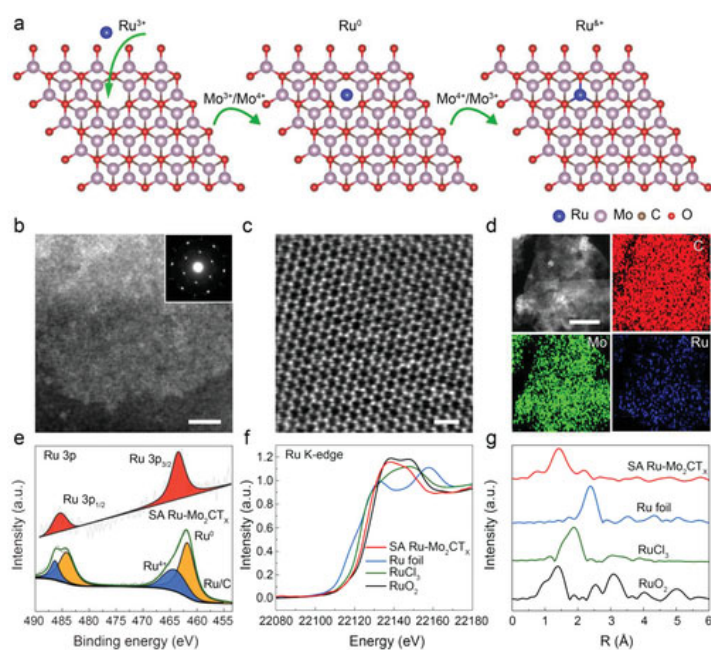
Fig. 34 **Fabrication and structure characteristics of SA Ru-Mo₂CTX. (a) Schematic illustration of the fabrication mechanism. (b) HAADF-STEM image of SA Ru-Mo₂CTX, insert is the corresponding SAED pattern. (c) The magnified HAADF STEM image of SA Ru-Mo₂CTX. (d) The STEM-EDS elemental mapping of SA Ru-Mo₂CTX. (e) XPS spectra of SA Ru-Mo₂CTX and commercial Ru/C in Ru 3p regions. (f) The normalized XANES spectra at the Ru K-edge of RuO₂, RuCl₃, Ru foil and SA Ru-Mo₂CTX. (g) The FT-EXAFS spectra derived from EXAFS of Ru K-edge of RuO₂, RuCl₃, Ru foil and SA Ru-Mo₂CTX. Scale bars: (b) 5 nm, (c) 1 nm, (d) 50 nm. Reproduced with permission from Ref. [954], Copyright 2020 John Wiley and Sons.**
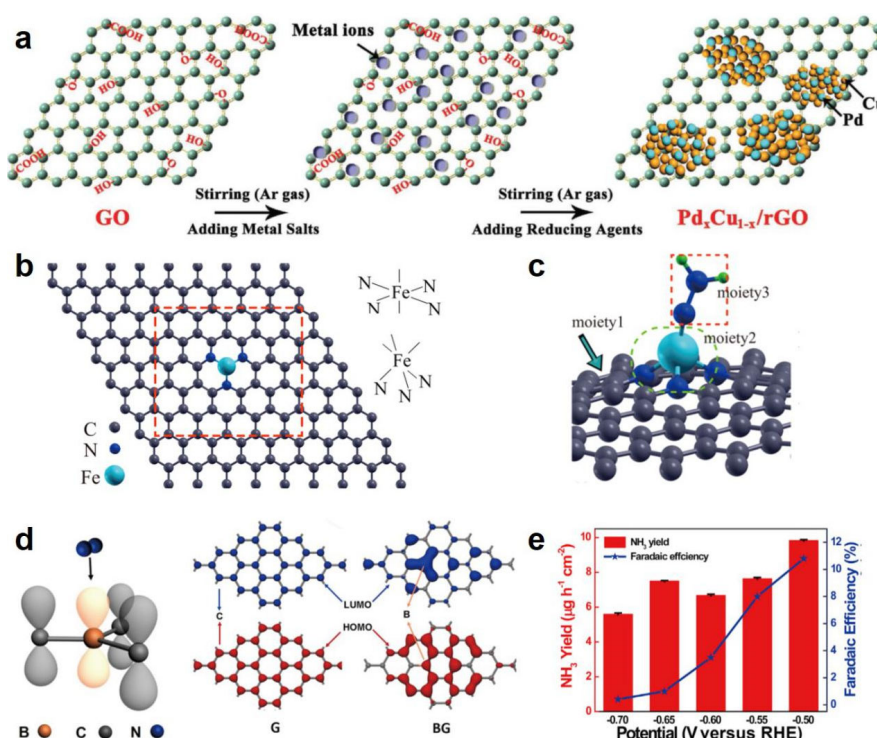
Fig. 35 **(a) Schematic illustration of the preparation of PdCu NPs/rGO composites; reproduced with permission from Ref. [941], Copyright 2018 John Wiley and Sons. (b) Optimized structure of FeN₃-graphene, (c) moieties of the Fe－N＝NH₂ intermediate; reproduced with permission from Ref. [978], Copyright 2016 American Chemical Society. (d) Schematic of the atomic orbital of BC₃ for binding N₂ and LUMO and HOMO of undoped graphene and B-doped graphene, (e) the NH₃ production rates and FE of B-doped graphene, the error bars represent the average of three measurements [983].**

catalyze the NRR at ambient conditions.

Compared to the heterogeneous composite catalysts, graphene delivers high conductivity, tunable structure and com

position, and strong tolerance to acidic/alkaline. The theoretical and experimental studies suggest that heteroatoms doping of graphene leads to effective enhanced of the electrocatalytic

properties [976,977]. For example, embedding Fe atom in N_3-graphene can well capture the N_2 molecules (Fig. 35b). Through the first-principles calculations, the superior N_2 fixation activity can be attributed to the high-spin polarization of the FeN_3 center (Fig. 35c) [978]. Xia *et al*. reported an S-doped graphene which possessed superior activity and stability for electrocatalytic NRR [979]. Further, Tian *et al*. reported an N, S co-doped graphene which could effectively boost the activity of NRR due to the enhanced N_2 adsorption and N≡N bond elongation [980]. Some recent studies show that doping oxygen atom is also effective to enhance the NRR performance. Usually, introducing O atom on carbon catalysts is *via* acid oxidation [389]. But Wang *et al*. adopted an Ar anneal method of sodium gluconate to obtain O-doped graphene (O-G). Under ambient condition, the O-G catalyst showed high catalytic activity with large NH_3 yield of 21.3 $\mu g \cdot h^{-1} \cdot mg^{-1}$ and high FE of 12.6% [981]. The key to design an effective NRR electrocatalyst is to build an active center which can effectively adsorb and activate the N_2 molecules. As N_2 is a Lewis base, it is ideal to create Lewis acid active center to bind N_2. Boron (B) is a natural Lewis acid due to the electron deficiency so the B is an important element to induce electron deficiency in graphene [982]. The B-doped graphene is synthesized by anneal H_3BO_3 and GO in H_2/Ar gas (Fig. 35d). When the amount of B doping is 6.2%, such a catalyst showed an excellent yield of NH_3 and high FE of 10.8% (Fig. 35e). With the further theoretical investigations, the B-C centers play a key role in N_2 adsorption and NH_3 production [983]. In addition, the defect-rich graphene can also as high efficiency NRR catalyst, but this has only a few reports before [984].

Although the research of electrochemical NRR have made some progress, there are still many problems and challenges that the yield and FE are far below the application level. How to improve the energy efficiency and to repress the side reaction of hydrogen evolution reaction (HER) by optimizing the physical and chemical properties of 2D catalysts remain the main direction to be explored. In addition, the research on the catalytic mechanism with 2D catalysts is still in its infancy and needs more in-depth research through more experiment and theoretical calculation to guide the design of NRR electrocatalysts in future.

4.3.1.4 Methanol oxidation reaction/ethanol oxidation reaction

Direct methanol fuel cells (DMFC) and direct ethanol fuel cells (DEFC) have received extensive interest because of the distinct advantages of ethanol and methanol fuels, such as low cost, easy availability, high energy density, abundance, safety for transportation and storage, *etc*. Therefore, DMFC and DEFC have been considered as promising power conversion devices and utilization technology in the future [985–987]. The anode half reactions of DMFC and DEFC correspond to methanol oxidation reaction (MOR) and ethanol oxidation reaction (EOR), respectively. Currently, noble metals Pt and Pd usually used as the electrocatalysts. In order to further enhance the reaction activity of the catalysts, while reducing the amounts of precious

metals, researchers have developed a series of Pt-based and Pd-based nanomaterials with ultra-thin 2D structures as high-efficiency MOR or EOR catalysts. Yang *et al*. found that the rGO can promote the generation of 2D Pt nanosheet with thickness of about 9.8 nm in a eutectic molten salt mixture of KNO_3 and $LiNO_3$. The growth mechanism study revealed that the aggregation and subsequent sintering of individual NPs along rGO surface were involved in the growth process of Pt nanosheets. The electrochemical measurements showed that the obtained composite possess an improved durability and activity toward MOR in comparison with commercial Pt/C catalyst [988]. Bu *et al*. synthesized PtPb/Pt core/shell hexagonal nanoplates (Fig. 36), which show excellent catalytic performance toward alcohol oxidation because of the large internal biaxial tensile strain. They can largely outperform the catalytic performances of PtPb nanoplates and commercial Pt/C in terms of MOR and EOR [989]. Luo *et al*. showed that spin control of Pd-Fe-Pt nanomeshes (NMs) could realize great enhancement for the electrooxidation of fuels. It was revealed that $Pd_{59}Fe_{27}Pt_{14}$ NMs possess the largest number of polarized spins, which can facilitate the adsorption of OH_{ads} and thus favor the oxidation of CO_{ads}. As a result, the optimized $Pd_{59}Fe_{27}Pt_{14}$ NMs show superior MOR stability and activity over those of Pt/C and PtRu/C. Furthermore, the optimized $Pd_{59}Fe_{27}Pt_{14}$ NMs also exhibit excellent catalytic performances toward both EOR and FAOR [990].

Recently, Saleem *et al*. reported the successful synthesis of free-standing ultrathin Pt-Cu nanosheets with controllable lateral size in the range of 10–50 nm. Benefit from its larger specific surface area (62.8 $m^2 \cdot g^{-1}$) and the alloying effect produced by the introduction of Cu, The Pt-Cu alloy nanosheets exhibit excellent catalytic activity in EOR. Electrochemical test results show that the mass activity of PtCu nanosheets is 19 and 2.7 times larger than that of Pt black and Pt/C catalysts, respectively. In addition, the catalytic performance of PtCu alloy nanosheets is also significantly higher than that of PtCu alloy nanocones with the same composition, which fully proves the advantages of 2D structure in MOR catalysis [991]. Hong *et al*. prepared ultrathin Pd-Pt-Ag nanosheets with thickness of around 3 nm. Because of their specific compositional and structural characteristics, the obtained Pd-Pt-Ag nanosheets demonstrated much enhanced electrocatalytic performance toward EOR in comparison with their NP counterparts and the commercial Pd/C and Pt/C catalysts [992]. Hong *et al*. synthesized hexagonal close packed (hcp) structure PtBi nanoplatelets (NPLs) with the average thickness of 6 nm. The mass activity for PtBi NPL/XC-72 is 470 $mA \cdot mg^{-1}$, which is much higher than 250 $mA \cdot mg^{-1}$ of commercial Pt/C. Furthermore, The Pt-Pt bond in the PtBi alloy phase becomes longer due to the insertion of Bi atoms, which weakens its combination with the CO intermediate species, and therefore exhibits better resistance to CO poisoning and catalytic stability than pure Pt. Compared with methanol, ethanol is less toxic and safer in transportation and operation. However, since
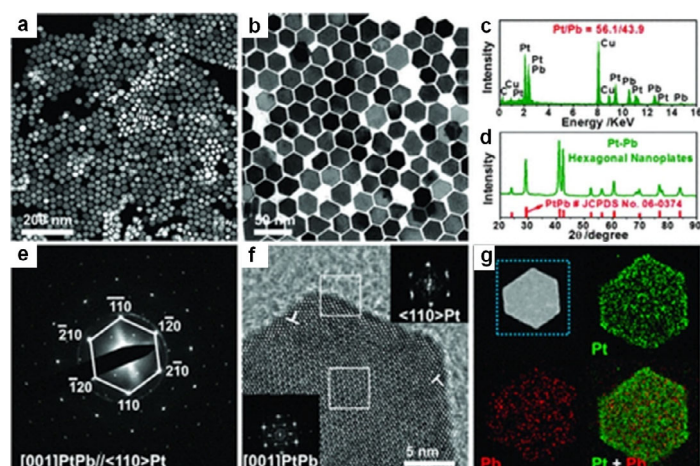
Fig. 36 **Morphology and structure characterization of PtPb hexagonal nanoplates. Representative (a) HAADF-STEM image, (b) TEM image,**
(c) TEM-EDX, and (d) PXRD pattern of PtPb hexagonal nanoplates. (e) SAED and (f) HRTEM of one single hexagonal nanoplate; insets in
(f) are the FFT patterns from the white squares at the edge of and inside the nanoplate, respectively. (g) STEM-EELS elemental
mapping of PtPb hexagonal nanoplates: HAADF-STEM image, Pt mapping in green, Pb mapping in red, and integrated mapping of Pt and
Pb are shown. The compositional ratio between Pt/Pb is 55.9/44.1, as revealed by ICP-AES. Reproduced with permission from Ref. [989]**,**
Copyright 2015 Association for the Advancement of Science.

the complete oxidation process of ethanol involves the breaking of C−C bonds, it has a higher reaction energy barrier [993–995].

4.3.1.5 Formic acid oxidation reaction

Direct formic acid fuel cell (DFAFC) has been considered as one of the most promising power supply for next-generation electronic equipments [996]. Pt and Pd are ordinarily known as efficient formic acid oxidation reaction (FAOR) catalysts, and have been investigated intensively [997–999]. However, the poor poisoning resistance as well as low mass activity of DFAFC limit their practical application. Recently, great efforts have been devoted to improving the stability and activity of the FAOR electrocatalysts. Lv *et al.* reported a new class of 2D PdIr bimetallenes with an average thickness of only ca. 1.0 nm for the FAOR (Fig. 37). The obtained PdIr bimetallenes possess an extremely large electrochemical active area of 127.5 ± 10.8 $m^2 \cdot g^{-1}$, and also demonstrate an ultrahigh activity, quite low overpotential and enhanced stability toward the FAOR. Theoretical calculations reveal the generation of concave-convex type electro-active areas *via* the effect of surface strain [1000].

4.3.1.6 Hydrogen evolution reaction

Hydrogen evolution reaction (HER) is the cathodic reaction of electrocatalytic water splitting, producing high-purity hydrogen, a promising type of clean and renewable energy [1001]. Many 2D materials are excellent HER catalysts, even showing comparable performance to the conventional noble metal catalysts.

4.3.1.6.1 Transition metal chalcogenides

Transition metal chalcogenides (TMCs) have been widely recognized as promising electrocatalysts due to their predicated low ΔG_H values [1002], low cost, and high stability [1003]. Various 2D TMCs have been prepared and studied for the HER, including Co_3S_4 [1004], Ni_3S_2 [1005,1006], NiS [1007], $NiCo_2S_4$ [1008], $NiSe_2$ [1009,1010], and so on [1011,1012]. Among which, transition metal sulfides have

been identified as the most promising ones. 2D MS_2 is a type of TMD materials, and similar to graphene, a vdW materials. The vdW gaps lead to a poor transmission of electrons between layers and weakens the overall conductivity of the materials [1013]. Tributsch *et al.* studied the electrocatalytic hydrogen production
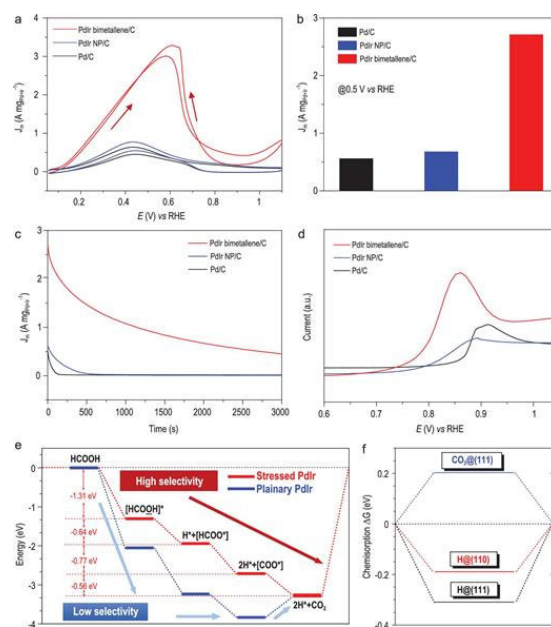
Fig. 37 **(a) CVs of PdIr bimetallene/C, PdIr NP/C and Pd/C for**
FAOR in 0.1 mol·L^{-1} HClO$_4$ containing 0.5 mol·L^{-1} HCOOH at the
scan rate of 50 mV·s^{-1}; (b) mass activities of different catalysts at the
potential of 0.5 V *vs.* RHE; (c) chronoamperometric curves of the
PdIr bimetallene/C, PdIr NP/C and Pd/C catalysts at 0.5 V *vs.* RHE;
(d) CO stripping tests of PdIr bimetallene/C, PdIr NP/C and Pd/C
catalysts conducted in 0.1 mol·L^{-1} HClO$_4$ at the scan rate of 50 mV·s^{-1};
(e) free energy pathway (ΔG) for FAOR under acidic conditions;
(f) chemisorption of H and CO$_2$ on the surface (111) [1000]**.**

of bulk MoS₂ and confirmed its poor activity due to both its low conductivity and less active sites [1014]. Therefore, TMDs were not regarded as promising candidates for electrocatalysis. In 2005, Hinnemann *et al*. predicted the high catalytic activity of the edge sites of MoS₂ by using density function calculations, and point out the potential HER performance of this material [1015]. Later, Jaramillo *et al*. experimentally proved the high catalytic activity of the edge sites of MoS₂ nanoplates. A linear relationship between catalytic activity and the number of edge sites were observed [1002]. These new findings demonstrate the huge potential of novel HER catalysts based on 2D materials [1016–1020]. Currently, the key development in this field is mainly built around the strategies to increase active sites such as the highly active edge sites, grain boundaries [1021], and sulfur vacancy [1022].

The various defect engineering strategies are built on the fact that defects inside or on the surface of the materials can change the coordination environment of the adjacent atoms, and consequently affect the electronic structure and surface properties [1016,1021–1025]. In an typical example, Li *et al*. study the Sulphur (S) vacancies and strain on the effect of the basal plane of monolayer 2H-phase MoS₂ for HER [1022]. The experimental and theoretical studies indicate that S-vacancies act as the new catalytic sites in MoS₂ basal plane. Hydrogen can bind directly to expose Mo atoms. The formation of S-vacancies in the basal plane can produce new bands in the gap near Fermi level. The new gap state is responsible for the hydrogen adsorption on S-vacancies. With the increasement of S-vacancies, the bands of MoS₂ move closer to Fermi level, and further enhance the H binding. When the concentration of S-vacancies is 12.5%, the free energy of hydrogen adsorption reached the optimum value and near zero. More than this, the adsorption of hydrogen atoms can be further modulated by strain. The positions of these new bands further shift towards the Fermi level as tensile strain is applied.

Designing 2D materials with heterostructures is another effective strategy towards enhanced HER performance [206,548,1026–1030]. The synergistic effect of composite materials along with and the enhanced charge transport property can improve the catalytic activity. Shah *et al*. prepared a nickel@nitrogen-doped carbon@MoS₂ nanosheets (Ni@NC@MoS₂) by a simple hydrothermal process for HER [1026]. The catalyst has shown an onset overpotential with 18 mV and Tafel slope with 47.5 mV·s⁻¹. The excellent performance can be ascribed to the synergistic effect between different composite materials, which including the dense catalytic sites with exposed edges on MoS₂ and the fast electron transfer from the substrate to MoS₂ nanosheets. Liu *et al*. also prepared a MoS₂/Ti₃C₂Tₓ hierarchical "nanoroll" [1027]. The hierarchical electrocatalyst was synthesized by combining liquid nitrogen-freezing and subsequent annealing. The Ti₃C₂Tₓ nanosheets with rolled structure and the vertically aligned MoS₂ crystallites can afford more active sites and facilitate the charge transfer process. The substrate can also influence the electrocatalysis [965]. Zhang *et al*. developed a

unique two-zone CVD technique and successfully grow 2D TaS₂ on different substrates like carbon fibers, Mo foil, glassy carbon, and Au foil. They studied the catalyst-substrate interaction and found TaS₂ on Au foils own the best performance with smallest overpotential and lowest charge transfer resistance. They ascribed the good performance to the charge injection and suitable lattice mismatch between Au and TaS₂ [211].

Metal-support interaction is a key role in heterogeneous catalysis. Turning the metal-support interaction is a feasible way to adjust the catalytic activity and electronic structure of supported metal catalyst. Shi *et al*. prepared four types of SA Pt catalysts on various TMDs supports by using a site-specific electro-deposition technique. They found that the electronic metal-support interaction can activate the acidic and alkaline HER by tailoring the oxidation state of single-atom Pt. They correlate the alkaline/acidic HER activity with Pt-H/Pt-OH interaction and average oxidation states of SA Pt [1031].

4.3.1.6.2 Xenes

As a typical 2D material, graphene is inert toward HER with a large ΔG_{H*} (1.85 eV) [1003]. However, various modifications of materials can change the properties and enhance the electrocatalytic performance. Heteroatomic doping into the graphene matrix can induce the redistribution of charge/spin to graphene layer, which has been confirmed a useful way to improve the HER activity. For instance, the B-doped graphene [1032] and n-doped graphene [1033,1034] all exhibit remarkable activity in electrocatalysis. Moreover, the co-doping strategy are increasing being used to achieve high HER performance. For example, N and S co-doped nonporous graphene has shown extremely high catalytic activity in HER, showing comparable performance to the best Pt-free HER catalyst [1035]. In another example, N and P co-doped graphene demonstrated greatly enhanced electrochemical performance in comparison with single doped counterparts [1036]. In order to explain the effectiveness of co-doping, they explored various nonmetallic elements doped graphene models using DFT calculations. It shows that the co-doping of P and N would decrease the ΔG_{H*} value to increase the original H* adsorption, resulted in the highest HER activity. Experimentally, the incorporating of both P and N heteroatoms to graphene matrix was realized *via* the chemical doping process. The co-doped graphene catalysts exhibited much higher exchange current density and lower HER overpotential than pure and doped samples. In addition, the synergistic effects of co-doping N and P heteroatoms favor the proton adsorption and reduction, further enhanced the electrocatalytic performance.

Combing 2D heterostructure with other components can providing large surface area and more exposed active sites, leading to high-efficiency HER activities. Zhang *et al*. developed a 2D NiS/graphene heterostructure composites using a novel deep eutectic solvents (DESs) as precursors. The homogeneous system can provide enough contact of different components and contribute the coupling of NiS nanosheets and graphene. The

compound exhibits high electrocatalytic efficiency and stability for HER and OER [1037]. In another example, the heterostructure of LDH nanosheet and defective graphene also show high activity for overall water splitting [1038]. Deng *et al.* designed a hierarchical architecture that composes of ultrathin graphene shell that encapsulates a uniform CoNi nanoalloy to boost its HER activity in acidic media. Base on the theoretical analysis in Fig. 38, it shows that the electron penetration from CoNi nanoalloy to graphene surface was greatly promoted due to the ultrathin graphene shells. By decreasing the number of graphene layer and increasing the amount of N dopant, the electron density in graphene shells were significantly increased, which further enhanced the HER activity [1039].

4.3.1.6.3 MXenes

MXenes with unique structure and electronic properties are regarded as promising electrocatalyst for HER. Among which, molybdenum carbide (Mo_2C) has attracted most attention due to its high electrical conductivity and optimal hydrogen-adsorption properties. Jia *et al.* prepared the ultrathin n-doped Mo_2C nanosheets (n-Mo_2C NSs) for the HER [1040]. The prepared materials own a single-crystal structure with a thickness of 1.0 nm. The Mo_2C NSs with large electrochemical area is beneficial to the diffusion of electrolyte, electrocatalyst, and gas. Besides, the surface of the n-Mo_2C NSs are encompass by apical Mo atoms, exposing more Mo active sites. The prepared n-Mo_2C NSs has shown high activity for HER, under the cathodic current density of 10 mA·cm^{-2}, with an onset potential of -48.3 mV *vs.* RHE, Tafel slope of 44.5 mV·s^{-1} and overpotential of 99 mV. The catalyst also shown excellent long-term stability.

Designing MXenes materials with hybrid structure can remarkably improve the catalytic activity [548,1027,1041–1044]. Du *et al.* prepared a nickel-based bimetal phosphorus trisulfide ($Ni_{1-x}Fe_xPS_3$) 0D-2D nanohybrids [1041]. Different Ni : Fe

compositions can be obtained by turning the ratio of Ni and Fe during the preparation. The lateral size of NFPS decreases from 50 to ca. 15 nm with the increasement Fe content. By changing the Ni : Fe ratio to 9 : 1, the obtained $Ni_{0.9}Fe_{0.1}PS_3$@MXene showed low overpotential (196 mV) for the HER in 1 mol·L^{-1} KOH solution. Besides, the $Ni_{0.7}Fe_{0.3}PS_3$@MXene ‖ $Ni_{0.9}Fe_{0.1}PS_3$@MXene couples show a low onset potential of 1.42 V and requires just 1.65 V to achieve a current density of 10 mA·cm^{-2}, which is much better than that of noble metal IrO_2 ‖ Pt/C electrocatalyst (1.71 mV@10 mA·cm^{-2}). Li *et al.* prepared a ternary PMo_{12}-PPy/rGO nanocomposite and studied the PMo_{12} content and carbonization temperature on the HER activity [1044]. The rGO-supported Mo-based catalysts may effectively hinder Mo sources and graphene from aggregating during the preparation process. In addition, the theoretical and experimental results show that the small size of Mo_2C NPs can exposure more active sites. And the introduction of heteroatoms (N, P) to the carbon structure leads to charge density distribution and asymmetry spin. During the carbonization process, rGO can improve the dispersion of PMo_{12} and further get highly dispersed Mo_2C. rGO with outstanding electrical conductivity can also promote the charge transport process. The conjugation between Mo_2C and NPC/NPrGO could favor fast electron transfer. These synergistic effects contribute the potent HER activity for Mo_2C@NPC/NPrGO.

4.3.1.6.4 Layered double hydroxides

LDH-based materials also have important applications in HER. As a typical work, Liu *et al.* synthesized the heterostructures composed of (Ni, Fe)S_2 nanobox and MoS_2 nanoarray based on NiFe-LDH precursors, which show greatly improved activity ($\eta_{10} = 130$ mV) and durability toward HER [1045]. The obtained (Ni, Fe)S_2@MoS_2 with abundant active sites offer favorable chemisorption of hydrogen, which account for the easy generation of S-H$_{ads}$ in the alkaline environment. In addition, LDHs can also be used as an excellent carrier to load other active materials to achieve synergistically enhanced HER performance. For example, Guo *et al.* found that anchoring Pd nanoparticles on the surface of NiFe-LDH nanosheet can improve HER performance [1046]. The introduction of Pd induces the defects and lattice distortion as additional active sites, facilitates charge transfer, and adjusted the electronic state of active sites, thus enhancing the adsorption capacity toward H and accelerating the reaction kinetics than NiFe-LDH.

4.3.1.7 Oxygen evolution reaction

Oxygen evolution reaction (OER) is the anode reaction of electrocatalytic water splitting [1047]. Typically, the OER half reaction significantly restricts the overall water splitting efficiency due to its sluggish reaction kinetics related to a complex four-electron redox process [1048–1050]. Great efforts have been made to solve this problem. Improving the catalytic activity and increasing the number of active sites are two common strategies to improve the OER performance. 2D materials with unique structures, facile surface reaction, fast electron transfer
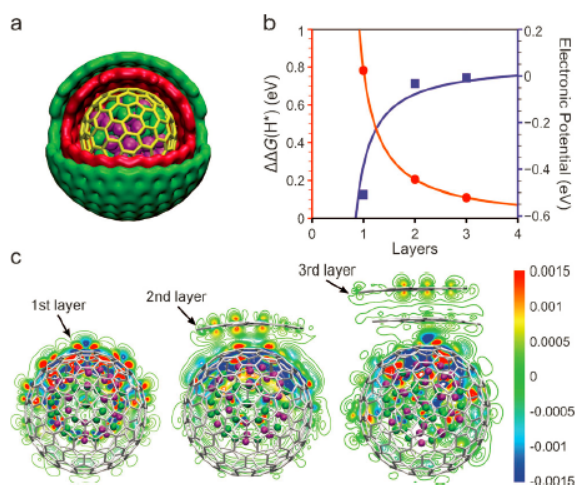

Fig. 38　(a) Diagram of CoNi alloy encapsulated by graphene with three-layer. (b) Plots of ∆G(H*) (red line) and electronic potential (blue line) *vs.* the graphene layers. (c) Electron density redistribution of CoNi covered by one to three layers of graphene. Reproduced with permission from Ref. [1039], Copyright 2015 John Wiley and Sons.

and mass transport, have shown excellent performance in the OER [1051,1052].

4.3.1.7.1 Metal organic frameworks

Metal organic frameworks (MOFs) have shown excellent electrocatalytic activity for OER [1053–1057]. MOFs are consisted of metal atom node and organic ligand with periodic units' structures. However, the poor mass permeability, low conductivity and blockage of active sites by organic ligands have limited their applications. On the other hand, the electron transfer and mass transport properties can be greatly improved by adopting 2D MOF structures [1058]. Ge *et al.* designed a simple way to prepare 2D MOF-Fe/Co nanosheets by stirring the mixture of Fe/Co salts and 1,4-BDC [1058]. Water and TEA are important additives to stabilize the MOF nanosheets. The obtained 2D MOF-Fe/Co nanosheets exhibit excellent performance for OER, which is better than the bulk and 3D MOF-Fe/Co samples. Both experiments and DFT calculation were employed to study the reaction mechanism. The introduction of Fe into MOF changes the electronic properties of Co, and reduces the free energy of rate-determining step.

Besides, the coordinatively unsaturated sites are favorable for adsorption [1059,1060]. Zhao *et al.* developed an ultrathin NiCo bimetal-organic framework nanosheet through a simple ultrasound approach for OER electrocatalysis [1059]. In 1 mol·L^{-1} KOH solution with O$_2$-saturated and scan rate of 5 mV·s^{-1}, the NiCo-UMOFNs electrode exhibits a quite low overpotential of 250 mV at 10 mA·cm^{-2}, much less than Co MOF nanosheets (371 mV), Ni MOF nanosheets (321 mV), bulky NiCo MOF nanosheets (317 mV), and the commercial RuO$_2$ (279 mV). The experiments results combined with the DFT calculations indicate that the exposed coordinatively unsaturated metal atoms act as the active centers for OER. The XPS results revealed that partial electron is transferred from Ni^{2+} to Co^{2+} *via* the ligands oxygen. As shown in Fig. 39, the charge transfer processes can be well explained in terms of the electronic structures. The coupling effects between Co and Ni contribute to the OER enhancement. All these results indicate that turning MOFs with 2D structure can be an effective strategy to construct highly active electrocatalysts.
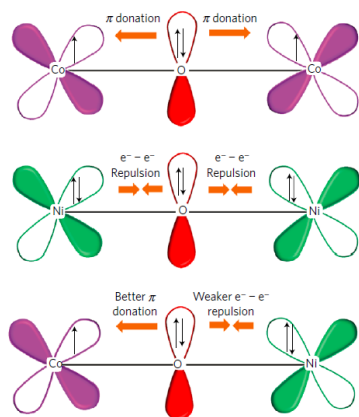
Fig. 39　Illustration of electronic coupling between Co and Ni [1059].

4.3.1.7.2 Transition metal chalcogenides

TMCs have excellent conductivity, which could be used as active electrocatalysts for water splitting both in HER and OER process [949,1061–1065]. Some TMCs materials can maintain stability during the OER process without damage. Others could be oxidized into the corresponding metal oxides/hydroxides under the strong oxidizing environments, forming an *in situ* heterostructure [317,1066,1067]. Modulate the spin states in uniquely exposed active planes can be an effective way for promoting the OER performance. Liu *et al.* prepared the Co$_3$S$_4$ nanosheets for high-efficient water oxidation in both alkaline and neutral environment [1061]. The HAADF image confirmed the exposed Jahn-Teller-distorted octahedra structure of the Co$_3$S$_4$ nanosheets. Moreover, as the nanosheet thins to atomic thickness, the spin state of Co^{3+} in the exposed octahedron adapts from the low spin state to the high spin state. The synergistic effect and electronic configuration contribute the high activity of Co$_3$S$_4$ nanosheets. The electrocatalyst exhibits an onset overpotential of 0.31 V and polarization current of 3.97 mA·cm^{-2} at neutral pH with overpotential of 0.7 V. The superior performance of Co$_3$S$_4$ have exceeded most other inorganic non-noble metal catalysts.

4.3.1.7.3 Layered double hydroxides

In recent years, LDHs, especially transition metal based LDHs, are regarded as one of ideal electrocatalysts toward water splitting because of their excellent OER activity, low cost and high stability in the basic condition [1068]. Li *et al.* firstly reported hierarchical MFe-LDHs (M = Ni, Co and Li) nanoplatelet array *via* a facile electrodeposition method [255]. Among them, the NiFe-LDH shows optimal activity (η_{10} = 224 mV) and long-term durability for OER. Ordered nanoplatelet array structure facilitates electron transport and electrolyte diffusion, while the good combination with the substrate enhances the stability of NiFe-LDH. However, the inferior electrical conductivity of pure LDHs restricts its further application to some extent. In view of this, Zhou *et al.* reported the CoMP (M = Fe, Ni and Mg) ultrathin nanosheet arrays by using CoM-LDH as precursors through an *in situ* phosphidation transformation [265]. The FeCoP exhibits significantly promoted activity toward water splitting with a cell potential of 1.60 V (at 10 mA cm^{-2}) benefitting from the modified electronic structure of active sites and enhanced electronic conductivity. In addition to water oxidation, LDH-based materials are also widely applied in the oxidation reaction of organic small molecules. Zhou *et al.* reported a synthesis of CoNi-alloy@CoNi-sulfide with hierarchical nanostructure by topotransformation of CoNi-LDH arrays, which displays excellent electrocatalytic activity and durability for hydrazine electrooxidation [264]. DFT calculation reveals that the enhanced activity is resulting from facile dehydrogenation process, increased electronic conductivity and ion transport on the surface of CoNi-sulfide. Liu *et al.* demonstrated NiFe-LDH can efficiently electrocatalyze the oxidation of 5-hydroxy-methylfurfural (HMF) to 2,5-furandicarboxylic acid with a

Faradaic efficiency of 99.4% [1069]. HMF oxidation on NiFe-LDH is kinetically more favorable than OER, which can replace OER in water splitting cells to promote H_2 evolution, as well as produce high-value chemicals.

4.3.2 Photocatalysis

Modern society remain highly dependent on fossil fuels for electricity generation and transportation, creating environmental problems (global warming) through the release of CO_2 into the atmosphere [1070]. Clean and sustainable renewable energy technologies must be found to allow a transition away from fossil fuel energy [1071], with semiconductor photocatalysis having long been considered a potential route towards alternative fuels, as well as environmental governance (Fig. 40) [1072,1073]. Whilst considerable fundamental advances have been made in recent years related to photocatalysis, many obstacles (especially the low solar conversion efficiency) need to be overcome [1074]. In an attempt to achieve step-change improvements in photocatalytic property for the energy and environmental sectors, researchers are increasingly turning to 2D photocatalysts as a strategy towards enhancing photocatalytic performance [1075]. Benefitting from the high specific surface area, tunable bandgap energies (band edge positions) and superior charge transfer performance, 2D photocatalysts have been shown to demonstrate remarkable performance (relative to traditional 3D photocatalysts) in a wide range of energy and environmental applications, including water splitting, CO_2 reduction and removal of organic pollutants, amongst others. In this section, we summarize recent advancements in the smart design of 2D photocatalysts for environmental (e.g., removal of organic pollutants or toxic chemicals, bacteria disinfection, antibiotic degradation) and energy applications (such as water splitting, CO_2 photoreduction, nitrogen photofixation and organic synthesis). 2D photocatalyst discovery, performance optimization and superiority in photocatalysis are prominently emphasized. It is expected to pave a novel avenue to rationally design and develop high-performance 2D photocatalysts for environmental pollution control and sustainable energy development.

4.3.2.1 Water splitting

The direct route of splitting pure water to H_2 and O_2 (including the reduction/oxidation process) H_2O using solar energy was considered as one of the most valuable
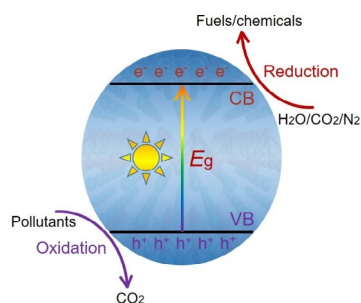
Fig. 40 Schematic illustration of the basic principles of photocatalysis (E_g: bandgap, CB: conduction band, VB: valence band).

photochemical reactions. To realize overall water splitting, semiconductors need to have an appropriate position of the valence band and conduction (H^+/H_2O 0 V *vs*. NHE at pH = 0 and H_2O/O_2 + 1.23 V *vs*. NHE at pH = 0) [1076]. Accordingly, the bandgap of the semiconductor must exceed 1.23 eV to initiate this reaction. Under photoexcitation, the excited electrons and holes can produce hydrogen and oxygen from water, also accompanied by the transportation and recombination of electrons and holes that are the main bottleneck, resulting in poor photocatalytic efficiency. Therefore, it is imperative to design and develop semiconductors with appropriate bandgap for efficient water splitting.

Recently, a range of 2D building blocks, e.g., graphene-based photocatalysts [1077,1078], 2D oxides [1079,1080], 2D chalcogenides [1081,1082], g-C_3N_4 [1083,1084], LDHs [1085,1086], and other 2D semiconductors [1087,1088] have been developed for photocatalytic water splitting. Further, a variety of strategies (such as doping, crystal facet/defect/strain engineering and modification) began to be widely utilized to boost the photocatalytic activity in terms of bandgap, photoinduced carriers' migration rate, recombination of electron-hole pairs, *etc*. For instance, Li *et al*. observed that the X (X = P, S, N, B, F, Br, C) is more favorable to substitute Cl in [Cl] layers [1089], rather than [Bi_3O_4] layers of constructed X-doped Bi_3O_4Cl models through the substitution energy calculations (Fig. 41a). The corresponding charge density contour plots demonstrated that C-doping intensified the nonuniform distribution of charge between [Cl] and [Bi_3O_4] slices to the most extent. Moreover, the electrostatic potential difference (ΔE) between [Cl] and [Bi_3O_4] slices of all constructed models revealed that carbon-doped Bi_3O_4Cl with the highest ΔE value of 7.36 eV than that of other samples, confirming carbon doping might be the best choice to enhance charge separation efficiency. Inspired by theoretical simulation results, they also synthesized carbon-doped Bi_3O_4Cl with different C-doped concentration for photocatalytic water oxidation. The pristine Bi_3O_4Cl is inactive for O_2 evolution, while the carbon-doped Bi_3O_4Cl achieved outstanding O_2-evolving activity originated from the enhanced charge separation efficiency by the carbon doping. In addition, owing to the special superiorities of 2D-2D coupled interfaces, the as-prepared interfaces/engineering have drawn great attention in photocatalysis when compared with 0D-1D, 0D-2D, 1D-1D, and 1D-2D interfaces [1076]. The generated 2D heterojunctions in recent years have been employed as high-performance photocatalysts toward photocatalytic water splitting. In 2016, Li *et al*. successfully designed 2D Janus (Cl_2)-($Bi_{12}O_{17}$)-(MoS_2) bilayer junctions, which were confirmed by AFM analysis and the advanced aberration-corrected high-angle annular dark-field scanning transmission electron microscopy (HAADF-STEM) (Fig. 41b–f) [1090]. The as-prepared Janus bilayers possessed an ultra-long carrier lifetime (3446 ns), leading to an advanced rate of photocatalytic hydrogen evolution (33 mmol·h^{-1}·g^{-1}) under visible-light irradiation. In recent years,

Fig. 41 (a) The constructed X-doped Bi_3O_4Cl crystal structure and corresponding electrostatic potential diagrams of X-doped Bi_3O_4Cl (X = P, S, N, B, F, Br, C); reproduced with permission from Ref. [1089], Copyright 2016 John Wiley and Sons. (b) Side-view 3D AFM images and (c) corresponding height profiles al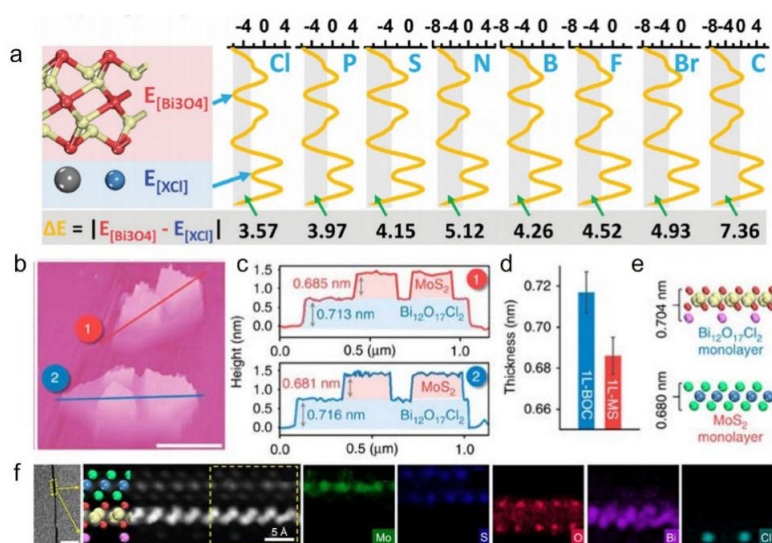ong the lines in (b); (d, e) the average measured thicknesses and theoretical thicknesses of mono-layered $Bi_{12}O_{17}Cl_2$ and MoS_2 in 2D Janus; (f) the corresponding EELS elemental maps of 2D Janus (Cl_2)-$(Bi_{12}O_{17})$-(MoS_2) bilayer junctions; scale bar is 10 nm [1090].

Zhao *et al.* synthesized boron-doped nitrogen-deficient carbon nitride-based Z-scheme heterostructure using the electrostatic self-assembly strategy [1091]. The obtained 2D-2D polymeric heterostructure exhibited an obvious increased photocatalytic performance for overall water splitting and the solar-to hydrogen efficiency with the presence of Pt and $Co(OH)_2$ co-catalysts can reach 1.16% under one-sun illumination conditions (AM 1.5G). This work presented a practical strategy for constructing efficient Z-scheme photocatalysts to boost solar conversion efficiency. Photocatalytic water splitting with 2D semiconductors offers ameliorative rates, though most of these works still focused on the semi reaction with the sacrificial agent, rather than for photocatalytic overall water splitting. Therefore, the solar-to-chemical efficiency is still too low to meet industrial requirements.

4.3.2.2　CO₂ photoreduction

CO_2 photoreduction to CO, CH_4, CH_3OH, HCOOH and other high value-added multi-carbon products has been considered as a clean and sustainable technique for CO_2 utilization and reclamation. However, chemical inertness of CO_2 molecule due to stable C=O bond (ca. 750 kJ·mol^{-1}) causes high reaction barrier and difficult to activation, so CO_2 photoreduction is still in its infancy. Meanwhile, the efficient generation, separation and migration of photogenerated electron-hole pairs in photocatalysis are extremely challenging. To break these obstacles, numerous modification strategies (doping, noble metal loading, crystal facet control and defect construction, *etc.*) and novel photocatalysts [1092], have been extensively investigated. Among these state-of-the-art photocatalysts, 2D photocatalytic materials attracted much attention due to their unique 2D confined structure and inherent physicochemical property, especially the shorter path for migration of electron and

hole to the surface [329,1075,1092–1096]. Herein, we divide them into metal-containing 2D photocatalysts (e.g., LDHs [275,1097–1105], TMDs [1098,1106–1109], MXenes-based catalysts [1098,1110,1111], 2D metal oxides [1098,1112–1118], *etc.*) and metal-free 2D photocatalysts (g-C_3N_4 [1098,1106,1119–1123], graphene [1098,1106,1120,1124,1125], BP [1093,1098,1119,1120,1126–1131], h-BN [1098,1120], *etc.*) for simplicity.

As representative 2D metal-containing materials, LDHs have received extensive interest for the selectivity regulation of CO_2 photoreduction as photocatalysts or precursor due to their controllable components [1102]. Xiong *et al.* synthesized a series of ZnM-LDH photocatalysts with different trivalent and tetravalent metal cations (M = Ti^{4+}, Fe^{3+}, Co^{3+}, Ga^{3+}, Al^{3+}), investigating the influence of controllable components on CO_2 reduction selectivity [1100]. The selectivity of CO_2 hydrogeneration can be further regulated *via* the design of catalyst. Chen *et al.* prepared a series of novel CoFe-based catalysts by the hydrogen reduction of CoFeAl-LDH nanosheets at the range of 300–700 °C [1097]. When the reduction temperature was increased, the catalytic selectivity of CoFe-*x* catalysts showed a shift from CO to CH_4, and eventually to high-value hydrocarbons (C_{2+}) (Fig. 42a). As for the improvement of activity, LDHs as alkaline photocatalysts also perform a promoted CO_2 photoreduction activity on account of the strong CO_2 adsorption capacity of mass alkaline OH groups on the surface of LDHs. For example, CoAl-LDH exhibited a twice capacity for CO_2 adsorption (2.95 cm^3·g^{-1}) than that of P25, leading to a 13 times higher CH_4 formation rate (4.2 mmol·g^{-1}·h^{-1}) than that of P25 (0.3 mmol·g^{-1}·h^{-1}) [1104]. Generally, the CO_2 adsorption capacity of LDHs can be modulated using different synthesis methods [1105]. Besides, the effect of external alkaline OH groups was also generalized in BP. Through the *in situ* modification by OH groups, Zhu *et al.* achieved a stable visible-light-driven photocatalytic CO
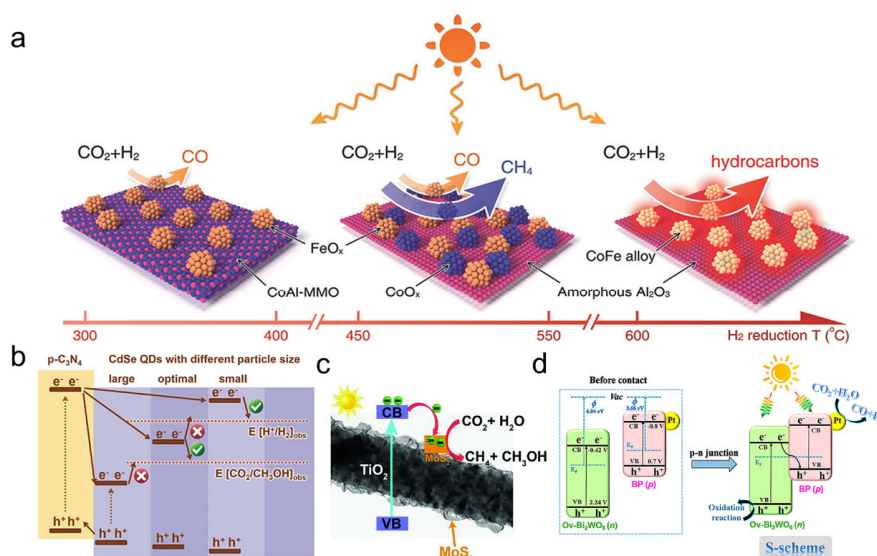
Fig. 42 **(a) Illustration of the different CoFe-*x* catalysts formed by hydrogen reduction of a CoFeAl-LDH nanosheet precursor at different temperatures and the CO_2 hydrogenation selectivity of each CoFe-*x* catalyst; reproduced with permission from Ref. [1097], Copyright 2017 John Wiley and Sons. (b) Illustration of the variation tendencies of different polymeric C_3N_4/CdSe QDs; reproduced with permission from Ref. [1121], Copyright 2019 John Wiley and Sons. (c) Schematic illustration of TiO_2 and MoS_2 heterojunction: charge transfer and separation under UV-visible light irradiation for CO_2 reduction. Reproduced with permission from Ref. [1132], Copyright 2018 John Wiley and Sons. (d) Mechanism diagram of the photocatalytic CO_2 reduction reaction over a Pt/BP-Bi_2WO_6 heterojunction under solar light irradiation. Reproduced with permission from Ref. [1126], Copyright 2021 American Chemical Society.**

production rate of 112.6 μmol·h^{-1}·g^{-1} on BP nanosheets (4 times higher than that of bulk BP) [1131]. In addition to surface treatment, the construction of effective heterojunction structures (0D/2D, 1D/2D or 2D/2D) is another effective strategy for retarding the recombination of photogenerated electrons/holes, further promoting the CO_2 photoreduction activity. Luo *et al*. reported that 0D/2D materials of g-C_3N_4 nanosheets and CdSe QDs can reduce the diffusion length of charge carriers, then enhancing the activity of CO_2 reduction [1121]. CdSe QDs with different sizes possessed the tunable energy level of the photogenerated electrons, which altered the selectivity of CO_2 (Fig. 42b).

A similar enhancement of activity in 1D/2D heterojunction material can be accomplished (Fig. 42c) [1132]. Moreover, a stable 2D/2D heterostructure of BP/bismuth tungstate (BP/Bi_2WO_6) with oxygen vacancy was reported for CO_2 photoreduction to syngas (Fig. 42d), whose generation rates of carbon monoxide and hydrogen (20.5 and 16.8 μmol·g^{-1}·h^{-1}) were remarkably higher than the reported BP-based materials [1126]. The construction of S-scheme 2D/2D heterostructure with coupled oxygen defects widely facilitates the charge transfer efficiency and photocatalytic activity. Although tremendous studies on the flourishing of CO_2 photoreduction of 2D materials have been concerned, there still are many unknown tracks to dig out. It is an emergency to develop novel *in situ* detection technologies to realize a visual observation on the migration of photo-electrons/holes or the variation of reaction intermediates, which is beneficial for a deep understanding of CO_2 photocatalysis, making a breakthrough on the activity and selectivity of CO_2 photoconversion.

4.3.2.3 Nitrogen reduction reaction

Photocatalytic NRR utilizing solar light under mild conditions is a green avenue for ammonia synthesis. Efficient photocatalytic NH_3 synthesis relies on a highly active catalytic site for N_2 activation and high-efficiency electrons transfer from photocatalyst into N_2 molecule to accomplish N_2 reduction [1133–1138]. As a kind of alternative photocatalysts for high-efficiency NRR, 2D semiconductor materials process atomic-level thickness with large lateral dimension, thereby resulting in the short path for migration of photogenerated carriers to surface and abundant surface active sites. In recent years, 2D materials such as bismuth oxyhalides (BiOX) [1139], g-C_3N_4 [1140], LDHs [1141], and BP [1142] have been widely reported for photocatalytic nitrogen fixation through various design strategies.

Recent progress indicated that O, N, and S vacancies exhibited promoting photocatalytic N_2 activation on account of their excess electrons and coordinately unsaturated metal sites [1143–1145]. Benefited from high surface atom exposure of 2D materials, anion vacancies could be simply constructed and adjusted on surface by the design of crystal facet, doping and strain [1146–1148]. Researchers reported that efficient activation and reduction of adsorbed N_2 to produce NH_3 were realized on oxygen vacancies (V_o) of BiOBr nanosheets (Fig. 43a, b) [1149–1151]. Furthermore, the distinct structures of V_o on {001} and {010} facets resulted in different ammonia synthesis pathways by altering the adsorption structure of N_2 [1152]. Unlike the 2D BiOX materials whose component modulation is restricted to a small scope, the tunability of cations within the layers of LDHs provide wide spaces for the design of defects. In 2017, ultrathin 2D $M^{II}M^{III}$-
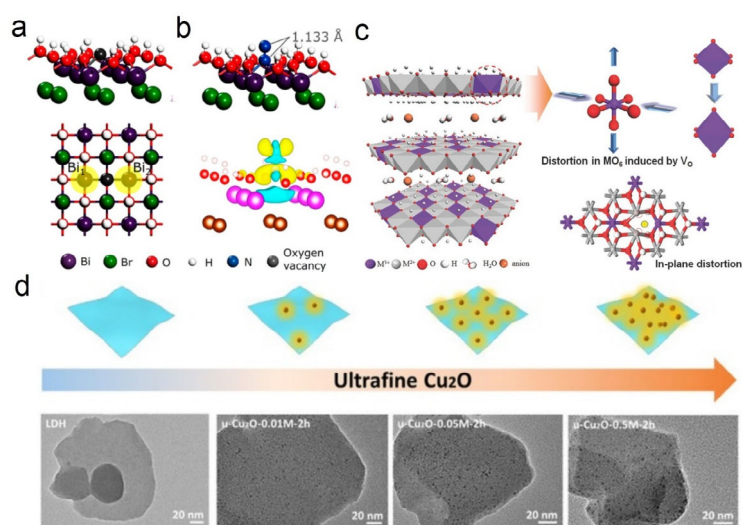
Fig. 43 **(a) Side and top view of (001) surface of BiOBr with a V_o. (b) The adsorption geometry of N_2 on the V_o of BiOBr (001) surface and corresponding charge density distribution; the yellow and blue contour represent charge accumulation and depletion in the space respectively [1149]. (c) Schematic polyhedral representation of the ultrathin LDH structure with defective MO_6 octahedra at the nanosheet edge or surface and the distortion structure induced by V_o (V_o marked by the yellow dot); reproduced with permission from Ref. [1153], Copyright 2017 John Wiley and Sons. (d) Schematic illustration and HRTEM images of the supported ultrafine Cu_2O prepared through *in situ* reduction of LDH using different concentrations of ascorbic acid; reproduced with permission from Ref. [1170], Copyright 2020 John Wiley and Sons.**

LDH (M^{II} = Zn, Ni, Cu; M^{III} = Al, Cr) nanosheets with abundant V_o were designed and exhibited superior photocatalytic activity for NRR than the bulk counterparts. Particularly, severely distorted structure and compressive strain caused by plentiful V_o was observed in ultrathin CuCr-LDH, leading to remarkable performance compared with other several LDHs (Fig. 43c). Furthermore, the doping of Cu^{2+} into ZnAl-LDH could introduce electron-rich $Cu^{\delta+}$ and surrounding V_o (Cu-V_o) at surface [1153]. The abundant Cu-V_o sites promoted N_2 activation and injection of photogenerated electron [1154], resulting in remarkable NRR performance of 110 $\mu mol \cdot g^{-1} \cdot h^{-1}$.

In addition to the construction of intrinsic vacancy defects, surface modification of 2D materials for photocatalytic NRR has also been widely reported in recent years [1155–1157]. For example, Zheng *et al*. decorated a series of single transition-metal atoms (Mn, Fe, Co, and Ni) onto MoS_2, prolonging the lifetime of photogenerated carriers, suggesting the single metal modification enhanced charge separation by trapping excited electrons [1158]. Anchoring single-atom onto carbon nitride can also construct new catalytic active centers and efficiently capture photogenerated electrons [1159,1160]. Huang *et al*. demonstrated a valence-electron cloud of single Cu atom on g-C_3N_4 isolated from the conjugated π electron of g-C_3N_4, thereby easily exciting to generate electrons with high energy level [1161]. Guo *et al*. reported coordinatively unsaturated single-atom Mo on g-C_3N_4 exhibited strong adsorption to N_2 molecule with a stretched length of N≡N bond from 1.11 to 1.15 Å [1162]. Besides, special bonding mode and topological structure enable 2D materials to construct hybrids with a variety of materials (Cu_2O, BiO, Ni_2P, *etc*.), achieving improved stable bonding and carrier separation efficiency [1163–1168]. For Ni_2P/BP, the Ni-P bond between BP and

Ni_2P could act as atomic level channels for charge transfer at the interface to supply photogenerated electron efficiently for N_2 reduction [1169]. Alike Ni_2P/BP photocatalysts, uniformly sized sub-3 nm Cu_2O platelets loaded on LDH nanosheets could be obtained *via* a simple *in situ* reduction of CuZnAl-LDH (Fig. 43d), exhibiting considerable performance and stability for visible-light-driven NRR [1170].

In spite of the rapid development of photocatalytic nitrogen reduction, there are still some bottlenecks restricting improvement of performance for ammonia production. Special optical and electrical properties of 2D materials are expected to provide new approaches to overcome these challenges in the future. Considering that most of current photocatalysts with low solar efficiency were excited by ultraviolet light [1169,1170], rational design of 2D materials with unique optical properties and wide absorption (up to visible or near-infrared light) is prime important to achieve remarkable nitrogen fixation performance. In addition, inspired by thermal catalytic ammonia synthesis, the enriching electron density of surface defects is a key to promote nitrogen activation [1171–1174]. Therefore, the construction of electron-rich structures at the surface of 2D materials in virtue of the confined electron in layered structure may be one of the avenues to high-performance photocatalyst for NRR.

4.3.2.4 Photocatalytic environmental treatment

Among these environmental treatment technologies employed thus far, the semiconductor photocatalysis as a new pollution control technology demonstrates the great potential of degrading and eliminating various emerging pollutants *via* advanced oxidation processes (AOPs) [1175]. In recent years, a large number of studies have confirmed that dyes, surfactants, organic halides, pesticides, oils, cyanides, *etc*. can be effectively removed

through photocatalytic decolourization, detoxification, and mineralization into inorganic small molecular substances (e.g., CO_2, H_2O and inorganic ions or acids), thereby eliminating environmental pollution [1176,1177]. Photocatalysis involving O_2 and H_2O as reaction species converted into high-reactivity oxygen species (ROS) [1178], *i.e.*, hydrogen peroxide (H_2O_2), superoxide anion radical ($\cdot O_2^-$), singlet oxygen ($^1O_2$) and hydroxyl radical ($\cdot OH$) in photocatalysis (Fig. 44).

Since the synthesis of ROS is the initial rate-limiting step for photocatalytic environmental pollutant treatment, designing catalyst for enhancing ROS generation is crucial. 2D photocatalysts emerge with great potential for settling this matter as they can convert solar energy to ROS efficiently [1179]. Nitric oxide and nitrogen dioxide (collectively referred to as NO_x) as one of the typical outdoor and indoor air pollutants, have attracted extensive environmental concern [1180]. In particular, the removal of indoor air pollutants at a realistic concentration (ppb level) is technically challenging with reasons for economic infeasibility [1181]. Dong *et al.* developed a novel *in situ* method for the synthesis of g-C_3N_4 on structured ceramic foam. The optimized supported g-C_3N_4 with a remarkable NO removal ratio of 77.1% can be obtained under real indoor illumination [1182]. Through EPR characterization, the reaction mechanism and ROS of photocatalytic NO oxidation were revealed. Further, owing to enough stable g-C_3N_4 on the structured ceramic foam with special chemical interaction, photocatalysts can be employed under the continuous airflow to promote the practical environmental application. Alike NO removal, photocatalysis was considered a presumably critical important technology for the removal of ammonia, which acted as a typical environmental pollutant in water originate from industry, agriculture and domestic sewage effluent [1183,1184]. Ultrathin g-C_3N_4 with 2.7 eV bandgap and suitable position of CB and VB was fabricated as a metal-free photocatalyst for ammonia removal from water [1185]. Compared with bulk g-C_3N_4, the ultrathin g-C_3N_4 can obviously improve photocatalytic performance. It attributed to the 2D ultrathin structure that shortened the photoinduced carriers' migration distance and accelerated separation efficiency to generate more hydroxyl radical for ammonia oxidation [1186]. Among these 2D photocatalysts studies, catalyst design and

Fig. 44 High-reactivity oxygen species generated in photocatalysis. Reproduced with permission from Ref. [1178], Copyright 2017 American Chemical Society.

screening are especially crucial in terms of extending the lifetime and understanding the kinetic synthesis of ROS in future photocatalytic applications for pollutants removal.

4.3.2.5 Photocatalytic organic synthesis

Photocatalytic organic synthesis is the valorization of small molecules beyond H_2O, CO_2, and N_2, and it has received growing interest and attention recently, albeit an emerging field. Within a few years, a number of systems were explored, including controlled photooxidation (e.g., oxidation of alcohols, amines, and cyclohexane; hydroxylation of benzene; epoxidation of alkenes) or photoreduction (e.g., reduction of nitroaromatics, unsaturated aldehydes, alkenes, and alkynes) of organic molecules. The outstanding electronic characteristics and versatility for structural modifications of 2D materials (g-C_3N_4, 2D COFs, graphene, BiOX, LDHs, *etc.*) project them into the field of heterogeneous photocatalytic organic synthesis [1187].

In a seminal report, graphene-supported copper NPs are feasible for igniting the coupling reaction of aromatic nitro compounds to corresponding azo- and azoxy-aromatic compounds under visible-light irradiation at 60 °C [1188]. The ignition is primarily ascribed to excited energetic electrons, which is originated from the localized surface Plasmon resonance effect of Cu and photoexcitation of the bound electrons, facilitating the cleavage of N—O bonds in the aromatic nitro compounds. Whereas Cu and graphene are expensive, many low-cost and metal-free materials have been exploring. For example, Chen *et al.* reported that a 2D porphyrin-based sp^2 carbon-conjugated COF can induce aerobic oxidation of amines to imines under visible light, and the COF is highly stable even under harsh pH condition [1189]. Dai *et al.* demonstrated that g-C_3N_4 can also selectively synthesize various azo- and azoxy-aromatic compounds from the corresponding nitroaromatics with isopropanol serving as electron donor, and the selectivity can be controlled by different irradiation wavelength [1190]. Since the oxygen removal process by two H atoms through the generation of H_2O is the key step of nitrobenzene reduction, photogenerated electrons and adsorbed hydrogen atoms (H_{ads}) of g-C_3N_4 are pivotal. *In situ* mass spectrometry ca. remaining O_2 after the deaerated conditions showed that g-C_3N_4 possesses the fastest O_2 depletion rates (Fig. 45a), hence the most efficient utilization of photogenerated electrons. Besides, the post-mortem temperature-programmed desorption suggested weak adsorption of H_{ads} on the g-C_3N_4 surface, thereby reacting rapidly with the surface absorbed nitrobenzene to azo- or azoxy-benzene (Fig. 45b–d). Xiao *et al.* demonstrated oxidative couplings of amines to imines by porous few-layer g-C_3N_4 with 2–15 nm pores (Fig. 45e, f) whereby diffusion of reactants and products are facilitating [1191]. However, g-C_3N_4 alone is unsuitable for selective oxidation of 5-hydroxymethylfurfural (HMF) because hydroxyl radicals generated over g-C_3N_4 are detrimental to the oxidation process *via* oxidizing HMF directly to CO_2 and H_2O [1192]. Xu *et al.* reported that C_3N_4/H_2O_2 adduct can acquire comparable HMF
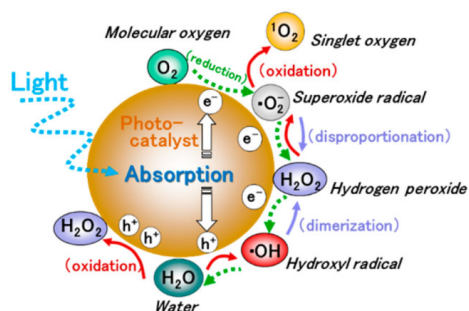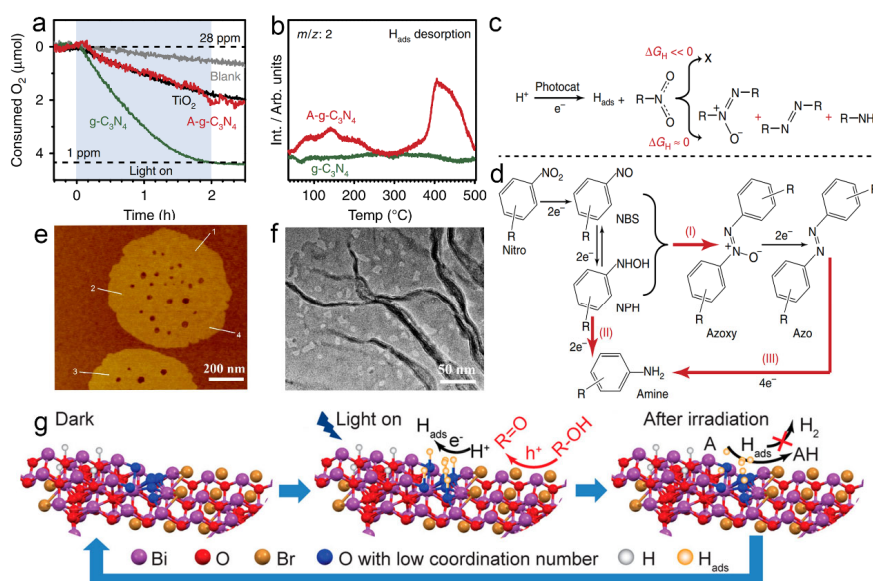
Fig. 45 (a) The consumption of dissolved O_2 under irradiation using various photocatalysts determined by *in situ* MS. (b) Post-mortem TPD spectra revealing the desorption of H_{ads} from the g-C_3N_4 and A-g-C_3N_4 surfaces. (c) Scheme of the suggested reaction pathway; the reduction reaction will be hindered if H_{ads} binds strongly to the catalyst. (d) Reaction path for the photoconversion of nitroaromatic compounds to azoxy-, azo-aromatic compounds, and amines. NBS = Nitrosobenzene, NPH = N-phenylhydroxylamine [1190]. (e) AFM and (f) TEM image of the few-layer C_3N_4; reproduced with permission from Ref. [1191], Copyright 2019 American Chemical Society. (g) Working principle of the $Bi_{24}O_{31}Br_{10}(OH)_\delta$ [1193].

conversion and higher selectivity of 2,5-furandicarboxaldehyde. Additionally, composite is an efficacious means to change properties of C_3N_4 and heavily improve catalytic conversion and selectivity as well. For instance, the strong interaction between cobalt thioporphyrazine (CoPz) and g-C_3N_4 in CoPz/g-C_3N_4 composite not only enhances the accessibility of the CoPz sites, but also boosts $^1O_2$ instead of hydroxyl radical generation, thus obviously promoting selective oxidation of HMF to 2,5-furandicarboxylic acid [1192]. Considering photocatalytic organic conversion involving the hydrogen transfer step is attractive while selectivity and efficiency driven by visible-light are still unsatisfactory. Dai *et al*. developed a basic-site engineered bismuth oxybromide [$Bi_{24}O_{31}Br_{10}(OH)_\delta$] that performs remarkably in photocatalytic redox reactions (e.g., thiones to thiols, quinones to quinols, nitrobenzene to azo/azoxybenzene, and alcohols to ketones) involving hydrogen transfer step [1193]. Such basic sites (OH and undercoordinated O atoms) on catalyst surface can favor the oxidation of alcohols (R—OH), then being donated protons (H*) through oxidative dehydrogenation of alcohols (Fig. 45g). The donated protons further accept the conduction band electrons to generate metastable H_{ads} under irradiation, which can then be rapidly scavenged by hydrogen acceptors (A) to form valuable organic compounds, rather than H_2 gas. Moreover, joint utilization of basic surface sites and active lattice oxygen in $Bi_{24}O_{31}Br_{10}(OH)_\delta$ is a promising way to selectively oxidize aliphatic and aromatic alcohols to the corresponding aldehydes/ketones due to boosted dehydrogenation in photooxidation of alcohols [1194]. Defect engineering in LDHs also play a vital role in the hydroxylation of benzene [1195], selective oxidation of aromatic alcohols [1196], and hydroxylation

of phenol [1197]. While photocatalytic organic synthesis has achieved huge advances in recent years, most of these works involved sacrificial agents, which make them far from energy economical and practical application. Coupling cathodic and anodic conversion is likely a promising route to efficiently utilize electron-hole pairs.

Demands for higher energy efficiency, coupled with environmentally-friendly premises provide growing impetus to explore new alternative green energy. Over the next 5–20 years, it is anticipated that photocatalysis combined with 2D materials will be widely adopted for practical energy and environmental applications owing to its technological advantages. Opportunities exist for the discovery of new photocatalytic systems and alternative methods with effective 2D materials. Certainly, how to fully strengthen the 2D photocatalysts' advantages (high surface area with the exposed active site, excellent charge transferability and tunable bandgap structure) is the key to promote solar-to-chemical conversion efficiency.

4.4 Energy storage

2D materials are widely employed for electrochemical energy storage applications due to their layered crystal structure for ion intercalation and diffusion, rich surface functional groups and high redox reactivity, tuneable conductivity as well as structural flexibility. A wide diversity of 2D materials have been studied for energy storage (see examples in Fig. 46), spanning from graphene, graphene analogues, COFs, to TMDs, MXenes, BP and 2D metal oxides [33,1198]. 2D materials are applied in both cathode, anode and electrolyte. More specifically, they can be electrochemical active materials (for bulk intercalation or surface adsorption), conductive additives (forming composites
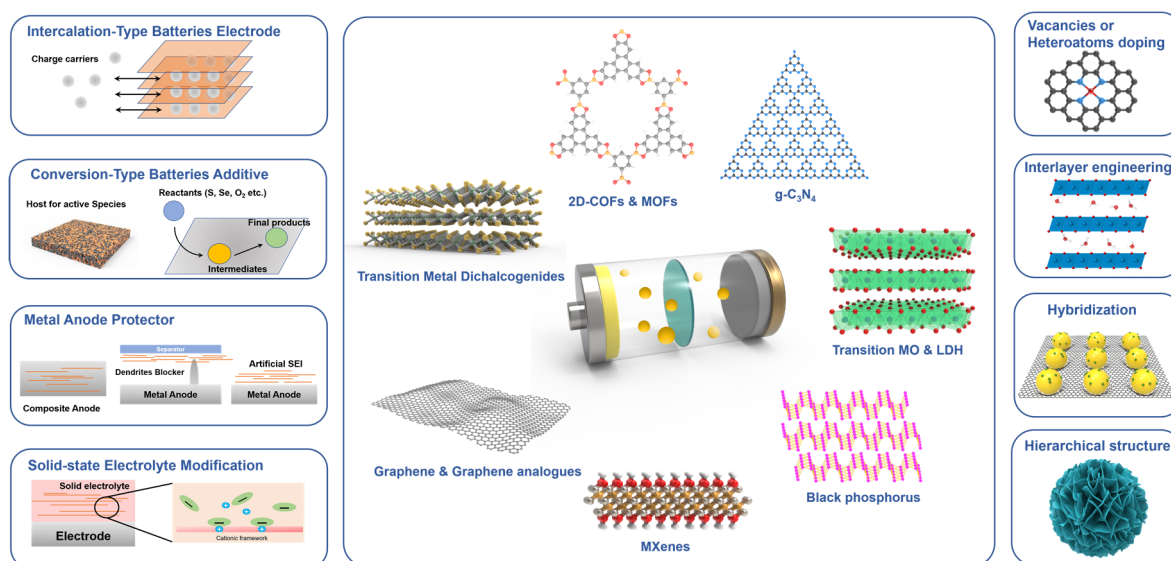
Fig. 46　Classification of 2D materials and modification strategies in application for rechargeable batteries.

with transition metal oxides or sulphides) and surface protectors (to suppress dendrites or pulverization). In this section, we will highlight with examples the application of typical 2D materials in secondary batteries, supercapacitors and micro-supercapacitors.

4.4.1　Batteries

According to the type of charge carriers (Li^+, Na^+, K^+, Mg^{2+}, Al^{3+}, and non-metal cations) and storage mechanisms, electrodes of batteries can be divided into two major types: conversion-type and intercalation-type. Examples for the former are Li-S, Li-Se, Na-S, $Li-O_2$, $Zn-O_2$ battery cathodes and the corresponding metal anodes; and examples for the later are the most common Li-ion, Na-ion, K-ion, Zn-ion battery cathodes or anodes. In the following, we will discuss the application of 2D materials in intercalation-type electrode, conversion-type additive, metal anode protection, and solid-state electrolyte (Fig. 46, left panel).

In the intercalation-type batteries, 2D materials with an open structure and weak interlayer bonding and adjustable interlayer distance provide more active sites for ions storage and easier ions transfer compared to bulk counterparts. Typical 2D organic materials employed for intercalation-type electrodes include graphene and derivatives, 2D polymers, 2D COFs and 2D MOFs [1199,1200]. The inorganic type is represented by TMDs, but other 2D graphene-analogous (Si, Ge, Sn, Sb, Bi, B_3P, ZnN, ZnP, LDHs, *etc.*) and are being attempted either experimentally or theoretically [1201–1204].

Graphene has been widely applied in the anode for insertion-type batteries. Li^+, Na^+, and K^+ can be inserted between the carbon layers and form metal carbides [1205,1206]. In Li-ion battery, reactive sites generated by the exposed graphene edges exhibit high binding energies between C and Li^+, rendering a high specific capacity around 1500 $mAh \cdot g^{-1}$ with the formation of LiC_6 [1207]. Heteroatom doping can further improve the conductivity and enhance the interaction between charge carriers and graphene layers, leading to improved activity [1208,1209].

Following the success of graphene, TMDs are widely employed as the anode host for alkane metal ions. Taking MoS_2 as an example, because of the weak vdW interaction between the interlayers, it suffers less volume expansion during the accommodation of metal cations than that of other alloying type anodes, such as 2D BP and bulk TMDs [1210]. However, the pitfall of most TMDs is that they usually have lower electrical conductivity than graphene, thus requires hybridization with conductive agents or creation of atomic vacancies [1211–1213]. Introducing guest ions or molecules to expand the interlayer distance of TMDs is beneficial to ion diffusion [1214]. In macroscopic level, engineering the porous or hierarchical structures is a widely employed method to shorten the mass transport pathway and also to alleviate the re-stacking and aggregation during the cycling process [1215]. Attention should be paid that most TMD semiconductors may experience a decomposition reaction at a lower discharge potential than the potential for intercalation reaction, and this decomposition could be irreversible [1216].

LDH-based materials have also been successfully applied in the field of energy storage like batteries. As a typical work, Li *et al*. reported a series of activated LDHs (CoFe, CoNi and CoAl-LDH) nanoarrays as cation supercapacitor materials through a facile electrochemical activation (ECA) method [1217]. The ECA process results in the generation of hydrogen vacancies (V_H) on LDH host layers, which can provide a 2D open channel for the reversible intercalation of metal cations. These activated LDH-V_H exhibits remarkable storage capacities for a wide range of metal cations (monovalent Li^+, Na^+ and K^+ and divalent Ca^{2+}, Mg^{2+} and Zn^{2+}) compared with pristine LDHs. Furthermore, both DFT calculations and experimental studies indicate that the V_H in the activated LDH plays an important role in the intercalation chemistry as well as energy storage performances. The ultrathin CoFe-LDH with active-oxygen-rich surface (ULDH-O) was further developed by Li *et al*. to modulate the

deposition/dissolution of Li metal anode for Li-metal batteries [1218]. The active oxygen on the lithiophilic surface of ULDH-O is thermodynamically favorable for Li atom adsorption and thus promotes the homogeneous nucleation and deposition of Li metal to suppress dendrite formation. Moreover, the ultrathin structures also promote the sufficient exposure of Li nucleation active site and guarantee efficient electron transfer between ULDH-O and conductive substrate. Furthermore, LDHs with inert metal ions (such as Mg^{2+}, Zn^{2+}, and Al^{3+}) have attracted widespread interest by assembling into the ultrathin film to suppress the "shuttle effect" of polysulfides because of the ultrathin nanosheet structures with positive charges [1219]. Cui *et al.* successfully fabricated an ultrathin separator by the assembly of MgAl-LDH nanosheets and GO on a commercial polypropylene separator ((LDH/GO)$_n$) and could effectively act as both a polysulfide barrier and Li^+ rectifier in the lithium-sulfur battery [1220]. The experimental results demonstrate that the (LDH/GO)$_{20}$-assembled lithium-sulfur battery exhibits excellent performance with a large initial discharge capacity, cycle stability and good heat resistance performance. The restricted pathways on the (LDH/GO)$_n$ film could effectively block polysulfides to stabilize the sulfur cathode but promote the uniform dispersion of Li^+ to inhibit the generation of Li dendrites on the Li-metal anode.

MXenes with high conductivity are being extensively studied for energy applications include battery anode [1221–1223]. Charge carriers are stored in the Ti_2C_3 layers. However, the remaining OH and F groups on Ti_2C_3 layers may lower the ions transfer, thus some guest dopants (N, Sn, S, P) are often introduced to modify the surface [1224–1227]. Similar to 2D MoS_2, the interlayer distance of MXenes can also be effectively expanded by filling with nano-structured materials such as CNT, polymers and large-sized metal ions to facilitate the ion intercalation [1228–1230].

For the conversion-type batteries, such as metal-sulfur, metal-selenium, metal-O_2 and metal-CO_2 batteries, 2D materials are often applied as a host, an additive to the cathode, or a coating layer on the separator. An important function of 2D materials is to catalyze the active species conversion or reduce the side reactions during the cycling [1231,1232].

In the metal-sulfur system, taking lithium-sulfur battery as an example, it suffers the shuttle effect of soluble intermediates-lithium polysulfides, low conductivity of sulfur and final products (Li_2S), and the large volume fluctuation during the cycling process (~76%). 2D materials with good conductivity such as graphene and g-C_3N_4 are often employed as the host for sulfur [1233]. The high porosity of such flexible sheet-like material can efficiently accommodate the volume expansion during the cycling. The non-polar carbon-based materials cannot thoroughly prevent the polysulfides shuttling. To enhance the immobilization of intermediates on the cathode, TMDs or MXenes with higher polarity and large exposed planar surface provide a better function owing to the strong Lewis-acid based interaction between the metal ions and polysulfides [1234,1235].

Vacancies and single atoms modification introduced into the 2D materials are proven useful to enhance the polysulfides conversion kinetics [1236,1237]. Because of low conductivity, a hybridization and a possible synergistic effect between the porous carbon and polar 2D metal compounds are beneficial to mitigate the issue of volume change and polysulfides shuttling [1238].

The role played by 2D materials in the metal-air batteries is similar to the metal sulfur batteries. Specifically, they may accelerate the electrocatalytic ORR and OER process and reduce the polarization during the cycling process [1239]. For example, graphene with homogeneous sp^2 hybridized electrons and high specific area can efficiently accommodate and regulate the distribution of insulating products Li_2O_2/LiO_2, avoid the blocking of O_2 in the cathode and facilitate the ORR and OER process [1240–1243]. To optimize the nucleation of LiO_2, graphene surface may be modified by noble metal or compounds with a similar crystallographic lattice to LiO_2, which further reduces the charge overpotential [1244]. In addition, 2D oxides and LDHs with exposed surface atoms, atomic steps and kinks can facilitate the chemical bonds breaking, and thus boost the OER/ORR process [1245,1246].

Generally speaking, for the conversion-type batteries, 2D materials are applied based on the unique interaction between their surface and the unstable or soluble active species since the active species will not be stored inside the crystalline framework. Thus, the anchoring sites for active species (e.g., edge sites, heteroatoms dopant or vacancies) and the transport of active species (generated by rational design of hierarchical structures) are both significant factors of 2D materials.

In the metal anode research area, prominent issues of dendrite growth and side reactions need to be solved. 2D materials are widely studied for anode protection because of their outstanding conductivity and mechanical flexibility [1247]. For example, the basal plane of graphene can serve as the nucleation template to guide the horizontal growth of the zinc metal which is effective in suppressing the Zn dendrite growth in Zn-ion battery [1248]. Apart from the nucleation template, graphene can also serve as physical confinement to reduce the dendrite formation by reducing the current density and enhancing the affinity of charge carriers on the surface [1249,1250]. MXenes with heteroatoms doping or modification are served as the host for Li, Na, Zn and K metal [1251,1252]. Other strategies are ex-situ artificial SEI layer on metal anode to induce uniform metal deposition [1253], or coating on separator to reduce the number of hotspots [1254]. These are both effective in preventing dendrites from piercing the separator.

In addition to the application as electrodes, 2D materials, especially when surface functionalized have also been added into the electrolyte (solid polymer electrolyte or gel electrolyte) to facilitate the dissociation of the metal salts [1247]. For example, in the solid lithium-ion battery, 2D graphene nanosheet modified by poly(ethylene glycol) and branched-graft copolymer could efficiently enhance the ionic conductivity by constructing Lewis acid-base interaction with lithium salts [1255]. Similarly, 2D

vermiculite sheets with the substitution of surface Si atoms by Al atoms bring about a negative surface charge state, corresponding to improved ability to dissociate Li salt by absorbing Li^+ [1256]. 2D COFs and h-BN can also be applied in this area to dissociate the ion pairing of the metal salts and enhance ion mobility [1257–1259].

In summary, this section highlights the application of 2D materials in different parts of electrochemical batteries. Typical strategies such as doping, hierarchical structures or heterostructures, and vacancies are discussed with respect to the charge storage mechanisms (Fig. 46). Typical strategies in enhancing the redox kinetics, reaction reversibility and electrode stability are presented.

4.4.2 Supercapacitors

Different from battery systems, supercapacitors (SCs) store energy *via* kinetically faster physisorptions or faradaic reactions on the electrode (near) surface, which are capable of achieving high power density and long cycle life. On the basis of the charge storage behaviours, SCs can are generally classified to electrochemical double-layer capacitors (EDLC) and pseudo-capacitors. The former stores charges at the "Helmholtz layer" formed through electrostatic interaction between electrode/electrolyte interface; while the latter stores by (near)surface-confined faradaic reactions. It is not surprising that 2D materials can be useful for both types because of much larger surface ratios than bulk [1260–1265], as illustrated in Fig. 47a, b. Their reactive basal planes or edges, tunable surface chemistry,

and interlayer spacing are desirable features to accommodate Faradaic reactions and insertion pseudo-capacitance.

In terms of EDLC, the capacitance is calculated solely according to a material's surface area. Hence graphene with extraordinarily high surface area of up to 2630 $m^2{\cdot}g^{-1}$ can theoretically achieve an EDL capacitance as high as ~550 $F{\cdot}g^{-1}$ [1266]. As reported, single-layer graphene achieved a high capacitance of ~21 $\mu F{\cdot}cm^{-2}$ superior to other carbon-based materials [1267]. Subsequently, explosion of publication on preparations of GO and rGO especially for large-scale or more facile fabrication has been observed. Defects and surface modification can enhance the capacitance by modulating graphene electronic structure and electrochemical properties. For example, an ~150% enhancement (~50 $\mu F{\cdot}cm^{-2}$) in measurable capacitance of few-layer graphene has been observed by defect incorporation [1268]. The great success of graphene in supercapacitors has intrigued attentions in other 2D single-elemental materials, such as borophene- [1269,1270], silicene- [1271–1273], and germanene-based [1274] materials. So far, silicene/germanene are mainly synthesized on substrates due to the lack of thermodynamic stability, so an in-depth study remains at a theoretical stage and advanced synthesis strategies are needed. As for EDL capacitive 2D materials like BP, h-BN, and g-C_3N_4, the reduction of their large electronic bandgap can be realized through a controlled doping process or forming heterostructures with graphene to mitigate the poor conductivity and restacking issues effectively [1275–1277].
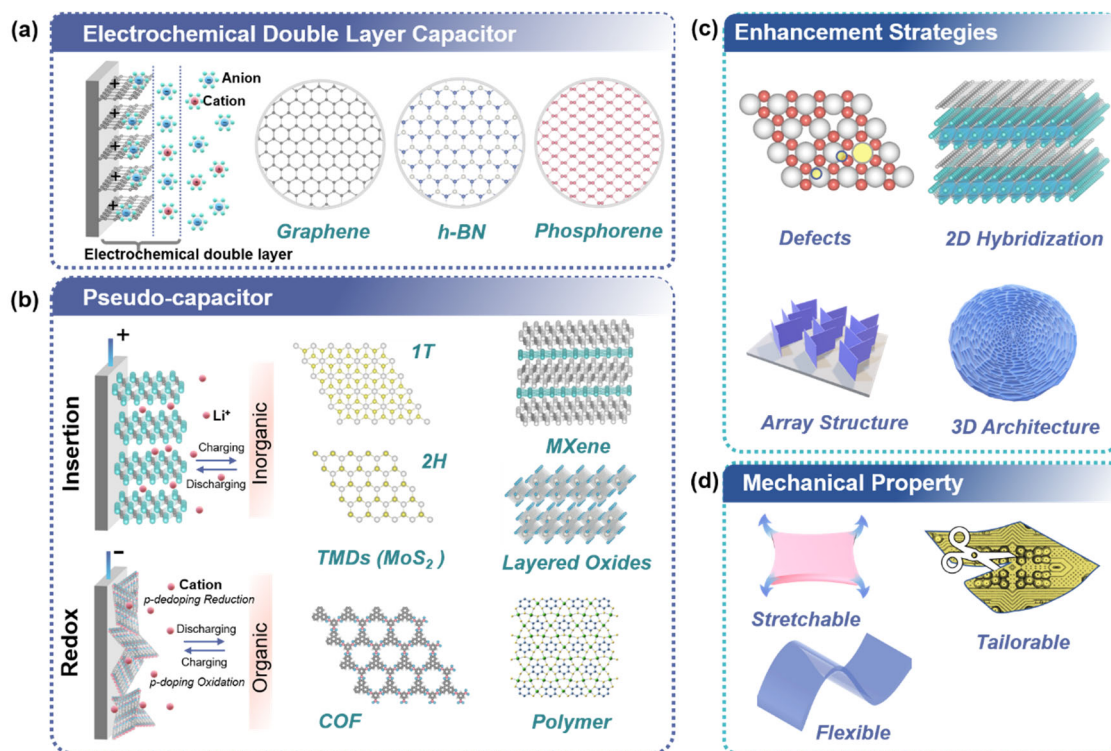

Fig. 47　Supercapacitors based on 2D material electrodes: (a) electrochemical double layer mechanism and (b) pseudocapacitance. (c) Various strategies to enhance the electrochemical properties of 2D materials. (d) Unique mechanical properties of 2D materials compared to bulk electrode materials.

In the domain of pseudocapacitor, we will exclude some 2D transition metal oxides such as LDHs as their pseudo-capacitive behavior is generally not intrinsic [1278,1279]. On the other hand, layered TMDs show strong pseudocapacitance behavior because of their large surface area and variable oxidation states. The most interesting attribute of TMDs is their different polymorphs structures (e.g., 1T and 2H phases) (Fig. 47b) [370]. Acerce *et al.* demonstrated that the high electrical conductivity and intrinsic hydrophilicity imparted 1T-phase MoS_2 the ability to intercalate various cations and interesting electrochemical properties for aqueous/organic supercapacitor devices [156]. Likewise, the exfoliated "distorted" 1T-phase (1T′) WTe_2 was reported to show good electrical conductivities and deliver a mass capacitance of 221 $F \cdot g^{-1}$ [1280]. 2H-phase MoS_2 and layered oxides (δ-MnO_2 and α-MoO_3) face some issues in common, namely, the poor electronic conductivity and inferior structural stability [32]. Previous works have tried to mitigate these two issues by foreign ion doping to narrow down the bandgap and improve electron transfer [1281,1282]. Of course, the most common strategy by hybridizing layered TMDs or oxides with conductive carbonaceous materials is always useful to facilitate charge transport, increase ion-accessible sites, enlarge interlayer space and impede restacking, thus giving rise to improved rate capability and cycling stability.

MXenes, particularly the conductive $Ti_3C_2T_x$, with high metallic conductivity and volumetric capacitance are widely explored in supercapacitors [1283]. In 2013, Lukatskaya *et al.* demonstrated that various cations (Li^+, Na^+, Mg^{2+}, K^+, NH_4^+, and Al^{3+} ions) could readily intercalate between 2D $Ti_3C_2T_x$ layers from aqueous solutions. Among which, binder-free $Ti_3C_2T_x$ paper in basic solutions exhibited the best performance and yielded volumetric capacitance of up to 350 $F \cdot cm^{-3}$ [948]. Subsequently, they continued to study the capacitive behavior of $Ti_3C_2T_x$ in organic electrolyte aiming at an extended voltage window and thus a larger energy density. It's found that solvated or desolvated Li^+ can be intercalated when different organic solvents were used, which delivered significantly different capacitance [1284]. The development of $Ti_3C_2T_x$ in SCs also inspires the research of other MXenes like Ti_2CT_x [1285] and V_2NT_x [1286].

Beyond inorganic ones, 2D organic materials offer chemical and structural tunability and physicochemical properties toward application in SCs (Fig. 47b). Typical examples are conductive polymers, MOFs, and COFs. In general, these organic materials or functionalized organic materials [1287,1288] exhibit pseudocapacitive behaviour *via* redox reactions. However, by virtue of their large compositional diversity, some 2D organic materials can store charge through EDL capacitive [1289–1291] and insertion pseudo-capacitive behaviour as well [1292]. Furthermore, 2D MOFs and COFs as a novel class of porous crystalline organic materials can be directly applied for capacitive energy storage [1293], or as sacrificial templates for resulting sulfide/carbon CoSNC [1294] and porous carbon [1295] for supercapacitor electrodes.

As above, a variety of 2D materials have emerged as favourable and competitive candidates in the application of supercapacitors. Modulation strategies, such as defect introduction, surface functionalization, and materials hybridization, are effective in enhancing the performance (Fig. 47c). In addition, architecture engineering also has profound effect on electrochemical properties by exposing more reactive sites and regulating charge transports, e.g., vertical alignment of 2D materials [1296], and restacking of exfoliated nanosheets into a 3D sponge [1297] or hydrogel electrodes [1298].

Finally, the high mechanical strength and flexibility of 2D materials at atomic dimensions make them promising for the preparation of electrodes that are stretchable, flexible and tailorable (Fig. 47d) [1283]. Research on that has proliferated over the recent years, like stretchable MXene/rGO-based supercapacitor (*i.e.*, up to 300% uniaxial and 200% × 200% biaxial strain) [1299], and flexible BP-CNTs-based supercapacitor (can withstand bending, rotating, twisting and folding deformation) [1300]. This will be a promising direction for 2D materials based electrodes in the study of device with both high mechanical robustness and electrochemical performance.

4.4.3 2D materials for micro-supercapacitors

The trend of miniaturizing electronic devices has pushed the development of integrated self-powered systems. The race to pack energy storage units with high energy, power density, low mass, and small volume into tiny devices is very competitive. While micro-batteries are undisputed in terms of energy density, the slow speed of charge-discharge and short cycling lifetime has limited the application in high-rate and cycling-intensive situations. This void has been filled by micro-supercapacitors (MSCs). The popularity of 2D materials as MSC electrode was not serendipitous; instead, their large specific surface area, high conductivity and inherent out-of-plane flexibility are essential for attaining high power density, decent energy density and robust mechanical properties of overall device. Moreover, stacked nanosheets are ideal high-rate electrodes for planar MSCs with interdigitated fingers since they feature more accessible surface and fast in-plane ion transport unhindered by separators used in typical sandwich MSCs, resulting in high power density [1301].

For MSCs, four classes of 2D materials have been extensively researched with great success. These include graphene, transition metal oxides (TMOs), TMDs and MXenes. Each of these has specific advantages and disadvantages which decides the target application. For example, graphene is highly conductive but exhibits only EDLC. This makes it suitable for high-rate applications like AC-line filtering over frequency range of 1–10000 Hz, retaining EDLC behaviour even at scan rates of 1000 $V \cdot s^{-1}$ [1302,1303]. MXene-based MSCs exhibit capacitance as high as hundreds or thousands of farads per unit volume [1304]. In the following, we briefly discuss the suitability and challenges of 2D materials for MSCs without going to

details of examples (Fig. 48).

The performance of MSCs is evaluated by three metrics of areal/volumetric capacitance, energy density and power density. At the microscopic scale we need be creative to achieve trade-offs. Conductive 2D materials readily overcome two bottlenecks of both the surface area and resistance. Typically, graphene is one of the most ideal materials to achieve this, and there has been significant related research into graphene [1305,1306]. Even graphene synthesized using simple laser-induced reduction of graphene oxide or polymer could achieve capacitance in the range of 10 mF·cm^{-2} and up to 32 mF·cm^{-2} using KOH activation [1307–1309]. Graphene's capacitance can be improved further by doping with electron donors or acceptors like N, S, B, which engineers its bandgap for better charge transfer/storage and enriches its surface chemistry by introducing defects and pseudocapacitance, thus increasing the activity [1310–1312]. Despite several other elemental nanosheets have been isolated, phosphorene is the only one that has been applied in MSCs due to the large interlayer space (5.3 Å) between its puckered lamellar structure allowing fast ion diffusion [1275]. Because of such unique advantages from 2D structure, it can achieve high power density of around 10 W·cm^{-3} and retain capacitive performance at 100 V·s^{-1} [1275,1313]. Most of its applications for MSCs hybridize it with other materials that offer protection from environment, improve inter-lamellar conduction and prevent reaggregation [1300,1314,1315].

The energy output of EDLC materials does not scale well into miniaturized devices. Therefore, it is necessary to employ pseudocapacitive materials (MXenes, metal oxides, *etc*.) functioning on Faradic reactions at electrode/electrolyte interface. These combine the structural advantage of 2D materials with rich electrochemistry. As discussed above, TMD and TMO nanosheets are attractive pseudocapacitive materials. The 1T phase TMDs have conductivity orders of magnitudes higher than 2H phase ones in addition to larger interlayer spacing and number of active sites [1316]. However, TMD nanosheets tend to be less flexible due to their multilayer structure and may easily crack if applied to MSC electrodes. Also, TMOs usually employ additional conductive fillers to compensate the poor conductivity. In addition, they are both prone to reaggregation which cuts off both electronic transport and access to active sites. To tackle this challenge, forming composites is an effective solution. Compositing with graphene preserves the active sites and provides fast electronic transport channel which is essential for exploiting their excellent pseudocapacitance. Very recently, an ultrafast photonic reduction technique was reported which could manufacture 30000 graphene/MnO$_2$ electrodes in 1 min, with high areal capacitance 128 mF·cm^{-2} [1317]. MXenes overcome the chemical inertness of graphene and low conductivity of TMO/TMDs, thus it is an ideal material for smaller, multifunctional and self-sufficient MSCs packing high energy and power [1221,1318–1320]. But this superstar material still face shortcomings of moisture-related degradation and brittleness. For instance, nanocellulose additive offers incredible mechanical strength (341 MPa with 20% nanocellulose) [1321], carbon or sodium ascorbate coating provides resistance against
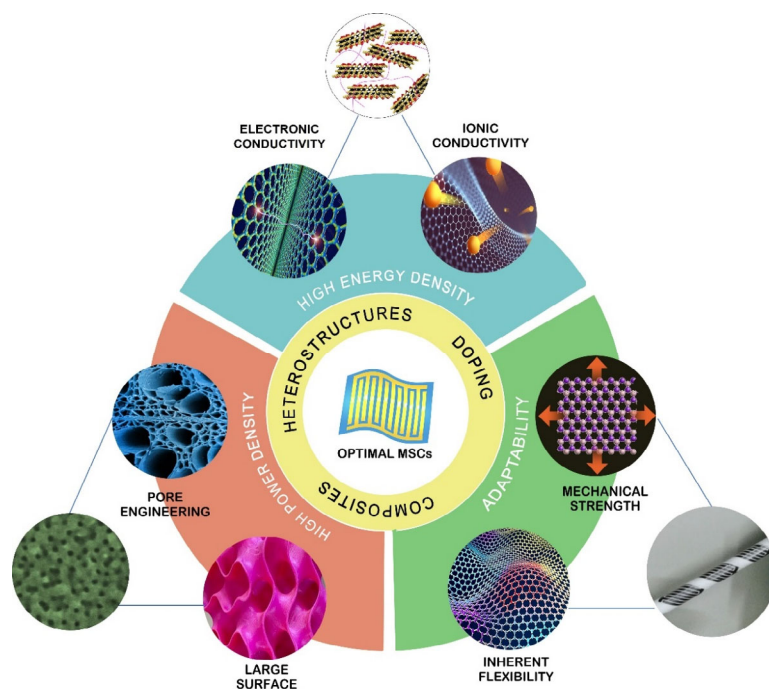
Fig. 48　Factors of 2D materials that are suitable micro-supercapacitors. High conductivity and fast ionic diffusion are essential for high power performance. The inherently large surface area and engineerable pores increase the possibility to pack high energy density. The mechanical strength and out-of-plane flexibility are attractive for all-weather, wearable MSCs for integrated electronics. Doping, composites, and or heterostructures are general and effective strategies to render high-performance and multifunctional MSC electrodes.

oxidation [1322,1323], and compositing with graphene makes MXene-based electrodes stretchable (300% under uniaxial strain) [1299]. Such enhancements are important to achieve all-weather MSCs that deliver desired electrochemical performance. Incorporation of new materials into MXene-framework may also impart unique functions like pressure sensing [1324] and self-healing [1325] which may not only reduce the footprint of integrated devices but also extend the usable life of such devices.

Finally, 2D materials provide a way for addressing the issue of close approach of ions to active material surface in the form of pore engineering [1326]. Through theoretical and *in situ* investigations the dependence of capacitive mechanism on pore size distribution through desolvation of electrolyte's ion hydration shell has been adequately established [1327–1329]. Porous nanosheets could be the essential building blocks for hierarchical porous structures with nano- and meso-pores that could provide a trade-off between diffusion and charge storage capacity, enabling highly tuneable performance in MSCs by simply changing some synthesis parameters. In this regard, ordered bulk materials with hierarchical porosity could act as source or templates for obtaining nanosheets that inherit the parent porosity [1330–1332]. For example, Lin *et al*. has made great progress in fabricating well-defined porous graphene from polyimide films using the cost-effective, high throughput laser-scribing method [1309]. This method can also be used for boron doping which increases capacitance by three times to 16.5 mF·cm^{-2} [1333]. The pore size can be tuned by controlling the laser power [1334]. Pore engineering of 2D materials is a superb strategy to activate intercalation pseudocapacitance in materials that may exhibit inherent redox activity and thus improve suitability of some materials for MSCs which were otherwise overlooked [1273,1335].

Despite the large number of reports, it is unlikely that a single 2D material will remove all the obstacles in the path of industry-level fabrication of MSCs. As human needs evolve, so will the demand for specific types of MSCs. For such situations we must build a repository of detailed information on protocols for rational hybridization of 2D materials and their mechanisms.

4.5 Solar cells

Solar cells, which directly convert the solar energy into electrical energy *via* photovoltaic effect, are multilayered devices, in which the light harvesting layer is sandwiched between the anode and cathode. In general, charge transport layers in terms of hole transport layer (HTL) and electron transport layer (ETL) are inserted between the photoactive layer and the anode or cathode, respectively, to facilitate the efficient collection of photogenerated charge carriers at respective electrodes. With the development trends in the community of solar cells stepping toward high flexibility, low cost and light weight, the unique mechanical and optoelectronic properties of 2D materials enabled them promising candidates in designing the next generation solar cells. These atomically thin 2D materials have exhibited very large light-matter interaction, unique electrical and structural properties, and controllable optical bandgap structures, making it possible to obtain a high conversion efficiency of solar energy using a minimal amount of active absorber materials [1336]. The structural properties of 2D materials, including the number of layers, defects and dopants, phase, strain, and composition, could greatly change their properties and thus affect the overall performance of solar devices [1337]. Recently, 2D materials have been widely explored in the fabrication of high-performance solar cells as electrodes, charge transport layers and photoactive layers (Fig. 49), respectively.

4.5.1 Electrodes

In general, indium-doped tin oxide (ITO) and fluorine-doped tin oxide (FTO) are frequently used transparent electrodes in solar cells, but their expensive price, time-consuming processing and brittle nature restricted their applications. In contrast, owing to the cost-effective manufacturing, ambipolar conductivities and robust mechanical properties, electrically conductive 2D materials in terms of graphene [1338] 2D MOFs with π-*d* conjugated coordination [1339] and MXenes [1340] *etc*., are promising candidates to replace the traditional ITO and FTO. It was noted that both the transmittance and conductivity of 2D materials vary with the number of layers. A compromise must be reached between the conductivity and transmittance of the transparent electrodes based on 2D materials, and chemical modifications and heteroatom doping have been realized as efficient strategies to reduce their sheet resistance while maintaining the high transmittance [1341,1342]. For examples, a single layer of chemically doped graphene was employed as transparent electrode in flexible perovskite solar cells, resulting in an efficiency up to 18% with excellent bending durability. Furthermore, 2D materials, especially graphene, can also be used as top electrode to replace the traditional metals (Au, Ag, Cu *etc*.), and some promising benefits can be obtained. For examples, graphene
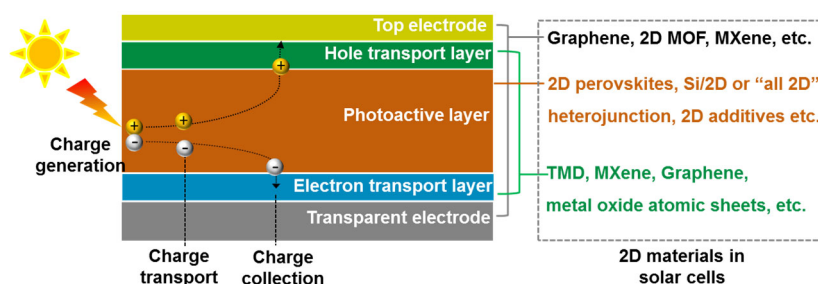

Fig. 49 **Device structure and work mechanism of solar cells, and the application of 2D materials in solar cells.**

electrodes enabled the fabrication of HTL-free perovskite solar cells [1343] and semitransparent solar cells [1344], which open new applications in power generating windows or tandem solar cells. Moreover, the application of 2D materials as electrode in solar cells can boost the device stability compared to the metal counterparts, because the carbon based materials are not diffusive into the neighboring layers and the thick and hydrophobic carbon materials can act as good encapsulating layers to prevent the moisture permeation [1345].

4.5.2 Charge transport layers

It is well established that the 2D materials are composed of a monolayer or multilayered nanosheets bonded *via* van der Walls forces. The dangling bonds and defect states are generally absent at the 2D thin film surface and their optoelectronic properties are adjustable by varying the number of layers [127]. Moreover, as-formed 2D thin films exhibit atomic-level smoothness, enabling fast charge transport and a good compatibility with the deposition of upper layers. Therefore, 2D materials can be functioned as charge transport layers in solar cells. For examples, TMDs, such as SnS_2 [1346], TiS_2 [1347] and MoS_2 [1348], are recently used as efficient electron and hole transport layers in solar cells. The electronic properties of the TMDs can be tuned by modifying the transition metals or chalcogens according to the properties of the photoactive layers, thus resulting in improved stability and efficiency. MXenes such as $Ti_3C_2T_x$ are another type of 2D materials based on transition metals with high versatile chemistry and metallic conductivity. After appropriate treatments, MXenes can be used as charge transport materials to improve the interface property between the MXene and photoactive layer with improved contact intimacy and well aligned energy level [1349]. And also, 2D metal oxide nanosheets made from conventional charge transport materials such as TiO_2 were also employed as ETL in perovskite solar cells. Compared to crystalline TiO_2, the multilayered 2D TiO_2 nanosheets prepared at low-temperature process exhibited excellent flexibility and good coverage on a variety of substrates, and also greatly inhibited the photoinduced performance degradation because of the low oxygen vacancy [1350]. In addition, some 2D materials such as MXenes [1351], BP [1352,1353], graphene [1354] and their derivatives were also considered to be incorporated into or combined with the conventional charge transporting layers to enhance their conductivity or optimize the electronic properties. Therefore, the application of 2D charge transport layers in solar cells can bring in synergistic effects with smoothened interface contact, well matched energy level, low defect density and high intrinsic conduction, thus resulting in reduced non-radiative charge recombination at the interface and hence improved device performance.

4.5.3 Photoactive layer

2D materials can principally be used as solely photoactive layers in ultrathin solar cells because of their good light absorbing ability and direct bandgap characters at the monolayer level. Particularly, 2D perovskites such as Ruddlesden-Popper (RP) phase and Dion-Jacobson (DJ) phase, have attracted extensive investigation because of their excellent operational stability compared to 3D perovskites [356]. In order to improve the efficiency of the 2D perovskite solar cells and make them competitive with their 3D counterparts, recent efforts have been focused on the understanding of the interlayer interaction between neighboring perovskite sheets, which can be strengthened *via* compositional modification on the 2D perovskites to introduce some additional high-energy bonds besides the Coulombic and hydrogen bonds [1355]. In addition, reducing the quantum well width distribution [1356] or even fabricating phase-pure quantum well films [1357] are another strategies to further enhance the device performance. As a result, efficiency up to 18% with significantly enhanced stability can be obtained in 2D perovskite solar cells. And also, 2D materials can be combined with other light harvesting materials to form Si/2D or "all 2D" heterojunction solar cells [1358]. In particular, a solar cell based on a monolayer MoS_2/monolayer WSe_2 can obtain an efficiency up to 2.56% [1359]. Even though the "all 2D" solar cells are not as effective as conventional solar cells because of the ultrathin layer thickness, the unique properties such as extremely high ratio of watt-per-gram, flexibility and transparency rendered them promising applications in the next-generation photovoltaics. Similarly, 2D materials including GO [1360], BP [1361], g-C_3N_4 [1362], 2D perovskites [1363], *etc.*, can also be incorporated into the photoactive layer or used as interface engineer to regulate the crystallization, passivate defect states or encapsulate the photoactive layer, and hence simultaneously improve the device efficiency and operational stability.

4.6 Biomedical applications

Graphene was first demonstrated as an efficient nanocarrier for a water-insoluble aromatic anticancer drug delivery in 2008 [1364]. Since then, 2D materials have been investigated extensively for various biomedical applications, such as drug delivery, biosensors, wearable/implantable devices, bio-imaging, diagnosis, therapeutics and regenerative medicine to surmount the limitations found in traditional modalities of diagnosis and treatment, owing to their unusual structure and properties deriving from the ultrathin atom-thick planar surfaces. To data, 2D materials have attained remarkable accomplishments and progresses in biomedical fields.

Some family members of 2D biomaterials have been exploited as cutting-edge tools for a host of biomedical utilizations, attributing to their following distinct characteristics, such as (i) the desirable atomic thickness for biosensing and gene-sequence detection; (ii) high near-infrared (NIR) absorption for photothermal therapy (PTT) and photoacoustic (PA) imaging at both the first and second biological window; (iii) substantial generation of reactive oxygen species (ROS) under the activation of endogenous chemical activators (e.g., H_2O_2) or external physical triggers (e.g., light, ultrasound and X-ray) for nanodynamic therapy (e.g., chemodynamic therapy (CDT), photodynamic therapy (PDT), sonodynamic therapy (SDT) and

radiodynamic therapy (RDT)); (iv) high atomic number elements allowing them as the contrast agents for precise computed tomography (CT) imaging; (v) effect on the proton relaxation of water enabling magnetic resonance (MR) imaging; (vi) ultrahigh specific surface area for utilization as drug delivery system with the capability of encapsulating plentiful guest molecules (e.g., small molecular drugs, genes, biomacromolecules and fluorescent dyes), controlling on-demand drug release and integrating other functional moieties (e.g., contrast agents) for implementing specific disease theragnostic.

As a typical type known for cancer treatment that utilizes drugs to eliminate tumor cells, chemotherapy has made a dramatic impact in prolonging survival of millions of patients [1365]. There exist three major challenges during cancer therapy, namely the early detection, tumor metastasis and multidrug resistance (MDR). Moreover, successful treatment cannot be implemented without precise diagnosis. To achieve effective utilization of delivered drugs, the augmented diagnostic imaging-guided and on-demand drug delivery is essential to maximize the use of drugs. Taking graphene for example, graphene modified with functional nanoparticles has been fabricated to provide additional properties and functions for tumor imaging and treatments. In 2014, Chen *et al.* successfully designed a multifunctional stimuli-responsive doxorubicin (DOX)-loaded nanosystem by co-integration of Fe_3O_4 and MnO_x onto GO using a double redox strategy (Fig. 50a) [1366]. MnO_x could realize the pH-/reduction-activated T_1-weighted magnetic resonance (MR) imaging. After Fe_3O_4 integration, this nanosystem was not only used for contrast-enhanced T_2-MRI, but also acted as a magnetic-hyperthermia nanoagent. By combined treatment with DOX-enabled chemotherapy, such a theranostic planar nanoplatform significantly inhibited the cancer metastasis and reversed the MDR of cancer cells. Notably, the strong and broad optical absorption in NIR region makes 2D materials possible to convert the light energy into heat energy for PTT. Beyond chemotherapy, PTT, PDT, radiotherapy (RT), magnetic hyperthermia and immunotherapy are the major types of monotherapies.

In view of the setbacks of monotherapy, combined therapy could offer superior advantages by making the best of the cooperative enhancement of each individual treatment. Dai *et al.* reported on the integration of graphene with TiO_2 and MnO_x, forming MnO_x/TiO_2-graphene nanocomposites, which could serve as constrast agents for pH-responsive T_1-weighed MRI and nanosonosensitizers for PTT-enhanced sonodynamic therapy on synergistically combating cancer [1368]. Encouraged by the success of graphene, monoelement 2D nanostructures, such as BP, are distinguished from other 2D materials by its easy and controllable degradation, and its degradation rate mainly relies on the oxygen content and thickness. In consideration of the degradation products such as phosphate anions those are essential for human health, Yang *et al.* constructed the multifunctional BP-integrated robust 3D-printed bioactive glass scaffold for therapeutic tissue engineering, which could be highlighted as the desirable countermeasure for the efficient topical treatment of osteosarcoma and simultaneous bone regeneration (Fig. 50b) [1367]. Hereafter, research indicates that the degradation behavior of BP in tumor cells is different from that in normal cells, which induces phosphate anions acute accumulation in cancer cells for selective chemotherapy [1369].

Through continuous exploration and innovation, we have witnessed enormous strides in biomedical application of 2D materials. Higher expectations are inevitably followed by more
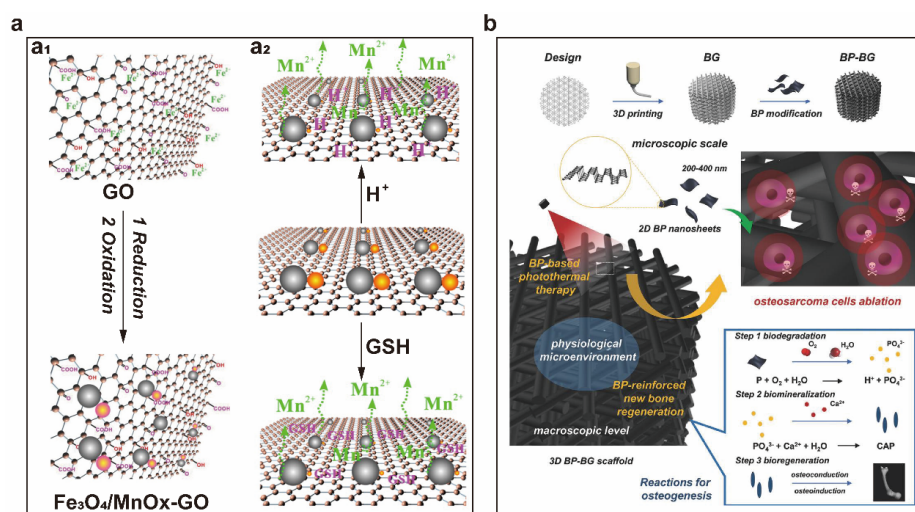
Fig. 50   Biomedical applications of 2D biomaterials. (a) Multifunctional GO-based stimuli-responsive nanotheranostics. (a₁) The scheme of double redox strategy to fabricate Fe_3O_4/MnO_x–GO composite nanosystems. (a₂) The scheme of MnO_x decomposition and Mn^{2+} release under either mild acidic or redox environment. (b) Schematic representation of the synthesis regarding BP-BG scaffold and the therapeutic countermeasure for osteosarcoma based on osteogenesis by BP-BG. (a) Reproduced with permission from Ref. [1366], Copyright 2014 John Wiley and Sons. (b) Reproduced with permission from Ref. [1367], Copyright 2018 John Wiley and Sons.

stringent standards. Obviously, each 2D material possess its own unique advantages and disadvantages. Although bold steps have been made toward 2D biomaterials up to now, they still encounter substantial hurdles for clinical translation. For example, the inextricable issues including difficult batch production, lacking reproducibility, uncontrollable number of layers, indisciplinable morphology and wide size distributions present the benchmarks of 2D materials in clinical trials. The dispersibility and stability of 2D materials in aqueous solutions are of both scientific and technological significance for biomedicine. Furthermore, the potential long-term side effects and cumulative toxicity remain the most important concerns for 2D materials and its derivatives, especially for inorganic 2D materials. According to the current findings, both surface chemistry and size effect play key roles in influencing the biological behaviors, fate and toxicity of 2D materials. However, at this point, much remains unknown regarding whether or not and how 2D materials could be biologically degraded or metabolized in living organism.

4.7 Sensing applications

Since the successful application of graphene in the construction of sensing platforms for chemical and biological molecules detection, 2D materials including TMDs (e.g., MoS_2 and WS_2), MXenes, BP, g-C_3N_4, graphyne, NMDs, h-BN and transition metal oxides (e.g., WO_3 and MnO_2) have been considered as powerful materials for the design of sensing platforms [49,1370–1373]. Combined with fluorescence, surface-enhanced Raman scattering (SERS), surface plasmon resonance (SPR), FET, electrochemistry and colorimetry, the 2D material-based sensing platforms have been employed to detect heavy metal ions, organic compounds, pesticides residues, antibiotics, nucleic acids, proteins, bacteria and cells [1374,1375].

4.7.1 Fluorescence sensing platforms

Since the theoretical and experimental evidence of the fluorescence quenching ability of graphene and its derivatives, hundreds of works have proved that 2D materials have this ability to efficiently quench the fluorescence of fluorophores [1376–1379]. As a proof of the concept, He *et al.* found that GO efficiently quenched the fluorescence of three dyes-labelled single-strand DNA (ssDNA) probes. With the addition of p 16, p 21 and p 53 genes, the corresponding fluorescence of carboxy fluorescein (FAM), cyanine 5 (Cy5) and 6-carboxy-X-rhodamine (ROX) were recovered. According to this phenomenon, this graphene-based sensing platform was used to simultaneously analyze three genes [1380]. Inspired by this interesting finding, Zhu *et al.* firstly reported a MoS_2-based fluorescence sensor. As we know, MoS_2 nanosheet has different affinity towards ssDNA and double-strand DNA (dsDNA), leading to the fluorescence intensity of dsDNA recovering after the addition of target DNA. As a result, the designed fluorescence biosensor can efficiently determine DNA and other biomolecules [1381]. Similarly, Ti_3C_2 nanosheets [1382], MXenes [1383], BP [1384] and MOFs [1385] have been successful used to construct fluorescence sensing platforms for HPV, bacteria,

ctDNA and cyanide detection, respectively.

Besides *in vitro* analysis, 2D material-based sensing platforms have been also used to analyze intracellular molecules. Li *et al.* immobilized FAM-labelled peptide onto polydopamine and PEG co-functionalized MoS_2 nanosheet to construct an intracellular sensing platform for the detection of caspase-3 activity. Taking human cervical carcinoma (HeLa) cells as a model, the designed MoS_2-based sensing platform can efficiently analyze intracellular caspase-3 activity, which was proved by confocal laser scanning microscopy and flow cytometry [1386]. To enhance the performance of 2D material-based sensing platforms, Zhu *et al.* introduced signal amplification strategy into MoS_2-based sensing platform. As shown in Fig. 51, three Cy3-labelled molecular beacons co-absorbed on the surface of MoS_2 nanosheet. With the addition of microRNA-21 (miRNA-21), "Y"-shaped three-branched duplex nanostructure was formed and released from MoS_2 surface, making the fluorescence recover. With the help of catalyzed hairpin assembly (CHA) reaction, the detection limit of this sensing platform was down to 75.6 amol·L^{-1}, which is much lower than other similar detection strategies [1387].

4.7.2 SPR sensing platforms

The introduction of 2D materials into SPR sensors can efficiently improve their sensitivity. A typical example was given by Wu *et al.*, who found that the sensitivity of SPR sensor improved with the increasing the graphene layer [1388]. This exciting work pave a way for application of 2D materials in SPR sensing platforms. According to this concept, Kumar *et al.* systematically studied the performance of SPR sensors based on WS_2, MoS_2 and graphene, respectively. The experimental results showed that monolayer WS_2-constructed SPR sensor has better sensitivity (180 (°)·RIU^{-1}) than those constructed by monolayer MoS_2 (174 (°)·RIU^{-1}) and graphene (157 (°)·RIU^{-1}), respectively. Unexpectedly, monolayer graphene-constructed SPR sensor has smaller full width at half maxima (FWHM), higher quality parameter and detection accuracy [1389]. In 2019, Xue *et al.* employed antimonene to develop a SPR sensing platform for ultrasensitive microRNA detection due to the strong
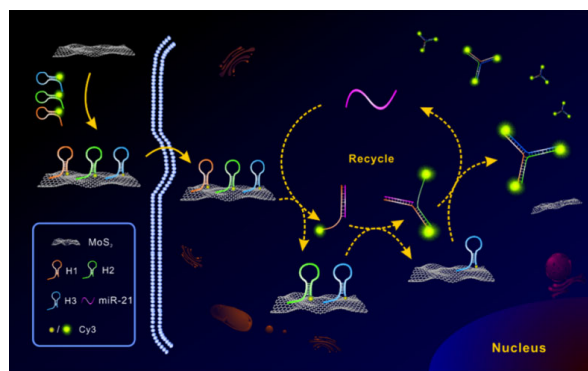

Fig. 51 Scheme of the MoS₂-based fluorescence sensing platform for detection and imaging of miRNA-21 in cells. Reproduced with permission from Ref. [1387], Copyright 2019 American Chemical Society.
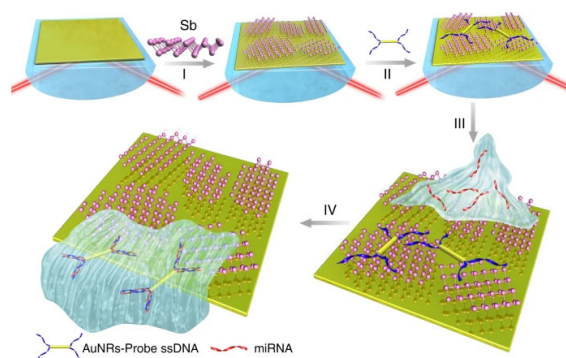
Fig. 52 Fabrication of antimonene-based SPR sensor for miRNA detection [1390].

affinity between antimonene and ssDNA (Fig. 52). More delocalized 5*s*/5*p* orbitals in antimonene led to lower detection limit (10 amol·L^{-1}) of this SPR sensor, which is much lower than those of published miRNA sensors [1390].

2D material-based SPR sensing platforms were also used to detect proteins and bacteria. For example, a SPR sensor was constructed for recognizing and detecting BSA protein based on carboxyl-MoS$_2$ nanosheet. Under the same detection condition, the SPR angle signal of carboxyl-MoS$_2$-based sensor was 3.1 folds than that of MoS$_2$-based sensor [1391]. Kaushik *et al.* developed a label-free SPR immunosensor for Escherichia coli detection based on biofunctionalized MoS$_2$ nanosheets. Under optimal condition, this SPR immunosensor exhibited low detection limit (94 CFU·mL^{-1}) and high sensitivity (2.9 nm/1000 CFU·mL^{-1}) for Escherichia coli detection [1392]. Construction of 2D materials-based nanoprobes is a popular way to improve the analytical performance of SPR sensing platforms. For example, Nie *et al.* developed a SPR sensing platform for ultrasensitive detection of miRNA-141 by using gold nanoparticles-decorated MoS$_2$ nanocomposites (AuNPs-MoS$_2$) as nanoprobes. Once the formation of a classical "sandwich" DNA structure, resonance angle of this SPR sensor obviously shifted. Therefore, this SPR sensing platform can detect as low as 0.5 fmol·L^{-1} miRNA-141 with the amplification effect of AuNPs-MoS$_2$ nanoprobe [1393].

4.7.3 Surface-enhanced Raman scattering sensing platforms

Compared with noble metal nanostructures, 2D materials have weaker Raman enhancement due to the chemical enhancement mechanism, which was proved Lin *et al.* [1394]. Subsequently, h-

BN, WS$_2$, MoS$_2$ and MXene have been reported as SERS-active substrates with small Raman enhancement factors ranging from 10 to 100 [1395–1397]. Unfortunately, these small enhancement factors limited the application of 2D materials in SERS sensors [1370].

To improve the Raman enhancement, hybridization of 2D materials with noble metal nanostructures is a useful way. It is well known that 2D materials possess large surface area, which can load a large number of noble metal nanostructures. As a result, the Raman enhancement of these 2D nanocomposites are much stronger than 2D materials. These exciting findings accelerated the development 2D material-based SERS sensors. For example, gold nanoparticles supported on the surface of MoS$_2$ nanosheet to form MoS$_2$-based nanocomposites (MoS$_2$-AuNPs), which exhibited stronger Raman enhancement than MoS$_2$ nanosheet [1398]. Similarly, Singha *et al.* reported the *in situ* growth of AuNPs on the surface of three-dimensional MoS$_2$ nanoflowers to construct SERS-active substrate for bilirubin detection. It should be noted that the enhancement factor of this nanocomposite is 10^9 [1399]. Xie *et al.* developed a SERS-active sensing platform for organic pollutants detection based on gold nanorods (AuNRs)-MXene (Ti$_3$C$_2$T$_x$) nanocomposites. Large amounts of AuNRs supported on the surface of MXene generated abundant "hot spot", making the detection limits of this sensing platform for rhodamine 6G, crystal violet, and malachite green detection are down to 1, 1, and 100 pmol·L^{-1}, respectively (Fig. 53) [1400]. For improving the detection selectivity, Shorie *et al.* combined aptamer with AuNPs-decorated WS$_2$ nanocomposite (WS$_2$-AuNPs) to construct a SERS sensing platform for cardiac marker myoglobin (Mb) analysis. Expectedly, this proposed sensing platform showed high detection performance included wide detection range (10 fg·mL^{-1} to 0.1 μg·mL^{-1}), which was ascribed to the high Raman enhancement generated from the synergistic effect of WS$_2$-AuNPs nanocomposites [1401].

2D materials are also promising candidates to construct Raman probes for signal amplification. For instance, Fu *et al.* constructed a SERS immunosensor for cardiac troponin I (cTnI) detection by using GO loaded with large amounts of antibody/Raman reporter-labeled AuNPs as SERS nanotags. With the signal amplification of GO-based SERS nanotags, this designed SERS sensing platform has a wide linear range (0.01–1000 ng·mL^{-1}) and a low detection limit (5 pg·mL^{-1}) for the
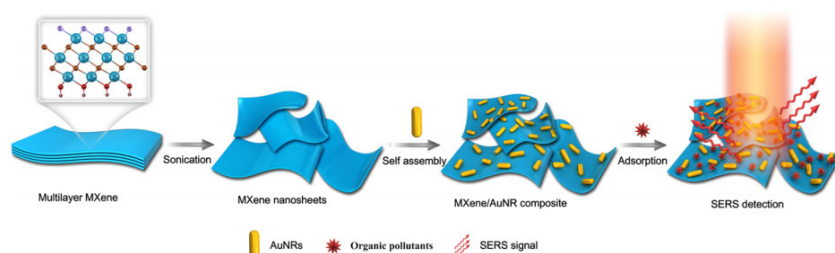

Fig. 53 Schematic illustration of SERS sensing platform for organic pollutants detection based on the MXene/AuNR composite.
Reproduced with permission from Ref. [1400], Copyright 2019 American Chemical Society.

detection of cTnI [1402]. Similarly, Achadu *et al.* group used GO as a SERS-active substrate and molybdenum trioxide nanocube as a SERS nanotag to construct an immunosensor for norovirus detection. Due to the synergistic effect of SERS substrate and nanotag, this proposed immunosensor obtained a ~10^9-fold signal amplification, resulting in an ultralow detection limit for norovirus detection (~5.2 fg·mL^{-1}). It should be noted that this immunosensor can determine as low as ~60 RNA copy·mL^{-1} in human fecal samples, which is much lower than that of a commercial kit [1403].

4.7.4 Field-effect transistor sensing platforms

FET is considered as a promising sensing platform for the analysis of chemical/biological molecules due to its rapid sensing capability and readable electrical signals. Since the discovery of graphene, 2D materials are extensively employed as ideal channel materials to construct FET sensing platform due to their high surface area, large transconductance and exceptional chemical stability and biocompatibility. Graphene has become the main focal point of 2D FET-based chemical and biological sensing, delivering excellent performance in at both single-nanosheet and thin-film level in various chemical and biological sensing [1404,1405]. Seo *et al.* utilized graphene to design FET sensing platform for severe acute respiratory syndrome coronavirus 2 (SARS-CoV-2) detection due to its high carrier mobility (15000 cm^2·V^{-1}·s^{-1}) and large surface area. As shown in Fig. 54, an obvious signal was observed when SARS-CoV-2 protein specifically bound with the corresponding spike antibody. This proposed FET sensing platform could determine 100 fg·mL^{-1} SARS-CoV-2 protein and 2.42 × 10^2 copy·mL^{-1} SARS-CoV-2 in clinical samples [1406], respectively. To improve the selectivity, Xu *et al.* immobilized aptamer on the surface of graphene to selectively recognize and detect adenosine triphosphate (ATP). Due to the special binding effect between aptamer and ATP, this FET sensing platform can selectively analyze 0.5 pmol·L^{-1} ATP, which is several orders lower than some published works [1407]. In 2021, the same group developed graphene-based FET sensing platform to monitor interactions between drug imatinib and Abl1 protein [1408]. Formation of noble metal nanostructures-supported graphene nanocomposites can efficiently improve the analytical performance of FET sensing

platform. For example, Zhang and co-worker designed a label-free FET sensor for brain natriuretic peptide (BNP) detection based on platinum nanoparticles (PtNPs)-decorated graphene nanocomposites. Experimental results suggested that this sensing platform could determine BNP in whole blood sample [1409].

Compared with graphene, MoS$_2$ possessed thickness-tunable bandgaps and excellent electrical properties, which is considered as an ideal channel material to construct next-generation of FET devices [1410]. In 2019, Gong *et al.* utilized MoS$_2$ nanosheet to design a label-free FET sensor for high-sensitive detection of fibroblast growth factor 21 (FGF21). As expected, this MoS$_2$-based FET sensing platform can analyze as low as 10 fg·mL^{-1} FGF21 without the assistance of additional adsorption layers. Moreover, this sensing platform can determine FGF21 in complex real samples [1411]. In the same year, Liu *et al.* developed a MoS$_2$-based FET sensing platform for screening of Down syndrome. The experimental test suggested that this proposed FET sensor has low detection limit of 100 amol·L^{-1}, high selectivity and high signal response for chromosome 21 detection. The real-time test further proved that this sensing platform could analyze chromosome 21 in the peripheral blood of pregnant women [1412]. Besides graphene and MoS$_2$, other 2D materials are also suitable for construction of FET sensing platform, such as MXene [1413] and BP [1414].

4.7.5 Electrochemical sensors

Since Zhou *et al.* successfully employed graphene to construct electrochemical sensing platforms for biological molecules detection [1415], 2D materials have attracted more and more attentions in sensing field because of their excellent physical and chemical properties, such as fast electron transfer kinetics, high electrical conductivity, large surface area and so on [1416]. Nowadays, constructing high-performance sensing platforms with new 2D materials is one of the hot research directions. Generally, 2D materials are often employed as electrode modifiers to construct sensing platforms. For example, Su *et al.* decorated AuNPs on the surface of MoS$_2$ nanosheet to obtain high-performance nanocomposites. Such nanocomposites modified electrodes have been proved as excellent sensing ability for dopamine, uric acid and glucose detection [1417–1419].
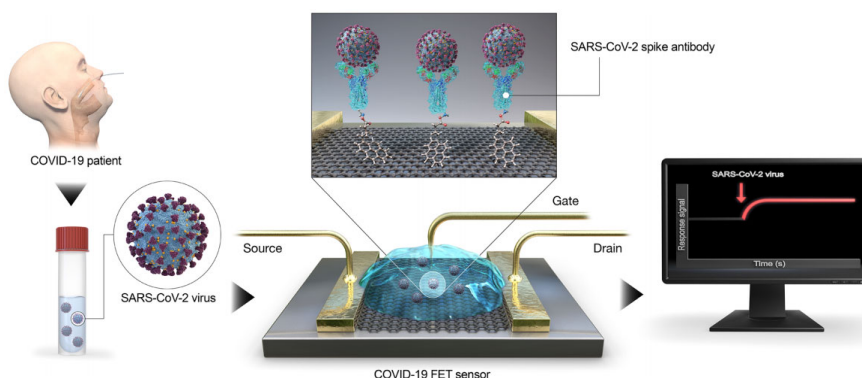

Fig. 54　Schematic of graphene-based FET sensor for COVID-19 detection [1406].

The further study suggested that MoS$_2$-based nanocomposites could efficiently load hemoglobin to construct an electro-chemical sensing platform for hydrogen peroxide (H$_2$O$_2$) detection due to their good biocompatibility [1420]. Besides MoS$_2$, black phosphorene and WS$_2$ were also employed to construct enzymatic sensing platforms [1421,1422]. These exciting findings attracted more researchers to develop 2D materials-based electrochemical sensing platforms with high-performance, accelerating the application of 2D materials in sensing field.

The introduction of 2D materials into electrochemical sensing platforms often bring high sensitivity, high selectivity and high stability. For example, Cai *et al*. fabricated an immunosensor for leptin detection based on porous graphene-black phosphorus nanocomposites. The conductive capability and protein loading capacity of this sensing platform were improved after the immobilization of nanocomposites. As a result, the analytical performance of this immunosensor was improved, which can detect 0.036 pg·mL^{-1} leptin with a wide linear range (0.150–2500 pg·mL^{-1}) [1423]. Su *et al*. combined methylene blue with MoS$_2$ nanosheet to construct a multifunctional electrochemical sensing platform for the label-free detection of miRNA-21. More interestingly, this designed sensing platform also possesses excellent electrocatalytic ability, which can be used to individually and simultaneously determine dopamine (DA) and uric acid (UA) with satisfactory results [1424]. Mahmoudian *et al*. synthesized a Pt/g-C$_3$N$_4$/polythiophene nanocomposite (Pt/g-C$_3$N$_4$/PTh NCs) and used it to construct electrochemical sensing platform for mercury ion detection. From electrochemical impedance spectroscopy (EIS) measurements, they found the introduction of g-C$_3$N$_4$ could efficiently improve the Pt adsorption, resulting in the electron transfer facilitating. As a result, introduction of g-C$_3$N$_4$ can efficiently improve the sensing performance, making the detection limit of this sensing platform down to 0.009 nmol·L^{-1} for Hg^{2+} detection [1425].

2D materials and their nanocomposites are also considered as promising candidates to construct nanoprobes, which can efficiently amplify electrochemical signals of sensing platforms. Su *et al*. assembled horseradish peroxidase (HRP)-labelled carcinoembryonic monoclonal antibody (anti-CEA) on the surface of MoS$_2$-AuNPs nanocomposites to construct nano-probes. Then, they used HRP instead of bovine serum albumin (BSA) to block the remaining active sites. With the assistance of enzymatic catalytic reaction, this nanoprobe efficiently amplified electrochemical responses of the designed immune-sensor for carcinoembryonic antigen (CEA) analysis due to the triple signal amplification strategy. It should be noted that MoS$_2$-AuNPs nanocomposite not only used as a substrate to load abundant anti-CEA and HRP, but also used as a nanocatalyst to amplify electrochemical signal [1426]. Two years later, the same group developed a multilayer nanoprobe (MLNP) for miRNA-21 detection based on MoS$_2$-AuNPs nanocomposites. Experi-mental data suggested MoS$_2$-based MLNPs brought the proposed sensing platform ultrawide dynamic range (10

amol·L^{-1}–1 μmol·L^{-1}) and ultralow detection limit (38 amol·L^{-1}) for miRNA-21 detection compared with single-layer nanoprobe (SLNP). Moreover, this sensing platform could analyze miRNA-21 in 100 HeLa cell lysates (Fig. 55) [1427].

4.7.6 Colorimetric sensors

Since the intrinsic enzyme mimetic activity of magnetite (Fe$_3$O$_4$) was discovered by Yan and co-worker, "nanoenzyme" have been received more and more scientists' recognition [1428]. The intrinsic peroxidase-like activity of carboxyl-modified graphene oxide (GO-COOH) was firstly reported by Song *et al*. [1429], 2D materials with peroxidase-like, glucose oxidase-like catalytic activities have aroused the interest of researchers in the construction of colorimetric sensors, including MoS$_2$, WS$_2$, Rh and g-C$_3$N$_4$ [1430–1433]. A typical example was offered by Lee *et al*. They combined G-quadruplex DNAzyme with GO to design a simple sensing platform for visual detection of microRNA. The application of GO concentrates the G-quadruplex DNAzyme, enhancing the analytical performance of this colorimetric sensing platform for 1 nmol·L^{-1} microRNA detection [1434]. Lan *et al*. investigated the analytical performance of WS$_2$-based colorimetric sensing platforms for DNA detection. Combined the different affinity of WS$_2$ towards ssDNA and dsDNA with the ion-induced aggregation, this proposed sensing platform can detect as low as 1.54 nmol·L^{-1} target DNA with high selectivity. After introduction of HCR amplification strategy, the detection limit of WS$_2$-based colorimetric sensing platforms was down to 0.23 nmol·L^{-1} [1435].

To improve the sensitivity of colorimetric sensing platforms, formation of 2D materials-based nanocomposites becomes a popular method. Generally, 2D materials-based nanocomposites bring better performances due to the synergistic effect of 2D materials and functionalized groups. For example, Wan *et al*. decorated high catalytic activity of gold@platinum (Au@Pt) bimetallic nanoparticles on MoS$_2$ surface to form MoS$_2$-based nanocomposites (MoS$_2$-Au@Pt). The proposed nanocomposites exhibited high peroxidase-mimicking activity towards 3,3',5,5'-
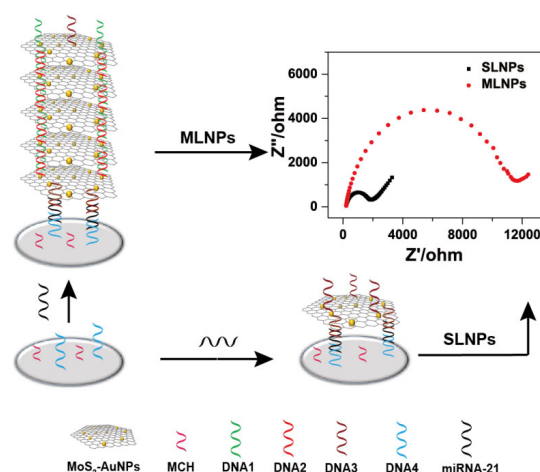

Fig. 55　Construction of electrochemical sensing platform for the detection of miRNA-21 based on MoS$_2$-based nanoprobes [1427].

tetramethylbenzidine (TMB) oxidation in the presence of H_2O_2. The added cysteine inhibited this catalytic reaction, making the solution change from blue to colorless. According to this phenomenon, they constructed a simple and label-free colorimetric sensing platform for cysteine detection with high sensitivity based on MoS_2-Au@Pt nanocomposites. More importantly, this sensing platform showed excellent selectivity, which can efficiently distinguish cysteine from homocysteine and 19 other amino acids [1436]. Similarly, Xiao *et al.* reported a colorimetric immunosensor for CEA detection based on the catalytic activity of AuNPs-supported Bi_2Se_3 (Au/Bi_2Se_3) nanocomposites. As shown in Fig. 56, the catalytic activity of Au/Bi_2Se_3 nanocomposites towards the reduction of 4-nitrophenol (4-NP) by sodium borohydride was inhibited after the immobilization of anti-CEA. The reason was ascribed to the catalytic sites of the nanocomposites were blocked by anti-CEA. When CEA added into the detection strategy, the catalytic activity of Au/Bi_2Se_3 nanocomposites recovered and made the solution changed from yellow to colorless. Under optimal condition, this colorimetric sensing platform can detect 160 pg·mL^{-1} CEA with high selectivity [1437]. Inspired by these exciting works, Zr-MOFs [1438], MoS_2-AuNPs nanocomposites [1439], Prussian blue (PB)-$Ti_3C_2T_x$ hybrid composites [1440], Pt-deposited NiCo-LDH [1441] and copper hydroxide nitrate [1442] have been employed to construct colorimetric sensing platforms for chemical/biological molecules detection.

4.8 Flexible electronics

In the recent 5 years, 2D materials for flexible electronics has been transited from the initial stage of demonstration into deeper understanding and real applications. Herein, we discuss the recent progress of 2D materials for flexible electronics from two aspects: graphene and other semiconducting 2D materials, and outlooked their future.

Due to the superior optoelectronic properties of graphene and the great success in synthesizing large-area graphene, it has attracted tremendous attention for flexible electronics, ranging from the flexible logic circuits [1443,1444], displays [1445,1446], energy

Fig. 56 Construction of colorimetric sensor for CEA detection based on Au/Bi_2Se_3 nanocomposites. Reproduced with permission from Ref. [1437], Copyright 2017 American Chemical Society.

storage and conversion [1447,1448] devices to wearable healthcare sensors [1449,1450]. As for the application of high-speed graphene FETs and RF devices, low contact resistance between graphene and metal electrode has been regarded as the prerequisite. Several works have been focused on optimizing the contact resistance by forming various types of graphene-metal geometries, such as bottom-, edge-, and top-contact [1451,1452]. Liu *et al.* developed a bottom-contact strategy by transferring CVD grown monolayer graphene onto Au electrode and achieved an ultralow contact resistance (65 Ω·μm) without harsh thermal annealing process (Fig. 57a), which is suitable for flexible electronics [1453].

Stretchable electronics, which require the devices to withstand a certain mechanical stress, is more challenging and particularly useful in wearable healthcare. Liu *et al.* achieved stretchable graphene electrodes by utilizing naturally CVD grown graphene to form graphene/graphene scrolls structure, and demonstrated all-carbon transistors which can function very well even up to 120% strain (Fig. 57b, c) [1454]. It is believed that graphene scrolls take the role of connecting cracked domains and increasing the interlayer sliding upon strain. Taking the advantage of this idea, Qiu *et al.* reported graphene-based epidermal electrodes that are able to endure the stretching of skin and sense weak electrophysiological signals such as electrocardiograms (ECG), electromyograms (EMG), and electroencephalograms (EEG) [1455]. By semi-embedding the graphene/graphene fibers into an elastomeric substrate, the entire electrode is similar to the structure of bird nest, and can be repetitively used for recording the electrophysiological signals (Fig. 57d). The semi-embedding design and 2D/1D hybrid structure enabled the "robustness" of graphene electrodes, pushing CVD graphene further for real applications in wearable healthcare. Although monolayer graphene grown by CVD on Cu foil features in high-conductivity and optical transparency, few-layer graphene obtained by solution-processing and laser-fabrication have been widely studied for flexible electronics due to the easy fabrication [1456]. They mostly start with GO and employ chemical or physical methods to reduce GO to be rGO for higher conductivity. Taking laser-fabrication graphene as an example, versatile flexible devices have been demonstrated, such as generators [1457,1458], supercapacitors [1459–1461], sensors [1462,1463], optoelectronic devices [1464,1465], electro-actuators [1466,1467] and integrated devices [1468,1469]. Sun *et al.* fabricated 3D patterned and porous graphene/elastomer sponges by laser induced technique, and demonstrated a gas-permeable and multi-functional device that can sense electrophysiological, hydration, temperature, joule-heating signals at the same time (Fig. 57e) [1462]. Compared with CVD monolayer graphene, laser-fabrication based graphene flexible electronics are advantageous in sensors and supercapacitors, which require massive production. But in terms of optical transparency and smooth surface of the electrode, CVD monolayer graphene show great strengths in optoelectronics, such as OLEDs [1470,1471], photodetectors [436,1465],
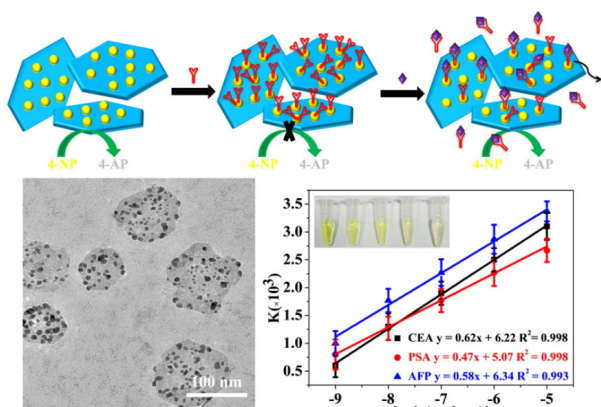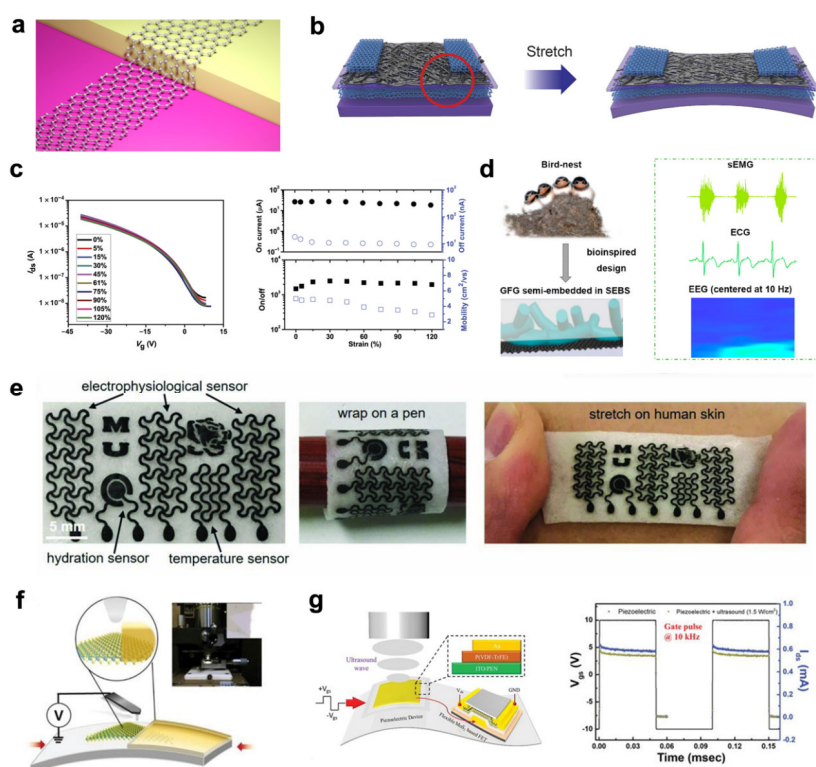
Fig. 57 **(a) Scheme of the concept of graphene-metal bottom contacts to achieve ultralow contact resistance; reproduced with permission from Ref. [1453], Copyright 2019 American Chemistry Society. (b) Scheme of all-carbon stretchable transistor, with graphene/graphene scrolls as source and drain electrodes and single-walled carbon nanotubes (SWNTs) as channel, (c) transfer curves, on and off current, on/off ratio, and mobility of such all-carbon transistor at different strains [1454]. (d) Left: scheme of fabrication of non-disposable graphene-based skin-electrodes by semi-embedding graphitized electrospun fiber/monolayer graphene into SEBS elastomer; right: such electrode as a robust and non-disposable skin-electrode for sEMG, ECG, and EEG detection; reproduced with permission from Ref. [1455], Copyright 2020 American Chemistry Society. (e) Optical images of the on-skin bioelectronic sensing systems, including electrophysiological sensors, hydration sensors, and temperature sensors; reproduced with permission from Ref. [1462], Copyright 2018 John Wiley and Sons. (f) Scheme of the MoS₂ /Au junction measured using Kelvin probe force microscope (KPFM); reproduced with permission from Ref. [1473], Copyright 2020 John Wiley and Sons. (g) Left: a schematic layout of the ultrasound detector combined with the flexible MoS₂ FET and piezoelectric device based on P(VDF-TrFE); right: the pulsed-gate switching responses of the ultrasound detector under the applied frequencies of 10 kHz; reproduced with permission from Ref. [1474], Copyright 2021 John Wiley and Sons.**

and tattoo-based epidermal electronics [1469,1472].

Many TMDs (e.g., MoS₂, WS₂, MoSe₂, WSe₂, *etc.*) are semiconductor with unique optoelectronic properties, such as layer-dependent bandgap and high charge mobility [2,1475]. When the layer number decreases to be monolayer, they exhibit strong photoluminescence due to large exciton binding energy by the nanoconfinement effect [1476], thus many monolayer 2D materials are very attractive in optoelectronic devices, such as transistors [1477,1478], photodetectors [1479,1480], light emitting diodes [1481,1482] and solar cells [1483,1484]. MoS₂ is the most studied 2D semiconducting material. The contact energy barrier between MoS₂ and metal contacts under stretching or bending was also investigated. Pak *et al*. fabricated two-terminal flexible MoS₂ devices and studied the contact barrier by kelvin probe force microscope [1473]. The observation is that tensile strain can increase electron affinity and lower the contact barrier, which will be beneficial to the optoelectronic performance (Fig. 57f). However, the biggest challenges for semiconducting 2D materials to be really applicable in flexible electronics are a

feasible synthetic strategy of large-area and high-quality materials, and a mature technique for processing these materials into devices on plastic or elastomeric substrates [1476,1485–1487]. Although MoS₂ ranks the most studied TMDs, achieving centi-meter scale and uniform monolayer MoS₂ by CVD and transfer on to flexible substrates is still not easy. Li *et al*. recently reported a modified CVD process to grow wafer-scale MoS₂ and transferred it onto a PET substrate, demonstrating large-scale flexible and transparent logic circuits based on MoS₂ FETs [774]. The FETs exhibited high mobilities (~55 cm²·V⁻¹·s⁻¹), on-off ratios (10^{10}), current densities (35 μA·μm⁻¹) and flexibility, with combinational performances superior than other candidates in semi-conductor industry [774]. Artificial intelligence and human-machine interfacing recently attract extensive attention. Integration another device structure such as pressure sensor or photodetector with MoS₂ FETs to form mechano-, photo- or sound- receptors is a very effective way to obtain high speed and sensitive detection, which are potential in artificial intelligence and human-machine interfacing [1488]. Naqi *et al*. reported an

ultrasonic detector by combining the flexible MoS₂ FETs with polyvinylidene fluoride trifluoro ethylene (PVDF-TrFE)) piezoelectric sensor on a polyimide substrate (Fig. 57g). Such detector is highly sensitive (Fig. 57g) to the ultrasound wave by shifting threshold voltage, showing pulsed gate switching [1474]. Besides, TMDs are layered materials with big surface area, attracting a lot of attention in flexible capacitive energy storage, such as battery [1489,1490] and supercapacitors [1280,1491].

Overall, 2D materials for flexible electronic devices is a rapidly expanding area, widely applicable in wearable logic circuits, energy storage and healthcare [1443,1444,1447,1448,1455,1469,1472,1483,1484]. However, their future largely depends on the development of material synthesis and technological processing for 2D devices on plastic or elastomeric substrates, requiring a lot of scientific understanding and material engineering.

4.9 Environmental applications

The family of 2D materials has attracted increasing attention in numerous environmental applications, ranging from the utilization of natural sources to exhaust treatments and pollution remediations [1264]. Owing to the intriguing physical and chemical properties, 2D materials and their assemblies have shown significant advantages over other dimensional materials. Firstly, the large surface area of 2D materials (e.g., 2630 cm²·g⁻¹ for monolayer graphene [1492], 5900 cm²·g⁻¹ for a 2D MOF called MIL-101 [1493], 2060 m²·g⁻¹ for an imine-linked 2D COF) [1494] endow them with large molecular adsorption capacity, making them ideal candidates in the gas, ion, and organic pollute adsorption. Additionally, a proper chemical modification of 2D materials can provide the host-guest recognition, and selectively separate the desired source from a mixture [1495]. The second advantage of 2D materials for environmental applications is the ultrahigh mass transport and size-exclusive selectivity in the confined space assembled by nanosheets. Nair *et al.* first reported the unimpeded permeation of water through the 2D capillary made by graphene oxide (GO) [1496], inspiring the applications of 2D materials in water treatments [1497]. Moreover, the ultrafast mass transport and molecular sieving properties in assembled 2D materials provide new opportunities to break through the "trade-off" limits between the selectivity and permeation, opening a new avenue for highly efficient

membrane separation technology [1498]. Thirdly, the unique properties of 2D materials provide new opportunities to utilize green and economic energy sources in environmental applications. For instance, Li *et al.* fabricated a GO lamellar structure to generate portable water by the solar-thermal energy [1499]. Additionally, these semiconducting 2D materials can be also used in the electrochemical and photoelectro-chemical degradation of organic pollutes [1500]. Taking of the above advantages in enormous adsorption, highly efficient separation, and diverse driven energy sources, 2D materials play a rising role in the environmental protection of the aquatic, atmospheric and terrestrial ecosystems.

4.9.1 Water treatments

To satisfy the increasing demand for civil and industrial water consumption, it is highly desired to develop economic and green technologies for water treatments. Recently, 2D materials have been used to adsorb, separate, or degrade hazardous compounds (e.g., salts, leaking oil, organic pollutes) to supply clean water.

The first route is to use the 2D materials as adsorbents. 2D materials can be used to adsorb organic pollutant [205,1501–1505] and metal ions [1506–1509] due to the large surface area and their diverse functional groups. Jiang *et al.* reported few-layered GO could remove 17β-Estradiol (E2) efficiently from aqueous solutions with the maximum adsorption capacity of 149.4 mg·g⁻¹ at 298 K [1510]. There are π-electron-rich regions on the GO surfaces which will interact with the π electrons of E2 — it comes to a π–π interaction to adsorption E2 onto GO. Besides, bountiful surface oxygen-containing groups of GO can also construct hydrogen bonds with E2. To remove toxic dyes such as methylene blue (MB), 3D rGO aerogels with different C/O ratios were prepared by grafting neutral, positive and negative redox mediator (Fig. 58a) [1511]. The neutral and cationic redox mediator were selectively adsorbed on rGO through π–π and non-covalent electrostatic interactions, respectively. On the contrary, the anionic redox mediator would not be adsorbed in the 3D rGO aerogel due to the repulsive force. High surface area porous h-BN nanosheets, synthesized by heating boron trioxide (B₂O₃) and guanidine hydrochloride under a cover of H₂ and N₂, have been used to remove pharmaceuticals such as antibiotics tetracycline, chlortetracycline hydrochloride, ciprofloxacin, and
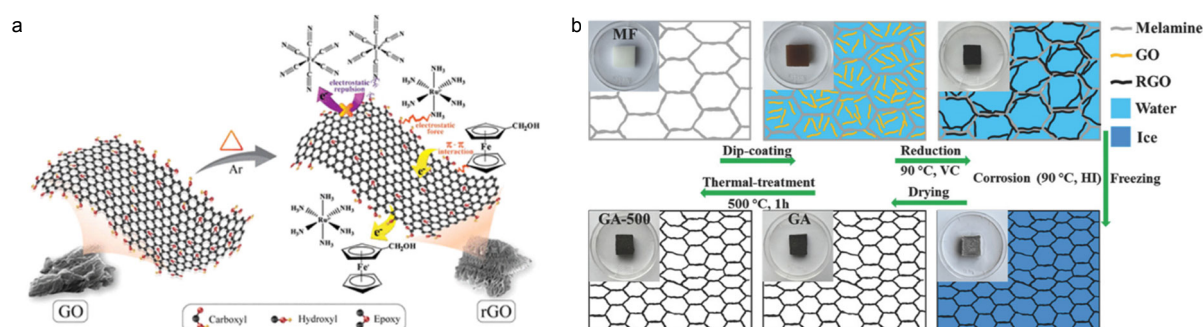

Fig. 58 (a) Schematic illustration of adsorption mechanisms by GO; reproduced with permission from Ref. [1511], Copyright 2020 American Chemical Society. (b) Schematic showing the formation of GA-500, inset: snapshots of stepwise fabrication process; reproduced with permission from Ref. [1513], Copyright 2018 John Wiley and Sons.

norfloxacin from aqueous solution [1512]. Ge *et al.* developed a Joule-heated graphene-wrapped sponge (GWS) to clean viscous crude-oil spill [1502]. The graphene is coated onto the skeletons of the sponge substrates to improve hydrophobic and conductive properties so that the GWS can selectively adsorb spilled oil and a voltage can be applied to generate Joule heat to accelerate the adsorption process. Liu's group reported a simple method about using melamine foam as a sacrificial framework to create a graphene aerogel with arbitrary shape, super elasticity and durability [1513]. The as-prepared graphene aerogel was applied to absorb various organic solvents depending on the type and density of the solvent (Fig. 58b). Graphene/δ-MnO_2 aerogels with interconnected 3D network microstructure that possesses abundant MnO_2 nanosheets are homogeneously deposited on the graphene framework show excellent adsorption capacity toward heavy metal ions such as Pb^{2+}, Cd^{2+}, Cu^{2+} and others [1514]. It expands the adsorption capacity by intercalating metal ions into the interlayer gaps of MnO_2 compared to GO which only adsorb ions on the surface. Yoon *et al.* reported the preparation of magnetite/non-oxidative graphene (M-nOG) for arsenic removal [1515]. M-nOG was found to retain 94.5% of the capacity for As^{3+} removal and 92% for As^{5+} compared to the first cycle after 5 consecutive reuses, which indicate its regeneration and re-usability. The low-cost 2D g-C_3N_4 nanosheets are also a kind of absorbent for both cationic and anionic heavy metals. Xiao *et al.* reported convenient one-step calcination to synthesize the g-C_3N_4 nanosheets as absorbents [1509]. They found besides the lone electrons on nitrogen, the tri-s-triazine units, terminal N-containing groups, and surface amino take part in the adsorption positively. Hazardous salts, such as Hg^{2+}, Cd^{2+}, AsO_5^{3-}, can be also adsorbed by 3D foams based on 2D materials [1516]. Furthermore, proper assembly and interface modification are able to enhance the adsorption capacity of 2D materials, e.g., MXenes, MOFs, COFs, *etc.* [1517–1520].

Another route is to generate clean water by steam generation or membrane separation technologies. Researcher developed the GO and 2D MOF membrane or their aerogel with highly efficient solar steam generation (Fig. 59a, b) [1499,1521,1522]. Recently, along with the understanding of ultrafast water transport in the 2D capillary (Fig. 59c, d) [1497,1523,1524], the
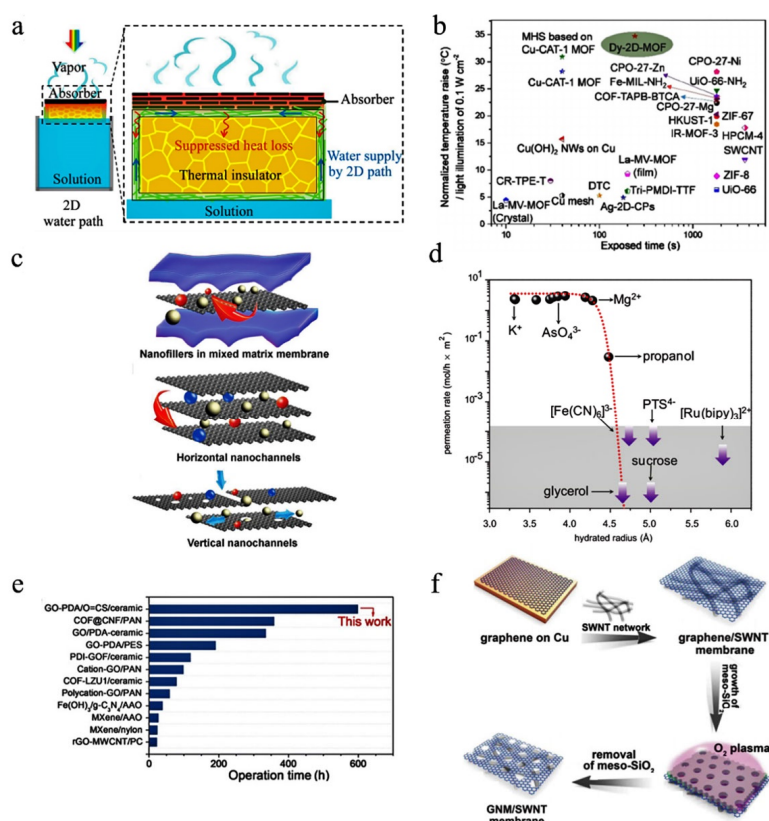
Fig. 59 **(a)** Schematic illustration of solar-thermal steam generator based on GO film; reproduced with permission from Ref. [1499], Copyright 2016 National Academy of Sciences. **(b)** The temperature raise for various solar-thermal steam generation materials under solar irradiation of 0.1 W·cm^{-2}; reproduced with permission from Ref. [1522], Copyright 2021 John Wiley and Sons. **(c)** Schematic illustrations of the separation mechanism of 2D material membranes; reproduced with permission from Ref. [1524], Copyright 2020 John Wiley and Sons. **(d)** The size-dependent molecular sieve based on GO lamellar; reproduced with permission from Ref. [1497], Copyright 2014 Association for the Advancement of Science. **(e)** Comparison of the long-term operation times for state-of-the-art two-dimensional material membranes applied in water separation; reproduced with permission from Ref. [1529], Copyright 2020 John Wiley and Sons. **(f)** CNT-assisted plasma perforation on CVD-growth graphene can provide a desalination membrane with high salt rejection and fast water permeation; reproduced with permission from Ref. [1532], Copyright 2019 Association for the Advancement of Science.

lamellar membranes made by 2D materials have attracted increasing attention in desalination, reverse osmosis, and nanofiltration [1525,1526]. Numerous chemical modification and cross-linking strategies have been developed to promote the permeation and lifetime of desalination and nanofiltration membranes based on the GO (Fig. 59e) [1527–1529], MoS_2 [1530], MOF [1531], and COF [848]. Perforation on the 2D membrane can also enhance the water permeation, and meanwhile, maintain the ion sieving performance (Fig. 59f) [159,1532].

Photocatalysis based on semiconducting 2D materials is another effective route to utilize economic solar energy to thoroughly degrade pollutants in an aquatic system, taking advantage of the enormous surface area and rational designed electronic band structures. For instance, 2D materials with bandgap absorption at near UV or visible region, such as *g*-C_3N_4 [1533], MOF [1534] and MoS_2 [1535], have been developed, and they can generate the radicals for photochemically or electrochemically driven degradation of organic pollutes [1536]. Furthermore, the membrane based on photocatalytic 2D

materials was applied to capture the organic pollutes by their size-exclusion properties, and meanwhile, convert them into innocuous compounds [1537].

4.9.2　Carbon neutralization and exhaust gas treatment

Due to increasing human activity, the emission of hazardous and greenhouse gases is becoming a topical issue of global climate change. For instance, CO_2 from the combustion of fossil fuels in the carbon cycle is contributing to the increasing greenhouse effect. Thus, it is urgent to develop efficient and economic CO_2 capture and separation technologies. 2D materials, such as GO, MOF, and LDHs, can be made into molecular sieves with low transport resistance and high permeation fluxes for gas separation, inspiring their applications in carbon neutralization and exhaust gas treatments.

Recently, a great deal of work has been reported in the area of CO_2 gas separation. In 2016, Shen *et al*. fabricated GO channels with an ordered height of 0.4 nm by designing external forces applied to the inside and outside of the GO sheet (Fig. 60a) [1538]. As shown in Fig. 60b, this sub-nano channel can provide 2–3
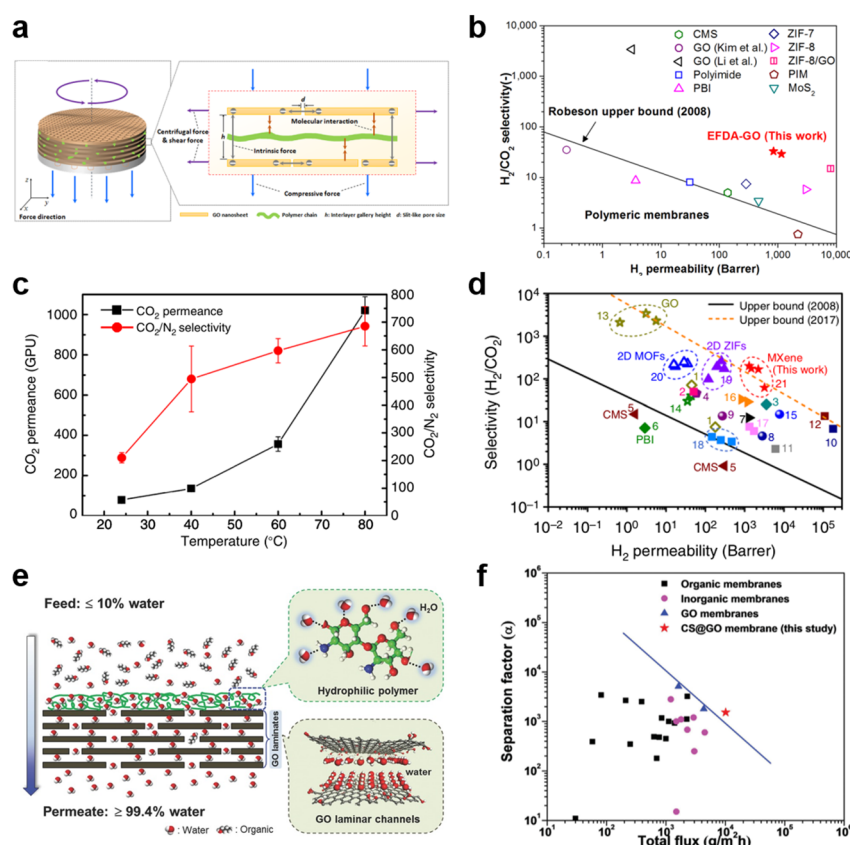
Fig. 60　(a) External force driven assembly approach for fabricating 2D channels, **(b)** H_2 /CO_2 separation performance of EFDA-GO membranes compared with state-of-the-art gas separation membranes; reproduced with permission from Ref. [1538], Copyright 2016 American Chemical Society. **(c)** Influence of temperature on GO-piperazine (GOP) hollow fiber membrane performance for mixed gas (CO_2 : N_2 =15% : 85%, volume fraction) separation under the wet condition [1539]. **(d)** H_2 /CO_2 separation performance of the MXene membrane compared with state-of-the-art gas separation membranes; the black line indicates the Robeson 2008 upper bound of polymeric membranes for H_2/CO_2 separation, and the orange dashed line represents the 2017 upper bound of the best current membranes for H_2 /CO_2 separation [1540]. **(e)** Schematic of the organic/water (butanol/water) separation process using the synergistic effect of a hydrophilic polymer and GO laminates, **(f)** comparison of GO membranes and the CS@GO membrane with state-of-the-art membranes for water/butanol dehydration; reproduced with permission from Ref. [1547], Copyright 2015 John Wiley and Sons.

orders of magnitude higher H_2 permeability and 3 times higher H_2/CO_2 selectivity compared to commercial membranes. Zhou *et al*. introduced CO_2-philic piperazine as a crosslinking agent into the GO interlayer [1539], the membrane shows excellent CO_2 permeability of 1020 GPU and a CO_2/N_2 selectivity bursting up to about 680 (Fig. 60c). MXenes with nonporous 2D structure also show excellent performance in gas separation. Ding *et al*. reported that lamellar stacked MXene membranes exhibit excellent gas performance with H_2 permeability above 2200 Barrer and H_2/CO_2 selectivity more than 160, better than many advanced membranes (Fig. 60d) [1540]. In previous work, it was discovered that LDHs have excellent gas barrier properties [1541–1544]. Comparing the permeation rates of a variety of gas molecules, it was found that there is a significant difference in the magnitude of the barrier effect of LDHs on different gas molecules. Some acidic gas molecules (e.g., CO_2) are subject to a higher permeation. Later on, they constructed LDH-based gas-selective barrier layers on microporous substrates to achieve efficient separation of CO_2 gas [1545]. Apart from nonporous 2D materials, there are also a significant amount of works devoted to the development of MOFs and COFs to capture CO_2. For example, Huang *et al*. constructed a Cu-based 2D MOF, FJI-H14, from 2,5-di(1H-1,2,4-triazol-1-yl) terephthalic acid (H_2BTTA) [1546]. The results show that the FJI-H14 exhibits an extremely high CO_2 capacity of 171 $cm^3 \cdot cm^{-3}$ at 1 atm and 298 K, with a CO_2/N_2 selectivity of up to 51 for CO_2/N_2 gases mixed at a ratio of 15/85.

The separation membranes based on 2D materials are also applied in biomass utilization, which can significantly reduce the consumption of fossil fuels and promote economic carbon neutralization. Huang *et al*. reported a polymer-coated GO laminate that can separate *n*-butanol from the mixture of *n*-butanol and water [1547]. Fig. 60e illustrates the organic/water (butanol/water) separation process based on the chitin-decorated GO membrane. With the ultrathin hydrophilic polymeric layer (< 10 nm), the water flux can reach 12 $kg \cdot m^{-2} \cdot h^{-1}$, and the separation factor can be enhanced up to 1523 for *n*-butanol/water mixture. (Fig. 60f) The surface modification strategy is also applicable to MXenes. Liu *et al*. inserted hyperbranched polyethyleneimine into Ti_2CT_x MXene nanosheets to form regular stacked structures, and then the interfacial polymerization with triformylchloride was applied to recover the potential defects [1548]. Owing to the highly ordered 2D nanochannels, it exhibits excellent separation performance: water content was enriched to > 99% (*w*) from a 10% (*w*) isopropanol aqueous.

Additionally, 2D materials play a rising role in the treatment of atmospheric pollution. Volatile organic compounds (VOCs) from industrial activities and transportation are generally considered to be one of the culprits of atmospheric pollution. VOCs, such as aromatic species, are extremely hazardous to living creatures, so it is important to develop efficient technologies and materials for the removal of VOCs. Xie *et al*. constructed two Zr-MOFs named BUT-66 and BUT-67 as

adsorbents, which showed the excellent performance to remove trace amounts of benzene in air [1549]. Furthermore, the combination of MOFs with carbon nanomaterials, such as carbon nanotubes and GO can improve their stability and adaptability, which makes 2D MOF composites more suitable to be operated in practical applications [1550].

4.9.3 Rare earth enrichments and soil remediation

Rare earth elements have been considered as one of the most important strategic resources. However, owing to their similar physical and chemical properties, it is a great challenge to achieve their selective separation and purification. The present industrial technologies for rare earth separation suffer from high energy consumption and pollutions from byproducts [1551]. Membrane separation technology has been considered as an ideal alternative way due to its simplicity, absence of energy consumption from phase change, low carbon emissions, ease of operation, and suitability for industrial automation applications [1527,1552,1553]. GO membranes are an emerging class of membranes with nanometer-scale pore sizes that can be used for precise ion and molecular sieving [1497,1527,1554]. However, the limitation of interlayer spacing in GO membranes leads to low ion penetration. In order to solve this problem, Tan *et al*. used confinement combustion to synthesize nitrogen-doped nanoporous graphene (NDNG) with adjustable pore size and controlled nitrogen content [1555]. The NDNG membranes exhibit good separation selectivity (~3.7) for Sc^{3+} from other rare-earth ions and ~1.7 for Tm^{3+}/Sm^{3+}. MOFs, as a group of emerging porous crystalline materials, are size-selective and can be used for the selective separation of rare earth elements (Fig. 61a, b). Recently, Wu *et al*. prepared Zn-BTC MOF/nanoporous graphene composites, showing selectivity of 10,000 for Ce/Lu and up to 9.8 between adjacent rare earth elements (e.g., Nd/Pr) (Fig. 61c, d) [1556].

Due to the industrial and agricultural developments, highly toxic organic pollutants and heavy metals have been released into the soil ecosphere and consequently entered the biosphere through the food chain. They are potentially mutagenic, teratogenic, and carcinogenic to living creatures [1557]. In recent years, nanomaterials have become a hot spot in the area of soil remediation due to their huge specific surface area and good catalytic reaction activity. The graphene with a huge surface area can act as an excellent adsorbent for organic pollutants owing to the π–π or steric interaction [1558]. Qi *et al*. found that 5.3–20.2 $mg \cdot L^{-1}$ GO significantly enhanced the migration-assistant recycling of 1-naphthol, an initiator to human colorectal tumors (Fig. 61e, f) [1559]. Among the families of 2D materials, MoS_2 nanosheets exhibit high adsorption capacity of both Hg(0) [1560] and Hg^{2+} [1561], providing a potential solution against the mercury pollution.

4.10 Proton permeation

It had long been assumed that despite of their mono-atomic-layer thickness, perfect graphene and related 2D materials are impermeable to all atoms and molecules at ambient conditions:
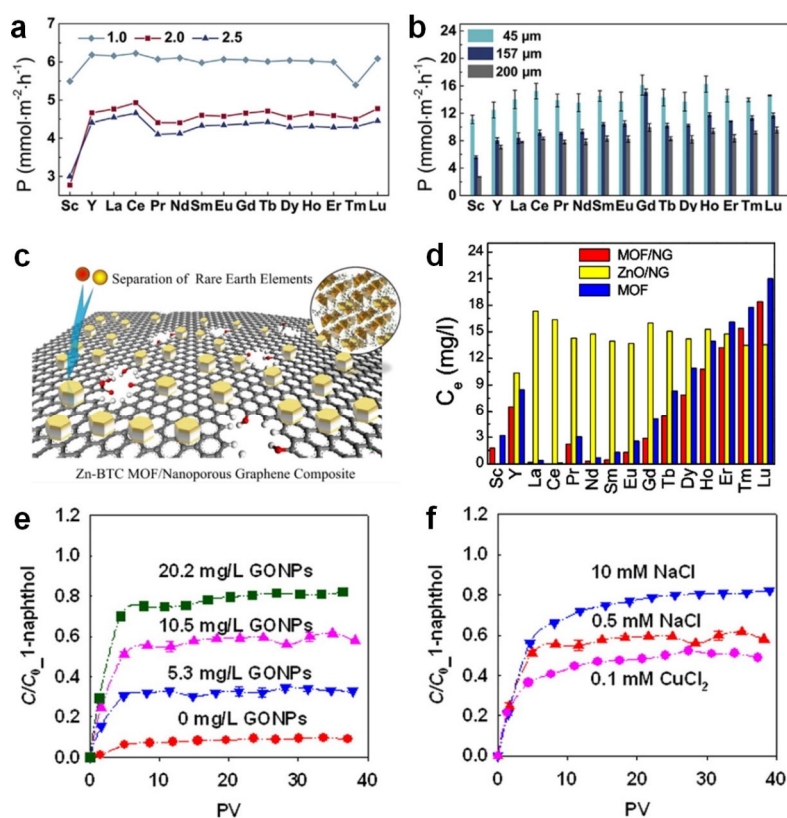
Fig. 61 (a) Effect of pH on the separation for NDNG-1 membrane, (b) permeation flux of REEs as a function of the NDNG-1 membrane thickness [1555]. (c) Schematic diagram Zn-BTC MOF/nanoporous graphene in the separation of REEs, (d) adsorption of ZnO/NG, MOF, and MOF/NG to RE^{3+} (C$_e$) at the same time (160 min) and pH (2.03); reproduced with permission from Ref. [1556], Copyright 2021 American Chemical Society. (e) Effect of concentration on the separation for GO nanoparticles (GONPs), (f) effect of solution chemistry on the separation for GO nanoparticles (GONPs); reproduced with permission from Ref. [1559], Copyright 2014 American Chemical Society.

even the smallest of atoms hydrogen is expected to take billions of years to penetrate through the dense electron cloud of graphene lattice [1562–1564]. On the other hand, it is well known that they are permeable to electrons either by conduction or tunneling. This raises a fundamental question: what about sub-atomic particles, *i.e.* protons, the nucleus of hydrogen atoms, permeation through these one-atom-thick crystals?

In 2014, Hu *et al.*, first demonstrated that protons are permeable through 2D materials [1565]. Surprisingly, protons pass through so easily with a remarkable proton conductance that at odds with the large energy barrier predicted by previous theories. Following that, considerable efforts have been devoted to the investigation of both related mechanisms and potential applications. To emphasize its contribution to the understanding of intrinsic properties of 2D materials, Pulizzi *et al.* list proton permeation as one of the 25 key discoveries that shaped the graphene field [1566].

4.10.1 Origin of the proton permeation

The origin of proton transport through 2D materials involves two essential steps (Fig. 62a). The first one is proton approaching the 2D surface, *i.e.* entry before jumping through the lattice. The zero point vibration of protons prior to permeation effectively reduces the activation barrier that leads to fast proton transport. For example, in the original experiments [1567], the initial state of

protons is transiently bonded to oxygen-containing chemical groups. The zero point energies of these hydrogen-oxygen bonds lift the protons in energy with respect to vacuum by 0.2 eV. It is quite remarkable that the zero point oscillation, a pure quantum behavior, is reserved even at room temperature, but seems reconcile with the discrepancy of the lower proton transport barrier found experimentally compared to that from simulations.

The second step is proton translocation, during which proton interacts with the electrons in the 2D lattice and its conductance is highly affected by the electron cloud density in the lattice pore. For example, h-BN with its valence electrons localized near the N atoms is more "porous" compare to graphene with delocalized π electrons [1565]. Due to its strong electric polarity, proton attracts electrons easily and are indistinguishable to hydrogen atoms when translocation. From this perspective, it is not difficult to understand the slow albeit detectable hydrogen atoms penetration through 2D materials [1571]. The interlayer stacking of 2D materials also affect the proton transport. The AB stacked bilayer graphene completely blocked the proton transport because, intuitively, the atoms in the second layer locates in the center of the hexagonal ring in the first one, while the AA' stacked bilayer h-BN remains permeable to protons [1565].

Despite the above discussed general processes, however, the detailed proton transport scenario is still under debate. Water and
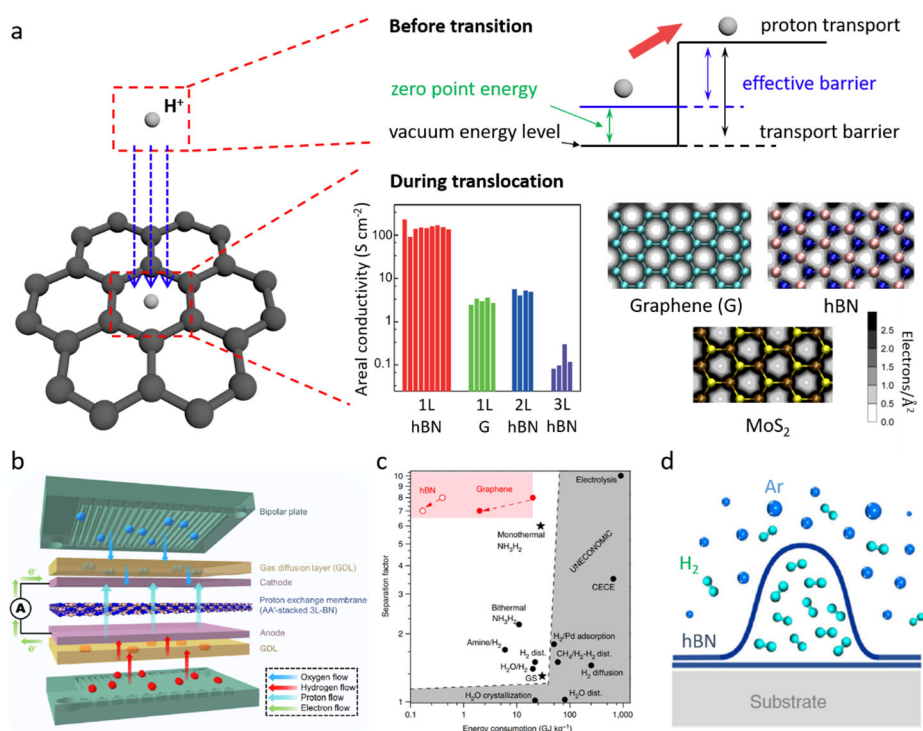
Fig. 62 **(a) Schematic of proton transport mechanism. Bottom right: proton conductivity through varies 2D materials with distinct electron density in their lattice [1565]. Typical applications of proton transport: (b) proton exchange membrane fuel cells made by few-layer h-BN, reproduced with permission from Ref. [1568], Copyright 2018 American Chemical Society; (c) comparison of 2D material-based H/D separation membrane performance with other techniques for heavy water separation [1569]; (d) isolating hydrogen gas using h-BN [1570].**

hydrogenation assisted proton transport models describe the proton-electron and proton-material interactions, though predict a considerably higher proton transport barrier compare to that observed in the experiments [1572,1573]. In addition, although the proton transport is thermally activated [1565], the contribution of possible proton tunneling through one-atom-thick membranes is unclear [1574,1575]. Recently, a few characterization techniques have been developed for the *in situ* observation of proton transport [1576,1577], which provides possible route for the understanding of the origin of proton permeation.

4.10.2　Applications of proton transport

　　Membranes that allow selective proton transport with high conductivities are at the core in some industrial applications, and proton permeable 2D materials should certainly offer a radically new direction for their development. The most commonly appeared such membrane is the proton exchange membranes (PEMs) in fuel cells. As a proof of concept, PEMs made of few layer h-BN and graphene have been demonstrated in the prototype of fuel cell [1568,1578] (Fig. 62b) and flow battery systems [1579]. Compared to conventional polymer-based PEMs, one of the advantages of using 2D materials is their stability at humid oxygen atmosphere at elevated temperature up to a few hundred degrees Celsius and thus they extend the devices operation temperature [1565,1580], yielding extremely high proton conductivities $> 10^3$ S·cm^{-2}.

　　An alternative but seemly promising application is to use 2D materials for the separation of hydrogen isotopes. It has been shown that monolayer h-BN and graphene is able to separate protons (H) from deuterons (D) [1567]. The origin of the isotope effect is attributed to that the energy barrier posed by 2D materials is affected by the zero point oscillation of nucleon, and thus is highly sensitive to its mass. The isotope separation factor between H and D is close to 10, almost one order of magnitude higher than several conventional methods, while with energy consumption being reduced by at least 50% (Fig. 62c) [1569,1581], importantly, the 2D materials-based electrochemical pump method is operable at room temperature without adding or producing any harmful chemical products. It has been estimated that a 2D membrane with an area of 30 m^2 produces 40 tons of heavy water per year, comparable with a typical annul output of existing heavy water production plants.

　　Proton permeation has also been utilized to tune the interaction between monolayer 2D materials and their substrates by proton penetration into the interlayer spacing. A direct outcome is protons/hydrogen atoms encapsulation between 2D materials and substrates (Fig. 62d), which offers a route for the application of isolating hydrogen gases [1570]. Reversibly switching the surface properties, e.g., stiction and adhesion to liquids, of 2D materials is also possible when hydrogen atoms present or absent in the space between 2D materials and substrates [1582]. In addition, such space provides a confined environment for chemical reactions [1583], where protons has been found to decouple the vdW interaction between substrate and 2D materials and assist the growth of ultra-flat 2D crystals [352].

4.10.3　Various approaches to enhance proton conductance

Improving the proton conductance through 2D materials is not only important in terms of highly efficient applications especially in membrane areas as mentioned above, but provides insights to the proton transport mechanism from fundamental level point of view. One strategy is to tune the electrons distribution on 2D materials using proton-binding metal nanoparticles decorated on 2D materials to form heterostructures [1565]. The built-in electric field at the material-nanoparticle interface can be further enhanced if illuminated with visible light, leading to a graphene areal proton conductance above 2 S·cm^{-2} at room temperature [1584].

Design of novel 2D materials is another approach of promoting proton transport. Atomically thin micas with proton areal conductivity exceeding that of defect-free graphene and h-BN by two orders of magnitudes is merely one of the examples [1580]. Theoretical simulations have predicted more than 10 novel 2D crystals being promising candidates for proton permeation [1572,1573,1585]. It is worth noting that "defect-free" may not necessarily be important when considering materials' proton transport properties [1586]. Recently, atomically thin carbon films with eight-atom-ring defects has been fabricated, showing a 10^3 times higher proton permeability than that of pristine graphene [1587]. Apart from enlarging the effective pore size for proton conduction, defects also play a positive role by accumulating high concentration of protons as proton source, as exemplified by Cd vacancies in CdPS$_3$ nanosheets [1588]. As a result, a record-high proton conductivity of 0.95 S·cm^{-1} has been achieved.

Proton permeation provides 2D crystal lattice as a novel subatomic sieve. However, there is still a long path towards the real applications. Scalable production of high quality 2D materials [1589], their wafer-scale transfer techniques and compatibility with support proton conductive substrate would be logical future investigation directions here.

4.11　Other applications

Besides various applications mentioned above, 2D materials also show application potentials in reinforcing filler, corrosion protection, pollutant adsorption, desalination and so on due to their layered structure, ultrahigh specific surface and excellent mechanical strength. These applications will be discussed in detail in this part.

Ultrathin 2D materials are competent as reinforcing filler [1590–1592], conductive filler [1593–1595] and anticorrosion filler [1596,1597] in polymer matrix composites. Liu *et al.* developed two fraction methods to prepare layered and scrolled nanocomposites with high-quality graphene [1598]. They prepared planar stacking composites of graphene and polycarbonate (PC) by repetition of quadrant fold or segmentation (Fig. 63a), and an Archimedean spiral fiber was fabricated with similar a method (Fig. 63b). These nanocomposites display substantial mechanical reinforcement and still retain high electrical conductivity and optical

transmittance even at very low loadings. Graphene/nanofiller nanocomposites are further developed to avoid graphene agglomeration [1599]. Song *et al.* reported the preparation of graphene wrapped B$_4$C nanowires (B$_4$C-NWs) which can strengthen the interfacial interaction between the B$_4$C-NWs and matrix [1600]. They directly synthesized B$_4$C-NWs@graphene by shear mixing the mixture of graphite powders and B$_4$C-NWs and found the graphene was successfully exfoliated then crumpled and self-assembled onto the B$_4$C-NWs (Fig. 63c, d). The three-point bending tests of the epoxy resin with a different fraction of B$_4$C-NWs@graphene indicate the flexural strength and elastic modulus increased with increasing nanofillers (Fig. 63e). 2D h-BN nanosheets are an acceptable solution when devices require both great electric insulation and thermal conduction. Cho *et al.* prepared polysiloxane/h-BN nanocomposite films by introducing 15% (volume percentage) h-BN nanosheets into a poly(dimethylsiloxane) elastomer whose thermal conductivity are 15 times that the polysiloxane matrix itself, and the composite can still maintain the electrically insulating nature because of the wide bandgap of h-BN [1601].

Many 2D materials such as graphene and h-BN are almost impermeable to all molecules with excellent chemical stability. Therefore, 2D materials can be used to cover the surface of the metal to protect them from corrosion. But sometimes pure 2D materials coating like graphene could not protect the metals effectively, or even accelerate the corrosion in a long term, due to the defects of graphene which may trap corrosive media such as H$_2$O and O$_2$ [1602], and the defective area behaves as a cathode
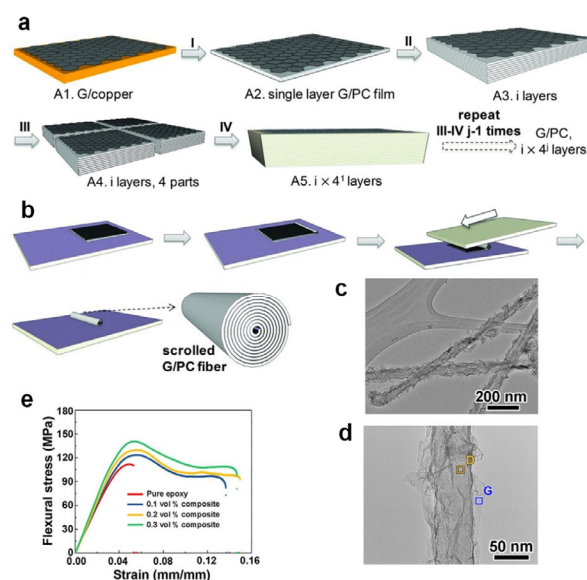
Fig. 63　(a, b) Schematic illustration of the method for planar stacking composites and the transverse shear method for scrolled nanocomposite fiber; reproduced with permission from Ref. [1598], Copyright 2016 Association for the Advancement of Science. (c, d) The TEM image of B$_4$C-NWs@graphene, (e) flexural stress-strain curves of epoxy and B$_4$C-NWs@graphene (0.1%, 0.2%, and 0.3%, volume percentage) reinforced composites [1600].

that accelerates the corrosion [1603]. The graphene composites are developed to solve the problems above instead of pure graphene coating. A nonconductive graphene composite through the Diels-Alder reaction between the exfoliated graphene and a bio-based epoxy monomer can work as a long-term anticorrosive coating [1604]. The insulating h-BN is also a good choice for anticorrosion which can suppress the galvanic corrosion under the ambient environment [1605].

Non-toxic 2D inorganic nanosheets can be used for food packaging films for the reason of their high aspect ratio platelet structures which can construct circuitous pathways to impede the diffusion of gas molecules [1606]. A platelet morphology sample of Mg_2Al-CO_3-LDH was calcined in the air and then put into the aqueous glycine solution to regenerate and exfoliate the LDH. Bilayer LDH nanosheets with well define shapes were obtained. The LDH nanosheets coating on the polyethylene terephthalate (PET) film show extremely excellent oxygen barrier performance (Fig. 64a) and water vapor barrier performance (Fig. 64b).

Hybrid GO/graphene with a large mechanical strength can withstand osmotic pressure and shear stress for desalination [1607]. Morelos-Gomez *et al*. reported a preparation of hybrid GO/graphene layered membranes deposited onto the polysulfone support membrane modified with polyvinyl alcohol (PVA), followed by the thermal treatment and Ca^{2+} crosslinking to enhance the mechanical strength furthermore [1608]. Water can flow within nanochannels adjacent to the edges of few-layered graphene and the NaCl will be rejected due to the Gibbs-Donnan exclusion. They found the PVA interfacial adhesive layers were the key to enhance the mechanical strength that the membranes with PVA would exhibit any observable peel-off under a strong 1000 mL·min^{-1} cross flow, meanwhile, the membranes without PVA started to peel up at 400 mL·min^{-1} after 120 h.

Besides the above discussions, there are also some interesting applications based on 2D materials due to the promising properties of 2D materials. For example, Luo *et al*. even developed a unique graphene hair dye [1609]. The GO or rGO are used to coat on the hair substituting the toxic small molecules which are added in common hair dyes. They found graphene hair

dye could improve comfort by enhancing antistatic performance and heat dissipation because of the good electrical conductivity and thermal conductivity of graphene. Also, we believe that the killer applications of 2D materials will be explored in the future and 2D materials will play more important roles in different applications.

5　Theoretical calculations and simulations

In parallel to the experimental investigations, tremendous efforts have also been dedicated into the development of 2D materials by adopting computational strategies, including DFT calculations, molecular dynamic (MD) simulations, Monte Carlo (MC) methods, machine learning (ML) algorithms, *etc*. On this basis, extraordinary progress has been made in various aspects of 2D materials, such as growth mechanism, stability, property and application. In this section, we will summarize recent advances in theoretical calculations and simulations of 2D materials, with an emphasis on the growth mechanism, surface reactivity and magnetism.

5.1　Growth mechanism of 2D materials *via* bottom-up synthesis

In history, most of the extensively explored 2D materials are first synthesized *via* the top-down approaches, such as the mechanical exfoliation method [1,128,1610,1611]. The top-down approaches generally produce very high quality 2D materials which are suitable for the exploration of their properties, prototype device fabrications and tests and, sometimes, also can produce 2D materials in large scale, such as graphene. While most of the top-down approaches suffer some acritical drawbacks. For example, 2D materials produced by top-down approaches are generally in small size and small quality. So, most of the top-down approaches do not fit the requirements for industrial applications of 2D materials, especially for integrated device fabrications [111,1612–1614]. In contrast, the bottom-up approaches, such as the PVD [1615–1617], CVD [1618–1620], and molecule beam epitaxy [1621–1623], can produce large area films of various 2D materials of different thickness, sometimes in the form of wafer-scale 2D single-crystalline thin films. During more than one decade of extensive study of 2D materials, the
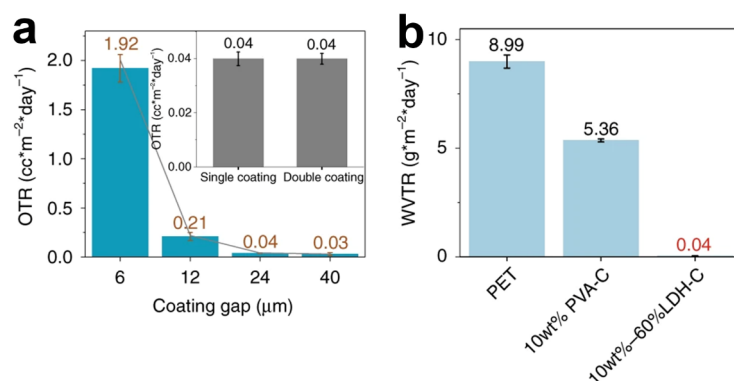

Fig. 64 **(a) The oxygen transmission rate (OTR) plot against coating gap, (b) the water vapor transmission rate (WVTR) plot against PET, 10% (*w*) PVA-C, and 10%–60%LDH-C [1606].**

bottom-up synthesis gradually becomes the main steam approach for synthesis of various 2D materials.

In contrast to the relatively simple top-down approaches, achieving growth of high quality 2D materials by the bottom-up synthesis requires the reactions of various precursors on a suitable substrate at an appropriate experiential condition, and thus many tunable experimental parameters determine the quality of the product [1624,1625]. To optimize the bottom-up experimental synthesis of 2D materials, a deep understanding on the growth mechanisms of various 2D materials is essential. In the past decade, great theoretical efforts have been dedicated to the theoretical study of the mechanism of 2D materials bottom-up synthesis. Here we will mainly summarize the recent achievements on the theoretical studies on the growth mechanisms of various 2D materials, including a general theory of 2D materials epitaxy; the mechanisms of graphene and h-BN epitaxial growth, the current understanding on growth of TMDs and the mechanism of graphene growth on insulating substrates.

5.1.1 Role of substrate in bottom-up synthesis of 2D materials

As shown in Fig. 65, the transitional epitaxial growth of thin film is significantly different from the bottom-up growth of 2D materials because of their interactions with the substrate is significantly different. For thin film grown on a substrate, the strong chemical bonding ensures an epitaxial relationship between the crystalline lattice of the overlayer material and that of the substrate (Fig. 65a) [1626,1627]. So, when the growth of 2D materials covering a polycrystalline substrate grain boundary, the 2D thin film have to change its crystallographic orientation to match its lattice orientation with the substrate [1626]. Therefore, a polycrystalline substrate cannot be used as the template for the growth of a single-crystalline thin film (Fig. 65b). In contrast, a stable 2D material generally interacts with most substrates through weak vdW interaction [1628–1632], which is not sensitive to the crystallographic orientation of 2D material (Fig. 65c) [1633,1634].

For example, DFT study has proved that the binding energy difference of graphene on a Cu surface for epitaxial growth is only a few meV different from the non-epitaxial growth. Such value is more than two orders of magnitudes lower than the chemical binding energy. Such a small driving force cannot ensure the epitaxial growth of a 2D material on a substrate. Therefore, graphene can pass through substrate grain boundaries easily without changing its crystalline orientation during growth (Fig. 65d) [1634,1635]. Besides, such phenomena have also been observed during the growth of many 2D materials [1636,1637], offering a possibility for synthesizing wafer-scale single-crystalline 2D materials on polycrystalline substrates [1638,1639].

The nucleation control for wafer-scale 2D single crystal growth requires the nucleation only one seed on a wafer scale substrate in a period of a few hours or longer, which is very challenging and, even it is possible, the productivity is generally very low. In comparison, the strategy of seamless stitching a mass of parallelly aligned 2D islands on a substrate is more practical and efficient. Therefore, it is very important to gain a deep understanding on the epitaxial growth mechanisms of 2D materials on various substrates in order to achieve the parallel alignment of millions of 2D islands on a wafer scale substrate. Recently, numerous DFT calculations have revealed that the alignment of 2D material on a substrate is determined by a simple principle that a high symmetric direction of the 2D material's crystallographic lattice tends to along a high symmetric direction of the lattice of the substrate [195,1640,1641]. Fig. 66 shows an example of graphene on the Cu(111) surface, the strongest binding energy between edge of the graphene and the Cu substrate appears when a high symmetric zigzag edge of graphene is along a high symmetric <110> direction of the Cu surface. From the charge density difference, we can clearly see that all the edge atoms are well passivated with such a configuration (Fig. 66b). In comparison, when the edge is not parallel to a high symmetric direction of the substrate, some
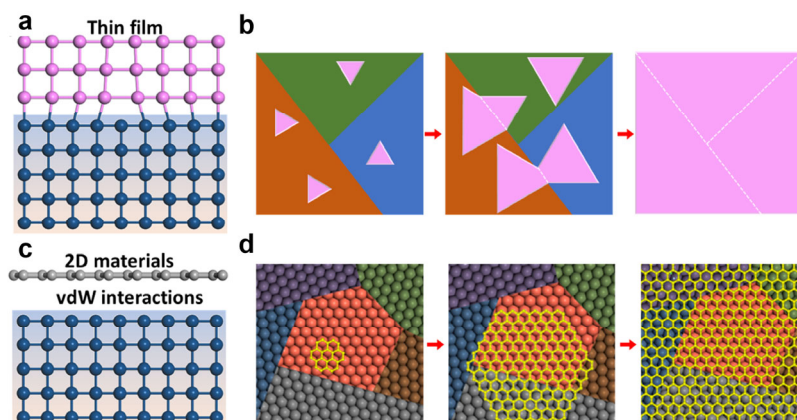
Fig. 65　The epitaxial growth of thin films *vs.* 2D materials. (a) Schematic of the chemical binding between a thin film and a substrate. (b) Illustration of a polycrystalline thin film growth on a polycrystalline substrate. (c) Schematic of the weak vdW interaction between a 2D material and a substrate. (d) Illustration of the growth of a single crystalline 2D material on a polycrystalline substrate *via* nucleation control. (d) Reproduced with permission from Ref. [1633]. Copyright 2012 American Chemical Society.
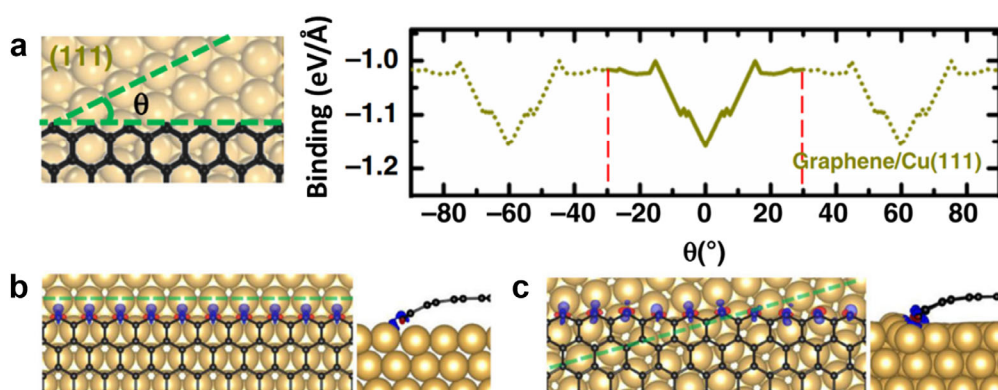
Fig. 66 The interaction between a 2D material and a substrate. (a) Model of a graphene zigzag edge on a Cu(111) surface and the binding energy of the edge on the substrate as a function of the alignment angle, *θ*. (b) Charge density differences with isovalue of 0.01 Bohr⁻³ of graphene on the Cu(111) surface with misorientation angles of 0° and 15.3°, where electron accumulation and depletion are denoted by Blue and red colors [1640].

atoms at edges are poorly passivated (Fig. 66c). This clearly shows that the high symmetric direction of a substrate is very beneficial for passivating the high symmetric edges of a 2D material. More extensive calculations prove that the principle is also applicable for other 2D materials on various substrates.

Based on the epitaxial relationship, Dong *et al*. reported that the equivalent but different alignment number of 2D materials on a substrate can be obtained *via* simple formula [1640]

$$N_{\text{2D@sub}} = \frac{|G_{\text{sub}}|}{|G_{\text{2D@sub}}|} \tag{1}$$

where $|G_{\text{sub}}|$ denotes the number of symmetric operations of the substrate and $|G_{\text{2D@sub}}|$ denotes that of the 2D material system on the substrate.

Fig. 67 presents the possible alignments of 2D materials with various symmetries on several high symmetric substrates, including the h-BN(0001) surface and three low index facets of face-centered cubic (FCC) crystal. The number of equivalent but different directions of these 2D materials on substrates are

strikingly in consistent with numerous experimental observations in 2D materials' epitaxial growth [99,213,908,924,1641–1654]. It can be clearly seen that the more symmetry operations will give rise to a greater number of equivalent but different directions of the grown 2D materials on the substrate. This implies that substrates with lower symmetries, such as high-index surfaces, are more promising for templating the epitaxial growth of 2D materials. As illustrated in Fig. 68, due to the existence of step edges, a high-index surface owns very low C_1 or C_s symmetry [1640,1655]. On such a substrate, the energetically most preferred orientations of a 2D material are not degenerated and, thus, uniformly aligned 2D islands may be grown under the optimized experimental condition.

5.1.2 Epitaxy of 2D materials on low-symmetry substrates

Recently, the alignment mechanisms of two most explored examples of 2D materials, graphene and h-BN, on various substrates containing step edges have been extensively studied. Both theoretical and experimental studies reveal that nucleation

Fig. 67 Alignment of 2D islands with various symmetries on the three low-index FCC crystal surfaces and the hBN (0001) surface. The high-symmetry crystallographic orientations of substrates are denoted by green lines. The symmetry groups of the 2D materials, substrates, and the systems of 2D islands on substrates are provided. Reproduced with permission from Ref. [1625]. Copyright 2021 American Chemical Society.

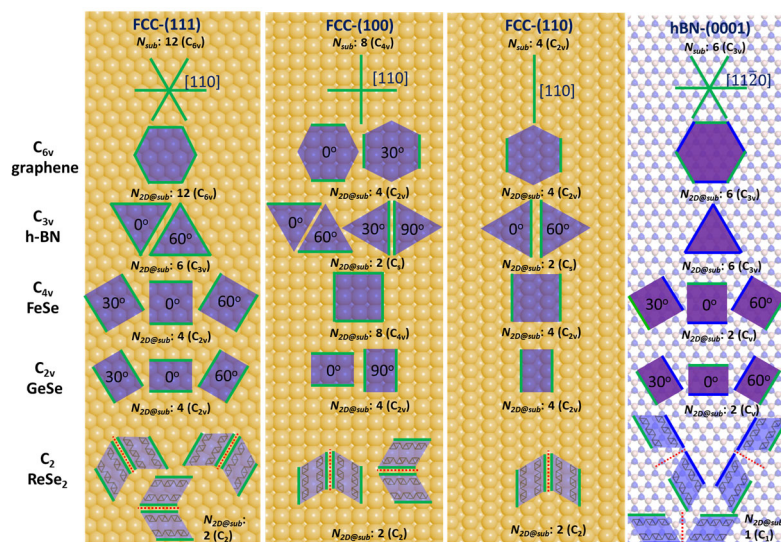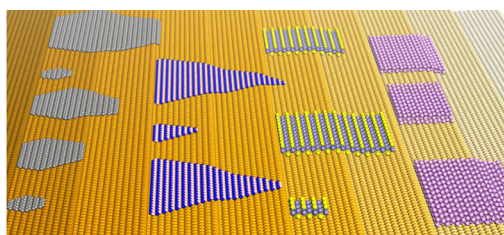**Fig. 68** Schematic of parallelly aligned 2D materials with different symmetries grown on a high-index substrate with steps [1640].

of a 2D material near a step edge is superior to that on a terrace, because of strong adhesion between the active step edges and the edge of 2D materials [1654,1656–1659].

Near a step edge, the alignment of a 2D material is determined by the interaction between the edge of the 2D material and the step edge of the substrate, or the interfacial formation energy [1655,1660]. Fig. 69a shows interfacial formation energy of various graphene edges on a <110> step edge of Cu(111) surface as a function of the tilt angle of the graphene edge [1660]. It can be seen that the global minimum corresponds to a configuration of a graphene zigzag edge attaching to the <110> step edge. This explains the broadly observed unidirectional alignment of graphene islands on near-Cu(111) surfaces, as illustrated in Fig. 69b. Ge(110) surface is a promising candidate for graphene synthesis on semiconductor compatible substrates [1661,1663]. Under the optimized experimental condition, high-quality wafer-scale single-crystalline graphene film was recently synthesized on a high index Ge surface which is 15° from the Ge(001) surface and the existence of step edges is critical for the success of the growth of unidirectionally aligned graphene islands, which further proves the effectiveness of using substrates with lower symmetry for single crystalline 2D materials synthesis [1664].

Besides the epitaxial growth of graphene, the h-BN epitaxial growth on high-index surfaces has also been studied extensively. As exhibited in Fig. 70a, on a high-index surface, which can be constructed by many low-index terraces and step edges, the alignment of h-BN islands highly depends on the types of the terrace and step edges [1655]. Zhao *et al.* investigated the alignments of triangular h-BN clusters on the (111) surface of

FCC metals and the (0001) surface of hexagonal close packed (HCP) metals, respectively (Fig. 70b–e) [1665]. It is revealed that, due to equivalence of ABC… and BCA… configurations of the neighboring terraces of a vicinal FCC(111) surface, h-BN islands tend to align parallelly on neighboring terraces of a vicinal FCC(111) surface. In contrast, the AB… and BA… configurations of the neighboring HCP(0001) surfaces are equivalent after a mirror symmetric operation, so the orientations of h-BN islands on neighboring terraces of a HCP(0001) surface are anti-parallel (Fig. 70b–e).

Both experimental and theoretical studies have showed that, the nucleation of 2D materials near a step edge of a high-index surface is energetically more preferred than that on a low index terrace [1658,1659,1666]. Generally, step edges of a high index surfaces may along any direction and can be classified into straight step edges and tilted ones [1655]. In general, a straight h-BN edge, such as armchair or zigzag, attaching to a straight step edge, such as the <110>, <100> or <211> step edge of a surface of a FCC crystal, is energetically most preferred. For example, Wang *et al.* synthesized vicinal Cu(110) substrates with straight Cu<211> step edges and observed the growth of unidirectional aligned h-BN islands (Fig. 70f, g) [214]. Combining DFT calculations and atomic-resolution STM image, nitrogen-terminated zigzag edge of h-BN attaching to the straight Cu<211> step edges was seen clearly. Chen *et al.* reported the epitaxial growth of h-BN single crystals on Cu(111) substrates with abundant step edges trending up and down (Fig. 70h, i) [99]. These step edges are highly curved and locally rugged. Atomically, a curved step edge can be constructed by using two types of straight <110> segments and the h-BN islands nucleation on them are antiparallelly aligned (Fig. 70h). To explain the unidirectional alignment of the h-BN, the authors used DFT calculations to reveal that the binding energy difference of h-BN islands attaching to the two types of step edges is large enough to drive the dominating nucleation of h-BN near one type only. Therefore, h-BN islands with one orientation will be suppressed under the optimized experimental condition.

In reality, high-index surfaces with straight step edges are rare and most high-index surfaces own tilted step edges and
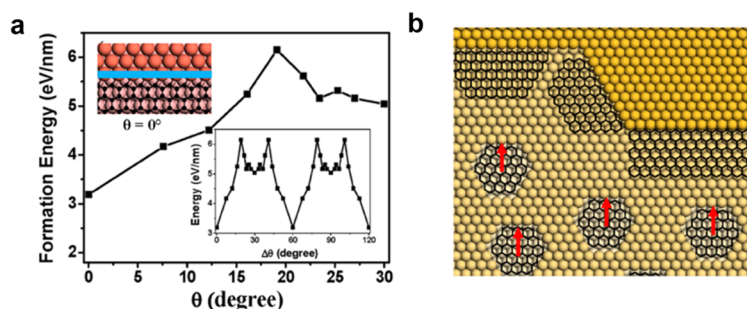
Fig. 69 Alignment of graphene on high-index substrates. (a) Formation energies of various graphene edges attaching to a Cu<110> step edge as a function of the graphene edge's tilt angle, *θ*, where *θ* = 0 and 30 degrees represent zigzag and armchair edges, respectively. (b) On a vicinal Cu(111) surface, all the nucleated graphene islands, either nucleated on the Cu(111) terrace or nearby the possible step edges, could be parallelly aligned. Reproduced with permission from Ref. [1660]. Copyright 2014 American Chemical Society.
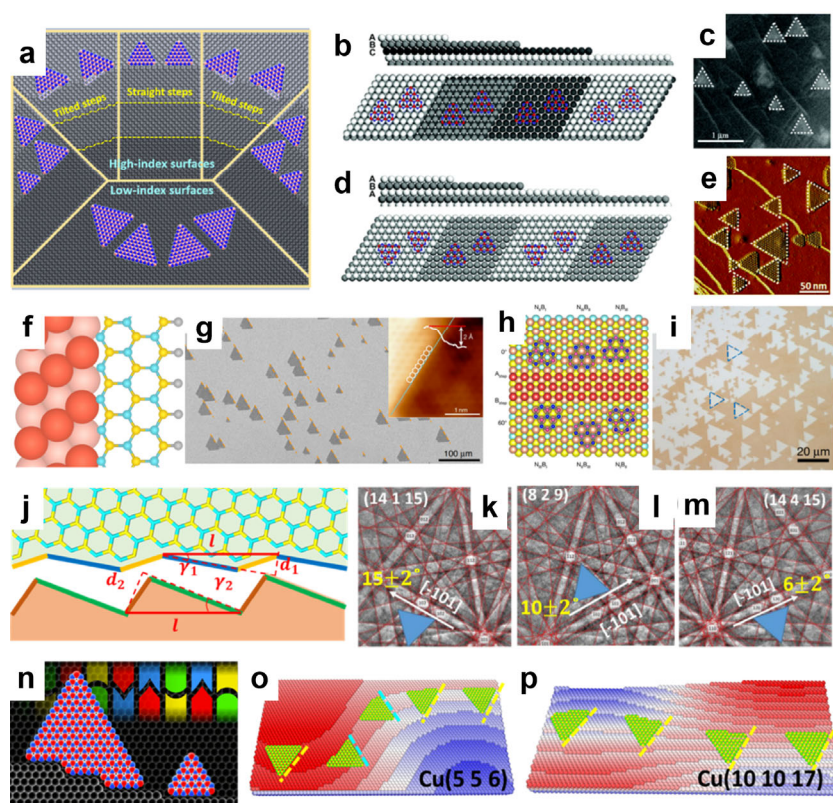
Fig. 70 **Alignment of h-BN on high-index metal substrates. (a) Schematic of hBN on various Cu surfaces and the configurations of various vicinal FCC(100) surfaces. (b–c) Schematic and experimental observation of triangular h-BN clusters on different terraces of the Ni(111) substrate. (d–e) Schematic and experimental observation of triangular h-BN clusters on different terraces of the Ru(0001) substrate. (f–g) Model of a h-BN zigzag edge attaching to the Cu<211> step of a vicinal Cu(110) surface and the experimental observation of h-BN epitaxial growth on vicinal Cu (110) surface with <211> step edges. (h–i) Model of h-BN clusters attaching to Cu<110> steps of a vicinal Cu(111) surface and the experimental observation of h-BN epitaxial growth. (j) Schematic of a tilted hBN edge attaching to a tilted step edge, where the kink heights of the h-BN edge and the step edge are shown. (k–m) Illustration of experimentally observed h-BN orientations on various high-index Cu surfaces, which agree well with theoretical predictions. (n) Schematic of h-BN alignment along a tilted step edge. (o–p) The alignment of h-BN islands on various high-index Cu surface under the same surface roughness. (a, j–m, o–p) Reproduced with permission from Ref. [1655], Copyright 2021 John Wiley and Sons. (b–e) Reproduced from Ref. [1665]. (f–g) Reproduced from Ref. [214]. (h–i) Reproduced from Ref. [99]. (n) Reproduced with permission from Ref. [1667], Copyright 2019 American Chemical Society.**

sometimes even highly curved ones. By using DFT calculations, Z hang *et al.* revealed that a tilted step edge is preferred to be attached by a tilted h-BN edge [1655], as illustrated in Fig. 70j. In this case, a misalignment angle, $\Delta\gamma$, between the high symmetric directions of the 2D materials and the substrate is no longer zero and its value can be calculated by:

$$\Delta\gamma = \gamma_2 - \gamma_1 = a\sin\frac{d_2}{l} - a\sin\frac{d_1}{l} \tag{2}$$

The calculated misalignment angles of h-BN grown on various Cu high-index surfaces are in perfect agreement with the experimentally observations shown in Fig. 70k–m. Similarly, Bets *et al.* propose that tilted step edges having similar kink size with the tilted edge of a 2D material are preferred the epitaxy growth of the 2D material (Fig. 70n) [1667].

Moreover, recent theoretical study also reveal that high-index surfaces with larger miscut angles or larger step densities are more robust in guiding the epitaxy growth of 2D materials than those with small miscut angles [1655]. Fig. 70o–p show examples

of two high-index surfaces with same surface roughness but different miscut angles. Clearly, the direction of step edges of the Cu(5 5 6) surface varies a lot, resulting in two possible h-BN orientations. In contrast, those step edges of the Cu(10 10 17) surface, which has a very larger step edge density than the Cu(5 5 6) surface, the variation step edges direction is very small and the unidirectional alignment of hBN islands is ensured.

5.1.3 Growth mechanisms of TMDs on gold substrates

TMDs have the same 3-fold symmetries with h-BN, and thus the alignments of TMDs on various substrates should be similar with those of h-BN. Inspired by the success of h-BN on vicinal Cu(111) surface [99], centimeter-scale single-crystalline MoS$_2$ monolayer has been recently successfully realized on vicinal Au(111) surfaces [924]. Soon after, the growth of centimeter-scale single-crystalline TMD monolayers, including WS$_2$, WSe$_2$, MoS$_2$, MoSe$_2$/WSe$_2$ heterostructure, and even W$_{1-x}$Mo$_x$S$_2$ alloy, on various high-index Au surfaces was reported [1668]. These experimental successes confirm the effectiveness of using low-

symmetry substrate to template 2D materials epitaxy. So, here we briefly introduce the recent understanding of TMD growth on Au surfaces.

In compare with the one-atomic-thick graphene and h-BN, the three-atomic-thick TMDs present various metastable phases, and their growth mechanisms are more complicated [1669–1671]. DFT-based molecular dynamic (MD) simulations provides an intuitive picture of MoS_2 growth on Au(111) surface (Fig. 71a) [1672]. Theoretical study reveals that the surface of Au(111) tends to be passivated by sulfurs atoms. Under a sulfur-rich environment, the metal precursor, MoO_3 molecules, can be gradually transformed into a MoS_3 molecule by reactions with the surface sulfur atoms. Then the reactions of MoS_3 molecules on the Au(111) surface firstly lead to a T-phase MoS_2 nucleus. As the growth continues, the T-phase MoS_2 nucleus will transform into an H-phase MoS_2 island when the size is large enough.

Sulfurization of pre-deposited transition metal containing films offers another strategy for synthesis of TMDs [1673–1676]. Fig. 71b presents an atomic-level mechanism for the initial sulfidation of a MoO_3 surface [1677]. In this study, a three-steps reaction process is proposed, which includes (i) the self-reduction of the MoO_3 surface, (ii) followed by SO/SO_2 formation and S_2-assisted reduction, and (iii) then the sulfidation of the reduced surface and formation of Mo－S bonds. In Fig. 71c, typical Mo－S termination and Mo－S－Mo bridge formed

during the simulation are shown. It is worth noting that the synthesized TMDs are generally multilayer and polycrystalline by this method.

5.1.4　Growth of polycrystalline 2D materials on liquid substrates

Liquid metal surfaces have also been widely used to grow 2D materials. Geng *et al*. reported the randomly aligned hexagonal graphene flakes at the initial stage of graphene growth on liquid Cu surface and, with the increasing of the graphene coverage, these islands become unidirectional aligned gradually [1678]. The parallel alignment of h-BN islands on liquid Au surfaces was also reported [1651]. However, the underlying mechanisms of the unidirectional alignment of 2D islands on liquid substrates is still unclear. Besides single-crystalline 2D materials, polycrystalline 2D materials with controlled misalignment angles or lattice orientations is also of great interests for both fundamental studies and practical applications.

In 2019, Dong *et al*. studied the formation mechanisms of polycrystalline graphene grown on liquid Cu surfaces [1679]. The grown graphene islands on liquid Cu surfaces are randomly aligned but can rotate freely because of the high mobility of the liquid substrate [1680]. The curve of the formation energy of grain boundary (GB) in graphene *vs*. the misalignment angle of the GB have two minima, zero degree corresponds a perfect single crystal and ~30° corresponds a highly stable GB with the
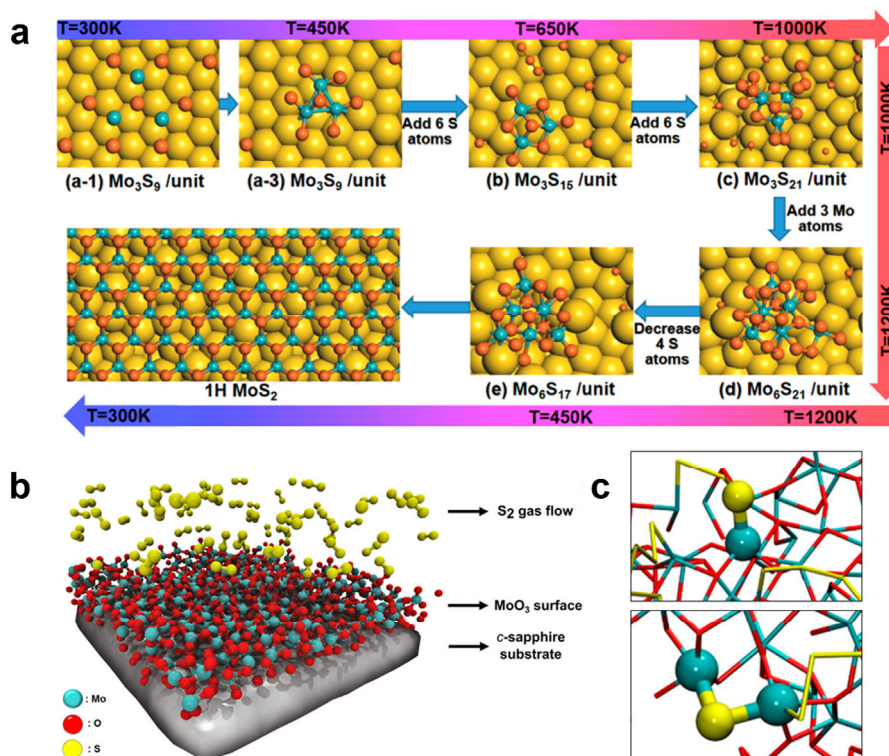
Fig. 71　Growth mechanism of TMD on various substrates. (a) First principal molecular dynamic (MD) simulations showing that the nucleation of T-phase MoS_2 on the Au(111) surface is preferred and the transformation from T-phase to H-phase will occur during the further growth process. (b) Schematic of the sulfidation of a MoO_3 surface to synthesize a MoS_2 film. (c) Close-up of Mo－S termination and Mo－S－Mo bridge structures created during reactive MD simulation. (a) Reproduced with permission from Ref. [1672], Copyright 2021 American Chemical Society. (b, c) Reproduced with permission from Ref. [1677], Copyright 2017 American Chemical Society.

formation of pentagon-heptagon lines. So, the coalescence of two graphene islands either leads to the seamless stitching of them or a polycrystal with ~30° GB, as shown in Fig. 72a, b. If many graphene islands coalescence together on a liquid surface, 30 types of graphene polycrystals with 30° GBs could be formed. As shown in Fig. 72c, 27 of 30 predicted graphene polycrystals are observed experimentally.

5.1.5 Growth mechanism of graphene on insulating substrates

For high performance device applications, it is of great important for synthesizing 2D materials directly on an insulating substrate. In experiments, great effort has been devoted to synthesizing graphene on various insulating substrates, such as SiO_2, Al_2O_3, and h-BN, to avoid the wrinkles and contaminations in graphene films formed during the transfer process [1623,1681–1685]. However, comparing with the growth of graphene on metal substrates, the growth mechanism of graphene on insulating substrates is still poorly understood, especially at the atomic scale.

As shown in Fig. 73a, the graphene growth rate on typical insulating substrates are about 3–5 orders of magnitude slower than that of on metal substrates. Besides, the type of insulating substrates has little impact on the growth behaviors of graphene, such as the growth rate and the shape [1686]. Recently, through extensive DFT calculations and modeling, Cheng *et al.* have successfully explained the slow growth rate and morphology of graphene grown on various insulating substrates [1686]. They unveiled that the CH_3 molecules in the gas phase are the key carbon precursors, and there are three typical main reactions during the addition of new hexagons onto a graphene edge: (i) feed the graphene growth by attaching a CH_3 radicles; (ii) remove the excessive H atoms of CH_3 *via* reaction of CH_3 + H → CH_4, and (iii) form a new hexagonal carbon ring, as illustrated in Fig. 73b. Therefore, the growth process on an insulating substrate can be attributed to a vapor-solid growth, which is different from the vapor-surface-solid growth on metal substrates. Besides, the type (ii) reaction is the threshold step that limits the growth rate. Fig. 73c exhibits the energy profiles of threshold step reactions for a graphene zigzag and armchair edge. The threshold reaction barrier are 1.94 and 3.00 eV, respectively and the growth rate of the armchair edge is slower than that of the zigzag edge. Based on the kinetic Wulff construction theory, the slowly growing armchair edge gradually dominate the circumference of a graphene island (Fig. 73d), which is similar to the experimental observations of graphene growth on the insulating substrates [1687–1689]. Based on such theory, the growth rate of a graphene edge could be estimated by

$$v = \frac{\Delta L \times C_p}{e^{(E_b - E_f)/k_B T}} \tag{3}$$
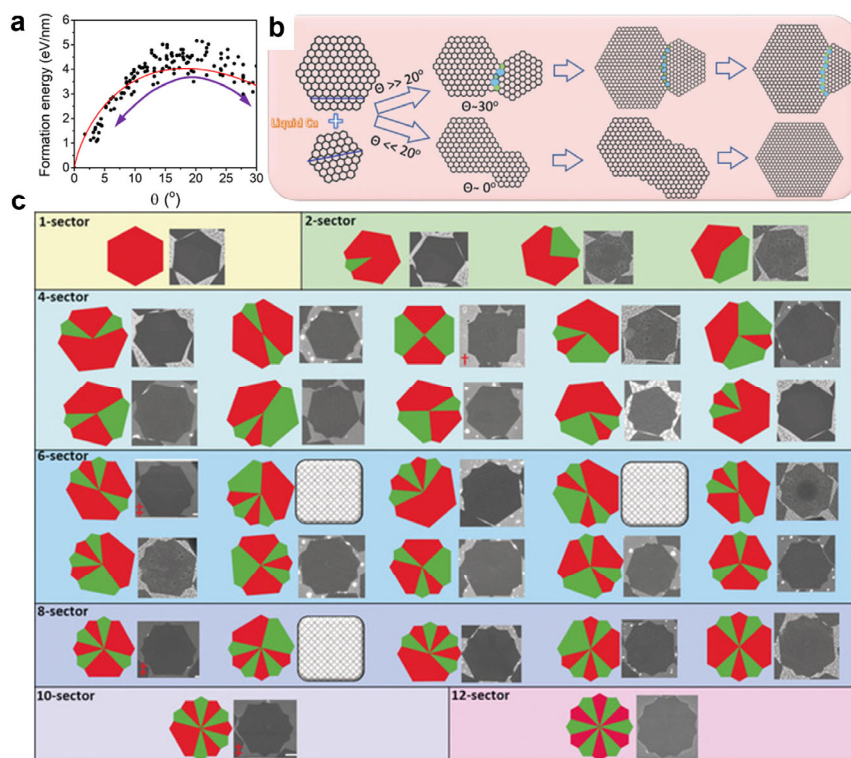
Fig. 72　Growth of graphene polycrystals on liquid Cu surface. (a) Formation energy of graphene grain boundary as a function of the misalignment angle of the two graphene grains. (b) Schematic showing two routes of graphene coalescence on liquid Cu surface, a single crystal *via* seamless stitching of two aligned graphene islands or a graphene polycrystal with a 30-degree GB. (c) The prediction and corresponding experimental observation of graphene polycrystals *via* coalescence of multi graphene islands on liquid Cu surfaces. Reproduced with permission from Ref. [1679], Copyright 2019 John Wiley and Sons.
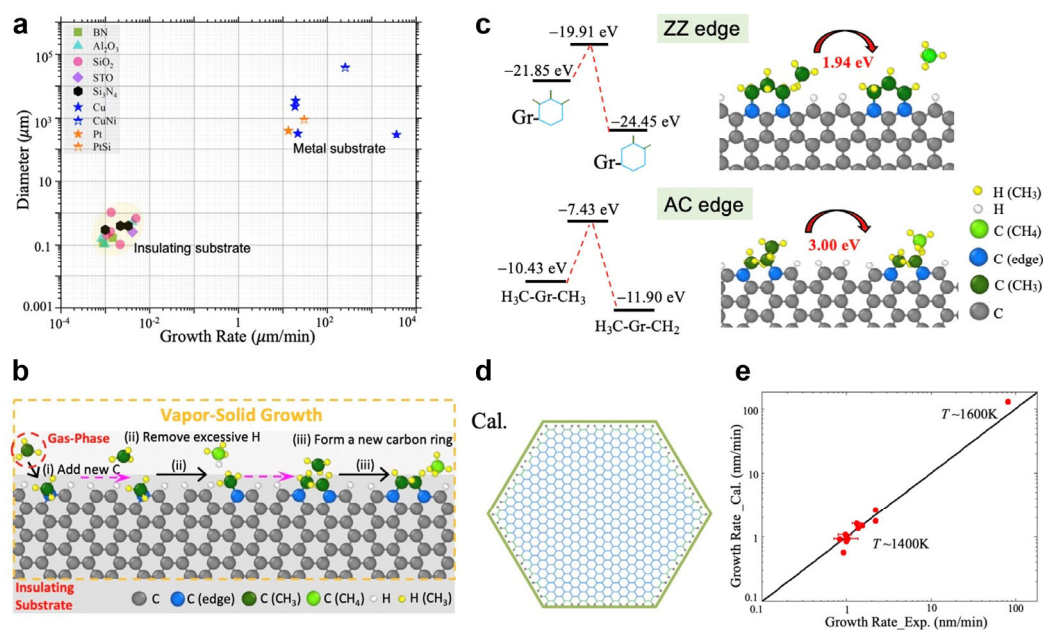
Fig. 73 **The mechanism of graphene growth on insulating substrates. (a) Summary of the experimental data (growth rates and sizes of grown graphene islands) of graphene growth on the insulating substrates and metal substrates. (b) Schematic of vapor-solid growth of graphene on insulating substrates. (c) Energy profile and reaction geometries of the threshold step for a graphene zigzag and armchair edge. (d) Morphology of a growing graphene island on the insulating substrates obtained by the kinetic Wulff plots in theory. (e) Comparison of the graphene growth rate between experimental results and calculated results based on the experimental conditions and Eq. (3). Reproduced with permission from Ref. [1686], Copyright 2021 American Chemical Society.**

where, $\Delta L = 0.142$ nm is the carbon-carbon bond length of graphene, E_b is the threshold barrier of growing graphene, E_f is the formation energy of a CH_3 attached at the edge, and C_p denotes the collision rate of a CH_3 to the growth site. Fig. 73e plots the calculated graphene growth rates at different experimental conditions and a perfect agreement is clearly seen when comparing with the experimental results [1686].

Based on the mechanism, using more active carbon source to lower the barrier of removing excess H atoms or growing graphene at a higher growth temperature (> 1600 K) were proposed as effective strategies for fast graphene growth on insulating substrates.

5.1.6 Summary

Although the growth mechanisms of 2D materials have been explored extensively in last decade, the deep understanding especially at the atomic level, is still very poor and many of the theoretical results are not in consistent with experimental observation. There are still many experimental puzzles, such as why the less active Cu is the best catalyst for graphene growth, how oxygen help the growth of graphene on Cu surface, are not properly explained. Besides, the lack of deep understanding on the atomic processes of 2D materials growth greatly hinders the applications of theory in experimental design and, thus, most of the experimental progresses of bottom-up synthesis of 2D materials are still based on a huge number of experimental tries. To realize true rational experimental design of 2D materials growth, developing new theoretical methods, such as machine learning force fields, to explore the atomic details of 2D

materials growth with a high accuracy and with a longer simulation time simulation is critical. On the other hand, the current theory of 2D materials epitaxy based on the symmetry analysis and some simple theoretical calculations are very successful and, based on it, experimental scientists can grow quite a few types of single-crystalline 2D materials in wafer scale. We believe that, in a long term before the theoretical methods allow us to simulate real and complicated experimental systems in a long term, the close collaborations between theoreticians and experimentalists are crucial for the further development of the theory and experimental approaches on the synthesis of 2D materials.

5.2 Surface reactivity of 2D materials

A distinctive feature of 2D materials is their atomic-thin thickness, which endows them unique physical and chemical properties [1690–1692]. However, the atomic-thin thickness also leads to the relatively high surface reactivity of 2D materials, leading to their environmental instability, as they may be corroded, decomposed, oxidized, segregated and so forth [1693]. In particular, the few-layer BP show visible surface oxidation within a few hours, resulting in the invalidity of the fabricated devices [1694]. Apart from BP, many other 2D materials also suffer from oxidation and degradation, such as metal chalcogenides (e.g., InSe and GaSe) and TMDs (e.g., WS_2 and HfS_2) [55,1695–1697]. In addition, the existence of surface defects can also lead to the further increase of surface reactivity, leading to the degradation of the stability, charge carrier mobility and optical properties. On the other hand, the increase of surface reactivity can significantly

affect their properties, offering new opportunities for their applications. For instance, surface vacancies can activate the inert basal planes of 2H-phase MoS_2 for HER [1022]; surface defects endow the carbon materials the capability of trapping the single metal atoms to form single atom catalysts (SACs) with enhanced activity [1698]; *etc*. Therefore, a fundamental understanding of the surface reactivity will help to identify the key factors that effecting the stability, property and performance for certain applications, as well as the corresponding strategies to enhance the stability and performance [1699]. In this section, we will summarize the surface reactivity of 2D materials at atomic level, with an emphasis on the oxidation/degradation mechanisms, role of surface vacancies on the properties and activities, as well as theoretical insights into the 2D materials supported SACs (SACs@2D).

5.2.1 Oxidation and degradation mechanisms

5.2.1.1 Light-induced oxidation

Based on the active species in air and the possible energy source, Zhou *et al*. firstly established a "three-step" mechanism of light induced BP degradation (Fig. 74a) [1700]. Specifically, superoxide (O_2^-) can be generated under light illumination on the surface of few-layer BP; the active superoxide then directly reacts with the surface P atoms to form phosphorus oxides; the H_2O molecules decompose the hydrophilic phosphorus oxides and finally causes the breakdown of BP layer. It should be noted

that the generation of superoxide is highly depending on the electronic structures of the system. As the energy levels of BP changes with the number of layers, which is also known as quantum confinement, the generation of superoxide can be limited and thus the photooxidation takes much longer for multi-layer BP than the thinner ones [1701].

5.2.1.2 Water catalyzed oxidation

In addition, the concentration of water is proven to play an important role in the oxidation of 2D materials. Hu *et al*. found that when the water molecules with high polarity gradually approached oxygen, the energy levels of $\pi*_{2p}$ of O_2 decrease and get close to the valence bands of BP (Fig. 74b) [1702] Consequently, the electrons from BP surface can be transferred to O_2 molecules with the assistance of water molecules, O_2^- anions are thus expected to be formed even without light irradiation. The theoretical results explain the experimental findings that both hole and electron motilies of the BP-based device decreased significantly after 19.5 h exposure in dark environment.

5.2.1.3 Defect induced oxidation

The pristine surfaces of TMDs and metal chalcogenides present higher stability than BP, the reported oxidation phenomenon can be attributed to defective sites such as surface vacancies and edges [1703,1707]. For the defective sites, metals and transitional metals can be exposed to air and react with either water or oxygen molecules. The reaction and the formation of
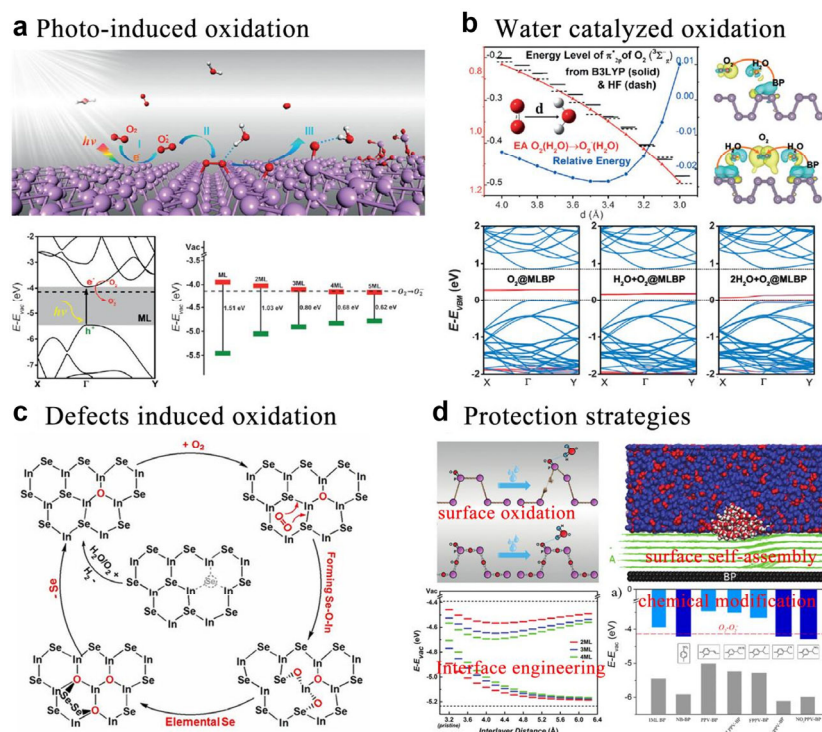
Fig. 74 **(a) Light induced oxidation: the light-induced ambient degradation process of BP and the electronic structures of BP with the redox potential of O_2/O_2^-; reproduced with permission from Ref. [1700], Copyright 2016 John Wiley and Sons. (b) Water catalyzed oxidation: the polarization effect of H_2O on O_2 illustrated by theoretical calculations; reproduced with permission from Ref. [1702], Copyright 2017 John Wiley and Sons. (c) Defect induced oxidation: schematic of the degradation mechanism for InSe; reproduced with permission from Ref. [1703], Copyright 2017 American Chemical Society. (d) Several proposed protection strategies by theoretical calculations and simulations; reproduced with permission from Ref. [1700,1704–1706], Copyright 2016 John Wiley and Sons, Copyright 2016 American Chemical Society, Copyright 2017 Royal Society of Chemistry.**

oxides leads to local deformation of the crystal lattice around the defective sites, and the insertion of oxygen atoms can activate surrounding metal-chalcogenide bonds (Fig. 74c). The high energy barrier required for the step-by-step intercalation of O_2 leads to a slow oxidation process that is observed from experiments.

To increase the stability, a direct and most commonly used approach is encapsulation or coating with other materials, include polymer, Al_2O_3, and h-BN [1708–1710]. Based on the understanding of oxidation mechanisms for many 2D systems, alternative approaches can be adopted to slow down the oxidation processes. For example, the electronic structures of BP layers can be modulated by several approaches, such as heteroatom doping, chemical modification, interface engineering by small molecule intercalation, covalent modification of polymers (Fig. 74d) [1705,1706,1711,1712]. These methods intend to decrease the energy level of the CBM so that superoxide generation can be restricted, thus the environmental stability of black phosphorus is improved. Combining with experiments, these modification methods are proven to be effective to increase the stability of BP to a large extent [1711–1713].

5.2.2 Surface vacancies and performance control

In the practical applications of 2D materials, the properties and performance can be largely affected by many kinds of defective sites, including vacancies, grain boundaries, edges, and substitutional impurities, in which surface vacancies are the most abundant and investigated type [1714]. It can be noticed in the reported literatures that many novel characters are attributed to the presence of defect sites, such as high catalytic activity, quantum states, and color centers [1715,1716]. With the help of first-principle methods, theoretical studies often get insights into the electronic structures and the modulation mechanisms of the defects, thus providing new perspectives for the experiments.

On the one hand, the defects can bring negative effects on the stability (as we discussed in the former section), charge carrier mobility and optical properties of 2D materials. For example, Qiu *et al*. proposed that the sulfur vacancy defect is the key factor of low mobility of MoS_2, and a charge hopping transport scheme mediated by localized defect states is established [750]. As shown in Fig. 75a, the existing sulfur vacancies introduces localized donor states inside the band gap. At low carrier concentration, the electron transport can only be realized by the transition between the induced gap states, which limits the intrinsic mobility of MoS_2 considerably; with the increase of carrier concentration, the gap states are filled and band-like transport is expected (Fig. 75b). The transport model is further validated by transmission electron microscopy and transport experiments. It is, therefore, explained that the actual device mobility is far lower than the theoretical value, which has been a long-standing problem in the field. In addition, thiol chemistry is introduced to the repair of the vacancy-sites based on the calculated reaction mechanisms [745]. Following the theoretical guidance, the carrier mobility of the repaired MoS_2-based device increased by 2–3 times, which further proved the transport model. Similarly, Jiang *et al*. demonstrated that defect engineering *via* molecule decoration can be used to efficiently modulate the trap states induced by vacancies in 2D ReS_2. The defects are then passivated and shallow traps and recombination centers dominate the photo-response, which show much improved response than the as-prepared device [1717]. By the listed examples, it can be noted that the thiol molecules are widely used to modify the properties of 2D materials, but the corresponding reaction mechanism is still unclear and controversial in experiments [1718]. One is that thiol molecules fill the vacancy, which leads to the significant improvement of mobility and optical absorption properties [1719]; another one is that the
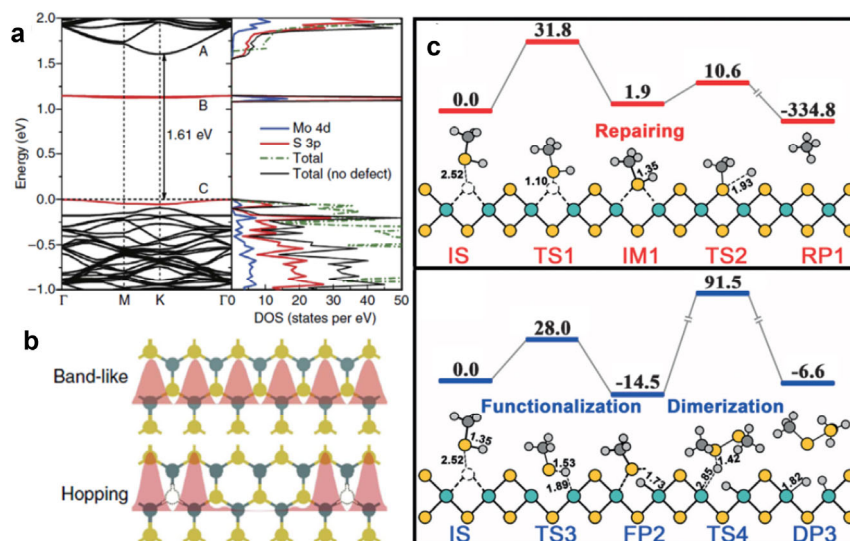
Fig. 75　**(a) Band structure and partial density of states for single-layer MoS₂ with an SV. The localized states are highlighted by red lines; (b) schematics of electron transport mechanism in perfect and defective MoS₂ [750]. (c) Two competing Reaction mechanisms between a thiol molecule and SV-MoS₂, energy units are in kJ·mol⁻¹ and the distances are in Å; reproduced with permission from Ref. [1722], Copyright 2017 John Wiley and Sons.**

molecules adsorb on the surfaces to realize the surface functionalization [1720–1721]. Accordingly, Li *et al.* performed detailed theoretical calculations on the reaction mechanisms between the defective MoS$_2$ and thiol molecules and found that the vacancies can catalyze the cleavage of S－H bond in thiol molecules with two competitive reaction mechanisms: the cleavage of S－C bond, which can repair defects, and the formation of Mo－S bond to modify the surface of MoS$_2$ (Fig. 75c). Further calculation shows that the two competitive reactions can be effectively controlled by the modification of functional groups (such as electron withdrawing group and electron donating group) and the control of reaction temperature [1722].

On the other hand, the high activity of the defective sites can be applied to modulate the properties of the system for specific applications such as sensors and catalysis. For instance, Nan *et al.* reported that defect engineering by oxygen bonding can be used as an effective strategy to enhance the photoluminescence (PL) of monolayer MoS$_2$ [1723]. The calculated band structure clear shows that that the existence of sulfur vacancy defects has n-type doping effect on MoS$_2$, which leads the neutral excitations into negative trions and the decreased PL efficiency. However, the defect sites can chemisorb oxygen molecules to form Mo－O bond and the defective states are thus removed. Moreover, oxygen molecules can extract electrons from MoS$_2$ to form p-type doping, which leads to the transition from charged excitation to neutral exciton, thus the luminescence efficiency can be improved. The utilization of defective sites as reactive centers for heterogeneous catalysis has been widely investigated [1724]. The theoretical studies can identify the reactive centers for certain reactions and thus can promote the improvement of the activity and the design of new catalysts. Ouyang *et al.* systematically evaluated the catalytic activity of hydrogen evolution by 16 intrinsic defects on basal planes of MoS$_2$, including point defects and grain boundaries [1725]. The results show that six of them (V$_s$, V$_{MoS3}$, Mo$_{S2}$ PDs; 4|8a, S bridge, and Mo－Mo bond GBs) can achieve promising HER performance. Furthermore, an amendatory band-center model is established to accounts for the different HER activities of defects, and can be applicable to a wide range of systems with localized defect states.

5.2.3　2D materials supported single atom catalysts

2D materials as the substrates for single atom catalysts (SACs) have several advantages as compared to 3D substrates: (1) single metal atoms supported on 2D materials could be more coordinatively unsaturated, which may lead to higher catalytic performance; (2) a more expedited mass-transfer process on SACs@2D, which maximizes the reaction rates; (3) well-defined structures of SACs@2D that can be accurately probed experimentally, which benefit the investigations on the reaction mechanisms and effect of geometric and electronic structures on the catalytic performance both the experimentally and theoretically [1726]. Therefore, SACs@2D has drawn great

attentions during the past years. Here we will focus on the computational investigations on SACs@2D, including the activity descriptors and strategies for the discovery of SACs@2D.

5.2.3.1　Activity descriptors

For SACs@2D, the single metal atom is usually the active center. Therefore, the inherent electronic structure of the supported single metal atom is found to be the determining factor that governs the binding strength with the reaction intermediates [1727–1729]. On this basis, the *d* band center (ε_d) of the supported single atom has been widely used as the activity descriptor of SACs@2D for various reactions. Ling *et al.* proposed that the OER activity of β_{12} boron monolayer (β_{12}-BM) supported SACs (SACs@β_{12}-BM) depend closely on the energy level of the ε_d. Specifically, the binding strength of all the reaction intermediates during the OER process (*OH, *O and *OOH) present good linear relation against the corresponding ε_d and the lowest overpotential for OER of SACs@β_{12}-BM can be obtained when the energy level of ε_d is about −2.82 eV (Fig. 76a) [1730]. Gao *et al.* reported that binding strengths of intermediates on n-doped graphene (N-G) supported SACs (Mn, Fe, Co, Ni, and Cu) will be weakened with the decrease of ε_d and Co@N-G possesses an optimal ε_d that leads to the appropriate binding strength with *OOH. As a result, the Co@N-G can present better ORR activity than the other four systems, which has also been confirmed by their experimental measurements [901].

Except for ε_d, some other activity descriptors based on the inherent electronic structure of single metal atom have also been developed. By using single Au (neutral, negatively and positively charged) embedding into C$_3$N as examples, Fu *et al.* demonstrated that spatial structures of frontier *d* orbitals determine the chemical and catalytic activities of Au@C$_3$N SACs [1727]. Liu *et al.* proposed that bonding/antibonding orbital population can well describe the binding strength of *N (key intermediate for NRR) on different nitrogen-doped carbon substrates supported SACs [1729]. Fu *et al.* found that the ORR and OER activity of Ti$_3$C$_2$O$_2$-based SACs is actually determined by the *d* electrons near the Fermi level instead of all the occupied *d* electrons (Fig. 76b) [1728].

In addition to the electronic structure of the single metal atom, the coordination environment of the single metal atom is another determining factor for the activity of the SACs [1731]. Using graphene-based SACs as examples, Xu *et al.* developed an activity descriptor for HER, OER and ORR, which takes both the intrinsic properties of metal center and coordination environment into account. This descriptor is defined as

$$\varphi = \theta_d \times \frac{E_M + \alpha \times (n_N \times E_N + n_C \times E_C)}{E_{OH}}$$, where the θ_d is

the number of the *d* electrons; E_M, E_N, E_C, E_O and E_H are the electronegativity of metal, N, C, O and H atom, respectively; n_N and n_C are the number of coordinated N and C atoms, respectively [1732]. Moreover, all the parameters involved in this equation are the intrinsic properties of the metal/coordination
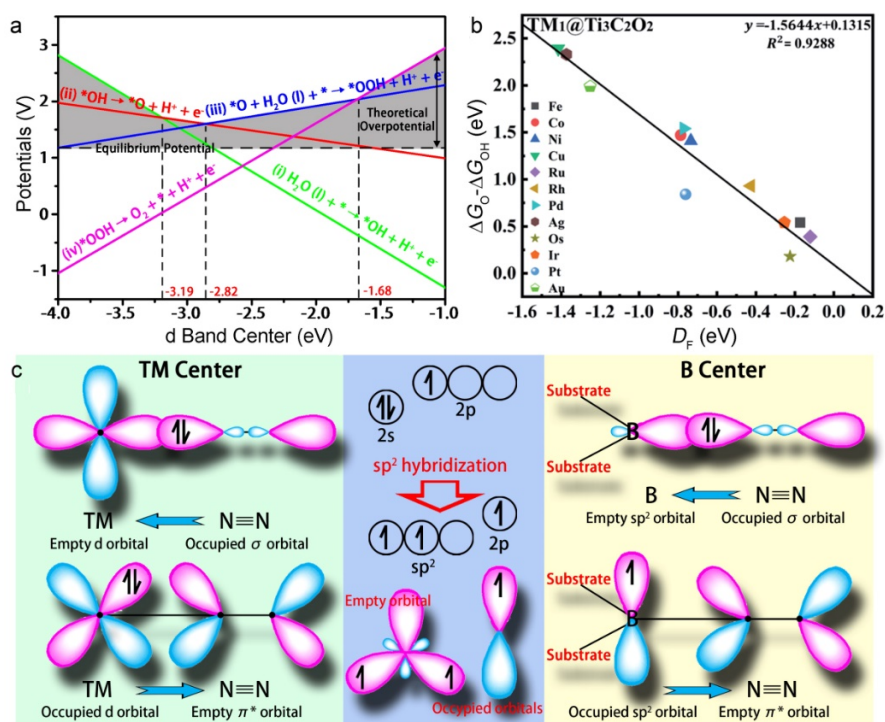
Fig. 76 (a) Calculated free energy change for each reaction of OER on different SACs@β_{12}-BM as a function of the *d* band center; reproduced with permission from Ref. [1730], Copyright 2017 American Chemical Society. (b) Calculated ΔG_O–ΔG_{OH} on Ti$_3$C$_2$O$_2$-based SACs catalysts as a function of the corresponding D_F (defined as $D_F = \dfrac{\int_{-\infty}^{+\infty} ED(E)W(E)\mathrm{d}E}{\int_{-\infty}^{+\infty} D(E)W(E)\mathrm{d}E}$, where $D(E)$ and E are the DOS and energy of *d* states of transition metal atoms, and $W(E)$ is the weight factor [1728]. (c) Simplified schematic of N$_2$ bonding to transition metals and B atom with *sp*^{3} hybridization; reproduced with permission from Ref. [1733], Copyright 2018 American Chemical Society.

atoms (electronegativity) and the structure feature (coordination number), which can be directly obtained and allow us to predict the activity without performing any DFT calculations.

5.2.3.2　Strategies for materials discovery

The large number of 2D materials, the diversity of metal center and coordination environment make the number of possible candidates for SACs@2D enormous. Therefore, it is very hard to synthesize and investigate the entire possible SACs@2D experimentally. Under this circumstance, computational discovery of SACs@2D has drawn great attention, owing to its advantages of low cost and short development period as compared to the experimental means. In this section, we will summarize recent computational strategies for the discovery of SACs@2D.

The first strategy is the rational design of SACs@2D for certain applications based on the basic chemical and physical concepts. For instance, strong binding strength and sufficient activation of N$_2$ is the prerequisite of efficient catalysts for NRR [976]. Some certain transition metal-based materials can bind N$_2$ at low temperatures, which can be ascribed to the co-existence of unoccupied and occupied *d* orbitals. The unoccupied *d* orbital can accept the lone-pair electrons, while the *d* electrons can be donated into antibonding orbitals of N$_2$ (π back donation, which can weaken the N≡N triple bond and simultaneously strengthen the metal-N bond). According to this

concept, Ling and coworkers proposed that two-coordinated B atom with *sp*^{3} hybridization possesses one occupied and one empty orbitals, thus can also bind and activate N$_2$ molecule (Fig. 76c). Moreover, they further designed g-C$_3$N$_4$ supported single B atom catalyst, which can catalyze NRR with a very low onset potential [1733]. The ability of B atom center to catalyze NRR has been confirmed by a series of experiments [955,983].

The second one is high-throughput screening, which can give a full assessment of the catalytic performance of a class of materials. Graphene-based SACs have been reported to have potential application in various electrochemical reactions. To fully understand the activity of this class of materials, a series of works by using high-throughput screening strategy have been done. Specifically, Choi *et al*. studied the stability and HER activity of 300 kinds of B, C, N, O and S coordinated SACs and 19 materials were selected with $|\Delta G_H|$ (free energy for H adsorption) lower than 0.2 eV [1734]. Back *et al*. systematically investigated the stability, activity, mechanism and selectivity for CO$_2$RR of 12 metals embedded into the single- and double-C vacancy site of graphene (labeled as sv-G and dv-G, respectively), where Ni@dv-G/Pt@dv-G and Os@dv-G/Ru@dv-G were found to be highly active for CH$_3$OH and CH$_4$ production, respectively [1735]. Ling and coworkers developed a general two-step strategy for the high-throughput screening of catalysts for NRR and on this basis, they extracted 10 promising

candidates from 270 kinds of graphene-based SACs [1736]. Moreover, the activity for certain reactions of some the predicted systems have been confirmed by available experimental reports, such as Co@G [1737] and Pt@G for HER [1738], Mo@G for NRR [945], *etc*.

　　The third one is the machine learning-aided catalysts screening, which can significantly reduce the computation cost and time bypassing complicated quantum mechanics [1739]. Wu *et al*. proved that machine learning-based screening of SACs for ORR is 130000 times faster than using DFT-based approach [1740]. Besides, machine learning-based prediction can also achieve high accuracy in addition to the high efficiency. Lin *et al*. built machine learning models to predict the limiting potentials of graphene-based SACs for ORR, OER and HER, where the mean square errors are only 0.027, 0.021 and 0.035 V, respectively, as compared to the DFT calculations [1741]. In general, high efficiency and accuracy make machine learning a powerful technique for materials discovery [1742]. With the development of machine learning algorithms and database, this technique will unquestionably draw growing attention.

5.3　2D magnetic materials

　　2D magnetic materials with abundant magnetic, electronic and optical properties promise the development of new magnetoelectronic and magneto-optical applications [1743]. First-principle calculations have been proven to be one of the most useful methods to investigate novel 2D magnetic materials, and provide valuable guidelines for experimental synthesis of high performance devices in spintronics [1744]. In this section, we will comprehensively review some of the key roles of theoretic calculations and simulations in 2D magnetic materials, including

determination of magnetic ground state, Curie temperature calculation, interlayer magnetic coupling, external field modulation, topological magnets and high throughput searching.

5.3.1　Magnetic ground state determination

　　The magnetic ground state plays a significant role in determining the fundamental magnetic properties of 2D magnetisms. As in magnetic materials, there are two competing energies in electronic states, one is the hopping energy of electrons between atoms, the other is electrostatic Coulomb energy between electrons, which can be described by a Hubbard model

$$\hat{H} = -\sum_{i,j \in \Lambda} \sum_{\sigma} t_{ij} c_{i\sigma}^{\dagger} c_{j\sigma} + U \sum_{i \in \Lambda} c_{i\uparrow}^{\dagger} c_{i\downarrow}^{\dagger} c_{i\downarrow} c_{i\uparrow} \quad (4)$$

where the hopping t_{ij} is often restricted to nearest-neighbor sites. The operator $c_{i\sigma}^{\dagger}$ creates an electron with spin σ on atom i and the operator $c_{i\sigma}^{\dagger}$ annihilates an electron with spin σ on atom i. An interesting example is CrI_3, intriguing layer-dependent magnetic order was reported in atomically thin CrI_3 films. Monolayer and trilayer CrI_3 remain ferromagnetic, whereas bilayer CrI_3 becomes antiferromagnetic (AFM) with FM monolayers coupled antiferromagnetically [514]. There are two phases of bilayer CrI_3, namely, rhombohedral structure with $R\bar{3}$ symmetry at low temperature (LT phase), and monoclinic structure with C$2/m$ space group symmetry at 210–220 K (HT phase). As shown in Fig. 77a, Jiang *et al*. investigated that the interlayer FM state is always kept under different U values [1745], indicating the preferred FM ground state in the LT phase, while HT phase is AFM under U larger than 2.1 eV, such a phenomenon is also obtained in other works [1746,1747]. Therefore, the interlayer AFM coupling of bilayer CrI_3 could be maintained
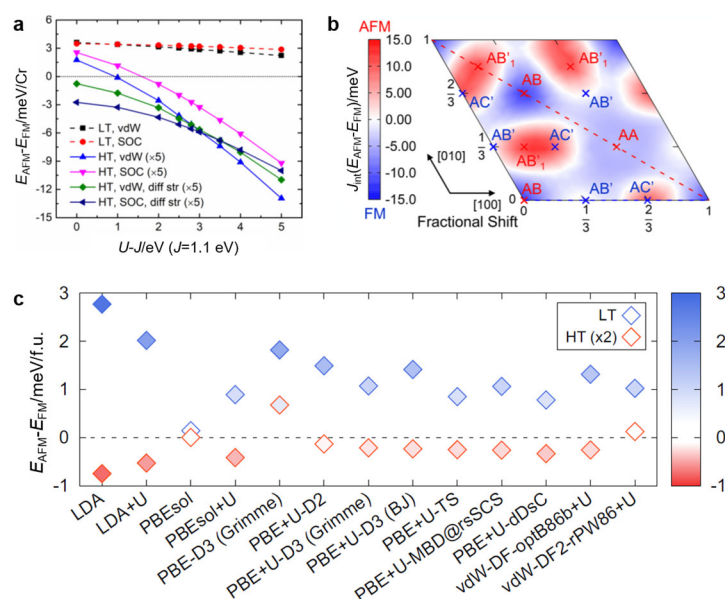
Fig. 77　**Energy difference between AFM and FM spin configurations of bilayer CrI₃ as a function of (a) on-site *U*, (b) interlayer stacking orders and (c) vdW functional corrections. (a) Reproduced with permission from Ref. [1745], Copyright 2019 American Physical Society.**

(b) Reproduced with permission from Ref. [1748], Copyright 2018 American Chemical Society. (c) Reproduced with permission from Ref. [1750], Copyright 2019 American Physical Society.

in the HT phase, rather than the presumed LT phase, even at low temperatures. Such a phenomenon may be ascribed to structural quenching under rapid cooling rates and/or vertical confinement of the capping layers in measurements.

The magnetic ground state of 2D magnetic materials can also be influenced by interlayer stacking because the superexchange interaction between magnetic atoms in different layers can be changed through interlayer translation. Sivadas *et al*. performed first-principle calculations for bilayer CrI₃ and found that the magnetic ground state is defined by stacking order (Fig. 77b) [1748]. This stacking-dependent magnetism stems from a competition between interlayer AFM super-superexchange (SSE) and interlayer FM SSE. The interlayer exchange interaction between AFM and FM can be tuned by changing the interlayer stacking order. The interlayer stacking order can also influence the interlayer magnetic coupling of 2D vdWHs. Shang *et al*. found that the preferred magnetic order and electronic properties are largely influenced by interlayer stacking in CrI₃/CrGeTe₃ heterostructure, which is caused by the competition between the nearest-neighbor and second nearest-neighbor superexchange [1749]. In addition, the relative energy is reliable to the choice of vdW functional (Fig. 77c) [1750–1752].

5.3.2 Curie temperature calculation

The most important feature of FM materials is the phase transition temperature, *i.e.*, Curie temperature (T_c), which defines many intrinsic macroscopic mechanisms of magnetic materials. The exchange interaction parameters, J_{ij}, are determined by the basic Heisenberg Hamiltonian as

$$H = -\sum_{ij} J_{ij} S_i S_j \tag{5}$$

where i and j are lattice sites of local magnetic moment, and S and J denote the spin operator and exchange interactions, respectively. Usually, it is enough to consider the exchange interactions between the nearest-neighbor magnetic atoms. In theoretical calculations, J_{ij} can be extracted from the energies of various spin configurations, such as FM, AF-Neel, AF-zigzag and AF-Stripy, and so on [1753]. Using Monte Carlo (MC) methods, one can obtain the T_c according to the relation between thermodynamic specific heat or magnetic moment and temperature. Moreover, a simpler method to roughly estimate T_c is the mean-field approximation of $k_B T_c = 2J/3$ (k_B is the Boltzmann constant), which, however, usually overestimates T_c. Other theories, such as Stoner, Hubbard and Ruderman-Kittel-Kasuya-Yosida (RKKY) mechanism, were also applied to deal with more complicated electron-electron exchange interactions in 2D magnetic materials. As CrI₃ monolayer is one of the most typical 2D ferromagnetisms, its T_c has been extensively studied. An overrated T_c of 80 K was predicted using the Ising model for the overestimation of anisotropic interactions [1754]. Researcher calculated the T_c of 40 K by MC simulations, which is close to the experimental value of 45 K [552,1746]. Lu *et al*. calculated T_c is 42 K using XXZ Heisenberg model and MC simulations [1755]. More importantly, it is found that within a wide range of

parameter space, T_c shows a linear relationship with magnetic interaction coefficients. As a consequence, T_c of 2D Heisenberg-type magnets can be predicted by the magnetic interactions rather than performing time-consuming MC simulations. Moreover, the selection of U also affects the calculated T_c, for a smaller U value corresponds to larger exchange parameters J since $J \sim t^2/U$ [1756].

In such a manner, one can predict 2D FM materials with T_c over room temperature to develop high-performance spintronic devices. Zheng *et al*. identified an ideal FM Fe₃P monolayer, whose T_c reaches ~420 K [1757]. Furthermore, it was reported that a new 2D pentagon-based monolayer, penta-MnN₂ displays a high T_c of 913 K that can be further improved to 956 K by biaxial tensile strain [1758].

5.3.3 Interlayer magnetic coupling

Interlayer coupling is of paramount importance in modulating physical properties of 2D materials. The layer-dependent magnetic coupling of 2D magnetisms originates from the strong wavefunction overlap in the vdW gap, which can form bonding and antibonding states to modulate the electronic and magnetic properties. Such orbital hybridization could lead to charge redistribution of both layers and thus may influence the intra- and interlayer magnetic coupling. As seen from the layer-dependent magnetism in CrI₃ [1745,1747,1748], the interlayer magnetic coupling might regulate the magnetic properties of 2D magnetisms. Wang *et al*. reported a Bethe-Slater-curve (BSC)-like phenomenon of energy difference between AFM and FM spin configurations in bilayer TMDs (MX₂, M = V, Cr, Mn; X = S, Se, Te) and set up the interlayer exchange coupling mechanism at the vdW spacing (Fig. 78a) [1759]. In addition, the in-plane magnetic orders of mono and few layers CrS₂ can be largely tuned between striped AFM and FM coupling by the charge transfer of Cr e_g and t_{2g} orbitals [1760]. In experiment, such an interlayer magnetic coupling can be tuned *via* pressure. Song *et al*. demonstrated that vdW engineering by hydrostatic pressure can modify the stacking order of CrI₃, which shows AFM-to-FM phase transition under a certain pressure [559].

With the stacking-dependence of interlayer coupling of vdW layers, it can also be expected that integration of 2D vdW magnets to form heterostructures could provide an efficient platform for spin control and novel physical phenomena. Combining a FM monolayer supported on a AFM substrate, Tong *et al*. demonstrated a new skyrmions origin in the 2D magnets by different atomic locations in moiré (Fig. 78b) [1761]. The moiré skyrmions strongly relies on the strength of interlayer magnetic coupling and can be largely modulated by strain and interlayer translation. They also investigated the magnetic proximity effect in a 2D vdW monolayer semiconductor/ ferromagnet heterostructure with a moiré pattern by the lattice mismatch and interlayer twisting [1762]. The heterostructure is modeled by a slab consisting of a 2 × 2 supercell of BAs on a 1 × 1 unit cell of CrI₃ with a lattice mismatch of 1.3%. The different spatial variations lead to lateral modulation of magnetic
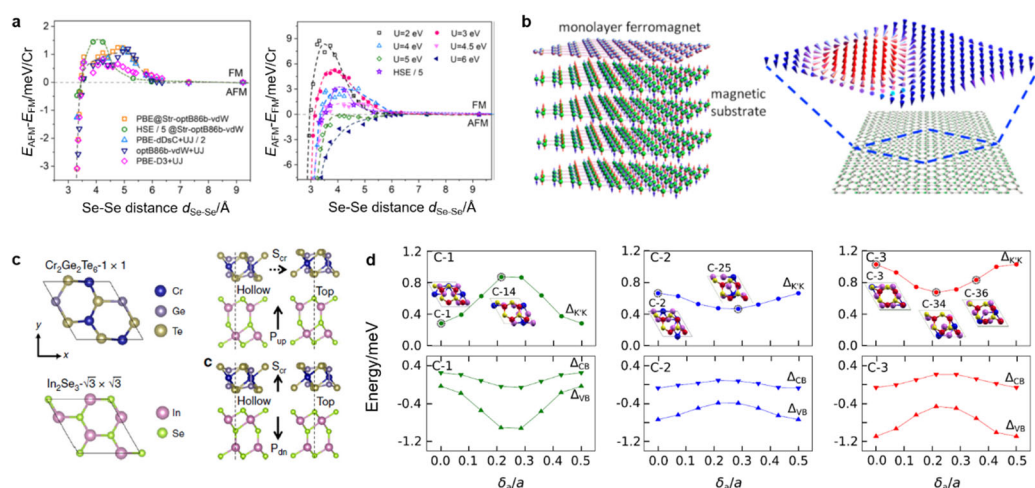
Fig. 78 **(a)** Bethe-Slater-curve-like behavior in bilayer CrSe$_2$; reproduced with permission from Ref. [1759], Copyright 2020 American Physical Society.
(b) Skyrmions in the Moiré of vdW 2D Magnets composed by a FM monolayer on an AFM substrate; reproduced with permission from Ref. [1761],
Copyright 2018 American Chemical Society. **(c)** 2D multiferroicity in vdW CrGeTe$_3$/In$_2$Se$_3$ heterostructure [572]. **(d)** Evolution of total valley splitting
($\Delta_{K'K}$, upper panels) and valance and conduction band valley splitting (Δ_{VB} and Δ_{CB}, bottom panels) for different displacements along lattice *a* of
CrI$_3$/WSe$_2$ heterostructure; reproduced with permission from Ref. [1763], Copyright 2019 American Physical Society.

proximity effect, which shows a miniband spin splitting strongly depending on the moiré periodicity.

2D vdWHs provide an ideal platform to combine materials with totally different electronic or magnetic properties together, such as multiferroics with both ferroelectric (FE) and FM properties, which possess potential abilities of regulating magnetism with electric polarization and vice versa [1764]. Gong *et al*. proposed the 2D heterostructure multiferroics by stacking 2D FM CrGeTe$_3$-1 × 1 on FE In$_2$Se$_3$- $\sqrt{3}$ × $\sqrt{3}$, leading to all-atomic multiferroicity (Fig. 78c) [572]. The magnetism of CrGeTe$_3$ is switched as the polarization of In$_2$Se$_3$ reversed, which can be achieved *via* lateral displacement of the middle most Se layer. The corresponding In$_2$Se$_3$ exhibits a tunable magnetic semiconductor for the proximity effect of CrGeTe$_3$. They chose U = 0.5 eV, J = 0.0 eV to reproduce the ferromagnetic ground state and small band gap of CrGeTe$_3$, which is consistent with experimental results [512]. Moreover, the interlayer magnetic coupling of 2D FM materials is tuned by changing electric polarization direction of 2D FE, which results from the dramatic band alignment changing by the strong built-in electric field in FE materials [1765].

The magnetic proximity effect of 2D ferromagnetisms could also be applied to manipulate the valley of TMDs by forming vdWHs for the strong charge transfer across the interface and spin-orbit coupling. The coupling between valley spin and the magnetic field of 2D FM substrates dominate the total valley splitting, which can be tuned by twisting, gating [1766] and interfacial superposition (Fig. 78d) [1763]. Zhang *et al*. reported large valley splitting of MoTe$_2$/CrBr$_3$, band inversion in WSe$_2$/CrBr$_3$ and MoTe$_2$/CrBr$_3$, and valley-polarized quantum anomalous Hall effect in WSe$_2$/CrBr$_3$ using first-principles calculations and the *kp* model [1767]. The generalized gradient approximation (GGA) + *U* method was employed to better

describe transition metals. Therefore, integration of TMDs with 2D FM materials can deepen the understanding of the magnetic proximity effect on the valley degeneracy lifting in TMD-based heterostructures, and provide valuable guidelines in valleytronic applications. In addition, the introduced extra superexchange paths can vastly increase the intralayer FM coupling of 2D ferromagnets [1768].

5.3.4 External field modulation

The magnetic ground state and exchange coupling strength of 2D magnetic materials are very sensitive to Fermi level, charge distribution, orbital occupation, symmetry, energy level, and *etc*. There have been theoretically proposed many strategies to modulate these parameters, including strain engineering, external electric/magnetic field and optical controlling.

After 2D layered magnets are exfoliated from their bulk forms or grown by MBE/CVD methods in experiments, they will be transferred on substrates, such as SiO$_2$ or other materials for further electric/magnetic measurement. The lattice mismatch between 2D magnets and substrates is thus inevitable and will introduce strain effect into 2D magnets. From the structural view, increasing biaxial tensile strain can be used as an effective strategy to increase the bond length and bond angle between magnetic atoms, while increasing compression strain will have the opposite effect. Therefore, the strain effect undoubtedly changes the orbital hybridization and determines the magnetic exchange parameters, which could cause FM and AFM phase transition. In this regard, it was theoretically reported that the biaxial tensile strain can lead to FM character in NbS$_2$ and NbSe$_2$ and the predicted T_c is above room temperature (Fig. 79a) [1769]. In addition, the tensile strain can significantly enhance the induced magnetic moments, resulting to a half-metallic character and a strong spin polarization near Fermi level. On the contrary, applying a compressive strain causes FM to AFM transition in
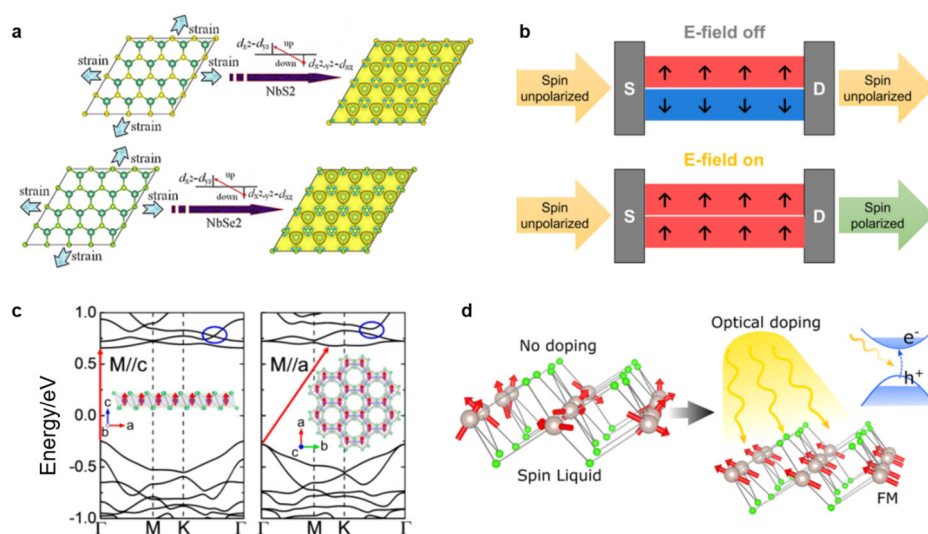
Fig. 79 **(a) Tensile strain switched ferromagnetism in layered NbS₂ and NbSe₂; reproduced with permission from Ref. [1769], Copyright 2012 American Chemical Society. (b) Bilayer CrI₃ based spin field-effect transistor with generation of spin-polarized current controlled by an electric field; reproduced with permission from Ref. [1771], Copyright 2020 American Chemical Society. (c) Band structures of monolayer CrI₃ with magnetic moment along the out-of-plane and in-plane, respectively; reproduced with permission from Ref. [1777], Copyright 2018 American Chemical Society. (d) Schematic plot of optically modulated magnetism in RuCl₃ monolayer; reproduced with permission from Ref. [565], Copyright 2019 American Chemical Society.**

monolayer CrX_3 (X = Cl, Br, I) and the magnetic anisotropy energy (MAE) can also be altered [1770].

In practice, it is essential to electrically control magnetism by electrostatic doping/ion liquid gating. The atomic thin 2D magnets provide a platform for electrostatic manipulating magnetic properties by changing orbital hopping, exchange splitting, crystalline splitting and carrier densities (Fig. 79b) [1771,1772]. Both electron and hole doping would render monolayer CrI_3 itinerant half-metallic, and steadily enhance the FM stability with T_c above 300 K [1773]. In addition, Wang *et al*. theoretically investigated that MAE of Fe_3GeTe_2 monolayer shows strongly oscillating behavior upon electron doping, totally different with hole-doping, which is caused by the great changes in the band structure around Fermi energy under electron doping. The $Te(p_z)$−$Fe(d_{z2})$ bond states occupation and splitting play a critical role in modulating MAE [1774]. Using MC simulations and mean-field solutions, Lei *et al*. predicted that vdW AFM bilayers with weak interlayer and strong intralyer FM coupling possess strong magnetoelectric response, which can be detected in dual-gated devices [1775]. Moreover, electric field can also induce half-metallicity in magnetic vdW $CrI_3/CrGeTe_3$ heterostructures by electric-controlled band alignment in the asymmetric band structures [1776].

It is natural to use magnetic field to control the magnetism in 2D magnets. On one hand, the Zeeman spin splitting induced by external magnetic field usually induces magnetic ordering. On the other hand, the external magnetic field can also make spin reoriented and thus determines the magnetic ground state. Jiang *et al*. theoretically demonstrated a direct-to-indirect bandgap transition by rotating the spin order of CrI_3 from out-of-plane to in-plane (Fig. 79c), and the Fermi surface can be significantly

changed with different magnetic directions, leading to giant anisotropic magnetoresistance [1777]. Using an optical-excited double-band-edge transition model, Guo *et al*. proposed that reversing the magnetization can switch the band alignment of $CrBr_3/CrCl_3$ heterostruction, which realizes the interlayer magnetic order and spin polarized band structure coupling [1778].

Optically modulating magnetic properties is also a promising strategy for its no destruction of geometrical and electronic structures and easily control. Based on first-principles calculations, Tian *et al*. predicted that the coupling between light and magnetism in monolayer $RuCl_3$ is strong, and in turn modulates its magnetic order (Fig. 79d). Both of the ferromagnetism and T_c are significantly enhanced with optical doping e-h pair density increasing, and particularly, T_c is close to room temperature as e-h concentration reaches 3×10^{13} cm^{-2} [565]. Using real-time time-dependent density functional theory (DFT) simulations, He and coworkers demonstrated that ultrafast spin-selective charge transfer between magnetic sublattices can be directly induced by laser pulses in a few femtoseconds in 2D MXenes [1021]. The magnetic structures show dramatic changes under laser excitation. In addition, they also studied that laser pulses can also induce significant spin injection from Fe_3GeTe_2 to 2D nonmagnetic layers within a few femtoseconds [1779].

5.3.5 2D topological magnets

2D materials with coexisting quantum phases provide exciting platforms for exploring novel physic phenomena induced by the interplay between topology and magnetism. Intrinsic topological magnets offer a promising platform for both exploring fundamental physical mechanism and developing next-generation technologies based on topological quantum states. Otrokov *et al*. predicted by ab initio calculations and further
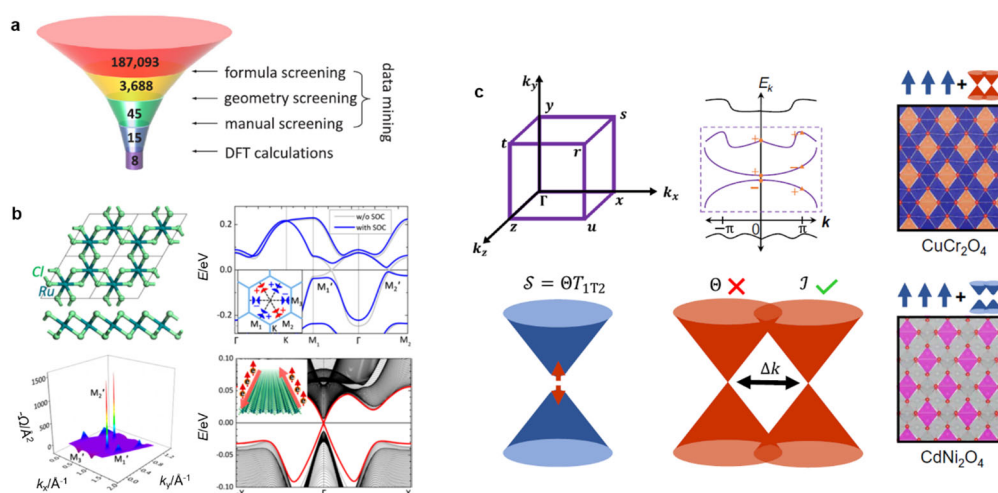
Fig. 80 (a) Schematic diagram of the search procedure for 2D FM materials; reproduced with permission from Ref. [1783], Copyright 2018 American Physical Society. (b) Quantum anomalous Hall state in FM monolayer RuCl$_3$, including atomic structure (upper left) and band structure with (blue line) and without spin orbital coupling (gray line) (upper right) of monolayer RuCl$_3$, Berry curvature in first Brillouin zone (left lower), and band structure of RuCl$_3$ nanoribbon with a width of 386 Å (low right); reproduced with permission from Ref. [1784], Copyright 2018 American Chemical Society. (c) Magnetic topological materials [1786].

confirm in experiments the realization of an AFM topological insulator (TI) in the layered vdW compound MnBi$_2$Te$_4$ [1780]. Li *et al*. also predicted a series of vdW layered MnBi$_2$Te$_4$-related materials showing intralayer FM and interlayer AFM exchange interactions [548]. Moreover, the electronic, magnetic and topological transitions in MnBi$_2$Te$_4$ are thickness dependent and can be magnetically controlled [1030].

5.3.6 High throughput search magnetism

According to the above reviews, there are tremendous excellent magnetic and electronic properties in 2D magnetic materials, which, however, always possess low Curie temperature, hindering further development of magnetic materials in spintronic applications. Currently, it is still an expensive process for the discovery of magnetic materials in experiment. Therefore, searching 2D ferromagnetic materials with T_c approaching room temperature is thus an urgent and challenging task. Theoretical simulation offers a more effective way to explore 2D intrinsic FM materials. The recent emergence of first-principle high-throughput calculations and machine learning (ML) techniques greatly accelerate such a process [1781,1782]. Zhu *et al*. performed a systematic search for 2D FM materials in the Inorganic Crystal Structure Database (ICSD) [1783]. From 187,093 entries in the ICSD, they identified eight 2D FM materials (Fig. 80a), including three known structural prototypes and two 2D experimentally-discovered FM materials. More importantly, they found two new prototypes of 2D ferromagnets and one promising candidate Cr$_3$Te$_4$ with the predicted T_c much higher than other 2D FM materials. In addition, Liu and co-authors carried out high-throughput first-principles screening to yield 89 magnetic monolayers including 56 FM and 33 AFM materials [1784]. Interestingly, 2D FM monolayers with high T_c and fascinating electronic phases were identified, including coexisting quantum anomalous Hall and valley Hall effect in

single materials and half-metals (Fig. 80b). In the later studies, combining advanced ML technologies with high-throughput DFT calculations, Lu *et al*. developed an adaptive framework to accelerate the search of 2D intrinsic ferromagnets [1785]. They screened out about 90 FM materials with both satisfactory bandgap and outstanding thermodynamic stability, and further set up a database containing 1459 2D magnets.

Beyond 2D FM materials, the discovery of MnBi$_2$Te$_4$, a typical intrinsic magnetic topological material, has motivates the exploring of systems with coexisting magnetism and topology. Frey *et al*. computed 27000 different magnetic orderings for more than 3000 transition metal oxides, and determined the ground states to estimate the effective exchange parameters and T_c [1786]. After performing high-throughput band topology analysis of centrosymmetric magnetic materials and calculating topological invariants, they identified 18 new potential FM topological semimetals (spinel CuCr$_2$O$_4$), axion insulators (spinel CdNi$_2$O$_4$), and AFM topological insulators (e.g., tetragonal Ca$_2$MnO$_3$) (Fig. 80c).

6 Conclusions and outlooks

Since 2004, it has been witnessed the development of 2D materials from springing up to prosperity not only in fundamental scientific research but also in promising technological innovation in various disciplines including condensed matter physics, materials science, chemistry and electronic engineering. The unique properties and striking applications of 2D materials have revolutionized our understanding on how they will make a big difference as compared to the bulk materials and 0D/1D nanomaterials. It is worth pointing out that on the basis of previous studies, some major breakthroughs have been made in this promising field from all aspects. In this Review, we have summarized the recent

progress in the field of 2D materials with a particular emphasis on that in the last five years. We have categorized the recent progress on 2D materials in the following sections: synthetic methods, properties, potential applications and theoretical calculations/simulations.

Although significant progress has been made in the field of 2D materials in the last decade, it is no doubt that this rapidly growing field still faces some challenges. First, one of the big challenges is how to synthesize 2D materials with desired structural characteristics in a highly controllable manner since the properties and applications of 2D materials are highly related to all these structural characteristics, such as size, layer number, doping, defects, vacancies, inter layer spacing, crystallinity and phase. For example, the phase of 2D materials has been considered as one of the critical parameters to affect their properties and application performance in recent years. However, it is still difficult to precisely engineer the purity of certain phase, the ratio of different phases, or phase patterning of 2D materials, *i.e.*, the research topics on phase engineering of nanomaterials (PEN), which are believed to be important for their further applications in catalysis and electronics. Second, another big challenge in 2D materials is how to realize the massive production of 2D materials or wafer-scale growth of high-quality 2D thin films for practical applications. The current wet-chemical synthesis and liquid exfoliation methods can produce 2D materials with promising performances in catalysis or batteries, but their production still cannot meet the requirement for practical industrial applications. In addition, the large lateral size and atomic thickness of 2D materials endow them with many excellent properties but also inevitably make them very easy to stack together during the storage and further usage, which will dramatically deactivate their advantages. Therefore, the third big challenge is how to prevent the stacking or aggregation of 2D nanosheets in storage and application processes and thus avoid the degradation of the excellent properties and performances of 2D materials. Considering that 2D materials have been widely explored for a wide range of applications, challenges still exist for each specific application. Although 2D materials indeed have the great potential to exceed the Moore's law by making shorter-channel transistor or constructing monolithic 3D integrated CMOS circuits based on 2D materials, the more realistic goal is to integrate 2D materials with silicon chips rather than to replace silicon. Fourthly, one of the big challenges for the application of 2D materials in electronics is to make the 2D materials processing processes compatible with current silicon semiconductor production technology. Although 2D materials have been demonstrated to be promising in construction of next-generation high-performance photodetectors, most of 2D materials have large bandgap and only can be used for fabrication of photodetectors to detect visible to near infrared light. Fifth, one of the big challenges for the application of 2D materials in optoelectronics is to design and synthesize narrow bandgap 2D semiconductors

for fabrication of photodetectors to detect infrared light, especially for the long-wave infrared light. Although 2D materials have been demonstrated to be excellent electrocatalysts in a number of reactions, such as HER, OER and CO₂RR, the performance of most of the 2D material-based electrocatalysts degrades fast in long term stability test, which is one of the major limitations for their practical applications in electrocatalysis. Sixth, one of the big challenges for the application of 2D materials in catalysis is to achieve long term stability in catalytic reactions. Although 2D materials have been extensively explored for energy storage, the understanding of the storage mechanisms is still insufficient and the energy storage devices normally are not very stable for long-term operation. Seventh, the challenge for the application of 2D materials in energy storage lies in how to understand and control of the storage mechanisms and achieive long-term electrochemical stability. Eeighth, although 2D materials have been widely used for solar cells, one of the major challenges for the application of 2D materials in solar cells is to synthesize diverse 2D materials with functional agents to bring in synergistic effects with eliminated nonradiative charge recombination and good compatibility with neighboring layers. Although 2D materials have shown promising application in biomedicine, the biomedical applications of 2D biomaterials still suffers from the critical issue of precise structure/composition control of 2D nanosystems for the strict biomedical utilization. Ninth, one of the big challenges for 2D materials in biologoical applciaiton is to precisely engeer the structure and compsotion of 2D materials for specific biologoical applciaiton. 2D material-based sensing platforms have been successfully applied in environmental monitoring, biochemical analysis, disease diagnosis, food safety, public health safety, and even homeland security due to their charming properties, such as excellent sensitivity, selectivity, stability and reproducibility. With the increasing practical detection need, 2D material-based sensing platforms face challenges. Tenth, one of the big challenges for the application of 2D materials in sensing platforms is to understand the interaction mechanism between target molecules and 2D materials, which is important for constructing high-performance sensing platforms. Eleventh, for the application of 2D materials in flexible electronics, one of the major challenges is how to achieve the processing compatibility of 2D materials with plastic substrates. Twelfth, for 2D materials in environmental application is how to reduce the interferences in the operation process, e.g., swelling, fouling and degradation, to maintain the long-term performance of the 2D materials in practical applications. Proton permeation provides 2D crystal lattice as a novel subatomic sieve. However, there is still a long path towards the real applications. Last but not least, one of the big challenges for the application of 2D materials in proton permeation is how to realize the scalable production of high quality 2D materials, their wafer-scale transfer techniques and compatibility with support proton conductive substrate.

Although research on 2D materials has been exponentially growing in last seventeen years, the history of 2D materials is still relatively short in comparison with conventional bulk materials and 0D/1D nanomaterials. Therefore, studies on 2D materials are still far from mature. Without a doubt, there are many opportunities in this bright research field on various aspects and thus lots of works can be carried out in the near future. First, the most straightforward direction in this field is to prepare and explore novel 2D materials despite the fact that a large number of 2D materials have been reported so far. Given that 2D materials are defined by the dimension, it is reasonable to predict that all of the existing materials have the possibility to be grown as 2D materials once proper synthetic methods are established. New 2D materials may exhibit unusual but important properties and innovative functionalities. Secondly, the growth of high-quality wafer-scale 2D thin films with controllable layer number is another promising research direction in this field. The ability to grow high-quality wafer-scale 2D thin films is critically important for their future applications in the large-area integration of 2D materials in electronics, optoelectronics and flexible electronics. Recent studies have successfully demonstrated the growth of high-quality wafer-scale 2D thin films, such as graphene, h-BN and MoS_2, by properly optimizing the synthetic conditions of the CVD technique. As a consequence, it is believed that many other 2D materials could also be grown into wafer-scale 2D thin films with high quality in the future. Third, another promising direction in this field is to precisely control or engineer the phase of novel 2D materials, *i.e.*, an important research topic of PEN. The crystal phase of 2D materials has been proven to play an important role in determining their properties and applications. Although some 2D materials with unconventional phases have been synthesized and explored in recent years, the study on phase of 2D materials is still in its early stage. To this end, more 2D materials with new phases would be synthesized in the near future. Fourth, exploring new properties and applications for 2D materials is one of the promising directions. For example, 2D materials have been found to show unexpected appealing magnetic properties in recent years. Most current research on 2D materials only focuses on studying certain properties or applications. Therefore, many new properties and innovative applications of 2D materials are still waiting to be explored in the near future. Last but not least, given that many 2D materials have been demonstrated to be promising in a given application in laboratory, one of the promising directions in this field is to push forward the replacement of some key commercialized materials by 2D materials in real products or by integrating 2D materials with existing technologies or products to further optimize their performances. For example, wafer-scale semiconducting 2D thin films have been used as active channel materials to fabricate integrated circuits. Therefore, wafer-scale high-quality 2D thin films could be used as active materials in the construction of next-generation monolithic 3D integrated CMOS circuits and high-performance room-temperature infrared imaging sensor systems in the near future.

References

(1)　Novoselov, K. S.; Geim, A. K.; Morozov, S. V.; Jiang, D.; Zhang, Y.; Dubonos, S. V.; Grigorieva, I. V.; Firsov, A. A. *Science* **2004**, *306*, 666. doi: 10.1126/science.1102896

(2)　Tan, C.; Cao, X.; Wu, X. J.; He, Q.; Yang, J.; Zhang, X.; Chen, J.; Zhao, W.; Han, S.; Nam, G. H.; *et al. Chem. Rev.* **2017**, *117*, 6225. doi: 10.1021/acs.chemrev.6b00558

(3)　Zhang, H. *ACS Nano* **2015**, *9*, 9451. doi: 10.1021/acsnano.5b05040

(4)　Mannix, A. J.; Kiraly, B.; Hersam, M. C.; Guisinger, N. P. *Nat. Rev. Chem.* **2017**, *1*, 0014. doi: 10.1038/s41570-016-0014

(5)　Akinwande, D.; Huyghebaert, C.; Wang, C.-H.; Serna, M. I.; Goossens, S.; Li, L.-J.; Wong, H. S. P.; Koppens, F. H. L. *Nature* **2019**, *573*, 507. doi: 10.1038/s41586-019-1573-9

(6)　Xiao, X.; Wang, H.; Urbankowski, P.; Gogotsi, Y. *Chem. Soc. Rev.* **2018**, *47*, 8744. doi: 10.1039/C8CS00649K

(7)　Tan, C.; Lai, Z.; Zhang, H. *Adv. Mater.* **2017**, *29*, 1701392. doi: 10.1002/adma.201701392

(8)　Zhai, W.; Xiong, T.; He, Z.; Lu, S.; Lai, Z.; He, Q.; Tan, C.; Zhang, H. *Adv. Mater.* **2021**, 2006661. doi: 10.1002/adma.202006661

(9)　Xiong, Y.; Wu, H.; Gao, J.; Chen, W.; Zhang, J.; Yue, Y. *Acta Phys. -Chim. Sin.* **2019**, *35*, 1150. doi: 10.3866/PKU.WHXB201901002

(10)　Liu, Q.; Wang, X.; Wang, J.; Huang, X. *Acta Phys. -Chim. Sin.* **2019**, *35*, 1099. doi: 10.3866/PKU.WHXB201811005

(11)　Zhao, C.; Tan, C.; Lien, D.-H.; Song, X.; Amani, M.; Hettick, M.; Nyein, H. Y. Y.; Yuan, Z.; Li, L.; Scott, M. C.; *et al. Nat. Nanotechnol.* **2020**, *15*, 53. doi: 10.1038/s41565-019-0585-9

(12)　Koman, V. B.; Liu, P.; Kozawa, D.; Liu, A. T.; Cottrill, A. L.; Son, Y.; Lebron, J. A.; Strano, M. S. *Nat. Nanotechnol.* **2018**, *13*, 819. doi: 10.1038/s41565-018-0194-z

(13)　Conti, S.; Pimpolari, L.; Calabrese, G.; Worsley, R.; Majee, S.; Polyushkin, D. K.; Paur, M.; Pace, S.; Keum, D. H.; Fabbri, F.; *et al. Nat. Commun.* **2020**, *11*, 3566. doi: 10.1038/s41467-020-17297-z

(14)　Zhu, W.; Low, T.; Wang, H.; Ye, P.; Duan, X. *2D Mater.* **2019**, *6*, 032004. doi: 10.1088/2053-1583/ab1ed9

(15)　Amani, M.; Tan, C.; Zhang, G.; Zhao, C.; Bullock, J.; Song, X.; Kim, H.; Shrestha, V. R.; Gao, Y.; Crozier, K. B.; *et al. ACS Nano* **2018**, *12*, 7253. doi: 10.1021/acsnano.8b03424

(16)　Mak, K. F.; Shan, J. *Nat. Photon.* **2016**, *10*, 216. doi: 10.1038/nphoton.2015.282

(17)　Huo, C.; Cai, B.; Yuan, Z.; Ma, B.; Zeng, H. *Small Methods* **2017**, *1*, 1600018. doi: 10.1002/smtd.201600018

(18)　Cheng, Z.; Cao, R.; Wei, K.; Yao, Y.; Liu, X.; Kang, J.; Dong, J.; Shi, Z.; Zhang, H.; Zhang, X. *Adv. Sci.* **2021**, *8*, 2003834.

doi: 10.1002/advs.202003834

(19) Li, J.; Ding, Y.; Zhang, D. W.; Zhou, P. *Acta Phys. -Chim. Sin.* **2019,** *35*, 1058. doi: 10.3866/PKU.WHXB201812020

(20) Ye, M.; Zha, J.; Tan, C.; Crozier, K. B. *Appl. Phys. Rev.* **2021,** *8*, 031303. doi: 10.1063/5.0049633

(21) Wang, H.; Liu, X.; Niu, P.; Wang, S.; Shi, J.; Li, L. *Matter* **2020,** *2*, 1377. doi: 10.1016/j.matt.2020.04.002

(22) Li, Z.; Zhang, X.; Cheng, H.; Liu, J.; Shao, M.; Wei, M.; Evans, D. G.; Zhang, H.; Duan, X. *Adv. Energy Mater.* **2020,** *10*, 1900486. doi: 10.1002/aenm.201900486

(23) Han, S.; Zhou, K.; Yu, Y.; Tan, C.; Chen, J.; Huang, Y.; Ma, Q.; Chen, Y.; Cheng, H.; Zhou, W. *Research* **2019,** *2019*, 6439734. doi: 10.34133/2019/6439734

(24) Chia, X.; Pumera, M. *Nat. Catal.* **2018,** *1*, 909. doi: 10.1038/s41929-018-0181-7

(25) Tan, C.; Luo, Z.; Chaturvedi, A.; Cai, Y.; Du, Y.; Gong, Y.; Huang, Y.; Lai, Z.; Zhang, X.; Zheng, L.; *et al. Adv. Mater.* **2018,** *30*, 1705509. doi: 10.1002/adma.201705509

(26) Chen, C.; Mao, S.; Tan, C.; Wang, Z.; Ge, Y.; Ma, Q.; Zhang, X.; Qi, G.; Xu, J.; Fan, Z.; *et al. Angew. Chem. Int. Ed.* **2021,** *60*, 15556. doi: 10.1002/anie.202104028

(27) Pomerantseva, E.; Gogotsi, Y. *Nat. Energy* **2017,** *2*, 17089. doi: 10.1038/nenergy.2017.89

(28) Kato, K.; Sayed, F. N.; Babu, G.; Ajayan, P. M. *2D Mater.* **2018,** *5*, 025016. doi: 10.1088/2053-1583/aaad29

(29) Zhang, P.; Wang, F.; Yu, M.; Zhuang, X.; Feng, X. *Chem. Soc. Rev.* **2018,** *47*, 7426. doi: 10.1039/C8CS00561C

(30) Zhou, Z.; Ma, L.; Tan, C. *Chem. J. Chin. Univ.* **2021,** *42*, 662. doi: 10.7503/cjcu20200609

(31) Yi, F.; Ren, H.; Shan, J.; Sun, X.; Wei, D.; Liu, Z. *Chem. Soc. Rev.* **2018,** *47*, 3152. doi: 10.1039/C7CS00849J

(32) Yun, Q.; Li, L.; Hu, Z.; Lu, Q.; Chen, B.; Zhang, H. *Adv. Mater.* **2020,** *32*, 1903826. doi: 10.1002/adma.201903826

(33) Zhang, X.; Hou, L.; Ciesielski, A.; Samorì, P. *Adv. Energy Mater.* **2016,** *6*, 1600671. doi: 10.1002/aenm.201600671

(34) Zhao, J.; Xu, Z.; Zhou, Z.; Xi, S.; Xia, Y.; Zhang, Q.; Huang, L.; Mei, L.; Jiang, Y.; Gao, J.; *et al. ACS Nano* **2021,** *15*, 10597. doi: 10.1021/acsnano.1c03341

(35) Bati, A. S. R.; Batmunkh, M.; Shapter, J. G. *Adv. Energy Mater.* **2020,** *10*, 1902253. doi: 10.1002/aenm.201902253

(36) Kakavelakis, G.; Kymakis, E.; Petridis, K. *Adv. Mater. Interfaces* **2018,** *5*, 1800339. doi: 10.1002/admi.201800339

(37) Das, S.; Pandey, D.; Thomas, J.; Roy, T. *Adv. Mater.* **2019,** *31*, 1802722. doi: 10.1002/adma.201802722

(38) Tan, C.; Zhao, W.; Chaturvedi, A.; Fei, Z.; Zeng, Z.; Chen, J.; Huang, Y.; Ercius, P.; Luo, Z.; Qi, X.; *et al. Small* **2016,** *12*, 1866.

doi: 10.1002/smll.201600014

(39) Kostarelos, K. *Nat. Rev. Mater.* **2016,** *1*, 16084. doi: 10.1038/natrevmats.2016.84

(40) Cheng, L.; Wang, X.; Gong, F.; Liu, T.; Liu, Z. *Adv. Mater.* **2020,** *32*, 1902333. doi: 10.1002/adma.201902333

(41) Lin, H.; Chen, Y.; Shi, J. *Adv. Sci.* **2018,** *5*, 1800518. doi: 10.1002/advs.201800518

(42) Liu, J.; Chen, C.; Zhao, Y. *Adv. Mater.* **2019,** *31*, 1804386. doi: 10.1002/adma.201804386

(43) Sun, W.; Wu, F.-G. *Chem. Asian J.* **2018,** *13*, 3378. doi: 10.1002/asia.201800851

(44) Zhou, Z.; Wang, X.; Zhang, H.; Huang, H.; Sun, L.; Ma, L.; Du, Y.; Pei, C.; Zhang, Q.; Li, H.; *et al. Small* **2021,** *17*, 2007486. doi: 10.1002/smll.202007486

(45) Zhou, Z.; Li, B.; Shen, C.; Wu, D.; Fan, H.; Zhao, J.; Li, H.; Zeng, Z.; Luo, Z.; Ma, L.; *et al. Small* **2020,** *16*, 2004173. doi: 10.1002/smll.202004173

(46) Yang, S.; Jiang, C.; Wei, S.-H. *Appl. Phys. Rev.* **2017,** *4*, 021304. doi: 10.1063/1.4983310

(47) Meng, Z.; Stolz, R. M.; Mendecki, L.; Mirica, K. A. *Chem. Rev.* **2019,** *119*, 478. doi: 10.1021/acs.chemrev.8b00311

(48) Jiang, H.; Zheng, L.; Liu, Z.; Wang, X. *InfoMat* **2020,** *2*, 1077. doi: 10.1002/inf2.12072

(49) Anichini, C.; Czepa, W.; Pakulski, D.; Aliprandi, A.; Ciesielski, A.; Samorì, P. *Chem. Soc. Rev.* **2018,** *47*, 4860. doi: 10.1039/c8cs00417j

(50) Balasubramaniam, B.; Singh, N.; Kar, P.; Tyagi, A.; Prakash, J.; Gupta, R. K. *Mol. Syst. Des. Eng.* **2019,** *4*, 804. doi: 10.1039/C8ME00116B

(51) Wang, Z.; Mi, B. *Environ. Sci. Technol.* **2017,** *51*, 8229. doi: 10.1021/acs.est.7b01466

(52) Chen, B.; Bi, H.; Ma, Q.; Tan, C.; Cheng, H.; Chen, Y.; He, X.; Sun, L.; Lim, T.-T.; Huang, L.; *et al. Sci. China Mater.* **2017,** *60*, 1102. doi: 10.1007/s40843-017-9150-7

(53) Sun, Y.; Li, Y. *Chemosphere* **2021,** *271*, 129578. doi: 10.1016/j.chemosphere.2021.129578

(54) Yu, Y.; Ma, Q.; Tan, C.; Wang, H.; Hu, Z.; Zhang, Q.; Zhang, H.; Zhang, B. *EcoMat* **2020,** *2*, e12041. doi: 10.1002/eom2.12041

(55) Manzeli, S.; Ovchinnikov, D.; Pasquier, D.; Yazyev, O. V.; Kis, A. *Nat. Rev. Mater.* **2017,** *2*, 17033. doi: 10.1038/Natrevmats.2017.33

(56) Huang, H.; Zha, J.; Li, S.; Tan, C. *Chin. Chem. Lett.* **2021,** doi: 10.1016/j.cclet.2021.06.004

(57) Zhang, J.; Tan, B.; Zhang, X.; Gao, F.; Hu, Y.; Wang, L.; Duan, X.; Yang, Z.; Hu, P. *Adv. Mater.* **2021,** *33*, 2000769. doi: 10.1002/adma.202000769

(58) Caldwell, J. D.; Aharonovich, I.; Cassabois, G.; Edgar, J. H.; Gil, B.; Basov, D. N. *Nat. Rev. Mater.* **2019,** *4*, 552. doi: 10.1038/s41578-019-0124-1

(59) Li, Y.; Xu, L.; Liu, H.; Li, Y. *Chem. Soc. Rev.* **2014,** *43*, 2572. doi: 10.1039/C3CS60388A

(60) Du, Y.; Zhou, W.; Gao, J.; Pan, X.; Li, Y. *Acc. Chem. Res.* **2020,** *53*, 459. doi: 10.1021/acs.accounts.9b00558

(61) Miró, P.; Ghorbani-Asl, M.; Heine, T. *Angew. Chem. Int. Ed.* **2014,** *53*, 3015. doi: 10.1002/anie.201309280

(62) Pi, L.; Li, L.; Liu, K.; Zhang, Q.; Li, H.; Zhai, T. *Adv. Energy Mater.* **2019,** *29*, 1904932. doi: 10.1002/adfm.201904932

(63) Si, J.; Yu, J.; Shen, Y.; Zeng, M.; Fu, L. *Small Struct.* **2021,** *2*, 2000101. doi: 10.1002/sstr.202000101

(64) Lin, Z.; Wang, C.; Chai, Y. *Small* **2020,** *16*, 2003319. doi: 10.1002/smll.202003319

(65) Mannix, A. J.; Zhang, Z.; Guisinger, N. P.; Yakobson, B. I.; Hersam, M. C. *Nat. Nanotechnol.* **2018,** *13*, 444. doi: 10.1038/s41565-018-0157-4

(66) Yang, T.; Song, T. T.; Callsen, M.; Zhou, J.; Chai, J. W.; Feng, Y. P.; Wang, S. J.; Yang, M. *Adv. Mater. Interfaces* **2019,** *6*, 1801160. doi: 10.1002/admi.201801160

(67) Kumbhakar, P.; Chowde Gowda, C.; Mahapatra, P. L.; Mukherjee, M.; Malviya, K. D.; Chaker, M.; Chandra, A.; Lahiri, B.; Ajayan, P. M.; Jariwala, D.; *et al. Mater. Today* **2021,** *45*, 142. doi: 10.1016/j.mattod.2020.11.023

(68) Lv, L.; Yang, Z.; Chen, K.; Wang, C.; Xiong, Y. *Adv. Energy Mater.* **2019,** *9*, 1803358. doi: 10.1002/aenm.201803358

(69) Chen, C.; Tao, L.; Du, S.; Chen, W.; Wang, Y.; Zou, Y.; Wang, S. *Adv. Energy Mater.* **2020,** *30*, 1909832. doi: 10.1002/adfm.201909832

(70) Wang, Y.; Liu, L.; Ma, T.; Zhang, Y.; Huang, H. *Adv. Funct. Mater.* **2021,** *31*, 2102540. doi: 10.1002/adfm.202102540

(71) Wang, Y.; Zhang, R.; Zhang, Z.; Cao, J.; Ma, T. *Adv. Mater. Interfaces* **2019,** *6*, 1901429. doi: 10.1002/admi.201901429

(72) Naguib, M.; Mochalin, V. N.; Barsoum, M. W.; Gogotsi, Y. *Adv. Mater.* **2014,** *26*, 992. doi: 10.1002/adma.201304138

(73) Chen, Y.; Fan, Z.; Zhang, Z.; Niu, W.; Li, C.; Yang, N.; Chen, B.; Zhang, H. *Chem. Rev.* **2018,** *118*, 6409. doi: 10.1021/acs.chemrev.7b00727

(74) Payamyar, P.; King, B. T.; Öttinger, H. C.; Schlüter, A. D. *Chem. Commun.* **2016,** *52*, 18. doi: 10.1039/C5CC07381B

(75) Yang, F.; Cheng, S.; Zhang, X.; Ren, X.; Li, R.; Dong, H.; Hu, W. *Adv. Mater.* **2018,** *30*, 1702415. doi: 10.1002/adma.201702415

(76) Jiang, Q.; Zhou, C.; Meng, H.; Han, Y.; Shi, X.; Zhan, C.; Zhang, R. *J. Mater. Chem. A* **2020,** *8*, 15271. doi: 10.1039/d0ta00468e

(77) Zhao, M.; Lu, Q.; Ma, Q.; Zhang, H. *Small Methods* **2017,** *1*, 1600030. doi: 10.1002/smtd.201600030

(78) Li, X.; Yadav, P.; Loh, K. P. *Chem. Soc. Rev.* **2020,** *49*, 4835. doi: 10.1039/D0CS00236D

(79) Bhunia, S.; Deo, K. A.; Gaharwar, A. K. *Adv. Energy Mater.* **2020,** *30*, 2002046. doi: 10.1002/adfm.202002046

(80) Dou, L.; Wong, A. B.; Yu, Y.; Lai, M.; Kornienko, N.; Eaton, S. W.; Fu, A.; Bischak, C. G.; Ma, J.; Ding, T.; *et al. Science* **2015,** *349*, 1518. doi: 10.1126/science.aac7660

(81) Zhang, F.; Lu, H.; Tong, J.; Berry, J. J.; Beard, M. C.; Zhu, K. *Energy Environ. Sci.* **2020,** *13*, 1154. doi: 10.1039/C9EE03757H

(82) Leng, K.; Abdelwahab, I.; Verzhbitskiy, I.; Telychko, M.; Chu, L.; Fu, W.; Chi, X.; Guo, N.; Chen, Z.; Chen, Z.; *et al. Nat. Mater.* **2018,** *17*, 908. doi: 10.1038/s41563-018-0164-8

(83) Huang, C.; Du, Y.; Wu, H.; Xiang, H.; Deng, K.; Kan, E. *Phys. Rev. Lett.* **2018,** *120*, 147601. doi: 10.1103/PhysRevLett.120.147601

(84) Sun, J.; Zhong, X.; Cui, W.; Shi, J.; Hao, J.; Xu, M.; Li, Y. *Phys. Chem. Chem. Phys.* **2020,** *22*, 2429. doi: 10.1039/C9CP05084A

(85) Yu, X.; Yu, P.; Wu, D.; Singh, B.; Zeng, Q.; Lin, H.; Zhou, W.; Lin, J.; Suenaga, K.; Liu, Z.; *et al. Nat. Commun.* **2018,** *9*, 1545. doi: 10.1038/s41467-018-03935-0

(86) Li, L.; Wang, W.; Chai, Y.; Li, H.; Tian, M.; Zhai, T. *Adv. Energy Mater.* **2017,** *27*, 1701011. doi: 10.1002/adfm.201701011

(87) Zhang, G.; Amani, M.; Chaturvedi, A.; Tan, C.; Bullock, J.; Song, X.; Kim, H.; Lien, D.-H.; Scott, M. C.; Zhang, H.; *et al. Appl. Phys. Lett.* **2019,** *114*, 253102. doi: 10.1063/1.5097825

(88) Wu, W.; Qiu, G.; Wang, Y.; Wang, R.; Ye, P. *Chem. Soc. Rev.* **2018,** *47*, 7203. doi: 10.1039/C8CS00598B

(89) Wang, Y.; Qiu, G.; Wang, R.; Huang, S.; Wang, Q.; Liu, Y.; Du, Y.; Goddard, W. A.; Kim, M. J.; Xu, X.; *et al. Nat. Electron.* **2018,** *1*, 228. doi: 10.1038/s41928-018-0058-4

(90) Qin, J.; Qiu, G.; Jian, J.; Zhou, H.; Yang, L.; Charnas, A.; Zemlyanov, D. Y.; Xu, C.-Y.; Xu, X.; Wu, W.; *et al. ACS Nano* **2017,** *11*, 10222. doi: 10.1021/acsnano.7b04786

(91) Azam, A.; Kim, J.; Park, J.; Novak, T. G.; Tiwari, A. P.; Song, S. H.; Kim, B.; Jeon, S. *Nano Lett.* **2018,** *18*, 5646. doi: 10.1021/acs.nanolett.8b02150

(92) Desai, S. B.; Madhvapathy, S. R.; Amani, M.; Kiriya, D.; Hettick, M.; Tosun, M.; Zhou, Y.; Dubey, M.; Ager Iii, J. W.; Chrzan, D.; *et al. Adv. Mater.* **2016,** *28*, 4053. doi: 10.1002/adma.201506171

(93) Wang, C.; He, Q.; Halim, U.; Liu, Y.; Zhu, E.; Lin, Z.; Xiao, H.; Duan, X.; Feng, Z.; Cheng, R.; *et al. Nature* **2018,** *555*, 231. doi: 10.1038/nature25774

(94) Lin, Z. Y.; Liu, Y.; Halim, U.; Ding, M. N.; Liu, Y. Y.; Wang, Y. L.; Jia, C. C.; Chen, P.; Duan, X. D.; Wang, C.; *et al. Nature* **2018,** *562*, 254. doi: 10.1038/s41586-018-0574-4

(95) Shi, H.; Li, M.; Shaygan Nia, A.; Wang, M.; Park, S.; Zhang, Z.; Lohe, M. R.; Yang, S.; Feng, X. *Adv. Mater.* **2020,** *32*, 1907244. doi: 10.1002/adma.201907244

(96) Li, S.; Wang, S.; Tang, D.-M.; Zhao, W.; Xu, H.; Chu, L.; Bando, Y.; Golberg, D.; Eda, G. *Appl. Mater. Today* **2015,** *1*, 60. doi: 10.1016/j.apmt.2015.09.001

(97) Zhou, J.; Lin, J.; Huang, X.; Zhou, Y.; Chen, Y.; Xia, J.; Wang, H.; Xie, Y.; Yu, H.; Lei, J.; *et al. Nature* **2018**, *556*, 355. doi: 10.1038/s41586-018-0008-3

(98) Yu, H.; Liao, M. Z.; Zhao, W. J.; Liu, G. D.; Zhou, X. J.; Wei, Z.; Xu, X. Z.; Liu, K. H.; Hu, Z. H.; Deng, K.; *et al. ACS Nano* **2017**, *11*, 12001. doi: 10.1021/acsnano.7b03819

(99) Chen, T.-A.; Chuu, C.-P.; Tseng, C.-C.; Wen, C.-K.; Wong, H. S. P.; Pan, S.; Li, R.; Chao, T.-A.; Chueh, W.-C.; Zhang, Y.; *et al. Nature* **2020**, *579*, 219. doi: 10.1038/s41586-020-2009-2

(100) Wu, Z.; Lyu, Y.; Zhang, Y.; Ding, R.; Zheng, B.; Yang, Z.; Lau, S. P.; Chen, X. H.; Hao, J. *Nat. Mater.* **2021**, *20*, 1203. doi: 10.1038/s41563-021-01001-7

(101) Lai, Z.; He, Q.; Tran, T. H.; Repaka, D. V. M.; Zhou, D.-D.; Sun, Y.; Xi, S.; Li, Y.; Chaturvedi, A.; Tan, C.; *et al. Nat. Mater.* **2021**, *20*, 1113. doi: 10.1038/s41563-021-00971-y

(102) Zavabeti, A.; Ou, J. Z.; Carey, B. J.; Syed, N.; Orrell-Trigg, R.; Mayes, E. L. H.; Xu, C.; Kavehei, O.; O'Mullane, A. P.; Kaner, R. B.; *et al. Science* **2017**, *358*, 332. doi: 10.1126/science.aao4249

(103) Seo, S.-Y.; Park, J.; Park, J.; Song, K.; Cha, S.; Sim, S.; Choi, S.-Y.; Yeom, H. W.; Choi, H.; Jo, M.-H. *Nat. Electron.* **2018**, *1*, 512. doi: 10.1038/s41928-018-0129-6

(104) Goossens, S.; Navickaite, G.; Monasterio, C.; Gupta, S.; Piqueras, J. J.; Pérez, R.; Burwell, G.; Nikitskiy, I.; Lasanta, T.; Galán, T.; *et al. Nat. Photon.* **2017**, *11*, 366. doi: 10.1038/nphoton.2017.75

(105) Chen, Y.; Lai, Z.; Zhang, X.; Fan, Z.; He, Q.; Tan, C.; Zhang, H. *Nat. Rev. Chem.* **2020**, *4*, 243. doi: 10.1038/s41570-020-0173-4

(106) Ge, Y.; Shi, Z.; Tan, C.; Chen, Y.; Cheng, H.; He, Q.; Zhang, H. *Chem* **2020**, *6*, 1237. doi: 10.1016/j.chempr.2020.04.004

(107) Cao, Y.; Fatemi, V.; Fang, S.; Watanabe, K.; Taniguchi, T.; Kaxiras, E.; Jarillo-Herrero, P. *Nature* **2018**, *556*, 43. doi: 10.1038/nature26160

(108) Cao, Y.; Fatemi, V.; Demir, A.; Fang, S.; Tomarken, S. L.; Luo, J. Y.; Sanchez-Yamagishi, J. D.; Watanabe, K.; Taniguchi, T.; Kaxiras, E.; *et al. Nature* **2018**, *556*, 80. doi: 10.1038/nature26154

(109) Ganz, E.; Sattler, K.; Clarke, J. *Phys. Rev. Lett.* **1988**, *60*, 1856. doi: 10.1103/PhysRevLett.60.1856

(110) Castellanos-Gomez, A.; Poot, M.; Steele, G. A.; van der Zant, H. S. J.; Agraït, N.; Rubio-Bollinger, G. *Adv. Mater.* **2012**, *24*, 772. doi: 10.1002/adma.201103965

(111) Novoselov, K. S.; Jiang, D.; Schedin, F.; Booth, T. J.; Khotkevich, V. V.; Morozov, S. V.; Geim, A. K. *Proc. Natl. Acad. Sci. U. S. A.* **2005**, *102*, 10451. doi: 10.1073/pnas.0502848102

(112) Mak, K. F.; Lee, C.; Hone, J.; Shan, J.; Heinz, T. F. *Phys. Rev. Lett.* **2010**, *105*, 136805. doi: 10.1103/PhysRevLett.105.136805

(113) Radisavljevic, B.; Radenovic, A.; Brivio, J.; Giacometti, V.; Kis, A. *Nat. Nanotechnol.* **2011**, *6*, 147. doi: 10.1038/nnano.2010.279

(114) Zhao, W.; Ghorannevis, Z.; Chu, L.; Toh, M.; Kloc, C.; Tan, P. H.; Eda, G. *ACS Nano* **2013**, *7*, 791. doi: 10.1021/nn305275h

(115) Huang, Y.; Sutter, E.; Sadowski, J.; Cotlet, M.; Monti, O.; Racke, D.; Neupane, M.; Wickramaratne, D.; Lake, R.; Parkinson, B.; *et al. ACS Nano* **2014**, *8*, 10743. doi: 10.1021/nn504481r

(116) Liu, H.; Neal, A. T.; Zhu, Z.; Luo, Z.; Xu, X.; Tomanek, D.; Ye, P. D. *ACS Nano* **2014**, *8*, 4033. doi: 10.1021/nn501226z

(117) Zhang, Y.; Tan, Y.-W.; Stormer, H. L.; Kim, P. *Nature* **2005**, *438*, 201. doi: 10.1038/nature04235

(118) Avouris, P. *Nano Lett.* **2010**, *10*, 4285. doi: 10.1021/nl102824h

(119) Amani, M.; Lien, D.-H.; Kiriya, D.; Xiao, J.; Azcatl, A.; Noh, J.; Madhvapathy, S. R.; Addou, R.; KC, S.; Dubey, M.; *et al. Science* **2015**, *350*, 1065. doi: 10.1126/science.aad2114

(120) Huang, Y.; Sutter, E.; Shi, N. N.; Zheng, J.; Yang, T.; Englund, D.; Gao, H. J.; Sutter, P. *ACS Nano* **2015**, *9*, 10612. doi: 10.1021/acsnano.5b04258

(121) Song, S. M.; Cho, B. J. *Nanotechnology* **2010**, *21*, 335706. doi: 10.1088/0957-4484/21/33/335706

(122) Xu, H.; Meng, L.; Li, Y.; Yang, T. Z.; Bao, L. H.; Liu, G. D.; Zhao, L.; Liu, T. S.; Xing, J.; Gao, H. J.; *et al. Acta Phys. Sin.* **2018**, *67*, 218201. doi: 10.7498/aps.67.20181636

(123) Huang, Y.; Wang, X.; Zhang, X.; Chen, X. J.; Li, B. W.; Wang, B.; Huang, M.; Zhu, C. Y.; Zhang, X. W.; Bacsa, W. S.; *et al. Phys. Rev. Lett.* **2018**, *120*, 186104. doi: 10.1103/PhysRevLett.120.186104

(124) Luo, H.; Li, X.; Zhao, Y.; Yang, R.; Bao, L.; Hao, Y.; Gao, Y.-N.; Shi, N. N.; Guo, Y.; Liu, G.; *et al. Phys. Rev. Mater.* **2020**, *4*, 074006. doi: 10.1103/PhysRevMaterials.4.074006

(125) Magda, G. Z.; Pető, J.; Dobrik, G.; Hwang, C.; Biró, L. P.; Tapasztó, L. *Sci. Rep.* **2015**, *5*, 14714. doi: 10.1038/srep14714

(126) Huang, Y.; Pan, Y.-H.; Yang, R.; Bao, L.-H.; Meng, L.; Luo, H.-L.; Cai, Y.-Q.; Liu, G.-D.; Zhao, W.-J.; Zhou, Z.; *et al. Nat. Commun.* **2020**, *11*, 2453. doi: 10.1038/s41467-020-16266-w

(127) Nicolosi, V.; Chhowalla, M.; Kanatzidis, M. G.; Strano, M. S.; Coleman, J. N. *Science* **2013**, *340*, 1226419. doi: 10.1126/science.1226419

(128) Coleman, J. N.; Lotya, M.; O'Neill, A.; Bergin, S. D.; King, P. J.; Khan, U.; Young, K.; Gaucher, A.; De, S.; Smith, R. J.; *et al. Science* **2011**, *331*, 568. doi: 10.1126/science.1194975

(129) Hernandez, Y.; Nicolosi, V.; Lotya, M.; Blighe, F. M.; Sun, Z.; De, S.; McGovern, I. T.; Holland, B.; Byrne, M.; Gun'Ko, Y. K.; *et al. Nat. Nanotechnol.* **2008**, *3*, 563. doi: 10.1038/nnano.2008.215

(130) Hanlon, D.; Backes, C.; Doherty, E.; Cucinotta, C. S.; Berner, N. C.; Boland, C.; Lee, K.; Harvey, A.; Lynch, P.; Gholamvand, Z.; *et al. Nat. Commun.* **2015**, *6*, 8563. doi: 10.1038/ncomms9563

(131) Sarkar, A. S.; Mushtaq, A.; Kushavah, D.; Pal, S. K. *npj 2D Mater. Appl.* **2020**, *4*, 1. doi: 10.1038/s41699-019-0135-1

(132) Sinha, S.; Zhu, T.; France-Lanord, A.; Sheng, Y.; Grossman, J. C.; Porfyrakis, K.; Warner, J. H. *Nat. Commun.* **2020,** *11*, 823. doi: 10.1038/s41467-020-14481-z

(133) Lê Anh, M.; Potapov, P.; Lubk, A.; Doert, T.; Ruck, M. *npj 2D Mater. Appl.* **2021,** *5*, 22. doi: 10.1038/s41699-021-00203-6

(134) Liao, W.-M.; Zhang, J.-H.; Yin, S.-Y.; Lin, H.; Zhang, X.; Wang, J.; Wang, H.-P.; Wu, K.; Wang, Z.; Fan, Y.-N.; *et al. Nat. Commun.* **2018,** *9*, 2401. doi: 10.1038/s41467-018-04833-1

(135) Puthirath Balan, A.; Radhakrishnan, S.; Woellner, C. F.; Sinha, S. K.; Deng, L.; de los Reyes, C.; Rao, B. M.; Paulose, M.; Neupane, R.; Apte, A.; *et al. Nat. Nanotechnol.* **2018,** *13*, 602. doi: 10.1038/s41565-018-0134-y

(136) Gong, F.; Cheng, L.; Yang, N.; Gong, Y.; Ni, Y.; Bai, S.; Wang, X.; Chen, M.; Chen, Q.; Liu, Z. *Nat. Commun.* **2020,** *11*, 3712. doi: 10.1038/s41467-020-17485-x

(137) Yano, S.; Sato, K.; Suzuki, J.; Imai, H.; Oaki, Y. *Commun. Chem.* **2019,** *2*, 97. doi: 10.1038/s42004-019-0201-9

(138) Dong, J.; Zhang, K.; Li, X.; Qian, Y.; Zhu, H.; Yuan, D.; Xu, Q.-H.; Jiang, J.; Zhao, D. *Nat. Commun.* **2017,** *8*, 1142. doi: 10.1038/s41467-017-01293-x

(139) Zhou, K.-G.; Mao, N.-N.; Wang, H.-X.; Peng, Y.; Zhang, H.-L. *Angew. Chem. Int. Ed.* **2011,** *50*, 10839. doi: 10.1002/anie.201105364

(140) Lotya, M.; Hernandez, Y.; King, P. J.; Smith, R. J.; Nicolosi, V.; Karlsson, L. S.; Blighe, F. M.; De, S.; Wang, Z.; McGovern, I. T.; *et al. J. Am. Chem. Soc.* **2009,** *131*, 3611. doi: 10.1021/ja807449u

(141) Lotya, M.; King, P. J.; Khan, U.; De, S.; Coleman, J. N. *ACS Nano* **2010,** *4*, 3155. doi: 10.1021/nn1005304

(142) Green, A. A.; Hersam, M. C. *Nano Lett.* **2009,** *9*, 4031. doi: 10.1021/nl902200b

(143) Bourlinos, A. B.; Georgakilas, V.; Zboril, R.; Steriotis, T. A.; Stubos, A. K.; Trapalis, C. *Solid State Commun.* **2009,** *149*, 2172. doi: 10.1016/j.ssc.2009.09.018

(144) Chen, Y.-W.; Shie, M.-Y.; Hsiao, C.-H.; Liang, Y.-C.; Wang, B.; Chen, I. W. P. *npj 2D Mater. Appl.* **2020,** *4*, 34. doi: 10.1038/s41699-020-00168-y

(145) Chhowalla, M.; Shin, H. S.; Eda, G.; Li, L.-J.; Loh, K. P.; Zhang, H. *Nat. Chem.* **2013,** *5*, 263. doi: 10.1038/nchem.1589

(146) Wang, Q. H.; Kalantar-Zadeh, K.; Kis, A.; Coleman, J. N.; Strano, M. S. *Nat. Nanotechnol.* **2012,** *7*, 699. doi: 10.1038/nnano.2012.193

(147) Zhang, Q.; Mei, L.; Cao, X.; Tang, Y.; Zeng, Z. *J. Mater. Chem. A* **2020,** *8*, 15417. doi: 10.1039/D0TA03727C

(148) Dines, M. B. *Mater. Res. Bull.* **1975,** *10*, 287. doi: 10.1016/0025-5408(75)90115-4

(149) Joensen, P.; Frindt, R. F.; Morrison, S. R. *Mater. Res. Bull.* **1986,** *21*, 457. doi: 10.1016/0025-5408(86)90011-5

(150) Walker, G. F.; Garrett, W. G. *Science* **1967,** *156*, 385. doi: 10.1126/science.156.3773.385

(151) Eda, G.; Yamaguchi, H.; Voiry, D.; Fujita, T.; Chen, M.; Chhowalla, M. *Nano Lett.* **2011,** *11*, 5111. doi: 10.1021/nl201874w

(152) Zeng, Z.; Yin, Z.; Huang, X.; Li, H.; He, Q.; Lu, G.; Boey, F.; Zhang, H. *Angew. Chem. Int. Ed.* **2011,** *50*, 11093. doi: 10.1002/anie.201106004

(153) Zeng, Z.; Sun, T.; Zhu, J.; Huang, X.; Yin, Z.; Lu, G.; Fan, Z.; Yan, Q.; Hng, H. H.; Zhang, H. *Angew. Chem. Int. Ed.* **2012,** *51*, 9052. doi: 10.1002/anie.201204208

(154) Voiry, D.; Yamaguchi, H.; Li, J.; Silva, R.; Alves, D. C. B.; Fujita, T.; Chen, M.; Asefa, T.; Shenoy, V. B.; Eda, G.; *et al. Nat. Mater.* **2013,** *12*, 850. doi: 10.1038/nmat3700

(155) Voiry, D.; Salehi, M.; Silva, R.; Fujita, T.; Chen, M.; Asefa, T.; Shenoy, V. B.; Eda, G.; Chhowalla, M. *Nano Lett.* **2013,** *13*, 6222. doi: 10.1021/nl403661s

(156) Acerce, M.; Voiry, D.; Chhowalla, M. *Nat. Nanotechnol.* **2015,** *10*, 313. doi: 10.1038/nnano.2015.40

(157) Chou, S. S.; Kaehr, B.; Kim, J.; Foley, B. M.; De, M.; Hopkins, P. E.; Huang, J.; Brinker, C. J.; Dravid, V. P. *Angew. Chem. Int. Ed.* **2013,** *52*, 4160. doi: 10.1002/anie.201209229

(158) Zeng, Z.; Tan, C.; Huang, X.; Bao, S.; Zhang, H. *Energy Environ. Sci.* **2014,** *7*, 797. doi: 10.1039/C3EE42620C

(159) Mei, L.; Gao, X.; Gao, Z.; Zhang, Q.; Yu, X.; Rogach, A. L.; Zeng, Z. *Chem. Commun.* **2021,** *57*, 2879. doi: 10.1039/D0CC08091H

(160) Watts, M. C.; Picco, L.; Russell-Pavier, F. S.; Cullen, P. L.; Miller, T. S.; Bartuś, S. P.; Payton, O. D.; Skipper, N. T.; Tileli, V.; Howard, C. A. *Nature* **2019,** *568*, 216. doi: 10.1038/s41586-019-1074-x

(161) Huang, X.; Zeng, Z.; Bao, S.; Wang, M.; Qi, X.; Fan, Z.; Zhang, H. *Nat. Commun.* **2013,** *4*, 1444. doi: 10.1038/ncomms2472

(162) Kim, B.-H.; Jang, M.-H.; Yoon, H.; Kim, H. J.; Cho, Y.-H.; Jeon, S.; Song, S.-H. *NPG Asia Mater.* **2021,** *13*, 41. doi: 10.1038/s41427-021-00305-z

(163) García-Dalí, S.; Paredes, J. I.; Munuera, J. M.; Villar-Rodil, S.; Adawy, A.; Martínez-Alonso, A.; Tascón, J. M. D. *ACS Appl. Mater. Interfaces* **2019,** *11*, 36991. doi: 10.1021/acsami.9b13484

(164) Zhang, L.; Nan, H.; Zhang, X.; Liang, Q.; Du, A.; Ni, Z.; Gu, X.; Ostrikov, K.; Xiao, S. *Nat. Commun.* **2020,** *11*, 5960. doi: 10.1038/s41467-020-19766-x

(165) Andrews, J. L.; De Jesus, L. R.; Tolhurst, T. M.; Marley, P. M.; Moewes, A.; Banerjee, S. *Chem. Mater.* **2017,** *29*, 3285. doi: 10.1021/acs.chemmater.7b00597

(166) Luo, F.; Wang, D.; Zhang, J.; Li, X.; Liu, D.; Li, H.; Lu, M.; Xie, X.; Huang, L.; Huang, W. *ACS Appl. Nano Mater.* **2019,** *2*, 3793. doi: 10.1021/acsanm.9b00667

(167) Omomo, Y.; Sasaki, T.; Wang, L. Z.; Watanabe, M. *J. Am. Chem.*

Soc. **2003**, *125*, 3568. doi: 10.1021/ja021364p

(168) Li, F.; Xue, M.; Zhang, X.; Chen, L.; Knowles, G. P.; MacFarlane, D. R.; Zhang, J. *Adv. Energy Mater.* **2018**, *8*, 1702794. doi: 10.1002/aenm.201702794

(169) Seiler, S.; Halbig, C. E.; Grote, F.; Rietsch, P.; Börrnert, F.; Kaiser, U.; Meyer, B.; Eigler, S. *Nat. Commun.* **2018**, *9*, 836. doi: 10.1038/s41467-018-03211-1

(170) Liu, N.; Kim, P.; Kim, J. H.; Ye, J. H.; Kim, S.; Lee, C. J. *ACS Nano* **2014**, *8*, 6902. doi: 10.1021/nn5016242

(171) Ambrosi, A.; Sofer, Z.; Luxa, J.; Pumera, M. *ACS Nano* **2016**, *10*, 11442. doi: 10.1021/acsnano.6b07096

(172) Su, C.-Y.; Lu, A.-Y.; Xu, Y.; Chen, F.-R.; Khlobystov, A. N.; Li, L.-J. *ACS Nano* **2011**, *5*, 2332. doi: 10.1021/nn200025p

(173) Liu, Z.; Sun, Y.; Cao, H.; Xie, D.; Li, W.; Wang, J.; Cheetham, A. K. *Nat. Commun.* **2020**, *11*, 3917. doi: 10.1038/s41467-020-17622-6

(174) Zhou, F.; Huang, H.; Xiao, C.; Zheng, S.; Shi, X.; Qin, J.; Fu, Q.; Bao, X.; Feng, X.; Müllen, K.; *et al. J. Am. Chem. Soc.* **2018**, *140*, 8198. doi: 10.1021/jacs.8b03235

(175) Zhai, X.; Zhang, R.; Sheng, H.; Wang, J.; Zhu, Y.; Lu, Z.; Li, Z.; Huang, X.; Li, H.; Lu, G. *ACS Nano* **2021**, *15*, 5661. doi: 10.1021/acsnano.1c00838

(176) Jeong, S.; Yoo, D.; Ahn, M.; Miró, P.; Heine, T.; Cheon, J. *Nat. Commun.* **2015**, *6*, 5763. doi: 10.1038/ncomms6763

(177) Kovtyukhova, N. I.; Wang, Y.; Berkdemir, A.; Cruz-Silva, R.; Terrones, M.; Crespi, V. H.; Mallouk, T. E. *Nat. Chem.* **2014**, *6*, 957. doi: 10.1038/nchem.2054

(178) Yang, K.; Zhou, Y.; Wang, Z.; Li, M.; Shi, D.; Wang, X.; Jiang, T.; Zhang, Q.; Ding, B.; You, J. *Adv. Mater.* **2021**, *33*, 2007596. doi: 10.1002/adma.202007596

(179) Ding, Y.; Chen, Y.-P.; Zhang, X.; Chen, L.; Dong, Z.; Jiang, H.-L.; Xu, H.; Zhou, H.-C. *J. Am. Chem. Soc.* **2017**, *139*, 9136. doi: 10.1021/jacs.7b04829

(180) Sun, Y.; Sun, Z.; Gao, S.; Cheng, H.; Liu, Q.; Piao, J.; Yao, T.; Wu, C.; Hu, S.; Wei, S.; *et al. Nat. Commun.* **2012**, *3*, 1057. doi: 10.1038/ncomms2066

(181) Pan, X.-F.; Gao, H.-L.; Lu, Y.; Wu, C.-Y.; Wu, Y.-D.; Wang, X.-Y.; Pan, Z.-Q.; Dong, L.; Song, Y.-H.; Cong, H.-P.; *et al. Nat. Commun.* **2018**, *9*, 2974. doi: 10.1038/s41467-018-05355-6

(182) Dakhchoune, M.; Villalobos, L. F.; Semino, R.; Liu, L.; Rezaei, M.; Schouwink, P.; Avalos, C. E.; Baade, P.; Wood, V.; Han, Y.; *et al. Nat. Mater.* **2021**, *20*, 362. doi: 10.1038/s41563-020-00822-2

(183) Li, J.; Song, P.; Zhao, J.; Vaklinova, K.; Zhao, X.; Li, Z.; Qiu, Z.; Wang, Z.; Lin, L.; Zhao, M.; *et al. Nat. Mater.* **2021**, *20*, 181. doi: 10.1038/s41563-020-00831-1

(184) Ugeda, M. M.; Bradley, A. J.; Zhang, Y.; Onishi, S.; Chen, Y.; Ruan, W.; Ojeda-Aristizabal, C.; Ryu, H.; Edmonds, M. T.; Tsai, H.-Z.;

et al. Nat. Phys. **2016**, *12*, 92. doi: 10.1038/nphys3527

(185) Wang, H.; Huang, X.; Lin, J.; Cui, J.; Chen, Y.; Zhu, C.; Liu, F.; Zeng, Q.; Zhou, J.; Yu, P.; *et al. Nat. Commun.* **2017**, *8*, 394. doi: 10.1038/s41467-017-00427-5

(186) Cai, Z.; Liu, B.; Zou, X.; Cheng, H.-M. *Chem. Rev.* **2018**, *118*, 6091. doi: 10.1021/acs.chemrev.7b00536

(187) Lin, L.; Deng, B.; Sun, J.; Peng, H.; Liu, Z. *Chem. Rev.* **2018**, *118*, 9281. doi: 10.1021/acs.chemrev.8b00325

(188) Jiang, J.; Li, N.; Zou, J.; Zhou, X.; Eda, G.; Zhang, Q.; Zhang, H.; Li, L.-J.; Zhai, T.; Wee, A. T. S. *Chem. Soc. Rev.* **2019**, *48*, 4639. doi: 10.1039/C9CS00348G

(189) Li, X.; Cai, W.; An, J.; Kim, S.; Nah, J.; Yang, D.; Piner, R.; Velamakanni, A.; Jung, I.; Tutuc, E.; *et al. Science* **2009**, *324*, 1312. doi: 10.1126/science.1171245

(190) Kim, K. K.; Lee, H. S.; Lee, Y. H. *Chem. Soc. Rev.* **2018**, *47*, 6342. doi: 10.1039/C8CS00450A

(191) Tang, L.; Tan, J.; Nong, H.; Liu, B.; Cheng, H.-M. *Acc. Mater. Res.* **2021**, *2*, 36. doi: 10.1021/accountsmr.0c00063

(192) Wang, H.; Chen, Y.; Duchamp, M.; Zeng, Q.; Wang, X.; Tsang, S. H.; Li, H.; Jing, L.; Yu, T.; Teo, E. H. T.; *et al. Adv. Mater.* **2018**, *30*, 1704382. doi: 10.1002/adma.201704382

(193) Liu, D.; Hong, J.; Li, X.; Zhou, X.; Jin, B.; Cui, Q.; Chen, J.; Feng, Q.; Xu, C.; Zhai, T.; *et al. Adv. Funct. Mater.* **2020**, *30*, 1910169. doi: 10.1002/adfm.201910169

(194) Meng, L.; Zhou, Z.; Xu, M.; Yang, S.; Si, K.; Liu, L.; Wang, X.; Jiang, H.; Li, B.; Qin, P.; *et al. Nat. Commun.* **2021**, *12*, 809. doi: 10.1038/s41467-021-21072-z

(195) Li, X.; Dai, X.; Tang, D.; Wang, X.; Hong, J.; Chen, C.; Yang, Y.; Lu, J.; Zhu, J.; Lei, Z.; *et al. Adv. Funct. Mater.* **2021**, *31*, 2102138. doi: 10.1002/adfm.202102138

(196) Gao, T.; Zhang, Q.; Li, L.; Zhou, X.; Li, L.; Li, H.; Zhai, T. *Adv. Opt. Mater.* **2018**, *6*, 1800058. doi: 10.1002/adom.201800058

(197) Tan, C.; Zhang, H. *J. Am. Chem. Soc.* **2015**, *137*, 12162. doi: 10.1021/jacs.5b03590

(198) Kang, K.; Xie, S.; Huang, L.; Han, Y.; Huang, P. Y.; Mak, K. F.; Kim, C.-J.; Muller, D.; Park, J. *Nature* **2015**, *520*, 656. doi: 10.1038/nature14417

(199) Yu, P.; Lin, J.; Sun, L.; Le, Q. L.; Yu, X.; Gao, G.; Hsu, C.-H.; Wu, D.; Chang, T.-R.; Zeng, Q.; *et al. Adv. Mater.* **2017**, *29*, 1603991. doi: 10.1002/adma.201603991

(200) Liu, X.; Wu, J.; Yu, W.; Chen, L.; Huang, Z.; Jiang, H.; He, J.; Liu, Q.; Lu, Y.; Zhu, D.; *et al. Adv. Funct. Mater.* **2017**, *27*, 1606469. doi: 10.1002/adfm.201606469

(201) Wu, J.; Yuan, H.; Meng, M.; Chen, C.; Sun, Y.; Chen, Z.; Dang, W.; Tan, C.; Liu, Y.; Yin, J.; *et al. Nat. Nanotechnol.* **2017**, *12*, 530. doi: 10.1038/nnano.2017.43

(202) Wu, J.; Tan, C.; Tan, Z.; Liu, Y.; Yin, J.; Dang, W.; Wang, M.; Peng, H. *Nano Lett.* **2017**, *17*, 3021. doi: 10.1021/acs.nanolett.7b00335

(203) Hong, Y.-L.; Liu, Z.; Wang, L.; Zhou, T.; Ma, W.; Xu, C.; Feng, S.; Chen, L.; Chen, M.-L.; Sun, D.-M.; *et al. Science* **2020**, *369*, 670. doi: 10.1126/science.abb7023

(204) Wang, H.; Xu, X.; Li, J.; Lin, L.; Sun, L.; Sun, X.; Zhao, S.; Tan, C.; Chen, C.; Dang, W.; *et al. Adv. Mater.* **2016**, *28*, 8968. doi: 10.1002/adma.201603579

(205) Xu, X.; Zhang, Z.; Qiu, L.; Zhuang, J.; Zhang, L.; Wang, H.; Liao, C.; Song, H.; Qiao, R.; Gao, P.; *et al. Nat. Nanotechnol.* **2016**, *11*, 930. doi: 10.1038/nnano.2016.132

(206) Lin, L.; Zhang, J.; Su, H.; Li, J.; Sun, L.; Wang, Z.; Xu, F.; Liu, C.; Lopatin, S.; Zhu, Y.; *et al. Nat. Commun.* **2019**, *10*, 1912. doi: 10.1038/s41467-019-09565-4

(207) Wang, R.; Muhammad, Y.; Xu, X.; Ran, M.; Zhang, Q.; Zhong, J.; Zhuge, F.; Li, H.; Gan, L.; Zhai, T. *Small Methods* **2020**, *4*, 2000102. doi: 10.1002/smtd.202000102

(208) Xu, H.; Huang, H.-P.; Fei, H.; Feng, J.; Fuh, H.-R.; Cho, J.; Choi, M.; Chen, Y.; Zhang, L.; Chen, D.; *et al. ACS Appl. Mater. Interfaces* **2019**, *11*, 8202. doi: 10.1021/acsami.8b19218

(209) Deng, B.; Pang, Z.; Chen, S.; Li, X.; Meng, C.; Li, J.; Liu, M.; Wu, J.; Qi, Y.; Dang, W.; *et al. ACS Nano* **2017**, *11*, 12337. doi: 10.1021/acsnano.7b06196

(210) Cui, F.; Zhao, X.; Xu, J.; Tang, B.; Shang, Q.; Shi, J.; Huan, Y.; Liao, J.; Chen, Q.; Hou, Y.; *et al. Adv. Mater.* **2020**, *32*, 1905896. doi: 10.1002/adma.201905896

(211) Zhang, Y.; Chu, J.; Yin, L.; Shifa, T. A.; Cheng, Z.; Cheng, R.; Wang, F.; Wen, Y.; Zhan, X.; Wang, Z.; *et al. Adv. Mater.* **2019**, *31*, 1900056. doi: 10.1002/adma.201900056

(212) Yang, P.; Zou, X.; Zhang, Z.; Hong, M.; Shi, J.; Chen, S.; Shu, J.; Zhao, L.; Jiang, S.; Zhou, X.; *et al. Nat. Commun.* **2018**, *9*, 979. doi: 10.1038/s41467-018-03388-5

(213) Xu, X.; Zhang, Z.; Dong, J.; Yi, D.; Niu, J.; Wu, M.; Lin, L.; Yin, R.; Li, M.; Zhou, J.; *et al. Sci. Bull.* **2017**, *62*, 1074. doi: 10.1016/j.scib.2017.07.005

(214) Wang, L.; Xu, X.; Zhang, L.; Qiao, R.; Wu, M.; Wang, Z.; Zhang, S.; Liang, J.; Zhang, Z.; Zhang, Z.; *et al. Nature* **2019**, *570*, 91. doi: 10.1038/s41586-019-1226-z

(215) Chubarov, M.; Choudhury, T. H.; Hickey, D. R.; Bachu, S.; Zhang, T.; Sebastian, A.; Bansal, A.; Zhu, H.; Trainor, N.; Das, S.; *et al. ACS Nano* **2021**, *15*, 2532. doi: 10.1021/acsnano.0c06750

(216) Zeng, L.-H.; Wu, D.; Lin, S.-H.; Xie, C.; Yuan, H.-Y.; Lu, W.; Lau, S. P.; Chai, Y.; Luo, L.-B.; Li, Z.-J.; *et al. Adv. Funct. Mater.* **2019**, *29*, 1806878. doi: 10.1002/adfm.201806878

(217) Yim, C.; McEvoy, N.; Riazimehr, S.; Schneider, D. S.; Gity, F.; Monaghan, S.; Hurley, P. K.; Lemme, M. C.; Duesberg, G. S. *Nano Lett.* **2018**, *18*, 1794. doi: 10.1021/acs.nanolett.7b05000

(218) Zhou, L.; Zubair, A.; Wang, Z.; Zhang, X.; Ouyang, F.; Xu, K.; Fang, W.; Ueno, K.; Li, J.; Palacios, T.; *et al. Adv. Mater.* **2016**, *28*, 9526. doi: 10.1002/adma.201602687

(219) Yu, F.; Liu, Q.; Gan, X.; Hu, M.; Zhang, T.; Li, C.; Kang, F.; Terrones, M.; Lv, R. *Adv. Mater.* **2017**, *29*, 1603266. doi: 10.1002/adma.201603266

(220) Lin, H.; Zhu, Q.; Shu, D.; Lin, D.; Xu, J.; Huang, X.; Shi, W.; Xi, X.; Wang, J.; Gao, L. *Nat. Mater.* **2019**, *18*, 602. doi: 10.1038/s41563-019-0321-8

(221) Serna, M. I.; Yoo, S. H.; Moreno, S.; Xi, Y.; Oviedo, J. P.; Choi, H.; Alshareef, H. N.; Kim, M. J.; Minary-Jolandan, M.; Quevedo-Lopez, M. A. *ACS Nano* **2016**, *10*, 6054. doi: 10.1021/acsnano.6b01636

(222) Seo, S.; Choi, H.; Kim, S.-Y.; Lee, J.; Kim, K.; Yoon, S.; Lee, B. H.; Lee, S. *Adv. Mater. Interfaces* **2018**, *5*, 1800524. doi: 10.1002/admi.201800524

(223) Apte, A.; Bianco, E.; Krishnamoorthy, A.; Yazdi, S.; Rao, R.; Glavin, N.; Kumazoe, H.; Varshney, V.; Roy, A.; Shimojo, F.; *et al. 2D Mater.* **2018**, *6*, 015013. doi: 10.1088/2053-1583/aae7f6

(224) Jiang, Y.; Yan, Y.; Chen, W.; Khan, Y.; Wu, J.; Zhang, H.; Yang, D. *Chem. Commun.* **2016**, *52*, 14204. doi: 10.1039/C6CC08464H

(225) Wang, L.; Zhu, Y.; Wang, J.-Q.; Liu, F.; Huang, J.; Meng, X.; Basset, J.-M.; Han, Y.; Xiao, F.-S. *Nat. Commun.* **2015**, *6*, 6957. doi: 10.1038/ncomms7957

(226) Wu, G.; Zheng, X.; Cui, P.; Jiang, H.; Wang, X.; Qu, Y.; Chen, W.; Lin, Y.; Li, H.; Han, X.; *et al. Nat. Commun.* **2019**, *10*, 4855. doi: 10.1038/s41467-019-12859-2

(227) Niu, J.; Wang, D.; Qin, H.; Xiong, X.; Tan, P.; Li, Y.; Liu, R.; Lu, X.; Wu, J.; Zhang, T. *Nat. Commun.* **2014**, *5*, 3313. doi: 10.1038/ncomms4313

(228) Luo, L.; Li, Y.; Sun, X.; Li, J.; Hu, E.; Liu, Y.; Tian, Y.; Yang, X.-Q.; Li, Y.; Lin, W.-F. *Chem* **2020**, *6*, 448. doi: 10.1016/j.chempr.2019.11.004

(229) Huang, W.; Kang, X.; Xu, C.; Zhou, J.; Deng, J.; Li, Y.; Cheng, S. *Adv. Mater.* **2018**, *30*, 1706962. doi: 10.1002/adma.201706962

(230) Zhao, L.; Xu, C.; Su, H.; Liang, J.; Lin, S.; Gu, L.; Wang, X.; Chen, M.; Zheng, N. *Adv. Sci.* **2015**, *2*, 1500100. doi: 10.1002/advs.201500100

(231) Luo, M.; Zhao, Z.; Zhang, Y.; Sun, Y.; Xing, Y.; Lv, F.; Yang, Y.; Zhang, X.; Hwang, S.; Qin, Y.; *et al. Nature* **2019**, *574*, 81. doi: 10.1038/s41586-019-1603-7

(232) Yang, N.; Zhang, Z.; Chen, B.; Huang, Y.; Chen, J.; Lai, Z.; Chen, Y.; Sindoro, M.; Wang, A. L.; Cheng, H.; *et al. Adv. Mater.* **2017**, *29*, 1700769. doi: 10.1002/adma.201700769

(233) Chen, L.; Ji, F.; Xu, Y.; He, L.; Mi, Y.; Bao, F.; Sun, B.; Zhang, X.;

Zhang, Q. *Nano Lett.* **2014**, *14*, 7201. doi: 10.1021/nl504126u

(234) Zhai, Y.; DuChene, J. S.; Wang, Y.-C.; Qiu, J.; Johnston-Peck, A. C.; You, B.; Guo, W.; DiCiaccio, B.; Qian, K.; Zhao, E. W. *Nat. Mater.* **2016**, *15*, 889. doi: 10.1038/nmat4683

(235) Qiu, X.; Zhang, H.; Wu, P.; Zhang, F.; Wei, S.; Sun, D.; Xu, L.; Tang, Y. *Adv. Funct. Mater.* **2017**, *27*, 1603852. doi: 10.1002/adfm.201603852

(236) Hong, X.; Tan, C.; Liu, J.; Yang, J.; Wu, X.-J.; Fan, Z.; Luo, Z.; Chen, J.; Zhang, X.; Chen, B. *J. Am. Chem. Soc.* **2015**, *137*, 1444. doi: 10.1021/ja513120u

(237) Wang, Y.; Peng, H.-C.; Liu, J.; Huang, C. Z.; Xia, Y. *Nano Lett.* **2015**, *15*, 1445. doi: 10.1021/acs.nanolett.5b00158

(238) Chhetri, M.; Rana, M.; Loukya, B.; Patil, P. K.; Datta, R.; Gautam, U. K. *Adv. Mater.* **2015**, *27*, 4430. doi: 10.1002/adma.201501056

(239) Ge, J.; Wei, P.; Wu, G.; Liu, Y.; Yuan, T.; Li, Z.; Qu, Y.; Wu, Y.; Li, H.; Zhuang, Z. *Angew. Chem. Int. Ed.* **2018**, *57*, 3435. doi: 10.1002/anie.201800552

(240) Luc, W.; Fu, X.; Shi, J.; Lv, J.-J.; Jouny, M.; Ko, B. H.; Xu, Y.; Tu, Q.; Hu, X.; Wu, J.; *et al. Nat. Catal.* **2019**, *2*, 423. doi: 10.1038/s41929-019-0269-8

(241) Luo, Y.; Liu, Z.; Wu, G.; Wang, G.; Chao, T.; Li, H.; Liu, J.; Hong, X. *Chin. Chem. Lett.* **2019**, *30*, 1093. doi: 10.1016/j.cclet.2018.11.008

(242) Yu, J.; Wang, Q.; O'Hare, D.; Sun, L. *Chem. Soc. Rev.* **2017**, *46*, 5950. doi: 10.1039/C7CS00318H

(243) Yi, H.; Liu, S.; Lai, C.; Zeng, G.; Li, M.; Liu, X.; Li, B.; Huo, X.; Qin, L.; Li, L.; *et al. Adv. Energy Mater.* **2021**, *11*, 2002863. doi: 10.1002/aenm.202002863

(244) Xie, W.; Song, Y.; Li, S.; Shao, M.; Wei, M. *Energy Environ. Mater.* **2019**, *2*, 158. doi: 10.1002/eem2.12033

(245) Yu, J.; Yu, F.; Yuen, M. F.; Wang, C. *J. Mater. Chem. A* **2021**, *9*, 9389. doi: 10.1039/D0TA11910E

(246) Xie, W. F.; Li, Z. H.; Jiang, S.; Li, J. B.; Shao, M. F.; Wei, M. *Chem. Eng. J.* **2019**, *373*, 734. doi: 10.1016/j.cej.2019.04.066

(247) Li, J.; Jiang, S.; Shao, M.; Wei, M. *Catalysts* **2018**, *8*, 214. doi: 10.3390/catal8050214

(248) Zhou, L.; Shao, M.; Wei, M.; Duan, X. *J. Energy Chem.* **2017**, *26*, 1094. doi: 10.1016/j.jechem.2017.09.015

(249) Seh, Z. W.; Kibsgaard, J.; Dickens, C. F.; Chorkendorff, I.; Norskov, J. K.; Jaramillo, T. F. *Science* **2017**, *355*, 1. doi: 10.1126/science.aad4998

(250) Li, M. M. J.; Chen, C.; Ayvalı, T.; Suo, H.; Zheng, J.; Teixeira, I. F.; Ye, L.; Zou, H.; O'Hare, D.; Tsang, S. C. E. *ACS Catal.* **2018**, *8*, 4390. doi: 10.1021/acscatal.8b00474

(251) Calhau, I. B.; Gomes, A. C.; Bruno, S. M.; Coelho, A. C.; Magalhães, C. I. R.; Romão, C. C.; Valente, A. A.; Gonçalves, I. S.;

Pillinger, M. *Eur. J. Inorg. Chem.* **2020**, *2020*, 2726. doi: 10.1002/ejic.202000202

(252) Lu, Z.; Qian, L.; Tian, Y.; Li, Y.; Sun, X.; Duan, X. *Chem. Commun.* **2016**, *52*, 908. doi: 10.1039/C5CC08845C

(253) Sun, H.; Zhang, W.; Li, J. G.; Li, Z.; Ao, X.; Xue, K. H.; Ostrikov, K. K.; Tang, J.; Wang, C. *Appl. Catal. B: Environ.* **2021**, *284*, 119740. doi: 10.1016/j.apcatb.2020.119740

(254) Li, T.; Hao, X.; Bai, S.; Zhao, Y.; Song, Y. *Acta Phys. -Chim. Sin.* **2020**, *36*, 1912005. doi: 10.3866/PKU.WHXB201912005

(255) Li, Z.; Shao, M.; An, H.; Wang, Z.; Xu, S.; Wei, M.; Evans, D. G.; Duan, X. *Chem. Sci.* **2015**, *6*, 6624. doi: 10.1039/c5sc02417j

(256) Jiang, S.; Liu, Y.; Xie, W.; Shao, M. *J. Energy Chem.* **2019**, *33*, 125. doi: 10.1016/j.jechem.2018.08.010

(257) Chen, F.; Chen, C.; Hu, Q.; Xiang, B.; Song, T.; Zou, X.; Li, W.; Xiong, B.; Deng, M. *Chem. Eng. J.* **2020**, *401*, 126145. doi: 10.1016/j.cej.2020.126145

(258) Mai, W.; Cui, Q.; Zhang, Z.; Zhang, K.; Li, G.; Tian, L.; Hu, W. *ACS Appl. Energy Mater.* **2020**, *3*, 8075. doi: 10.1021/acsaem.0c01538

(259) Wang, Y.; Zhang, Y.; Liu, Z.; Xie, C.; Feng, S.; Liu, D.; Shao, M.; Wang, S. *Angew. Chem. Int. Ed.* **2017**, *56*, 5867. doi: 10.1002/anie.201701477

(260) Zhao, J.; Xu, S.; Tschulik, K.; Compton, R. G.; Wei, M.; O'Hare, D.; Evans, D. G.; Duan, X. *Adv. Funct. Mater.* **2015**, *25*, 2745. doi: 10.1002/adfm.201500408

(261) Chen, Z.; Ha, Y.; Jia, H.; Yan, X.; Chen, M.; Liu, M.; Wu, R. *Adv. Energy Mater.* **2019**, *9*, 1803918. doi: 10.1002/aenm.201803918

(262) Li, J.; Li, Z.; Ning, F.; Zhou, L.; Zhang, R.; Shao, M.; Wei, M. *ACS Omega* **2018**, *3*, 1675. doi: 10.1021/acsomega.7b01832

(263) Li, Z. H.; Shao, M. F.; Yang, Q. H.; Tang, Y.; Wei, M.; Evans, D. G.; Duan, X. *Nano Energy* **2017**, *37*, 98. doi: 10.1016/j.nanoen.2017.05.016

(264) Zhou, L.; Shao, M. F.; Zhang, C.; Zhao, J.; He, S.; Rao, D.; Wei, M.; Evans, D. G.; Duan, X. *Adv. Mater.* **2017**, *29*, 1604080. doi: 10.1002/adma.201604080

(265) Zhou, L.; Shao, M. F.; Li, J. B.; Jiang, S.; Wei, M.; Duan, X. *Nano Energy* **2017**, *41*, 583. doi: 10.1016/j.nanoen.2017.10.009

(266) Xiao, K.; Zhou, L.; Shao, M.; Wei, M. *J. Mater. Chem. A* **2018**, *6*, 7585. doi: 10.1039/C8TA01067F

(267) Fan, K.; Li, Z.; Song, Y.; Xie, W.; Shao, M.; Wei, M. *Adv. Funct. Mater.* **2021**, *31*, 2008064. doi: 10.1002/adfm.202008064

(268) Bing, W.; Wang, H.; Zheng, L.; Rao, D.; Yang, Y.; Zheng, L.; Wang, B.; Wang, Y.; Wei, M. *Green Chem.* **2018**, *20*, 3071. doi: 10.1039/C8GC00851E

(269) Yuan, Z.; Bak, S.; Li, P.; Jia, Y.; Zheng, L.; Zhou, Y.; Bai, L.; Hu, E.; Yang, X.; Cai, Z.; *et al. ACS Energy Lett.* **2019**, *4*, 1412.

doi: 10.1021/acsenergylett.9b00867

(270) Sakata, Y.; Furukawa, S.; Kondo, M.; Hirai, K.; Horike, N.; Takashima, Y.; Uehara, H.; Louvain, N.; Meilikhov, M.; Tsuruoka, T.; *et al. Science* **2013**, *339*, 193. doi: 10.1126/science.1231451

(271) Hu, B.; Wu, P. *Nano Res.* **2020**, *13*, 868. doi: 10.1007/s12274-020-2709-9

(272) Zhu, D.; Guo, C.; Liu, J.; Wang, L.; Du, Y.; Qiao, S.-Z. *Chem. Commun.* **2017**, *53*, 10906. doi: 10.1039/C7CC06378D

(273) Hai, G.; Jia, X.; Zhang, K.; Liu, X.; Wu, Z.; Wang, G. *Nano Energy* **2018**, *44*, 345. doi: 10.1016/j.nanoen.2017.11.071

(274) Wang, Y.; Zhao, M.; Ping, J.; Chen, B.; Cao, X.; Huang, Y.; Tan, C.; Ma, Q.; Wu, S.; Yu, Y.; *et al. Adv. Mater.* **2016,** *28*, 4149. doi: 10.1002/adma.201600108

(275) Zhao, M.; Wang, Y.; Ma, Q.; Huang, Y.; Zhang, X.; Ping, J.; Zhang, Z.; Lu, Q.; Yu, Y.; Xu, H.; *et al. Adv. Mater.* **2015,** *27*, 7372. doi: 10.1002/adma.201503648

(276) Huang, Y.; Zhao, M.; Han, S.; Lai, Z.; Yang, J.; Tan, C.; Ma, Q.; Lu, Q.; Chen, J.; Zhang, X.; *et al. Adv. Mater.* **2017,** *29*, 1700102. doi: 10.1002/adma.201700102

(277) Rodenas, T.; Luz, I.; Prieto, G.; Seoane, B.; Miro, H.; Corma, A.; Kapteijn, F.; Llabres, I. X. F. X.; Gascon, J. *Nat. Mater.* **2015**, *14*, 48. doi: 10.1038/nmat4113

(278) Zhao, L.; Dong, B.; Li, S.; Zhou, L.; Lai, L.; Wang, Z.; Zhao, S.; Han, M.; Gao, K.; Lu, M.; *et al. ACS Nano* **2017**, *11*, 5800. doi: 10.1021/acsnano.7b01409

(279) Huang, X.; Sheng, P.; Tu, Z.; Zhang, F.; Wang, J.; Geng, H.; Zou, Y.; Di, C.-A.; Yi, Y.; Sun, Y.; *et al. Nat. Commun.* **2015**, *6*, 7408. doi: 10.1038/ncomms8408

(280) Lahiri, N.; Lotfizadeh, N.; Tsuchikawa, R.; Deshpande, V. V.; Louie, J. *J. Am. Chem. Soc.* **2017**, *139*, 19. doi: 10.1021/jacs.6b09889

(281) Cliffe, M. J.; Castillo-Martínez, E.; Wu, Y.; Lee, J.; Forse, A. C.; Firth, F. C. N.; Moghadam, P. Z.; Fairen-Jimenez, D.; Gaultois, M. W.; Hill, J. A.; *et al. J. Am. Chem. Soc.* **2017**, *139*, 5397. doi: 10.1021/jacs.7b00106

(282) Chandrasekhar, P.; Mukhopadhyay, A.; Savitha, G.; Moorthy, J. N. *J. Mater. Chem. A* **2017**, *5*, 5402. doi: 10.1039/C6TA11110F

(283) Wu, J.-X.; Yuan, W.-W.; Xu, M.; Gu, Z.-Y. *Chem. Commun.* **2019**, *55*, 11634. doi: 10.1039/C9CC05487A

(284) Zhu, D.; Liu, J.; Zhao, Y.; Zheng, Y.; Qiao, S.-Z. *Small* **2019**, *15*, 1805511. doi: 10.1002/smll.201805511

(285) Ashworth, D. J.; Foster, J. A. *J. Mater. Chem. A* **2018**, *6*, 16292. doi: 10.1039/C8TA03159B

(286) Zhao, M.; Huang, Y.; Peng, Y.; Huang, Z.; Ma, Q.; Zhang, H. *Chem. Soc. Rev.* **2018**, *47*, 6267. doi: 10.1039/c8cs00268a

(287) Zhao, W.; Peng, J.; Wang, W.; Liu, S.; Zhao, Q.; Huang, W. *Coord. Chem. Rev.* **2018**, *377*, 44. doi: 10.1016/j.ccr.2018.08.023

(288) Wang, B.; Zhao, M.; Li, L.; Huang, Y.; Zhang, X.; Guo, C.; Zhang, Z.; Cheng, H.; Liu, W.; Shang, J.; *et al. Natl. Sci. Rev.* **2019**, *7*, 46. doi: 10.1093/nsr/nwz118

(289) Zhuang, L.; Ge, L.; Liu, H.; Jiang, Z.; Jia, Y.; Li, Z.; Yang, D.; Hocking, R. K.; Li, M.; Zhang, L.; *et al. Angew. Chem. Int. Ed.* **2019**, *58*, 13565. doi: 10.1002/anie.201907600

(290) Zhang, F.; Zhang, J.; Zhang, B.; Zheng, L.; Cheng, X.; Wan, Q.; Han, B.; Zhang, J. *Nat. Commun.* **2020,** *11*, 1431. doi: 10.1038/s41467-020-15200-4

(291) Li, L.; Yi, J.-D.; Fang, Z.-B.; Wang, X.-S.; Liu, N.; Chen, Y.-N.; Liu, T.-F.; Cao, R. *Chem. Mater.* **2019**, *31*, 7584. doi: 10.1021/acs.chemmater.9b02375

(292) Au, V. K.-M.; Nakayashiki, K.; Huang, H.; Suginome, S.; Sato, H.; Aida, T. *J. Am. Chem. Soc.* **2019**, *141*, 53. doi: 10.1021/jacs.8b09987

(293) Wu, Z.; Qi, J.; Wang, W.; Zeng, Z.; He, Q. *J. Mater. Chem. A* **2021,** *9*, 18793. doi: 10.1039/D1TA03676A

(294) Mannix, A. J.; Zhou, X.-F.; Kiraly, B.; Wood, J. D.; Alducin, D.; Myers, B. D.; Liu, X.; Fisher, B. L.; Santiago, U.; Guest, J. R.; *et al. Science* **2015**, *350*, 1513. doi: 10.1126/science.aad1080

(295) Tao, M.-L.; Tu, Y.-B.; Sun, K.; Wang, Y.-L.; Xie, Z.-B.; Liu, L.; Shi, M.-X.; Wang, J.-Z. *2D Mater.* **2018**, *5*, 035009. doi: 10.1088/2053-1583/aaba3a

(296) Cherukara, M. J.; Narayanan, B.; Chan, H.; Sankaranarayanan, S. K. *Nanoscale* **2017**, *9*, 10186. doi: 10.1039/C7NR03153J

(297) Yuhara, J.; Shimazu, H.; Ito, K.; Ohta, A.; Araidai, M.; Kurosawa, M.; Nakatake, M.; Le Lay, G. *ACS Nano* **2018**, *12*, 11632. doi: 10.1021/acsnano.8b07006

(298) Yuhara, J.; Fujii, Y.; Nishino, K.; Isobe, N.; Nakatake, M.; Xian, L.; Rubio, A.; Le Lay, G. *2D Mater.* **2018**, *5*, 025002. doi: 10.1088/2053-1583/aa9ea0

(299) Yuhara, J.; He, B.; Matsunami, N.; Nakatake, M.; Le Lay, G. *Adv. Mater.* **2019**, *31*, 1901017. doi: 10.1002/adma.201901017

(300) Wang, Z.; Zhou, X.-F.; Zhang, X.; Zhu, Q.; Dong, H.; Zhao, M.; Oganov, A. R. *Nano Lett.* **2015**, *15*, 6182. doi: 10.1021/acs.nanolett.5b02512

(301) Zhang, S.; Zhou, J.; Wang, Q.; Chen, X.; Kawazoe, Y.; Jena, P. *Proc. Natl. Acad. Sci. U. S. A.* **2015**, *112*, 2372. doi: 10.1073/pnas.1416591112

(302) Zhang, Y.; Wang, L.; Xu, H.; Cao, J.; Chen, D.; Han, W. *Adv. Funct. Mater.* **2020**, *30*, 1909372. doi: 10.1002/adfm.201909372

(303) Wang, X.; He, J.; Zhou, B.; Zhang, Y.; Wu, J.; Hu, R.; Liu, L.; Song, J.; Qu, J. *Angew. Chem. Int. Ed.* **2018**, *130*, 8804. doi: 10.1002/ange.201804886

(304) Zhou, J.; Chen, J.; Chen, M.; Wang, J.; Liu, X.; Wei, B.; Wang, Z.; Li, J.; Gu, L.; Zhang, Q.; *et al. Adv. Mater.* **2019**, *31*, 1807874.

doi: 10.1002/adma.201807874

(305) Beladi-Mousavi, S. M.; Pourrahimi, A. M.; Sofer, Z.; Pumera, M. *Adv. Funct. Mater.* **2019**, *29*, 1807004. doi: 10.1002/adfm.201807004

(306) Chen, J.; Dai, Y.; Ma, Y.; Dai, X.; Ho, W.; Xie, M. *Nanoscale* **2017**, *9*, 15945. doi: 10.1039/C7NR04085G

(307) Singh, D.; Gupta, S. K.; Lukačević, I.; Sonvane, Y. *RSC Adv.* **2016**, *6*, 8006. doi: 10.1039/C5RA25773E

(308) Qian, M.; Xu, Z.; Wang, Z.; Wei, B.; Wang, H.; Hu, S.; Liu, L.-M.; Guo, L. *Adv. Mater.* **2020**, *32*, 2004835. doi: 10.1002/adma.202004835

(309) Vishnoi, P.; Mazumder, M.; Pati, S. K.; R. Rao, C. N. *New J. Chem.* **2018**, *42*, 14091. doi: 10.1039/C8NJ03186J

(310) Tian, W.; Zhang, S.; Huo, C.; Zhu, D.; Li, Q.; Wang, L.; Ren, X.; Xie, L.; Guo, S.; Chu, P. K.; *et al. ACS Nano* **2018**, *12*, 1887. doi: 10.1021/acsnano.7b08714

(311) Kamal, C.; Ezawa, M. *Phys. Rev. B* **2015**, *91*, 085423. doi: 10.1103/PhysRevB.91.085423

(312) Del Rio Castillo, A. E.; Pellegrini, V.; Sun, H.; Buha, J.; Dinh, D. A.; Lago, E.; Ansaldo, A.; Capasso, A.; Manna, L.; Bonaccorso, F. *Chem. Mater.* **2018**, *30*, 506. doi: 10.1021/acs.chemmater.7b04628

(313) Peng, B.; Zhang, H.; Shao, H.; Xu, K.; Ni, G.; Li, J.; Zhu, H.; Soukoulis, C. M. *J. Mater. Chem. A* **2018**, *6*, 2018. doi: 10.1039/C7TA09480A

(314) Meng, Z.; Zhuang, J.; Xu, X.; Hao, W.; Dou, S. X.; Du, Y. *Adv. Mater. Interfaces* **2018**, *5*, 1800749. doi: 10.1002/admi.201800749

(315) Qiu, M.; Sun, Z. T.; Sang, D. K.; Han, X. G.; Zhang, H.; Niu, C. M. *Nanoscale* **2017**, *9*, 13384. doi: 10.1039/C7NR03318D

(316) Xu, Y.; Shi, Z.; Shi, X.; Zhang, K.; Zhang, H. *Nanoscale* **2019**, *11*, 14491. doi: 10.1039/C9NR04348A

(317) Lang, J.; Ding, B.; Zhang, S.; Su, H.; Ge, B.; Qi, L.; Gao, H.; Li, X.; Li, Q.; Wu, H. *Adv. Mater.* **2017**, *29*, 1701777. doi: 10.1002/adma.201701777

(318) Ghosh, T.; Samanta, M.; Vasdev, A.; Dolui, K.; Ghatak, J.; Das, T.; Sheet, G.; Biswas, K. *Nano Lett.* **2019**, *19*, 5703. doi: 10.1021/acs.nanolett.9b02312

(319) Ali Umar, A.; Md Saad, S. K.; Mat Salleh, M. *ACS Omega* **2017**, *2*, 3325. doi: 10.1021/acsomega.7b00580

(320) De Padova, P.; Quaresima, C.; Ottaviani, C.; Sheverdyaeva, P. M.; Moras, P.; Carbone, C.; Topwal, D.; Olivieri, B.; Kara, A.; Oughaddou, H. J. A. P. L. *Appl. Phys. Lett.* **2010**, *96*, 261905. doi: 10.1063/1.3459143

(321) Qin, Z.; Pan, J.; Lu, S.; Shao, Y.; Wang, Y.; Du, S.; Gao, H.-J.; Cao, G. *Adv. Mater.* **2017**, *29*, 1606046. doi: 10.1002/adma.201606046

(322) Peng, L.; Ye, S.; Song, J.; Qu, J. *Angew. Chem. Int. Ed.* **2019**, *58*, 9891. doi: 10.1002/anie.201900802

(323) Xu, H.; Yang, S.; Li, B. *J. Mater. Chem. A* **2020**, *8*, 149. doi: 10.1039/C9TA11079H

(324) Antonatos, N.; Luxa, J.; Sturala, J.; Sofer, Z. *Nanoscale* **2020**, *12*, 5397. doi: 10.1039/C9NR10257D

(325) Côté, A. P.; Benin, A. I.; Ockwig, N. W.; O'Keeffe, M.; Matzger, A. J.; Yaghi, O. M. *Science* **2005**, *310*, 1166. doi: 10.1126/science.1120411

(326) Gao, Q.; Bai, L.; Zhang, X.; Wang, P.; Li, P.; Zeng, Y.; Zou, R.; Zhao, Y. *Chin. J. Chem.* **2015**, *33*, 90. doi: 10.1002/cjoc.201400550

(327) Doonan, C. J.; Tranchemontagne, D. J.; Glover, T. G.; Hunt, J. R.; Yaghi, O. M. *Nat. Chem.* **2010**, *2*, 235. doi: 10.1038/nchem.548

(328) Ge, L.; Qiao, C.; Tang, Y.; Zhang, X.; Jiang, X. *Nano Lett.* **2021**, *21*, 3218. doi: 10.1021/acs.nanolett.1c00488

(329) Zhao, Y.; Waterhouse, G. I. N.; Chen, G.; Xiong, X.; Wu, L. Z.; Tung, C. H.; Zhang, T. *Chem. Soc. Rev.* **2019**, *48*, 1972. doi: 10.1039/c8cs00607e

(330) Romero-Muñiz, I.; Mavrandonakis, A.; Albacete, P.; Vega, A.; Briois, V.; Zamora, F.; Platero-Prats, A. E. *Angew. Chem. Int. Ed.* **2020**, *59*, 13013. doi: 10.1002/anie.202004197

(331) Aiyappa, H. B.; Thote, J.; Shinde, D. B.; Banerjee, R.; Kurungot, S. *Chem. Mater.* **2016**, *28*, 4375. doi: 10.1021/acs.chemmater.6b01370

(332) Zhi, Y.; Wang, Z.; Zhang, H.-L.; Zhang, Q. *Small* **2020**, *16*, 2001070. doi: 10.1002/smll.202001070

(333) Ding, X.; Chen, L.; Honsho, Y.; Feng, X.; Saengsawang, O.; Guo, J.; Saeki, A.; Seki, S.; Irle, S.; Nagase, S.; *et al. J. Am. Chem. Soc.* **2011**, *133*, 14510. doi: 10.1021/ja2052396

(334) Zhang, P.; Chen, S.; Zhu, C.; Hou, L.; Xian, W.; Zuo, X.; Zhang, Q.; Zhang, L.; Ma, S.; Sun, Q. *Nat. Commun.* **2021**, *12*, 1844. doi: 10.1038/s41467-021-22141-z

(335) Sun, T.; Li, Z.-J.; Yang, X.; Wang, S.; Zhu, Y.-H.; Zhang, X.-B. *CCS Chemistry* **2019**, *1*, 365. doi: 10.31635/ccschem.019.20190003

(336) Bhanja, P.; Das, S. K.; Bhunia, K.; Pradhan, D.; Hayashi, T.; Hijikata, Y.; Irle, S.; Bhaumik, A. *ACS Sus. Chem. Eng.* **2018**, *6*, 202. doi: 10.1021/acssuschemeng.7b02234

(337) Gao, C.; Li, J.; Yin, S.; Lin, G.; Ma, T.; Meng, Y.; Sun, J.; Wang, C. *Angew. Chem. Int. Ed.* **2019**, *58*, 9770. doi: 10.1002/anie.201905591

(338) Yao, C.-J.; Wu, Z.; Xie, J.; Yu, F.; Guo, W.; Xu, Z. J.; Li, D.-S.; Zhang, S.; Zhang, Q. *ChemSusChem* **2020**, *13*, 2457. doi: 10.1002/cssc.201903007

(339) Evans, A. M.; Parent, L. R.; Flanders, N. C.; Bisbey, R. P.; Vitaku, E.; Kirschner, M. S.; Schaller, R. D.; Chen, L. X.; Gianneschi, N. C.; Dichtel, W. R. *Science* **2018**, *361*, 52. doi: 10.1126/science.aar7883

(340) Wan, S.; Guo, J.; Kim, J.; Ihee, H.; Jiang, D. *Angew. Chem. Int. Ed.* **2008**, *47*, 8826. doi: 10.1002/anie.200803826

(341) Dalapati, S.; Jin, E.; Addicoat, M.; Heine, T.; Jiang, D. *J. Am. Chem.*

Soc. **2016**, *138*, 5797. doi: 10.1021/jacs.6b02700

(342) Haldar, S.; Chakraborty, D.; Roy, B.; Banappanavar, G.; Rinku, K.; Mullangi, D.; Hazra, P.; Kabra, D.; Vaidhyanathan, R. *J. Am. Chem. Soc.* **2018**, *140*, 13367. doi: 10.1021/jacs.8b08312

(343) Zeng, J.-Y.; Wang, X.-S.; Xie, B.-R.; Li, M.-J.; Zhang, X.-Z. *Angew. Chem. Int. Ed.* **2020**, *59*, 10087. doi: 10.1002/anie.201912594

(344) Wang, S.; Ma, L.; Wang, Q.; Shao, P.; Ma, D.; Yuan, S.; Lei, P.; Li, P.; Feng, X.; Wang, B. *J. Mater. Chem. C* **2018**, *6*, 5369. doi: 10.1039/C8TC01559G

(345) Li, C.; Wang, K.; Li, J.; Zhang, Q. *ACS Mater. Lett.* **2020**, *2*, 779. doi: 10.1021/acsmaterialslett.0c00148

(346) Dalapati, S.; Jin, S.; Gao, J.; Xu, Y.; Nagai, A.; Jiang, D. *J. Am. Chem. Soc.* **2013**, *135*, 17310. doi: 10.1021/ja4103293

(347) Zhang, Y.; Shen, X.; Feng, X.; Xia, H.; Mu, Y.; Liu, X. *Chem. Commun.* **2016**, *52*, 11088. doi: 10.1039/C6CC05748A

(348) Yu, F.; Liu, W.; Li, B.; Tian, D.; Zuo, J.-L.; Zhang, Q. *Angew. Chem. Int. Ed.* **2019**, *58*, 16101. doi: 10.1002/anie.201909613

(349) Yu, F.; Liu, W.; Ke, S.-W.; Kurmoo, M.; Zuo, J.-L.; Zhang, Q. *Nat. Commun.* **2020**, *11*, 5534. doi: 10.1038/s41467-020-19315-6

(350) Ning, G.-H.; Chen, Z.; Gao, Q.; Tang, W.; Chen, Z.; Liu, C.; Tian, B.; Li, X.; Loh, K. P. *J. Am. Chem. Soc.* **2017**, *139*, 8897. doi: 10.1021/jacs.7b02696

(351) Chandra, S.; Kundu, T.; Kandambeth, S.; BabaRao, R.; Marathe, Y.; Kunjir, S. M.; Banerjee, R. *J. Am. Chem. Soc.* **2014**, *136*, 6570. doi: 10.1021/ja502212v

(352) Yuan, G. W.; Lin, D. J.; Wang, Y.; Huang, X. L.; Chen, W.; Xie, X. D.; Zong, J. Y.; Yuan, Q. Q.; Zheng, H.; Wang, D.; *et al Nature* **2020**, *577*, 204. doi: 10.1038/s41586-019-1870-3

(353) Sun, T.; Xie, J.; Guo, W.; Li, D.-S.; Zhang, Q. *Adv. Energy Mater.* **2020**, *10*, 1904199. doi: 10.1002/aenm.201904199

(354) Li, T.; Tu, T.; Sun, Y.; Fu, H.; Yu, J.; Xing, L.; Wang, Z.; Wang, H.; Jia, R.; Wu, J.; *et al Nat. Electron.* **2020**, *3*, 473. doi: 10.1038/s41928-020-0444-6

(355) Mao, L.; Stoumpos, C. C.; Kanatzidis, M. G. *J. Am. Chem. Soc.* **2019**, *141*, 1171. doi: 10.1021/jacs.8b10851

(356) Tsai, H. H.; Nie, W. Y.; Blancon, J. C.; Toumpos, C. C. S.; Asadpour, R.; Harutyunyan, B.; Neukirch, A. J.; Verduzco, R.; Crochet, J. J.; Tretiak, S.; *et al Nature* **2016**, *536*, 312. doi: 10.1038/nature18306

(357) Gan, Z.; Cheng, Y.; Chen, W.; Loh, K. P.; Jia, B.; Wen, X. *Adv. Sci.* **2021**, *8*, 2001843. doi: 10.1002/advs.202001843

(358) Sun, Y.; Yin, Y.; Pols, M.; Zhong, J.; Huang, Z.; Liu, B.; Liu, J.; Wang, W.; Xie, H.; Zhan, G.; *et al Adv. Mater.* **2020**, *32*, 2002392. doi: 10.1002/adma.202002392

(359) Leng, K.; Fu, W.; Liu, Y.; Chhowalla, M.; Loh, K. P. *Nat. Rev. Mater.* **2020**, *5*, 482. doi: 10.1038/s41578-020-0185-1

(360) Gao, Y.; Shi, E.; Deng, S.; Shiring, S. B.; Snaider, J. M.; Liang, C.; Yuan, B.; Song, R.; Janke, S. M.; Liebman-Peláez, A.; *et al. Nat. Chem.* **2019**, *11*, 1151. doi: 10.1038/s41557-019-0354-2

(361) Hart, J. L.; Hantanasirisakul, K.; Lang, A. C.; Anasori, B.; Pinto, D.; Pivak, Y.; van Omme, J. T.; May, S. J.; Gogotsi, Y.; Taheri, M. L. *Nat. Commun.* **2019**, *10*, 522. doi: 10.1038/s41467-018-08169-8

(362) Anasori, B.; Lukatskaya, M. R.; Gogotsi, Y. *Nat. Rev. Mater.* **2017**, *2*, 16098. doi: 10.1038/natrevmats.2016.98

(363) Li, P.; Lv, H.; Li, Z.; Meng, X.; Lin, Z.; Wang, R.; Li, X. *Adv. Mater.* **2021**, *33*, 2007803. doi: 10.1002/adma.202007803

(364) Chen, W. Y.; Jiang, X.; Lai, S.-N.; Peroulis, D.; Stanciu, L. *Nat. Commun.* **2020**, *11*, 1302. doi: 10.1038/s41467-020-15092-4

(365) Hou, T.; Luo, Q.; Li, Q.; Zu, H.; Cui, P.; Chen, S.; Lin, Y.; Chen, J.; Zheng, X.; Zhu, W.; *et al Nat. Commun.* **2020**, *11*, 4251. doi: 10.1038/s41467-020-18091-7

(366) Kuznetsov, D. A.; Chen, Z.; Kumar, P. V.; Tsoukalou, A.; Kierzkowska, A.; Abdala, P. M.; Safonova, O. V.; Fedorov, A.; Müller, C. R. *J. Am. Chem. Soc.* **2019**, *141*, 17809. doi: 10.1021/jacs.9b08897

(367) Natu, V.; Hart, J. L.; Sokol, M.; Chiang, H.; Taheri, M. L.; Barsoum, M. W. *Angew. Chem. Int. Ed.* **2019**, *58*, 12655. doi: 10.1002/anie.201906138

(368) Kuznetsov, D. A.; Chen, Z.; Abdala, P. M.; Safonova, O. V.; Fedorov, A.; Müller, C. R. *J. Am. Chem. Soc.* **2021**, *143*, 5771. doi: 10.1021/jacs.1c00504

(369) VahidMohammadi, A.; Mojtabavi, M.; Caffrey, N. M.; Wanunu, M.; Beidaghi, M. *Adv. Mater.* **2019**, *31*, 1806931. doi: 10.1002/adma.201806931

(370) Li, H.; Zhou, X.; Zhai, W.; Lu, S.; Liang, J.; He, Z.; Long, H.; Xiong, T.; Sun, H.; He, Q.; *et al Adv. Energy Mater.* **2020**, *10*, 2002019. doi: 10.1002/aenm.202002019

(371) Py, M. A.; Haering, R. R. *Can. J. Phys.* **1983**, *61*, 76. doi: 10.1139/p83-013

(372) Yu, Y. F.; Nam, G. H.; He, Q. Y.; Wu, X. J.; Zhang, K.; Yang, Z. Z.; Chen, J. Z.; Ma, Q. L.; Zhao, M. T.; Liu, Z. Q.; *et al Nat. Chem.* **2018**, *10*, 638. doi: 10.1038/s41557-018-0035-6

(373) Kappera, R.; Voiry, D.; Yalcin, S. E.; Branch, B.; Gupta, G.; Mohite, A. D.; Chhowalla, M. *Nat. Mater.* **2014**, *13*, 1128. doi: 10.1038/nmat4080

(374) Tan, C.; Zhang, H. *Chem. Soc. Rev.* **2015**, *44*, 2713. doi: 10.1039/C4CS00182F

(375) Voiry, D.; Mohite, A.; Chhowalla, M. *Chem. Soc. Rev.* **2015**, *44*, 2702. doi: 10.1039/C5CS00151J

(376) He, Q.; Lin, Z.; Ding, M.; Yin, A.; Halim, U.; Wang, C.; Liu, Y.; Cheng, H.-C.; Huang, Y.; Duan, X. *Nano Lett.* **2019**, *19*, 6819. doi: 10.1021/acs.nanolett.9b01898

(377) Lin, Y.-C.; Dumcenco, D. O.; Huang, Y.-S.; Suenaga, K. *Nat. Nanotechnol.* **2014**, *9*, 391. doi: 10.1038/nnano.2014.64

(378) Kang, Y.; Najmaei, S.; Liu, Z.; Bao, Y.; Wang, Y.; Zhu, X.; Halas, N. J.; Nordlander, P.; Ajayan, P. M.; Lou, J.; *et al. Adv. Mater.* **2014**, *26*, 6467. doi: 10.1002/adma.201401802

(379) Wu, S.; Zeng, Z.; He, Q.; Wang, Z.; Wang, S. J.; Du, Y.; Yin, Z.; Sun, X.; Chen, W.; Zhang, H. *Small* **2012**, *8*, 2264. doi: 10.1002/smll.201200044

(380) Wang, Y.; Xiao, J.; Zhu, H.; Li, Y.; Alsaid, Y.; Fong, K. Y.; Zhou, Y.; Wang, S.; Shi, W.; Wang, Y.; *et al. Nature* **2017**, *550*, 487. doi: 10.1038/nature24043

(381) Cho, S.; Kim, S.; Kim, J. H.; Zhao, J.; Seok, J.; Keum, D. H.; Baik, J.; Choe, D.-H.; Chang, K. J.; Suenaga, K.; *et al. Science* **2015**, *349*, 625. doi: 10.1126/science.aab3175

(382) Song, S.; Keum, D. H.; Cho, S.; Perello, D.; Kim, Y.; Lee, Y. H. *Nano Lett.* **2016**, *16*, 188. doi: 10.1021/acs.nanolett.5b03481

(383) Nayak, A. P.; Bhattacharyya, S.; Zhu, J.; Liu, J.; Wu, X.; Pandey, T.; Jin, C.; Singh, A. K.; Akinwande, D.; Lin, J.-F. *Nat. Commun.* **2014**, *5*, 3731. doi: 10.1038/ncomms4731

(384) Zhu, J.; Wang, Z.; Yu, H.; Li, N.; Zhang, J.; Meng, J.; Liao, M.; Zhao, J.; Lu, X.; Du, L.; *et al. J. Am. Chem. Soc.* **2017**, *139*, 10216. doi: 10.1021/jacs.7b05765

(385) Voiry, D.; Goswami, A.; Kappera, R.; SilvaCecilia de Carvalho, C. S.; Kaplan, D.; Fujita, T.; Chen, M.; Asefa, T.; Chhowalla, M. *Nat. Chem.* **2015**, *7*, 45. doi: 10.1038/nchem.2108

(386) Sokolikova, M. S.; Sherrell, P. C.; Palczynski, P.; Bemmer, V. L.; Mattevi, C. *Nat. Commun.* **2019**, *10*, 712. doi: 10.1038/s41467-019-08594-3

(387) Liu, Z.; Zhang, X.; Gong, Y.; Lu, Q.; Zhang, Z.; Cheng, H.; Ma, Q.; Chen, J.; Zhao, M.; Chen, B.; *et al. Nano Res.* **2019**, *12*, 1301. doi: 10.1007/s12274-018-2212-8

(388) Finklea, H. O.; Hanshew, D. D. *J. Am. Chem. Soc.* **1992**, *114*, 3173. doi: 10.1021/ja00035a001

(389) Liu, C.; Zheng, L.; Song, Q.; Xue, Z.; Huang, C.; Liu, L.; Qiao, X.; Li, X.; Liu, K.; Wang, T. *Angew. Chem. Int. Ed.* **2019**, *58*, 2055. doi: 10.1002/anie.201812911

(390) Tao, Q.; Dahlqvist, M.; Lu, J.; Kota, S.; Meshkian, R.; Halim, J.; Palisaitis, J.; Hultman, L.; Barsoum, M. W.; Persson, P. O. Å.; *et al. Nat. Commun.* **2017**, *8*, 14949. doi: 10.1038/ncomms14949

(391) Zhou, W.; Zhou, P.; Lei, X.; Fang, Z.; Zhang, M.; Liu, Q.; Chen, T.; Zeng, H.; Ding, L.; Zhu, J.; *et al. ACS Appl. Mater. Interfaces* **2018**, *10*, 1897. doi: 10.1021/acsami.7b15008

(392) Fan, Z.; Bosman, M.; Huang, X.; Huang, D.; Yu, Y.; Ong, K. P.; Akimov, Y. A.; Wu, L.; Li, B.; Wu, J.; *et al. Nat. Commun.* **2015**, *6*, 7684. doi: 10.1038/ncomms8684

(393) Fan, Z.; Huang, X.; Han, Y.; Bosman, M.; Wang, Q.; Zhu, Y.; Liu,

Q.; Li, B.; Zeng, Z.; Wu, J.; *et al. Nat. Commun.* **2015**, *6*, 6571. doi: 10.1038/ncomms7571

(394) Huang, X.; Li, S.; Huang, Y.; Wu, S.; Zhou, X.; Li, S.; Gan, C. L.; Boey, F.; Mirkin, C. A.; Zhang, H. *Nat. Commun.* **2011**, *2*, 292. doi: 10.1038/ncomms1291

(395) Fan, Z.; Luo, Z.; Huang, X.; Li, B.; Chen, Y.; Wang, J.; Hu, Y.; Zhang, H. *J. Am. Chem. Soc.* **2016**, *138*, 1414. doi: 10.1021/jacs.5b12715

(396) Wang, G.; Ma, C.; Zheng, L.; Chen, Y. *J. Mater. Chem. A* **2021**, *9*, 19534. doi: 10.1039/D1TA03666A

(397) Fan, Z.; Chen, Y.; Zhu, Y.; Wang, J.; Li, B.; Zong, Y.; Han, Y.; Zhang, H. *Chem. Sci.* **2017**, *8*, 795. doi: 10.1039/C6SC02953A

(398) Yun, Q.; Lu, Q.; Li, C.; Chen, B.; Zhang, Q.; He, Q.; Hu, Z.; Zhang, Z.; Ge, Y.; Yang, N.; *et al. ACS Nano* **2019**, *13*, 14329. doi: 10.1021/acsnano.9b07775

(399) Lin, Z.; Du, C.; Yan, B.; Wang, C.; Yang, G. *Nat. Commun.* **2018**, *9*, 4036. doi: 10.1038/s41467-018-06456-y

(400) Yang, N.; Cheng, H.; Liu, X.; Yun, Q.; Chen, Y.; Li, B.; Chen, B.; Zhang, Z.; Chen, X.; Lu, Q.; *et al. Adv. Mater.* **2018**, *30*, 1803234. doi: 10.1002/adma.201803234

(401) Koningsberger, D. C.; Prins, R. *X-ray Absorption: Principles, Applications, Techniques of EXAFS, SEXAFS and XANES*; Wiley: New York, 1988.

(402) Giorgetti, M. *ISRN Mater. Sci.* **2013**, *2013*, 1. doi: 10.1155/2013/938625

(403) Yano, J.; Yachandra, V. K. *Photosynth. Res.* **2009**, *102*, 241. doi: 10.1007/s11120-009-9473-8

(404) Bunker, G. *Introduction to XAFS: A Practical Guide to X-ray Absorption Fine Structure Spectroscopy*; Cambridge University Press: Cambridge, 2010.

(405) Jin, H.; Li, L.; Liu, X.; Tang, C.; Xu, W.; Chen, S.; Song, L.; Zheng, Y.; Qiao, S. Z. *Adv. Mater.* **2019**, *31*, 1902709. doi: 10.1002/adma.201902709

(406) Chen, Z.; Leng, K.; Zhao, X.; Malkhandi, S.; Tang, W.; Tian, B.; Dong, L.; Zheng, L.; Lin, M.; Yeo, B. S.; *et al. Nat. Commun.* **2017**, *8*, 14548. doi: 10.1038/ncomms14548

(407) Muhammad, Z.; Zhang, B.; Lv, H.; Shan, H.; ur Rehman, Z.; Chen, S.; Sun, Z.; Wu, X.; Zhao, A.; Song, L. *ACS Nano* **2020**, *14*, 835. doi: 10.1021/acsnano.9b07931

(408) Strocov, V. N.; Wang, X.; Shi, M.; Kobayashi, M.; Krempasky, J.; Hess, C.; Schmitt, T.; Patthey, L. *J. Synchrotron Radiat.* **2014**, *21*, 32. doi: 10.1107/S1600577513019085

(409) Han, T. T.; Chen, L.; Cai, C.; Wang, Z. G.; Wang, Y. D.; Xin, Z. M.; Zhang, Y. *Phys. Rev. Lett.* **2021**, *126*, 106602. doi: 10.1103/PhysRevLett.126.106602

(410) Muhammad, Z.; Mu, K.; Lv, H.; Wu, C.; ur Rehman, Z.; Habib, M.;

Sun, Z.; Wu, X.; Song, L. *Nano Res.* **2018**, *11*, 4914. doi: 10.1007/s12274-018-2081-1

(411) ur Rehman, Z.; Wang, S.; Lawan, M. A.; Zareen, S.; Moses, O. A.; Zhu, W.; Wu, X.; Sun, Z.; Song, L. *Appl. Phys. Lett.* **2019**, *115*, 213102. doi: 10.1063/1.5115280

(412) Li, L. K.; Kim, J.; Jin, C. H.; Ye, G. J.; Qiu, D. Y.; da Jornada, F. H.; Shi, Z. W.; Chen, L.; Zhang, Z. C.; Yang, F. Y.; *et al. Nat. Nanotechnol.* **2017**, *12*, 21. doi: 10.1038/nnano.2016.171

(413) Li, L.; Han, W.; Pi, L. J.; Niu, P.; Han, J. B.; Wang, C. L.; Su, B.; Li, H. Q.; Xiong, J.; Bando, Y.; *et al. Infomat* **2019**, *1*, 54. doi: 10.1002/inf2.12005

(414) Zhang, G. W.; Chaves, A.; Huang, S. Y.; Wang, F. J.; Xing, Q. X.; Low, T.; Yan, H. G. *Sci. Adv.* **2018**, *4*, eaap9977. doi: 10.1126/sciadv.aap9977

(415) Yong, C. K.; Utama, M. I. B.; Ong, C. S.; Cao, T.; Regan, E. C.; Horng, J.; Shen, Y. X.; Cai, H.; Watanabe, K.; Taniguchi, T.; *et al. Nat. Mater.* **2019**, *18*, 1065. doi: 10.1038/s41563-019-0447-8

(416) Sim, S.; Lee, D.; Noh, M.; Cha, S.; Soh, C. H.; Sung, J. H.; Jo, M. H.; Choi, H. *Nat. Commun.* **2016**, *7*, 13569. doi: 10.1038/ncomms13569

(417) Yong, C. K.; Horng, J.; Shen, Y. X.; Cai, H.; Wang, A.; Yang, C. S.; Lin, C. K.; Zhao, S. L.; Watanabe, K.; Taniguchi, T.; *et al. Nat. Phys.* **2018**, *14*, 1092. doi: 10.1038/s41567-018-0216-7

(418) Christiansen, D.; Selig, M.; Berghauser, G.; Schmidt, R.; Niehues, I.; Schneider, R.; Arora, A.; de Vasconcellos, S. M.; Bratschitsch, R.; Malic, E.; *et al. Phys. Rev. Lett.* **2017**, *119*, 187402. doi: 10.1103/PhysRevLett.119.187402

(419) Selig, M.; Berghauser, G.; Raja, A.; Nagler, P.; Schuller, C.; Heinz, T. F.; Korn, T.; Chernikov, A.; Malic, E.; Knorr, A. *Nat. Commun.* **2016**, *7*, 13279. doi: 10.1038/ncomms13279

(420) Deng, S. B.; Shi, E. Z.; Yuan, L.; Jin, L. R.; Dou, L. T.; Huang, L. B. *Nat. Commun.* **2020**, *11*, 664. doi: 10.1038/s41467-020-14403-z

(421) Leisgang, N.; Shree, S.; Paradisanos, I.; Sponfeldner, L.; Robert, C.; Lagarde, D.; Balocchi, A.; Watanabe, K.; Taniguchi, T.; Marie, X.; *et al. Nat. Nanotechnol.* **2020**, *15*, 901. doi: 10.1038/s41565-020-0750-1

(422) Paradisanos, I.; Shree, S.; George, A.; Leisgang, N.; Robert, C.; Watanabe, K.; Taniguchi, T.; Warburton, R. J.; Turchanin, A.; Marie, X.; *et al. Nat. Commun.* **2020**, *11*, 2391. doi: 10.1038/s41467-020-16023-z

(423) Wu, F. C.; Lovorn, T.; MacDonald, A. H. *Phys. Rev. B* **2018**, *97*, 35306. doi: 10.1103/PhysRevB.97.035306

(424) Zhong, M. Z.; Meng, H. T.; Liu, S. J.; Yang, H.; Shen, W. F.; Hu, C. G.; Yang, J. H.; Ren, Z. H.; Li, B.; Liu, Y. Y.; *et al. ACS Nano* **2021**, *15*, 1701. doi: 10.1021/acsnano.0c09357

(425) Aslan, O. B.; Chenet, D. A.; van der Zande, A. M.; Hone, J. C.;

Heinz, T. F. *ACS Photon.* **2016**, *3*, 96. doi: 10.1021/acsphotonics.5b00486

(426) Liu, F. C.; Zheng, S. J.; He, X. X.; Chaturvedi, A.; He, J. F.; Chow, W. L.; Mion, T. R.; Wang, X. L.; Zhou, J. D.; Fu, Q. D.; *et al. Adv. Funct. Mater.* **2016**, *26*, 1169. doi: 10.1002/adfm.201504546

(427) Sim, S.; Lee, D.; Trifonov, A. V.; Kim, T.; Cha, S.; Sung, J. H.; Cho, S.; Shim, W.; Jo, M. H.; Choi, H. *Nat. Commun.* **2018**, *9*, 351. doi: 10.1038/s41467-017-02802-8

(428) Zuo, N.; Nie, A. M.; Hu, C. G.; Shen, W. F.; Jin, B.; Hu, X. Z.; Liu, Z. Y.; Zhou, X.; Zhai, T. Y. *Small* **2021**, *17*, 2008078. doi: 10.1002/smll.202008078

(429) Guo, P. J.; Huang, W.; Stoumpos, C. C.; Mao, L. L.; Gong, J.; Zeng, L.; Diroll, B. T.; Xia, Y.; Ma, X. D.; Gosztola, D. J.; *et al. Phys. Rev. Lett.* **2018**, *121*, 127401. doi: 10.1103/PhysRevLett.121.127401

(430) Raja, A.; Chaves, A.; Yu, J.; Arefe, G.; Hill, H. M.; Rigosi, A. F.; Berkelbach, T. C.; Nagler, P.; Schuller, C.; Korn, T.; *et al. Nat. Commun.* **2017**, *8*, 15251. doi: 10.1038/ncomms15251

(431) Scuri, G.; Zhou, Y.; High, A. A.; Wild, D. S.; Shu, C.; De Greve, K.; Jauregui, L. A.; Taniguchi, T.; Watanabe, K.; Kim, P.; *et al. Phys. Rev. Lett.* **2018**, *120*, 37402. doi: 10.1103/PhysRevLett.120.037402

(432) Qiu, Z. Z.; Trushin, M.; Fang, H. Y.; Verzhbitskiy, I.; Gao, S. Y.; Laksono, E.; Yang, M.; Lyu, P.; Li, J.; Su, J.; *et al. Sci. Adv.* **2019**, *5*, eaaw2347. doi: 10.1126/sciadv.aaw2347

(433) Xie, H. C.; Jiang, S. W.; Rhodes, D. A.; Hone, J. C.; Shan, J.; Mak, K. F. *Nano Lett.* **2021**, *21*, 2538. doi: 10.1021/acs.nanolett.0c05089

(434) Wei, J.; Xu, C.; Dong, B.; Qiu, C.-W.; Lee, C. *Nat. Photon.* **2021**, *15*, 614. doi: 10.1038/s41566-021-00819-6

(435) Lin, H. T.; Song, Y.; Huang, Y. Z.; Kita, D.; Deckoff-Jones, S.; Wang, K. Q.; Li, L.; Li, J. Y.; Zheng, H. Y.; Luo, Z. Q.; *et al. Nat. Photon.* **2017**, *11*, 798. doi: 10.1038/s41566-017-0033-z

(436) Lin, H.; Sturmberg, B. C. P.; Lin, K. T.; Yang, Y. Y.; Zheng, X. R.; Chong, T. K.; de Sterke, C. M.; Jia, B. H. *Nat. Photon.* **2019**, *13*, 270. doi: 10.1038/s41566-019-0389-3

(437) Lukman, S.; Ding, L.; Xu, L.; Tao, Y.; Riis-Jensen, A. C.; Zhang, G.; Wu, Q. Y. S.; Yang, M.; Luo, S.; Hsu, C. H.; *et al. Nat. Nanotechnol.* **2021**, *16*, 354. doi: 10.1038/s41565-021-00865-9

(438) Ergoktas, M. S.; Bakan, G.; Kovalska, E.; Le Fevre, L. W.; Fields, R. P.; Steiner, P.; Yu, X. X.; Salihoglu, O.; Balci, S.; Fal'ko, V. I.; *et al. Nat. Photon.* **2021**, *15*, 493. doi: 10.1038/s41566-021-00791-1

(439) Chen, K.; Zhou, X.; Cheng, X.; Qiao, R. X.; Cheng, Y.; Liu, C.; Xie, Y. D.; Yu, W. T.; Yao, F. R.; Sun, Z. P.; *et al. Nat. Photon.* **2019**, *13*, 754. doi: 10.1038/s41566-019-0492-5

(440) Huang, B.; Cenker, J.; Zhang, X. O.; Ray, E. L.; Song, T. C.; Taniguchi, T.; Watanabe, K.; McGuire, M. A.; Xiao, D.; Xu, X. D. *Nat. Nanotechnol.* **2020**, *15*, 212. doi: 10.1038/s41565-019-0598-4

(441) Yang, S. X.; Zhang, T. L.; Jiang, C. B. *Adv. Sci.* **2021**, *8*, 2002488.

doi: 10.1002/advs.202002488

(442) Guo, Y.; Zhang, W. X.; Wu, H. C.; Han, J. F.; Zhang, Y. L.; Lin, S. H.; Liu, C. R.; Xu, K.; Qiao, J. S.; Ji, W.; *et al. Sci. Adv.* **2018**, *4*, eaau6252. doi: 10.1126/sciadv.aau6252

(443) Carvalho, B. R.; Wang, Y. X.; Mignuzzi, S.; Roy, D.; Terrones, M.; Fantini, C.; Crespi, V. H.; Malard, L. M.; Pimenta, M. A. *Nat. Commun.* **2017**, *8*, 14670. doi: 10.1038/ncomms14670

(444) Lin, M. L.; Zhou, Y.; Wu, J. B.; Cong, X.; Liu, X. L.; Zhang, J.; Li, H.; Yao, W.; Tan, P. H. *Nat. Commun.* **2019**, *10*, 2419. doi: 10.1038/s41467-019-10400-z

(445) Palacios-Berraquero, C.; Barbone, M.; Kara, D. M.; Chen, X. L.; Goykhman, I.; Yoon, D.; Ott, A. K.; Beitner, J.; Watanabe, K.; Taniguchi, T.; *et al. Nat. Commun.* **2016**, *7*, 12978. doi: 10.1038/ncomms12978

(446) Pu, J.; Takenobu, T. *Adv. Mater.* **2018**, *30*, 1707627. doi: 10.1002/adma.201707627

(447) Xu, W. G.; Liu, W. W.; Schmidt, J. F.; Zhao, W. J.; Lu, X.; Raab, T.; Diederichs, C.; Gao, W. B.; Seletskiy, D. V.; Xiong, Q. H. *Nature* **2017**, *541*, 62. doi: 10.1038/nature20601

(448) Su, L. M.; Fan, X.; Yin, T.; Wang, H. D.; Li, Y.; Liu, F. S.; Li, J. Q.; Zhang, H.; Xie, H. P. *Adv. Opt. Mater.* **2020**, *8*, 1900978. doi: 10.1002/adom.201900978

(449) Riccardi, E.; Measson, M. A.; Cazayous, M.; Sacuto, A.; Gallais, Y. *Phys. Rev. Lett.* **2016**, *116*, 066805. doi: 10.1103/PhysRevLett.116.066805

(450) Sonntag, J.; Reichardt, S.; Beschoten, B.; Stampfer, C. *Nano Lett.* **2021**, *21*, 2898. doi: 10.1021/acs.nanolett.0c05043

(451) Sheng, S. X.; Wu, J. B.; Cong, X.; Li, W. B.; Gou, J.; Zhong, Q.; Cheng, P.; Tan, P. H.; Chen, L.; Wu, K. H. *Phys. Rev. Lett.* **2017**, *119*, 196803. doi: 10.1103/PhysRevLett.119.196803

(452) Gadelha, A. C.; Ohlberg, D. A. A.; Rabelo, C.; Neto, E. G. S.; Vasconcelos, T. L.; Campos, J. L.; Lemos, J. S.; Ornelas, V.; Miranda, D.; Nadas, R.; *et al. Nature* **2021**, *590*, 405. doi: 10.1038/s41586-021-03252-5

(453) Lien, D.-H.; Uddin, S. Z.; Yeh, M.; Amani, M.; Kim, H.; Ager, J. W.; Yablonovitch, E.; Javey, A. *Science* **2019**, *364*, 468. doi: 10.1126/science.aaw8053

(454) Liao, F.; Yu, J. X.; Gu, Z. Q.; Yang, Z. Y.; Hasan, T.; Linghu, S. Y.; Peng, J.; Fang, W.; Zhuang, S. L.; Gu, M.; *et al. Sci. Adv.* **2019**, *5*, eaax7398. doi: 10.1126/sciadv.aax7398

(455) Kim, H.; Ahn, G. H.; Cho, J.; Amani, M.; Mastandrea, J. P.; Groschner, C. K.; Lien, D. H.; Zhao, Y. B.; Ager, J. W.; Scott, M. C.; *et al. Sci. Adv.* **2019**, *5*, eaau4728. doi: 10.1126/sciadv.aau4728

(456) Kim, H.; Uddin, S. Z.; Higashitarumizu, N.; Rabani, E.; Javey, A. *Science* **2021**, *373*, 448. doi: 10.1126/science.abi9193

(457) Li, Z.; Wang, T.; Lu, Z.; Jin, C.; Chen, Y.; Meng, Y.; Lian, Z.;

Taniguchi, T.; Watanabe, K.; Zhang, S.; *et al. Nat. Commun.* **2018**, *9*, 3719. doi: 10.1038/s41467-018-05863-5

(458) Ye, Z.; Waldecker, L.; Ma, E. Y.; Rhodes, D.; Antony, A.; Kim, B.; Zhang, X.-X.; Deng, M.; Jiang, Y.; Lu, Z.; *et al. Nat. Commun.* **2018**, *9*, 3718. doi: 10.1038/s41467-018-05917-8

(459) Chen, S.-Y.; Goldstein, T.; Taniguchi, T.; Watanabe, K.; Yan, J. *Nat. Commun.* **2018**, *9*, 3717. doi: 10.1038/s41467-018-05558-x

(460) Barbone, M.; Montblanch, A. R. P.; Kara, D. M.; Palacios-Berraquero, C.; Cadore, A. R.; De Fazio, D.; Pingault, B.; Mostaani, E.; Li, H.; Chen, B.; *et al. Nat. Commun.* **2018**, *9*, 3721. doi: 10.1038/s41467-018-05632-4

(461) Klein, J.; Lorke, M.; Florian, M.; Sigger, F.; Sigl, L.; Rey, S.; Wierzbowski, J.; Cerne, J.; Muller, K.; Mitterreiter, E.; *et al. Nat. Commun.* **2019**, *10*, 2755. doi: 10.1038/s41467-019-10632-z

(462) He, Y. M.; Iff, O.; Lundt, N.; Baumann, V.; Davanco, M.; Srinivasan, K.; Hofling, S.; Schneider, C. *Nat. Commun.* **2016**, *7*, 13409. doi: 10.1038/ncomms13409

(463) Kianinia, M.; Bradac, C.; Sontheimer, B.; Wang, F.; Tran, T. T.; Nguyen, M.; Kim, S.; Xu, Z. Q.; Jin, D. Y.; Schell, A. W.; *et al. Nat. Commun.* **2018**, *9*, 874. doi: 10.1038/s41467-018-03290-0

(464) Chen, X. T.; Lu, X.; Dubey, S.; Yao, Q.; Liu, S.; Wang, X. Z.; Xiong, Q. H.; Zhang, L. F.; Srivastava, A. *Nat. Phys.* **2019**, *15*, 221. doi: 10.1038/s41567-018-0366-7

(465) Onga, M.; Zhang, Y. J.; Ideue, T.; Iwasa, Y. *Nat. Mater.* **2017**, *16*, 1193. doi: 10.1038/nmat4996

(466) Mak, K. F.; Xiao, D.; Shan, J. *Nat. Photon.* **2018**, *12*, 451. doi: 10.1038/s41566-018-0204-6

(467) Guo, L.; Wu, M.; Cao, T.; Monahan, D. M.; Lee, Y. H.; Louie, S. G.; Fleming, G. R. *Nat. Phys.* **2019**, *15*, 228. doi: 10.1038/s41567-018-0362-y

(468) Hao, K.; Moody, G.; Wu, F. C.; Dass, C. K.; Xu, L. X.; Chen, C. H.; Sun, L. Y.; Li, M. Y.; Li, L. J.; MacDonald, A. H.; *et al. Nat. Phys.* **2016**, *12*, 677. doi: 10.1038/nphys3674

(469) Rivera, P.; Seyler, K. L.; Yu, H. Y.; Schaibley, J. R.; Yan, J. Q.; Mandrus, D. G.; Yao, W.; Xu, X. D. *Science* **2016**, *351*, 688. doi: 10.1126/science.aac7820

(470) Jauregui, L. A.; Joe, A. Y.; Pistunova, K.; Wild, D. S.; High, A. A.; Zhou, Y.; Scuri, G.; De Greve, K.; Sushko, A.; Yu, C. H.; *et al. Science* **2019**, *366*, 870. doi: 10.1126/science.aaw4194

(471) Wang, Z. F.; Rhodes, D. A.; Watanabe, K.; Taniguchi, T.; Hone, J. C.; Shan, J.; Mak, K. F. *Nature* **2019**, *574*, 76. doi: 10.1038/s41586-019-1591-7

(472) Seyler, K. L.; Rivera, P.; Yu, H. Y.; Wilson, N. P.; Ray, E. L.; Mandrus, D. G.; Yan, J. Q.; Yao, W.; Xu, X. D. *Nature* **2019**, *567*, 66. doi: 10.1038/s41586-019-0957-1

(473) Tran, K.; Moody, G.; Wu, F. C.; Lu, X. B.; Choi, J.; Kim, K.; Rai,

A.; Sanchez, D. A.; Quan, J. M.; Singh, A.; *et al. Nature* **2019**, *567*, 71. doi: 10.1038/s41586-019-0975-z

(474) Jin, C. H.; Regan, E. C.; Yan, A. M.; Utama, M. I. B.; Wang, D. Q.; Zhao, S. H.; Qin, Y.; Yang, S. J.; Zheng, Z. R.; Shi, S. Y.; *et al. Nature* **2019**, *567*, 76. doi: 10.1038/s41586-019-0976-y

(475) Alexeev, E. M.; Ruiz-Tijerina, D. A.; Danovich, M.; Hamer, M. J.; Terry, D. J.; Nayak, P. K.; Ahn, S.; Pak, S.; Lee, J.; Sohn, J. I.; *et al. Nature* **2019**, *567*, 81. doi: 10.1038/s41586-019-0986-9

(476) Bai, Y. S.; Zhou, L.; Wang, J.; Wu, W. J.; McGilly, L. J.; Halbertal, D.; Lo, C. F. B.; Liu, F.; Ardelean, J.; Rivera, P.; *et al. Nat. Mater.* **2020**, *19*, 1068. doi: 10.1038/s41563-020-0730-8

(477) Shimazaki, Y.; Schwartz, I.; Watanabe, K.; Taniguchi, T.; Kroner, M.; Imamoğlu, A. *Nature* **2020**, *580*, 472. doi: 10.1038/s41586-020-2191-2

(478) Liu, E.; Barré, E.; van Baren, J.; Wilson, M.; Taniguchi, T.; Watanabe, K.; Cui, Y.-T.; Gabor, N. M.; Heinz, T. F.; Chang, Y.-C.; *et al. Nature* **2021**, *594*, 46. doi: 10.1038/s41586-021-03541-z

(479) Lundt, N.; Klembt, S.; Cherotchenko, E.; Betzold, S.; Iff, O.; Nalitov, A. V.; Klaas, M.; Dietrich, C. P.; Kavokin, A. V.; Hofling, S.; *et al. Nat. Commun.* **2016**, *7*, 13328. doi: 10.1038/ncomms13328

(480) Zhao, J. X.; Su, R.; Fieramosca, A.; Zhao, W. J.; Du, W.; Liu, X.; Diederichs, C.; Sanvitto, D.; Liew, T. C. H.; Xiong, Q. H. *Nano Lett.* **2021**, *21*, 3331. doi: 10.1021/acs.nanolett.1c01162

(481) Zhang, L.; Gogna, R.; Burg, W.; Tutuc, E.; Deng, H. *Nat. Commun.* **2018**, *9*, 713. doi: 10.1038/s41467-018-03188-x

(482) Fieramosca, A.; Polimeno, L.; Ardizzone, V.; De Marco, L.; Pugliese, M.; Maiorano, V.; De Giorgi, M.; Dominici, L.; Gigli, G.; Gerace, D. *Sci. Adv.* **2019**, *5*, eaav9967. doi: 10.1126/sciadv.aav9967

(483) Tian, Q.; Yin, P.; Zhang, T.; Zhou, L.; Xu, B.; Luo, Z.; Liu, H.; Ge, Y.; Zhang, J.; Liu, P.; *et al. Nanophotonics* **2020**, *9*, 2495. doi: 10.1515/nanoph-2020-0005

(484) Yin, P.; Jiang, X.; Huang, R.; Wang, X.; Ge, Y.; Ma, C.; Zhang, H. *Adv. Mater. Interfaces* **2021**, *8*, 2100367. doi: 10.1002/admi.202100367

(485) Yin, P.; Xu, X.; Jiang, Z. *Opt. Commun.* **2017**, *402*, 678. doi: 10.1016/j.optcom.2017.06.088

(486) Yin, P.; Xu, X.; Jiang, Z.; Hai, Y. *Opt. Commun.* **2017**, *405*, 378. doi: 10.1016/j.optcom.2017.08.046

(487) Gao, S.; Xu, X.; Yin, P. *Renew. Energy* **2020**, *150*, 1178. doi: 10.1016/j.renene.2019.11.125

(488) Lv, J.; Xu, X.; Yin, P. *Sol. Energy* **2019**, *194*, 554. doi: 10.1016/j.solener.2019.10.056

(489) Lv, J.; Xu, X.; Yin, P. *J. Clean. Prod.* **2020**, *266*, 121895. doi: 10.1016/j.jclepro.2020.121895

(490) Yin, P.; Lv, J.; Wang, X.; Huang, R. *Renew. Energy* **2021**, *179*, 778. doi: 10.1016/j.renene.2021.07.100

(491) Yin, P.; Bao, W.; Gao, L.; Kang, J.; Huang, R.; Wang, X.; Wei, S.; Ge, Y.; Zhang, H. *Nanophotonics* **2021**, *10*, 2833. doi: 10.1515/nanoph-2021-0074

(492) Ma, C.; Yin, P.; Khan, K.; Tareen, A. K.; Huang, R.; Du, J.; Zhang, Y.; Shi, Z.; Cao, R.; Wei, S.; *et al. Small* **2021**, *17*, 2006891. doi: 10.1002/smll.202006891

(493) Shi, X.; Wang, T.; Wang, J.; Xu, Y.; Yang, Z.; Yu, Q.; Wu, J.; Zhang, K.; Zhou, P. *Opt. Mater. Express* **2019**, *9*, 2348. doi: 10.1364/OME.9.002348

(494) Tian, X.; Luo, H.; Wei, R.; Zhu, C.; Guo, Q.; Yang, D.; Wang, F.; Li, J.; Qiu, J. *Adv. Mater.* **2018**, *30*, 1801021. doi: 10.1002/adma.201801021

(495) Wu, K.; Yang, Z.; Pan, S. *Angew. Chem. Int. Ed.* **2016**, *55*, 6713. doi: 10.1002/anie.201602317

(496) Guo, J.; Zhang, Y.; Wang, Z.; Shu, Y.; He, Z.; Zhang, F.; Gao, L.; Li, C.; Wang, C.; Song, Y. *Appl. Mater. Today* **2020**, *20*, 100657. doi: 10.1016/j.apmt.2020.100657

(497) Saouma, F. O.; Stoumpos, C. C.; Wong, J.; Kanatzidis, M. G.; Jang, J. I. *Nat. Commun.* **2017**, *8*, 742. doi: 10.1038/s41467-017-00788-x

(498) Wang, J.; Mi, Y.; Gao, X.; Li, J.; Li, J.; Lan, S.; Fang, C.; Shen, H.; Wen, X.; Chen, R.; *et al. Adv. Opt. Mater.* **2019**, *7*, 1900398. doi: 10.1002/adom.201900398

(499) Abdelwahab, I.; Dichtl, P.; Grinblat, G.; Leng, K.; Chi, X.; Park, I.-H.; Nielsen, M. P.; Oulton, R. F.; Loh, K. P.; Maier, S. A. *Adv. Mater.* **2019**, *31*, 1902685. doi: 10.1002/adma.201902685

(500) Jiang, X.; Zhang, L.; Liu, S.; Zhang, Y.; He, Z.; Li, W.; Zhang, F.; Shi, Y.; Lü, W.; Li, Y.; *et al. Adv. Opt. Mater.* **2018**, *6*, 1800561. doi: 10.1002/adom.201800561

(501) Cheng, X.; Yao, J.; Zhang, H.; Wang, X.; Bai, J. *J. Alloys Compd.* **2021**, *855*, 157433. doi: 10.1016/j.jallcom.2020.157433

(502) Biswal, B. P.; Valligatla, S.; Wang, M.; Banerjee, T.; Saad, N. A.; Mariserla, B. M. K.; Chandrasekhar, N.; Becker, D.; Addicoat, M.; Senkovska, I.; *et al. Angew. Chem. Int. Ed.* **2019**, *58*, 6896. doi: 10.1002/anie.201814412

(503) Song, Y.-D.; Wang, Q.-T. *Optik* **2020**, *220*, 164947. doi: 10.1016/j.ijleo.2020.164947

(504) Li, X.; Li, S. *J. Mater. Chem. C* **2019**, *7*, 1630. doi: 10.1039/C8TC05392H

(505) Chen, E.; Xu, W.; Chen, J.; Warner, J. H. *Mater. Today Adv.* **2020**, *7*, 100076. doi: 10.1016/j.mtadv.2020.100076

(506) Yang, Y.; Liu, W. G.; Lin, Z. T.; Pan, R. H.; Gu, C. Z.; Li, J. J. *Mater. Today Phys.* **2021**, *17*, 100343. doi: 10.1016/j.mtphys.2021.100343

(507) Yao, Y.; Zhang, F.; Chen, B.; Zhao, Y.; Cui, N.; Sun, D.; Liu, S.; Zhang, Y.; Zhang, H.; Zhang, H. *Opt. Laser Technol.* **2021**, *139*, 106983. doi: 10.1016/j.optlastec.2021.106983

(508) Moujaes, E. A.; Diery, W. A. *Phys. E: Low-Dimens. Syst. Nanostructures* **2021**, *128*, 114611.
doi: 10.1016/j.physe.2020.114611

(509) Tang, C. Y.; Cheng, P. K.; Wang, X. Y.; Ma, S.; Long, H.; Tsang, Y. H. *Opt. Mater.* **2020**, *101*, 109694.
doi: 10.1016/j.optmat.2020.109694

(510) Zhou, L.; Zhang, Y.; Zhuo, Z.; Neukirch, A. J.; Tretiak, S. *J. Phys. Chem. Lett.* **2018**, *9*, 6915. doi: 10.1021/acs.jpclett.8b03077

(511) Jiang, X.; Kuklin, A. V.; Baev, A.; Ge, Y.; Ågren, H.; Zhang, H.; Prasad, P. N. *Phys. Rep.* **2020**, *848*, 1.
doi: 10.1016/j.physrep.2019.12.006

(512) Gong, C.; Li, L.; Li, Z.; Ji, H.; Stern, A.; Xia, Y.; Cao, T.; Bao, W.; Wang, C.; Wang, Y.; *et al. Nature* **2017**, *546*, 265.
doi: 10.1038/nature22060

(513) Gong, C.; Zhang, X. *Science* **2019**, *363*, eaav4450.
doi: 10.1126/science.aav4450

(514) Huang, B.; Clark, G.; Navarro-Moratalla, E.; Klein, D. R.; Cheng, R.; Seyler, K. L.; Zhong, D.; Schmidgall, E.; McGuire, M. A.; Cobden, D. H.; *et al. Nature* **2017**, *546*, 270.
doi: 10.1038/nature22391

(515) Burch, K. S.; Mandrus, D.; Park, J.-G. *Nature* **2018**, *563*, 47.
doi: 10.1038/s41586-018-0631-z

(516) Gibertini, M.; Koperski, M.; Morpurgo, A. F.; Novoselov, K. S. *Nat. Nanotechnol.* **2019**, *14*, 408. doi: 10.1038/s41565-019-0438-6

(517) Zhang, X.-X.; Li, L.; Weber, D.; Goldberger, J.; Mak, K. F.; Shan, J. *Nat. Mater.* **2020**, *19*, 838. doi: 10.1038/s41563-020-0713-9

(518) Žutić, I.; Matos-Abiague, A.; Scharf, B.; Dery, H.; Belashchenko, K. *Mater. Today* **2019**, *22*, 85. doi: 10.1016/j.mattod.2018.05.003

(519) Zhong, D.; Seyler, K. L.; Linpeng, X.; Cheng, R.; Sivadas, N.; Huang, B.; Schmidgall, E.; Taniguchi, T.; Watanabe, K.; McGuire, M. A.; *et al. Sci. Adv.* **2017**, *3*, e1603113.
doi: 10.1126/sciadv.1603113

(520) Wu, Y.; Zhang, S.; Zhang, J.; Wang, W.; Zhu, Y. L.; Hu, J.; Yin, G.; Wong, K.; Fang, C.; Wan, C.; *et al. Nat. Commun.* **2020**, *11*, 3860.
doi: 10.1038/s41467-020-17566-x

(521) Ji, H.; Stokes, R. A.; Alegria, L. D.; Blomberg, E. C.; Tanatar, M. A.; Reijnders, A.; Schoop, L. M.; Liang, T.; Prozorov, R.; Burch, K. S.; *et al. J. Appl. Phys.* **2013**, *114*, 114907. doi: 10.1063/1.4822092

(522) Karpiak, B.; Cummings, A. W.; Zollner, K.; Vila, M.; Khokhriakov, D.; Hoque, A. M.; Dankert, A.; Svedlindh, P.; Fabian, J.; Roche, S.; *et al. 2D Mater.* **2019**, *7*, 015026. doi: 10.1088/2053-1583/ab5915

(523) Song, T.; Cai, X.; Tu, M. W.-Y.; Zhang, X.; Huang, B.; Wilson, N. P.; Seyler, K. L.; Zhu, L.; Taniguchi, T.; Watanabe, K.; *et al. Science* **2018**, *360*, 1214. doi: 10.1126/science.aar4851

(524) Klein, D. R.; MacNeill, D.; Lado, J. L.; Soriano, D.; Navarro-Moratalla, E.; Watanabe, K.; Taniguchi, T.; Manni, S.; Canfield, P.;
Fernández-Rossier, J.; *et al. Science* **2018**, *360*, 1218.
doi: 10.1126/science.aar3617

(525) Kim, H. H.; Yang, B.; Patel, T.; Sfigakis, F.; Li, C.; Tian, S.; Lei, H.; Tsen, A. W. *Nano Lett.* **2018**, *18*, 4885.
doi: 10.1021/acs.nanolett.8b01552

(526) Wang, Z.; Gutiérrez-Lezama, I.; Ubrig, N.; Kroner, M.; Gibertini, M.; Taniguchi, T.; Watanabe, K.; Imamoğlu, A.; Giannini, E.; Morpurgo, A. F. *Nat. Commun.* **2018**, *9*, 2516.
doi: 10.1038/s41467-018-04953-8

(527) Mermin, N. D.; Wagner, H. *Phys. Rev. Lett.* **1966**, *17*, 1133.
doi: 10.1103/PhysRevLett.17.1133

(528) Ugeda, M. M.; Brihuega, I.; Guinea, F.; Gómez-Rodríguez, J. M. *Phys. Rev. Lett.* **2010**, *104*, 096804.
doi: 10.1103/PhysRevLett.104.096804

(529) González-Herrero, H.; Gómez-Rodríguez, J. M.; Mallet, P.; Moaied, M.; Palacios, J. J.; Salgado, C.; Ugeda, M. M.; Veuillen, J.-Y.; Yndurain, F.; Brihuega, I. *Science* **2016**, *352*, 437.
doi: 10.1126/science.aad8038

(530) Červenka, J.; Katsnelson, M. I.; Flipse, C. F. J. *Nat. Phys.* **2009**, *5*, 840. doi: 10.1038/nphys1399

(531) Uchoa, B.; Kotov, V. N.; Peres, N. M. R.; Castro Neto, A. H. *Phys. Rev. Lett.* **2008**, *101*, 026805. doi: 10.1103/PhysRevLett.101.026805

(532) Sepioni, M.; Nair, R. R.; Tsai, I. L.; Geim, A. K.; Grigorieva, I. V. *EPL* **2012**, *97*, 47001. doi: 10.1209/0295-5075/97/47001

(533) Wang, Z.; Tang, C.; Sachs, R.; Barlas, Y.; Shi, J. *Phys. Rev. Lett.* **2015**, *114*, 016603. doi: 10.1103/PhysRevLett.114.016603

(534) Wei, P.; Lee, S.; Lemaitre, F.; Pinel, L.; Cutaia, D.; Cha, W.; Katmis, F.; Zhu, Y.; Heiman, D.; Hone, J.; *et al. Nat. Mater.* **2016**, *15*, 711.
doi: 10.1038/nmat4603

(535) Gong, S. J.; Li, Z. Y.; Yang, Z. Q.; Gong, C.; Duan, C.-G.; Chu, J. H. *J. Appl. Phys.* **2011**, *110*, 043704. doi: 10.1063/1.3622618

(536) Castro, E. V.; Peres, N. M. R.; Stauber, T.; Silva, N. A. P. *Phys. Rev. Lett.* **2008**, *100*, 186803. doi: 10.1103/PhysRevLett.100.186803

(537) Cao, T.; Li, Z.; Louie, S. G. *Phys. Rev. Lett.* **2015**, *114*, 236602.
doi: 10.1103/PhysRevLett.114.236602

(538) Sharpe, A. L.; Fox, E. J.; Barnard, A. W.; Finney, J.; Watanabe, K.; Taniguchi, T.; Kastner, M. A.; Goldhaber-Gordon, D. *Science* **2019**, *365*, 605. doi: 10.1126/science.aaw3780

(539) Chen, G.; Sharpe, A. L.; Fox, E. J.; Zhang, Y.-H.; Wang, S.; Jiang, L.; Lyu, B.; Li, H.; Watanabe, K.; Taniguchi, T.; *et al. Nature* **2020**, *579*, 56. doi: 10.1038/s41586-020-2049-7

(540) Tu, Z.; Xie, T.; Lee, Y.; Zhou, J.; Admasu, A. S.; Gong, Y.; Valanoor, N.; Cumings, J.; Cheong, S.-W.; Takeuchi, I.; *et al. npj 2D Mater. Appl.* **2021**, *5*, 62. doi: 10.1038/s41699-021-00242-z

(541) Zhang, X.; Zhao, Y.; Song, Q.; Jia, S.; Shi, J.; Han, W. *Jpn. J. Appl. Phys.* **2016**, *55*, 033001. doi: 10.7567/jjap.55.033001

(542) Deng, Y.; Yu, Y.; Song, Y.; Zhang, J.; Wang, N. Z.; Sun, Z.; Yi, Y.; Wu, Y. Z.; Wu, S.; Zhu, J.; *et al. Nature* **2018**, *563*, 94. doi: 10.1038/s41586-018-0626-9

(543) Fei, Z.; Huang, B.; Malinowski, P.; Wang, W.; Song, T.; Sanchez, J.; Yao, W.; Xiao, D.; Zhu, X.; May, A. F.; *et al. Nat. Mater.* **2018**, *17*, 778. doi: 10.1038/s41563-018-0149-7

(544) Tan, C.; Lee, J.; Jung, S.-G.; Park, T.; Albarakati, S.; Partridge, J.; Field, M. R.; McCulloch, D. G.; Wang, L.; Lee, C. *Nat. Commun.* **2018**, *9*, 1554. doi: 10.1038/s41467-018-04018-w

(545) May, A. F.; Calder, S.; Cantoni, C.; Cao, H.; McGuire, M. A. *Phys. Rev. B* **2016**, *93*, 014411. doi: 10.1103/PhysRevB.93.014411

(546) May, A. F.; Ovchinnikov, D.; Zheng, Q.; Hermann, R.; Calder, S.; Huang, B.; Fei, Z.; Liu, Y.; Xu, X.; McGuire, M. A. *ACS Nano* **2019**, *13*, 4436. doi: 10.1021/acsnano.8b09660

(547) Seo, J.; Kim, D. Y.; An, E. S.; Kim, K.; Kim, G.-Y.; Hwang, S.-Y.; Kim, D. W.; Jang, B. G.; Kim, H.; Eom, G.; *et al. Sci. Adv.* **2020**, *6*, eaay8912. doi: 10.1126/sciadv.aay8912

(548) Li, J. H.; Li, Y.; Du, S. Q.; Wang, Z.; Gu, B. L.; Zhang, S. C.; He, K.; Duan, W. H.; Xu, Y. *Sci. Adv.* **2019**, *5*, eaaw5685. doi: 10.1126/sciadv.aaw5685

(549) Deng, Y.; Yu, Y.; Shi, M. Z.; Guo, Z.; Xu, Z.; Wang, J.; Chen, X. H.; Zhang, Y. *Science* **2020**, *367*, 895. doi: 10.1126/science.aax8156

(550) Jiang, S.; Li, L.; Wang, Z.; Mak, K. F.; Shan, J. *Nat. Nanotechnol.* **2018**, *13*, 549. doi: 10.1038/s41565-018-0135-x

(551) Jiang, S.; Shan, J.; Mak, K. F. *Nat. Mater.* **2018**, *17*, 406. doi: 10.1038/s41563-018-0040-6

(552) Huang, B.; Clark, G.; Klein, D. R.; MacNeill, D.; Navarro-Moratalla, E.; Seyler, K. L.; Wilson, N.; McGuire, M. A.; Cobden, D. H.; Xiao, D.; *et al. Nat. Nanotechnol.* **2018**, *13*, 544. doi: 10.1038/s41565-018-0121-3

(553) Wang, Z.; Zhang, T.; Ding, M.; Dong, B.; Li, Y.; Chen, M.; Li, X.; Huang, J.; Wang, H.; Zhao, X.; *et al. Nat. Nanotechnol.* **2018**, *13*, 554. doi: 10.1038/s41565-018-0186-z

(554) Verzhbitskiy, I. A.; Kurebayashi, H.; Cheng, H.; Zhou, J.; Khan, S.; Feng, Y. P.; Eda, G. *Nat. Electron.* **2020**, *3*, 460. doi: 10.1038/s41928-020-0427-7

(555) Gong, S.-J.; Gong, C.; Sun, Y.-Y.; Tong, W.-Y.; Duan, C.-G.; Chu, J.-H.; Zhang, X. *Proc. Natl. Acad. Sci. U. S. A.* **2018**, *115*, 8511. doi: 10.1073/pnas.1715465115

(556) Du, E.-W.; Gong, S.-J.; Tang, X.; Chu, J.; Rappe, A. M.; Gong, C. *Nano Lett.* **2020**, *20*, 7230. doi: 10.1021/acs.nanolett.0c02584

(557) Alghamdi, M.; Lohmann, M.; Li, J.; Jothi, P. R.; Shao, Q.; Aldosary, M.; Su, T.; Fokwa, B. P. T.; Shi, J. *Nano Lett.* **2019**, *19*, 4400. doi: 10.1021/acs.nanolett.9b01043

(558) Gupta, V.; Cham, T. M.; Stiehl, G. M.; Bose, A.; Mittelstaedt, J. A.; Kang, K.; Jiang, S.; Mak, K. F.; Shan, J.; Buhrman, R. A.; *et al.*

Nano Lett. **2020**, *20*, 7482. doi: 10.1021/acs.nanolett.0c02965

(559) Song, T.; Fei, Z.; Yankowitz, M.; Lin, Z.; Jiang, Q.; Hwangbo, K.; Zhang, Q.; Sun, B.; Taniguchi, T.; Watanabe, K.; *et al. Nat. Mater.* **2019**, *18*, 1298. doi: 10.1038/s41563-019-0505-2

(560) Li, T.; Jiang, S.; Sivadas, N.; Wang, Z.; Xu, Y.; Weber, D.; Goldberger, J. E.; Watanabe, K.; Taniguchi, T.; Fennie, C. J.; *et al. Nat. Mater.* **2019**, *18*, 1303. doi: 10.1038/s41563-019-0506-1

(561) Sun, Y.; Xiao, R. C.; Lin, G. T.; Zhang, R. R.; Ling, L. S.; Ma, Z. W.; Luo, X.; Lu, W. J.; Sun, Y. P.; Sheng, Z. G. *Appl. Phys. Lett.* **2018**, *112*, 072409. doi: 10.1063/1.5016568

(562) Lin, Z.; Lohmann, M.; Ali, Z. A.; Tang, C.; Li, J.; Xing, W.; Zhong, J.; Jia, S.; Han, W.; Coh, S.; *et al. Phys. Rev. Mater.* **2018**, *2*, 051004. doi: 10.1103/PhysRevMaterials.2.051004

(563) Wang, Y.; Ying, J.; Zhou, Z.; Sun, J.; Wen, T.; Zhou, Y.; Li, N.; Zhang, Q.; Han, F.; Xiao, Y.; *et al. Nat. Commun.* **2018**, *9*, 1914. doi: 10.1038/s41467-018-04326-1

(564) Liu, B.; Liu, S.; Yang, L.; Chen, Z.; Zhang, E.; Li, Z.; Wu, J.; Ruan, X.; Xiu, F.; Liu, W.; *et al. Phys. Rev. Lett.* **2020**, *125*, 267205. doi: 10.1103/PhysRevLett.125.267205

(565) Tian, Y. Z.; Gao, W. W.; Henriksen, E. A.; Chelikowsky, J. R.; Yang, L. *Nano Lett.* **2019**, *19*, 7673. doi: 10.1021/acs.nanolett.9b02523

(566) Lee, J.-U.; Lee, S.; Ryoo, J. H.; Kang, S.; Kim, T. Y.; Kim, P.; Park, C.-H.; Park, J.-G.; Cheong, H. *Nano Lett.* **2016**, *16*, 7433. doi: 10.1021/acs.nanolett.6b03052

(567) Kang, S.; Kim, K.; Kim, B. H.; Kim, J.; Sim, K. I.; Lee, J.-U.; Lee, S.; Park, K.; Yun, S.; Kim, T.; *et al. Nature* **2020**, *583*, 785. doi: 10.1038/s41586-020-2520-5

(568) Hwangbo, K.; Zhang, Q.; Jiang, Q.; Wang, Y.; Fonseca, J.; Wang, C.; Diederich, G. M.; Gamelin, D. R.; Xiao, D.; Chu, J.-H.; *et al. Nat. Nanotechnol.* **2021**, *16*, 655. doi: 10.1038/s41565-021-00873-9

(569) Wang, X.; Cao, J.; Lu, Z.; Cohen, A.; Kitadai, H.; Li, T.; Tan, Q.; Wilson, M.; Lui, C. H.; Smirnov, D.; *et al. Nat. Mater.* **2021**, *20*, 964. doi: 10.1038/s41563-021-00968-7

(570) Sun, Z.; Yi, Y.; Song, T.; Clark, G.; Huang, B.; Shan, Y.; Wu, S.; Huang, D.; Gao, C.; Chen, Z.; *et al. Nature* **2019**, *572*, 497. doi: 10.1038/s41586-019-1445-3

(571) Ni, Z.; Haglund, A. V.; Wang, H.; Xu, B.; Bernhard, C.; Mandrus, D. G.; Qian, X.; Mele, E. J.; Kane, C. L.; Wu, L. *Nat. Nanotechnol.* **2021**, *16*, 782. doi: 10.1038/s41565-021-00885-5

(572) Gong, C.; Kim, E. M.; Wang, Y.; Lee, G.; Zhang, X. *Nat. Commun.* **2019**, *10*, 2657. doi: 10.1038/s41467-019-10693-0

(573) Lan, S.; Liu, X.; Wang, S.; Zhu, H.; Liu, Y.; Gong, C.; Yang, S.; Shi, J.; Wang, Y.; Zhang, X. *Nat. Commun.* **2021**, *12*, 2088. doi: 10.1038/s41467-021-22412-9

(574) Tan, G.; Zhao, L. D.; Kanatzidis, M. G. *Chem. Rev.* **2016**, *116*, 12123. doi: 10.1021/acs.chemrev.6b00255

(575) Hicks, L. D.; Dresselhaus, M. S. *Phys. Rev. B* **1993**, *47*, 12727.
doi: 10.1103/physrevb.47.12727

(576) Dresselhaus, M. S.; Chen, G.; Tang, M. Y.; Yang, R.; Lee, H.; Wang,
D.; Ren, Z.; Fleurial, J. P.; Gogna, P. *Adv. Mater.* **2007**, *19*, 1043.
doi: 10.1002/adma.200600527

(577) Zhou, Y.; Zhao, L. D. *Adv. Mater.* **2017**, *29*, 1702676.
doi: 10.1002/adma.201702676

(578) Zhao, L. D.; Tan, G.; Hao, S.; He, J.; Pei, Y.; Chi, H.; Wang, H.;
Gong, S.; Xu, H.; Dravid, V. P.; *et al. Science* **2016**, *351*, 141.
doi: 10.1126/science.aad3749

(579) He, W. K.; Wang, D. Y.; Wu, H. J.; Xiao, Y.; Zhang, Y.; He, D. S.;
Feng, Y.; Hao, Y.-J.; Dong, J.-F.; Chetty, R.; *et al. Science* **2019**,
365, 1418. doi: 10.1126/science.aax5123

(580) Zhao, L. D.; Lo, S. H.; Zhang, Y.; Sun, H.; Tan, G.; Uher, C.;
Wolverton, C.; Dravid, V. P.; Kanatzidis, M. G. *Nature* **2014**, *508*,
373. doi: 10.1038/nature13184

(581) Qin, G.; Zhang, X.; Yue, S.-Y.; Qin, Z.; Wang, H.; Han, Y.; Hu, M.
Phys. Rev. B **2016**, *94*, 165445 doi: 10.1103/PhysRevB.94.165445

(582) Voneshen, D. J.; Refson, K.; Borissenko, E.; Krisch, M.; Bosak, A.;
Piovano, A.; Cemal, E.; Enderle, M.; Gutmann, M. J.; Hoesch, M.;
et al. Nat. Mater. **2013**, *12*, 1028. doi: 10.1038/nmat3739

(583) Li, C. W.; Hong, J.; May, A. F.; Bansal, D.; Chi, S.; Hong, T.;
Ehlers, G.; Delaire, O. *Nat. Phys.* **2015**, *11*, 1063.
doi: 10.1038/nphys3492

(584) Chang, C.; Zhao, L. D. *Mater. Today Phys.* **2018**, *4*, 50.
doi: 10.1016/j.mtphys.2018.02.005

(585) Chang, C.; Wu, M.; He, D.; Pei, Y.; Wu, C. F.; Wu, X.; Yu, H.; Zhu,
F.; Wang, K.; Chen, Y.; *et al. Science* **2018**, *360*, 778.
doi: 10.1126/science.aaq1479

(586) Lu, Q.; Wu, M.; Wu, D.; Chang, C.; Guo, Y. P.; Zhou, C. S.; Li, W.;
Ma, X. M.; Wang, G.; Zhao, L. D.; *et al. Phys. Rev. Lett.* **2017**, *119*,
116401. doi: 10.1103/PhysRevLett.119.116401

(587) Kim, S. I.; Lee, K. H.; Mun, H. A.; Kim, H. S.; Hwang, S. W.; Roh,
J. W.; Yang, D. J.; Shin, W. H.; Li, X. S.; Lee, Y. H.; *et al. Science*
2015, *348*, 109. doi: 10.1126/science.aaa4166

(588) Zhao, L. D.; He, J.; Berardan, D.; Lin, Y.; Li, J. F.; Nan, C. W.;
Dragoe, N. *Energy Environ. Sci.* **2014**, *7*, 2900.
doi: 10.1039/c4ee00997e

(589) Wang, H.; Liu, Z. R.; Yoong, H. Y.; Paudel, T. R.; Xiao, J. X.; Guo,
R.; Lin, W. N.; Yang, P.; Wang, J.; Chow, G. M.; *et al. Nat.
Commun.* **2018**, *9*, 3319. doi: 10.1038/s41467-018-05662-y

(590) Bune, A. V.; Fridkin, V. M.; Ducharme, S.; Blinov, L. M.; Palto, S.
P.; Sorokin, A. V.; Yudin, S. G.; Zlatkin, A. *Nature* **1998**, *391*, 874.
doi: 10.1038/36069

(591) Birol, T. *Nature* **2018**, *560*, 174. doi: 10.1038/d41586-018-05807-5

(592) Nordlander, J.; Campanini, M.; Rossell, M. D.; Erni, R.; Meier, Q.

N.; Cano, A.; Spaldin, N. A.; Fiebig, M.; Trassin, M. *Nat. Commun.*
2019, *10*, 5591. doi: 10.1038/s41467-019-13474-x

(593) Barraza-Lopez, S.; Fregoso, B. M.; Villanova, J. W.; Parkin, S. S. P.;
Chang, K. *Rev. Mod. Phys.* **2021**, *93*, 011001.
doi: 10.1103/RevModPhys.93.011001

(594) Haleoot, R.; Paillard, C.; Kaloni, T. P.; Mehboudi, M.; Xu, B.;
Bellaiche, L.; Barraza-Lopez, S. *Phys. Rev. Lett.* **2017**, *118*, 227401.
doi: 10.1103/PhysRevLett.118.227401

(595) Mehboudi, M.; Fregoso, B. M.; Yang, Y.; Zhu, W.; van der Zande,
A.; Ferrer, J.; Bellaiche, L.; Kumar, P.; Barraza-Lopez, S. *Phys. Rev.
Lett.* **2016**, *117*, 246802. doi: 10.1103/PhysRevLett.117.246802

(596) Fei, R.; Kang, W.; Yang, L. *Phys. Rev. Lett.* **2016**, *117*, 097601.
doi: 10.1103/PhysRevLett.117.097601

(597) Chang, K.; Liu, J. W.; Lin, H. C.; Wang, N.; Zhao, K.; Zhang, A.
M.; Jin, F.; Zhong, Y.; Hu, X. P.; Duan, W. H.; *et al. Science* **2016**,
353, 274. doi: 10.1126/science.aad8609

(598) Higashitarumizu, N.; Kawamoto, H.; Lee, C.-J.; Lin, B.-H.; Chu, F.-
H.; Yonemori, I.; Nishimura, T.; Wakabayashi, K.; Chang, W.-H.;
Nagashio, K. *Nat. Commun.* **2020**, *11*, 2428.
doi: 10.1038/s41467-020-16291-9

(599) Bao, Y.; Song, P.; Liu, Y.; Chen, Z.; Zhu, M.; Abdelwahab, I.; Su, J.;
Fu, W.; Chi, X.; Yu, W.; *et al. Nano Lett.* **2019**, *19*, 5109.
doi: 10.1021/acs.nanolett.9b01419

(600) Hanakata, P. Z.; Carvalho, A.; Campbell, D. K.; Park, H. S. *Phys.
Rev. B* **2016**, *94*, 035304. doi: 10.1103/PhysRevB.94.035304

(601) Chang, K.; Küster, F.; Miller, B. J.; Ji, J.-R.; Zhang, J.-L.; Sessi, P.;
Barraza-Lopez, S.; Parkin, S. S. P. *Nano Lett.* **2020**, *20*, 6590.
doi: 10.1021/acs.nanolett.0c02357

(602) Qiao, H.; Wang, C.; Choi, W. S.; Park, M. H.; Kim, Y. *Mater. Sci.
Eng. R Rep.* **2021**, *145*, 100622. doi: 10.1016/j.mser.2021.100622

(603) Susner, M. A.; Chyasnavichyus, M.; McGuire, M. A.; Ganesh, P.;
Maksymovych, P. *Adv. Mater.* **2017**, *29*, 1602852.
doi: 10.1002/adma.201602852

(604) Belianinov, A.; He, Q.; Dziaugys, A.; Maksymovych, P.; Eliseev, E.;
Borisevich, A.; Morozovska, A.; Banys, J.; Vysochanskii, Y.;
Kalinin, S. V. *Nano Lett.* **2015**, *15*, 3808.
doi: 10.1021/acs.nanolett.5b00491

(605) Chyasnavichyus, M.; Susner, M. A.; Ievlev, A. V.; Eliseev, E. A.;
Kalinin, S. V.; Balke, N.; Morozovska, A. N.; McGuire, M. A.;
Maksymovych, P. *Appl. Phys. Lett.* **2016**, *109*, 172901.
doi: 10.1063/1.4965837

(606) Liu, F.; You, L.; Seyler, K. L.; Li, X.; Yu, P.; Lin, J.; Wang, X.;
Zhou, J.; Wang, H.; He, H.; *et al. Nat. Commun.* **2016**, *7*, 12357.
doi: 10.1038/ncomms12357

(607) Deng, J.; Liu, Y.; Li, M.; Xu, S.; Lun, Y.; Lv, P.; Xia, T.; Gao, P.;
Wang, X.; Hong, J. *Small* **2020**, *16*, 1904529.

doi: 10.1002/smll.201904529

(608) Wu, J.; Chen, H.-Y.; Yang, N.; Cao, J.; Yan, X.; Liu, F.; Sun, Q.; Ling, X.; Guo, J.; Wang, H. *Nat. Electron.* **2020**, *3*, 466. doi: 10.1038/s41928-020-0441-9

(609) Wang, X.; Yu, P.; Lei, Z.; Zhu, C.; Cao, X.; Liu, F.; You, L.; Zeng, Q.; Deng, Y.; Zhu, C.; *et al. Nat. Commun.* **2019**, *10*, 3037. doi: 10.1038/s41467-019-10738-4

(610) Niu, L.; Liu, F.; Zeng, Q.; Zhu, X.; Wang, Y.; Yu, P.; Shi, J.; Lin, J.; Zhou, J.; Fu, Q.; *et al. Nano Energy* **2019**, *58*, 596. doi: 10.1016/j.nanoen.2019.01.085

(611) Ding, W.; Zhu, J.; Wang, Z.; Gao, Y.; Xiao, D.; Gu, Y.; Zhang, Z.; Zhu, W. *Nat. Commun.* **2017**, *8*, 14956. doi: 10.1038/ncomms14956

(612) Zhou, Y.; Wu, D.; Zhu, Y.; Cho, Y.; He, Q.; Yang, X.; Herrera, K.; Chu, Z.; Han, Y.; Downer, M. C.; *et al. Nano Lett.* **2017**, *17*, 5508. doi: 10.1021/acs.nanolett.7b02198

(613) Cui, C.; Hu, W.-J.; Yan, X.; Addiego, C.; Gao, W.; Wang, Y.; Wang, Z.; Li, L.; Cheng, Y.; Li, P.; *et al. Nano Lett.* **2018**, *18*, 1253. doi: 10.1021/acs.nanolett.7b04852

(614) Si, M.; Saha, A. K.; Gao, S.; Qiu, G.; Qin, J.; Duan, Y.; Jian, J.; Niu, C.; Wang, H.; Wu, W.; *et al. Nat. Electron.* **2019**, *2*, 580. doi: 10.1038/s41928-019-0338-7

(615) Poh, S. M.; Tan, S. J. R.; Wang, H.; Song, P.; Abidi, I. H.; Zhao, X.; Dan, J.; Chen, J.; Luo, Z.; Pennycook, S. J.; *et al. Nano Lett.* **2018**, *18*, 6340. doi: 10.1021/acs.nanolett.8b02688

(616) Wang, S.; Liu, L.; Gan, L.; Chen, H.; Hou, X.; Ding, Y.; Ma, S.; Zhang, D. W.; Zhou, P. *Nat. Commun.* **2021**, *12*, 53. doi: 10.1038/s41467-020-20257-2

(617) Lv, B.; Yan, Z.; Xue, W.; Yang, R.; Li, J.; Ci, W.; Pang, R.; Zhou, P.; Liu, G.; Liu, Z.; *et al. Mater. Horiz.* **2021**, *8*, 1472. doi: 10.1039/D0MH01863E

(618) Xu, C.; Chen, Y.; Cai, X.; Meingast, A.; Guo, X.; Wang, F.; Lin, Z.; Lo, T. W.; Maunders, C.; Lazar, S.; *et al. Phys. Rev. Lett.* **2020**, *125*, 047601. doi: 10.1103/PhysRevLett.125.047601

(619) Xue, F.; Hu, W.; Lee, K.-C.; Lu, L.-S.; Zhang, J.; Tang, H.-L.; Han, A.; Hsu, W.-T.; Tu, S.; Chang, W.-H.; *et al. Adv. Funct. Mater.* **2018**, *28*, 1803738. doi: 10.1002/adfm.201803738

(620) Zheng, C. X.; Yu, L.; Zhu, L.; Collins, J. L.; Kim, D.; Lou, Y. D.; Xu, C.; Li, M.; Wei, Z.; Zhang, Y. P.; *et al. Sci. Adv.* **2018**, *4*, eaar7720. doi: 10.1126/sciadv.aar7720

(621) Shirodkar, S. N.; Waghmare, U. V. *Phys. Rev. Lett.* **2014**, *112*, 157601. doi: 10.1103/PhysRevLett.112.157601

(622) Fei, Z.; Zhao, W.; Palomaki, T. A.; Sun, B.; Miller, M. K.; Zhao, Z.; Yan, J.; Xu, X.; Cobden, D. H. *Nature* **2018**, *560*, 336. doi: 10.1038/s41586-018-0336-3

(623) Ma, X.-Y.; Lyu, H.-Y.; Hao, K.-R.; Zhao, Y.-M.; Qian, X.; Yan, Q.-B.; Su, G. *Sci. Bull.* **2021**, *66*, 233. doi: 10.1016/j.scib.2020.09.010

(624) Yuan, S.; Luo, X.; Chan, H. L.; Xiao, C.; Dai, Y.; Xie, M.; Hao, J. *Nat. Commun.* **2019**, *10*, 1775. doi: 10.1038/s41467-019-09669-x

(625) Zheng, Z.; Ma, Q.; Bi, Z.; de la Barrera, S.; Liu, M.-H.; Mao, N.; Zhang, Y.; Kiper, N.; Watanabe, K.; Taniguchi, T.; *et al. Nature* **2020**, *588*, 71. doi: 10.1038/s41586-020-2970-9

(626) Jing, Y. M.; Liu, B. Z.; Zhu, X. K.; Ouyang, F. P.; Sun, J.; Zhou, Y. *Nanophotonics* **2020**, *9*, 1675. doi: 10.1515/nanoph-2019-0574

(627) Guan, Z.; Hu, H.; Shen, X. W.; Xiang, P. H.; Zhong, N.; Chu, J. H.; Duan, C. G. *Adv. Electron. Mater.* **2020**, *6*, 1900818. doi: 10.1002/aelm.201900818

(628) Fu, C. F.; Sun, J. Y.; Luo, Q. Q.; Li, X. X.; Hu, W.; Yang, J. L. *Nano Lett.* **2018**, *18*, 6312. doi: 10.1021/acs.nanolett.8b02561

(629) Bardeen, J.; Cooper, L. N.; Schrieffer, J. R. *Phys. Rev.* **1957**, *108*, 1175. doi: 10.1103/PhysRev.108.1175

(630) Xu, C.; Wang, L.; Liu, Z.; Chen, L.; Guo, J.; Kang, N.; Ma, X. L.; Cheng, H. M.; Ren, W. *Nat. Mater.* **2015**, *14*, 1135. doi: 10.1038/nmat4374

(631) Xi, X.; Zhao, L.; Wang, Z.; Berger, H.; Forro, L.; Shan, J.; Mak, K. F. *Nat. Nanotechnol.* **2015**, *10*, 765. doi: 10.1038/nnano.2015.143

(632) Sohn, E.; Xi, X.; He, W. Y.; Jiang, S.; Wang, Z.; Kang, K.; Park, J. H.; Berger, H.; Forro, L.; Law, K. T.; *et al. Nat. Mater.* **2018**, *17*, 504. doi: 10.1038/s41563-018-0061-1

(633) Yu, Y.; Yang, F.; Lu, X. F.; Yan, Y. J.; Cho, Y. H.; Ma, L.; Niu, X.; Kim, S.; Son, Y. W.; Feng, D.; *et al. Nat. Nanotechnol.* **2015**, *10*, 270. doi: 10.1038/nnano.2014.323

(634) Lian, C. S.; Si, C.; Duan, W. *Nano Lett.* **2018**, *18*, 2924. doi: 10.1021/acs.nanolett.8b00237

(635) Wang, C.; Lian, B.; Guo, X.; Mao, J.; Zhang, Z.; Zhang, D.; Gu, B. L.; Xu, Y.; Duan, W. *Phys. Rev. Lett.* **2019**, *123*, 126402. doi: 10.1103/PhysRevLett.123.126402

(636) Falson, J.; Xu, Y.; Liao, M.; Zang, Y.; Zhu, K.; Wang, C.; Zhang, Z.; Liu, H.; Duan, W.; He, K.; *et al. Science* **2020**, *367*, 1454. doi: 10.1126/science.aax3873

(637) Qiu, D.; Gong, C.; Wang, S.; Zhang, M.; Yang, C.; Wang, X.; Xiong, J. *Adv. Mater.* **2021**, *33*, 2006124. doi: 10.1002/adma.202006124

(638) Saito, Y.; Nojima, T.; Iwasa, Y. *Nat. Rev. Mater.* **2017**, *2*, 16094. doi: 10.1038/natrevmats.2016.94

(639) Yang, C.; Liu, Y.; Wang, Y.; Feng, L.; He, Q.; Sun, J.; Tang, Y.; Wu, C.; Xiong, J.; Zhang, W.; *et al. Science* **2019**, *366*, 1505. doi: 10.1126/science.aax5798

(640) Ge, J. F.; Liu, Z. L.; Liu, C.; Gao, C. L.; Qian, D.; Xue, Q. K.; Liu, Y.; Jia, J. F. *Nat. Mater.* **2015**, *14*, 285. doi: 10.1038/nmat4153

(641) Yu, Y.; Ma, L.; Cai, P.; Zhong, R.; Ye, C.; Shen, J.; Gu, G. D.; Chen, X. H.; Zhang, Y. *Nature* **2019**, *575*, 156. doi: 10.1038/s41586-019-1718-x

(642) Bistritzer, R.; MacDonald, A. H. *Proc. Natl. Acad. Sci. U. S. A.* **2011**, *108*, 12233. doi: 10.1073/pnas.1108174108

(643) Cao, Y.; Luo, J. Y.; Fatemi, V.; Fang, S.; Sanchez-Yamagishi, J. D.; Watanabe, K.; Taniguchi, T.; Kaxiras, E.; Jarillo-Herrero, P. *Phys. Rev. Lett.* **2016,** *117*, 116804. doi: 10.1103/PhysRevLett.117.116804

(644) Kim, K.; Yankowitz, M.; Fallahazad, B.; Kang, S.; Movva, H. C. P.; Huang, S.; Larentis, S.; Corbet, C. M.; Taniguchi, T.; Watanabe, K.; *et al. Nano Lett.* **2016**, *16*, 1989. doi: 10.1021/acs.nanolett.5b05263

(645) Sun, L.; Wang, Z.; Wang, Y.; Zhao, L.; Li, Y.; Chen, B.; Huang, S.; Zhang, S.; Wang, W.; Pei, D.; *et al. Nat. Commun.* **2021,** *12*, 2391. doi: 10.1038/s41467-021-22533-1

(646) Gao, Z. L.; Zhao, M. Q.; Ashik, M. M. A.; Johnson, A. T. C. *J. Phys.-Mater.* **2020,** *3*, 042003. doi: 10.1088/2515-7639/abb58d

(647) Sun, Z. X.; Hu, Y. H. *Matter* **2020,** *2*, 1106. doi: 10.1016/j.matt.2020.03.010

(648) Polshyn, H.; Yankowitz, M.; Chen, S.; Zhang, Y.; Watanabe, K.; Taniguchi, T.; Dean, C. R.; Young, A. F. *Nat. Phys.* **2019,** *15*, 1011. doi: 10.1038/s41567-019-0596-3

(649) Jiang, Y.; Lai, X.; Watanabe, K.; Taniguchi, T.; Haule, K.; Mao, J.; Andrei, E. Y. *Nature* **2019,** *573*, 91. doi: 10.1038/s41586-019-1460-4

(650) Yankowitz, M.; Chen, S. W.; Polshyn, H.; Zhang, Y. X.; Watanabe, K.; Taniguchi, T.; Graf, D.; Young, A. F.; Dean, C. R. *Science* **2019,** *363*, 1059. doi: 10.1126/science.aav1910

(651) Chen, G.; Jiang, L.; Wu, S.; Lyu, B.; Li, H.; Chittari, B. L.; Watanabe, K.; Taniguchi, T.; Shi, Z.; Jung, J.; *et al. Nat. Phys.* **2019,** *15*, 237. doi: 10.1038/s41567-018-0387-2

(652) Chen, G.; Sharpe, A. L.; Gallagher, P.; Rosen, I. T.; Fox, E. J.; Jiang, L.; Lyu, B.; Li, H.; Watanabe, K.; Taniguchi, T.; *et al. Nature* **2019,** *572*, 215. doi: 10.1038/s41586-019-1393-y

(653) Liu, X.; Hao, Z.; Khalaf, E.; Lee, J. Y.; Ronen, Y.; Yoo, H.; Haei Najafabadi, D.; Watanabe, K.; Taniguchi, T.; Vishwanath, A.; *et al. Nature* **2020,** *583*, 221. doi: 10.1038/s41586-020-2458-7

(654) Shen, C.; Chu, Y.; Wu, Q.; Li, N.; Wang, S.; Zhao, Y.; Tang, J.; Liu, J.; Tian, J.; Watanabe, K.; *et al. Nat. Phys.* **2020,** *16*, 520. doi: 10.1038/s41567-020-0825-9

(655) Hao, Z.; Zimmerman, A. M.; Ledwith, P.; Khalaf, E.; Najafabadi, D. H.; Watanabe, K.; Taniguchi, T.; Vishwanath, A.; Kim, P. *Science* **2021,** *371*, 1133. doi: 10.1126/science.abg0399

(656) Lu, X.; Stepanov, P.; Yang, W.; Xie, M.; Aamir, M. A.; Das, I.; Urgell, C.; Watanabe, K.; Taniguchi, T.; Zhang, G.; *et al. Nature* **2019,** *574*, 653. doi: 10.1038/s41586-019-1695-0

(657) Liu, M.; Zhang, L.; Wang, T. *Chem. Rev.* **2015,** *115*, 7304. doi: 10.1021/cr500671p

(658) Dong, Y.; Zhang, Y.; Li, X.; Feng, Y.; Zhang, H.; Xu, J. *Small* **2019,** *15*, 1902237. doi: 10.1002/smll.201902237

(659) Long, G.; Sabatini, R.; Saidaminov, M. I.; Lakhwani, G.; Rasmita, A.; Liu, X.; Sargent, E. H.; Gao, W. *Nat. Rev. Mater.* **2020,** *5*, 423. doi: 10.1038/s41578-020-0181-5

(660) Dang, Y.; Liu, X.; Cao, B.; Tao, X. *Matter* **2021,** *4*, 794. doi: 10.1016/j.matt.2020.12.018

(661) Ma, J.; Wang, H.; Li, D. *Adv. Mater.* **2021,** *33*, 2008785. doi: 10.1002/adma.202008785

(662) Zhao, B.; Yang, S.; Deng, J.; Pan, K. *Adv. Sci.* **2021,** *8*, 2003681. doi: 10.1002/advs.202003681

(663) Chen, Y.; Ma, J.; Liu, Z.; Li, J.; Duan, X.; Li, D. *ACS Nano* **2020,** *14*, 15154. doi: 10.1021/acsnano.0c05343

(664) Huang, P. J.; Taniguchi, K.; Shigefuji, M.; Kobayashi, T.; Matsubara, M.; Sasagawa, T.; Sato, H.; Miyasaka, H. *Adv. Mater.* **2021,** *33*, 2008611. doi: 10.1002/adma.202008611

(665) Jana, M. K.; Song, R.; Liu, H.; Khanal, D. R.; Janke, S. M.; Zhao, R.; Liu, C.; Valy Vardeny, Z.; Blum, V.; Mitzi, D. B. *Nat. Commun.* **2020,** *11*, 4699. doi: 10.1038/s41467-020-18485-7

(666) Lu, H.; Xiao, C.; Song, R.; Li, T.; Maughan, A. E.; Levin, A.; Brunecky, R.; Berry, J. J.; Mitzi, D. B.; Blum, V.; *et al. J. Am. Chem. Soc.* **2020,** *142*, 13030. doi: 10.1021/jacs.0c03899

(667) Shi, C.; Ye, L.; Gong, Z. X.; Ma, J. J.; Wang, Q. W.; Jiang, J. Y.; Hua, M. M.; Wang, C. F.; Yu, H.; Zhang, Y.; *et al. J. Am. Chem. Soc.* **2020,** *142*, 545. doi: 10.1021/jacs.9b11697

(668) Zeng, Y. L.; Huang, X. Q.; Huang, C. R.; Zhang, H.; Wang, F.; Wang, Z. X. *Angew. Chem. Int. Ed.* **2021,** *60*, 10730. doi: 10.1002/anie.202102195

(669) Zhao, Y.; Qiu, Y.; Feng, J.; Zhao, J.; Chen, G.; Gao, H.; Zhao, Y.; Jiang, L.; Wu, Y. *J. Am. Chem. Soc.* **2021,** *143*, 8437. doi: 10.1021/jacs.1c02675

(670) Chen, Y.; Liu, Z.; Li, J.; Cheng, X.; Ma, J.; Wang, H.; Li, D. *ACS Nano* **2020,** *14*, 10258. doi: 10.1021/acsnano.0c03624

(671) Nishitani, S.; Sekiya, R.; Haino, T. *Angew. Chem. Int. Ed.* **2020,** *59*, 669. doi: 10.1002/anie.201910040

(672) Suzuki, N.; Wang, Y.; Elvati, P.; Qu, Z. B.; Kim, K.; Jiang, S.; Baumeister, E.; Lee, J.; Yeom, B.; Bahng, J. H.; *et al. ACS Nano* **2016,** *10*, 1744. doi: 10.1021/acsnano.5b06369

(673) Xu, Z.; Gao, C. *Nat. Commun.* **2011,** *2*, 571. doi: 10.1038/ncomms1583

(674) Ahmed, S. R.; Neethirajan, S. *Glob. Chall.* **2018,** *2*, 1700071. doi: 10.1002/gch2.201700071

(675) Lin, H.-T.; Chang, C.-Y.; Cheng, P.-J.; Li, M.-Y.; Cheng, C.-C.; Chang, S.-W.; Li, L. L. J.; Chu, C.-W.; Wei, P.-K.; Shih, M.-H. *ACS Appl. Mater. Interfaces* **2018,** *10*, 15996. doi: 10.1021/acsami.8b01472

(676) Purcell-Milton, F.; McKenna, R.; Brennan, L. J.; Cullen, C. P.; Guillemeney, L.; Tepliakov, N. V.; Baimuratov, A. S.; Rukhlenko, I. D.; Perova, T. S.; Duesberg, G. S.; *et al. ACS Nano* **2018,** *12*, 954.

doi: 10.1021/acsnano.7b06691

(677) Zhang, H.; He, H.; Jiang, X.; Xia, Z.; Wei, W. *ACS Appl. Mater. Interfaces* **2018,** *10*, 30680. doi: 10.1021/acsami.8b10594

(678) Shen, B.; Kim, Y.; Lee, M. *Adv. Mater.* **2020,** *32*, 1905669. doi: 10.1002/adma.201905669

(679) Ahn, J.; Ma, S.; Kim, J.-Y.; Kyhm, J.; Yang, W.; Lim, J. A.; Kotov, N. A.; Moon, J. *J. Am. Chem. Soc.* **2020,** *142*, 4206. doi: 10.1021/jacs.9b11453

(680) Trujillo-Hernandez, K.; Rodriguez-Lopez, G.; Espinosa-Roa, A.; Gonzalez-Roque, J.; Gomora-Figueroa, A. P.; Zhang, W.; Halasyamani, P. S.; Jancik, V.; Gembicky, M.; Pirruccio, G.; *et al. J. Mater. Chem. C* **2020,** *8*, 9602. doi: 10.1039/d0tc02118k

(681) Zhou, C.; Chu, Y.; Ma, L.; Zhong, Y.; Wang, C.; Liu, Y.; Zhang, H.; Wang, B.; Feng, X.; Yu, X.; *et al. Phys. Chem. Chem. Phys.* **2020,** *22*, 17299. doi: 10.1039/d0cp02530e

(682) Huang, H.; Hu, L.; Sun, Y.; Liu, Y.; Kang, Z.; MacFarlane, D. R. *Microchim. Acta* **2019,** *186*, 298. doi: 10.1007/s00604-019-3415-8

(683) Mo, Z.; Gou, H.; He, J.; Yang, P.; Feng, C.; Guo, R. *Appl. Surf. Sci.* **2012,** *258*, 8623. doi: 10.1016/j.apsusc.2012.05.063

(684) Si, K.; Sun, C.; Cheng, S.; Wang, Y.; Hu, W. *Anal. Methods* **2018,** *10*, 3660. doi: 10.1039/c8ay00664d

(685) Han, X.; Zhang, J.; Huang, J.; Wu, X.; Yuan, D.; Liu, Y.; Cui, Y. *Nat. Commun.* **2018,** *9*, 1294. doi: 10.1038/s41467-018-03689-9

(686) Ahn, J.; Lee, E.; Tan, J.; Yang, W.; Kim, B.; Moon, J. *Mater. Horiz.* **2017,** *4*, 851. doi: 10.1039/c7mh00197e

(687) He, T.; Li, J.; Li, X.; Ren, C.; Luo, Y.; Zhao, F.; Chen, R.; Lin, X.; Zhang, J. *Appl. Phys. Lett.* **2017,** *111*, 151102. doi: 10.1063/1.5001151

(688) Dang, Y.; Liu, X.; Sun, Y.; Song, J.; Hu, W.; Tao, X. *J. Phys. Chem. Lett.* **2020,** *11*, 1689. doi: 10.1021/acs.jpclett.9b03718

(689) Ben-Moshe, A.; Govorov, A. O.; Markovich, G. *Angew. Chem. Int. Ed.* **2013,** *52*, 1275. doi: 10.1002/anie.201207489

(690) Cheng, J.; Hao, J.; Liu, H.; Li, J.; Li, J.; Zhu, X.; Lin, X.; Wang, K.; He, T. *ACS Nano* **2018,** *12*, 5341. doi: 10.1021/acsnano.8b00112

(691) Evans, P. J.; Ouyang, J.; Favereau, L.; Crassous, J.; Fernandez, I.; Perles, J.; Martin, N. *Angew. Chem. Int. Ed.* **2018,** *57*, 6774. doi: 10.1002/anie.201800798

(692) Cruz, C. M.; Marquez, I. R.; Mariz, I. F. A.; Blanco, V.; Sanchez-Sanchez, C.; Sobrado, J. M.; Martin-Gago, J. A.; Cuerva, J. M.; Macoas, E.; Campana, A. G. *Chem. Sci.* **2018,** *9*, 3917. doi: 10.1039/c8sc00427g

(693) Kato, K.; Segawa, Y.; Scott, L. T.; Itami, K. *Angew. Chem. Int. Ed.* **2018,** *57*, 1337. doi: 10.1002/anie.201711985

(694) Billing, D. G.; Lemmerer, A. *Acta Crystallogr. Sect. E Struct. Rep. Online* **2003,** *59*, M381. doi: 10.1107/s1600536803010985

(695) Billing, D. G.; Lemmerer, A. *Crystengcomm* **2006, 8,** 686.

doi: 10.1039/b606987h

(696) Lemmerer, A.; Billing, D. G. *S. Afr. J. Chem.* **2013,** *66*, 263.

(697) Chen, C.; Gao, L.; Gao, W.; Ge, C.; Du, X.; Li, Z.; Yang, Y.; Niu, G.; Tang, J. *Nat. Commun.* **2019,** *10*, 1927. doi: 10.1038/s41467-019-09942-z

(698) Kim, Y.-H.; Zhai, Y.; Lu, H.; Pan, X.; Xiao, C.; Gaulding, E. A.; Harvey, S. P.; Berry, J. J.; Vardeny, Z. V.; Luther, J. M.; *et al. Science* **2021,** *371*, 1129. doi: 10.1126/science.abf5291

(699) Yang, C.-K.; Chen, W.-N.; Ding, Y.-T.; Wang, J.; Rao, Y.; Liao, W.-Q.; Tang, Y.-Y.; Li, P.-F.; Wang, Z.-X.; Xiong, R.-G. *Adv. Mater.* **2019,** *31*, 1808088. doi: 10.1002/adma.201808088

(700) Sun, B.; Liu, X.-F.; Li, X.-Y.; Zhang, Y.; Shao, X.; Yang, D.; Zhang, H.-L. *Chem. Mater.* **2020,** *32*, 8914. doi: 10.1021/acs.chemmater.0c02729

(701) Ma, J.; Fang, C.; Chen, C.; Jin, L.; Wang, J.; Wang, S.; Tang, J.; Li, D. *ACS Nano* **2019,** *13*, 3659. doi: 10.1021/acsnano.9b00302

(702) Wang, J.; Fang, C.; Ma, J.; Wang, S.; Jin, L.; Li, W.; Li, D. *ACS Nano* **2019,** *13*, 9473. doi: 10.1021/acsnano.9b04437

(703) Ishii, A.; Miyasaka, T. *Sci. Adv.* **2020,** *6*, eabd3274. doi: 10.1126/sciadv.abd3274

(704) Wang, L.; Xue, Y.; Cui, M.; Huang, Y.; Xu, H.; Qin, C.; Yang, J.; Dai, H.; Yuan, M. *Angew. Chem. Int. Ed.* **2020,** *59*, 6442. doi: 10.1002/anie.201915912

(705) Li, D.; Liu, X.; Wu, W.; Peng, Y.; Zhao, S.; Li, L.; Hong, M.; Luo, J. *Angew. Chem. Int. Ed.* **2021,** *60*, 8415. doi: 10.1002/anie.202013947

(706) Long, G.; Jiang, C.; Sabatini, R.; Yang, Z.; Wei, M.; Quan, L. N.; Liang, Q.; Rasmita, A.; Askerka, M.; Walters, G.; *et al. Nat. Photon.* **2018,** *12*, 528. doi: 10.1038/s41566-018-0220-6

(707) Di Nuzzo, D.; Cui, L.; Greenfield, J. L.; Zhao, B.; Friend, R. H.; Meskers, S. C. J. *ACS Nano* **2020,** *14*, 7610. doi: 10.1021/acsnano.0c03628

(708) Peng, Y.; Yao, Y.; Li, L.; Wu, Z.; Wang, S.; Luo, J. *J. Mater. Chem. C* **2018,** *6*, 6033. doi: 10.1039/c8tc01150h

(709) Yuan, C.; Li, X.; Semin, S.; Feng, Y.; Rasing, T.; Xu, J. *Nano Lett.* **2018,** *18*, 5411. doi: 10.1021/acs.nanolett.8b01616

(710) Peng, Y.; Yao, Y.; Li, L.; Liu, X.; Zhang, X.; Wu, Z.; Wang, S.; Ji, C.; Zhang, W.; Luo, J. *Chem. Asian J.* **2019,** *14*, 2273. doi: 10.1002/asia.201900288

(711) Moon, T. H.; Oh, S.-J.; Ok, K. M. *ACS Omega* **2018,** *3*, 17895. doi: 10.1021/acsomega.8b02877

(712) Hajlaoui, F.; Sadok, I. B. H.; Aeshah, H. A.; Audebrand, N.; Roisnel, T.; Zouari, N. *J. Mol. Struct.* **2019,** *1182*, 47. doi: 10.1016/j.molstruc.2019.01.035

(713) Guo, Z.; Li, J.; Wang, C.; Liu, R.; Liang, J.; Gao, Y.; Cheng, J.; Zhang, W.; Zhu, X.; Pan, R.; *et al. Angew. Chem. Int. Ed.* **2021,** *60*, 8441. doi: 10.1002/anie.202015445

(714) Dehnhardt, N.; Axt, M.; Zimmermann, J.; Yang, M.; Mette, G.; Heine, J. *Chem. Mater.* **2020**, *32*, 4801. doi: 10.1021/acs.chemmater.0c01605

(715) Ai, Y.; Chen, X.-G.; Shi, P.-P.; Tang, Y.-Y.; Li, P.-F.; Liao, W.-Q.; Xiong, R.-G. *J. Am. Chem. Soc.* **2019**, *141*, 4474. doi: 10.1021/jacs.9b00886

(716) Hu, Y.; Florio, F.; Chen, Z.; Phelan, W. A.; Siegler, M. A.; Zhou, Z.; Guo, Y.; Hawks, R.; Jiang, J.; Feng, J.; *et al. Sci. Adv.* **2020**, *6*, eaay4213. doi: 10.1126/sciadv.aay4213

(717) Huang, P. J.; Taniguchi, K.; Miyasaka, H. *J. Am. Chem. Soc.* **2019**, *141*, 14520. doi: 10.1021/jacs.9b06815

(718) Wang, J.; Lu, H.; Pan, X.; Xu, J.; Liu, H.; Liu, X.; Khanal, D. R.; Toney, M. F.; Beard, M. C.; Vardeny, Z. V. *ACS Nano* **2021**, *15*, 588. doi: 10.1021/acsnano.0c05980

(719) Lu, H.; Wang, J.; Xiao, C.; Pan, X.; Chen, X.; Brunecky, R.; Berry, J. J.; Zhu, K.; Beard, M. C.; Vardeny, Z. V. *Sci. Adv.* **2019**, *5*, eaay0571. doi: 10.1126/sciadv.aay0571

(720) Huang, Z.; Bloom, B. P.; Ni, X.; Georgieva, Z. N.; Marciesky, M.; Vetter, E.; Liu, F.; Waldeck, D. H.; Sun, D. *ACS Nano* **2020**, *14*, 10370. doi: 10.1021/acsnano.0c04017

(721) Lin, W.; Hong, W.; Sun, L.; Yu, D.; Yu, D.; Chen, X. *Chemsuschem* **2018**, *11*, 114. doi: 10.1002/cssc.201701984

(722) Chhowalla, M.; Jena, D.; Zhang, H. *Nat. Rev. Mater.* **2016**, *1*, 16052. doi: 10.1038/natrevmats2016.52

(723) Sze, S. M.; Li, Y.; Ng, K. K. *Physics of Semiconductor Devices,* 4th ed.; John Wiley & Sons, Inc.: Hoboken, NJ, USA, 2021.

(724) Tung, R. T. *Appl. Phys. Rev.* **2014**, *1*, 11304. doi: 10.1063/1.4858400

(725) Mott, N. F. *Proc. R. Soc. Lond. A* **1939**, *171*, 27. doi: 10.1098/rspa.1939.0051

(726) Fang, H.; Tosun, M.; Seol, G.; Chang, T. C.; Takei, K.; Guo, J.; Javey, A. *Nano Lett.* **2013**, *13*, 1991. doi: 10.1021/nl400044m

(727) Das, S.; Chen, H. Y.; Penumatcha, A. V.; Appenzeller, J. *Nano Lett.* **2013**, *13*, 100. doi: 10.1021/nl303583v

(728) Kim, C.; Moon, I.; Lee, D.; Choi, M. S.; Ahmed, F.; Nam, S.; Cho, Y.; Shin, H. J.; Park, S.; Yoo, W. J. *ACS Nano* **2017**, *11*, 1588. doi: 10.1021/acsnano.6b07159

(729) Liu, Y.; Guo, J.; Zhu, E. B.; Liao, L.; Lee, S. J.; Ding, M. N.; Shakir, I.; Gambin, V.; Huang, Y.; Duan, X. F. *Nature* **2018**, *557*, 696. doi: 10.1038/s41586-018-0129-8

(730) Chee, S. S.; Seo, D.; Kim, H.; Jang, H.; Lee, S.; Moon, S. P.; Lee, K. H.; Kim, S. W.; Choi, H.; Ham, M. H. *Adv. Mater.* **2019**, *31*, 1804422. doi: 10.1002/adma.201804422

(731) Cao, Z. H.; Lin, F. R.; Gong, G.; Chen, H.; Martin, J. *Appl. Phys. Lett.* **2020**, *116*, 22101. doi: 10.1063/1.5094890

(732) Wang, Y.; Kim, J. C.; Wu, R. J.; Martinez, J.; Song, X. J.; Yang, J.;

Zhao, F.; Mkhoyan, K. A.; Jeong, H. Y.; Chhowalla, M. *Nature* **2019**, *568*, 70. doi: 10.1038/s41586-019-1052-3

(733) Cui, X.; Shih, E. M.; Jauregui, L. A.; Chae, S. H.; Kim, Y. D.; Li, B. C.; Seo, D.; Pistunova, K.; Yin, J.; Park, J. H.; *et al. Nano Lett.* **2017**, *17*, 4781. doi: 10.1021/acs.nanolett.7b01536

(734) Jung, Y.; Choi, M. S.; Nipane, A.; Borah, A.; Kim, B.; Zangiabadi, A.; Taniguchis, T.; Watanabe, K.; Yoo, W. J.; Hone, J.; *et al. Nat. Electron.* **2019**, *2*, 187. doi: 10.1038/s41928-019-0245-y

(735) Farmanbar, M.; Brocks, G. *Phys. Rev. B* **2015**, *91*, 161304. doi: 10.1103/PhysRevB.91.161304

(736) Shen, P. C.; Su, C.; Lin, Y. X.; Chou, A. S.; Cheng, C. C.; Park, J. H.; Chiu, M. H.; Lu, A. Y.; Tang, H. L.; Tavakoli, M. M.; *et al. Nature* **2021**, *593*, 211. doi: 10.1038/s41586-021-03472-9

(737) Liu, Y.; Duan, X. D.; Huang, Y.; Duan, X. F. *Chem. Soc. Rev.* **2018**, *47*, 6388. doi: 10.1039/c8cs00318a

(738) Gao, J.; Kim, Y. D.; Liang, L.; Idrobo, J. C.; Chow, P.; Tan, J.; Li, B.; Li, L.; Sumpter, B. G.; Lu, T.-M.; *et al. Adv. Mater.* **2016**, *28*, 9735. doi: 10.1002/adma.201601104

(739) Gao, H.; Suh, J.; Cao, M. C.; Joe, A. Y.; Mujid, F.; Lee, K. H.; Xie, S. E.; Poddar, P.; Lee, J. U.; Kang, K.; *et al. Nano Lett.* **2020**, *20*, 4095. doi: 10.1021/acs.nanolett.9b05247

(740) Fang, H.; Chuang, S.; Chang, T. C.; Takei, K.; Takahashi, T.; Javey, A. *Nano Lett.* **2012**, *12*, 3788. doi: 10.1021/nl301702r

(741) Cernetic, N.; Wu, S. F.; Davies, J. A.; Krueger, B. W.; Hutchins, D. O.; Xu, X. D.; Ma, H.; Jen, A. K. Y. *Adv. Funct. Mater.* **2014**, *24*, 3464. doi: 10.1002/adfm.201303952

(742) Liu, C. S.; Chen, H. W.; Wang, S. Y.; Liu, Q.; Jiang, Y. G.; Zhang, D. W.; Liu, M.; Zhou, P. *Nat. Nanotechnol.* **2020**, *15*, 545. doi: 10.1038/s41565-020-0724-3

(743) Kaasbjerg, K.; Thygesen, K. S.; Jacobsen, K. W. *Phys. Rev. B* **2012**, *85*, 115317. doi: 10.1103/PhysRevB.85.115317

(744) Zhang, W.; Huang, Z.; Zhang, W.; Li, Y. *Nano Res.* **2014**, *7*, 1731. doi: 10.1007/s12274-014-0532-x

(745) Yu, Z. H.; Pan, Y. M.; Shen, Y. T.; Wang, Z. L.; Ong, Z. Y.; Xu, T.; Xin, R.; Pan, L. J.; Wang, B. G.; Sun, L. T.; *et al. Nat. Commun.* **2014**, *5*, 5290. doi: 10.1038/ncomms6290

(746) Yu, Z.; Ong, Z.-Y.; Li, S.; Xu, J.-B.; Zhang, G.; Zhang, Y.-W.; Shi, Y.; Wang, X. *Adv. Funct. Mater.* **2017**, *27*, 1604093. doi: 10.1002/adfm.201604093

(747) Hwang, E. H.; Adam, S.; Das Sarma, S. *Phys. Rev. Lett.* **2007**, *98*, 186806. doi: 10.1103/PhysRevLett.98.186806

(748) Ong, Z. Y.; Fischetti, M. V. *Phys. Rev. B* **2013**, *88*, 165316. doi: 10.1103/PhysRevB.88.165316

(749) Radisavljevic, B.; Kis, A. *Nat. Mater.* **2013**, *12*, 815. doi: 10.1038/Nmat3687

(750) Qiu, H.; Xu, T.; Wang, Z. L.; Ren, W.; Nan, H. Y.; Ni, Z. H.; Chen,

Q.; Yuan, S. J.; Miao, F.; Song, F. Q.; *et al. Nat. Commun.* **2013**, *4*, 2642. doi: 10.1038/ncomms3642

(751) Xie, H.; Alves, H.; Morpurgo, A. F. *Phys. Rev. B* **2009**, *80*, 245305. doi: 10.1103/PhysRevB.80.245305

(752) Ghatak, S.; Ghosh, A. *Appl. Phys. Lett.* **2013**, *103*, 122103. doi: 10.1063/1.4821185

(753) Chen, W.; Zhao, J.; Zhang, J.; Gu, L.; Yang, Z. Z.; Li, X. M.; Yu, H.; Zhu, X. T.; Yang, R.; Shi, D. X.; *et al. J. Am. Chem. Soc.* **2015**, *137*, 15632. doi: 10.1021/jacs.5b10519

(754) Qiu, H.; Pan, L. J.; Yao, Z. N.; Li, J. J.; Shi, Y.; Wang, X. R. *Appl. Phys. Lett.* **2012**, *100*, 123104. doi: 10.1063/1.3696045

(755) Cui, Y.; Xin, R.; Yu, Z. H.; Pan, Y. M.; Ong, Z. Y.; Wei, X. X.; Wang, J. Z.; Nan, H. Y.; Ni, Z. H.; Wu, Y.; *et al. Adv. Mater.* **2015**, *27*, 5230. doi: 10.1002/adma.201502222

(756) Lee, G. H.; Cui, X.; Kim, Y. D.; Arefe, G.; Zhang, X.; Lee, C. H.; Ye, F.; Watanabe, K.; Taniguchi, T.; Kim, P.; *et al. ACS Nano* **2015**, *9*, 7019. doi: 10.1021/acsnano.5b01341

(757) Yu, Z.; Ong, Z.-Y.; Pan, Y.; Cui, Y.; Xin, R.; Shi, Y.; Wang, B.; Wu, Y.; Chen, T.; Zhang, Y.-W.; *et al. Adv. Mater.* **2016**, *28*, 547. doi: 10.1002/adma.201503033

(758) Li, W.-S.; Zhou, J.; Wang, H.-C.; Wang, S.-X.; Yu, Z.-H.; Li, S.-L.; Yi, S.; Wang, X.-R. *Acta Phys. Sin.* **2017**, *66*, 218503. doi: 10.7498/aps.66.218503

(759) Su, S.-K.; Chuu, C.-P.; Li, M.-Y.; Cheng, C.-C.; Wong, H.-S. P.; Li, L.-J. *Small Struct.* **2021**, *2*, 2000103. doi: 10.1002/sstr.202000103

(760) Azcatl, A.; McDonnell, S.; Santosh, K. C.; Peng, X.; Dong, H.; Qin, X. Y.; Addou, R.; Mordi, G. I.; Lu, N.; Kim, J.; *et al. Appl. Phys. Lett.* **2014**, *104*, 111601. doi: 10.1063/1.4869149

(761) Islam, M. R.; Kang, N.; Bhanu, U.; Paudel, H. P.; Erementchouk, M.; Tetard, L.; Leuenberger, M. N.; Khondaker, S. I. *Nanoscale* **2014**, *6*, 10033. doi: 10.1039/c4nr02142h

(762) Su, T. H.; Lin, Y. J. *Appl. Phys. Lett.* **2016**, *108*, 33103. doi: 10.1063/1.4939978

(763) Lin, Y. S.; Hoo, J. Y.; Chung, T. F.; Yang, J. R.; Chen, M. J. *ACS Appl. Electron. Interfaces* **2020**, *2*, 1289. doi: 10.1021/acsaelm.0c00089

(764) Son, S.; Yu, S.; Choi, M.; Kim, D.; Choi, C. *Appl. Phys. Lett.* **2015**, *106*, 21601. doi: 10.1063/1.4905634

(765) Tselev, A.; Sangwan, V. K.; Jariwala, D.; Marks, T. J.; Lauhon, L. J.; Hersam, M. C.; Kalinin, S. V. *Appl. Phys. Lett.* **2013**, *103*, 243105. doi: 10.1063/1.4847675

(766) Li, W. S.; Zhou, J.; Cai, S. H.; Yu, Z. H.; Zhang, J. L.; Fang, N.; Li, T. T.; Wu, Y.; Chen, T. S.; Xie, X. Y.; *et al. Nat. Electron.* **2019**, *2*, 563. doi: 10.1038/s41928-019-0334-y

(767) Yu, Z.; Ning, H.; Cheng, C. C.; Li, W.; Liu, L.; Meng, W.; Luo, Z.; Li, T.; Cai, S.; Wang, P.; *et al. In Reliability of Ultrathin High-κ*

Dielectrics on Chemical-vapor Deposited 2D Semiconductors, 2020 IEDM, 12-18 Dec. 2020; pp. 3.2.1.

(768) Ang, Y. S.; Cao, L. M.; Ang, L. K. *Infomat* **2021**, *3*, 502. doi: 10.1002/inf2.12168

(769) Liang, S. J.; Cheng, B.; Cui, X. Y.; Miao, F. *Adv. Mater.* **2020**, *32*, 1903800. doi: 10.1002/adma.201903800

(770) Desai, S. B.; Madhvapathy, S. R.; Sachid, A. B.; Llinas, J. P.; Wang, Q. X.; Ahn, G. H.; Pitner, G.; Kim, M. J.; Bokor, J.; Hu, C. M.; *et al. Science* **2016**, *354*, 99. doi: 10.1126/science.aah4698

(771) Dathbun, A.; Kim, Y.; Kim, S.; Yoo, Y.; Kang, M. S.; Lee, C.; Cho, J. H. *Nano Lett.* **2017**, *17*, 2999. doi: 10.1021/acs.nanolett.7b00315

(772) Yu, L. L.; El-Damak, D.; Radhakrishna, U.; Ling, X.; Zubair, A.; Lin, Y. X.; Zhang, Y. H.; Chuang, M. H.; Lee, Y. H.; Antoniadis, D.; *et al. Nano Lett.* **2016**, *16*, 6349. doi: 10.1021/acs.nanolett.6b02739

(773) Wachter, S.; Polyushkin, D. K.; Bethge, O.; Mueller, T. *Nat. Commun.* **2017**, *8*, 14948. doi: 10.1038/ncomms14948

(774) Li, N.; Wang, Q. Q.; Shen, C.; Wei, Z.; Yu, H.; Zhao, J.; Lu, X. B.; Wang, G. L.; He, C. L.; Xie, L.; *et al. Nat. Electron.* **2020**, *3*, 711. doi: 10.1038/s41928-020-00475-8

(775) Zhang, Q.; Wang, X. F.; Shen, S. H.; Lu, Q.; Liu, X. Z.; Li, H. Y.; Zheng, J. Y.; Yu, C. P.; Zhong, X. Y.; Gu, L.; *et al. Nat. Electron.* **2019**, *2*, 164. doi: 10.1038/s41928-019-0233-2

(776) Kong, L. G.; Zhang, X. D.; Tao, Q. Y.; Zhang, M. L.; Dang, W. Q.; Li, Z. W.; Feng, L. P.; Liao, L.; Duan, X. F.; Liu, Y. *Nat. Commun.* **2020**, *11*, 1866. doi: 10.1038/s41467-020-15776-x

(777) Resta, G. V.; Balaji, Y.; Lin, D.; Radu, I. P.; Catthoor, F.; Gaillardon, P. E.; De Micheli, G. *ACS Nano* **2018**, *12*, 7039. doi: 10.1021/acsnano.8b02739

(778) Yi, J.; Sun, X.; Zhu, C.; Li, S.; Liu, Y.; Zhu, X.; You, W.; Liang, D.; Shuai, Q.; Wu, Y.; *et al. Adv. Mater.* **2021**, *33*, 2101036. doi: 10.1002/adma.202101036

(779) Sachid, A. B.; Desai, S. B.; Javey, A.; Hu, C. *Appl. Phys. Lett.* **2017**, *111*, 222101. doi: 10.1063/1.5004669

(780) Liu, Y.; Zhang, G.; Zhou, H. L.; Li, Z.; Cheng, R.; Xu, Y.; Gambin, V.; Huang, Y.; Duan, X. F. *Nano Lett.* **2017**, *17*, 1448. doi: 10.1021/acs.nanolett.6b04417

(781) Kim, J. S.; Jeon, P. J.; Lee, J.; Choi, K.; Lee, H. S.; Cho, Y.; Lee, Y. T.; Hwang, D. K.; Im, S. *Nano Lett.* **2015**, *15*, 5778. doi: 10.1021/acs.nanolett.5b01746

(782) Xiong, X.; Huang, M. Q.; Hu, B.; Li, X. F.; Liu, F.; Li, S. C.; Tian, M. C.; Li, T. Y.; Song, J.; Wu, Y. Q. *Nat. Electron.* **2020**, *3*, 106. doi: 10.1038/s41928-019-0364-5

(783) Pan, C.; Wang, C. Y.; Liang, S. J.; Wang, Y.; Cao, T. J.; Wang, P. F.; Wang, C.; Wang, S.; Cheng, B.; Gao, A. Y.; *et al. Nat. Electron.* **2020**, *3*, 383. doi: 10.1038/s41928-020-0433-9

(784) Wu, P.; Reis, D.; Hu, X. B. S.; Appenzeller, J. *Nat. Electron.* **2021**,

4, 45. doi: 10.1038/s41928-020-00511-7

(785) Liu, C. S.; Chen, H. W.; Hou, X.; Zhang, H.; Han, J.; Jiang, Y. G.; Zeng, X. Y.; Zhang, D. W.; Zhou, P. *Nat. Nanotechnol.* **2019**, *14*, 662. doi: 10.1038/s41565-019-0462-6

(786) Huang, M.; Li, S.; Zhang, Z.; Xiong, X.; Li, X.; Wu, Y. *Nat. Nanotechnol.* **2017**, *12*, 1148. doi: 10.1038/nnano.2017.208

(787) Chen, H. W.; Xue, X. Y.; Liu, C. S.; Fang, J. B.; Wang, Z.; Wang, J. L.; Zhang, D. W.; Hu, W. D.; Zhou, P. *Nat. Electron.* **2021**, *4*, 399. doi: 10.1038/s41928-021-00591-z

(788) Sebastian, A.; Le Gallo, M.; Khaddam-Aljameh, R.; Eleftheriou, E. *Nat. Nanotechnol.* **2020**, *15*, 529. doi: 10.1038/s41565-020-0655-z

(789) Ielmini, D.; Wong, H. S. P. *Nat. Electron.* **2018**, *1*, 333. doi: 10.1038/s41928-018-0092-2

(790) Christensen, D. V.; Dittmann, R.; Linares-Barranco, B.; Sebastian, A.; Le Gallo, M.; Redaelli, A.; Slesazeck, S.; Mikolajick, T.; Spiga, S.; Menzel, S.; *et al.* **2021**, arXiv:2105.05956.

(791) Wu, L.; Wang, A.; Shi, J.; Yan, J.; Zhou, Z.; Bian, C.; Ma, J.; Ma, R.; Liu, H.; Chen, J.; *et al. Nat. Nanotechnol.* **2021**, *16*, 882. doi: 10.1038/s41565-021-00904-5

(792) Liu, L.; Liu, C.; Jiang, L.; Li, J.; Ding, Y.; Wang, S.; Jiang, Y.-G.; Sun, Y.-B.; Wang, J.; Chen, S.; *et al. Nat. Nanotechnol.* **2021**, *16*, 874. doi: 10.1038/s41565-021-00921-4

(793) Tang, J.; He, C. L.; Tang, J. S.; Yue, K.; Zhang, Q. T.; Liu, Y. Z.; Wang, Q. Q.; Wang, S. P.; Li, N.; Shen, C.; *et al. Adv. Funct. Mater.* **2021**, *31*, 2011083. doi: 10.1002/adfm.202011083

(794) Marega, G. M.; Zhao, Y. F.; Avsar, A.; Wang, Z. Y.; Tripathi, M.; Radenovic, A.; Kis, A. *Nature* **2020**, *587*, 72. doi: 10.1038/s41586-020-2861-0

(795) Wang, M.; Cai, S. H.; Pan, C.; Wang, C. Y.; Lian, X. J.; Zhuo, Y.; Xu, K.; Cao, T. J.; Pan, X. Q.; Wang, B. G.; *et al. Nat. Electron.* **2018**, *1*, 130. doi: 10.1038/s41928-018-0021-4

(796) Chen, S. C.; Mahmoodi, M. R.; Shi, Y. Y.; Mahata, C.; Yuan, B.; Liang, X. H.; Wen, C.; Hui, F.; Akinwande, D.; Strukov, D. B.; *et al. Nat. Electron.* **2020**, *3*, 638. doi: 10.1038/s41928-020-00473-w

(797) Shi, Y. Y.; Liang, X. H.; Yuan, B.; Chen, V.; Li, H. T.; Hui, F.; Yu, Z. C. W.; Yuan, F.; Pop, E.; Wong, H. S. P.; *et al. Nat. Electron.* **2018**, *1*, 458. doi: 10.1038/s41928-018-0118-9

(798) Hus, S. M.; Ge, R. J.; Chen, P. A.; Liang, L. B.; Donnelly, G. E.; Ko, W.; Huang, F. M.; Chiang, M. H.; Li, A. P.; Akinwande, D. *Nat. Nanotechnol.* **2021**, *16*, 58. doi: 10.1038/s41565-020-00789-w

(799) Ge, R. J.; Wu, X. H.; Kim, M.; Shi, J. P.; Sonde, S.; Tao, L.; Zhang, Y. F.; Lee, J. C.; Akinwande, D. *Nano Lett.* **2018**, *18*, 434. doi: 10.1021/acs.nanolett.7b04342

(800) Sangwan, V. K.; Lee, H. S.; Bergeron, H.; Balla, I.; Beck, M. E.; Chen, K. S.; Hersam, M. C. *Nature* **2018**, *554*, 500. doi: 10.1038/nature25747

(801) Zhu, X. J.; Li, D.; Liang, X. G.; Lu, W. D. *Nat. Mater.* **2019**, *18*, 141. doi: 10.1038/s41563-018-0248-5

(802) Huo, N.; Konstantatos, G. *Adv. Mater.* **2018**, *30*, 1801164. doi: 10.1002/adma.201801164

(803) Lv, L.; Zhuge, F.; Xie, F.; Xiong, X.; Zhang, Q.; Zhang, N.; Huang, Y.; Zhai, T. *Nat. Commun.* **2019**, *10*, 3331. doi: 10.1038/s41467-019-11328-0

(804) Lee, C.-H.; Lee, G.-H.; van der Zande, A. M.; Chen, W.; Li, Y.; Han, M.; Cui, X.; Arefe, G.; Nuckolls, C.; Heinz, T. F.; *et al. Nat. Nanotechnol.* **2014**, *9*, 676. doi: 10.1038/nnano.2014.150

(805) Tan, C.; Yin, S.; Chen, J.; Lu, Y.; Wei, W.; Du, H.; Liu, K.; Wang, F.; Zhai, T.; Li, L. *ACS Nano* **2021**, *15*, 8328. doi: 10.1021/acsnano.0c09593

(806) Murali, K.; Dandu, M.; Das, S.; Majumdar, K. *ACS Appl. Mater. Interfaces* **2018**, *10*, 5657. doi: 10.1021/acsami.7b18242

(807) Younis, U.; Luo, X.; Dong, B.; Huang, L.; Vanga, S. K.; Lim, A. E.-J.; Lo, P. G.-Q.; Lee, C.; Bettiol, A. A.; Ang, K.-W. *J. Phys. Commun.* **2018**, *2*, 045029. doi: 10.1088/2399-6528/aaba24

(808) Wu, F.; Li, Q.; Wang, P.; Xia, H.; Wang, Z.; Wang, Y.; Luo, M.; Chen, L.; Chen, F.; Miao, J.; *et al. Nat. Commun.* **2019**, *10*, 4663. doi: 10.1038/s41467-019-12707-3

(809) Chen, Y.; Wang, Y.; Wang, Z.; Gu, Y.; Ye, Y.; Chai, X.; Ye, J.; Chen, Y.; Xie, R.; Zhou, Y.; *et al. Nat. Electron.* **2021**, *4*, 357. doi: 10.1038/s41928-021-00586-w

(810) Pospischil, A.; Furchi, M. M.; Mueller, T. *Nat. Nanotechnol.* **2014**, *9*, 257. doi: 10.1038/nnano.2014.14

(811) Baugher, B. W. H.; Churchill, H. O. H.; Yang, Y.; Jarillo-Herrero, P. *Nat. Nanotechnol.* **2014**, *9*, 262. doi: 10.1038/nnano.2014.25

(812) Wang, L.; Huang, L.; Tan, W. C.; Feng, X.; Chen, L.; Huang, X.; Ang, K.-W. *Small Methods* **2018**, *2*, 1700294. doi: 10.1002/smtd.201700294

(813) He, T.; Li, S.; Jiang, Y.; Qin, C.; Cui, M.; Qiao, L.; Xu, H.; Yang, J.; Long, R.; Wang, H.; *et al. Nat. Commun.* **2020**, *11*, 1672. doi: 10.1038/s41467-020-15451-1

(814) Liu, M.; Yin, X.; Ulin-Avila, E.; Geng, B.; Zentgraf, T.; Ju, L.; Wang, F.; Zhang, X. *Nature* **2011**, *474*, 64. doi: 10.1038/nature10067

(815) Liu, M.; Liu, W.; Liu, X.; Wang, Y.; Wei, Z. *Nano Select* **2021**, *2*, 37. doi: 10.1002/nano.202000047

(816) Li, Y.; Zhang, J.; Huang, D.; Sun, H.; Fan, F.; Feng, J.; Wang, Z.; Ning, C. Z. *Nat. Nanotechnol.* **2017**, *12*, 987. doi: 10.1038/nnano.2017.128

(817) Paik, E. Y.; Zhang, L.; Burg, G. W.; Gogna, R.; Tutuc, E.; Deng, H. *Nature* **2019**, *576*, 80. doi: 10.1038/s41586-019-1779-x

(818) Wu, S.; Buckley, S.; Schaibley, J. R.; Feng, L.; Yan, J.; Mandrus, D. G.; Hatami, F.; Yao, W.; Vučković, J.; Majumdar, A.; *et al. Nature*

2015, *520*, 69. doi: 10.1038/nature14290

(819) Zhang, Y.; Wang, S.; Chen, S.; Zhang, Q.; Wang, X.; Zhu, X.; Zhang, X.; Xu, X.; Yang, T.; He, M.; *et al. Adv. Mater.* **2020,** *32*, 1808319. doi: 10.1002/adma.201808319

(820) Zhao, L.; Shang, Q.; Gao, Y.; Shi, J.; Liu, Z.; Chen, J.; Mi, Y.; Yang, P.; Zhang, Z.; Du, W.; *et al. ACS Nano* **2018,** *12*, 9390. doi: 10.1021/acsnano.8b04511

(821) Lu, X.; Sun, L.; Jiang, P.; Bao, X. *Adv. Mater.* **2019,** *31*, 1902044. doi: 10.1002/adma.201902044

(822) Yang, Y. S.; Liu, S. C.; Wang, X.; Li, Z. B.; Zhang, Y.; Zhang, G. M.; Xue, D. J.; Hu, J. S. *Adv. Funct. Mater.* **2019,** *29*, 1900411. doi: 10.1002/Adfm.201900411

(823) Yan, Y.; Yang, J.; Du, J.; Zhang, X.; Liu, Y. Y.; Xia, C.; Wei, Z. *Adv. Mater.* **2021,** *33*, 2008761. doi: 10.1002/adma.202008761

(824) Zhou, X.; Hu, X. Z.; Zhou, S. S.; Zhang, Q.; Li, H. Q.; Zhai, T. Y. *Adv. Funct. Mater.* **2017,** *27*, 1703858. doi: 10.1002/Adfm.201703858

(825) Yan, Y.; Xiong, W.; Li, S.; Zhao, K.; Wang, X.; Su, J.; Song, X.; Li, X.; Zhang, S.; Yang, H.; *et al. Adv. Opt. Mater.* **2019,** *7*, 1900622. doi: 10.1002/adom.201900622

(826) Han, W.; Li, C.; Yang, S.; Luo, P.; Wang, F.; Feng, X.; Liu, K.; Pei, K.; Li, Y.; Li, H.; *et al. Small* **2020,** *16*, 2000228. doi: 10.1002/smll.202000228

(827) Zhang, Y.; Li, S.; Li, Z.; Liu, H.; Liu, X.; Chen, J.; Fang, X. *Nano Lett.* **2021,** *21*, 382. doi: 10.1021/acs.nanolett.0c03759

(828) Xia, F. N.; Wang, H.; Hwang, J. C. M.; Neto, A. H. C.; Yang, L. *Nat. Rev. Phys.* **2019,** *1*, 306. doi: 10.1038/s42254-019-0043-5

(829) Huang, L.; Dong, B.; Guo, X.; Chang, Y.; Chen, N.; Huang, X.; Liao, W.; Zhu, C.; Wang, H.; Lee, C.; *et al. ACS Nano* **2019,** *13*, 913. doi: 10.1021/acsnano.8b08758

(830) Hu, Z.; Li, Q.; Lei, B.; Wu, J.; Zhou, Q.; Gu, C.; Wen, X.; Wang, J.; Liu, Y.; Li, S.; *et al. Adv. Mater.* **2018,** *30*, 1801931. doi: 10.1002/adma.201801931

(831) Yuan, S.; Shen, C.; Deng, B.; Chen, X.; Guo, Q.; Ma, Y.; Abbas, A.; Liu, B.; Haiges, R.; Ott, C.; *et al. Nano Lett.* **2018,** *18*, 3172. doi: 10.1021/acs.nanolett.8b00835

(832) Long, M.; Gao, A.; Wang, P.; Xia, H.; Ott, C.; Pan, C.; Fu, Y.; Liu, E.; Chen, X.; Lu, W.; *et al. Sci. Adv.* **2017,** *3*, e1700589. doi: 10.1126/sciadv.1700589

(833) Amani, M.; Regan, E.; Bullock, J.; Ahn, G. H.; Javey, A. *ACS Nano* **2017,** *11*, 11724. doi: 10.1021/acsnano.7b07028

(834) Yu, P.; Zeng, Q.; Zhu, C.; Zhou, L.; Zhao, W.; Tong, J.; Liu, Z.; Yang, G. *Adv. Mater.* **2021,** *33*, 2005607. doi: 10.1002/adma.202005607

(835) Wang, Y.; Wu, P.; Wang, Z.; Luo, M.; Zhong, F.; Ge, X.; Zhang, K.; Peng, M.; Ye, Y.; Li, Q.; *et al. Adv. Mater.* **2020,** *32*, 2005037.

doi: 10.1002/adma.202005037

(836) Yin, C.; Gong, C.; Chu, J.; Wang, X.; Yan, C.; Qian, S.; Wang, Y.; Rao, G.; Wang, H.; Liu, Y.; *et al. Adv. Mater.* **2020,** *32*, 2002237. doi: 10.1002/adma.202002237

(837) Guo, J.; Liu, Y.; Ma, Y.; Zhu, E.; Lee, S.; Lu, Z.; Zhao, Z.; Xu, C.; Lee, S. J.; Wu, H.; *et al. Adv. Mater.* **2018,** *30*, 1705934. doi: 10.1002/adma.201705934

(838) Krishnamurthi, V.; Khan, H.; Ahmed, T.; Zavabeti, A.; Tawfik, S. A.; Jain, S. K.; Spencer, M. J. S.; Balendhran, S.; Crozier, K. B.; Li, Z.; *et al. Adv. Mater.* **2020,** *32*, 2004247. doi: 10.1002/adma.202004247

(839) Li, L.; Wang, W.; Gan, L.; Zhou, N.; Zhu, X.; Zhang, Q.; Li, H.; Tian, M.; Zhai, T. *Adv. Funct. Mater.* **2016,** *26*, 8281. doi: 10.1002/adfm.201603804

(840) Tong, L.; Huang, X.; Wang, P.; Ye, L.; Peng, M.; An, L.; Sun, Q.; Zhang, Y.; Yang, G.; Li, Z.; *et al. Nat. Commun.* **2020,** *11*, 2308. doi: 10.1038/s41467-020-16125-8

(841) Tutihasi, S.; Roberts, G. G.; Keezer, R. C.; Drews, R. E. *Phys. Rev.* **1969,** *177*, 1143. doi: 10.1103/PhysRev.177.1143

(842) Furukawa, T.; Shimokawa, Y.; Kobayashi, K.; Itou, T. *Nat. Commun.* **2017,** *8*, 954. doi: 10.1038/s41467-017-01093-3

(843) Bandurin, D. A.; Svintsov, D.; Gayduchenko, I.; Xu, S. G.; Principi, A.; Moskotin, M.; Tretyakov, I.; Yagodkin, D.; Zhukov, S.; Taniguchi, T.; *et al. Nat. Commun.* **2018,** *9*, 5392. doi: 10.1038/s41467-018-07848-w

(844) Guo, Q.; Yu, R.; Li, C.; Yuan, S.; Deng, B.; García de Abajo, F. J.; Xia, F. *Nat. Mater.* **2018,** *17*, 986. doi: 10.1038/s41563-018-0157-7

(845) Yu, X.; Li, Y.; Hu, X.; Zhang, D.; Tao, Y.; Liu, Z.; He, Y.; Haque, M. A.; Wu, T.; Wang, Q. *J. Nat. Commun.* **2018,** *9*, 4299. doi: 10.1038/s41467-018-06776-z

(846) Castilla, S.; Vangelidis, I.; Pusapati, V.-V.; Goldstein, J.; Autore, M.; Slipchenko, T.; Rajendran, K.; Kim, S.; Watanabe, K.; Taniguchi, T.; *et al. Nat. Commun.* **2020,** *11*, 4872. doi: 10.1038/s41467-020-18544-z

(847) Guo, C.; Hu, Y.; Chen, G.; Wei, D.; Zhang, L.; Chen, Z.; Guo, W.; Xu, H.; Kuo, C.-N.; Lue, C. S.; *et al. Sci. Adv.* **2020,** *6*, eabb6500. doi: 10.1126/sciadv.abb6500

(848) Yang, H.; Yang, L.; Wang, H.; Xu, Z.; Zhao, Y.; Luo, Y.; Nasir, N.; Song, Y.; Wu, H.; Pan, F.; *et al. Nat. Commun.* **2019,** *10*, 1. doi: 1038/s41467-019-10157-5

(849) Dong, X.; Wang, M.; Yan, D.; Peng, X.; Li, J.; Xiao, W.; Wang, Q.; Han, J.; Ma, J.; Shi, Y.; *et al. ACS Nano* **2019,** *13*, 9571. doi: 10.1021/acsnano.9b04573

(850) Ji, Z.; Liu, G.; Addison, Z.; Liu, W.; Yu, P.; Gao, H.; Liu, Z.; Rappe, A. M.; Kane, C. L.; Mele, E. J.; *et al. Nat. Mater.* **2019,** *18*, 955. doi: 10.1038/s41563-019-0421-5

(851) Lai, J.; Liu, X.; Ma, J.; Wang, Q.; Zhang, K.; Ren, X.; Liu, Y.; Gu, Q.; Zhuo, X.; Lu, W.; *et al. Adv. Mater.* **2018,** *30*, 1707152.

doi: 10.1002/adma.201707152

(852) Ma, J.; Gu, Q.; Liu, Y.; Lai, J.; Yu, P.; Zhuo, X.; Liu, Z.; Chen, J. H.; Feng, J.; Sun, D. *Nat. Mater.* **2019**, *18*, 476. doi: 10.1038/s41563-019-0296-5

(853) Wang, Q.; Zheng, J.; He, Y.; Cao, J.; Liu, X.; Wang, M.; Ma, J.; Lai, J.; Lu, H.; Jia, S.; *et al. Nat. Commun.* **2019**, *10*, 5736. doi: 10.1038/s41467-019-13713-1

(854) Novoselov, K. S.; Mishchenko, A.; Carvalho, A.; Castro Neto, A. H. *Science* **2016**, *353*, aac9439. doi: 10.1126/science.aac9439

(855) Lin, Z.; Huang, Y.; Duan, X. *Nat. Electron.* **2019**, *2*, 378. doi: 10.1038/s41928-019-0301-7

(856) Long, M.; Wang, Y.; Wang, P.; Zhou, X.; Xia, H.; Luo, C.; Huang, S.; Zhang, G.; Yan, H.; Fan, Z.; *et al. ACS Nano* **2019**, *13*, 2511. doi: 10.1021/acsnano.8b09476

(857) Gao, A.; Lai, J.; Wang, Y.; Zhu, Z.; Zeng, J.; Yu, G.; Wang, N.; Chen, W.; Cao, T.; Hu, W.; *et al. Nat. Nanotechnol.* **2019**, *14*, 217. doi: 10.1038/s41565-018-0348-z

(858) Lukman, S.; Ding, L.; Xu, L.; Tao, Y.; Riis-Jensen, A. C.; Zhang, G.; Wu, Q. Y. S.; Yang, M.; Luo, S.; Hsu, C.; *et al. Nat. Nanotechnol.* **2020**, *15*, 675. doi: 10.1038/s41565-020-0717-2

(859) Unuchek, D.; Ciarrocchi, A.; Avsar, A.; Sun, Z.; Watanabe, K.; Taniguchi, T.; Kis, A. *Nat. Nanotechnol.* **2019**, *14*, 1104. doi: 10.1038/s41565-019-0559-y

(860) Long, M.; Wang, P.; Fang, H.; Hu, W. *Adv. Funct. Mater.* **2019**, *29*, 1803807. doi: 10.1002/adfm.201803807

(861) Wang, X.; Cui, Y.; Li, T.; Lei, M.; Li, J.; Wei, Z. *Adv. Opt. Mater.* **2019**, *7*, 1801274. doi: 10.1002/adom.201801274

(862) Xia, F.; Mueller, T.; Lin, Y.-M.; Valdes-Garcia, A.; Avouris, P. *Nat. Nanotechnol.* **2009**, *4*, 839. doi: 10.1038/nnano.2009.292

(863) Xie, C.; Mak, C.; Tao, X.; Yan, F. *Adv. Funct. Mater.* **2017**, *27*, 1603886. doi: 10.1002/adfm.201603886

(864) Gupta, S.; Shirodkar, S. N.; Kutana, A.; Yakobson, B. I. *ACS Nano* **2018**, *12*, 10880. doi: 10.1021/acsnano.8b03754

(865) Zhao, M.; Su, J.; Zhao, Y.; Luo, P.; Wang, F.; Han, W.; Li, Y.; Zu, X.; Qiao, L.; Zhai, T. *Adv. Funct. Mater.* **2020**, *30*, 1909849. doi: 10.1002/adfm.201909849

(866) Tang, B.; Hou, L.; Sun, M.; Lv, F.; Liao, J.; Ji, W.; Chen, Q. *Nanoscale* **2019**, *11*, 12817. doi: 10.1039/C9NR03077H

(867) Jia, C.; Huang, X.; Wu, D.; Tian, Y.; Guo, J.; Zhao, Z.; Shi, Z.; Tian, Y.; Jie, J.; Li, X. *Nanoscale* **2020**, *12*, 4435. doi: 10.1039/C9NR10348A

(868) Lu, Z.; Xu, Y.; Yu, Y.; Xu, K.; Mao, J.; Xu, G.; Ma, Y.; Wu, D.; Jie, J. *Adv. Funct. Mater.* **2020**, *30*, 1907951. doi: 10.1002/adfm.201907951

(869) Xiao, R.; Lan, C.; Li, Y.; Zeng, C.; He, T.; Wang, S.; Li, C.; Yin, Y.; Liu, Y. *Adv. Mater. Interfaces* **2019**, *6*, 1901304. doi: 10.1002/admi.201901304

(870) Xu, S.-Y.; Ma, Q.; Gao, Y.; Kogar, A.; Zong, A.; Mier Valdivia, A. M.; Dinh, T. H.; Huang, S.-M.; Singh, B.; Hsu, C.-H.; *et al. Nature* **2020**, *578*, 545. doi: 10.1038/s41586-020-2011-8

(871) Yuan, H.; Liu, X.; Afshinmanesh, F.; Li, W.; Xu, G.; Sun, J.; Lian, B.; Curto, A. G.; Ye, G.; Hikita, Y.; *et al. Nat. Nanotechnol.* **2015**, *10*, 707. doi: 10.1038/nnano.2015.112

(872) Luo, Y.; Hu, Y.; Xie, Y. *J. Mater. Chem. A* **2019**, *7*, 27503. doi: 10.1039/C9TA10473A

(873) Zhao, S.; Luo, P.; Yang, S.; Zhou, X.; Wang, Z.; Li, C.; Wang, S.; Zhai, T.; Tao, X. *Adv. Opt. Mater.* **2021**, *9*, 2100198. doi: 10.1002/adom.202100198

(874) Qiao, J.; Feng, F.; Wang, Z.; Shen, M.; Zhang, G.; Yuan, X.; Somekh, M. G. *ACS Appl. Mater. Interfaces* **2021**, *13*, 17948. doi: 10.1021/acsami.1c00268

(875) Zhou, Z.; Cui, Y.; Tan, P. H.; Liu, X.; Wei, Z. *J. Semicond.* **2019**, *40*, 061001. doi: 10.1088/1674-4926/40/6/061001

(876) Lu, L.; Ma, Y.; Wang, J.; Liu, Y.; Han, S.; Liu, X.; Guo, W.; Xu, H.; Luo, J.; Sun, Z. *Chem. Eur. J.* **2021**, *27*, 9267. doi: 10.1002/chem.202100691

(877) Pi, L.; Hu, C.; Shen, W.; Li, L.; Luo, P.; Hu, X.; Chen, P.; Li, D.; Li, Z.; Zhou, X.; *et al. Adv. Funct. Mater.* **2021**, *31*, 2006774. doi: 10.1002/adfm.202006774

(878) Wu, D.; Guo, J.; Du, J.; Xia, C.; Zeng, L.; Tian, Y.; Shi, Z.; Tian, Y.; Li, X. J.; Tsang, Y. H.; *et al. ACS Nano* **2019**, *13*, 9907. doi: 10.1021/acsnano.9b03994

(879) Wang, X.; Zhong, F.; Kang, J.; Liu, C.; Lei, M.; Pan, L.; Wang, H.; Wang, F.; Zhou, Z.; Cui, Y.; *et al. Sci. China Mater.* **2021**, *64*, 1230. doi: 10.1007/s40843-020-1535-9

(880) Choi, C.; Choi, M. K.; Liu, S.; Kim, M. S.; Park, O. K.; Im, C.; Kim, J.; Qin, X.; Lee, G. J.; Cho, K. W.; *et al. Nat. Commun.* **2017**, *8*, 1664. doi: 10.1038/s41467-017-01824-6

(881) Tian, H.; Wang, X.; Wu, F.; Yang, Y.; Ren, T. In *High Performance 2D Perovskite/Graphene Optical Synapses as Artificial Eyes*, 2018 IEDM, 2018; pp. 38.6.1.

(882) Zhou, F.; Zhou, Z.; Chen, J.; Choy, T. H.; Wang, J.; Zhang, N.; Lin, Z.; Yu, S.; Kang, J.; Wong, H. S. P.; *et al. Nat. Nanotechnol.* **2019**, *14*, 776. doi: 10.1038/s41565-019-0501-3

(883) Seo, S.; Jo, S. H.; Kim, S.; Shim, J.; Oh, S.; Kim, J. H.; Heo, K.; Choi, J. W.; Choi, C.; Oh, S.; *et al. Nat. Commun.* **2018**, *9*, 5106. doi: 10.1038/s41467-018-07572-5

(884) Gu, L.; Poddar, S.; Lin, Y.; Long, Z.; Zhang, D.; Zhang, Q.; Shu, L.; Qiu, X.; Kam, M.; Javey, A.; *et al. Nature* **2020**, *581*, 278. doi: 10.1038/s41586-020-2285-x

(885) Wang, C. Y.; Liang, S. J.; Wang, S.; Wang, P. F.; Li, Z.; Wang, Z. R.; Gao, A. Y.; Pan, C.; Liu, C.; Liu, J.; *et al. Sci. Adv.* **2020**, *6*, eaba6173. doi: 10.1126/sciadv.aba6173

(886) Jang, H.; Liu, C. Y.; Hinton, H.; Lee, M. H.; Kim, H.; Seol, M.; Shin, H. J.; Park, S.; Ham, D. *Adv. Mater.* **2020**, *32*, 2002431. doi: 10.1002/adma.202002431

(887) Mennel, L.; Symonowicz, J.; Wachter, S.; Polyushkin, D. K.; Molina-Mendoza, A. J.; Mueller, T. *Nature* **2020**, *579*, 62. doi: 10.1038/s41586-020-2038-x

(888) Zhou, F. C.; Chai, Y. *Nat. Electron.* **2020**, *3*, 664. doi: 10.1038/s41928-020-00501-9

(889) Wang, S. Y.; Chen, C. S.; Yu, Z. H.; He, Y. L.; Chen, X. Y.; Wan, Q.; Shi, Y.; Zhang, D. W.; Zhou, H.; Wang, X. R.; *et al. Adv. Mater.* **2019**, *31*, 1806227. doi: 10.1002/adma.201806227

(890) Hou, X.; Liu, C.; Ding, Y.; Liu, L.; Wang, S.; Zhou, P. *Adv. Sci.* **2020**, *7*, 2002072. doi: 10.1002/advs.202002072

(891) Wang, S.; Wang, C. Y.; Wang, P. F.; Wang, C.; Li, Z. A.; Pan, C.; Dai, Y. T.; Gao, A. Y.; Liu, C.; Liu, J.; *et al. Natl. Sci. Rev.* **2021**, *8*, nwaa172. doi: 10.1093/nsr/nwaa172

(892) Zhu, Q. B.; Li, B.; Yang, D. D.; Liu, C.; Feng, S.; Chen, M. L.; Sun, Y.; Tian, Y. N.; Su, X.; Wang, X. M.; *et al. Nat. Commun.* **2021**, *12*, 1798. doi: 10.1038/s41467-021-22047-w

(893) Choi, C.; Leem, J.; Kim, M. S.; Taqieddin, A.; Cho, C.; Cho, K. W.; Lee, G. J.; Seung, H.; Jong, H.; Song, Y. M.; *et al. Nat. Commun.* **2020**, *11*, 5934. doi: 10.1038/s41467-020-19806-6

(894) Seo, S.; Kang, B. S.; Lee, J. J.; Ryu, H. J.; Kim, S.; Kim, H.; Oh, S.; Shim, J.; Heo, K.; Oh, S.; *et al. Nat. Commun.* **2020**, *11*, 3936. doi: 10.1038/s41467-020-17849-3

(895) Jayachandran, D.; Oberoi, A.; Sebastian, A.; Choudhury, T. H.; Shankar, B.; Redwing, J. M.; Das, S. *Nat. Electron.* **2020**, *3*, 646. doi: 10.1038/s41928-020-00466-9

(896) Sun, L. F.; Wang, Z. R.; Jiang, J.; Kim, Y.; Joo, B.; Zheng, S.; Lee, S.; Yu, W. J.; Kong, B. S.; Yang, H. *Sci. Adv.* **2021**, *7*, eabg1455. doi: 10.1126/sciadv.abg1455

(897) Setzler, B. P.; Zhuang, Z.; Wittkopf, J. A.; Yan, Y. *Nat. Nanotechnol.* **2016**, *11*, 1020. doi: 10.1038/nnano.2016.265

(898) Debe, M. K. *Nature* **2012**, *486*, 43. doi: 10.1038/nature11115

(899) Fu, S.; Zhu, C.; Song, J.; Du, D.; Lin, Y. *Adv. Energy Mater.* **2017**, *7*, 1700363. doi: 10.1002/aenm.201700363

(900) Cano, Z. P.; Banham, D.; Ye, S.; Hintennach, A.; Lu, J.; Fowler, M.; Chen, Z. *Nat. Energy* **2018**, *3*, 279. doi: 10.1038/s41560-018-0108-1

(901) Gao, J. J.; Yang, H. B.; Huang, X.; Hung, S. F.; Cai, W. Z.; Jia, C. M.; Miao, S.; Chen, H. M.; Yang, X. F.; Huang, Y. Q.; *et al. Chem* **2020**, *6*, 658. doi: 10.1016/j.chempr.2019.12.008

(902) Choi, C. H.; Kwon, H. C.; Yook, S.; Shin, H.; Kim, H.; Choi, M. *J. Phys. Chem. C* **2014**, *118*, 30063. doi: 10.1021/jp5113894

(903) Verdaguer-Casadevall, A.; Deiana, D.; Karamad, M.; Siahrostami, S.; Malacrida, P.; Hansen, T. W.; Rossmeisl, J.; Chorkendorff, I.; Stephens, I. E. *Nano Lett.* **2014**, *14*, 1603. doi: 10.1021/nl500037x

(904) Jirkovsky, J. S.; Panas, I.; Ahlberg, E.; Halasa, M.; Romani, S.; Schiffrin, D. J. *J. Am. Chem. Soc.* **2011**, *133*, 19432. doi: 10.1021/ja206477z

(905) Wang, Y.; Li, J.; Wei, Z. *ChemElectroChem* **2018**, *5*, 1764. doi: 10.1002/celc.201701335

(906) Shao, Y.; Jiang, Z.; Zhang, Q.; Guan, J. *ChemSusChem* **2019**, *12*, 2133. doi: 10.1002/cssc.201900060

(907) Komba, N.; Wei, Q.; Zhang, G.; Rosei, F.; Sun, S. *Appl. Catal. B: Environ.* **2019**, *243*, 373. doi: 10.1016/j.apcatb.2018.10.070

(908) Zhang, X.; Choudhury, T. H.; Chubarov, M.; Xiang, Y.; Jariwala, B.; Zhang, F.; Alem, N.; Wang, G. C.; Robinson, J. A.; Redwing, J. M. *Nano Lett.* **2018**, *18*, 1049. doi: 10.1021/acs.nanolett.7b04521

(909) Qu, Y.; Wang, L.; Li, Z.; Li, P.; Zhang, Q.; Lin, Y.; Zhou, F.; Wang, H.; Yang, Z.; Hu, Y.; *et al. Adv. Mater.* **2019**, *31*, 1904496. doi: 10.1002/adma.201904496

(910) Hu, Y.; Zhu, M.; Luo, X.; Wu, G.; Chao, T.; Qu, Y.; Zhou, F.; Sun, R.; Han, X.; Li, H.; *et al. Angew. Chem. Int. Ed.* **2021**, *60*, 6533. doi: 10.1002/anie.202014857

(911) Wu, H.; Wang, J.; Jin, W.; Wu, Z. *Nanoscale* **2020**, *12*, 18497. doi: 10.1039/d0nr04458j

(912) Zhu, D.; Qiao, M.; Liu, J.; Tao, T.; Guo, C. *J. Mater. Chem. A* **2020**, *8*, 8143. doi: 10.1039/d0ta03138k

(913) Zhong, H.; Ly, K. H.; Wang, M.; Krupskaya, Y.; Han, X.; Zhang, J.; Zhang, J.; Kataev, V.; Buchner, B.; Weidinger, I. M.; *et al. Angew. Chem. Int. Ed.* **2019**, *58*, 10677. doi: 10.1002/anie.201907002

(914) Cheng, W.; Zhao, X.; Su, H.; Tang, F.; Che, W.; Zhang, H.; Liu, Q. *Nat. Energy* **2019**, *4*, 115. doi: 10.1038/s41560-018-0308-8

(915) Jiang, L.; Duan, J.; Zhu, J.; Chen, S.; Antonietti, M. *ACS Nano* **2020**, *14*, 2436. doi: 10.1021/acsnano.9b09912

(916) Peng, J.; Chen, X.; Ong, W. J.; Zhao, X.; Li, N. *Chem* **2019**, *5*, 18. doi: 10.1016/j.chempr.2018.08.037

(917) Duarte, M. F. P.; Rocha, I. M.; Figueiredo, J. L.; Freire, C.; Pereira, M. F. R. *Catal. Today* **2018**, *301*, 17. doi: 10.1016/j.cattod.2017.03.046

(918) Guo, X.; Hu, X.; Wu, D.; Jing, C.; Liu, W.; Ren, Z.; Zhao, Q.; Jiang, X.; Xu, C.; Zhang, Y.; *et al. ACS Appl. Mater. Interfaces* **2019**, *11*, 21506. doi: 10.1021/acsami.9b04217

(919) Buitenwerf, R.; Rose, L.; Higgins, S. I. *Nat. Clim. Change* **2015**, *5*, 364. doi: 10.1038/nclimate2533

(920) Gusmão, R.; Veselý, M.; Sofer, Z. *ACS Catal.* **2020**, *10*, 9634. doi: 10.1021/acscatal.0c02388

(921) Sun, Z.; Ma, T.; Tao, H.; Fan, Q.; Han, B. *Chem* **2017**, *3*, 560. doi: 10.1016/j.chempr.2017.09.009

(922) Liu, S.; Tao, H.; Zeng, L.; Liu, Q.; Xu, Z.; Liu, Q.; Luo, J. L. *J. Am. Chem. Soc.* **2017**, *139*, 2160. doi: 10.1021/jacs.6b12103

(923) Yang, J.; Wang, X.; Qu, Y.; Wang, X.; Huo, H.; Fan, Q.; Wang, J.; Yang, L. M.; Wu, Y. *Adv. Energy Mater.* **2020**, *10*, 2001709.

doi: 10.1002/aenm.202001709

(924) Yang, P.; Zhang, S.; Pan, S.; Tang, B.; Liang, Y.; Zhao, X.; Zhang, Z.; Shi, J.; Huan, Y.; Shi, Y.; *et al. ACS Nano* **2020**, *14*, 5036. doi: 10.1021/acsnano.0c01478

(925) Pan, F.; Li, B.; Xiang, X.; Wang, G.; Li, Y. *ACS Catal.* **2019**, *9*, 2124. doi: 10.1021/acscatal.9b00016

(926) Yi, J. D.; Xie, R.; Xie, Z. L.; Chai, G. L.; Liu, T. F.; Chen, R. P.; Huang, Y. B.; Cao, R. *Angew. Chem. Int. Ed.* **2020**, *59*, 23641. doi: 10.1002/anie.202010601

(927) Cao, R.; Yi, J. D.; Si, D. H.; Xie, R.; Yin, Q.; Zhang, M. D.; Wu, Q.; Chai, G. L.; Huang, Y. B. *Angew. Chem. Int. Ed.* **2021**, *60*, 17108. doi: 10.1002/anie.202104564

(928) Meng, Z.; Luo, J.; Li, W.; Mirica, K. A. *J. Am. Chem. Soc.* **2020**, *142*, 21656. doi: 10.1021/jacs.0c07041

(929) Wu, Q.; Mao, M. J.; Wu, Q. J.; Liang, J.; Huang, Y. B.; Cao, R. *Small* **2021**, *17*, e2004933. doi: 10.1002/smll.202004933

(930) Wu, Q.; Xie, R.-K.; Mao, M.-J.; Chai, G.-L.; Yi, J.-D.; Zhao, S.-S.; Huang, Y.-B.; Cao, R. *ACS Energy Lett.* **2020**, *5*, 1005. doi: 10.1021/acsenergylett.9b02756

(931) Asadi, M.; Kim, K.; Liu, C.; Ad Depalli, A. V.; Abbasi, P.; Yasaei, P.; Phillips, P.; Behranginia, A.; Cerrato, J. M.; Haasch, R. *Science* **2016**, *353*, 467. doi: 10.1126/science.aaf4767

(932) Li, W.; Hou, P.; Wang, Z.; Kang, P. *Sustain. Energy Fuels* **2019**, *3*, 1455. doi: 10.1039/C9SE00056A

(933) Rafiqul, I.; Weber, C.; Lehmann, B.; Voss, A. *Energy* **2005**, *30*, 2487. doi: 10.1016/j.energy.2004.12.004

(934) Service, R. F. *Science* **2014**, *345*, 610. doi: 10.1126/science.345.6197.610

(935) van Kessel, M. A. H. J.; Speth, D. R.; Albertsen, M.; Nielsen, P. H.; Op den Camp, H. J. M.; Kartal, B.; Jetten, M. S. M.; Lücker, S. *Nature* **2015**, *528*, 555. doi: 10.1038/nature16459

(936) Fryzuk, M. D. *Chem. Commun.* **2013**, *49*, 4866. doi: 10.1039/C3CC42001A

(937) Wei, Z.; He, J.; Yang, Y.; Xia, Z.; Feng, Y.; Ma, J. *J. Energy Chem.* **2021**, *53*, 303. doi: 10.1016/j.jechem.2020.04.014

(938) Zhang, L.; Ji, X.; Ren, X.; Ma, Y.; Shi, X.; Tian, Z.; Asiri, A. M.; Chen, L.; Tang, B.; Sun, X. *Adv. Mater.* **2018**, *30*, 1800191. doi: 10.1002/adma.201800191

(939) Cui, X.; Tang, C.; Zhang, Q. *Adv. Energy Mater.* **2018**, *8*, 1800369. doi: 10.1002/aenm.201800369

(940) Guo, C.; Ran, J.; Vasileff, A.; Qiao, S.-Z. *Energy Environ. Sci.* **2018**, *11*, 45. doi: 10.1039/C7EE02220D

(941) Shi, M.-M.; Bao, D.; Li, S.-J.; Wulan, B.-R.; Yan, J.-M.; Jiang, Q. *Adv. Energy Mater.* **2018**, *8*, 1800124. doi: 10.1002/aenm.201800124

(942) Reis-Dennis, S. *Monash Bioeth. Rev.* **2020**, *38*, 83. doi: 10.1007/s40592-020-00107-z

(943) Chen, G. F.; Cao, X.; Wu, S.; Zeng, X.; Ding, L. X.; Zhu, M.; Wang, H. *J. Am. Chem. Soc.* **2017**, *139*, 9771. doi: 10.1021/jacs.7b04393

(944) Zhao, J.; Chen, Z. *J. Am. Chem. Soc.* **2017**, *139*, 12480. doi: 10.1021/jacs.7b05213

(945) Han, L.; Liu, X.; Chen, J.; Lin, R.; Liu, H.; Lu, F.; Bak, S.; Liang, Z.; Zhao, S.; Stavitski, E.; *et al. Angew. Chem. Int. Ed.* **2019**, *58*, 2321. doi: 10.1002/anie.201811728

(946) Ding, L.; Wei, Y.; Wang, Y.; Chen, H.; Caro, J.; Wang, H. *Angew. Chem. Int. Ed.* **2017**, *56*, 1825. doi: 10.1002/anie.201609306

(947) Liang, X.; Garsuch, A.; Nazar, L. F. *Angew. Chem. Int. Ed.* **2015**, *54*, 3907. doi: 10.1002/anie.201410174

(948) Lukatskaya, M. R.; Mashtalir, O.; Ren, C. E.; Dall'Agnese, Y.; Rozier, P.; Taberna, P. L.; Naguib, M.; Simon, P.; Barsoum, M. W.; Gogotsi, Y. *Science* **2013**, *341*, 1502. doi: 10.1126/science.1241488

(949) Ma, T. Y.; Cao, J. L.; Jaroniec, M.; Qiao, S. Z. *Angew. Chem. Int. Ed.* **2016**, *55*, 1138. doi: 10.1002/anie.201509758

(950) Ran, J.; Gao, G.; Li, F. T.; Ma, T. Y.; Du, A.; Qiao, S. Z. *Nat. Commun.* **2017**, *8*, 13907. doi: 10.1038/ncomms13907

(951) Azofra, L. M.; Li, N.; MacFarlane, D. R.; Sun, C. *Energy Environ. Sci.* **2016**, *9*, 2545. doi: 10.1039/c6ee01800a

(952) Mashtalir, O.; Naguib, M.; Mochalin, V. N.; Dall'Agnese, Y.; Heon, M.; Barsoum, M. W.; Gogotsi, Y. *Nat. Commun.* **2013**, *4*, 1716. doi: 10.1038/ncomms2664

(953) Gao, G.; O'Mullane, A. P.; Du, A. *ACS Catal.* **2016**, *7*, 494. doi: 10.1021/acscatal.6b02754

(954) Peng, W.; Luo, M.; Xu, X.; Jiang, K.; Peng, M.; Chen, D.; Chan, T. S.; Tan, Y. *Adv. Energy Mater.* **2020**, *10*, 1803935. doi: 10.1002/aenm.202001364

(955) Qiu, W.; Xie, X. Y.; Qiu, J.; Fang, W. H.; Liang, R.; Ren, X.; Ji, X.; Cui, G.; Asiri, A. M.; Cui, G.; *et al. Nat. Commun.* **2018**, *9*, 3485. doi: 10.1038/s41467-018-05758-5

(956) Jin, H.; Guo, C.; Liu, X.; Liu, J.; Vasileff, A.; Jiao, Y.; Zheng, Y.; Qiao, S. Z. *Chem. Rev.* **2018**, *118*, 6337. doi: 10.1021/acs.chemrev.7b00689

(957) Zheng, Y.; Jiao, Y.; Zhu, Y.; Cai, Q.; Vasileff, A.; Li, L. H.; Han, Y.; Chen, Y.; Qiao, S. Z. *J. Am. Chem. Soc.* **2017**, *139*, 3336. doi: 10.1021/jacs.6b13100

(958) Yao, Y.; Huang, Z.; Xie, P.; Lacey, S. D.; Jacob, R. J.; Xie, H.; Chen, F.; Nie, A.; Pu, T.; Rehwoldt, M.; *et al. Science* **2018**, *359*, 1489. doi: 10.1126/science.aan5412

(959) Liu, Y.; Cheng, H.; Lyu, M.; Fan, S.; Liu, Q.; Zhang, W.; Zhi, Y.; Wang, C.; Xiao, C.; Wei, S.; *et al. J. Am. Chem. Soc.* **2014**, *136*, 15670. doi: 10.1021/ja5085157

(960) Yu, H.; Yang, X.; Xiao, X.; Chen, M.; Zhang, Q.; Huang, L.; Wu, J.; Li, T.; Chen, S.; Song, L.; *et al. Adv. Mater.* **2018**, *30*, 1805655. doi: 10.1002/adma.201805655

(961) Gao, S.; Sun, Z.; Liu, W.; Jiao, X.; Zu, X.; Hu, Q.; Sun, Y.; Yao, T.;

Zhang, W.; Wei, S.; *et al. Nat. Commun.* **2017**, *8*, 14503. doi: 10.1038/ncomms14503

(962) Liu, H.-M.; Han, S.-H.; Zhao, Y.; Zhu, Y.-Y.; Tian, X.-L.; Zeng, J.-H.; Jiang, J.-X.; Xia, B. Y.; Chen, Y. *J. Mater. Chem. A* **2018**, *6*, 3211. doi: 10.1039/c7ta10866d

(963) He, S.; Ni, F.; Ji, Y.; Wang, L.; Wen, Y.; Bai, H.; Liu, G.; Zhang, Y.; Li, Y.; Zhang, B.; *et al. Angew. Chem. Int. Ed.* **2018**, *57*, 16114. doi: 10.1002/anie.201810538

(964) Qu, L.; Liu, Y.; Baek, J.-B.; Dai, L. *ACS Nano* **2010**, *4*, 1321. doi: 10.1021/nn901850u

(965) Li, Y.; Wang, H.; Xie, L.; Liang, Y.; Hong, G.; Dai, H. *J. Am. Chem. Soc.* **2011**, *133*, 7296. doi: 10.1021/ja201269b

(966) Liang, Y.; Wang, H.; Zhou, J.; Li, Y.; Wang, J.; Regier, T.; Dai, H. *J. Am. Chem. Soc.* **2012**, *134*, 3517. doi: 10.1021/ja210924t

(967) Chen, H.; Zhu, X.; Huang, H.; Wang, H.; Wang, T.; Zhao, R.; Zheng, H.; Asiri, A. M.; Luo, Y.; Sun, X. *Chem. Commun.* **2019**, *55*, 3152. doi: 10.1039/C9CC00461K

(968) Li, S.-J.; Bao, D.; Shi, M.-M.; Wulan, B.-R.; Yan, J.-M.; Jiang, Q. *Adv. Mater.* **2017**, *29*, 1700001. doi: 10.1002/adma.201700001

(969) Zhang, X.; Liu, Q.; Shi, X.; Asiri, A. M.; Luo, Y.; Sun, X.; Li, T. *J. Mater. Chem. A* **2018**, *6*, 17303. doi: 10.1039/C8TA05627G

(970) Wang, F.; Liu, Y.-P.; Zhang, H.; Chu, K. *ChemCatChem* **2019**, *11*, 1441. doi: 10.1002/cctc.201900041

(971) Huang, H.; Gong, F.; Wang, Y.; Wang, H.; Wu, X.; Lu, W.; Zhao, R.; Chen, H.; Shi, X.; Asiri, A. M.; *et al. Nano Res.* **2019**, *12*, 1093. doi: 10.1007/s12274-019-2352-5

(972) Zhou, Y.; Yu, X.; Sun, F.; Zhang, J. *Dalton Trans.* **2020**, *49*, 988. doi: 10.1039/C9DT04441H

(973) Li, X.; Ren, X.; Liu, X.; Zhao, J.; Sun, X.; Zhang, Y.; Kuang, X.; Yan, T.; Wei, Q.; Wu, D. *J. Mater. Chem. A* **2019**, *7*, 2524. doi: 10.1039/C8TA10433F

(974) Chu, K.; Liu, Y.-P.; Li, Y.-B.; Zhang, H.; Tian, Y. *J. Mater. Chem. A* **2019**, *7*, 4389. doi: 10.1039/C9TA00016J

(975) Chu, K.; Liu, Y.-P.; Wang, J.; Zhang, H. *ACS Appl. Energy Mater.* **2019**, *2*, 2288. doi: 10.1021/acsaem.9b00102

(976) Légaré, M.-A.; Bélanger-Chabot, G.; Dewhurst, R. D.; Welz, E.; Krummenacher, I.; Engels, B.; Braunschweig, H. *Science* **2018**, *359*, 896. doi: 10.1126/science.aaq1684

(977) Wei, Z.; Feng, Y.; Ma, J. *J. Energy Chem.* **2020**, *48*, 322. doi: 10.1016/j.jechem.2020.02.014

(978) Li, X.-F.; Li, Q.-K.; Cheng, J.; Liu, L.; Yan, Q.; Wu, Y.; Zhang, X.-H.; Wang, Z.-Y.; Qiu, Q.; Luo, Y. *J. Am. Chem. Soc.* **2016**, *138*, 8706. doi: 10.1021/jacs.6b04778

(979) Xia, L.; Yang, J.; Wang, H.; Zhao, R.; Chen, H.; Fang, W.; Asiri, A. M.; Xie, F.; Cui, G.; Sun, X. *Chem. Commun.* **2019**, *55*, 3371. doi: 10.1039/C9CC00602H

(980) Tian, Y.; Xu, D.; Chu, K.; Wei, Z.; Liu, W. *J. Mater. Sci.* **2019**, *54*, 9088. doi: 10.1007/s10853-019-03538-0

(981) Wang, T.; Xia, L.; Yang, J.-J.; Wang, H.; Fang, W.-H.; Chen, H.; Tang, D.; Asiri, A. M.; Luo, Y.; Cui, G.; *et al. Chem. Commun.* **2019**, *55*, 7502. doi: 10.1039/C9CC01999E

(982) Liu, Q.; Wang, S.; Chen, G.; Liu, Q.; Kong, X. *Inorg. Chem.* **2019**, *58*, 11843. doi: 10.1021/acs.inorgchem.9b02280

(983) Yu, X.; Han, P.; Wei, Z.; Huang, L.; Gu, Z.; Peng, S.; Ma, J.; Zheng, G. *Joule* **2018**, *2*, 1610. doi: 10.1016/j.joule.2018.06.007

(984) Zhao, J.; Yang, J.; Ji, L.; Wang, H.; Chen, H.; Niu, Z.; Liu, Q.; Li, T.; Cui, G.; Sun, X. *Chem. Commun.* **2019**, *55*, 4266. doi: 10.1039/C9CC01920K

(985) Feng, Y.; Liu, H.; Yang, J. *Sci. Adv.* **2017**, *3*, e1700580. doi: 10.1126/sciadv.1700580

(986) Shih, C. F.; Zhang, T.; Li, J.; Bai, C. *Joule* **2018**, *2*, 1925. doi: 10.1016/j.joule.2018.08.016

(987) Huang, W.; Wang, H.; Zhou, J.; Wang, J.; Duchesne, P. N.; Muir, D.; Zhang, P.; Han, N.; Zhao, F.; Zeng, M.; *et al. Nat. Commun.* **2015**, *6*, 10035. doi: 10.1038/ncomms10035

(988) Yang, S.; Qiu, P.; Yang, G. *Carbon* **2014**, *77*, 1123. doi: 10.1016/j.carbon.2014.06.030

(989) Bu, L.; Zhang, N.; Guo, S.; Zhang, X.; Li, J.; Yao, J.; Wu, T.; Lu, G.; Ma, J. Y.; Su, D.; *et al. Science* **2016**, *354*, 1410. doi: 10.1126/science.aah6133

(990) Luo, X.; Liu, C.; Wang, X.; Shao, Q.; Pi, Y.; Zhu, T.; Li, Y.; Huang, X. *Nano Lett.* **2020**, *20*, 1967. doi: 10.1021/acs.nanolett.9b05250

(991) Saleem, F.; Zhang, Z.; Xu, B.; Xu, X.; He, P.; Wang, X. *J. Am. Chem. Soc.* **2013**, *135*, 18304. doi: 10.1021/ja4101968

(992) Hong, J. W.; Kim, Y.; Wi, D. H.; Lee, S.; Lee, S. U.; Lee, Y. W.; Choi, S. I.; Han, S. W. *Angew. Chem. Int. Ed.* **2016**, *55*, 2753. doi: 10.1002/anie.201510460

(993) Liao, H.; Zhu, J.; Hou, Y. *Nanoscale* **2014**, *6*, 1049. doi: 10.1039/c3nr05590f

(994) Kowal, A.; Li, M.; Shao, M.; Sasaki, K.; Vukmirovic, M. B.; Zhang, J.; Marinkovic, N. S.; Liu, P.; Frenkel, A. I.; Adzic, R. R. *Nat. Mater.* **2009**, *8*, 325. doi: 10.1038/nmat2359

(995) Rizo, R.; Aran-Ais, R. M.; Padgett, E.; Muller, D. A.; Lazaro, M. J.; Solla-Gullon, J.; Feliu, J. M.; Pastor, E.; Abruna, H. D. *J. Am. Chem. Soc.* **2018**, *140*, 3791. doi: 10.1021/jacs.8b00588

(996) Yu, X.; Pickup, P. G. *J. Power Sources* **2008**, *182*, 124. doi: 10.1016/j.jpowsour.2008.03.075

(997) Vidal-Iglesias, F. J.; Lopez-Cudero, A.; Solla-Gullon, J.; Feliu, J. M. *Angew. Chem. Int. Ed.* **2013**, *52*, 964. doi: 10.1002/anie.201207517

(998) Zeb Gul Sial, M. A.; Ud Din, M. A.; Wang, X. *Chem. Soc. Rev.* **2018**, *47*, 6175. doi: 10.1039/c8cs00113h

(999) Su, N.; Chen, X.; Ren, Y.; Yue, B.; Wang, H.; Cai, W.; He, H. *Chem. Commun.* **2015**, *51*, 7195. doi: 10.1039/c5cc00353a

(1000) Lv, F.; Huang, B.; Feng, J.; Zhang, W.; Wang, K.; Li, N.; Zhou, J.; Zhou, P.; Yang, W.; Du, Y.; *et al. Natl. Sci. Rev.* **2021**, *8*, nwab019. doi: 10.1093/nsr/nwab019

(1001) Lewis, N. S.; Nocera, D. G. *Proc. Natl. Acad. Sci. U. S. A.* **2006**, *103*, 15729. doi: 10.1073/pnas.0603395103

(1002) Jaramillo, T. F.; Jørgensen, K. P.; Bonde, J.; Nielsen, J. H.; Horch, S.; Chorkendorff, I. *Science* **2007**, *317*, 100. doi: 10.1126/science.1141483

(1003) Wang, Y.; Zhang, Z.; Mao, Y.; Wang, X. *Energy Environ. Sci.* **2020**, *13*, 3993. doi: 10.1039/d0ee01714k

(1004) Zhang, C.; Shi, Y.; Yu, Y.; Du, Y.; Zhang, B. *ACS Catal.* **2018**, *8*, 8077. doi: 10.1021/acscatal.8b02056

(1005) Wu, C.; Liu, B.; Wang, J.; Su, Y.; Yan, H.; Ng, C.; Li, C.; Wei, J. *Appl. Surf. Sci.* **2018**, *441*, 1024. doi: 10.1016/j.apsusc.2018.02.076

(1006) Ho, T. A.; Bae, C.; Nam, H.; Kim, E.; Lee, S. Y.; Park, J. H.; Shin, H. *ACS Appl. Mater. Interfaces* **2018**, *10*, 12807. doi: 10.1021/acsami.8b00813

(1007) Long, X.; Li, G.; Wang, Z.; Zhu, H.; Zhang, T.; Xiao, S.; Guo, W.; Yang, S. *J. Am. Chem. Soc.* **2015**, *137*, 11900. doi: 10.1021/jacs.5b07728

(1008) Ma, L.; Hu, Y.; Chen, R.; Zhu, G.; Chen, T.; Lv, H.; Wang, Y.; Liang, J.; Liu, H.; Yan, C.; *et al. Nano Energy* **2016**, *24*, 139. doi: 10.1016/j.nanoen.2016.04.024

(1009) Wang, F.; Li, Y.; Shifa, T. A.; Liu, K.; Wang, F.; Wang, Z.; Xu, P.; Wang, Q.; He, J. *Angew. Chem. Int. Ed.* **2016**, *55*, 6919. doi: 10.1002/anie.201602802

(1010) Liang, H.; Li, L.; Meng, F.; Dang, L.; Zhuo, J.; Forticaux, A.; Wang, Z.; Jin, S. *Chem. Mater.* **2015**, *27*, 5702. doi: 10.1021/acs.chemmater.5b02177

(1011) Zhou, Y.; Song, E.; Zhou, J.; Lin, J.; Ma, R.; Wang, Y.; Qiu, W.; Shen, R.; Suenaga, K.; Liu, Q.; *et al. ACS Nano* **2018**, *12*, 4486. doi: 10.1021/acsnano.8b00693

(1012) Liu, Y.; Hua, X.; Xiao, C.; Zhou, T.; Huang, P.; Guo, Z.; Pan, B.; Xie, Y. *J. Am. Chem. Soc.* **2016**, *138*, 5087. doi: 10.1021/jacs.6b00858

(1013) Faber, M. S.; Jin, S. *Energy Environ. Sci.* **2014**, *7*, 3519. doi: 10.1039/c4ee01760a

(1014) Tributsch, H. *Ber. Bunsenges. Physikalische Chem.* **1977**, *81*, 361. doi: 10.1002/bbpc.19770810403

(1015) Hinnemann, B.; Moses, P. G.; Bonde, J.; Jørgensen, K. P.; Nielsen, J. H.; Horch, S.; Chorkendorff, I.; Nørskov, J. K. *J. Am. Chem. Soc.* **2005**, *127*, 5308. doi: 10.1021/ja0504690

(1016) Xie, J.; Zhang, H.; Li, S.; Wang, R.; Sun, X.; Zhou, M.; Zhou, J.; Lou, X. W.; Xie, Y. *Adv. Mater.* **2013**, *25*, 5807.

doi: 10.1002/adma.201302685

(1017) Gopalakrishnan, D.; Damien, D.; Shaijumon, M. M. *ACS Nano* **2014**, *8*, 5297. doi: 10.1021/nn501479e

(1018) Kibsgaard, J.; Chen, Z.; Reinecke, B. N.; Jaramillo, T. F. *Nat. Mater.* **2012**, *11*, 963. doi: 10.1038/nmat3439

(1019) Wang, H.; Lu, Z.; Xu, S.; Kong, D.; Cha, J. J.; Zheng, G.; Hsu, P.-C.; Yan, K.; Bradshaw, D.; Prinz, F. B.; *et al. Proc. Natl. Acad. Sci. U. S. A.* **2013**, *110*, 19701. doi: 10.1073/pnas.1316792110

(1020) He, Y.; He, Q.; Wang, L.; Zhu, C.; Golani, P.; Handoko, A. D.; Yu, X.; Gao, C.; Ding, M.; Wang, X.; *et al. Nat. Mater.* **2019**, *18*, 1098. doi: 10.1038/s41563-019-0426-0

(1021) He, J. J.; Frauenheim, T. *J. Phys. Chem. Lett.* **2020**, *11*, 6219. doi: 10.1021/acs.jpclett.0c02007

(1022) Li, H.; Tsai, C.; Koh, A. L.; Cai, L.; Contryman, A. W.; Fragapane, A. H.; Zhao, J.; Han, H. S.; Manoharan, H. C.; Abild-Pedersen, F.; *et al. Nat. Mater.* **2016**, *15*, 48. doi: 10.1038/nmat4465

(1023) Zhang, J.; Wang, Y.; Cui, J.; Wu, J.; Li, Y.; Zhu, T.; Kang, H.; Yang, J.; Sun, J.; Qin, Y.; *et al. J. Phys. Chem. Lett.* **2019**, *10*, 3282. doi: 10.1021/acs.jpclett.9b01121

(1024) Xie, J.; Yang, X.; Xie, Y. *Nanoscale* **2020**, *12*, 4283. doi: 10.1039/c9nr09753h

(1025) Wu, T.; Dong, C.; Sun, D.; Huang, F. *Nanoscale* **2021**, *13*, 1581. doi: 10.1039/d0nr08009h

(1026) Shah, S. A.; Shen, X.; Xie, M.; Zhu, G.; Ji, Z.; Zhou, H.; Xu, K.; Yue, X.; Yuan, A.; Zhu, J.; *et al. Small* **2019**, *15*, e1804545. doi: 10.1002/smll.201804545

(1027) Liu, J.; Liu, Y.; Xu, D.; Zhu, Y.; Peng, W.; Li, Y.; Zhang, F.; Fan, X. *Appl. Catal. B: Environ.* **2019**, *241*, 89. doi: 10.1016/j.apcatb.2018.08.083

(1028) Yu, C.; Cao, Z.-F.; Yang, F.; Wang, S.; Zhong, H. *Int. J. Hydrog. Energy* **2019**, *44*, 28151. doi: 10.1016/j.ijhydene.2019.09.052

(1029) Gao, M. R.; Liang, J. X.; Zheng, Y. R.; Xu, Y. F.; Jiang, J.; Gao, Q.; Li, J.; Yu, S. H. *Nat. Commun.* **2015**, *6*, 5982. doi: 10.1038/ncomms6982

(1030) Otrokov, M. M.; Rusinov, I. P.; Blanco-Rey, M.; Hoffmann, M.; Vyazovskaya, A. Y.; Eremeev, S. V.; Ernst, A.; Echenique, P. M.; Arnau, A.; Chulkov, E. V. *Phys. Rev. Lett.* **2019**, *122*, 107202. doi: 10.1103/PhysRevLett.122.107202

(1031) Shi, Y.; Ma, Z. R.; Xiao, Y. Y.; Yin, Y. C.; Huang, W. M.; Huang, Z. C.; Zheng, Y. Z.; Mu, F. Y.; Huang, R.; Shi, G. Y.; *et al. Nat. Commun.* **2021**, *12*, 3021. doi: 10.1038/s41467-021-23306-6

(1032) Sathe, B. R.; Zou, X.; Asefa, T. *Catal. Sci. Technol.* **2014**, *4*, 2023. doi: 10.1039/c4cy00075g

(1033) Zhang, S.; Yu, X.; Yan, F.; Li, C.; Zhang, X.; Chen, Y. *J. Mater. Chem. A* **2016**, *4*, 12046. doi: 10.1039/c6ta04365h

(1034) Yang, Y.; Lun, Z.; Xia, G.; Zheng, F.; He, M.; Chen, Q. *Energy*

Environ. Sci. **2015**, *8*, 3563. doi: 10.1039/c5ee02460a

(1035) Ito, Y.; Cong, W.; Fujita, T.; Tang, Z.; Chen, M. *Angew. Chem. Int. Ed.* **2015**, *54*, 2131. doi: 10.1002/anie.201410050

(1036) Zheng, Y.; Jiao, Y.; Li, L. H.; Xing, T.; Chen, Y.; Jaroniec, M.; Qiao, S. Z. *ACS Nano* **2014**, *8*, 5290. doi: 10.1021/nn501434a

(1037) Zhang, D.; Mou, H.; Lu, F.; Song, C.; Wang, D. *Appl. Catal. B: Environ.* **2019**, *254*, 471. doi: 10.1016/j.apcatb.2019.05.029

(1038) Jia, Y.; Zhang, L.; Gao, G.; Chen, H.; Wang, B.; Zhou, J.; Soo, M. T.; Hong, M.; Yan, X.; Qian, G.; *et al. Adv. Mater.* **2017**, *29*, 1700017. doi: 10.1002/adma.201700017

(1039) Deng, J.; Ren, P.; Deng, D.; Bao, X. *Angew. Chem. Int. Ed.* **2015**, *54*, 2100. doi: 10.1002/anie.201409524

(1040) Jia, J.; Xiong, T.; Zhao, L.; Wang, F.; Liu, H.; Hu, R.; Zhou, J.; Zhou, W.; Chen, S. *ACS Nano* **2017**, *11*, 12509. doi: 10.1021/acsnano.7b06607

(1041) Du, C.-F.; Dinh, K. N.; Liang, Q.; Zheng, Y.; Luo, Y.; Zhang, J.; Yan, Q. *Adv. Energy Mater.* **2018**, *8*, 1801127. doi: 10.1002/aenm.201801127

(1042) Yu, M.; Zhou, S.; Wang, Z.; Zhao, J.; Qiu, J. *Nano Energy* **2018**, *44*, 181. doi: 10.1016/j.nanoen.2017.12.003

(1043) Liu, Y.; Yu, G.; Li, G.-D.; Sun, Y.; Asefa, T.; Chen, W.; Zou, X. *Angew. Chem. Int. Ed.* **2015**, *54*, 10752. doi: 10.1002/anie.201504376

(1044) Li, J.-S.; Wang, Y.; Liu, C.-H.; Li, S.-L.; Wang, Y.-G.; Dong, L.-Z.; Dai, Z.-H.; Li, Y.-F.; Lan, Y.-Q. *Nat. Commun.* **2016**, *7*, 11204. doi: 10.1038/ncomms11204

(1045) Liu, Y.; Jiang, S.; Li, S.; Zhou, L.; Li, Z.; Li, J.; Shao, M. *Appl. Catal. B: Environ.* **2019**, *247*, 107. doi: 10.1016/j.apcatb.2019.01.094

(1046) Guo, J.; Sun, J.; Sun, Y.; Liu, Q.; Zhang, X. *Mater. Chem. Front.* **2019**, *3*, 842. doi: 10.1039/C9QM00052F

(1047) Qi, J.; Zhang, W.; Cao, R. *Adv. Energy Mater.* **2018**, *8*, 1701620. doi: 10.1002/aenm.201701620

(1048) Suen, N.-T.; Hung, S.-F.; Quan, Q.; Zhang, N.; Xu, Y.-J.; Chen, H. M. *Chem. Soc. Rev.* **2017**, *46*, 337. doi: 10.1039/C6CS00328A

(1049) Han, L.; Dong, S.; Wang, E. *Adv. Mater.* **2016**, *28*, 9266. doi: 10.1002/adma.201602270

(1050) Hunter, B. M.; Gray, H. B.; Müller, A. M. *Chem. Rev.* **2016**, *116*, 14120. doi: 10.1021/acs.chemrev.6b00398

(1051) Pawar, S. M.; Pawar, B. S.; Hou, B.; Kim, J.; Aqueel Ahmed, A. T.; Chavan, H. S.; Jo, Y.; Cho, S.; Inamdar, A. I.; Gunjakar, J. L.; *et al. J. Mater. Chem. A* **2017**, *5*, 12747. doi: 10.1039/C7TA02835K

(1052) Sun, Y.; Gao, S.; Lei, F.; Liu, J.; Liang, L.; Xie, Y. *Chem. Sci.* **2014**, *5*, 3976. doi: 10.1039/C4SC00565A

(1053) Li, W.; Fang, W.; Wu, C.; Dinh, K. N.; Ren, H.; Zhao, L.; Liu, C.; Yan, Q. *J. Mater. Chem. A* **2020**, *8*, 3658.

doi: 10.1039/C9TA13473E

(1054) Rui, K.; Zhao, G.; Chen, Y.; Lin, Y.; Zhou, Q.; Chen, J.; Zhu, J.; Sun, W.; Huang, W.; Dou, S. X. *Adv. Funct. Mater.* **2018**, *28*, 1801554. doi: 10.1002/adfm.201801554

(1055) Huang, J.; Wu, J.-Q.; Shao, B.; Lan, B.-L.; Yang, F.-J.; Sun, Y.; Tan, X.-Q.; He, C.-T.; Zhang, Z. *ACS Sus. Chem. Eng.* **2020**, *8*, 10554. doi: 10.1021/acssuschemeng.0c03376

(1056) Lu, Z.; Wang, K.; Cao, Y.; Li, Y.; Jia, D. *J. Alloys Compd.* **2021**, *871*, 159580. doi: 10.1016/j.jallcom.2021.159580

(1057) Rodenas, T.; Beeg, S.; Spanos, I.; Neugebauer, S.; Girgsdies, F.; Algara-Siller, G.; Schleker, P. P. M.; Jakes, P.; Pfänder, N.; Willinger, M.; *et al. Adv. Energy Mater.* **2018**, *8*, 1802404. doi: 10.1002/aenm.201802404

(1058) Ge, K.; Sun, S.; Zhao, Y.; Yang, K.; Wang, S.; Zhang, Z.; Cao, J.; Yang, Y.; Zhang, Y.; Pan, M.; *et al. Angew. Chem. Int. Ed.* **2021**, *60*, 12097. doi: 10.1002/anie.202102632

(1059) Zhao, S.; Wang, Y.; Dong, J.; He, C.-T.; Yin, H.; An, P.; Zhao, K.; Zhang, X.; Gao, C.; Zhang, L.; *et al. Nat. Energy* **2016**, *1*, 16184. doi: 10.1038/nenergy.2016.184

(1060) Xu, Y.; Li, B.; Zheng, S.; Wu, P.; Zhan, J.; Xue, H.; Xu, Q.; Pang, H. *J. Mater. Chem. A* **2018**, *6*, 22070. doi: 10.1039/C8TA03128B

(1061) Liu, Y.; Xiao, C.; Lyu, M.; Lin, Y.; Cai, W.; Huang, P.; Tong, W.; Zou, Y.; Xie, Y. *Angew. Chem. Int. Ed.* **2015**, *54*, 11231. doi: 10.1002/anie.201505320

(1062) Liu, H.; Xu, C.-Y.; Du, Y.; Ma, F.-X.; Li, Y.; Yu, J.; Zhen, L. *Sci. Rep.* **2019**, *9*, 1951. doi: 10.1038/s41598-018-35831-4

(1063) Souleymen, R.; Wang, Z.; Qiao, C.; Naveed, M.; Cao, C. *J. Mater. Chem. A* **2018**, *6*, 7592. doi: 10.1039/c8ta01266k

(1064) Feng, L.-L.; Yu, G.; Wu, Y.; Li, G.-D.; Li, H.; Sun, Y.; Asefa, T.; Chen, W.; Zou, X. *J. Am. Chem. Soc.* **2015**, *137*, 14023. doi: 10.1021/jacs.5b08186

(1065) Wu, J.; Liu, M.; Chatterjee, K.; Hackenberg, K. P.; Shen, J.; Zou, X.; Yan, Y.; Gu, J.; Yang, Y.; Lou, J.; *et al. Adv. Mater. Interfaces* **2016**, *3*, 1500669. doi: 10.1002/admi.201500669

(1066) Xie, J.; Zhang, X.; Xie, Y. *ChemCatChem* **2019**, *11*, 4662. doi: 10.1002/cctc.201901088

(1067) Xie, J.; Xin, J.; Wang, R.; Zhang, X.; Lei, F.; Qu, H.; Hao, P.; Cui, G.; Tang, B.; Xie, Y. *Nano Energy* **2018**, *53*, 74. doi: 10.1016/j.nanoen.2018.08.045

(1068) Bodhankar, P. M.; Sarawade, P. B.; Singh, G.; Vinu, A.; Dhawale, D. S. *J. Mater. Chem. A* **2021**, *9*, 3180. doi: 10.1039/D0TA10712C

(1069) Deng, J.; Iñiguez, J. A.; Liu, C. *Joule* **2018**, *2*, 846. doi: 10.1016/j.joule.2018.04.014

(1070) Dincer, I. *Renew. Sustain. Energy Rev.* **2000**, *4*, 157. doi: 10.1016/S1364-0321(99)00011-8

(1071) Lim, X. *Nat. News* **2015**, *526*, 628. doi: 10.1038/526628a

(1072) Wang, H.; Zhang, L.; Chen, Z.; Hu, J.; Li, S.; Wang, Z.; Liu, J.; Wang, X. *Chem. Soc. Rev.* **2014,** *43*, 5234. doi: 10.1039/C4CS00126E

(1073) Fujishima, A.; Honda, K. *Nature* **1972,** *238*, 37. doi: 10.1038/238037a0

(1074) Hisatomi, T.; Kubota, J.; Domen, K. *Chem. Soc. Rev.* **2014,** *43*, 7520. doi: 10.1039/C3CS60378D

(1075) Zhao, Y.; Zhang, S.; Shi, R.; Waterhouse, G. I. N.; Tang, J.; Zhang, T. *Mater. Today* **2020,** *34*, 78. doi: 10.1016/j.mattod.2019.10.022

(1076) Su, T.; Shao, Q.; Qin, Z.; Guo, Z.; Wu, Z. *ACS Catal.* **2018,** *8*, 2253. doi: 10.1021/acscatal.7b03437

(1077) Putri, L. K.; Ng, B.-J.; Ong, W.-J.; Lee, H. W.; Chang, W. S.; Chai, S.-P. *ACS Appl. Mater. Interfaces* **2017,** *9*, 4558. doi: 10.1021/acsami.6b12060

(1078) Li, M.; Wang, Y.; Tang, P.; Xie, N.; Zhao, Y.; Liu, X.; Hu, G.; Xie, J.; Zhao, Y.; Tang, J. *Chem. Mater.* **2017,** *29*, 2769. doi: 10.1021/acs.chemmater.6b04622

(1079) Tao, J.; Luttrell, T.; Batzill, M. *Nat. Chem.* **2011,** *3*, 296. doi: 10.1038/nchem.1006

(1080) Zhou, C.; Zhao, Y.; Shang, L.; Shi, R.; Wu, L.-Z.; Tung, C.-H.; Zhang, T. *Chem. Commun.* **2016,** *52*, 8239. doi: 10.1039/C6CC03739A

(1081) Mahler, B.; Hoepfner, V.; Liao, K.; Ozin, G. A. *J. Am. Chem. Soc.* **2014,** *136*, 14121. doi: 10.1021/ja506261t

(1082) Sun, Y.; Cheng, H.; Gao, S.; Sun, Z.; Liu, Q.; Liu, Q.; Lei, F.; Yao, T.; He, J.; Wei, S.; *et al. Angew. Chem. Int. Ed.* **2012,** *51*, 8727. doi: 10.1002/anie.201204675

(1083) Yu, H.; Shi, R.; Zhao, Y.; Bian, T.; Zhao, Y.; Zhou, C.; Waterhouse, G. I.; Wu, L. Z.; Tung, C. H.; Zhang, T. *Adv. Mater.* **2017,** *29*, 1605148. doi: 10.1002/adma.201605148

(1084) Chen, X.; Shi, R.; Chen, Q.; Zhang, Z.; Jiang, W.; Zhu, Y.; Zhang, T. *Nano Energy* **2019,** *59*, 644. doi: 10.1016/j.nanoen.2019.03.010

(1085) Xu, S.-M.; Pan, T.; Dou, Y.-B.; Yan, H.; Zhang, S.-T.; Ning, F.-Y.; Shi, W.-Y.; Wei, M. *J. Phys. Chem. C* **2015,** *119*, 18823. doi: 10.1021/acs.jpcc.5b01819

(1086) Xu, S.-M.; Yan, H.; Wei, M. *J. Phys. Chem. C* **2017,** *121*, 2683. doi: 10.1021/acs.jpcc.6b10159

(1087) Di, J.; Xiong, J.; Li, H.; Liu, Z. *Adv. Mater.* **2018,** *30*, 1704548. doi: 10.1002/adma.201704548

(1088) Wu, J.; Li, X.; Shi, W.; Ling, P.; Sun, Y.; Jiao, X.; Gao, S.; Liang, L.; Xu, J.; Yan, W.; *et al. Angew. Chem. Int. Ed.* **2018,** *57*, 8719. doi: 10.1002/anie.201803514

(1089) Li, J.; Cai, L.; Shang, J.; Yu, Y.; Zhang, L. *Adv. Mater.* **2016,** *28*, 4059. doi: 10.1002/adma.201600301

(1090) Li, J.; Zhan, G.; Yu, Y.; Zhang, L. *Nat. Commun.* **2016,** *7*, 11480. doi: 10.1038/ncomms11480

(1091) Zhao, D.; Wang, Y.; Dong, C.-L.; Huang, Y.-C.; Chen, J.; Xue, F.; Shen, S.; Guo, L. *Nat. Energy* **2021,** *6*, 388. doi: 10.1038/s41560-021-00795-9

(1092) Xie, Z.; Kuang, Q.; Chen, Q. *Acta Chim. Sin.* **2021,** *79*, 10. doi: 10.6023/a20080384

(1093) Zheng, Y.; Chen, Y.; Gao, B.; Lin, B.; Wang, X. *Adv. Funct. Mater.* **2020,** *30*, 2002021. doi: 10.1002/adfm.202002021

(1094) Jiao, X.; Zheng, K.; Liang, L.; Li, X.; Sun, Y.; Xie, Y. *Chem. Soc. Rev.* **2020,** *49*, 6592. doi: 10.1039/d0cs00332h

(1095) Xiong, J.; Song, P.; Di, J.; Li, H. *Appl. Catal. B: Environ.* **2019,** *256*, 117788. doi: 10.1016/j.apcatb.2019.117788

(1096) Xu, B.; Qi, S.; Jin, M.; Cai, X.; Lai, L.; Sun, Z.; Han, X.; Lin, Z.; Shao, H.; Peng, P.; *et al. Chin. Chem. Lett.* **2019,** *30*, 2053. doi: 10.1016/j.cclet.2019.10.028

(1097) Chen, G.; Gao, R.; Zhao, Y.; Li, Z.; Waterhouse, G. I. N.; Shi, R.; Zhao, J.; Zhang, M.; Shang, L.; Sheng, G.; *et al. Adv. Mater.* **2018,** *30*, 1704663. doi: 10.1002/adma.201704663

(1098) Qin, D.; Zhou, Y.; Wang, W.; Zhang, C.; Zeng, G.; Huang, D.; Wang, L.; Wang, H.; Yang, Y.; Lei, L.; *et al. J. Mater. Chem. A* **2020,** *8*, 19156. doi: 10.1039/d0ta07460h

(1099) Tan, L.; Wang, Z.; Zhao, Y.; Song, Y. F. *Chem. Asian J.* **2020,** *15*, 3380. doi: 10.1002/asia.202000963

(1100) Xiong, X.; Zhao, Y.; Shi, R.; Yin, W.; Zhao, Y.; Waterhouse, G. I. N.; Zhang, T. *Sci. Bull.* **2020,** *65*, 987. doi: 10.1016/j.scib.2020.03.032

(1101) Zhao, X.; Zhao, X.; Ullah, I.; Gao, L.; Zhang, J.; Lu, J. *Catal. Lett.* **2020,** *151*, 1683. doi: 10.1007/s10562-020-03426-2

(1102) Ahmed, N.; Shibata, Y.; Taniguchi, T.; Izumi, Y. *J. Catal.* **2011,** *279*, 123. doi: 10.1016/j.jcat.2011.01.004

(1103) Razzaq, A.; Ali, S.; Asif, M.; In, S.-I. *Catalysts* **2020,** *10*, 998. doi: 10.3390/catal10101185

(1104) Wang, K.; Zhang, L.; Su, Y.; Shao, D.; Zeng, S.; Wang, W. *J. Mater. Chem. A* **2018,** *6*, 8366. doi: 10.1039/C8TA01309H

(1105) Yang, Z.-Z.; Wei, J.-J.; Zeng, G.-M.; Zhang, H.-Q.; Tan, X.-F.; Ma, C.; Li, X.-C.; Li, Z.-H.; Zhang, C. *Coord. Chem. Rev.* **2019,** *386*, 154. doi: 10.1016/j.ccr.2019.01.018

(1106) Fung, C.-M.; Tang, J.-Y.; Tan, L.-L.; Mohamed, A. R.; Chai, S.-P. *Mater. Today Sustain.* **2020,** *9*, 100037. doi: 10.1016/j.mtsust.2020.100037

(1107) Kim; Kim; Do; Seo; Kang *Catalysts* **2019,** *9*, 998. doi: 10.3390/catal9120998

(1108) Meier, A. J.; Garg, A.; Sutter, B.; Kuhn, J. N.; Bhethanabotla, V. R. *ACS Sus. Chem. Eng.* **2018,** *7*, 265. doi: 10.1021/acssuschemeng.8b03168

(1109) Chen, S.; Wang, H.; Kang, Z.; Jin, S.; Zhang, X.; Zheng, X.; Qi, Z.; Zhu, J.; Pan, B.; Xie, Y. *Nat. Commun.* **2019,** *10*, 788.

doi: 10.1038/s41467-019-08697-x

(1110) Xie, X.; Zhang, N. *Adv. Funct. Mater.* **2020**, *30*, 2002528.
doi: 10.1002/adfm.202002528

(1111) Ma, J.; Jiang, Q.; Zhou, Y.; Chu, W.; Perathoner, S.; Jiang, C.; Wu, K. H.; Centi, G.; Liu, Y. *Small* **2021**, *17*, 2007509.
doi: 10.1002/smll.202007509

(1112) Di, J.; Zhao, X.; Lian, C.; Ji, M.; Xia, J.; Xiong, J.; Zhou, W.; Cao, X.; She, Y.; Liu, H.; *et al. Nano Energy* **2019**, *61*, 54.
doi: 10.1016/j.nanoen.2019.04.029

(1113) Dong, L.; Xiong, Z.; Zhou, Y.; Zhao, J.; Li, Y.; Wang, J.; Chen, X.; Zhao, Y.; Zhang, J. *J. CO₂ Util.* **2020**, *41*, 101262.
doi: 10.1016/j.jcou.2020.101262

(1114) Du, Z. Y.; Chen, Z.; Kang, R. K.; Han, Y. M.; Ding, J.; Cao, J. P.; Jiang, W.; Fang, M.; Mei, H.; Xu, Y. *Inorg. Chem.* **2020**, *59*, 12876.
doi: 10.1021/acs.inorgchem.0c01941

(1115) Liu, L.; Huang, H.; Chen, F.; Yu, H.; Tian, N.; Zhang, Y.; Zhang, T. *Sci. Bull.* **2020**, *65*, 934. doi: 10.1016/j.scib.2020.02.019

(1116) Qi, Y.; Song, L.; Ouyang, S.; Liang, X.; Ning, S.; Zhang, Q.; Ye, J. *Adv. Mater.* **2020**, *32*, 1903915. doi: 10.1002/adma.201903915

(1117) Wang, L.; Zhao, X.; Lv, D.; Liu, C.; Lai, W.; Sun, C.; Su, Z.; Xu, X.; Hao, W.; Dou, S. X.; *et al. Adv. Mater.* **2020**, *32*, 2004311.
doi: 10.1002/adma.202004311

(1118) Xiong, X.; Mao, C.; Yang, Z.; Zhang, Q.; Waterhouse, G. I. N.; Gu, L.; Zhang, T. *Adv. Energy Mater.* **2020**, *10*, 2002928.
doi: 10.1002/aenm.202002928

(1119) Yang, J.; Guo, Y.; Jiang, R.; Qin, F.; Zhang, H.; Lu, W.; Wang, J.; Yu, J. C. *J. Am. Chem. Soc.* **2018**, *140*, 8497.
doi: 10.1021/jacs.8b03537

(1120) Lai, C.; An, N.; Li, B.; Zhang, M.; Yi, H.; Liu, S.; Qin, L.; Liu, X.; Li, L.; Fu, Y.; *et al. Chem. Eng. J.* **2021**, *406*, 126780.
doi: 10.1016/j.cej.2020.126780

(1121) Li, A.; Wang, T.; Li, C.; Huang, Z.; Luo, Z.; Gong, J. *Angew. Chem. Int. Ed.* **2019**, *58*, 3804. doi: 10.1002/anie.201812773

(1122) Liu, C.; Zhang, Y.; Dong, F.; Reshak, A. H.; Ye, L.; Pinna, N.; Zeng, C.; Zhang, T.; Huang, H. *Appl. Catal. B: Environ.* **2017**, *203*, 465. doi: 10.1016/j.apcatb.2016.10.002

(1123) Xu, Y.; Jin, X.; Ge, T.; Xie, H.; Sun, R.; Su, F.; Li, X.; Ye, L. *Chem. Eng. J.* **2021**, *409*, 128178. doi: 10.1016/j.cej.2020.128178

(1124) Ong, W. J.; Putri, L. K.; Mohamed, A. R. *Chem. Eur. J.* **2020**, *26*, 9710. doi: 10.1002/chem.202000708

(1125) Xia, Y.; Tian, Z.; Heil, T.; Meng, A.; Cheng, B.; Cao, S.; Yu, J.; Antonietti, M. *Joule* **2019**, *3*, 2792.
doi: 10.1016/j.joule.2019.08.011

(1126) Chen, C.; Hu, J.; Yang, X.; Yang, T.; Qu, J.; Guo, C.; Li, C. M. *ACS Appl. Mater. Interfaces* **2021**, *13*, 20162.
doi: 10.1021/acsami.1c03482

(1127) Hu, Z.; Guo, W. *Small* **2021**, *17*, e2008004.
doi: 10.1002/smll.202008004

(1128) Ji, X.; Kang, Y.; Fan, T.; Xiong, Q.; Zhang, S.; Tao, W.; Zhang, H. *J. Mater. Chem. A* **2020**, *8*, 323. doi: 10.1039/c9ta11167k

(1129) Li, J.; Liu, P.; Huang, H.; Li, Y.; Tang, Y.; Mei, D.; Zhong, C. *ACS Sus. Chem. Eng.* **2020**, *8*, 5175.
doi: 10.1021/acssuschemeng.9b07591

(1130) Wang, X.; He, J.; Li, J.; Lu, G.; Dong, F.; Majima, T.; Zhu, M. *Appl. Catal. B: Environ.* **2020**, *277*, 119230.
doi: 10.1016/j.apcatb.2020.119230

(1131) Zhu, X.; Huang, S.; Yu, Q.; She, Y.; Yang, J.; Zhou, G.; Li, Q.; She, X.; Deng, J.; Li, H.; *et al. Appl. Catal. B: Environ.* **2020**, *269*, 118760. doi: 10.1016/j.apcatb.2020.118760

(1132) Xu, F.; Zhu, B.; Cheng, B.; Yu, J.; Xu, J. *Adv. Opt. Mater.* **2018**, *6*, 1800911. doi: 10.1002/adom.201800911

(1133) Medford, A. J.; Hatzell, M. C. *ACS Catal.* **2017**, *7*, 2624.
doi: 10.1021/acscatal.7b00439

(1134) Wang, S.; Ichihara, F.; Pang, H.; Chen, H.; Ye, J. *Adv. Funct. Mater.* **2018**, *28*, 1803309. doi: 10.1002/adfm.201803309

(1135) Zhang, S.; Zhao, Y.; Shi, R.; Waterhouse, G. I.; Zhang, T. *EnergyChem* **2019**, *1*, 100013. doi: 10.1016/j.enchem.2019.100013

(1136) Lu, Y.; Yang, Y.; Zhang, T.; Ge, Z.; Chang, H.; Xiao, P.; Xie, Y.; Hua, L.; Li, Q.; Li, H. *ACS Nano* **2016**, *10*, 10507.
doi: 10.1021/acsnano.6b06472

(1137) Chen, X.; Li, N.; Kong, Z.; Ong, W.-J.; Zhao, X. *Mater. Horiz.* **2018**, *5*, 9. doi: 10.1039/C7MH00557A

(1138) Li, H.; Mao, C.; Shang, H.; Yang, Z.; Ai, Z.; Zhang, L. *Nanoscale* **2018**, *10*, 15429. doi: 10.1039/C8NR04277B

(1139) Shiraishi, Y.; Hashimoto, M.; Chishiro, K.; Moriyama, K.; Tanaka, S.; Hirai, T. *J. Am. Chem. Soc.* **2020**, *142*, 7574.
doi: 10.1021/jacs.0c01683

(1140) Cao, S.; Zhou, N.; Gao, F.; Chen, H.; Jiang, F. *Appl. Catal. B: Environ.* **2017**, *218*, 600. doi: 10.1016/j.apcatb.2017.07.013

(1141) Zhao, Y.; Zheng, L.; Shi, R.; Zhang, S.; Bian, X.; Wu, F.; Cao, X.; Waterhouse, G. I.; Zhang, T. *Adv. Energy Mater.* **2020**, *10*, 2002199. doi: 10.1002/aenm.202002199

(1142) Bian, S.; Wen, M.; Wang, J.; Yang, N.; Chu, P. K.; Yu, X.-F. *J. Phys. Chem. Lett.* **2020**, *11*, 1052. doi: 10.1021/acs.jpclett.9b03507

(1143) Mao, C.; Wang, J.; Zou, Y.; Li, H.; Zhan, G.; Li, J.; Zhao, J.; Zhang, L. *Green Chem.* **2019**, *21*, 2852.
doi: 10.1039/C9GC01010F

(1144) Zhao, W.; Liu, B.; Qin, J.; Ke, J.; Yu, L.; Hu, X. *ChemPhotoChem* **2020**, *4*, 5322. doi: 10.1002/cptc.202000114

(1145) Shi, R.; Zhao, Y.; Waterhouse, G. I.; Zhang, S.; Zhang, T. *ACS Catal.* **2019**, *9*, 9739. doi: 10.1021/acscatal.9b03246

(1146) Dong, G.; Ho, W.; Wang, C. *J. Mater. Chem. A* **2015**, *3*, 23435.

doi: 10.1039/C5TA06540B

(1147) Sun, S.; Li, X.; Wang, W.; Zhang, L.; Sun, X. *Appl. Catal. B: Environ.* **2017,** *200*, 323. doi: 10.1016/j.apcatb.2016.07.025

(1148) Hu, S.; Chen, X.; Li, Q.; Zhao, Y.; Mao, W. *Catal. Sci. Technol.* **2016,** *6*, 5884. doi: 10.1039/c6cy00622a

(1149) Li, H.; Shang, J.; Ai, Z.; Zhang, L. *J. Am. Chem. Soc.* **2015,** *137*, 6393. doi: 10.1021/jacs.5b03105

(1150) Li, J.; Li, H.; Zhan, G.; Zhang, L. *Acc. Chem. Res.* **2017,** *50*, 112. doi: 10.1021/acs.accounts.6b00523

(1151) Wang, S.; Hai, X.; Ding, X.; Chang, K.; Xiang, Y.; Meng, X.; Yang, Z.; Chen, H.; Ye, J. *Adv. Mater.* **2017,** *29*, 1701774. doi: 10.1002/adma.201701774

(1152) Li, H.; Shang, J.; Shi, J.; Zhao, K.; Zhang, L. *Nanoscale* **2016,** *8*, 1986. doi: 10.1039/c5nr07380d

(1153) Zhao, Y.; Zhao, Y.; Waterhouse, G. I.; Zheng, L.; Cao, X.; Teng, F.; Wu, L. Z.; Tung, C. H.; O'Hare, D.; Zhang, T. *Adv. Mater.* **2017,** *29*, 1703828. doi: 10.1002/adma.201703828

(1154) Zhang, S.; Zhao, Y.; Shi, R.; Zhou, C.; Waterhouse, G. I.; Wu, L. Z.; Tung, C. H.; Zhang, T. *Adv. Energy Mater.* **2020,** *10*, 1901973. doi: 10.1002/aenm.201901973

(1155) Li, H.; Gu, S.; Sun, Z.; Guo, F.; Xie, Y.; Tao, B.; He, X.; Zhang, W.; Chang, H. *J. Mater. Chem. A* **2020,** *8*, 13038. doi: 10.1039/d0ta04251j

(1156) Liu, Y.; Hu, Z.; Yu, J. C. *Chem. Mater.* **2020,** *32*, 1488. doi: 10.1021/acs.chemmater.9b04448

(1157) Liang, C.; Niu, H.-Y.; Guo, H.; Niu, C.-G.; Huang, D.-W.; Yang, Y.-Y.; Liu, H.-Y.; Shao, B.-B.; Feng, H.-P. *Chem. Eng. J.* **2020,** *396*, 125395. doi: 10.1016/j.cej.2020.125395

(1158) Zheng, J.; Lu, L.; Lebedev, K.; Wu, S.; Zhao, P.; McPherson, I. J.; Wu, T.-S.; Kato, R.; Li, Y.; Ho, P.-L.; *et al. Chem Catal.* **2021,** *1*, 162. doi: 10.1016/j.checat.2021.03.002

(1159) Yao, C.; Wang, R.; Wang, Z.; Lei, H.; Dong, X.; He, C. *J. Mater. Chem. A* **2019,** *7*, 27547. doi: 10.1039/c9ta09201c

(1160) Zhang, W.; Fu, Y.; Peng, Q.; Yao, Q.; Wang, X.; Yu, A.; Chen, Z. *Chem. Eng. J.* **2020,** *394*, 124822. doi: 10.1016/j.cej.2020.124822

(1161) Huang, P.; Liu, W.; He, Z.; Xiao, C.; Yao, T.; Zou, Y.; Wang, C.; Qi, Z.; Tong, W.; Pan, B. *Sci. China Chem.* **2018,** *61*, 1187. doi: 10.1007/s11426-018-9273-1

(1162) Guo, X.-W.; Chen, S.-M.; Wang, H.-J.; Zhang, Z.-M.; Lin, H.; Song, L.; Lu, T.-B. *J. Mater. Chem. A* **2019,** *7*, 19831. doi: 10.1039/c9ta06653e

(1163) Qiu, P.; Xu, C.; Zhou, N.; Chen, H.; Jiang, F. *Appl. Catal. B: Environ.* **2018,** *221*, 27. doi: 10.1016/j.apcatb.2017.09.010

(1164) Liao, Y.; Qian, J.; Xie, G.; Han, Q.; Dang, W.; Wang, Y.; Lv, L.; Zhao, S.; Luo, L.; Zhang, W. *Appl. Catal. B: Environ.* **2020,** *273*, 119054. doi: 10.1016/j.apcatb.2020.119054

(1165) Shen, Z.-K.; Yuan, Y.-J.; Wang, P.; Bai, W.; Pei, L.; Wu, S.; Yu, Z.-T.; Zou, Z. *ACS Appl. Mater. Interfaces* **2020,** *12*, 17343. doi: 10.1021/acsami.9b21167

(1166) Fang, Y.; Xue, Y.; Hui, L.; Yu, H.; Li, Y. *Angew. Chem. Int. Ed.* **2021,** *60*, 3170. doi: 10.1002/anie.202012357

(1167) Liang, C.; Niu, H.-Y.; Guo, H.; Niu, C.-G.; Yang, Y.-Y.; Liu, H.-Y.; Tang, W.-W.; Feng, H.-P. *Chem. Eng. J.* **2021,** *406*, 126868. doi: 10.1016/j.cej.2020.126868

(1168) Zhang, K.; Ai, Z.; Huang, M.; Shi, D.; Shao, Y.; Hao, X.; Zhang, B.; Wu, Y. *J. Catal.* **2021,** *395*, 273. doi: 10.1016/j.jcat.2021.01.013

(1169) Shen, Z.-K.; Cheng, M.; Yuan, Y.-J.; Pei, L.; Zhong, J.; Guan, J.; Li, X.; Li, Z.-J.; Bao, L.; Zhang, X. *Appl. Catal. B: Environ.* **2021,** *295*, 120274. doi: 10.1016/j.apcatb.2021.120274

(1170) Zhang, S.; Zhao, Y.; Shi, R.; Zhou, C.; Waterhouse, G. I.; Wang, Z.; Weng, Y.; Zhang, T. *Angew. Chem. Int. Ed.* **2021,** *60*, 2554. doi: 10.1002/anie.202013594

(1171) Ye, T.-N.; Park, S.-W.; Lu, Y.; Li, J.; Sasase, M.; Kitano, M.; Tada, T.; Hosono, H. *Nature* **2020,** *583*, 391. doi: 10.1038/s41586-020-2464-9

(1172) Hattori, M.; Iijima, S.; Nakao, T.; Hosono, H.; Hara, M. *Nat. Commun.* **2020,** *11*, 2001. doi: 10.1038/s41467-020-15868-8

(1173) Mao, C.; Yu, L.; Li, J.; Zhao, J.; Zhang, L. *Appl. Catal. B: Environ.* **2018,** *224*, 612. doi: 10.1016/j.apcatb.2017.11.010

(1174) Fu, R.; Wu, Z.; Pan, Z.; Gao, Z.; Li, Z.; Kong, X.; Li, L. *Angew. Chem. Int. Ed.* **2021,** *60*, 11173. doi: 10.1002/anie.202100572

(1175) Hoffmann, M. R.; Martin, S. T.; Choi, W.; Bahnemann, D. W. *Chem. Rev.* **1995,** *95*, 69. doi: 10.1021/cr00033a004

(1176) Dalrymple, O. K.; Yeh, D. H.; Trotz, M. A. *J. Chem. Technol. Biotechnol.* **2007,** *82*, 121. doi: 10.1002/jctb.1657

(1177) Kanakaraju, D.; Glass, B. D.; Oelgemoller, M. *J. Environ. Manage.* **2018,** *219*, 189. doi: 10.1016/j.jenvman.2018.04.103

(1178) Nosaka, Y.; Nosaka, A. Y. *Chem. Rev.* **2017,** *117*, 11302. doi: 10.1021/acs.chemrev.7b00161

(1179) Chen, T.; Liu, L.; Hu, C.; Huang, H. *Chin. J. Catal.* **2021,** *42*, 1413. doi: 10.1016/s1872-2067(20)63769-x

(1180) Brickus, L. S.; Cardoso, J. N.; de Aquino Neto, F. R. *Environ. Sci. Technol.* **1998,** *32*, 3485. doi: 10.1021/es980336x

(1181) Ai, Z.; Ho, W.; Lee, S.; Zhang, L. *Environ. Sci. Technol.* **2009,** *43*, 4143. doi: 10.1021/es9004366

(1182) Dong, F.; Wang, Z.; Li, Y.; Ho, W. K.; Lee, S. C. *Environ. Sci. Technol.* **2014,** *48*, 10345. doi: 10.1021/es502290f

(1183) Randall, D. J.; Tsui, T. *Mar. Pollut. Bull.* **2002,** *45*, 17. doi: 10.1016/S0025-326X(02)00227-8

(1184) Sun, H.; Lü, K.; Minter, E. J.; Chen, Y.; Yang, Z.; Montagnes, D. J. *J. Hazard. Mater.* **2012,** *221*, 213. doi: 10.1016/j.jhazmat.2012.04.036

(1185) Wang, H.; Su, Y.; Zhao, H.; Yu, H.; Chen, S.; Zhang, Y.; Quan, X. *Environ. Sci. Technol.* **2014,** *48*, 11984. doi: 10.1021/es503073z

(1186) Ong, W.-J.; Tan, L.-L.; Ng, Y. H.; Yong, S.-T.; Chai, S.-P. *Chem. Rev.* **2016,** *116*, 7159. doi: 10.1021/acs.chemrev.6b00075

(1187) Rosso, C.; Filippini, G.; Criado, A.; Melchionna, M.; Fornasiero, P.; Prato, M. *ACS Nano* **2021,** *15*, 3621.
doi: 10.1021/acsnano.1c00627

(1188) Guo, X.; Hao, C.; Jin, G.; Zhu, H. Y.; Guo, X. Y. *Angew. Chem. Int. Ed.* **2014,** *53*, 1973. doi: 10.1002/anie.201309482

(1189) Chen, R.; Shi, J.-L.; Ma, Y.; Lin, G.; Lang, X.; Wang, C. *Angew. Chem. Int. Ed.* **2019,** *58*, 6430. doi: 10.1002/anie.201902543

(1190) Dai, Y.; Li, C.; Shen, Y.; Lim, T.; Xu, J.; Li, Y.; Niemantsverdriet, H.; Besenbacher, F.; Lock, N.; Su, R. *Nat. Commun.* **2018,** *9*, 60.
doi: 10.1038/s41467-017-02527-8

(1191) Xiao, Y.; Tian, G.; Li, W.; Xie, Y.; Jiang, B.; Tian, C.; Zhao, D.; Fu, H. *J. Am. Chem. Soc.* **2019,** *141*, 2508. doi: 10.1021/jacs.8b12428

(1192) Xu, S.; Zhou, P.; Zhang, Z.; Yang, C.; Zhang, B.; Deng, K.; Bottle, S.; Zhu, H. *J. Am. Chem. Soc.* **2017,** *139*, 14775.
doi: 10.1021/jacs.7b08861

(1193) Dai, Y.; Li, C.; Shen, Y.; Zhu, S.; Hvid, M. S.; Wu, L. C.; Skibsted, J.; Li, Y.; Niemantsverdriet, J. W. H.; Besenbacher, F.; *et al. J. Am. Chem. Soc.* **2018,** *140*, 16711. doi: 10.1021/jacs.8b09796

(1194) Dai, Y.; Ren, P.; Li, Y.; Lv, D.; Shen, Y.; Li, Y.; Niemantsverdriet, H.; Besenbacher, F.; Xiang, H.; Hao, W.; *et al. Angew. Chem. Int. Ed.* **2019,** *58*, 6265. doi: 10.1002/anie.201900773

(1195) Li, J.; Xu, Y.; Ding, Z.; Mahadi, A. H.; Zhao, Y.; Song, Y.-F. *Chem. Eng. J.* **2020,** *388*, 124248. doi: 10.1016/j.cej.2020.124248

(1196) Zou, J.; Wang, Z.; Guo, W.; Guo, B.; Yu, Y.; Wu, L. *Appl. Catal. B: Environ.* **2020,** *260*, 118185. doi: 10.1016/j.apcatb.2019.118185

(1197) Wang, J.; Xu, Y.; Li, J.; Ma, X.; Xu, S.-M.; Gao, R.; Zhao, Y.; Song, Y.-F. *Green Chem.* **2020,** *22*, 8604. doi: 10.1039/d0gc02786c

(1198) Zhang, C.; Pan, H.; Sun, L.; Xu, F.; Ouyang, Y.; Rosei, F. *Energy Storage Mater.* **2021,** *38*, 354. doi: 10.1016/j.ensm.2021.03.007

(1199) Li, J.; Jing, X.; Li, Q.; Li, S.; Gao, X.; Feng, X.; Wang, B. *Chem. Soc. Rev.* **2020,** *49*, 3565. doi: 10.1039/d0cs00017e

(1200) Zhang, H.; Sun, W.; Chen, X.; Wang, Y. *ACS Nano* **2019,** *13*, 14252. doi: 10.1021/acsnano.9b07360

(1201) Zhang, W.; Mao, J.; Li, S.; Chen, Z.; Guo, Z. *J. Am. Chem. Soc.* **2017,** *139*, 3316. doi: 10.1021/jacs.6b12185

(1202) Abbas, G.; Alay-e-Abbas, S. M.; Laref, A.; Li, Y.; Zhang, W. X. *Mater. Today Energy* **2020,** *17*, 100486.
doi: 10.1016/j.mtener.2020.100486

(1203) Younis, U.; Muhammad, I.; Qayyum, F.; Wu, W.; Sun, Q. *Mater. Today Energy* **2021,** *20*, 100664.
doi: 10.1016/j.mtener.2021.100664

(1204) Mortazavi, B.; Bafekry, A.; Shahrokhi, M.; Rabczuk, T.; Zhuang, X. *Mater. Today Energy* **2020,** *16*, 100392.
doi: 10.1016/j.mtener.2020.100392

(1205) Wang, Y.-X.; Chou, S.-L.; Liu, H.-K.; Dou, S.-X. *Carbon* **2013,** *57*, 202. doi: 10.1016/j.carbon.2013.01.064

(1206) Yang, J.; Yuan, Y.; Chen, G. *Mol. Phys.* **2019,** *118*, e1581291.
doi: 10.1080/00268976.2019.1581291

(1207) Hassoun, J.; Bonaccorso, F.; Agostini, M.; Angelucci, M.; Betti, M. G.; Cingolani, R.; Gemmi, M.; Mariani, C.; Panero, S.; Pellegrini, V.; *et al. Nano Lett.* **2014,** *14*, 4901. doi: 10.1021/nl502429m

(1208) Ma, G.; Xiang, Z.; Huang, K.; Ju, Z.; Zhuang, Q.; Cui, Y. *Part. Part. Syst. Charact.* **2017,** *34*, 1600315.
doi: 10.1002/ppsc.201600315

(1209) Qiao, Y.; Cheng, X.; Liu, Y.; Han, R.; Ma, M.; Li, Q.; Dong, H.; Li, X.; Yang, S. *Inorg. Chem. Front.* **2017,** *4*, 2017.
doi: 10.1039/c7qi00574a

(1210) Chen, K.-S.; Balla, I.; Luu, N. S.; Hersam, M. C. *ACS Energy Lett.* **2017,** *2*, 2026. doi: 10.1021/acsenergylett.7b00476

(1211) Choi, S. H.; Ko, Y. N.; Lee, J.-K.; Kang, Y. C. *Adv. Funct. Mater.* **2015,** *25*, 1780. doi: 10.1002/adfm.201402428

(1212) Xie, X.; Ao, Z.; Su, D.; Zhang, J.; Wang, G. *Adv. Funct. Mater.* **2015,** *25*, 1393. doi: 10.1002/adfm.201404078

(1213) Lu, Y.; Zhao, Q.; Zhang, N.; Lei, K.; Li, F.; Chen, J. *Adv. Funct. Mater.* **2016,** *26*, 911. doi: 10.1002/adfm.201504062

(1214) Xu, Y.; Bahmani, F.; Zhou, M.; Li, Y.; Zhang, C.; Liang, F.; Kazemi, S. H.; Kaiser, U.; Meng, G.; Lei, Y. *Nanoscale Horiz.* **2019,** *4*, 202. doi: 10.1039/c8nh00305j

(1215) Zhu, C.; Mu, X.; van Aken, P. A.; Yu, Y.; Maier, J. *Angew. Chem. Int. Ed.* **2014,** *53*, 2152. doi: 10.1002/anie.201308354

(1216) Jia, G.; Chao, D.; Tiep, N. H.; Zhang, Z.; Fan, H. J. *Energy Storage Mater.* **2018,** *14*, 136. doi: 10.1016/j.ensm.2018.02.019

(1217) Li, Z.; Duan, H.; Shao, M.; Li, J.; O'Hare, D.; Wei, M.; Wang, Z. L. *Chem* **2018,** *4*, 2168. doi: 10.1016/j.chempr.2018.06.007

(1218) Li, Z.; Liu, K.; Fan, K.; Yang, Y.; Shao, M.; Wei, M.; Duan, X. *Angew. Chem. Int. Ed.* **2019,** *58*, 3962.
doi: 10.1002/anie.201814705

(1219) Cui, J.; Li, Z.; Wang, G.; Guo, J.; Shao, M. *J. Mater. Chem. A* **2020,** *8*, 23738. doi: 10.1039/d0ta08573a

(1220) Cui, J.; Li, Z.; Li, J.; Li, S.; Liu, J.; Shao, M.; Wei, M. *J. Mater. Chem. A* **2020,** *8*, 1896. doi: 10.1039/c9ta11250b

(1221) Hemanth, N. R.; Kandasubramanian, B. *Chem. Eng. J.* **2020,** *392*, 123678. doi: 10.1016/j.cej.2019.123678

(1222) Tang, X.; Guo, X.; Wu, W.; Wang, G. *Adv. Energy Mater.* **2018,** *8*, 1801897. doi: 10.1002/aenm.201801897

(1223) Pang, J.; Mendes, R. G.; Bachmatiuk, A.; Zhao, L.; Ta, H. Q.; Gemming, T.; Liu, H.; Liu, Z.; Rummeli, M. H. *Chem. Soc. Rev.* **2019,** *48*, 72. doi: 10.1039/c8cs00324f

(1224) Luo, J.; Tao, X.; Zhang, J.; Xia, Y.; Huang, H.; Zhang, L.; Gan, Y.; Liang, C.; Zhang, W. *ACS Nano* **2016**, *10*, 2491. doi: 10.1021/acsnano.5b07333

(1225) Liu, Y.; Han, M.; Xiong, Q.; Zhang, S.; Zhao, C.; Gong, W.; Wang, G.; Zhang, H.; Zhao, H. *Adv. Energy Mater.* **2019**, *9*, 1803935. doi: 10.1002/aenm.201803935

(1226) Zhu, J.; Schwingenschlögl, U. *2D Mater.* **2017**, *4*, 025073. doi: 10.1088/2053-1583/aa69fe

(1227) Li, J.; Yan, D.; Hou, S.; Li, Y.; Lu, T.; Yao, Y.; Pan, L. *J. Mater. Chem. A* **2018**, *6*, 1234. doi: 10.1039/c7ta08261d

(1228) Xie, X.; Zhao, M.-Q.; Anasori, B.; Maleski, K.; Ren, C. E.; Li, J.; Byles, B. W.; Pomerantseva, E.; Wang, G.; Gogotsi, Y. *Nano Energy* **2016**, *26*, 513. doi: 10.1016/j.nanoen.2016.06.005

(1229) Zhang, Z.; Weng, L.; Rao, Q.; Yang, S.; Hu, J.; Cai, J.; Min, Y. *J. Power Sources* **2019**, *439*, 227107. doi: 10.1016/j.jpowsour.2019.227107

(1230) Lian, P.; Dong, Y.; Wu, Z.-S.; Zheng, S.; Wang, X.; Sen, W.; Sun, C.; Qin, J.; Shi, X.; Bao, X. *Nano Energy* **2017**, *40*, 1. doi: 10.1016/j.nanoen.2017.08.002

(1231) Hu, A.; Shu, C.; Qiu, X.; Li, M.; Zheng, R.; Long, J. *ACS Sus. Chem. Eng.* **2019**, *7*, 6929. doi: 10.1021/acssuschemeng.8b06496

(1232) Cai, Y. *ACS Omega* **2020**, *5*, 13424. doi: 10.1021/acsomega.0c01692

(1233) Ye, C.; Chao, D.; Shan, J.; Li, H.; Davey, K.; Qiao, S.-Z. *Matter* **2020**, *2*, 323. doi: 10.1016/j.matt.2019.12.020

(1234) Liang, X.; Rangom, Y.; Kwok, C. Y.; Pang, Q.; Nazar, L. F. *Adv. Mater.* **2017**, *29*, 27859697. doi: 10.1002/adma.201603040

(1235) Wang, H.; Zhang, Q.; Yao, H.; Liang, Z.; Lee, H. W.; Hsu, P. C.; Zheng, G.; Cui, Y. *Nano Lett.* **2014**, *14*, 7138. doi: 10.1021/nl503730c

(1236) Zhang, L.; Liu, D.; Muhammad, Z.; Wan, F.; Xie, W.; Wang, Y.; Song, L.; Niu, Z.; Chen, J. *Adv. Mater.* **2019**, *31*, 1903955. doi: 10.1002/adma.201903955

(1237) Lin, H.; Yang, L.; Jiang, X.; Li, G.; Zhang, T.; Yao, Q.; Zheng, G. W.; Lee, J. Y. *Energy Environ. Sci.* **2017**, *10*, 1476. doi: 10.1039/c7ee01047h

(1238) Sun, Z.; Zhang, J.; Yin, L.; Hu, G.; Fang, R.; Cheng, H. M.; Li, F. *Nat. Commun.* **2017**, *8*, 14627. doi: 10.1038/ncomms14627

(1239) Ding, Y.; Li, Y.; Wu, M.; Zhao, H.; Li, Q.; Wu, Z.-S. *Energy Storage Mater.* **2020**, *31*, 470. doi: 10.1016/j.ensm.2020.07.041

(1240) Li, Q.; Xu, P.; Gao, W.; Ma, S.; Zhang, G.; Cao, R.; Cho, J.; Wang, H. L.; Wu, G. *Adv. Mater.* **2014**, *26*, 1378. doi: 10.1002/adma.201304218

(1241) Huang, Y.; Wang, Y.; Tang, C.; Wang, J.; Zhang, Q.; Wang, Y.; Zhang, J. *Adv. Mater.* **2019**, *31*, 1803800. doi: 10.1002/adma.201803800

(1242) Feng, J.; Sun, X.; Wu, C.; Peng, L.; Lin, C.; Hu, S.; Yang, J.; Xie, Y. *J. Am. Chem. Soc.* **2011**, *133*, 17832. doi: 10.1021/ja207176c

(1243) Wu, G.; Mack, N. H.; Gao, W.; Ma, S.; Zhong, R.; Han, J.; Baldwin, J. K.; Zelenay, P. *ACS Nano* **2012**, *6*, 9764. doi: 10.1021/nn303275d

(1244) Lu, J.; Jung Lee, Y.; Luo, X.; Chun Lau, K.; Asadi, M.; Wang, H.-H.; Brombosz, S.; Wen, J.; Zhai, D.; Chen, Z.; *et al. Nature* **2016**, *529*, 377. doi: 10.1038/nature16484

(1245) Wang, Q.; Shang, L.; Shi, R.; Zhang, X.; Zhao, Y.; Waterhouse, G. I. N.; Wu, L.-Z.; Tung, C.-H.; Zhang, T. *Adv. Energy Mater.* **2017**, *7*, 1700467. doi: 10.1002/aenm.201700467

(1246) Jia, Q.; Ghoshal, S.; Li, J.; Liang, W.; Meng, G.; Che, H.; Zhang, S.; Ma, Z. F.; Mukerjee, S. *J. Am. Chem. Soc.* **2017**, *139*, 7893. doi: 10.1021/jacs.7b02378

(1247) Zhang, C.; Wang, A.; Zhang, J.; Guan, X.; Tang, W.; Luo, J. *Adv. Energy Mater.* **2018**, *8*, 1802833. doi: 10.1002/aenm.201802833

(1248) Zheng, J.; Zhao, Q.; Tang, T.; Yin, J.; Quilty, C. D.; Renderos, G. D.; Liu, X.; Deng, Y.; Wang, L.; Bock, D. C.; *et al. Science* **2019**, *366*, 6465. doi: 10.1126/science.aax6873

(1249) Wang, H.; Wang, C.; Matios, E.; Li, W. *Nano Lett.* **2017**, *17*, 6808. doi: 10.1021/acs.nanolett.7b03071

(1250) Lin, D.; Liu, Y.; Liang, Z.; Lee, H. W.; Sun, J.; Wang, H.; Yan, K.; Xie, J.; Cui, Y. *Nat. Nanotechnol.* **2016**, *11*, 626. doi: 10.1038/nnano.2016.32

(1251) Tian, Y.; An, Y.; Wei, C.; Xi, B.; Xiong, S.; Feng, J.; Qian, Y. *ACS Nano* **2019**, *13*, 11676. doi: 10.1021/acsnano.9b05599

(1252) Zhang, X.; Lv, R.; Wang, A.; Guo, W.; Liu, X.; Luo, J. *Angew. Chem. Int. Ed.* **2018**, *57*, 15028. doi: 10.1002/anie.201808714

(1253) Liu, Q. C.; Xu, J. J.; Yuan, S.; Chang, Z. W.; Xu, D.; Yin, Y. B.; Li, L.; Zhong, H. X.; Jiang, Y. S.; Yan, J. M.; *et al. Adv. Mater.* **2015**, *27*, 5241. doi: 10.1002/adma.201501490

(1254) Yan, K.; Lee, H. W.; Gao, T.; Zheng, G.; Yao, H.; Wang, H.; Lu, Z.; Zhou, Y.; Liang, Z.; Liu, Z.; *et al. Nano Lett.* **2014**, *14*, 6016. doi: 10.1021/nl503125u

(1255) Shim, J.; Kim, D.-G.; Kim, H. J.; Lee, J. H.; Baik, J.-H.; Lee, J.-C. *J. Mater. Chem. A* **2014**, *2*, 13873. doi: 10.1039/c4ta02667e

(1256) Tang, W.; Tang, S.; Zhang, C.; Ma, Q.; Xiang, Q.; Yang, Y. W.; Luo, J. *Adv. Energy Mater.* **2018**, *8*, 1800866. doi: 10.1002/aenm.201800866

(1257) Shim, J.; Kim, H. J.; Kim, B. G.; Kim, Y. S.; Kim, D.-G.; Lee, J.-C. *Energy Environ. Sci.* **2017**, *10*, 1911. doi: 10.1039/c7ee01095h

(1258) Chen, H.; Tu, H.; Hu, C.; Liu, Y.; Dong, D.; Sun, Y.; Dai, Y.; Wang, S.; Qian, H.; Lin, Z.; *et al. J. Am. Chem. Soc.* **2018**, *140*, 896. doi: 10.1021/jacs.7b12292

(1259) Li, M.; Zhu, W.; Zhang, P.; Chao, Y.; He, Q.; Yang, B.; Li, H.; Borisevich, A.; Dai, S. *Small* **2016**, *12*, 3535.

doi: 10.1002/smll.201600358

(1260) Kumar, K. S.; Choudhary, N.; Jung, Y.; Thomas, J. *ACS Energy Lett.* **2018,** *3*, 482. doi: 10.1021/acsenergylett.7b01169

(1261) Han, D.; Zhang, J.; Weng, Z.; Kong, D.; Tao, Y.; Ding, F.; Ruan, D.; Yang, Q.-H. *Mater. Today Energy* **2019,** *11*, 30. doi: 10.1016/j.mtener.2018.10.013

(1262) Liu, Y.; Peng, X. *Appl. Mater. Today* **2017,** *8*, 104. doi: 10.1016/j.apmt.2017.05.002

(1263) Wu, Y.; Yuan, W.; Xu, M.; Bai, S.; Chen, Y.; Tang, Z.; Wang, C.; Yang, Y.; Zhang, X.; Yuan, Y.; *et al. Chem. Eng. J.* **2021,** *412*, 128744. doi: 10.1016/j.cej.2021.128744

(1264) Jeong, G. H.; Sasikala, S. P.; Yun, T.; Lee, G. Y.; Lee, W. J.; Kim, S. O. *Adv. Mater.* **2020,** *32*, 1907006. doi: 10.1002/adma.201907006

(1265) Gu, T.-H.; Kwon, N. H.; Lee, K.-G.; Jin, X.; Hwang, S.-J. *Coord. Chem. Rev.* **2020,** *421*, 213439. doi: 10.1016/j.ccr.2020.213439

(1266) El-Kady, M. F.; Shao, Y.; Kaner, R. B. *Nat. Rev. Mater.* **2016,** *1*, 16033. doi: 10.1038/natrevmats.2016.33

(1267) Xia, J.; Chen, F.; Li, J.; Tao, N. *Nat. Nanotechnol.* **2009,** *4*, 505. doi: 10.1038/nnano.2009.177

(1268) Zhu, J.; Childress, A. S.; Karakaya, M.; Dandeliya, S.; Srivastava, A.; Lin, Y.; Rao, A. M.; Podila, R. *Adv. Mater.* **2016,** *28*, 7185. doi: 10.1002/adma.201602028

(1269) Li, H.; Jing, L.; Liu, W.; Lin, J.; Tay, R. Y.; Tsang, S. H.; Teo, E. H. T. *ACS Nano* **2018,** *12*, 1262. doi: 10.1021/acsnano.7b07444

(1270) Lv, Z.-L.; Cui, H.-L.; Wang, H.; Li, X.-H. *Appl. Surf. Sci.* **2021,** *562*, 150154. doi: 10.1016/j.apsusc.2021.150154

(1271) Yang, G. M.; Xu, Q.; Fan, X.; Zheng, W. T. *J. Phys. Chem. C* **2018,** *122*, 1903. doi: 10.1021/acs.jpcc.7b08955

(1272) Gao, R.; Tang, J.; Yu, X.; Lin, S.; Zhang, K.; Qin, L. C. *Adv. Funct. Mater.* **2020,** *30*, 2002200. doi: 10.1002/adfm.202002200

(1273) Krishnamoorthy, K.; Pazhamalai, P.; Kim, S.-J. *Energy Environ. Sci.* **2018,** *11*, 1595. doi: 10.1039/c8ee00160j

(1274) Xu, Q.; Si, X.; She, W. H.; Yang, G. M.; Fan, X.; Zheng, W. T. *J. Phys. Chem. C* **2020,** *124*, 12346. doi: 10.1021/acs.jpcc.0c00354

(1275) Hao, C. X.; Yang, B. C.; Wen, F. S.; Xiang, J. Y.; Li, L.; Wang, W. H.; Zeng, Z. M.; Xu, B.; Zhao, Z. S.; Liu, Z. Y.; *et al. Adv. Mater.* **2016,** *28*, 3194. doi: 10.1002/adma.201505730

(1276) Chen, H.; Yang, Z.; Guo, W.; Dunlap, J. R.; Liang, J.; Sun, Y.; Jie, K.; Wang, S.; Fu, J.; Dai, S. *Adv. Funct. Mater.* **2019,** *29*, 1906284. doi: 10.1002/adfm.201906284

(1277) Bai, L.; Huang, H.; Zhang, S.; Hao, L.; Zhang, Z.; Li, H.; Sun, L.; Guo, L.; Huang, H.; Zhang, Y. *Adv. Sci.* **2020,** *7*, 2001939. doi: 10.1002/advs.202001939

(1278) Mathis, T. S.; Kurra, N.; Wang, X.; Pinto, D.; Simon, P.; Gogotsi, Y. *Adv. Energy Mater.* **2019,** *9*, 1902007.

doi: 10.1002/aenm.201902007

(1279) Fan, H. J. *Joule* **2019,** *3*, 317. doi: 10.1016/j.joule.2019.01.014

(1280) Yu, P.; Fu, W.; Zeng, Q.; Lin, J.; Yan, C.; Lai, Z.; Tang, B.; Suenaga, K.; Zhang, H.; Liu, Z. *Adv. Mater.* **2017,** *29*, 1701909. doi: 10.1002/adma.201701909

(1281) Zhao, Y.; Fang, Q.; Zhu, X.; Xue, L.; Ni, M.; Qiu, C.; Huang, H.; Sun, S.; Li, S.; Xia, H. *J. Mater. Chem. A* **2020,** *8*, 8969. doi: 10.1039/d0ta01480j

(1282) Jabeen, N.; Hussain, A.; Xia, Q.; Sun, S.; Zhu, J.; Xia, H. *Adv. Mater.* **2017,** *29*, 1700804. doi: 10.1002/adma.201700804

(1283) Hu, M.; Zhang, H.; Hu, T.; Fan, B.; Wang, X.; Li, Z. *Chem. Soc. Rev.* **2020,** *49*, 6666. doi: 10.1039/d0cs00175a

(1284) Wang, X.; Mathis, T. S.; Li, K.; Lin, Z.; Vlcek, L.; Torita, T.; Osti, N. C.; Hatter, C.; Urbankowski, P.; Sarycheva, A.; *et al. Nat. Energy* **2019,** *4*, 241. doi: 10.1038/s41560-019-0339-9

(1285) Wang, X.; Kajiyama, S.; Iinuma, H.; Hosono, E.; Oro, S.; Moriguchi, I.; Okubo, M.; Yamada, A. *Nat. Commun.* **2015,** *6*, 6544. doi: 10.1038/ncomms7544

(1286) Venkateshalu, S.; Cherusseri, J.; Karnan, M.; Kumar, K. S.; Kollu, P.; Sathish, M.; Thomas, J.; Jeong, S. K.; Grace, A. N. *ACS Omega* **2020,** *5*, 17983. doi: 10.1021/acsomega.0c01215

(1287) Khayum M, A.; Vijayakumar, V.; Karak, S.; Kandambeth, S.; Bhadra, M.; Suresh, K.; Acharambath, N.; Kurungot, S.; Banerjee, R. *ACS Appl. Mater. Interfaces* **2018,** *10*, 28139. doi: 10.1021/acsami.8b10486

(1288) Kandambeth, S.; Jia, J.; Wu, H.; Kale, V. S.; Parvatkar, P. T.; Czaban-Jóźwiak, J.; Zhou, S.; Xu, X.; Ameur, Z. O.; Abou-Hamad, E. *Adv. Energy Mater.* **2020,** *10*, 2001673. doi: 10.1002/aenm.202001673

(1289) Liu, W.; Ulaganathan, M.; Abdelwahab, I.; Luo, X.; Chen, Z.; Tan, S. J. R.; Wang, X.; Liu, Y.; Geng, D.; Bao, Y.; *et al. ACS Nano* **2018,** *12*, 852. doi: 10.1021/acsnano.7b08354

(1290) Wang, M.; Shi, H.; Zhang, P.; Liao, Z.; Wang, M.; Zhong, H.; Schwotzer, F.; Nia, A. S.; Zschech, E.; Zhou, S.; *et al. Adv. Funct. Mater.* **2020,** *30*, 2002664. doi: 10.1002/adfm.202002664

(1291) Yusran, Y.; Li, H.; Guan, X.; Li, D.; Tang, L.; Xue, M.; Zhuang, Z.; Yan, Y.; Valtchev, V.; Qiu, S.; *et al. Adv. Mater.* **2020,** *32*, 1907289. doi: 10.1002/adma.201907289

(1292) Banda, H.; Dou, J. H.; Chen, T.; Libretto, N. J.; Chaudhary, M.; Bernard, G. M.; Miller, J. T.; Michaelis, V. K.; Dinca, M. *J. Am. Chem. Soc.* **2021,** *143*, 2285. doi: 10.1021/jacs.0c10849

(1293) Kandambeth, S.; Kale, V. S.; Shekhah, O.; Alshareef, H. N.; Eddaoudi, M. *Adv. Energy Mater.* **2021,** 2100177. doi: 10.1002/aenm.202100177

(1294) Cao, F.; Zhao, M.; Yu, Y.; Chen, B.; Huang, Y.; Yang, J.; Cao, X.; Lu, Q.; Zhang, X.; Zhang, Z.; *et al. J. Am. Chem. Soc.* **2016,** *138*,

6924. doi: 10.1021/jacs.6b02540

(1295) Sun, J.; Klechikov, A.; Moise, C.; Prodana, M.; Enachescu, M.; Talyzin, A. V. *Angew. Chem. Int. Ed.* **2018,** *57*, 1034. doi: 10.1002/anie.201710502

(1296) Xia, Y.; Mathis, T. S.; Zhao, M. Q.; Anasori, B.; Dang, A.; Zhou, Z.; Cho, H.; Gogotsi, Y.; Yang, S. *Nature* **2018,** *557*, 409. doi: 10.1038/s41586-018-0109-z

(1297) Wen, M.; Liu, D.; Kang, Y.; Wang, J.; Huang, H.; Li, J.; Chu, P. K.; Yu, X.-F. *Mater. Horiz.* **2019,** *6*, 176. doi: 10.1039/c8mh00708j

(1298) Lukatskaya, M. R.; Kota, S.; Lin, Z.; Zhao, M.-Q.; Shpigel, N.; Levi, M. D.; Halim, J.; Taberna, P.-L.; Barsoum, M. W.; Simon, P.; *et al. Nat. Energy* **2017,** *2*, 17105. doi: 10.1038/nenergy.2017.105

(1299) Zhou, Y.; Maleski, K.; Anasori, B.; Thostenson, J. O.; Pang, Y.; Feng, Y.; Zeng, K.; Parker, C. B.; Zauscher, S.; Gogotsi, Y.; *et al. ACS Nano* **2020,** *14*, 3576. doi: 10.1021/acsnano.9b10066

(1300) Wu, X. J.; Xu, Y. J.; Hu, Y.; Wu, G.; Cheng, H. Y.; Yu, Q.; Zhang, K.; Chen, W.; Chen, S. *Nat. Commun.* **2018,** *9*, 11. doi: 10.1038/s41467-018-06914-7

(1301) Beidaghi, M.; Wang, C. *Adv. Funct. Mater.* **2012,** *22*, 4501. doi: 10.1002/adfm.201201292

(1302) Wu, Z. S.; Parvez, K.; Feng, X.; Müllen, K. *Nat. Commun.* **2013,** *4*, 2487. doi: 10.1038/ncomms3487

(1303) Wu, M.; Chi, F.; Geng, H.; Ma, H.; Zhang, M.; Gao, T.; Li, C.; Qu, L. *Nat. Commun.* **2019,** *10*, 2855. doi: 10.1038/s41467-019-10886-7

(1304) Jiang, Q.; Lei, Y.; Liang, H.; Xi, K.; Xia, C.; Alshareef, H. N. *Energy Storage Mater.* **2020,** *27*, 78. doi: 10.1016/j.ensm.2020.01.018

(1305) Lu, B.; Jin, X.; Han, Q.; Qu, L. *Small* **2021**, 2006827. doi: 10.1002/smll.202006827

(1306) Wang, C.; Muni, M.; Strauss, V.; Borenstein, A.; Chang, X.; Huang, A.; Qu, S.; Sung, K.; Gilham, T.; Kaner, R. B. *Small* **2021**, 2006875. doi: 10.1002/smll.202006875

(1307) El-Kady, M. F.; Kaner, R. B. *Nat. Commun.* **2013,** *4*, 1475. doi: 10.1038/ncomms2446

(1308) Liu, H.; Xie, Y.; Liu, J.; Moon, K.-S.; Lu, L.; Lin, Z.; Yuan, W.; Shen, C.; Zang, X.; Lin, L.; *et al. Chem. Eng. J.* **2020,** *393*, 124672. doi: 10.1016/j.cej.2020.124672

(1309) Lin, J.; Peng, Z.; Liu, Y.; Ruiz-Zepeda, F.; Ye, R.; Samuel, E. L. G.; Yacaman, M. J.; Yakobson, B. I.; Tour, J. M. *Nat. Commun.* **2014,** *5*, 5714. doi: 10.1038/ncomms6714

(1310) Wu, Z.-S.; Tan, Y.-Z.; Zheng, S.; Wang, S.; Parvez, K.; Qin, J.; Shi, X.; Sun, C.; Bao, X.; Feng, X.; *et al. J. Am. Chem. Soc.* **2017,** *139*, 4506. doi: 10.1021/jacs.7b00805

(1311) Wu, Z. S.; Parvez, K.; Winter, A.; Vieker, H.; Liu, X.; Han, S.; Turchanin, A.; Feng, X.; Müllen, K. *Adv. Mater.* **2014,** *26*, 4552. doi: 10.1002/adma.201401228

(1312) Wang, Y.; Zhang, Y.; Liu, J.; Wang, G.; Pu, F.; Ganesh, A.; Tang, C.; Shi, X.; Qiao, Y.; Chen, Y.; *et al. Energy Storage Mater.* **2020,** *30*, 412. doi: 10.1016/j.ensm.2020.05.034

(1313) Yang, J.; Pan, Z.; Yu, Q.; Zhang, Q.; Ding, X.; Shi, X.; Qiu, Y.; Zhang, K.; Wang, J.; Zhang, Y. *ACS Appl. Mater. Interfaces* **2019,** *11*, 5938. doi: 10.1021/acsami.8b18172

(1314) Zahed, M. A.; Barman, S. C.; Sharifuzzaman, M.; Zhang, S.; Yoon, H.; Park, C.; Yoon, S. H.; Park, J. Y. *Adv. Funct. Mater.* **2021,** *31*, 2009018. doi: 10.1002/adfm.202009018

(1315) Xiao, H.; Wu, Z.-S.; Chen, L.; Zhou, F.; Zheng, S.; Ren, W.; Cheng, H.-M.; Bao, X. *ACS Nano* **2017,** *11*, 7284. doi: 10.1021/acsnano.7b03288

(1316) Xiang, T.; Tao, S.; Xu, W.; Fang, Q.; Wu, C.; Liu, D.; Zhou, Y.; Khalil, A.; Muhammad, Z.; Chu, W.; *et al. ACS Nano* **2017,** *11*, 6483. doi: 10.1021/acsnano.7b03329

(1317) Yuan, Y.; Jiang, L.; Li, X.; Zuo, P.; Xu, C.; Tian, M.; Zhang, X.; Wang, S.; Lu, B.; Shao, C.; *et al. Nat. Commun.* **2020,** *11*, 6185. doi: 10.1038/s41467-020-19985-2

(1318) Zhang, Y.-Z.; Wang, Y.; Jiang, Q.; El-Demellawi, J. K.; Kim, H.; Alshareef, H. N. *Adv. Mater.* **2020,** *32*, 1908486. doi: 10.1002/adma.201908486

(1319) Li, H.; Liang, J. *Adv. Mater.* **2020,** *32*, 1805864. doi: 10.1002/adma.201805864

(1320) Pomerantseva, E.; Bonaccorso, F.; Feng, X.; Cui, Y.; Gogotsi, Y. *Science* **2019,** *366*, eaan8285. doi: 10.1126/science.aan8285

(1321) Tian, W.; VahidMohammadi, A.; Reid, M. S.; Wang, Z.; Ouyang, L.; Erlandsson, J.; Pettersson, T.; Wågberg, L.; Beidaghi, M.; Hamedi, M. M. *Adv. Mater.* **2019,** *31*, 1902977. doi: 10.1002/adma.201902977

(1322) Zhang, P.; Soomro, R. A.; Guan, Z.; Sun, N.; Xu, B. *Energy Storage Mater.* **2020,** *29*, 163. doi: 10.1016/j.ensm.2020.04.016

(1323) Wu, C.-W.; Unnikrishnan, B.; Chen, I. W. P.; Harroun, S. G.; Chang, H.-T.; Huang, C.-C. *Energy Storage Mater.* **2020,** *25*, 563. doi: 10.1016/j.ensm.2019.09.026

(1324) Zhang, Y.; Wang, L.; Zhao, L.; Wang, K.; Zheng, Y.; Yuan, Z.; Wang, D.; Fu, X.; Shen, G.; Han, W. *Adv. Mater.* **2021,** *33*, 2007890. doi: 10.1002/adma.202007890

(1325) Yue, Y.; Liu, N.; Ma, Y.; Wang, S.; Liu, W.; Luo, C.; Zhang, H.; Cheng, F.; Rao, J.; Hu, X.; *et al. ACS Nano* **2018,** *12*, 4224. doi: 10.1021/acsnano.7b07528

(1326) Huang, H.; Shi, H.; Das, P.; Qin, J.; Li, Y.; Wang, X.; Su, F.; Wen, P.; Li, S.; Lu, P.; *et al. Adv. Funct. Mater.* **2020,** *30*, 1909035. doi: 10.1002/adfm.201909035

(1327) Griffin, J. M.; Forse, A. C.; Tsai, W. Y.; Taberna, P. L.; Simon, P.; Grey, C. P. *Nat. Mater.* **2015,** *14*, 812. doi: 10.1038/nmat4318

(1328) Chmiola, J.; Yushin, G.; Gogotsi, Y.; Portet, C.; Simon, P.; Taberna,

P. L. *Science* **2006,** *313*, 1760. doi: 10.1126/science.1132195

(1329) Chmiola, J.; Largeot, C.; Taberna, P.-L.; Simon, P.; Gogotsi, Y. *Angew. Chem. Int. Ed.* **2008,** *47*, 3392. doi: 10.1002/anie.200704894

(1330) Dai, F.; Wang, X.; Zheng, S.; Sun, J.; Huang, Z.; Xu, B.; Fan, L.; Wang, R.; Sun, D.; Wu, Z.-S. *Chem. Eng. J.* **2021,** *413*, 127520. doi: 10.1016/j.cej.2020.127520

(1331) Yao, L.; Wu, Q.; Zhang, P.; Zhang, J.; Wang, D.; Li, Y.; Ren, X.; Mi, H.; Deng, L.; Zheng, Z. *Adv. Mater.* **2018,** *30*, 1706054. doi: 10.1002/adma.201706054

(1332) Tan, K. W.; Jung, B.; Werner, J. G.; Rhoades, E. R.; Thompson, M. O.; Wiesner, U. *Science* **2015,** *349*, 54. doi: 10.1126/science.aab0492

(1333) Peng, Z.; Ye, R.; Mann, J. A.; Zakhidov, D.; Li, Y.; Smalley, P. R.; Lin, J.; Tour, J. M. *ACS Nano* **2015,** *9*, 5868. doi: 10.1021/acsnano.5b00436

(1334) Ye, R.; James, D. K.; Tour, J. M. *Adv. Mater.* **2019,** *31*, 1803621. doi: 10.1002/adma.201803621

(1335) Pazhamalai, P.; Krishnamoorthy, K.; Sahoo, S.; Mariappan, V. K.; Kim, S. J. *Inorg. Chem. Front.* **2019,** *6*, 2387. doi: 10.1039/c9qi00623k

(1336) Li, C. L.; Cao, Q.; Wang, F. Z.; Xiao, Y. Q.; Li, Y. B.; Delaunay, J. J.; Zhu, H. W. *Chem. Soc. Rev.* **2018,** *47*, 4981. doi: 10.1039/c8cs00067k

(1337) Li, X. M.; Tao, L.; Chen, Z. F.; Fang, H.; Li, X. S.; Wang, X. R.; Xu, J. B.; Zhu, H. W. *Appl. Phys. Rev.* **2017,** *4*, 21306. doi: 10.1063/1.4983646

(1338) Yoon, J.; Sung, H.; Lee, G.; Cho, W.; Ahn, N.; Jung, H. S.; Choi, M. *Energy Environ. Sci.* **2017,** *10*, 337. doi: 10.1039/c6ee02650h

(1339) Jin, Z. W.; Yan, J.; Huang, X.; Xu, W.; Yang, S. Y.; Zhu, D. B.; Wang, J. Z. *Nano Energy* **2017,** *40*, 376. doi: 10.1016/j.nanoen.2017.08.028

(1340) Ahn, S.; Han, T. H.; Maleski, K.; Song, J. N.; Kim, Y. H.; Park, M. H.; Zhou, H. Y.; Yoo, S.; Gogotsi, Y.; Lee, T. W. *Adv. Mater.* **2020,** *32*, 2000919. doi: 10.1002/adma.202000919

(1341) Heo, J. H.; Shin, D. H.; Song, D. H.; Kim, D. H.; Lee, S. J.; Im, S. H. *J. Mater. Chem. A* **2018,** *6*, 8251. doi: 10.1039/c8ta02672f

(1342) Heo, J. H.; Shin, D. H.; Jang, M. H.; Lee, M. L.; Kang, M. G.; Im, S. H. *J. Mater. Chem. A* **2017,** *5*, 21146. doi: 10.1039/c7ta06465a

(1343) Zhu, Y. Y.; Jia, S. P.; Zheng, J. F.; Lin, Y. L.; Wu, Y. R.; Wang, J. *J. Mater. Chem. C* **2018,** *6*, 3097. doi: 10.1039/c8tc00086g

(1344) Chang, J. K.; Huang, Y. Y.; Lin, D. L.; Tau, J. I.; Chen, T. H.; Chen, M. H. *Sci. Rep.* **2020,** *10*, 20010. doi: 10.1038/s41598-020-77012-2

(1345) You, P.; Tang, G. Q.; Yan, F. *Mater. Today Energy* **2019,** *11*, 128. doi: 10.1016/j.mtener.2018.11.006

(1346) Zhao, X. J.; Liu, S. S.; Zhang, H. T.; Chang, S. Y.; Huang, W. C.;

Zhu, B. W.; Shen, Y.; Shen, C.; Wang, D. Y.; Yang, Y.; *et al. Adv. Funct. Mater.* **2019,** *29*, 1805168. doi: 10.1002/adfm.201805168

(1347) Huang, P.; Yuan, L.; Zhang, K.; Chen, Q.; Zhou, Y.; Song, B.; Li, Y. *ACS Appl. Mater. Int.* **2018,** *10*, 14796. doi: 10.1021/acsami.8b03225

(1348) Singh, R.; Giri, A.; Pal, M.; Thiyagarajan, K.; Kwak, J.; Lee, J. J.; Jeong, U.; Cho, K. *J. Mater. Chem. A* **2019,** *7*, 7151. doi: 10.1039/c8ta12254g

(1349) Yang, L.; Dall'Agnese, C.; Dall'Agnese, Y.; Chen, G.; Gao, Y.; Sanehira, Y.; Jena, A. K.; Wang, X. F.; Gogotsi, Y.; Miyasaka, T. *Adv. Funct. Mater.* **2019,** *29*, 1905694. doi: 10.1002/adfm.201905694

(1350) Chen, T. P.; Lin, C. W.; Li, S. S.; Tsai, Y. H.; Wen, C. Y.; Lin, W. J.; Hsiao, F. M.; Chiu, Y. P.; Tsukagoshi, K.; Osada, M.; *et al. Adv. Energy Mater.* **2018,** *8*, 1701722. doi: 10.1002/aenm.201701722

(1351) Yang, L.; Dall'Agnese, Y.; Hantanasirisakul, K.; Shuck, C. E.; Maleski, K.; Alhabeb, M.; Chen, G.; Gao, Y.; Sanehira, Y.; Jena, A. K.; *et al. J. Mater. Chem. A* **2019,** *7*, 5635. doi: 10.1039/c8ta12140k

(1352) Fu, N. Q.; Huang, C.; Lin, P.; Zhu, M. S.; Li, T.; Ye, M.; Lin, S. H.; Zhang, G. G.; Du, J.; Liu, C.; *et al. J. Mater. Chem. A* **2018,** *6*, 8886. doi: 10.1039/c8ta01408f

(1353) Batmunkh, M.; Vimalanathan, K.; Wu, C. C.; Bati, A. S. R.; Yu, L. P.; Tawfik, S. A.; Ford, M. J.; Macdonald, T. J.; Raston, C. L.; Priya, S.; *et al. Small Methods* **2019,** *3*, 1800521. doi: 10.1002/smtd.201800521

(1354) Zhao, X. J.; Tao, L. M.; Li, H.; Huang, W. C.; Sun, P. Y.; Liu, J.; Liu, S. S.; Sun, Q.; Cui, Z. F.; Sun, L. J.; *et al. Nano Lett.* **2018,** *18*, 2442. doi: 10.1021/acs.nanolett.8b00025

(1355) Ren, H.; Yu, S. D.; Chao, L. F.; Xia, Y. D.; Sun, Y. H.; Zuo, S. W.; Li, F.; Niu, T. T.; Yang, Y. G.; Ju, H. X.; *et al. Nat. Photon.* **2020,** *14*, 154. doi: 10.1038/s41566-019-0572-6

(1356) Yang, R.; Li, R. Z.; Cao, Y.; Wei, Y. Q.; Miao, Y. F.; Tan, W. L.; Jiao, X. C.; Chen, H.; Zhang, L. D.; Chen, Q.; *et al. Adv. Mater.* **2018,** *30*, 1804771. doi: 10.1002/adma.201804771

(1357) Liang, C.; Gu, H.; Xia, Y. D.; Wang, Z.; Liu, X. T.; Xia, J. M.; Zuo, S. W.; Hu, Y.; Gao, X. Y.; Hui, W.; *et al. Nat. Energy* **2021,** *6*, 38. doi: 10.1038/s41560-020-00721-5

(1358) Rehman, A. U.; Khan, M. F.; Shehzad, M. A.; Hussain, S.; Bhopal, M. F.; Lee, S. H.; Eom, J.; Seo, Y.; Jung, J.; Lee, S. H. *ACS Appl. Mater. Interfaces* **2016,** *8*, 29383. doi: 10.1021/acsami.6b07064

(1359) Tsai, M. L.; Li, M. Y.; Retamal, J. R. D.; Lam, K. T.; Lin, Y. C.; Suenaga, K.; Chen, L. J.; Liang, G.; Li, L. J.; He, J. H. *Adv. Mater.* **2017,** *29*, 1701168. doi: 10.1002/adma.201701168

(1360) Hadadian, M.; Correa-Baena, J. P.; Goharshadi, E. K.; Ummadisingu, A.; Seo, J. Y.; Luo, J. S.; Gholipour, S.;

Zakeeruddin, S. M.; Saliba, M.; Abate, A.; *et al. Adv. Mater.* **2016,** *28*, 8681. doi: 10.1002/adma.201602785

(1361) Gong, X.; Guan, L.; Li, Q. W.; Li, Y.; Zhang, T.; Pan, H.; Sun, Q.; Shen, Y.; Gratzel, C.; Zakeeruddin, S. M.; *et al. Sci. Adv.* **2020,** *6*, eaay5661. doi: 10.1126/sciadv.aay5661

(1362) Jiang, L. L.; Wang, Z. K.; Li, M.; Zhang, C. C.; Ye, Q. Q.; Hu, K. H.; Lu, D. Z.; Fang, P. F.; Liao, L. S. *Adv. Funct. Mater.* **2018,** *28*, 1705875. doi: 10.1002/adfm.201705875

(1363) Jung, E. H.; Jeon, N. J.; Park, E. Y.; Moon, C. S.; Shin, T. J.; Yang, T. Y.; Noh, J. H.; Seo, J. *Nature* **2019,** *567*, 511. doi: 10.1038/s41586-019-1036-3

(1364) Liu, Z.; Robinson, J. T.; Sun, X.; Dai, H. *J. Am. Chem. Soc.* **2008,** *130*, 10876. doi: 10.1021/ja803688x

(1365) Qin, S. Y.; Zhang, A. Q.; Cheng, S. X.; Rong, L.; Zhang, X. Z. *Biomaterials* **2017,** *112*, 234. doi: 10.1016/j.biomaterials.2016.10.016

(1366) Chen, Y.; Xu, P.; Shu, Z.; Wu, M.; Wang, L.; Zhang, S.; Zheng, Y.; Chen, H.; Wang, J.; Li, Y.; *et al. Adv. Funct. Mater.* **2014,** *24*, 4386. doi: 10.1002/adfm.201400221

(1367) Yang, B.; Yin, J.; Chen, Y.; Pan, S.; Yao, H.; Gao, Y.; Shi, J. *Adv. Mater.* **2018,** *30*, 1705611. doi: 10.1002/adma.201705611

(1368) Dai, C.; Zhang, S.; Liu, Z.; Wu, R.; Chen, Y. *ACS Nano* **2017,** *11*, 9467. doi: 10.1021/acsnano.7b05215

(1369) Zhou, W.; Pan, T.; Cui, H.; Zhao, Z.; Chu, P. K.; Yu, X. F. *Angew. Chem. Int. Ed.* **2019,** *58*, 769. doi: 10.1002/anie.201810878

(1370) Chen, M.; Liu, D.; Du, X.; Lo, K. H.; Wang, S.; Zhou, B.; Pan, H. *TrAC-Trends Anal. Chem* **2020,** *130*, 115983. doi: 10.1016/j.trac.2020.115983

(1371) Pumera, M. *TrAC-Trends Anal. Chem* **2017,** *93*, 1. doi: 10.1016/j.trac.2017.05.002

(1372) Zhang, H. *Chem. Rev.* **2018,** *118*, 6089. doi: 10.1021/acs.chemrev.8b00278

(1373) Chi, J.; Li, J.; Ren, S.; Su, S.; Wang, L. *Acta Chim. Sin.* **2019,** *77*, 1230. doi: 10.6023/A19070262

(1374) Su, S.; Chao, J.; Pan, D.; Wang, L.; Fan, C. *Electroanalysis* **2015,** *27*, 1062. doi: 10.1002/elan.201400655

(1375) Su, S.; Sun, Q.; Gu, X.; Xu, Y.; Shen, J.; Zhu, D.; Chao, J.; Fan, C.; Wang, L. *TrAC-Trends Anal. Chem* **2019,** *119*, 115610. doi: 10.1016/j.trac.2019.07.021

(1376) Li, F.; Huang, Y.; Yang, Q.; Zhong, Z.; Li, D.; Wang, L.; Song, S.; Fan, C. *Nanoscale* **2010,** *2*, 1021. doi: 10.1039/b9nr00401g

(1377) Wu, W.; Hu, H.; Li, F.; Wang, L.; Gao, J.; Lu, J.; Fan, C. *Chem. Commun.* **2011,** *47*, 1201. doi: 10.1039/c0cc04312e

(1378) Tan, C.; Yu, P.; Hu, Y.; Chen, J.; Huang, Y.; Cai, Y.; Luo, Z.; Li, B.; Lu, Q.; Wang, L. *J. Am. Chem. Soc.* **2015,** *137*, 10430. doi: 10.1021/jacs.5b06982

(1379) Zhang, Y.; Zheng, B.; Zhu, C.; Zhang, X.; Tan, C.; Li, H.; Chen, B.; Yang, J.; Chen, J.; Huang, Y. *Adv. Mater.* **2015,** *27*, 935. doi: 10.1002/adma.201404568

(1380) He, S.; Song, B.; Li, D.; Zhu, C.; Qi, W.; Wen, Y.; Wang, L.; Song, S.; Fang, H.; Fan, C. *Adv. Funct. Mater.* **2010,** *20*, 453. doi: 10.1002/adfm.200901639

(1381) Zhu, C.; Zeng, Z.; Li, H.; Li, F.; Fan, C.; Zhang, H. *J. Am. Chem. Soc.* **2013,** *135*, 5998. doi: 10.1021/ja4019572

(1382) Peng, X.; Zhang, Y.; Lu, D.; Guo, Y.; Guo, S. *Sens. Actuators B Chem.* **2019,** *286*, 222. doi: 10.1016/j.snb.2019.01.158

(1383) Sheng, A.; Wang, P.; Yang, J.; Tang, L.; Chen, F.; Zhang, J. *Anal. Chem.* **2021,** *93*, 4676. doi: 10.1021/acs.analchem.1c00371

(1384) Huang, C.; Hu, S.; Zhang, X.; Cui, H.; Wu, L.; Yang, N.; Zhou, W.; Chu, P. K.; Yu, X.-F. *Biosens. Bioelectron.* **2020,** *165*, 112384. doi: 10.1016/j.bios.2020.112384

(1385) Li, J.; Yuan, S.; Qin, J. S.; Pang, J.; Zhang, P.; Zhang, Y.; Huang, Y.; Drake, H. F.; Liu, W. R.; Zhou, H. C. *Angew. Chem. Int. Ed.* **2020,** *59*, 9319. doi: 10.1002/anie.202000702

(1386) Li, X.; Li, Y.; Qiu, Q.; Wen, Q.; Zhang, Q.; Yang, W.; Yuwen, L.; Weng, L.; Wang, L. *J. Colloid Interface Sci.* **2019,** *543*, 96. doi: 10.1016/j.jcis.2019.02.011

(1387) Zhu, D.; Huang, J.; Lu, B.; Zhu, Y.; Wei, Y.; Zhang, Q.; Guo, X.; Yuwen, L.; Su, S.; Chao, J. *ACS Appl. Mater. Interfaces* **2019,** *11*, 20725. doi: 10.1021/acsami.9b04883

(1388) Wu, L.; Chu, H.; Koh, W.; Li, E. *Opt. Express* **2010,** *18*, 14395. doi: 10.1364/OE.18.014395

(1389) Kumar, A.; Yadav, A. K.; Kushwaha, A. S.; Srivastava, S. *Sens. Actuators Rep.* **2020,** *2*, 100015. doi: 10.1016/j.snr.2020.100015

(1390) Xue, T.; Liang, W.; Li, Y.; Sun, Y.; Xiang, Y.; Zhang, Y.; Dai, Z.; Duo, Y.; Wu, L.; Qi, K.; *et al. Nat. Commun.* **2019,** *10*, 28. doi: 10.1038/s41467-018-07947-8

(1391) Chiu, N.-F.; Lin, T.-L. *Talanta* **2018,** *185*, 174. doi: 10.1016/j.talanta.2018.03.073

(1392) Kaushik, S.; Tiwari, U. K.; Pal, S. S.; Sinha, R. K. *Biosens. Bioelectron.* **2019,** *126*, 501. doi: 10.1016/j.bios.2018.11.006

(1393) Nie, W.; Wang, Q.; Yang, X.; Zhang, H.; Li, Z.; Gao, L.; Zheng, Y.; Liu, X.; Wang, K. *Anal. Chim. Acta* **2017,** *993*, 55. doi: 10.1016/j.aca.2017.09.015

(1394) Ling, X.; Xie, L.; Fang, Y.; Xu, H.; Zhang, H.; Kong, J.; Dresselhaus, M. S.; Zhang, J.; Liu, Z. *Nano Lett.* **2010,** *10*, 553. doi: 10.1021/nl903414x

(1395) Li, Z.; Jiang, S.; Xu, S.; Zhang, C.; Qiu, H.; Chen, P.; Gao, S.; Man, B.; Yang, C.; Liu, M. *J. Alloys Compd.* **2016,** *666*, 412. doi: 10.1016/j.jallcom.2016.01.126

(1396) Ling, X.; Fang, W.; Lee, Y.-H.; Araujo, P. T.; Zhang, X.; Rodriguez-Nieva, J. F.; Lin, Y.; Zhang, J.; Kong, J.; Dresselhaus,

M. S. *Nano Lett.* **2014**, *14*, 3033. doi: 10.1021/nl404610c

(1397) Sarycheva, A.; Makaryan, T.; Maleski, K.; Satheeshkumar, E.; Melikyan, A.; Minassian, H.; Yoshimura, M.; Gogotsi, Y. *J. Phys. Chem. C* **2017**, *121*, 19983. doi: 10.1021/acs.jpcc.7b08180

(1398) Su, S.; Zhang, C.; Yuwen, L.; Chao, J.; Zuo, X.; Liu, X.; Song, C.; Fan, C.; Wang, L. *ACS Appl. Mater. Interfaces* **2014**, *6*, 18735. doi: 10.1021/am5043092

(1399) Singha, S. S.; Mondal, S.; Bhattacharya, T. S.; Das, L.; Sen, K.; Satpati, B.; Das, K.; Singha, A. *Biosens. Bioelectron.* **2018**, *119*, 10. doi: 10.1016/j.bios.2018.07.061

(1400) Xie, H.; Li, P.; Shao, J.; Huang, H.; Chen, Y.; Jiang, Z.; Chu, P. K.; Yu, X.-F. *ACS Sensors* **2019**, *4*, 2303. doi: 10.1021/acssensors.9b00778

(1401) Shorie, M.; Kumar, V.; Kaur, H.; Singh, K.; Tomer, V. K.; Sabherwal, P. *Microchimica Acta* **2018**, *185*, 158. doi: 10.1007/s00604-018-2705-x

(1402) Fu, X.; Wang, Y.; Liu, Y.; Liu, H.; Fu, L.; Wen, J.; Li, J.; Wei, P.; Chen, L. *Analyst* **2019**, *144*, 1582. doi: 10.1039/c8an02022a

(1403) Achadu, O. J.; Abe, F.; Suzuki, T.; Park, E. Y. *ACS Appl. Mater. Interfaces* **2020**, *12*, 43522. doi: 10.1021/acsami.0c14729

(1404) Mao, S.; Chang, J.; Pu, H.; Lu, G.; He, Q.; Zhang, H.; Chen, J. *Chem. Soc. Rev.* **2017**, *46*, 6872. doi: 10.1039/C6CS00827E

(1405) He, Q.; Wu, S.; Gao, S.; Cao, X.; Yin, Z.; Li, H.; Chen, P.; Zhang, H. *ACS Nano* **2011**, *5*, 5038. doi: 10.1021/nn201118c

(1406) Seo, G.; Lee, G.; Kim, M. J.; Baek, S.-H.; Choi, M.; Ku, K. B.; Lee, C.-S.; Jun, S.; Park, D.; Kim, H. G. *ACS nano* **2020**, *14*, 5135. doi: 10.1021/acsnano.0c02823

(1407) Xu, S.; Zhang, C.; Jiang, S.; Hu, G.; Li, X.; Zou, Y.; Liu, H.; Li, J.; Li, Z.; Wang, X. *Sens. Actuators B Chem.* **2019**, *284*, 125. doi: 10.1016/j.snb.2018.12.129

(1408) Xu, S.; Wang, T.; Liu, G.; Cao, Z.; Frank, L. A.; Jiang, S.; Zhang, C.; Li, Z.; Krasitskaya, V. V.; Li, Q. *Sens. Actuators B Chem.* **2021**, *326*, 128991. doi: 10.1016/j.snb.2020.128991

(1409) Lei, Y.-M.; Xiao, M.-M.; Li, Y.-T.; Xu, L.; Zhang, H.; Zhang, Z.-Y.; Zhang, G.-J. *Biosens. Bioelectron.* **2017**, *91*, 1. doi: 10.1016/j.bios.2016.12.018

(1410) Sarkar, D.; Liu, W.; Xie, X.; Anselmo, A. C.; Mitragotri, S.; Banerjee, K. *ACS Nano* **2014**, *8*, 3992. doi: 10.1021/nn5009148

(1411) Gong, X.; Liu, Y.; Xiang, H.; Liu, H.; Liu, Z.; Zhao, X.; Li, J.; Li, H.; Hong, G.; Hu, T. S. *Sci. China Mater.* **2019**, *62*, 1479. doi: 10.1007/s40843-019-9444-y

(1412) Liu, J.; Chen, X.; Wang, Q.; Xiao, M.; Zhong, D.; Sun, W.; Zhang, G.; Zhang, Z. *Nano Lett.* **2019**, *19*, 1437. doi: 10.1021/acs.nanolett.8b03818

(1413) Hao, S.; Liu, C.; Chen, X.; Zong, B.; Wei, X.; Li, Q.; Qin, H.; Mao, S. *J. Hazard. Mater.* **2021**, *418*, 126301.

doi: 10.1016/j.jhazmat.2021.126301

(1414) Chen, Y.; Ren, R.; Pu, H.; Chang, J.; Mao, S.; Chen, J. *Biosens. Bioelectron.* **2017**, *89*, 505. doi: 10.1016/j.bios.2016.03.059

(1415) Zhou, M.; Zhai, Y.; Dong, S. *Anal. Chem.* **2009**, *81*, 5603. doi: 10.1021/ac900136z

(1416) Bollella, P.; Fusco, G.; Tortolini, C.; Sanzò, G.; Favero, G.; Gorton, L.; Antiochia, R. *Biosens. Bioelectron.* **2017**, *89*, 152. doi: 10.1016/j.bios.2016.03.068

(1417) Su, S.; Sun, H.; Xu, F.; Yuwen, L.; Wang, L. *Electroanalysis* **2013**, *25*, 2523. doi: 10.1002/elan.201300332

(1418) Su, S.; Lu, Z.; Li, J.; Hao, Q.; Liu, W.; Zhu, C.; Shen, X.; Shi, J.; Wang, L. *New J. Chem.* **2018**, *42*, 6750. doi: 10.1039/C8NJ00940F

(1419) Sun, H.; Chao, J.; Zuo, X.; Su, S.; Liu, X.; Yuwen, L.; Fan, C.; Wang, L. *RSC Adv.* **2014**, *4*, 27625. doi: 10.1039/C4RA04046E

(1420) Chao, J.; Zou, M.; Zhang, C.; Sun, H.; Pan, D.; Pei, H.; Su, S.; Yuwen, L.; Fan, C.; Wang, L. *Nanotechnology* **2015**, *26*, 274005. doi: 10.1088/0957-4484/26/27/274005

(1421) Li, X.; Niu, X.; Zhao, W.; Chen, W.; Yin, C.; Men, Y.; Li, G.; Sun, W. *Electrochem. Commun.* **2018**, *86*, 68. doi: 10.1016/j.elecom.2017.11.017

(1422) Niu, Y.; Zou, R.; Yones, H. A.; Li, X.; Li, X.; Niu, X.; Chen, Y.; Li, P.; Sun, W. *J. Chin. Chem. Soc.* **2018**, *65*, 1127. doi: 10.1002/jccs.201800054

(1423) Cai, J.; Gou, X.; Sun, B.; Li, W.; Li, D.; Liu, J.; Hu, F.; Li, Y. *Biosens. Bioelectron.* **2019**, *137*, 88. doi: 10.1016/j.bios.2019.04.045

(1424) Su, S.; Hao, Q.; Yan, Z.; Dong, R.; Yang, R.; Zhu, D.; Chao, J.; Zhou, Y.; Wang, L. *Microchimica Acta* **2019**, *186*, 607. doi: 10.1007/s00604-019-3678-0

(1425) Mahmoudian, M.; Basirun, W.; Alias, Y.; Pei, M. *J. Environ. Chem. Eng.* **2020**, *8*, 104204. doi: 10.1016/j.jece.2020.104204

(1426) Su, S.; Sun, Q.; Wan, L.; Gu, X.; Zhu, D.; Zhou, Y.; Chao, J.; Wang, L. *Biosens. Bioelectron.* **2019**, *140*, 111353. doi: 10.1016/j.bios.2019.111353

(1427) Su, S.; Sun, Q.; Ma, J.; Zhu, D.; Wang, F.; Chao, J.; Fan, C.; Li, Q.; Wang, L. *Chem. Commun.* **2020**, *56*, 9012. doi: 10.1039/D0CC03845H

(1428) Gao, L.; Zhuang, J.; Nie, L.; Zhang, J.; Zhang, Y.; Gu, N.; Wang, T.; Feng, J.; Yang, D.; Perrett, S. *Nat. Nanotechnol.* **2007**, *2*, 577. doi: 10.1038/nnano.2007.260

(1429) Song, Y.; Qu, K.; Zhao, C.; Ren, J.; Qu, X. *Adv. Mater.* **2010**, *22*, 2206. doi: 10.1002/adma.200903783

(1430) Cai, S.; Xiao, W.; Duan, H.; Liang, X.; Wang, C.; Yang, R.; Li, Y. *Nano Res.* **2018**, *11*, 6304. doi: 10.1007/s12274-018-2154-1

(1431) Lin, T.; Zhong, L.; Song, Z.; Guo, L.; Wu, H.; Guo, Q.; Chen, Y.; Fu, F.; Chen, G. *Biosens. Bioelectron.* **2014**, *62*, 302.

doi: 10.1016/j.bios.2014.07.001

(1432) Park, Y.; Ryu, B.; Ki, S. J.; McCracken, B.; Pennington, A.; Ward, K. R.; Liang, X.; Kurabayashi, K. *ACS Nano* **2021**, *15*, 7722. doi: 10.1021/acsnano.1c01394

(1433) Wu, Y.; Chen, Q.; Liu, S.; Xiao, H.; Zhang, M.; Zhang, X. *Chin. Chem. Lett.* **2019**, *30*, 2186. doi: 10.1016/j.cclet.2019.08.014

(1434) Lee, J.; Kim, Y.-K.; Lee, S.; Yoon, S.; Kim, W.-K. *Sens. Actuators B Chem.* **2019**, *282*, 861. doi: 10.1016/j.snb.2018.11.149

(1435) Lan, L.; Yao, Y.; Ping, J.; Ying, Y. *Sens. Actuators B Chem.* **2019**, *290*, 565. doi: 10.1016/j.snb.2019.04.016

(1436) Wan, L.; Wu, L.; Su, S.; Zhu, D.; Chao, J.; Wang, L. *Chem. Commun.* **2020**, *56*, 12351. doi: 10.1039/d0cc05152g

(1437) Xiao, L.; Zhu, A.; Xu, Q.; Chen, Y.; Xu, J.; Weng, J. *ACS Appl. Mater. Interfaces* **2017**, *9*, 6931. doi: 10.1021/acsami.6b15750

(1438) Sun, Z.; Wu, S.; Ma, J.; Shi, H.; Wang, L.; Sheng, A.; Yin, T.; Sun, L.; Li, G. *ACS Appl. Mater. Interfaces* **2019**, *11*, 36316. doi: 10.1021/acsami.9b10729

(1439) Su, S.; Li, J.; Yao, Y.; Sun, Q.; Zhao, Q.; Wang, F.; Li, Q.; Liu, X.; Wang, L. *ACS Appl. Bio Mater.* **2019**, *2*, 292. doi: 10.1021/acsabm.8b00598

(1440) He, Y.; Zhou, X.; Zhou, L.; Zhang, X.; Ma, L.; Jiang, Y.; Gao, J. *Ind. Eng. Chem. Res.* **2020**, *59*, 15556. doi: 10.1021/acs.iecr.0e02154

(1441) Cao, X.; Yang, H.; Wei, Q.; Yang, Y.; Liu, M.; Liu, Q.; Zhang, X. *Inorg. Chem. Commun.* **2021**, *123*, 108331. doi: 10.1016/j.inoche.2020.108331

(1442) Munyemana, J. C.; Chen, J.; Wei, X.; Ali, M. C.; Han, Y.; Qiu, H. *Anal. Bioanal. Chem.* **2020**, *412*, 4629. doi: 10.1007/s00216-020-02712-7

(1443) Friedman, J. S.; Girdhar, A.; Gelfand, R. M.; Memik, G.; Mohseni, H.; Taflove, A.; Wessels, B. W.; Leburton, J. P.; Sahakian, A. V. *Nat. Commun.* **2017**, *8*, 15635. doi: 10.1038/ncomms15635

(1444) Shim, J.; Jo, S. H.; Kim, M.; Song, Y. J.; Kim, J.; Park, J. H. *ACS Nano* **2017**, *11*, 6319. doi: 10.1021/acsnano.7b02635

(1445) Cartamil-Bueno, S. J.; Davidovikj, D.; Centeno, A.; Zurutuza, A.; van der Zant, H. S. J.; Steeneken, P. G.; Houri, S. *Nat. Commun.* **2018**, *9*, 4837. doi: 10.1038/s41467-018-07230-w

(1446) Xie, H.; Cui, K.; Cui, L.; Liu, B.; Yu, Y.; Tan, C.; Zhang, Y.; Zhang, Y.; Liu, Z. *Small* **2020**, *16*, e1905485. doi: 10.1002/smll.201905485

(1447) Sun, H.; Mei, L.; Liang, J.; Zhao, Z.; Lee, C.; Fei, H.; Ding, M.; Lau, J.; Li, M.; Wang, C.; *et al. Science* **2017**, *356*, 599. doi: 10.1126/science.aam5852

(1448) Mo, R.; Rooney, D.; Sun, K.; Yang, H. Y. *Nat. Commun.* **2017**, *8*, 13949. doi: 10.1038/ncomms13949

(1449) Guan, S. L.; Wang, J. F.; Fang, Y. *Nano Today* **2019**, *26*, 13.

doi: 10.1016/j.nantod.2019.01.003

(1450) Yin, R.; Xu, Z.; Mei, M.; Chen, Z.; Wang, K.; Liu, Y.; Tang, T.; Priydarshi, M. K.; Meng, X.; Zhao, S.; *et al. Nat. Commun.* **2018**, *9*, 2334. doi: 10.1038/s41467-018-04781-w

(1451) Giubileo, F.; Di Bartolomeo, A. *Prog. Surf. Sci.* **2017**, *92*, 143. doi: 10.1016/j.progsurf.2017.05.002

(1452) Schulman, D. S.; Arnold, A. J.; Das, S. *Chem. Soc. Rev.* **2018**, *47*, 3037. doi: 10.1039/c7cs00828g

(1453) Liu, F.; Navaraj, W. T.; Yogeswaran, N.; Gregory, D. H.; Dahiya, R. *ACS Nano* **2019**, *13*, 3257. doi: 10.1021/acsnano.8b09019

(1454) Liu, N.; Chortos, A.; Lei, T.; Jin, L.; Kim, T. R.; Bae, W. G.; Zhu, C.; Wang, S.; Pfattner, R.; Chen, X.; *et al. Sci. Adv.* **2017**, *3*, e1700159. doi: 10.1126/sciadv.1700159

(1455) Qiu, J. K.; Yu, T. H.; Zhang, W. F.; Zhao, Z. H.; Zhang, Y.; Ye, G.; Zhao, Y.; Du, X. J.; Liu, X.; Yang, L.; *et al. ACS Mater. Lett.* **2020**, *2*, 999. doi: 10.1021/acsmaterialslett.0c00203

(1456) You, R.; Liu, Y. Q.; Hao, Y. L.; Han, D. D.; Zhang, Y. L.; You, Z. *Adv. Mater.* **2020**, *32*, e1901981. doi: 10.1002/adma.201901981

(1457) Yang, C.; Huang, Y.; Cheng, H.; Jiang, L.; Qu, L. *Adv. Mater.* **2019**, *31*, 1805705. doi: 10.1002/adma.201805705

(1458) Cheng, H.; Huang, Y.; Qu, L.; Cheng, Q.; Shi, G.; Jiang, L. *Nano Energy* **2018**, *45*, 37. doi: 10.1016/j.nanoen.2017.12.033

(1459) Wang, S.; Liu, N.; Su, J.; Li, L.; Long, F.; Zou, Z.; Jiang, X.; Gao, Y. *ACS Nano* **2017**, *11*, 2066. doi: 10.1021/acsnano.6b08262

(1460) Fan, Z.; Wang, Y.; Xie, Z.; Wang, D.; Yuan, Y.; Kang, H.; Su, B.; Cheng, Z.; Liu, Y. *Adv. Sci.* **2018**, *5*, 1800750. doi: 10.1002/advs.201800750

(1461) Chmiola, J.; Largeot, C.; Taberna, P. L.; Simon, P.; Gogotsi, Y. *Science* **2010**, *328*, 480. doi: 10.1126/science.1184126

(1462) Sun, B.; McCay, R. N.; Goswami, S.; Xu, Y.; Zhang, C.; Ling, Y.; Lin, J.; Yan, Z. *Adv. Mater.* **2018**, *30*, 1804327. doi: 10.1002/adma.201804327

(1463) Qiao, Y.; Wang, Y.; Tian, H.; Li, M.; Jian, J.; Wei, Y.; Tian, Y.; Wang, D. Y.; Pang, Y.; Geng, X.; *et al. ACS Nano* **2018**, *12*, 8839. doi: 10.1021/acsnano.8b02162

(1464) Jiang, T.; Huang, D.; Cheng, J.; Fan, X.; Zhang, Z.; Shan, Y.; Yi, Y.; Dai, Y.; Shi, L.; Liu, K.; *et al. Nat. Photon.* **2018**, *12*, 430. doi: 10.1038/s41566-018-0175-7

(1465) An, J.; Le, T. D.; Lim, C. H. J.; Tran, V. T.; Zhan, Z.; Gao, Y.; Zheng, L.; Sun, G.; Kim, Y. J. *Adv. Sci.* **2018**, *5*, 1800496. doi: 10.1002/advs.201800496

(1466) Zhu, L.; Gao, Y. Y.; Han, B.; Zhang, Y. L.; Sun, H. B. *Opt. Lett.* **2019**, *44*, 1363. doi: 10.1364/OL.44.001363

(1467) Chen, L. Z.; Weng, M. C.; Zhou, P. D.; Huang, F.; Liu, C. H.; Fan, S. S.; Zhang, W. *Adv. Funct. Mater.* **2019**, *29*, 1806057. doi: 10.1002/adfm.201806057

(1468) Tao, L. Q.; Tian, H.; Liu, Y.; Ju, Z. Y.; Pang, Y.; Chen, Y. Q.; Wang, D. Y.; Tian, X. G.; Yan, J. C.; Deng, N. Q.; *et al. Nat. Commun.* **2017**, *8*, 14579. doi: 10.1038/ncomms14579

(1469) Kabiri Ameri, S.; Ho, R.; Jang, H.; Tao, L.; Wang, Y.; Wang, L.; Schnyer, D. M.; Akinwande, D.; Lu, N. *ACS Nano* **2017**, *11*, 7634. doi: 10.1021/acsnano.7b02182

(1470) Seo, H. K.; Kim, H.; Lee, J.; Park, M. H.; Jeong, S. H.; Kim, Y. H.; Kwon, S. J.; Han, T. H.; Yoo, S.; Lee, T. W. *Adv. Mater.* **2017**, *29*, 1605587. doi: 10.1002/adma.201605587

(1471) Park, I. J.; Kim, T. I.; Yoon, T.; Kang, S.; Cho, H.; Cho, N. S.; Lee, J. I.; Kim, T. S.; Choi, S. Y. *Adv. Funct. Mater.* **2018**, *28*, 1704435. doi: 10.1002/adfm.201704435

(1472) Kireev, D.; Ameri, S. K.; Nederveld, A.; Kampfe, J.; Jang, H.; Lu, N.; Akinwande, D. *Nat. Protoc.* **2021**, *16*, 2395. doi: 10.1038/s41596-020-00489-8

(1473) Pak, S.; Lee, J.; Jang, A. R.; Kim, S.; Park, K. H.; Sohn, J. I.; Cha, S. *Adv. Funct. Mater.* **2020**, *30*, 2002023. doi: 10.1002/adfm.202002023

(1474) Naqi, M.; Kim, B.; Kim, S. W.; Kim, S. *Adv. Funct. Mater.* **2020**, *31*, 2007389. doi: 10.1002/adfm.202007389

(1475) Choi, W.; Choudhary, N.; Han, G. H.; Park, J.; Akinwande, D.; Lee, Y. H. *Mater. Today* **2017**, *20*, 116. doi: 10.1016/j.mattod.2016.10.002

(1476) Xie, C.; Yan, F. *Small* **2017**, *13*, 1701822. doi: 10.1002/smll.201701822

(1477) Okogbue, E.; Han, S. S.; Ko, T. J.; Chung, H. S.; Ma, J.; Shawkat, M. S.; Kim, J. H.; Kim, J. H.; Ji, E.; Oh, K. H.; *et al. Nano Lett.* **2019**, *19*, 7598. doi: 10.1021/acs.nanolett.9b01726

(1478) Rahman, M.; Davey, K.; Qiao, S. Z. *Adv. Funct. Mater.* **2017**, *27*, 1606129. doi: 10.1002/adfm.201606129

(1479) Li, L.; Guo, Y.; Sun, Y.; Yang, L.; Qin, L.; Guan, S.; Wang, J.; Qiu, X.; Li, H.; Shang, Y.; *et al. Adv. Mater.* **2018**, *30*, 1706215. doi: 10.1002/adma.201706215

(1480) Choi, J. M.; Jang, H. Y.; Kim, A. R.; Kwon, J. D.; Cho, B.; Park, M. H.; Kim, Y. *Nanoscale* **2021**, *13*, 672. doi: 10.1039/d0nr07091b

(1481) Gu, J.; Chakraborty, B.; Khatoniar, M.; Menon, V. M. *Nat. Nanotechnol.* **2019**, *14*, 1024. doi: 10.1038/s41565-019-0543-6

(1482) Bie, Y. Q.; Grosso, G.; Heuck, M.; Furchi, M. M.; Cao, Y.; Zheng, J.; Bunandar, D.; Navarro-Moratalla, E.; Zhou, L.; Efetov, D. K.; *et al. Nat. Nanotechnol.* **2017**, *12*, 1124. doi: 10.1038/nnano.2017.209

(1483) Tebyetekerwa, M.; Zhang, J.; Liang, K.; Duong, T.; Neupane, G. P.; Zhang, L.; Liu, B.; Truong, T. N.; Basnet, R.; Qiao, X.; *et al. Adv. Mater.* **2019**, *31*, 1900522. doi: 10.1002/adma.201900522

(1484) Lin, Y.; Adilbekova, B.; Firdaus, Y.; Yengel, E.; Faber, H.; Sajjad, M.; Zheng, X.; Yarali, E.; Seitkhan, A.; Bakr, O. M.; *et al. Adv. Mater.* **2019**, *31*, 1902965. doi: 10.1002/adma.201902965

(1485) Gao, L. *Small* **2017**, *13*, 1603994. doi: 10.1002/smll.201603994

(1486) Li, G.; Wang, X.; Han, B.; Zhang, W.; Qi, S.; Zhang, Y.; Qiu, J.; Gao, P.; Guo, S.; Long, R.; *et al. J. Phys. Chem. Lett.* **2020**, *11*, 1570. doi: 10.1021/acs.jpclett.9b03879

(1487) Zhang, W.; Zhang, Y.; Qiu, J.; Zhao, Z.; Liu, N. *InfoMat* **2020**, *3*, 133. doi: 10.1002/inf2.12156

(1488) Pang, Y.; Yang, Z.; Yang, Y.; Ren, T. L. *Small* **2020**, *16*, e1901124. doi: 10.1002/smll.201901124

(1489) Babu, G.; Masurkar, N.; Al Salem, H.; Arava, L. M. *J. Am. Chem. Soc.* **2017**, *139*, 171. doi: 10.1021/jacs.6b08681

(1490) Sun, R. M.; Wei, Q. L.; Sheng, J. Z.; Shi, C. W.; An, Q. Y.; Liu, S. J.; Mai, L. Q. *Nano Energy* **2017**, *35*, 396. doi: 10.1016/j.nanoen.2017.03.036

(1491) Guo, Z. L.; Yang, L.; Wang, W.; Cao, L. X.; Dong, B. H. *J. Mater. Chem. A* **2018**, *6*, 14681. doi: 10.1039/c8ta03812k

(1492) Peigney, A.; Laurent, C.; Flahaut, E.; Bacsa, R.; Rousset, A. *Carbon* **2001**, *39*, 507. doi: 10.1016/S0008-6223(00)00155-X

(1493) Férey, G.; Mellot-Draznieks, C.; Serre, C.; Millange, F.; Dutour, J.; Surblé, S.; Margiolaki, I. *Science* **2005**, *309*, 2040. doi: 10.1126/science.1116275

(1494) Feriante, C. H.; Jhulki, S.; Evans, A. M.; Dasari, R. R.; Slicker, K.; Dichtel, W. R.; Marder, S. R. *Adv. Mater.* **2020**, *32*, 1905776. doi: 10.1002/adma.201905776

(1495) Le, T.-H.; Oh, Y.; Kim, H.; Yoon, H. *Chem. Eur. J.* **2020**, *26*, 6360. doi: 10.1002/chem.202000223

(1496) Nair, R.; Wu, H.; Jayaram, P.; Grigorieva, I.; Geim, A. *Science* **2012**, *335*, 442. doi: 10.1126/science.1211694

(1497) Joshi, R. K.; Carbone, P.; Wang, F. C.; Kravets, V. G.; Su, Y.; Grigorieva, I. V.; Wu, H. A.; Geim, A. K.; Nair, R. R. *Science* **2014**, *343*, 752. doi: 10.1126/science.1245711

(1498) Cheng, L.; Liu, G.; Jin, W. *Acta Phys. -Chim. Sin.* **2019**, *35*, 1090. doi: 10.3866/PKU.WHXB201810059

(1499) Li, X.; Xu, W.; Tang, M.; Zhou, L.; Zhu, B.; Zhu, S.; Zhu, J. *Proc. Natl. Acad. Sci. U. S. A.* **2016**, *113*, 13953. doi: 10.1073/pnas.1613031113

(1500) Deng, D.; Novoselov, K.; Fu, Q.; Zheng, N.; Tian, Z.; Bao, X. *Nat. Nanotechnol.* **2016**, *11*, 218. doi: 10.1038/NNANO.2015.340

(1501) Konicki, W.; Aleksandrzak, M.; Mijowska, E. *Chem. Eng. Res. Des.* **2017**, *123*, 35. doi: 10.1016/j.cherd.2017.03.036

(1502) Ge, J.; Shi, L.-A.; Wang, Y.-C.; Zhao, H.-Y.; Yao, H.-B.; Zhu, Y.-B.; Zhang, Y.; Zhu, H.-W.; Wu, H.-A.; Yu, S.-H. *Nat. Nanotechnol.* **2017**, *12*, 434. doi: 10.1038/nnano.2017.33

(1503) Cao, M.; Shen, Y.; Yan, Z.; Wei, Q.; Jiao, T.; Shen, Y.; Han, Y.; Wang, Y.; Wang, S.; Xia, Y.; *et al. Chem. Eng. J.* **2021**, *405*, 126647. doi: 10.1016/j.cej.2020.126647

(1504) Lei, W.; Portehault, D.; Liu, D.; Qin, S.; Chen, Y. *Nat. Commun.*

2013, *4*, 1777. doi: 10.1038/ncomms2818

(1505) Li, Q.; Yang, T.; Yang, Q.; Wang, F.; Chou, K.-C.; Hou, X. *Ceram. Int.* **2016**, *42*, 8754. doi: 10.1016/j.ceramint.2016.02.114

(1506) Zhao, G.; Ren, X.; Gao, X.; Tan, X.; Li, J.; Chen, C.; Huang, Y.; Wang, X. *Dalton Trans.* **2011**, *40*, 10945. doi: 10.1039/C1DT11005E

(1507) Zhao, G.; Wen, T.; Yang, X.; Yang, S.; Liao, J.; Hu, J.; Shao, D.; Wang, X. *Dalton Trans.* **2012**, *41*, 6182. doi: 10.1039/C2DT00054G

(1508) Liao, Q.; Pan, W.; Zou, D.; Shen, R.; Sheng, G.; Li, X.; Zhu, Y.; Dong, L.; Asiri, A. M.; Alamry, K. A.; *et al. J. Mol. Liq.* **2018**, *261*, 32. doi: 10.1016/j.molliq.2018.03.093

(1509) Xiao, G.; Wang, Y.; Xu, S.; Li, P.; Yang, C.; Jin, Y.; Sun, Q.; Su, H. *Chin. J. Chem. Eng.* **2019**, *27*, 305. doi: 10.1016/j.cjche.2018.09.028

(1510) Jiang, L.-H.; Liu, Y.-G.; Zeng, G.-M.; Xiao, F.-Y.; Hu, X.-J.; Hu, X.; Wang, H.; Li, T.-T.; Zhou, L.; Tan, X.-F. *Chem. Eng. J.* **2016**, *284*, 93. doi: 10.1016/j.cej.2015.08.139

(1511) Sroysee, W.; Suktha, P.; Kongsawatvoragul, K.; Vadivel, S.; Sawangphruk, M. *Ind. Eng. Chem. Res.* **2020**, *59*, 20719. doi: 10.1021/acs.iecr.0c04026

(1512) Liu, D.; Lei, W.; Qin, S.; Klika, K. D.; Chen, Y. *Phys. Chem. Chem. Phys.* **2016**, *18*, 84. doi: 10.1039/C5CP06399J

(1513) Li, C. W.; Jiang, D. G.; Liang, H.; Huo, B. B.; Liu, C. Y.; Yang, W. R.; Liu, J. Q. *Adv. Funct. Mater.* **2018**, *28*, 1704674. doi: 10.1002/adfm.201704674

(1514) Liu, J.; Ge, X.; Ye, X.; Wang, G.; Zhang, H.; Zhou, H.; Zhang, Y.; Zhao, H. *J. Mater. Chem. A* **2016**, *4*, 1970. doi: 10.1039/C5TA08106H

(1515) Yoon, Y.; Zheng, M.; Ahn, Y.-T.; Park, W. K.; Yang, W. S.; Kang, J.-W. *Sep. Purif. Technol.* **2017**, *178*, 40. doi: 10.1016/j.seppur.2017.01.025

(1516) Yousefi, N.; Lu, X.; Elimelech, M.; Tufenkji, N. *Nat. Nanotechnol.* **2019**, *14*, 107. doi: 10.1038/s41565-018-0325-6

(1517) Luo, J.; Fu, K.; Yu, D.; Hristovski, K. D.; Westerhoff, P.; Crittenden, J. C. *ACS EST Eng.* **2021**, *1*, 623. doi: 10.1021/acsestengg.0c00174

(1518) Wang, D.; Saleh, N. B.; Sun, W.; Park, C. M.; Shen, C.; Aich, N.; Peijnenburg, W. J.; Zhang, W.; Jin, Y.; Su, C. *Environ. Sci. Technol.* **2019**, *53*, 7265. doi: 10.1021/acs.est.9b01453

(1519) Li, H.; Gao, K.; Mo, B.; Meng, Q.; Li, K.; Wu, J.; Hou, H. *Dalton Trans.* **2021**, *50*, 3348. doi: 10.1039/d0dt04143b

(1520) Wang, Q.; Gao, Q.; Al-Enizi, A. M.; Nafady, A.; Ma, S. *Inorg. Chem. Front.* **2020**, *7*, 300. doi: 10.1039/c9qi01120j

(1521) Hu, X.; Xu, W.; Zhou, L.; Tan, Y.; Wang, Y.; Zhu, S.; Zhu, J. *Adv. Mater.* **2017**, *29*, 1604031. doi: 10.1002/adma.201604031

(1522) Su, J.; Xu, N.; Murase, R.; Yang, Z. M.; D'Alessandro, D. M.; Zuo, J. L.; Zhu, J. *Angew. Chem. Int. Ed.* **2021**, *60*, 4789. doi: 10.1002/anie.202013811

(1523) Perreault, F.; De Faria, A. F.; Elimelech, M. *Chem. Soc. Rev.* **2015**, *44*, 5861. doi: 10.1039/c5cs00021a

(1524) Sui, X.; Yuan, Z. W.; Yu, Y. X.; Goh, K.; Chen, Y. *Small* **2020**, *16*, 2003400. doi: 10.1002/smll.202003400

(1525) Shen, J.; Liu, G.; Han, Y.; Jin, W. *Nat. Rev. Mater.* **2021**, *6*, 294. doi: 10.1038/s41578-020-00268-7

(1526) Abraham, J.; Vasu, K. S.; Williams, C. D.; Gopinadhan, K.; Su, Y.; Cherian, C. T.; Dix, J.; Prestat, E.; Haigh, S. J.; Grigorieva, I. V. *Nat. Nanotechnol.* **2017**, *12*, 546. doi: 10.1038/NNANO.2017.21

(1527) Chen, L.; Shi, G.; Shen, J.; Peng, B.; Zhang, B.; Wang, Y.; Bian, F.; Wang, J.; Li, D.; Qian, Z. *Nature* **2017**, *550*, 415. doi: 10.1038/nature24044

(1528) Thebo, K. H.; Qian, X.; Zhang, Q.; Chen, L.; Cheng, H.-M.; Ren, W. *Nat. Commun.* **2018**, *9*, 1486. doi: 10.1038/s41467-018-03919-0

(1529) Zhang, M. C.; Mao, Y. Y.; Liu, G. Z.; Liu, G. P.; Fan, Y. Q.; Jin, W. Q. *Angew. Chem. Int. Ed.* **2020**, *59*, 1689. doi: 10.1002/ange.201913010

(1530) Ries, L.; Petit, E.; Michel, T.; Diogo, C. C.; Gervais, C.; Salameh, C.; Bechelany, M.; Balme, S.; Miele, P.; Onofrio, N. *Nat. Mater.* **2019**, *18*, 1112. doi: 10.1038/s41563-019-0464-7

(1531) Peng, Y.; Yao, R.; Yang, W. *Chem. Commun.* **2019**, *55*, 3935. doi: 10.1039/c9cc00349e

(1532) Yang, Y.; Yang, X.; Liang, L.; Gao, Y.; Cheng, H.; Li, X.; Zou, M.; Ma, R.; Yuan, Q.; Duan, X. *Science* **2019**, *364*, 1057. doi: 10.1126/science.aau5321

(1533) Kessler, F. K.; Zheng, Y.; Schwarz, D.; Merschjann, C.; Schnick, W.; Wang, X.; Bojdys, M. J. *Nat. Rev. Mater.* **2017**, *2*, 17030. doi: 10.1038/natrevmats.2017.30

(1534) Chakraborty, G.; Park, I.-H.; Medishetty, R.; Vittal, J. J. *Chem. Rev.* **2021**, *121*, 3751. doi: 10.1021/acs.chemrev.0c01049

(1535) Yuan, Y.; Shen, P.; Li, Q.; Chen, G.; Zhang, H.; Zhu, L.; Zou, B.; Liu, B. *J. Alloys Compd.* **2017**, *700*, 12. doi: 10.1016/j.jallcom.2017.01.027

(1536) Guan, G.; Ye, E.; You, M.; Li, Z. *Small* **2020**, *16*, 1907087. doi: 10.1002/smll.201907087

(1537) Zhou, K.-G.; McManus, D.; Prestat, E.; Zhong, X.; Shin, Y.; Zhang, H.-L.; Haigh, S. J.; Casiraghi, C. *J. Mater. Chem. A* **2016**, *4*, 11666. doi: 10.1039/c5ta09152g

(1538) Shen, J.; Liu, G.; Huang, K.; Chu, Z.; Jin, W.; Xu, N. *ACS Nano* **2016**, *10*, 3398. doi: 10.1021/acsnano.5b07304

(1539) Zhou, F.; Tien, H. N.; Xu, W. L.; Chen, J. T.; Liu, Q.; Hicks, E.; Fathizadeh, M.; Li, S.; Yu, M. *Nat. Commun.* **2017**, *8*, 2107. doi: 10.1038/s41467-017-02318-1

(1540) Ding, L.; Wei, Y.; Li, L.; Zhang, T.; Wang, H.; Xue, J.; Ding, L. X.; Wang, S.; Caro, J.; Gogotsi, Y. *Nat. Commun.* **2018,** *9*, 155. doi: 10.1038/s41467-017-02529-6

(1541) Dou, Y. B.; Pan, T.; Xu, S. M.; Yan, H.; Han, J. B.; Wei, M.; Evans, D. G.; Duan, X. *Angew. Chem. Int. Ed.* **2015,** *54*, 9673. doi: 10.1002/anie.201503797

(1542) Dou, Y.; Xu, S.; Liu, X.; Han, J.; Yan, H.; Wei, M.; Evans, D. G.; Duan, X. *Adv. Funct. Mater.* **2014,** *24*, 514. doi: 10.1002/adfm.201301775

(1543) Xu, X.; Wang, L.; Wang, J.; Yin, Q.; Dong, S.; Han, J.; Min, W. *Chem. Commun.* **2018,** *54*, 7778. doi: 10.1039/c8cc02900h

(1544) Wang, J.; Xu, X.; Jian, Z.; Chen, M.; Dong, S.; Han, J.; Min, W. *ACS Appl. Mater. Interfaces* **2018,** *10*, 28130. doi: 10.1021/acsami.8b09740

(1545) Xu, X.; Wang, J.; Zhou, A.; Dong, S.; Shi, K.; Li, B.; Han, J.; O'Hare, D. *Nat. Commun.* **2021,** *12*, 3069. doi: 10.1038/s41467-021-23121-z

(1546) Liang, L.; Liu, C.; Jiang, F.; Chen, Q.; Zhang, L.; Xue, H.; Jiang, H. L.; Qian, J.; Yuan, D.; Hong, M. *Nat. Commun.* **2017,** *8*, 1233. doi: 10.1038/s41467-017-01166-3

(1547) Huang, K.; Liu, G.; Shen, J.; Chu, Z.; Zhou, H.; Gu, X.; Jin, W.; Xu, N. *Adv. Funct. Mater.* **2015,** *25*, 5809. doi: 10.1002/adfm.201502205

(1548) Liu, G.; Shen, J.; Ji, Y.; Liu, Q.; Yang, J.; Liu, G.; Jin, W. *J. Mater. Chem. A* **2019,** *7*, 12095. doi: 10.1039/C9TA01507H

(1549) Xie, L. H.; Liu, X. M.; He, T.; Li, J. R. *Chem* **2018,** *4*, 1911. doi: 10.1016/j.chempr.2018.05.017

(1550) Zhu, L.; Meng, L.; Shi, J.; Li, J.; Zhang, X.; Feng, M. *J. Environ. Manag.* **2019,** *232*, 964. doi: 10.1016/j.jenvman.2018.12.004

(1551) Gannaz, B. T.; Antonio, M. R.; Chiarizia, R.; Hill, C. M.; Cote, G. R. *Dalton Trans.* **2006**, 4553. doi: 10.1039/b609492a

(1552) Seo, D. H.; Pineda, S.; Woo, Y. C.; Xie, M.; Murdock, A. T.; Ang, E.; Jiao, Y.; Park, M. J.; Lim, S. I.; Lawn, M. *Nat. Commun.* **2018,** *9*, 683. doi: 10.1038/s41467-018-02871-3

(1553) Werber, J. R.; Osuji, C. O.; Elimelech, M. *Nat. Rev. Mater.* **2016,** *1*, 16018. doi: 10.1038/natrevmats.2016.18

(1554) Huang, K.; Liu, G.; Lou, Y.; Dong, Z.; Shen, J.; Jin, W. *Angew. Chem. Int. Ed.* **2014,** *53*, 6929. doi: 10.1002/anie.201401061

(1555) Tan, H.; Zhang, X.; Li, Z.; Liang, Q.; Wu, J.; Yuan, Y.; Cao, S.; Chen, J.; Liu, J.; Qiu, H. *iScience* **2021,** *24*, 101920. doi: 10.1016/j.isci.2020.101920

(1556) Wu, J.; Li, Z.; Tan, H.; Du, S.; Liu, T.; Yuan, Y.; Liu, X.; Qiu, H. *Anal. Chem.* **2021,** *93*, 1732. doi: 10.1021/acs.analchem.0c04407

(1557) Megharaj, M.; Ramakrishnan, B.; Venkateswarlu, K.; Sethunathan, N.; Naidu, R. *Environ. Int.* **2011,** *37*, 1362. doi: 10.1016/j.envint.2011.06.003

(1558) Li, Q.; Chen, X.; Zhuang, J.; Chen, X. *Environ. Sci. Pollut. Res.* **2016,** *23*, 11533. doi: 10.1007/s11356-016-6255-7

(1559) Qi, Z.; Hou, L.; Zhu, D.; Ji, R.; Chen, W. *Environ. Sci. Technol.* **2014,** *48*, 10136. doi: 10.1021/es500833z

(1560) Zhao, H.; Fan, H.; Yang, G.; Lu, L.; Zheng, C.; Gao, X.; Wu, T. *Energy Fuels* **2018,** *32*, 5338. doi: 10.1021/acs.energyfuels.8b00099

(1561) Ai, K.; Ruan, C.; Shen, M.; Lu, L. *Adv. Funct. Mater.* **2016,** *26*, 5542. doi: 10.1002/adfm.201601338

(1562) Bunch, J. S.; Verbridge, S. S.; Alden, J. S.; van der Zande, A. M.; Parpia, J. M.; Craighead, H. G.; McEuen, P. L. *Nano Lett.* **2008,** *8*, 2458. doi: 10.1021/nl801457b

(1563) Leenaerts, O.; Partoens, B.; Peeters, F. M. *Appl. Phys. Lett.* **2008,** *93*, 193107. doi: 10.1063/1.3021413

(1564) Tsetseris, L.; Pantelides, S. T. *Carbon* **2014,** *67*, 58. doi: 10.1016/j.carbon.2013.09.055

(1565) Hu, S.; Lozada-Hidalgo, M.; Wang, F. C.; Mishchenko, A.; Schedin, F.; Nair, R. R.; Hill, E. W.; Boukhvalov, D. W.; Katsnelson, M. I.; Dryfe, R. A. W.; *et al. Nature* **2014,** *516*, 227. doi: 10.1038/nature14015

(1566) Pulizzi, F.; Bubnova, O.; Milana, S.; Schilter, D.; Abergel, D.; Moscatelli, A. *Nat. Nanotechnol.* **2019,** *14*, 914. doi: 10.1038/s41565-019-0552-5

(1567) Lozada-Hidalgo, M.; Hu, S.; Marshall, O.; Mishchenko, A.; Grigorenko, A. N.; Dryfe, R. A. W.; Radha, B.; Grigorieva, I. V.; Geim, A. K. *Science* **2016,** *351*, 68. doi: 10.1126/science.aac9726

(1568) Yoon, S. I.; Seo, D. J.; Kim, G.; Kim, M.; Jung, C. Y.; Yoon, Y. G.; Joo, S. H.; Kim, T. Y.; Shin, H. S. *ACS Nano* **2018,** *12*, 10764. doi: 10.1021/acsnano.8b06268

(1569) Lozada-Hidalgo, M.; Zhang, S.; Hu, S.; Esfandiar, A.; Grigorieva, I. V.; Geim, A. K. *Nat. Commun.* **2017,** *8*, 15215. doi: 10.1038/ncomms15215

(1570) He, L.; Wang, H.; Chen, L.; Wang, X.; Xie, H.; Jiang, C.; Li, C.; Elibol, K.; Meyer, J.; Watanabe, K.; *et al. Nat. Commun.* **2019,** *10*, 2815. doi: 10.1038/s41467-019-10660-9

(1571) Sun, P. Z.; Yang, Q.; Kuang, W. J.; Stebunov, Y. V.; Xiong, W. Q.; Yu, J.; Nair, R. R.; Katsnelson, M. I.; Yuan, S. J.; Grigorieva, I. V.; *et al. Nature* **2020,** *579*, 229. doi: 10.1038/s41586-020-2070-x

(1572) Shi, L.; Xu, A.; Chen, G.; Zhao, T. *J. Phys. Chem. Lett.* **2017,** *8*, 4354. doi: 10.1021/acs.jpclett.7b01999

(1573) Feng, Y.; Chen, J.; Fang, W.; Wang, E. G.; Michaelides, A.; Li, X. Z. *J. Phys. Chem. Lett.* **2017,** *8*, 6009. doi: 10.1021/acs.jpclett.7b02820

(1574) Poltavsky, I.; Zheng, L.; Mortazavi, M.; Tkatchenko, A. *J. Chem. Phys.* **2018,** *148*, 204707. doi: 10.1063/1.5024317

(1575) Mazzuca, J. W.; Haut, N. K. *J. Chem. Phys.* **2018,** *148*, 224301. doi: 10.1063/1.5027821

(1576) Zhu, D.; Liu, X.; Gao, Y.; Li, Y.; Wang, R.; Xu, Z.; Ji, G.; Jiang, S.; Zhao, B.; Yin, G.; *et al. ACS Nano* **2017,** *11*, 8970. doi: 10.1021/acsnano.7b03359

(1577) Jung, M.; Park, J.; Muhammad, R.; Kim, J. Y.; Grzimek, V.; Russina, M.; Moon, H. R.; Park, J. T.; Oh, H. *Adv. Mater.* **2021,** *33*, 2007412. doi: 10.1002/adma.202007412

(1578) Holmes, S. M.; Balakrishnan, P.; Kalangi, V. S.; Zhang, X.; Lozada-Hidalgo, M.; Ajayan, P. M.; Nair, R. R. *Adv. Energy Mater.* **2017,** *7*, 1601216. doi: 10.1002/aenm.201601216

(1579) Liu, J.; Yu, L.; Cai, X.; Khan, U.; Cai, Z.; Xi, J.; Liu, B.; Kang, F. *ACS Nano* **2019,** *13*, 2094. doi: 10.1021/acsnano.8b08680

(1580) Mogg, L.; Hao, G. P.; Zhang, S.; Bacaksiz, C.; Zou, Y. C.; Haigh, S. J.; Peeters, F. M.; Geim, A. K.; Lozada-Hidalgo, M. *Nat. Nanotechnol.* **2019,** *14*, 962. doi: 10.1038/s41565-019-0536-5

(1581) Bukola, S.; Liang, Y.; Korzeniewski, C.; Harris, J.; Creager, S. *J. Am. Chem. Soc.* **2018,** *140*, 1743. doi: 10.1021/jacs.7b10853

(1582) Mertens, S. F.; Hemmi, A.; Muff, S.; Groning, O.; De Feyter, S.; Osterwalder, J.; Greber, T. *Nature* **2016,** *534*, 676. doi: 10.1038/nature18275

(1583) Fu, Y.; Rudnev, A. V.; Wiberg, G. K. H.; Arenz, M. *Angew. Chem. Int. Ed.* **2017,** *56*, 12883. doi: 10.1002/anie.201705952

(1584) Lozada-Hidalgo, M.; Zhang, S.; Hu, S.; Kravets, V. G.; Rodriguez, F. J.; Berdyugin, A.; Grigorenko, A.; Geim, A. K. *Nat. Nanotechnol.* **2018,** *13*, 300. doi: 10.1038/s41565-017-0051-5

(1585) Fu, W.; Wang, Y.; Hu, S.; Zhou, X.; Long, X. *J. Phys. Chem. Lett.* **2019,** *10*, 4618. doi: 10.1021/acs.jpclett.9b01354

(1586) An, Y.; Oliveira, A. F.; Brumme, T.; Kuc, A.; Heine, T. *Adv. Mater.* **2020,** *32*, 2002442. doi: 10.1002/adma.202002442

(1587) Griffin, E.; Mogg, L.; Hao, G. P.; Kalon, G.; Bacaksiz, C.; Lopez-Polin, G.; Zhou, T. Y.; Guarochico, V.; Cai, J.; Neumann, C.; *et al. ACS Nano* **2020,** *14*, 7280. doi: 10.1021/acsnano.0c02496

(1588) Qian, X. T.; Chen, L.; Yin, L. C.; Liu, Z. B.; Pei, S. F.; Li, F.; Hou, G. J.; Chen, S. M.; Song, L.; Thebo, K. H.; *et al. Science* **2020,** *370*, 596. doi: 10.1126/science.abb9704

(1589) Jiang, B.; Sun, J.; Liu, Z. *Acta Phys. -Chim. Sin.* **2020,** *37*, 2007068. doi: 10.3866/PKU.WHXB202007068

(1590) Vlassiouk, I.; Polizos, G.; Cooper, R.; Ivanov, I.; Keum, J. K.; Paulauskas, F.; Datskos, P.; Smirnov, S. *ACS Appl. Mater. Interfaces* **2015,** *7*, 10702. doi: 10.1021/acsami.5b01367

(1591) Young, R. J.; Gong, L.; Kinloch, I. A.; Riaz, I.; Jalil, R.; Novoselov, K. S. *ACS Nano* **2011,** *5*, 3079. doi: 10.1021/nn2002079

(1592) Huang, Y.; Bazarnik, P.; Wan, D.; Luo, D.; Pereira, P. H. R.; Lewandowska, M.; Yao, J.; Hayden, B. E.; Langdon, T. G. *Acta Mater.* **2019,** *164*, 499. doi: 10.1016/j.actamat.2018.10.060

(1593) Stankovich, S.; Dikin, D. A.; Dommett, G. H. B.; Kohlhaas, K. M.; Zimney, E. J.; Stach, E. A.; Piner, R. D.; Nguyen, S. T.; Ruoff, R. S. *Nature* **2006,** *442*, 282. doi: 10.1038/nature04969

(1594) Guerra, V.; Wan, C.; McNally, T. *Prog. Mater. Sci.* **2019,** *100*, 170. doi: 10.1016/j.pmatsci.2018.10.002

(1595) Cai, Q.; Scullion, D.; Gan, W.; Falin, A.; Zhang, S.; Watanabe, K.; Taniguchi, T.; Chen, Y.; Santos, E. J. G.; Li, L. H. *Sci. Adv.* **2019,** *5*, eaav0129. doi: 10.1126/sciadv.aav0129

(1596) Liu, Z.; Gong, Y.; Zhou, W.; Ma, L.; Yu, J.; Idrobo, J. C.; Jung, J.; MacDonald, A. H.; Vajtai, R.; Lou, J.; *et al. Nat. Commun.* **2013,** *4*, 2541. doi: 10.1038/ncomms3541

(1597) Zhao, H.; Ding, J.; Yu, H. *New J. Chem.* **2018,** *42*, 14433. doi: 10.1039/C8NJ03113D

(1598) Liu, P.; Jin, Z.; Katsukis, G.; Drahushuk, L. W.; Shimizu, S.; Shih, C.-J.; Wetzel, E. D.; Taggart-Scarff, J. K.; Qing, B.; Van Vliet, K. J.; *et al. Science* **2016,** *353*, 364. doi: 10.1126/science.aaf4362

(1599) Papageorgiou, D. G.; Kinloch, I. A.; Young, R. J. *Prog. Mater. Sci.* **2017,** *90*, 75. doi: 10.1016/j.pmatsci.2017.07.004

(1600) Song, N.; Gao, Z.; Li, X. *Sci. Adv.* **2020,** *6*, eaba7016. doi: 10.1126/sciadv.aba7016

(1601) Cho, H.-B.; Nakayama, T.; Suematsu, H.; Suzuki, T.; Jiang, W.; Niihara, K.; Song, E.; Eom, N. S. A.; Kim, S.; Choa, Y.-H. *Compos. Sci. Technol.* **2016,** *129*, 205. doi: 10.1016/j.compscitech.2016.04.033

(1602) Lee, J.; Berman, D. *Carbon* **2018,** *126*, 225. doi: 10.1016/j.carbon.2017.10.022

(1603) Hsieh, Y.-P.; Hofmann, M.; Chang, K.-W.; Jhu, J. G.; Li, Y.-Y.; Chen, K. Y.; Yang, C. C.; Chang, W.-S.; Chen, L.-C. *ACS Nano* **2014,** *8*, 443. doi: 10.1021/nn404756q

(1604) Ding, J.-H.; Zhao, H.-R.; Zheng, Y.; Zhao, X.; Yu, H.-B. *Carbon* **2018,** *138*, 197. doi: 10.1016/j.carbon.2018.06.018

(1605) Shen, L.; Zhao, Y.; Wang, Y.; Song, R.; Yao, Q.; Chen, S.; Chai, Y. *J. Mater. Chem. A* **2016,** *4*, 5044. doi: 10.1039/C6TA01604A

(1606) Yu, J.; Ruengkajorn, K.; Crivoi, D.-G.; Chen, C.; Buffet, J.-C.; O'Hare, D. *Nat. Commun.* **2019,** *10*, 2398. doi: 10.1038/s41467-019-10362-2

(1607) Cohen-Tanugi, D.; Grossman, J. C. *Nano Lett.* **2014,** *14*, 6171. doi: 10.1021/nl502399y

(1608) Morelos-Gomez, A.; Cruz-Silva, R.; Muramatsu, H.; Ortiz-Medina, J.; Araki, T.; Fukuyo, T.; Tejima, S.; Takeuchi, K.; Hayashi, T.; Terrones, M.; *et al. Nat. Nanotechnol.* **2017,** *12*, 1083. doi: 10.1038/nnano.2017.160

(1609) Luo, C.; Zhou, L.; Chiou, K.; Huang, J. *Chem* **2018,** *4*, 784. doi: 10.1016/j.chempr.2018.02.021

(1610) Meyer, J. C.; Chuvilin, A.; Algara-Siller, G.; Biskupek, J.; Kaiser, U. *Nano Lett.* **2009,** *9*, 2683. doi: 10.1021/nl9011497

(1611) Smith, R. J.; King, P. J.; Lotya, M.; Wirtz, C.; Khan, U.; De, S.;

O'Neill, A.; Duesberg, G. S.; Grunlan, J. C.; Moriarty, G.; *et al. Adv. Mater.* **2011,** *23*, 3944. doi: 10.1002/adma.201102584

(1612) Tao, H.; Zhang, Y.; Gao, Y.; Sun, Z.; Yan, C.; Texter, J. *Phys. Chem. Chem. Phys.* **2017,** *19*, 921. doi: 10.1039/C6CP06813H

(1613) Liang, X.; Fu, Z.; Chou, S. Y. *Nano Lett.* **2007,** *7*, 3840. doi: 10.1021/nl072566s

(1614) Huo, C.; Yan, Z.; Song, X.; Zeng, H. *Sci. Bull.* **2015,** *60*, 1994. doi: 10.1007/s11434-015-0936-3

(1615) Narula, U.; Tan, C. M.; Lai, C. S. *Microelectron. Reliab.* **2016,** *61*, 87. doi: 10.1016/j.microrel.2016.01.005

(1616) Glavin, N. R.; Jespersen, M. L.; Check, M. H.; Hu, J.; Hilton, A. M.; Fisher, T. S.; Voevodin, A. A. *Thin Solid Films* **2014,** *572*, 245. doi: 10.1016/j.tsf.2014.07.059

(1617) Yang, Z.; Hao, J. *J. Mater. Chem. C* **2016,** *4*, 8859. doi: 10.1039/C6TC01602B

(1618) Zhang, Y.; Zhang, L.; Zhou, C. *Acc. Chem. Res.* **2013,** *46*, 2329. doi: 10.1021/ar300203n

(1619) Strupinski, W.; Grodecki, K.; Wysmolek, A.; Stepniewski, R.; Szkopek, T.; Gaskell, P. E.; Grüneis, A.; Haberer, D.; Bozek, R.; Krupka, J.; *et al. Nano Lett.* **2011,** *11*, 1786. doi: 10.1021/nl200390e

(1620) Sutter, P.; Lahiri, J.; Zahl, P.; Wang, B.; Sutter, E. *Nano Lett.* **2013,** *13*, 276. doi: 10.1021/nl304080y

(1621) Wofford, J. M.; Oliveira, M. H.; Schumann, T.; Jenichen, B.; Ramsteiner, M.; Jahn, U.; Fölsch, S.; Lopes, J. M. J.; Riechert, H. *New J. Phys.* **2014,** *16*, 093055. doi: 10.1088/1367-2630/16/9/093055

(1622) Nakhaie, S.; Wofford, J. M.; Schumann, T.; Jahn, U.; Ramsteiner, M.; Hanke, M.; Lopes, J. M. J.; Riechert, H. *Appl. Phys. Lett.* **2015,** *106*, 213108. doi: 10.1063/1.4921921

(1623) Chen, M.-W.; Ovchinnikov, D.; Lazar, S.; Pizzochero, M.; Whitwick, M. B.; Surrente, A.; Baranowski, M.; Sanchez, O. L.; Gillet, P.; Plochocka, P.; *et al. ACS Nano* **2017,** *11*, 6355. doi: 10.1021/acsnano.7b02726

(1624) Dong, J.; Zhang, L.; Ding, F. *Adv. Mater.* **2019,** *31*, 1801583. doi: 10.1002/adma.201801583

(1625) Zhang, L.; Dong, J.; Ding, F. *Chem. Rev.* **2021,** *121*, 6321. doi: 10.1021/acs.chemrev.0c01191

(1626) Woo, S.; Lee, S. A.; Mun, H.; Choi, Y. G.; Zhung, C. J.; Shin, S.; Lacotte, M.; David, A.; Prellier, W.; Park, T.; *et al. Nanoscale* **2018,** *10*, 4377. doi: 10.1039/C7NR09627E

(1627) Yan, T.; Huang, Y. C.; Hou, Y. C.; Chang, L. *J. Electrochem. Soc.* **2018,** *165*, D743. doi: 10.1149/2.0831814jes

(1628) Giovannetti, G.; Khomyakov, P. A.; Brocks, G.; Karpan, V. M.; van den Brink, J.; Kelly, P. J. *Phys. Rev. Lett.* **2008,** *101*, 026803. doi: 10.1103/PhysRevLett.101.026803

(1629) Gong, C.; Lee, G.; Shan, B.; Vogel, E. M.; Wallace, R. M.; Cho, K. *J. Appl. Phys.* **2010,** *108*, 123711. doi: 10.1063/1.3524232

(1630) Koitz, R.; Seitsonen, A. P.; Iannuzzi, M.; Hutter, J. *Nanoscale* **2013,** *5*, 5589. doi: 10.1039/c3nr00709j

(1631) Qi, Y.; Han, N.; Li, Y.; Zhang, Z.; Zhou, X.; Deng, B.; Li, Q.; Liu, M.; Zhao, J.; Liu, Z.; *et al. ACS Nano* **2017,** *11*, 1807. doi: 10.1021/acsnano.6b07773

(1632) Deng, S.; Gao, E.; Xu, Z.; Berry, V. *ACS Appl. Mater. Interfaces* **2017,** *9*, 7812. doi: 10.1021/acsami.6b16175

(1633) Zhang, X.; Xu, Z.; Hui, L.; Xin, J.; Ding, F. *J. Phys. Chem. Lett.* **2012,** *3*, 2822. doi: 10.1021/jz301029g

(1634) Dong, J.; Zhang, L.; Zhang, K.; Ding, F. *Nanoscale* **2018,** *10*, 6878. doi: 10.1039/C7NR06840A

(1635) Yu, Q.; Jauregui, L. A.; Wu, W.; Colby, R.; Tian, J.; Su, Z.; Cao, H.; Liu, Z.; Pandey, D.; Wei, D.; *et al. Nat. Mater.* **2011,** *10*, 443. doi: 10.1038/nmat3010

(1636) Ji, Y.; Calderon, B.; Han, Y.; Cueva, P.; Jungwirth, N. R.; Alsalman, H. A.; Hwang, J.; Fuchs, G. D.; Muller, D. A.; Spencer, M. G. *ACS Nano* **2017,** *11*, 12057. doi: 10.1021/acsnano.7b04841

(1637) Shi, J.; Zhang, X.; Ma, D.; Zhu, J.; Zhang, Y.; Guo, Z.; Yao, Y.; Ji, Q.; Song, X.; Zhang, Y.; *et al. ACS Nano* **2015,** *9*, 4017. doi: 10.1021/acsnano.5b00081

(1638) Wu, T.; Zhang, X.; Yuan, Q.; Xue, J.; Lu, G.; Liu, Z.; Wang, H.; Wang, H.; Ding, F.; Yu, Q.; *et al. Nat. Mater.* **2016,** *15*, 43. doi: 10.1038/nmat4477

(1639) Vlassiouk, I. V.; Stehle, Y.; Pudasaini, P. R.; Unocic, R. R.; Rack, P. D.; Baddorf, A. P.; Ivanov, I. N.; Lavrik, N. V.; List, F.; Gupta, N.; *et al. Nat. Mater.* **2018,** *17*, 318. doi: 10.1038/s41563-018-0019-3

(1640) Dong, J.; Zhang, L.; Dai, X.; Ding, F. *Nat. Commun.* **2020,** *11*, 5862. doi: 10.1038/s41467-020-19752-3

(1641) Song, X.; Gao, J.; Nie, Y.; Gao, T.; Sun, J.; Ma, D.; Li, Q.; Chen, Y.; Jin, C.; Bachmatiuk, A.; *et al. Nano Res.* **2015,** *8*, 3164. doi: 10.1007/s12274-015-0816-9

(1642) Murdock, A. T.; Koos, A.; Britton, T. B.; Houben, L.; Batten, T.; Zhang, T.; Wilkinson, A. J.; Dunin-Borkowski, R. E.; Lekka, C. E.; Grobert, N. *ACS Nano* **2013,** *7*, 1351. doi: 10.1021/nn3049297

(1643) Ogawa, Y.; Hu, B.; Orofeo, C. M.; Tsuji, M.; Ikeda, K.-I.; Mizuno, S.; Hibino, H.; Ago, H. *J. Phys. Chem. Lett.* **2012,** *3*, 219. doi: 10.1021/jz2015555

(1644) Uchida, Y.; Iwaizako, T.; Mizuno, S.; Tsuji, M.; Ago, H. *Phys. Chem. Chem. Phys.* **2017,** *19*, 8230. doi: 10.1039/C6CP08903H

(1645) Wood, G. E.; Marsden, A. J.; Mudd, J. J.; Walker, M.; Asensio, M.; Avila, J.; Chen, K.; Bell, G. R.; Wilson, N. R. *2D Mater.* **2015,** *2*, 025003. doi: 10.1088/2053-1583/2/2/025003

(1646) Tay, R. Y.; Park, H. J.; Ryu, G. H.; Tan, D.; Tsang, S. H.; Li, H.; Liu, W.; Teo, E. H. T.; Lee, Z.; Lifshitz, Y.; *et al. Nanoscale* **2016,**

8, 2434. doi: 10.1039/C5NR08036C

(1647) Gronborg, S. S.; Ulstrup, S.; Bianchi, M.; Dendzik, M.; Sanders, C. E.; Lauritsen, J. V.; Hofmann, P.; Miwa, J. A. *Langmuir* **2015**, *31*, 9700. doi: 10.1021/acs.langmuir.5b02533

(1648) Aljarb, A.; Cao, Z.; Tang, H.-L.; Huang, J.-K.; Li, M.; Hu, W.; Cavallo, L.; Li, L.-J. *ACS Nano* **2017**, *11*, 9215. doi: 10.1021/acsnano.7b04323

(1649) Dumcenco, D.; Ovchinnikov, D.; Marinov, K.; Lazić, P.; Gibertini, M.; Marzari, N.; Sanchez, O. L.; Kung, Y.-C.; Krasnozhon, D.; Chen, M.-W.; *et al. ACS Nano* **2015**, *9*, 4611. doi: 10.1021/acsnano.5b01281

(1650) Ruzmetov, D.; Zhang, K.; Stan, G.; Kalanyan, B.; Bhimanapati, G. R.; Eichfeld, S. M.; Burke, R. A.; Shah, P. B.; O'Regan, T. P.; Crowne, F. J.; *et al. ACS Nano* **2016**, *10*, 3580. doi: 10.1021/acsnano.5b08008

(1651) Lee, J. S.; Choi, S. H.; Yun, S. J.; Kim, Y. I.; Boandoh, S.; Park, J.-H.; Shin, B. G.; Ko, H.; Lee, S. H.; Kim, Y.-M.; *et al. Science* **2018**, *362*, 817. doi: 10.1126/science.aau2132

(1652) Wang, S.; Dearle, A. E.; Maruyama, M.; Ogawa, Y.; Okada, S.; Hibino, H.; Taniyasu, Y. *Adv. Mater.* **2019**, *31*, 1900880. doi: 10.1002/adma.201900880

(1653) Li, J.; Li, Y.; Yin, J.; Ren, X.; Liu, X.; Jin, C.; Guo, W. *Small* **2016**, *12*, 3645. doi: 10.1002/smll.201600681

(1654) Chen, L.; Liu, B.; Ge, M.; Ma, Y.; Abbas, A. N.; Zhou, C. *ACS Nano* **2015**, *9*, 8368. doi: 10.1021/acsnano.5b03043

(1655) Zhang, L.; Peng, P.; Ding, F. *Adv. Funct. Mater.* **2021**, *31*, 2100503. doi: 10.1002/adfm.202100503

(1656) Gao, J.; Yip, J.; Zhao, J.; Yakobson, B. I.; Ding, F. *J. Am. Chem. Soc.* **2011**, *133*, 5009. doi: 10.1021/ja110927p

(1657) Gao, J.; Yuan, Q.; Hu, H.; Zhao, J.; Ding, F. *J. Phys. Chem. C* **2011**, *115*, 17695. doi: 10.1021/jp2051454

(1658) Griep, M. H.; Sandoz-Rosado, E.; Tumlin, T. M.; Wetzel, E. *Nano Lett.* **2016**, *16*, 1657. doi: 10.1021/acs.nanolett.5b04531

(1659) Felter, J.; Raths, M.; Franke, M.; Kumpf, C. *2D Mater.* **2019**, *6*, 045005. doi: 10.1088/2053-1583/ab2926

(1660) Yuan, Q.; Yakobson, B. I.; Ding, F. *J. Phys. Chem. Lett.* **2014**, *5*, 3093. doi: 10.1021/jz5015899

(1661) Scaparro, A. M.; Miseikis, V.; Coletti, C.; Notargiacomo, A.; Pea, M.; De Seta, M.; Di Gaspare, L. *ACS Appl. Mater. Interfaces* **2016**, *8*, 33083. doi: 10.1021/acsami.6b11701

(1662) Wang, G.; Zhang, M.; Zhu, Y.; Ding, G.; Jiang, D.; Guo, Q.; Liu, S.; Xie, X.; Chu, P. K.; Di, Z.; *et al. Sci. Rep.* **2013**, *3*, 2465. doi: 10.1038/srep02465

(1663) Lee, J.-H.; Lee, E. K.; Joo, W.-J.; Jang, Y.; Kim, B.-S.; Lim, J. Y.; Choi, S.-H.; Ahn, S. J.; Ahn, J. R.; Park, M.-H.; *et al. Science* **2014**, *344*, 286. doi: 10.1126/science.1252268

(1664) Li, P.; Wei, W.; Zhang, M.; Mei, Y.; Chu, P. K.; Xie, X.; Yuan, Q.; Di, Z. *Nano Today* **2020**, *34*, 100908. doi: 10.1016/j.nantod.2020.100908

(1665) Zhao, R.; Zhao, X.; Liu, Z.; Ding, F.; Liu, Z. *Nanoscale* **2017**, *9*, 3561. doi: 10.1039/C6NR09368J

(1666) Ni, B.; Huang, M.; Chen, Z.; Chen, Y.; Hsu, C. H.; Li, Y.; Pochan, D.; Zhang, W. B.; Cheng, S. Z.; Dong, X. H. *J. Am. Chem. Soc.* **2015**, *137*, 1392. doi: 10.1021/ja511694a

(1667) Bets, K. V.; Gupta, N.; Yakobson, B. I. *Nano Lett.* **2019**, *19*, 2027. doi: 10.1021/acs.nanolett.9b00136

(1668) Choi, S. H.; Kim, H.-J.; Song, B.; Kim, Y. I.; Han, G.; Nguyen, H. T. T.; Ko, H.; Boandoh, S.; Choi, J. H.; Oh, C. S.; *et al. Adv. Mater.* **2021**, *33*, 2006601. doi: 10.1002/adma.202006601

(1669) Duerloo, K.-A. N.; Li, Y.; Reed, E. J. *Nat. Commun.* **2014**, *5*, 4214. doi: 10.1038/ncomms5214

(1670) Liu, L.; Wu, J.; Wu, L.; Ye, M.; Liu, X.; Wang, Q.; Hou, S.; Lu, P.; Sun, L.; Zheng, J.; *et al. Nat. Mater.* **2018**, *17*, 1108. doi: 10.1038/s41563-018-0187-1

(1671) Zhao, W.; Ding, F. *Nanoscale* **2017**, *9*, 2301. doi: 10.1039/C6NR08628D

(1672) Shao, P.; Ding, L.-P.; Ding, F. *Chem. Mater.* **2021**, *33*, 3241. doi: 10.1021/acs.chemmater.1c00116

(1673) Zhan, Y.; Liu, Z.; Najmaei, S.; Ajayan, P. M.; Lou, J. *Small* **2012**, *8*, 966. doi: 10.1002/smll.201102654

(1674) Wang, X.; Feng, H.; Wu, Y.; Jiao, L. *J. Am. Chem. Soc.* **2013**, *135*, 5304. doi: 10.1021/ja4013485

(1675) Lin, Y.-C.; Zhang, W.; Huang, J.-K.; Liu, K.-K.; Lee, Y.-H.; Liang, C.-T.; Chu, C.-W.; Li, L.-J. *Nanoscale* **2012**, *4*, 6637. doi: 10.1039/C2NR31833D

(1676) Liu, K.-K.; Zhang, W.; Lee, Y.-H.; Lin, Y.-C.; Chang, M.-T.; Su, C.-Y.; Chang, C.-S.; Li, H.; Shi, Y.; Zhang, H.; *et al. Nano Lett.* **2012**, *12*, 1538. doi: 10.1021/nl2043612

(1677) Hong, S.; Krishnamoorthy, A.; Rajak, P.; Tiwari, S.; Misawa, M.; Shimojo, F.; Kalia, R. K.; Nakano, A.; Vashishta, P. *Nano Lett.* **2017**, *17*, 4866. doi: 10.1021/acs.nanolett.7b01727

(1678) Geng, D.; Wu, B.; Guo, Y.; Huang, L.; Xue, Y.; Chen, J.; Yu, G.; Jiang, L.; Hu, W.; Liu, Y. *Proc. Natl. Acad. Sci. U. S. A.* **2012**, *109*, 7992. doi: 10.1073/pnas.1200339109

(1679) Dong, J.; Geng, D.; Liu, F.; Ding, F. *Angew. Chem. Int. Ed.* **2019**, *58*, 7723. doi: 10.1002/anie.201902441

(1680) Guo, W.; Wu, B.; Li, Y.; Wang, L.; Chen, J.; Chen, B.; Zhang, Z.; Peng, L.; Wang, S.; Liu, Y. *ACS Nano* **2015**, *9*, 5792. doi: 10.1021/acsnano.5b01827

(1681) Chen, J.; Wen, Y.; Guo, Y.; Wu, B.; Huang, L.; Xue, Y.; Geng, D.; Wang, D.; Yu, G.; Liu, Y. *J. Am. Chem. Soc.* **2011**, *133*, 17548. doi: 10.1021/ja2063633

(1682) Chen, J.; Guo, Y.; Jiang, L.; Xu, Z.; Huang, L.; Xue, Y.; Geng, D.; Wu, B.; Hu, W.; Yu, G.; *et al. Adv. Mater.* **2014**, *26*, 1348. doi: 10.1002/adma.201304872

(1683) Wang, H.; Xue, X.; Jiang, Q.; Wang, Y.; Geng, D.; Cai, L.; Wang, L.; Xu, Z.; Yu, G. *J. Am. Chem. Soc.* **2019**, *141*, 11004. doi: 10.1021/jacs.9b05705

(1684) Xie, Y.; Cheng, T.; Liu, C.; Chen, K.; Cheng, Y.; Chen, Z.; Qiu, L.; Cui, G.; Yu, Y.; Cui, L.; *et al. ACS Nano* **2019**, *13*, 10272. doi: 10.1021/acsnano.9b03596

(1685) Chen, Z.; Chang, H. l.; Cheng, T.; Wei, T.; Wang, R.; Yang, S.; Dou, Z.; Liu, B.; Zhang, S.; Xie, Y.; *et al. Adv. Funct. Mater.* **2020,** *30*, 2001483. doi: 10.1002/adfm.202001483

(1686) Cheng, T.; Liu, Z.; Liu, Z.; Ding, F. *ACS Nano* **2021**, *15*, 7399. doi: 10.1021/acsnano.1c00776

(1687) Rutter, G. M.; Guisinger, N. P.; Crain, J. N.; First, P. N.; Stroscio, J. A. *Phys. Rev. B* **2010**, *81*, 245408. doi: 10.1103/PhysRevB.81.245408

(1688) Tang, S.; Wang, H.; Zhang, Y.; Li, A.; Xie, H.; Liu, X.; Liu, L.; Li, T.; Huang, F.; Xie, X.; *et al. Sci. Rep.* **2013**, *3*, 2666. doi: 10.1038/srep02666

(1689) Chen, L.; Wang, H.; Tang, S.; He, L.; Wang, H. S.; Wang, X.; Xie, H.; Wu, T.; Xia, H.; Li, T.; *et al. Nanoscale* **2017,** *9*, 11475. doi: 10.1039/c7nr02578e

(1690) Rohaizad, N.; Mayorga-Martinez, C. C.; Fojtů, M.; Latiff, N. M.; Pumera, M. *Chem. Soc. Rev.* **2021,** *50*, 619. doi: 10.1039/D0CS00150C

(1691) Qi, L.; Ruan, S.; Zeng, Y.-J. *Adv. Mater.* **2021,** *33*, 2005098. doi: 10.1002/adma.202005098

(1692) Kanahashi, K.; Pu, J.; Takenobu, T. *Adv. Energy Mater.* **2020**, *10*, 1902842. doi: 10.1002/aenm.201902842

(1693) Geim, A. K.; Grigorieva, I. V. *Nature* **2013**, *499*, 419. doi: 10.1038/nature12385

(1694) Island, J. O.; Steele, G. A.; Zant, H. S. J. v. d.; Castellanos-Gomez, A. *2D Mater.* **2015**, *2*, 011002. doi: 10.1088/2053-1583/2/1/011002

(1695) Ho, P. H.; Chang, Y. R.; Chu, Y. C.; Li, M. K.; Tsai, C. A.; Wang, W. H.; Ho, C. H.; Chen, C. W.; Chiu, P. W. *ACS Nano* **2017**, *11*, 7362. doi: 10.1021/acsnano.7b03531

(1696) Bergeron, A.; Ibrahim, J.; Leonelli, R.; Francoeur, S. *Appl. Phys. Lett.* **2017**, *110*, 241901. doi: 10.1063/1.4986189

(1697) Chae, S. H.; Jin, Y.; Kim, T. S.; Chung, D. S.; Na, H.; Nam, H.; Kim, H.; Perello, D. J.; Jeong, H. Y.; Ly, T. H.; *et al. ACS Nano* **2016,** *10*, 1309. doi: 10.1021/acsnano.5b06680

(1698) Fei, H. L.; Dong, J. C.; Feng, Y. X.; Allen, C. S.; Wan, C. Z.; Volosskiy, B.; Li, M. F.; Zhao, Z. P.; Wang, Y. L.; Sun, H. T.; *et al. Nat. Catal.* **2018**, *1*, 63. doi: 10.1038/s41929-017-0008-y

(1699) Li, Q.; Zhou, Q. H.; Shi, L.; Chen, Q.; Wang, J. L. *J. Mater. Chem.*

(1700) Zhou, Q.; Chen, Q.; Tong, Y.; Wang, J. *Angew. Chem. Int. Ed.* **2016**, *55*, 11437. doi: 10.1002/anie.201605168

(1701) Favron, A.; Gaufres, E.; Fossard, F.; Phaneuf-L'Heureux, A. L.; Tang, N. Y.; Levesque, P. L.; Loiseau, A.; Leonelli, R.; Francoeur, S.; Martel, R. *Nat. Mater.* **2015,** *14*, 826. doi: 10.1038/nmat4299

(1702) Hu, Z.; Li, Q.; Lei, B.; Zhou, Q.; Xiang, D.; Lyu, Z.; Hu, F.; Wang, J.; Ren, Y.; Guo, R.; *et al. Angew. Chem. Int. Ed.* **2017**, *56*, 9131. doi: 10.1002/anie.201705012

(1703) Shi, L.; Zhou, Q.; Zhao, Y.; Ouyang, Y.; Ling, C.; Li, Q.; Wang, J. *J. Phys. Chem. Lett.* **2017**, *8*, 4368. doi: 10.1021/acs.jpclett.7b02059

(1704) Zhou, Q.; Li, Q.; Yuan, S.; Chen, Q.; Wang, J. *Phys. Chem. Chem. Phys.* **2017,** *19*, 29232. doi: 10.1039/C7CP05730J

(1705) Zhao, Y.; Zhou, Q.; Li, Q.; Yao, X.; Wang, J. *Adv. Mater.* **2017,** *29*, 1603990. doi: 10.1002/adma.201603990

(1706) Li, Q.; Zhou, Q.; Niu, X.; Zhao, Y.; Chen, Q.; Wang, J. *J. Phys. Chem. Lett.* **2016,** *7*, 4540. doi: 10.1021/acs.jpclett.6b02192

(1707) Li, Q.; Shi, L.; Wu, R.; Lin, C.; Bai, X.; Ouyang, Y.; Baraiya, B. A.; Jha, P. K.; Wang, J. *Phys. Chem. Chem. Phys.* **2019,** *21*, 17010. doi: 10.1039/C9CP02985K

(1708) Illarionov, Y. Y.; Waltl, M.; Rzepa, G.; Kim, J.-S.; Kim, S.; Dodabalapur, A.; Akinwande, D.; Grasser, T. *ACS Nano* **2016**, *10*, 9543. doi: 10.1021/acsnano.6b04814

(1709) Constantinescu, G. C.; Hine, N. D. *Nano Lett.* **2016**, *16*, 2586. doi: 10.1021/acs.nanolett.6b00154

(1710) Wood, J. D.; Wells, S. A.; Jariwala, D.; Chen, K. S.; Cho, E.; Sangwan, V. K.; Liu, X.; Lauhon, L. J.; Marks, T. J.; Hersam, M. C. *Nano Lett.* **2014**, *14*, 6964. doi: 10.1021/nl5032293

(1711) Bensong, W.; Qionghua, Z.; Junying, Z.; Yue, W.; Bingchao, Y.; Weiming, L.; Baoshun, Z.; Zhongming, Z.; Qian, C.; Jinlan, W.; *et al. Adv. Electron. Mater.* **2018,** *4*, 1700455. doi: 10.1002/aelm.201700455

(1712) Yang, B.; Wan, B.; Zhou, Q.; Wang, Y.; Hu, W.; Lv, W.; Chen, Q.; Zeng, Z.; Wen, F.; Xiang, J.; *et al. Adv. Mater.* **2016,** *28*, 9408. doi: 10.1002/adma.201603723

(1713) Ryder, C. R.; Wood, J. D.; Wells, S. A.; Yang, Y.; Jariwala, D.; Marks, T. J.; Schatz, G. C.; Hersam, M. C. *Nat. Chem.* **2016**, *8*, 597. doi: 10.1038/nchem.2505

(1714) Liu, Y.; Xiao, C.; Li, Z.; Xie, Y. *Adv. Energy Mater.* **2016,** *6*, 1600436. doi: 10.1002/aenm.201600436

(1715) Turiansky, M. E.; Alkauskas, A.; Van de Walle, C. G. *Nat. Mater.* **2020,** *19*, 487. doi: 10.1038/s41563-020-0668-x

(1716) Zou, X.; Yakobson, B. I. *Acc. Chem. Res.* **2015**, *48*, 73. doi: 10.1021/ar500302q

(1717) Jiang, J.; Ling, C.; Xu, T.; Wang, W.; Niu, X.; Zafar, A.; Yan, Z.;

A **2019,** *7*, 4291. doi: 10.1039/c8ta10306b

Wang, X.; You, Y.; Sun, L.; *et al. Adv. Mater.* **2018**, *30*, 1804332. doi: 10.1002/adma.201804332

(1718) Chen, X.; Berner, N. C.; Backes, C.; Duesberg, G. S.; McDonald, A. R. *Angew. Chem. Int. Ed.* **2016,** *55*, 5803. doi: 10.1002/anie.201510219

(1719) Wiegenstein, C. G.; Schulz, K. H. *J. Phys. Chem. B* **1999**, *103*, 6913. doi: 10.1021/jp990896y

(1720) Sim, D. M.; Kim, M.; Yim, S.; Choi, M.-J.; Choi, J.; Yoo, S.; Jung, Y. S. *ACS Nano* **2015,** *9*, 12115. doi: 10.1021/acsnano.5b05173

(1721) Chou, S. S.; De, M.; Kim, J.; Byun, S.; Dykstra, C.; Yu, J.; Huang, J.; Dravid, V. P. *J. Am. Chem. Soc.* **2013,** *135*, 4584. doi: 10.1021/ja310929s

(1722) Li, Q.; Zhao, Y.; Ling, C.; Yuan, S.; Chen, Q.; Wang, J. *Angew. Chem. Int. Ed.* **2017,** *56*, 10501. doi: 10.1002/anie.201706038

(1723) Nan, H.; Wang, Z.; Wang, W.; Liang, Z.; Lu, Y.; Chen, Q.; He, D.; Tan, P.; Miao, F.; Wang, X.; *et al. ACS Nano* **2014,** *8*, 5738. doi: 10.1021/nn500532f

(1724) Hong, J.; Jin, C.; Yuan, J.; Zhang, Z. *Adv. Mater.* **2017,** *29*, 1606434. doi: 10.1002/adma.201606434

(1725) Ouyang, Y.; Ling, C.; Chen, Q.; Wang, Z.; Shi, L.; Wang, J. *Chem. Mater.* **2016,** *28*, 4390. doi: 10.1021/acs.chemmater.6b01395

(1726) Wang, Y.; Mao, J.; Meng, X.; Yu, L.; Deng, D.; Bao, X. *Chem. Rev.* **2019,** *119*, 1806. doi: 10.1021/acs.chemrev.8b00501

(1727) Fu, Z. M.; Yang, B. W.; Wu, R. Q. *Phys. Rev. Lett.* **2020,** *125*, 156001. doi: 10.1103/Physrevlett.125.156001

(1728) Fu, Z. Z.; Ling, C. Y.; Wang, J. L. *J. Mater. Chem. A* **2020,** *8*, 7801. doi: 10.1039/d0ta01047b

(1729) Liu, X.; Jiao, Y.; Zheng, Y.; Jaroniec, M.; Qiao, S. Z. *J. Am. Chem. Soc.* **2019,** *141*, 9664. doi: 10.1021/jacs.9b03811

(1730) Ling, C.; Shi, L.; Ouyang, Y.; Zeng, X. C.; Wang, J. *Nano Lett.* **2017,** *17*, 5133. doi: 10.1021/acs.nanolett.7b02518

(1731) Zhang, J. C.; Yang, H. B.; Liu, B. *Adv. Energy Mater.* **2021,** *11*, 2002473. doi: 10.1002/Aenm.202002473

(1732) Xu, H.; Cheng, D.; Cao, D.; Zeng, X. C. *Nat. Catal.* **2018,** *1*, 339. doi: 10.1038/s41929-018-0063-z

(1733) Ling, C.; Niu, X.; Li, Q.; Du, A.; Wang, J. *J. Am. Chem. Soc.* **2018,** *140*, 14161. doi: 10.1021/jacs.8b07472

(1734) Choi, W. I.; Wood, B. C.; Schwegler, E.; Ogitsu, T. *Adv. Energy Mater.* **2015,** *5*, 1501423. doi: 10.1002/aenm.201501423

(1735) Back, S.; Lim, J.; Kim, N.-Y.; Kim, Y.-H.; Jung, Y. *Chem. Sci.* **2017,** *8*, 1090. doi: 10.1039/c6sc03911a

(1736) Ling, C.; Ouyang, Y.; Li, Q.; Bai, X.; Mao, X.; Du, A.; Wang, J. *Small Methods* **2019,** *3*, 1800376. doi: 10.1002/smtd.201800376

(1737) Fei, H.; Dong, J.; Arellano-Jimenez, M. J.; Ye, G.; Dong Kim, N.; Samuel, E. L.; Peng, Z.; Zhu, Z.; Qin, F.; Bao, J.; *et al. Nat. Commun.* **2015,** *6*, 8668. doi: 10.1038/ncomms9668

(1738) Cheng, N. C.; Stambula, S.; Wang, D.; Banis, M. N.; Liu, J.; Riese, A.; Xiao, B. W.; Li, R. Y.; Sham, T. K.; Liu, L. M.; *et al. Nat. Commun.* **2016,** *7*, 13638. doi: 10.1038/Ncomms13638

(1739) Lu, S. H.; Zhou, Q. H.; Ouyang, Y. X.; Guo, Y. L.; Li, Q.; Wang, J. L. *Nat. Commun.* **2018,** *9*, 3405. doi: 10.1038/S41467-018-05761-W

(1740) Wu, L. P.; Guo, T.; Li, T. *J. Mater. Chem. A* **2020,** *8*, 19290. doi: 10.1039/d0ta06207c

(1741) Lin, S. R.; Xu, H. X.; Wang, Y. K.; Zeng, X. C.; Chen, Z. F. *J. Mater. Chem. A* **2020,** *8*, 5663. doi: 10.1039/c9ta13404b

(1742) Zhou, Q. H.; Lu, S. H.; Wu, Y. L.; Wang, J. L. *J. Phys. Chem. Lett.* **2020,** *11*, 3920. doi: 10.1021/acs.jpclett.0c00665

(1743) Sethulakshmi, N.; Mishra, A.; Ajayan, P. M.; Kawazoe, Y.; Roy, A. K.; Singh, A. K.; Tiwary, C. S. *Mater. Today* **2019,** *27*, 107. doi: 10.1016/j.mattod.2019.03.015

(1744) Miao, N. H.; Sun, Z. M. *Wiley Interdiscip. Rev. Comput. Mol. Sci.* **2021**, e1545. doi: 10.1002/wcms.1545

(1745) Jiang, P. H.; Wang, C.; Chen, D. C.; Zhong, Z. C.; Yuan, Z.; Lu, Z. Y.; Ji, W. *Phys. Rev. B* **2019,** *99*, 144401. doi: 10.1103/PhysRevB.99.144401

(1746) Liu, N.; Zhou, S.; Zhao, J. *Phys. Rev. Mater.* **2020,** *4*, 094003. doi: 10.1103/PhysRevMaterials.4.094003

(1747) Soriano, D.; Cardoso, C.; Fernández-Rossier, J. *Solid State Commun.* **2019,** *299*, 113662. doi: 10.1016/j.ssc.2019.113662

(1748) Sivadas, N.; Okamoto, S.; Xu, X.; Fennie, C. J.; Xiao, D. *Nano Lett.* **2018,** *18*, 7658. doi: 10.1021/acs.nanolett.8b03321

(1749) Shang, J.; Tang, X.; Tan, X.; Du, A. J.; Liao, T.; Smith, S. C.; Gu, Y. T.; Li, C.; Kou, L. Z. *ACS Appl. Nano Mater.* **2020,** *3*, 1282. doi: 10.1021/acsanm.9b02055

(1750) Jang, S. W.; Jeong, M. Y.; Yoon, H.; Ryee, S.; Han, M. J. *Phys. Rev. Mater.* **2019,** *3*, 031001. doi: 10.1103/PhysRevMaterials.3.031001

(1751) Esters, M.; Hennig, R. G.; Johnson, D. C. *Phys. Rev. B* **2017,** *96*, 235147. doi: 10.1103/PhysRevB.96.235147

(1752) Zhuang, H. L.; Hennig, R. G. *Phys. Rev. B* **2016,** *93*, 054429. doi: 10.1103/PhysRevB.93.054429

(1753) Sivadas, N.; Daniels, M. W.; Swendsen, R. H.; Okamoto, S.; Xiao, D. *Phys. Rev. B* **2015,** *91*, 235425. doi: 10.1103/PhysRevB.91.235425

(1754) Lado, J. L.; Fernandez-Rossier, J. *2D Mater.* **2017,** *4*, 035002. doi: 10.1088/2053-1583/aa75ed

(1755) Lu, X. B.; Fei, R. X.; Yang, L. *Phys. Rev. B* **2019,** *100*, 205409. doi: 10.1103/PhysRevB.100.205409

(1756) Xiang, H. J.; Wei, S. H.; Whangbo, M. H. *Phys. Rev. Lett.* **2008,** *100*, 167207. doi: 10.1103/PhysRevLett.100.167207

(1757) Zheng, S.; Huang, C. X.; Yu, T.; Xu, M. L.; Zhang, S. T.; Xu, H. Y.; Liu, Y. C.; Kan, E. J.; Wang, Y. C.; Yang, G. C. *J. Phys. Chem. Lett.* **2019,** *10*, 2733. doi: 10.1021/acs.jpclett.9b00970

(1758) Zhao, K.; Wang, Q. *Appl. Surf. Sci.* **2020**, *505*, 144620.
doi: 10.1016/j.apsusc.2019.144620

(1759) Wang, C.; Zhou, X. Y.; Zhou, L. W.; Pan, Y. H.; Lu, Z. Y.; Wan, X.
G.; Wang, X. Q.; Ji, W. *Phys. Rev. B* **2020**, *102*, 020402.
doi: 10.1103/PhysRevB.102.020402

(1760) Wang, C.; Zhou, X. Y.; Pan, Y. H.; Qiao, J. S.; Kong, X. H.; Kaun,
C. C.; Ji, W. *Phys. Rev. B* **2018**, *97*, 245409.
doi: 10.1103/PhysRevB.97.245409

(1761) Tong, Q. J.; Liu, F.; Xiao, J.; Yao, W. *Nano Lett.* **2018**, *18*, 7194.
doi: 10.1021/acs.nanolett.8b03315

(1762) Tong, Q. J.; Chen, M. X.; Yao, W. *Phys. Rev. Appl.* **2019**, *12*,
024031. doi: 10.1103/PhysRevApplied.12.024031

(1763) Zhang, Z. Y.; Ni, X. J.; Huang, H. Q.; Hu, L.; Liu, F. *Phys. Rev. B*
2019, *99*, 115441. doi: 0.1103/PhysRevB.99.115441

(1764) Zhao, Y. H.; Zhang, J. J.; Yuan, S. J.; Chen, Z. F. *Adv. Funct. Mater.*
2019, *29*, 1901420. doi: 10.1002/adfm.201901420

(1765) Lu, Y.; Fei, R. X.; Lu, X. B.; Zhu, L. H.; Wang, L.; Yang, L. *ACS
Appl. Mater. Interfaces* **2020**, *12*, 6243.
doi: 10.1021/acsami.9b19320

(1766) Zollner, K.; Faria, J. P. E.; Fabian, J. *Phys. Rev. B* **2019**, *100*,
085128. doi: 10.1103/PhysRevB.100.085128

(1767) Zhang, H. S.; Yang, W. J.; Ning, Y. H.; Xu, X. H. *Phys. Rev. B*
2020, *101*, 205404. doi: 10.1103/PhysRevB.101.205404

(1768) Chen, S. B.; Huang, C. X.; Sun, H. S.; Ding, J. F.; Jena, P.; Kan, E.
J. *J. Phys. Chem. C* **2019**, *123*, 17987.
doi: 10.1021/acs.jpcc.9b04631

(1769) Zhou, Y. G.; Wang, Z. G.; Yang, P.; Zu, X. T.; Yang, L.; Sun, X.;
Gao, F. *ACS Nano* **2012**, *6*, 9727. doi: 10.1021/nn303198w

(1770) Webster, L.; Yan, J. A. *Phys. Rev. B* **2018**, *98*, 144411.
doi: 10.1103/PhysRevB.98.144411

(1771) Xu, R. Z.; Zou, X. L. *J. Phys. Chem. Lett.* **2020**, *11*, 3152.
doi: 10.1021/acs.jpclett.0c00567

(1772) Morell, E. S.; Leon, A.; Miwa, R. H.; Vargas, P. *2D Mater.* **2019**, *6*,
025020. doi: 10.1088/2053-1583/ab04fb

(1773) Wang, H.; Fan, F.; Zhu, S.; Wu, H. *EPL* **2016**, *114*, 47001.
doi: 10.1209/0295-5075/114/47001

(1774) Wang, Y. P.; Chen, X. Y.; Long, M. Q. *Appl. Phys. Lett.* **2020**, *116*,
092404. doi: 10.1063/1.5144032

(1775) Lei, C.; Chittari, B. L.; Nomura, K.; Banerjee, N.; Jung, J.;
MacDonald, A. H. *Nano Lett.* **2021**, *21*, 1948.
doi: 10.1021/acs.nanolett.0c04242

(1776) Tang, C.; Zhang, L.; Sanvito, S.; Du, A. J. *J. Mater. Chem. A* **2020**,
8, 7034. doi: 10.1039/d0tc01541e

(1777) Jiang, P. H.; Li, L.; Liao, Z. L.; Zhao, Y. X.; Zhong, Z. C. *Nano
Lett.* **2018**, *18*, 3844. doi: 10.1021/acs.nanolett.8b01125

(1778) Guo, Y.; Zhang, Y. H.; Zhou, Z. B.; Zhang, X. W.; Wang, B.; Yuan,
S. J.; Dong, S.; Wang, J. L. *Mater. Horiz.* **2021**, *8*, 1323.
doi: 10.1039/d0mh01480j

(1779) He, J. J.; Li, S.; Bandyopadhyay, A.; Frauenheim, T. *Nano Lett.*
2021, *21*, 3237. doi: 10.1021/acs.nanolett.1c00520

(1780) Otrokov, M. M.; Klimovskikh, I. I.; Bentmann, H.; Estyunin, D.;
Zeugner, A.; Aliev, Z. S.; Gass, S.; Wolter, A. U. B.; Koroleva, A.
V.; Shikin, A. M.; *et al. Nature* **2019**, *576*, 416.
doi: 10.1038/s41586-019-1840-9

(1781) Kabiraj, A.; Kumar, M.; Mahapatra, S. *npj Comput. Mater.* **2020**, *6*,
1. doi: 10.1038/s41524-020-0300-2

(1782) Torelli, D.; Moustafa, H.; Jacobsen, K. W.; Olsen, T. *npj Comput.
Mater.* **2020**, *6*, 1. doi: 10.1038/s41524-020-00428-x

(1783) Zhu, Y.; Kong, X. H.; Rhone, T. D.; Guo, H. *Phys. Rev. Mater.*
2018, *2*, 081001. doi: 10.1103/PhysRevMaterials.2.081001

(1784) Liu, H.; Sun, J. T.; Liu, M.; Meng, S. *J. Phys. Chem. Lett.* **2018**, *9*,
6709. doi: 10.1021/acs.jpclett.8b02783

(1785) Lu, S. H.; Zhou, Q. H.; Guo, Y. L.; Zhang, Y. H.; Wu, Y. L.; Wang,
J. L. *Adv. Mater.* **2020**, *32*, 2002658. doi: 10.1002/adma.202002658

(1786) Frey, N. C.; Horton, M. K.; Munro, J. M.; Griffin, S. M.; Persson,
K. A.; Shenoy, V. B. *Sci. Adv.* **2020**, *6*, eabd1076.
doi: 10.1126/sciadv.abd1076